Can stem cells cure an ailing fetus? *p. 284*

Will that reaction work for my molecule? *p. 294*

Migrating cells fix tears after a tight squeeze *pp. 295, 353, & 359*

Science

$15
15 APRIL 2016
sciencemag.org

AAAS

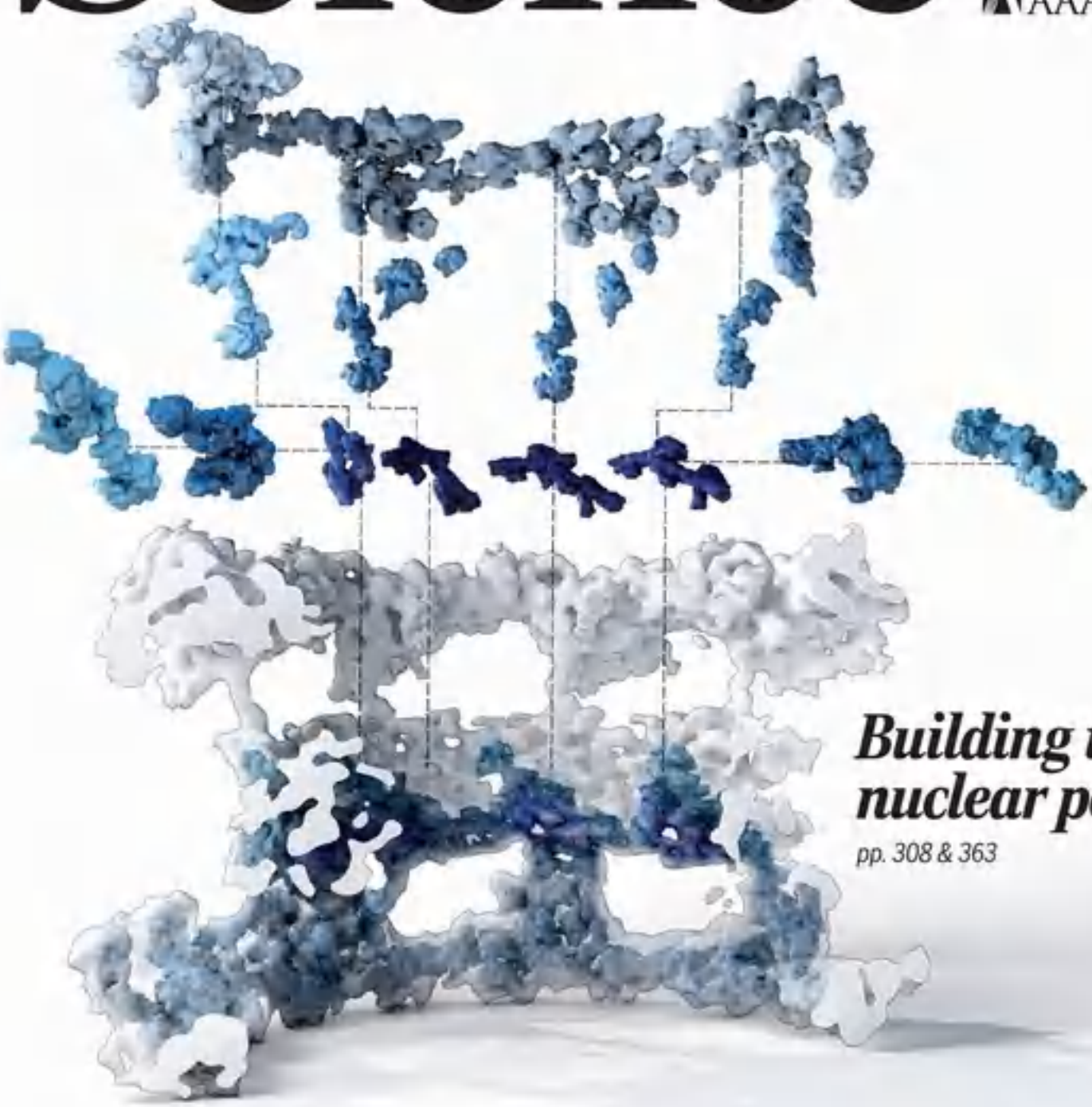

Building the nuclear pore

pp. 308 & 363

CONTENTS

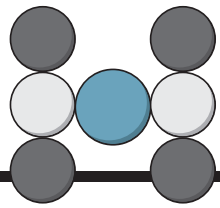

296 & 318
Long-lived atomic magnets

15 APRIL 2016 • VOLUME 352 • ISSUE 6283

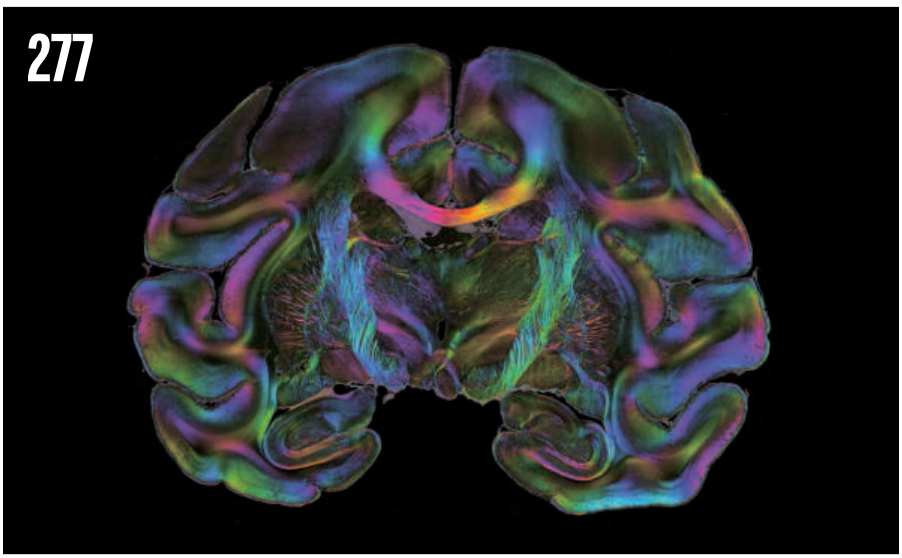

IMAGE: KATRIN AMUNTS, MARKUS AXER, ROGER WOODS AND KARL ZILLES, RESEARCH CENTRE JUELICH, GERMANY (K.A, MA, KZ) AND UCLA SCHOOL OF MEDICINE, USA(RW).

NEWS

IN BRIEF

274 News at a glance

IN DEPTH

277 INTERNATIONAL BRAIN PROJECTS PROPOSED
Meeting attendees debate big science ideas, including need for global data hub *By E. Underwood*

278 ARCTIC NATIONS EYE FISHING BAN
As ice recedes in central Arctic Ocean, officials meet to discuss catch moratorium until stocks can be studied *By E. Kintisch*

279 DUTCH PUSH FOR A QUANTUM LEAP IN OPEN ACCESS
E.U. urged to free all papers by 2020
By M. Enserink

280 MEGAPROJECT ASKS: WHAT DROVE THE VIKINGS?
Researchers suggest that the nature of pre-Viking society spurred a drive for slaves *By A. Lawler*

281 OBSOLESCENCE LOOMS FOR BALLOON DATA
United States falls behind Europe in adopting modern data format
By E. Hand

283 RURAL CHINA IS NO COUNTRY FOR OLD PEOPLE
Erosion of families sparks an epidemic of suicides among the elderly
By K. McLaughlin

FEATURE

284 THE SAVIOR CELLS?
After a painstaking journey, researchers are preparing to test stem cell therapy in ailing fetuses
By J. Couzin-Frankel

286 Gene therapy gets a high-stakes test
By J. Couzin-Frankel

INSIGHTS

PERSPECTIVES

288 TACKLING MINE WASTES
Global collaboration is needed to mitigate the environmental impacts of mine wastes *By K. Hudson-Edwards*

290 UNDERGROUND NETWORKING
Fungal networks transfer carbon between forest trees *By M. G. A. van der Heijden*
▸ REPORT P. 342

292 OPPORTUNITIES FOR ADVANCES IN CLIMATE CHANGE ECONOMICS
Target carbon's costs, policy designs, and developing countries *By M. Burke* et al.

294 THE STRAIGHT DOPE ON THE SCOPE OF CHEMICAL REACTIONS
Complementary strategies are needed for the analysis and reporting of synthetic methods *By T. Gensch and F. Glorius*

295 WHEN CELLS PUSH THE ENVELOPE
Nuclear integrity is temporarily compromised to accommodate cell migration *By B. Burke*
▸ REPORTS PP. 353 & 359

296 TOWARD SINGLE-ATOM MEMORY
Single holmium atoms can be used as a stable magnetic memory
By A. A. Khajetoorians and A. J. Heinrich
▸ REPORT P. 318

298 A SCAFFOLD IMMUNE MICROENVIRONMENT
Local immune cells create conditions that support tissue regeneration
By S. F. Badylak
▸ REPORT P. 366

BOOKS *ET AL.*

299 FINDING TIME
By H. Boushey; reviewed by J. Gornick

300 BLACK HOLE BLUES
By J. Levin; reviewed by A. Cho

LETTERS

301 FINANCIAL COMPLEXITY: REGULATING REGULATION
By J. B. Ruhl

301 FINANCIAL COMPLEXITY: ACCOUNTING FOR FRAUD
By D. Witzling

302 RESPONSE
By S. Battiston et al.

DEPARTMENTS

273 EDITORIAL
The UK: Thinking big or small?
By Dame Anne Glover

378 WORKING LIFE
Orchestrating a powerful group
By Jeffrey J. McDonnell

Science Staff 270
New Products 371
Science Careers 372

Published by AAAS

CONTENTS

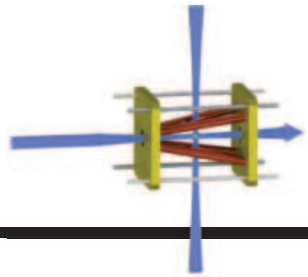

325
The smallest engine

15 APRIL 2016 • VOLUME 352 • ISSUE 6283

RESEARCH

IN BRIEF

304 From *Science* and other journals

REVIEW

307 PHOTOVOLTAICS
Photovoltaic materials: Present efficiencies and future challenges
A. Polman et al.
REVIEW SUMMARY; FOR FULL TEXT: dx.doi.org/10.1126/science.aad4424

RESEARCH ARTICLES

308 STRUCTURAL BIOLOGY
Architecture of the symmetric core of the nuclear pore *D. H. Lin* et al.
RESEARCH ARTICLE SUMMARY; FOR FULL TEXT: dx.doi.org/10.1126/science.aaf1015
▸ REPORT P. 363

309 STRUCTURAL BIOLOGY
Crystallographic capture of a radical *S*-adenosylmethionine enzyme in the act of modifying tRNA *E. L. Schwalm* et al.

312 INTERSTELLAR DUST
Flux and composition of interstellar dust at Saturn from Cassini's Cosmic Dust Analyzer *N. Altobelli* et al.

REPORTS

318 MOLECULAR MAGNETISM
Magnetic remanence in single atoms
F. Donati et al.
▸ PERSPECTIVE P. 296

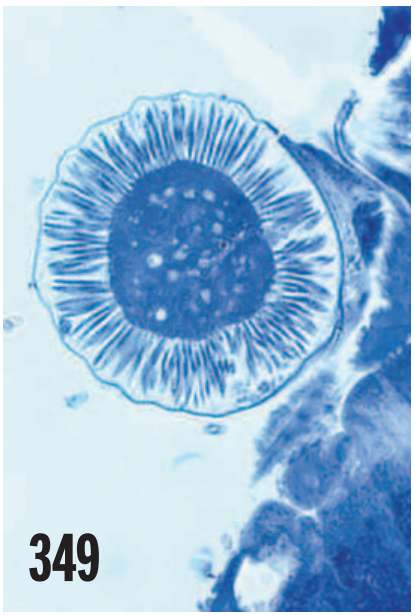

321 HYDROGEN BONDING
Nuclear quantum effects of hydrogen bonds probed by tip-enhanced inelastic electron tunneling *J. Guo* et al.

325 THERMODYNAMICS
A single-atom heat engine
J. Roßnagel et al.

329 ORGANOMETALLICS
Pre-transmetalation intermediates in the Suzuki-Miyaura reaction revealed: The missing link *A. A. Thomas and S. E. Denmark*

333 ELECTROCHEMISTRY
Homogeneously dispersed multimetal oxygen-evolving catalysts *B. Zhang* et al.

338 CORAL REEFS
Climate change disables coral bleaching protection on the Great Barrier Reef
T. D. Ainsworth et al.

342 FOREST ECOLOGY
Belowground carbon trade among tall trees in a temperate forest *T. Klein* et al.
▸ PERSPECTIVE P. 290

345 ZIKA VIRUS OUTBREAK
Zika virus in the Americas: Early epidemiological and genetic findings
N. R. Faria et al.
▸ PODCAST

349 MALARIA DRUGS
Parasites resistant to the antimalarial atovaquone fail to transmit by mosquitoes *C. D. Goodman* et al.

CELL BIOLOGY

353 Nuclear envelope rupture and repair during cancer cell migration
C. M. Denais et al.

359 ESCRT III repairs nuclear envelope ruptures during cell migration to limit DNA damage and cell death
M. Raab et al.
▸ PERSPECTIVE P. 295

363 STRUCTURAL BIOLOGY
Molecular architecture of the inner ring scaffold of the human nuclear pore complex *J. Kosinski* et al.
▸ RESEARCH ARTICLE P. 308

366 BIOMATERIALS
Developing a pro-regenerative biomaterial scaffold microenvironment requires T helper 2 cells *K. Sadtler* et al.
▸ PERSPECTIVE P. 298

ON THE COVER

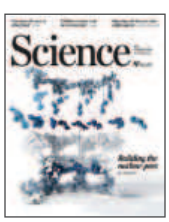

The nuclear pore complex is the sole gateway for macromolecules to enter or exit the nucleus and is one of the largest assemblies in eukaryotic cells. This illustration depicts the integrative approach used to determine structures of the individual protein components (blue), their connectivity (dashed lines), and their arrangement in the intact assembly (inside the transparent nuclear envelope). See pages 308 and 363. *Illustration: Valerie Altounian/* Science*; Crystallography data: André Hoelz; Electron density map: Martin Beck*

PHOTO: (BOTTOM RIGHT) PETER MUMBY

SCIENCE (ISSN 0036-8075) is published weekly on Friday, except the last week in December, by the American Association for the Advancement of Science, 1200 New York Avenue, NW, Washington, DC 20005. Periodicals mail postage (publication No. 484460) paid at Washington, DC, and additional mailing offices. Copyright © 2016 by the American Association for the Advancement of Science. The title SCIENCE is a registered trademark of the AAAS. Domestic individual membership and subscription (51 issues): $165 ($74 allocated to subscription). Domestic institutional subscription (51 issues): $1522; Foreign postage extra: Mexico, Caribbean (surface mail) $55; other countries (air assist delivery) $89. First class, airmail, student, and emeritus rates on request. Canadian rates with GST available upon request, GST #1254 88122. Publications Mail Agreement Number 1069624. **Printed in the U.S.A.**
Change of address: Allow 4 weeks, giving old and new addresses and 8-digit account number. **Postmaster:** Send change of address to AAAS, P.O. Box 96178, Washington, DC 20090–6178. **Single-copy sales:** $15.00 current issue, $20.00 back issue prepaid includes surface postage; bulk rates on request. **Authorization to photocopy** material for internal or personal use under circumstances not falling within the fair use provisions of the Copyright Act is granted by AAAS to libraries and other users registered with the Copyright Clearance Center (CCC) Transactional Reporting Service, provided that $35.00 per article is paid directly to CCC, 222 Rosewood Drive, Danvers, MA 01923. The identification code for *Science* is 0036-8075. *Science* is indexed in the *Reader's Guide to Periodical Literature* and in several specialized indexes.

Published by AAAS

Science

AAAS

1200 New York Avenue, NW, Washington, DC 20005
Bateman House, 82-88 Hills Road, Cambridge, UK CB2 1LQ

Editor-in-Chief Marcia McNutt

Executive Editor Monica M. Bradford **News Editor** Tim Appenzeller

Managing Editor, Research Journals Katrina L. Kelner

Deputy Editors Lisa D. Chong, Andrew M. Sugden(UK), Valda J. Vinson, Jake S. Yeston

Research and Insights

DEPUTY EDITOR, EMERITUS Barbara R. Jasny **SR. EDITORS** Caroline Ash(UK), Gilbert J. Chin, Julia Fahrenkamp-Uppenbrink(UK), Pamela J. Hines, Stella M. Hurtley(UK), Paula A. Kiberstis, Marc S. Lavine(Canada), Kristen L. Mueller, Ian S. Osborne(UK), Beverly A. Purnell, L. Bryan Ray, Guy Riddihough, H. Jesse Smith, Jelena Stajic, Peter Stern(UK), Phillip D. Szuromi, Sacha Vignieri, Brad Wible, Nicholas S. Wigginton, Laura M. Zahn **ASSOCIATE EDITORS** Brent Grocholski, Keith T. Smith **ASSOCIATE BOOK REVIEW EDITOR** Valerie B. Thompson **ASSOCIATE LETTERS EDITOR** Jennifer Sills **CHIEF CONTENT PRODUCTION EDITOR** Cara Tate **SR. CONTENT PRODUCTION EDITORS** Harry Jach, Lauren Kmec **CONTENT PRODUCTION EDITORS** Jeffrey E. Cook, Chris Filiatreau, Cynthia Howe, Barbara P. Ordway, Catherine Wolner **SR. EDITORIAL COORDINATORS** Carolyn Kyle, Beverly Shields **EDITORIAL COORDINATORS** Aneera Dobbins, Joi S. Granger, Lisa Johnson, Anita Wynn **PUBLICATIONS ASSISTANTS** Jeffrey Hearn, Dona Mathieu, Le-Toya Mayne Flood, Shannon McMahon, Scott Miller, Caitlyn Phillips, Jerry Richardson, Alice Whaley(UK), Brian White **EXECUTIVE ASSISTANT** Anna Bashkirova **ADMINISTRATIVE SUPPORT** Janet Clements(UK), Lizanne Newton(UK), Maryrose Madrid

News

NEWS MANAGING EDITOR John Travis **INTERNATIONAL EDITOR** Richard Stone **DEPUTY NEWS EDITORS** Robert Coontz, Elizabeth Culotta, David Grimm, David Malakoff, Leslie Roberts **CONTRIBUING EDITOR** Martin Enserink(Europe) **SR. CORRESPONDENTS** Daniel Clery(UK), Jeffrey Mervis, Elizabeth Pennisi **NEWS WRITERS** Adrian Cho, Jon Cohen, Jennifer Couzin-Frankel, Carolyn Gramling, Eric Hand, Jocelyn Kaiser, Catherine Matacic, Kelly Servick, Robert F. Service, Erik Stokstad(Cambridge, UK), Emily Underwood **INTERNS** Patrick Monahan **CONTRIBUTING CORRESPONDENTS** John Bohannon, Warren Cornwall, Ann Gibbons, Mara Hvistendahl, Sam Kean, Eli Kintisch, Kai Kupferschmidt(Berlin), Andrew Lawler, Christina Larson(Beijing), Mitch Leslie, Charles C. Mann, Eliot Marshall, Virginia Morell, Dennis Normile(Shanghai), Heather Pringle, Tania Rabesandratana(London), Gretchen Vogel(Berlin), Lizzie Wade(Mexico City) **CAREERS** Donisha Adams, Rachel Bernstein(Editor) **COPY EDITORS** Julia Cole, Dorie Chevlen, Jennifer Levin (Chief) **ADMINISTRATIVE SUPPORT** Jessica Adams

Executive Publisher Rush D. Holt

Interim Publisher Bill Moran **Chief Digital Media Officer** Rob Covey

BUSINESS OPERATIONS AND PORTFOLIO MANAGEMENT DIRECTOR Sarah Whalen **PRODUCT DEVELOPMENT DIRECTOR** Will Schweitzer **PRODUCT DEVELOPMENT ASSOCIATE** Hal Moore **BUSINESS SYSTEMS AND FINANCIAL ANALYSIS DIRECTOR** Randy Yi **MANAGER OF FULFILLMENT SYSTEMS** Neal Hawkins **SYSTEMS ANALYST** Nicole Mehmedovich **ASSISTANT DIRECTOR, BUSINESS OPERATIONS** Eric Knott **MANAGER, BUSINESS OPERATIONS** Jessica Tierney **SENIOR BUSINESS ANALYST** Cory Lipman **BUSINESS ANALYSTS** Sandy Kim, Meron Kebede **FINANCIAL ANALYST** Robert Clark **DIRECTOR, COPYRIGHTS LICENSING SPECIAL PROJECTS** Emilie David **PERMISSIONS ASSOCIATE** Elizabeth Sandler **RIGHTS, CONTRACTS, AND LICENSING ASSOCIATE** Lili Kiser

MARKETING DIRECTOR Elise Swinehart **ASSOCIATE MARKETING DIRECTOR** Christina Schlecht **MARKETING MANAGER** Elizabeth Sattler **MARKETING ASSOCIATE** Steven Goodman **CREATIVE DIRECTOR** Scott Rodgerson **SENIOR ART ASSOCIATES** Seil Lee, Paula Fry **ART ASSOCIATE** Kim Huynh **PROGRAM DIRECTOR, AAAS MEMBER CENTRAL** Peggy Mihelich **FULFILLMENT SYSTEMS AND OPERATIONS** membership@aaas.org **MANAGER, MEMBER SERVICES** Pat Butler **SPECIALISTS** Terrance Morrison, Latasha Russell **MANAGER, DATA ENTRY** Mickie Napoleoni **DATA ENTRY SPECIALISTS** Brenden Aquilino, Fiona Giblin

PUBLISHER RELATIONS MANAGER Catherine Holland **PUBLISHER RELATIONS, EASTERN REGION** Keith Layson **PUBLISHER RELATIONS, WESTERN REGION** Ryan Rexroth **SALES RESEARCH COORDINATOR** Aiesha Marshall **MANAGER, SITE LICENSE OPERATIONS** Iquo Edim **SENIOR OPERATIONS ANALYST** Lana Guz **FULFILLMENT ANALYST** Judy Lillibridge **ASSOCIATE DIRECTOR, MARKETING** Christina Schlecht **MARKETING ASSOCIATE** Isa Sesay-Bah

WEB TECHNOLOGIES SR. DEVELOPER Chris Coleman **DEVELOPERS** Dan Berger, Jimmy Marks, Ryan Jensen **SR. PROJECT MANAGER** Trista Smith **PROJECT MANAGER** Nick Fletcher

DIGITAL MEDIA DIRECTOR OF ANALYTICS Enrique Gonzales **DIGITAL REPORTING ANALYST** Eric Hossinger **SR. WEB PRODUCER** Sarah Crespi **WEB PRODUCER** Alison Crawford **VIDEO PRODUCER** Nguyen Nguyen **SOCIAL MEDIA PRODUCER** Brice Russ

DIRECTOR OF OPERATIONS PRINT AND ONLINE Lizabeth Harman **DIGITAL/PRINT STRATEGY MANAGER** Jason Hillman **QUALITY TECHNICAL MANAGER** Marcus Spiegler **PROJECT ACCOUNT MANAGER** Tara Kelly **DIGITAL PRODUCTION MANAGER** Lisa Stanford **ASSISTANT MANAGER DIGITAL/PRINT** Rebecca Doshi **SENIOR CONTENT SPECIALISTS** Steve Forrester, Antoinette Hodal, Lori Murphy, Anthony Rosen **CONTENT SPECIALISTS** Jacob Hedrick, Kimberley Oster

DESIGN DIRECTOR Beth Rakouskas **DESIGN EDITOR** Marcy Atarod **SENIOR DESIGNER** Garvin Grullón **DESIGNER** Chrystal Smith **GRAPHICS MANAGING EDITOR** Alberto Cuadra **SENIOR SCIENTIFIC ILLUSTRATORS** Chris Bickel, Katharine Sutliff **SCIENTIFIC ILLUSTRATOR** Valerie Altounian **SENIOR ART ASSOCIATES** Holly Bishop, Nathalie Cary, Preston Huey **PHOTOGRAPHY MANAGING EDITOR** William Douthitt **PHOTO EDITORS** Leslie Blizard, Christy Steele

DIRECTOR, GLOBAL COLLABORATION, CUSTOM PUBLICATIONS, ADVERTISING Bill Moran **EDITOR, CUSTOM PUBLISHING** Sean Sanders: 202-326-6430 **ADVERTISING MARKETING MANAGER** Justin Sawyers: 202-326-7061 science_advertising@aaas.org **ADVERTISING SUPPORT MANAGER** Karen Foote: 202-326-6740 **ADVERTISING PRODUCTION OPERATIONS MANAGER** Deborah Tompkins **SR. PRODUCTION SPECIALIST/GRAPHIC DESIGNER** Amy Hardcastle **SR. TRAFFIC ASSOCIATE** Christine Hall **SALES COORDINATOR** Shirley Young **ASSOCIATE DIRECTOR, COLLABORATION, CUSTOM PUBLICATIONS/CHINA/TAIWAN/KOREA/SINGAPORE** Ruolei Wu: +86-186 0082 9345, rwu@aaas.org **COLLABORATION/CUSTOM PUBLICATIONS/JAPAN** Adarsh Sandhu + 81532-81-5142 asandhu@aaas.org **EAST COAST/E. CANADA** Laurie Faraday: 508-747-9395, FAX 617-507-8189 **WEST COAST/W. CANADA** Lynne Stickrod: 415-931-9782, FAX 415-520-6940 **MIDWEST** Jeffrey Dembksi: 847-498-4520 x3005, Steven Loerch: 847-498-4520 x3006 **UK EUROPE/ASIA** Roger Goncalves: TEL/FAX +41 43 243 1358 **JAPAN** Katsuyoshi Fukamizu(Tokyo): +81-3-3219-5777 kfukamizu@aaas.org **CHINA/TAIWAN** Ruolei Wu: +86-186 0082 9345, rwu@aaas.org

WORLDWIDE ASSOCIATE DIRECTOR OF SCIENCE CAREERS Tracy Holmes: +44 (0) 1223 326525, FAX +44 (0) 1223 326532 tholmes@science-int. co.uk **CLASSIFIED** advertise@sciencecareers.org **U.S. SALES** Tina Burks: 202-326-6577, Nancy Toema: 202-326-6578 **EUROPE/ROW SALES** Sarah Lelarge **SALES ASSISTANT** Kelly Grace **JAPAN** Hiroyuki Mashiki(Kyoto): +81-75-823-1109 hmashiki@aaas.org **CHINA/TAIWAN** Ruolei Wu: +86-186 0082 9345 rwu@aaas.org **MARKETING MANAGER** Allison Pritchard **MARKETING ASSOCIATE** Aimee Aponte

AAAS BOARD OF DIRECTORS, CHAIR Geraldine L. Richmond **PRESIDENT** Barbara A. Schaal **PRESIDENT-ELECT** Susan Hockfield **TREASURER** David Evans Shaw **CHIEF EXECUTIVE OFFICER** Rush D. Holt **BOARD** Cynthia M. Beall, May R. Berenbaum, Carlos J. Bustamante, Stephen P.A. Fodor, Claire M. Fraser, Michael S. Gazzaniga, Laura H. Greene, Elizabeth Loftus, Mercedes Pascual

SUBSCRIPTION SERVICES For change of address, missing issues, new orders and renewals, and payment questions: 866-434-AAAS (2227) or 202-326-6417, FAX 202-842-1065. Mailing addresses: AAAS, P.O. Box 96178, Washington, DC 20090-6178 or AAAS Member Services, 1200 New York Avenue, NW, Washington, DC 20005

INSTITUTIONAL SITE LICENSES 202-326-6730 **REPRINTS:** Author Inquiries 800-635-7181 **COMMERCIAL INQUIRIES** 803-359-4578 **PERMISSIONS** 202-326-6765, permissions@aaas.org **AAAS Member Services** 202-326-6417 or http://membercentral.aaas.org/discounts

Science serves as a forum for discussion of important issues related to the advancement of science by publishing material on which a consensus has been reached as well as including the presentation of minority of conflicting points of view. Accordingly, all articles published in *Science*—including editorials, news and comment, and book reviews—are signed and reflect the individual views of the authors and not official points of view adopted by AAAS or the institutions with which the authors are affiliated.

INFORMATION FOR AUTHORS See pages 624 and 625 of the 5 February 2016 issue or access www.sciencemag.org/authors/science-information-authors

SENIOR EDITORIAL BOARD

Gary King, *Harvard University,* **Susan M. Rosenberg,** *Baylor College of Medicine,* **Ali Shilatifard,** *Northwestern University Feinberg School of Medicine*

BOARD OF REVIEWING EDITORS (Statistics board members indicated with **($)**)

Adriano Aguzzi, *U. Hospital Zürich*
Takuzo Aida, *U. of Tokyo*
Leslie Aiello, *Wenner-Gren Foundation*
Judith Allen, *U. of Edinburgh*
Sonia Altizer, *U. of Georgia*
Sebastian Amigorena, *Institut Curie*
Kathryn Anderson, *Memorial Sloan-Kettering Cancer Center*
Meinrat O. Andreae, *Max-Planck Inst. Mainz*
Paola Arlotta, *Harvard U.*
Johan Auwerx, *EPFL*
David Awschalom, *U. of Chicago*
Clare Baker, *University of Cambridge*
Nenad Ban, *ETH Zurich*
Jordi Bascompte, *University of Zurich*
Ray H. Baughman, *U. of Texas, Dallas*
David Baum, *U. of Wisconsin*
Carlo Beenakker, *Leiden U.*
Kamran Behnia, *ESPCI-ParisTech*
Yasmine Belkaid, *NIAID, NIH*
Philip Benfey, *Duke U.*
May Berenbaum, *U. of Illinois*
Gabriele Bergers, *U. of California, San Francisco*
Bradley Bernstein, *Massachusettes General Hospital*
Peer Bork, *EMBL*
Bernard Bourdon, *Ecole Normale Supérieure de Lyon*
Chris Bowler, *École Normale Supérieure*
Ian Boyd, *U. of St. Andrews*
Emily Brodsky, *U. of California, Santa Cruz*
Ron Brookmeyer, *U. of California Los Angeles* **($)**
Christian Büchel, *U. Hamburg-Eppendorf*
Joseph A. Burns, *Cornell U.*
Carter Tribley Butts, *U. of California, Irvine*
Gyorgy Buzsaki, *New York U. School of Medicine*
Blanche Capel, *Duke U.*
Mats Carlsson, *U. of Oslo*
Ib Chorkendorff, *U. of Denmark*
David Clapham, *Children's Hospital Boston*
Joel Cohen, *Rockefeller U., Columbia U.*
James J. Collins, *MIT*
Robert Cook-Deegan, *Duke U.*
Lisa Coussens, *Oregon Health & Science U.*
Alan Cowman, *Walter & Eliza Hall Inst.*
Robert H. Crabtree, *Yale U.*
Roberta Croce, *Vrije Universiteit*
Janet Currie, *Princeton U.*
Jeff L. Dangl, *U. of North Carolina*
Tom Daniel, *U. of Washington*
Frans de Waal, *Emory U.*
Stanislas Dehaene, *Collège de France*
Robert Desimone, *MIT*
Claude Desplan, *New York U.*
Dennis Discher, *U. of Pennsylvania*
Gerald W. Dorn II, *Washington U. School of Medicine*
Jennifer A. Doudna, *U. of California, Berkeley*
Bruce Dunn, *U. of California, Los Angeles*
William Dunphy, *Caltech*
Christopher Dye, *WHO*
Todd Ehlers, *U. of Tuebingen*
David Ehrhardt, *Carnegie Inst. of Washington*
Tim Elston, *U. of North Carolina at Chapel Hill*
Gerhard Ertl, *Fritz-Haber-Institut, Berlin*
Barry Everitt, *U. of Cambridge*
Ernst Fehr, *U. of Zurich*
Anne C. Ferguson-Smith, *U. of Cambridge*
Michael Feuer, *The George Washington U.*
Toren Finkel, *NHLBI, NIH*
Kate Fitzgerald, *U. of Massachusetts*
Peter Fratzl, *Max-Planck Inst.*
Elaine Fuchs, *Rockefeller U.*
Daniel Geschwind, *UCLA*
Karl-Heinz Glassmeier, *TU Braunschweig*
Ramon Gonzalez, *Rice U.*
Julia R. Greer, *Caltech*
Elizabeth Grove, *U. of Chicago*
Nicolas Gruber, *ETH Zurich*
Kip Guy, *St. Jude's Children's Research Hospital*
Taekjip Ha, *U. of Illinois at Urbana-Champaign*
Wolf-Dietrich Hardt, *ETH Zurich*
Christian Haass, *Ludwig Maximilians U.*
Sharon Hammes-Schiffer, *U. of Illinois at Urbana–Champaign*
Michael Hasselmo, *Boston U.*
Martin Heimann, *Max-Planck Inst. Jena*
Yka Helariutta, *U. of Cambridge*
James A. Hendler, *Rensselaer Polytechnic Inst.*
Janet G. Hering, *Swiss Fed. Inst. of Aquatic Science & Technology*
Kai-Uwe Hinrichs, *U. of Bremen*
David Hodell, *U. of Cambridge*
Lora Hooper, *UT Southwestern Medical Ctr. at Dallas*
Tamas Horvath, *Yale University*
Raymond Huey, *U. of Washington*
Fred Hughson, *Princeton U.*
Auke Ijspeert, *EPFL Lausanne*
Stephen Jackson, *USGS and U. of Arizona*
Steven Jacobsen, *U. of California, Los Angeles*
Kai Johnsson, *EPFL Lausanne*
Peter Jonas, *Inst. of Science & Technology (IST) Austria*
Matt Kaeberlein, *U. of Washington*
William Kaelin Jr., *Dana-Farber Cancer Inst.*
Daniel Kahne, *Harvard U.*
Daniel Kammen, *U. of California, Berkeley*
Abby Kavner, *U. of California, Los Angeles*
Masashi Kawasaki, *U. of Tokyo*
V. Narry Kim, *Seoul National U.*
Joel Kingsolver, *U. of North Carolina at Chapel Hill*
Robert Kingston, *Harvard Medical School*
Etienne Koechlin, *Ecole Normale Suprieure*
Alexander Kolodkin, *Johns Hopkins U.*
Thomas Langer, *U. of Cologne*
Mitchell A. Lazar, *U. of Pennsylvania*
David Lazer, *Harvard U.*
Thomas Lecuit, *IBDM*
Virginia Lee, *U. of Pennsylvania*
Stanley Lemon, *U. of North Carolina at Chapel Hill*
Ottoline Leyser, *Cambridge U.*
Wendell Lim, *U.C. San Francisco*
Marcia C. Linn, *U. of California, Berkeley*
Jianguo Liu, *Michigan State U.*
Luis Liz-Marzan, *CIC biomaGUNE*
Jonathan Losos, *Harvard U.*
Ke Lu, *Chinese Acad. of Sciences*
Christian Lüscher, *U. of Geneva*
Laura Machesky, *CRUK Beatson Inst. for Cancer Research*
Anne Magurran, *U. of St. Andrews*
Oscar Marin, *CSIC & U. Miguel Hernández*
Charles Marshall, *U. of California, Berkeley*
C. Robertson McClung, *Dartmouth College*
Graham Medley, *U. of Warwick*
Tom Misteli, *NCI*
Yasushi Miyashita, *U. of Tokyo*
Mary Ann Moran, *U. of Georgia*
Richard Morris, *U. of Edinburgh*
Alison Motsinger-Reif, *NC State U.* **($)**
Thomas Murray, *The Hastings Center*
Daniel Neumark, *U. of California, Berkeley*
Kitty Nijmeijer, *U. of Twente*
Pär Nordlund, *Karolinska Inst.*
Helga Nowotny, *European Research Advisory Board*
Ben Olken, *MIT*
Joe Orenstein, *U. of California Berkeley & Lawrence Berkeley National Lab*
Harry Orr, *U. of Minnesota*
Pilar Ossorio, *U. of Wisconsin*
Andrew Oswald, *U. of Warwick*
Steve Palumbi, *Stanford U.*
Jane Parker, *Max-Planck Inst. of Plant Breeding Research*
Giovanni Parmigiani, *Dana-Farber Cancer Inst.* **($)**
John H. J. Petrini, *Memorial Sloan-Kettering Cancer Center*
Samuel Pfaff, *Salk Institute for Biological Studies*
Joshua Plotkin, *U. of Pennsylvania*
Albert Polman, *FOM Institute AMOLF*
Philippe Poulin, *CNRS*
Jonathan Pritchard, *Stanford U.*
David Randall, *Colorado State U.*
Felix Rey, *Institut Pasteur*
Trevor Robbins, *U. of Cambridge*
Jim Roberts, *Fred Hutchinson Cancer Research Ctr.*
Barbara A. Romanowicz, *U. of California,Berkeley*
Amy Rosenzweig, *Northwestern University*
Mike Ryan, *U. of Texas, Austin*
Mitinori Saitou, *Kyoto U.*
Shimon Sakaguchi, *Kyoto U.*
Miquel Salmeron, *Lawrence Berkeley National Lab*
Jürgen Sandkühler, *Medical U. of Vienna*
Alexander Schier, *Harvard U.*
Vladimir Shalaev, *Purdue U.*
Robert Siliciano, *Johns Hopkins School of Medicine*
Denis Simon, *Arizona State U.*
Uri Simonsohn, *U. of Pennsylvania*
Alison Smith, *John Innes Centre*
Richard Smith, *U. of North Carolina* **($)**
John Speakman, *U. of Aberdeen*
Allan C. Spradling, *Carnegie Institution of Washington*
Jonathan Sprent, *Garvan Inst. of Medical Research*
Eric Steig, *U. of Washington*
Paula Stephan, *Georgia State U. and National Bureau of Economic Research*
Molly Stevens, *Imperial College London*
V. S. Subrahmanian, *U. of Maryland*
Ira Tabas, *Columbia U.*
Sarah Teichmann, *Cambridge U.*
John Thomas, *North Carolina State U.*
Shubha Tole, *Tata Institute of Fundamental Research*
Christopher Tyler-Smith, *The Wellcome Trust Sanger Inst.*
Herbert Virgin, *Washington U.*
Bert Vogelstein, *Johns Hopkins U.*
Cynthia Volkert, *U. of Göttingen*
David Wallach, *Weizmann Inst. of Science*
Ian Walmsley, *U. of Oxford*
Jane-Ling Wang, *U. of California, Davis* **($)**
David A. Wardle, *Swedish U. of Agric. Sciences*
David Waxman, *Fudan U.*
Jonathan Weissman, *U. of California, San Francisco*
Chris Wikle, *U. of Missouri* **($)**
Ian A. Wilson, *The Scripps Res. Inst.* **($)**
Timothy D. Wilson, *U. of Virginia*
Rosemary Wyse, *Johns Hopkins U.*
Jan Zaanen, *Leiden U.*
Kenneth Zaret, *U. of Pennsylvania School of Medicine*
Jonathan Zehr, *U. of California, Santa Cruz*
Len Zon, *Children's Hospital Boston*
Maria Zuber, *MIT*

BOOK REVIEW BOARD

David Bloom, *Harvard U.,* **Samuel Bowring,** *MIT,* **Angela Creager,** *Princeton U.,* **Richard Shweder,** *U. of Chicago,* **Ed Wasserman,** *DuPont*

Published by AAAS

EDITORIAL

The UK: Thinking big or small?

No member state has ever left the European Union (EU), and so the idea that the United Kingdom (UK) might leave has stirred fierce debate ever since Prime Minister David Cameron promised a referendum on membership nearly a year ago. On 23 June 2016, British citizens have a choice to make. Public opinion in the UK is split on a British exit from the EU, or a "Brexit." A recent survey indicates that the majority of researchers favor the UK remaining in the EU.* As a British scientist and former Chief Scientific Adviser to the President of the European Commission, I believe that it benefits the UK, the EU, and global science for the UK to remain a strong committed member of the EU.

Established in 1951 to cement nations through common trade interests, the EU reflects a unified movement toward peace, prosperity, and stability. Now a family of 28 nations, this union shares economic goals and social and cultural values, and solves problems and exerts global influence through partnerships. As a result, the EU leads some of the most successful scientific enterprises in the world.

A vote to leave the EU amounts to turning Britain's back on a demonstrably valuable venture that supports the UK's scientific success. The UK would face having a minor role in scientific endeavor rather than one of leadership and common vision. Science would survive, of course, and the UK could try to agree to terms with the remaining EU members (not a foregone conclusion) to secure "associated country" status for major science projects such as Horizon 2020, the largest EU Framework Programme for Research and Innovation. But the UK would say goodbye to influence, and the ability to achieve scientific ambitions would diminish as it attempted to compete globally as a small island nation.

Would this really matter? If the UK aspires to deliver a robust and sustainable economy fit for the 21st century, that economy must be based on science, engineering, and technology. It is difficult to see how that will be achieved if the best researchers in the UK are distanced from the best in Europe and other global partners. Science is an international pursuit. It relies on the best infrastructure, which cannot easily be delivered by single nations. British scientists currently have leadership roles in, and benefit from, the European Southern Observatory, the European Space Agency, the European Molecular Biology Laboratories, ITER (European nuclear fusion project), and ELIXIR (European infrastructure for biological information), to name a few. This involvement supports the UK's scientific aspirations, industries, and economy.

"...it benefits the UK... to remain a strong committed member of the EU."

The UK currently attracts the best scientists in the world, who understand that by being there, they can influence and take part in EU research programs, move freely between EU member states, form powerful scientific networks, and access the best infrastructure. It is hard to imagine that the UK would remain attractive to the best global scientific minds if distanced from the EU. Worse yet, would the UK close its borders to European scientists? Consider how the UK would deliver its European networks if the UK government chose not to replace funding received from Horizon 2020, an amount that substantially exceeds its proportionate contribution.

Without doubt, there are challenges for the European Commission as it struggles to support the rapid expansion of the EU. Tensions about debt crises and immigration loom large over Europe. But what would a Brexit reflect as far as the British attitude toward an alliance that represents the hope of further strengthening stability and security? Rather, the UK should be working with its European partners to make the EU the best it can be.

– Anne Glover

Dame Anne Glover is a professor at the University of Aberdeen, UK, and served as Chief Scientific Adviser to the President of the European Commission from 2012 to 2014. Email: l.a.glover @abdn.ac.uk; Twitter: @AnneGlover_EU

ILLUSTRATION: *SCIENCE*; PHOTO: EUROPEAN PARLIAMENT

*D. Cressy, *Nature* **531**, 559 (2016).

10.1126/science.aaf8180

Published by AAAS

NEWS

$250,000,000

Amount donated by tech entrepreneur and philanthropist **Sean Parker** for the new Parker Institute for Cancer Immunotherapy, announced 13 April. The institute will involve five major cancer centers and more than 300 researchers.

IN BRIEF

Mekong drought erodes food security

The megadrought is hammering Vietnamese agriculture, including crops like rambutan.

The worst drought ever recorded in Vietnam is stoking fears of a food security crisis. On 12 April, a Hanoi-based research team with the International Center for Tropical Agriculture briefed Vietnamese officials on how water scarcity and climate change are imperiling key crops—rice, cassava, maize, coffee, and cashew nuts—across the country. Since the end of 2015, water levels in the lower Mekong River have been at their lowest since records began nearly 100 years ago, according to a United Nations report released last month; as of mid-March, nearly a million people in central and southern Vietnam lacked access to fresh drinking water. Water levels customarily drop during the dry season, resulting in saltwater intrusion from the South China Sea. But a combination of factors—reduced rain due to El Niño, possibly exacerbated by climate change, as well as the impact of upstream dams—have dramatically constricted the river's flow. As a result, the saltwater intrusion began 2 months early, tainting groundwater and rice paddies as far as 90 kilometers inland. The Vietnamese government has approved $23.3 million in emergency funds to compensate hard-hit farmers and provide water tanks and other critical provisions. http://scim.ag/Mekongdrought

AROUND THE WORLD

NIH seeks money for Zika, Ebola

WASHINGTON, D.C. | The White House's decision this week to shift $589 million in unspent Ebola response funding to fighting Zika won't require cutting any Ebola research supported by the National Institutes of Health (NIH). But the Obama administration is requesting more help from Congress both to fund Zika efforts and to replenish money shifted away from Ebola, says Anthony Fauci, the head of NIH's National Institute of Allergy and Infectious Diseases (NIAID) in Bethesda, Maryland. Some $47 million of the shifted funds will go to NIAID to support Zika research, Fauci says; none of that comes from Ebola research at NIAID, which has already spent its $238 million share of Ebola response funding authorized by Congress last year. Meanwhile, Obama administration officials are still pushing Congress to approve a nearly $2 billion emergency Zika funding request the White House made earlier this year.
http://scim.ag/Zikafundingshift

Team to test drug for pedophiles

STOCKHOLM | Swedish researchers have begun a clinical trial to assess whether a prostate cancer drug called Firmagon could help prevent pedophilic behavior—and they're counting on online donations to help finish it. The team is reaching out to the public to collect £38,000 ($53,000) through a campaign launched last week on Walacea, a U.K. crowdfunding website for scientific research. They hope to show that the drug, which lowers testosterone levels in the body, will reduce the pedophilic impulses that might cause people to abuse a child. The trial participants are recruited through Preventell, a Swedish "helpline for unwanted sexuality" run by the Centre for Andrology and Sexual Medicine at the Karolinska University Hospital here. The trial will not enroll sex offenders, said the trial's principal investigator, psychiatric researcher Christoffer Rahm of the Karolinska Institute, at a press briefing to announce the campaign in London on 6 April. On the contrary, he said, the

PHOTO: THOMAS SCHOCH/CREATIVE COMMONS

Published by AAAS

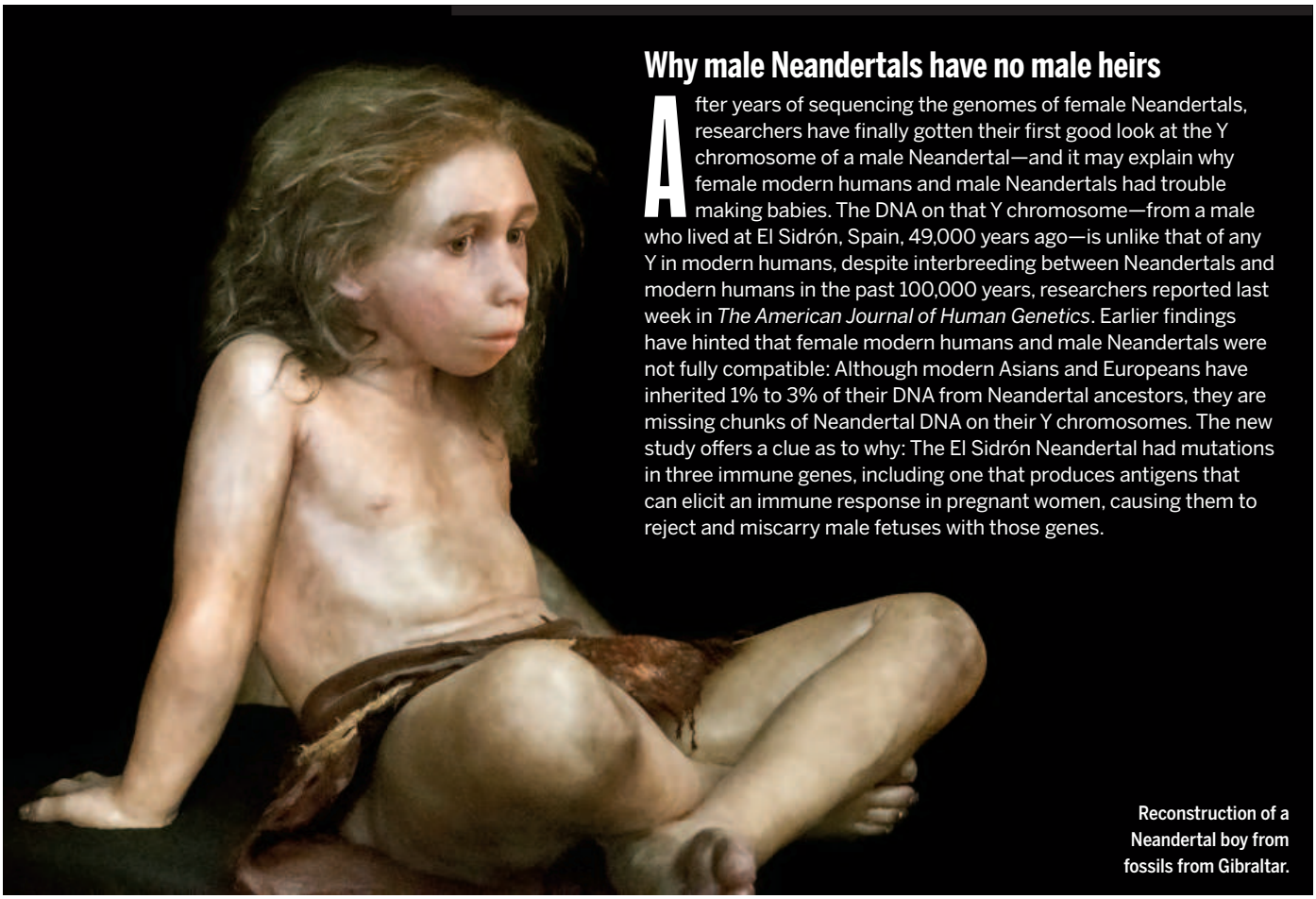

Why male Neandertals have no male heirs

After years of sequencing the genomes of female Neandertals, researchers have finally gotten their first good look at the Y chromosome of a male Neandertal—and it may explain why female modern humans and male Neandertals had trouble making babies. The DNA on that Y chromosome—from a male who lived at El Sidrón, Spain, 49,000 years ago—is unlike that of any Y in modern humans, despite interbreeding between Neandertals and modern humans in the past 100,000 years, researchers reported last week in *The American Journal of Human Genetics*. Earlier findings have hinted that female modern humans and male Neandertals were not fully compatible: Although modern Asians and Europeans have inherited 1% to 3% of their DNA from Neandertal ancestors, they are missing chunks of Neandertal DNA on their Y chromosomes. The new study offers a clue as to why: The El Sidrón Neandertal had mutations in three immune genes, including one that produces antigens that can elicit an immune response in pregnant women, causing them to reject and miscarry male fetuses with those genes.

Reconstruction of a Neandertal boy from fossils from Gibraltar.

project "wants to shift the focus [to] preventing child sexual abuse from happening in the first place" by targeting men who have sought help to deal with their pedophilic impulses. **http://scim.ag/pedodrugtrial**

Logging looms for famous forest

WARSAW | The Białowieża Forest is the largest remaining old-growth forest in Europe, covering 142,000 hectares in Poland and Belarus. It is a United Nations Educational, Scientific and Cultural Organization World Heritage Site, which includes both natural and managed forests and contains hundreds of European bison, Europe's heaviest land animal. On 25 March, the Polish government announced it would increase logging permits in 2470 hectares outside a national park and nature reserves, as a response to an outbreak of European spruce bark beetle that began in 2013. That will increase the logging intensity by an order of magnitude compared with 2012, says ornithologist Przemek Chylarecki of the Polish Academy of Sciences here. "I see this logging intensity as virtually incompatible with the need to maintain [ecological] integrity," he says. And logging outside the old-growth forest could still be harmful, says Stephen Woodward, a tree pathologist at the University of Aberdeen in the United Kingdom. "If they log right up to the boundary of the nature reserve, that could have serious impacts." Meanwhile, the European Commission last week began investigating whether the logging is compatible with E.U. protections of nature reserves.

Logging plans may threaten one of Europe's last primeval forests.

CSIRO chief defends divisive plan

CANBERRA | Speaking at a Senate budget hearing on 7 April, Larry Marshall, the chief executive of Australia's premier research agency, the Commonwealth Scientific and Industrial Organisation (CSIRO), sought to allay fears of job losses while defending the agency's new priorities. The controversy over the scientific direction and staffing of CSIRO had heated up again last week with the release of 700 pages of internal documents suggesting that CSIRO's management disdains "public good" research. Among those documents, released by a Senate panel investigating job cuts at the agency, were emails written by division Deputy Director Andreas Schiller to agency leaders suggesting that "public good is not good enough, [it] needs to be linked to jobs and growth," and advising that CSIRO make a "clean cut" and eliminate 120 staff engaged in "public good/government-funded climate research." Marshall said he was surprised by the "extremely negative" response to his February announcement of plans to "realign and restore our business growth." He said new jobs would be created in

IMAGES: (TOP TO BOTTOM) SEBASTIEN PLAILLY/SCIENCE SOURCE; MARC VERAART/FLICKR

Published by AAAS

areas such as carbon capture and storage, emission reduction measures, and photovoltaics. http://scim.ag/CSIROclimcuts

'Starshot' probes aim for stars

NEW YORK CITY | Russian internet billionaire Yuri Milner, teaming up with physicist Stephen Hawking and Facebook co-founder Mark Zuckerberg, announced this week the start of a project to send miniaturized spacecraft to the nearest nearby stars. The Breakthrough Starshot initiative will use cellphone technology to make a postage stamp–sized spacecraft-on-a-chip, with camera, thrusters, and communications. Thousands of these will be launched into space, each equipped with a solar sail a few meters across. Rather than rely on the weak power of the sun for propulsion, an array of powerful ground-based lasers will fire a 100-gigawatt beam to boost the tiny craft on their way. At 20% of the speed of light, the craft will reach the nearest star, Alpha Centauri, in 20 years. They will flash by in about an hour, sending back pictures and other data about any planets. "For the first time in human history, we can do more than just stare at the stars," Milner said 12 April at a press conference in New York.

NEWSMAKERS

Three Qs

In November, **Hugh Possingham**, an Australian mathematical ecologist at the University of Queensland, St. Lucia, in Brisbane, will become the next chief scientist of The Nature Conservancy (TNC), based in Arlington, Virginia. Possingham, 53, led a group that developed conservation planning software, called Marxan, that has been used in more than 150 countries for designing nature reserves, zoning plans, and other purposes—including rezoning the Great Barrier Reef Marine Park in 2004. *Science* spoke with Possingham about his new position. http://scim.ag/Possingham

Q: What will you do as chief scientist?
A: I wish I knew! I'm not starting until November, so I'm still in a learning curve. [TNC] has been rapidly changing from being largely U.S.-based and acquiring land as their main strategy. Now, they're in many more countries with many other methods to advance conservation. They're moving into areas like climate, water, and cities.

Q: What's going on with science at TNC?
A: They're interested in diversifying their science base, encompassing the whole of land-use planning. We need a lot of people with diverse backgrounds. This covers economics, social science, political science, engineering, mathematics.

Q: You're an advocate of "conservation triage." How will you apply that at TNC?
A: Triage is just prioritization, and every manager prioritizes. [TNC is] facing important questions: How do you allocate resources? How much effort do you spend on reaching out to policymakers? What's the business case for these diverse activities? And what new knowledge do we need to make these decisions? To me it's a massive intellectual problem in allocation of resources.

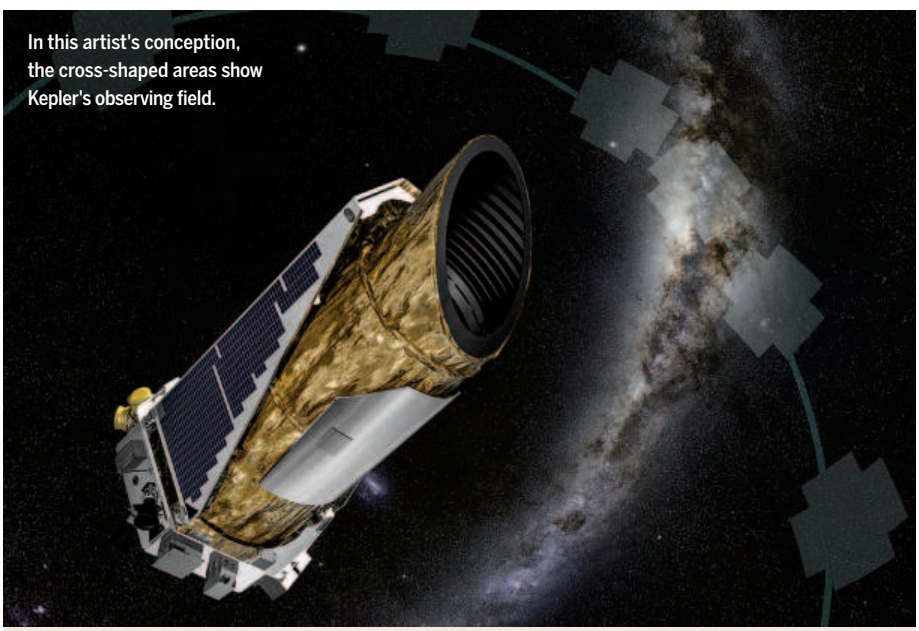

In this artist's conception, the cross-shaped areas show Kepler's observing field.

NASA's planet hunter safe again, for now

NASA has regained control of its exoplanet discovery satellite, Kepler, after a fraught few days during which the spacecraft put itself into a protective "emergency mode." Kepler, launched in 2009 to search out roughly Earth-sized planets around sunlike stars, had finished its last observing campaign on 23 March and was in a "rest" state before beginning a campaign to detect exoplanets by gravitational microlensing, due to begin last week. But during a check in with the spacecraft on 7 April, mission controllers found that it had put itself into emergency mode. By 10 April, controllers had the spacecraft in a stable state with its communications antenna pointing toward Earth; they are now downloading data from the spacecraft to examine what went wrong. Kepler, which has far outlasted its designed mission length, has previously faced and overcome technical problems, including the failure of two of its four reaction wheels, which keep the spacecraft pointed accurately; mission engineers worked out a solution using a combination of thrusters, surviving reaction wheels, and the pressure of sunlight. This is the first time Kepler has had to resort to emergency mode. http://scim.ag/Keplerback

FINDINGS

Embryo-editing study fuels debate

Chinese researchers have used the CRISPR gene-editing technique to modify the genome of a human embryo in an effort to make it resistant to HIV infection. The paper is only the second on the ethically fraught use of gene editing in human embryos. According to a 6 April report in the *Journal of Assisted Reproduction and Genetics*, researchers at Guangzhou Medical University in China attempted—with limited success—to modify the *CCR5* gene so that HIV could not enter immune cells. The team used nonviable embryos that were destroyed after 3 days. A similar paper published by a Chinese team in April 2015 led to an international summit on human gene editing. It concluded that although the clinical use of embryo editing should be off-limits, basic research should continue.

IMAGE: NASA AMES/JPL-CALTECH/T PYLE

Published by AAAS

IN DEPTH

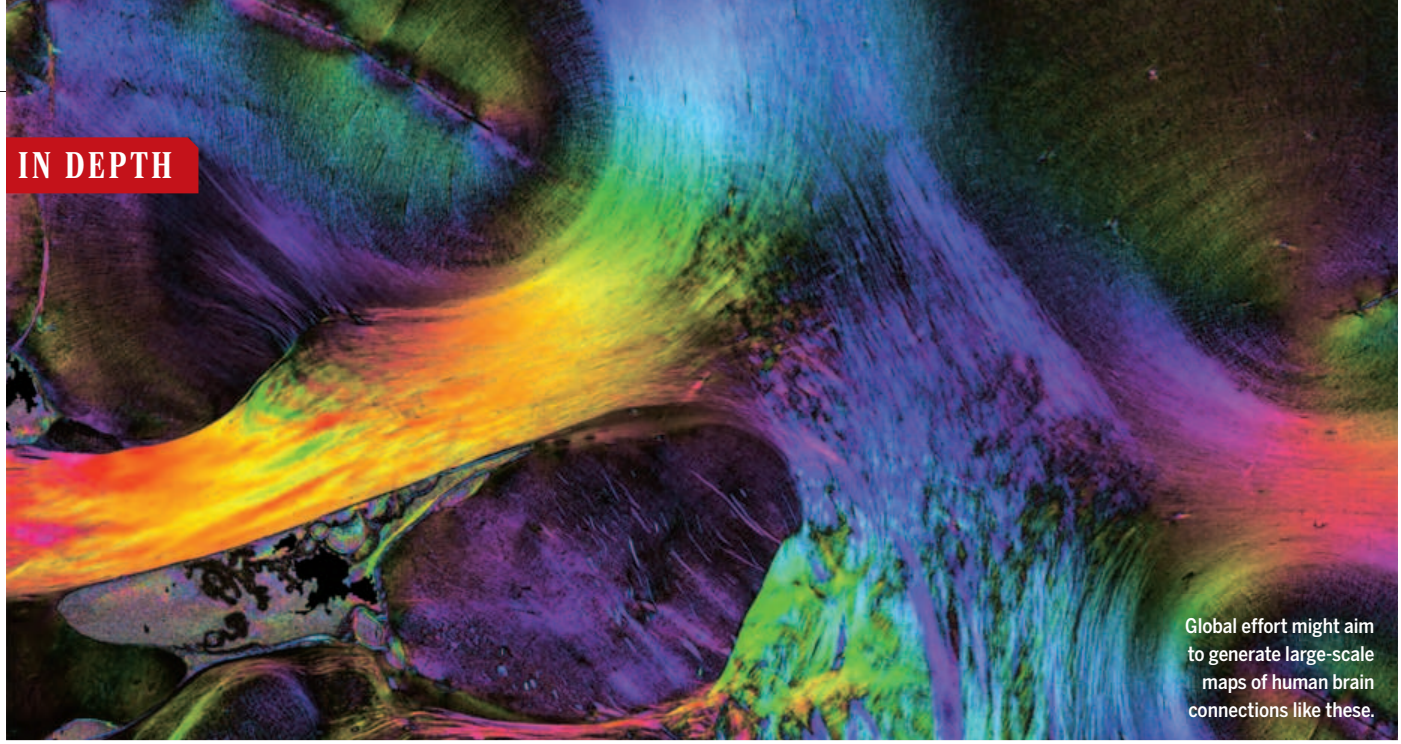

Global effort might aim to generate large-scale maps of human brain connections like these.

NEUROSCIENCE

International brain projects proposed

Meeting attendees debate big science ideas, including need for global data hub

By **Emily Underwood**, *in Baltimore, Maryland*

Neuroscience is becoming big science, with the 2013 launches of the European Union's Human Brain Project and the United States's Brain Research through Advancing Innovative Neurotechnologies (BRAIN) initiative setting the pace. Last week, leaders of these massive, multi-institution projects and others around the world met here at Johns Hopkins University to discuss an even loftier goal: a global neuroscience collaboration that would link their efforts and rival big science investments in astronomy and physics.

More than 60 neuroscientists from 12 countries pitched diverse visions for such a project at the meeting, sponsored by the Kavli Foundation and the National Science Foundation. Some called for a global effort to cure a single illness or disorder, such as depression, Alzheimer's disease, or stroke. Others argued for more detailed maps of brain connections in humans or nonhuman primates. Yet another contingent advocated creating a worldwide coalition of researchers to "crack" for the first time a single, complex behavior in a mammal, such as how a rat's brain controls foraging for food.

Long-standing tensions between clinical and basic research quickly emerged in the discussion. "We need to think about people—a depressed relative, a paralyzed relative," said neuroengineer Miguel Nicolelis of the Duke University School of Medicine in Durham, North Carolina, arguing for the disease-centered approach. Choosing just one condition to focus on, however, could "disenfranchise" people with other disorders, cautioned neurobiologist Story Landis, former director of the National Institute of Neurological Disorders and Stroke in Bethesda, Maryland, who lobbied for more basic science. "Real progress will depend on much better understanding of [neural] circuitry—how it's established, how it's modulated," she said.

Mu-Ming Poo, director of the Institute of Neuroscience at the Chinese Academy of Sciences in Shanghai, proposed an all-out effort to study brain wiring. Noting China's large supply of rhesus macaques and researchers' increasing ability to genetically engineer the animals to carry mutations for brain diseases such as autism, the neuroscientist proposed a 10- to 20-year global effort to complete the first map of brain connections in a nonhuman primate, which would include information about cell types, gene expression, and neural activity patterns. (Poo also provided some initial details about China's pending national brain project, saying it will encompass research into the neural basis of high cognition, artificial intelligence, and "early diagnosis" of brain diseases based on large medical and cognitive data sets collected by the Chinese health care system.)

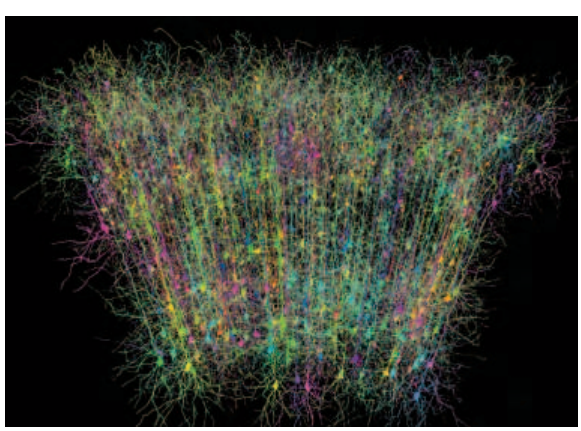

Some participants at the neuroscience meeting lobbied for a project to explain complex behaviors, including with simulations such as this one of a network of neurons in the cerebral cortex.

Attendees did converge on several guiding principles for an international project. All agreed, for example, on the need for better vetting, sharing, and storing of neuroscience data. "The raw data gathered by generations of graduate students and postdocs has been lost because we haven't come up with a good system for archiving and

IMAGES: (TOP TO BOTTOM) KATRIN AMUNTS, MARKUS AXER, ROGER WOODS AND KARL ZILLES, RESEARCH CENTRE JUELICH, GERMANY (KA, MA, KZ)/UCLA SCHOOL OF MEDICINE; HERMANN CUNTZ AND MICHAEL HAUSSER/UCL

Published by AAAS

sharing data," said neuroscientist Michael Hausser of University College London.

To address that problem, the group proposed creating an online resource tentatively dubbed the International Brain Station. Inspired in part by the Sloan Digital Sky Survey, a digital repository of telescope images containing hundreds of thousands of galaxies and other heavenly bodies, the brain counterpart would provide a portal into vast amounts of neuroscience data, which both scientists and the general public could access by computer.

Neurostatistician Joshua Vogelstein of Johns Hopkins, a meeting organizer, emphasized another key principle: encouraging participation from all nations. Although only about 450 laboratory heads are pursuing basic neuroscience research in India, for example, these researchers are "seeking and amenable to taking an international role," said neuroscientist Sandhya Koushika of the Tata Institute of Fundamental Research in Mumbai, India. A global neuroscience project should allow scientists from all countries to make intellectual contributions that go beyond "patronizing" requests for data analysis or technical support, she said. It should also avoid a narrow focus on problems that disproportionately afflict Western countries, she added. Whereas the United States is preoccupied with combating diseases of age such as Alzheimer's, Koushika noted, India's younger population is in greater need of interventions targeted to neurodevelopment and learning.

The group agreed on three basic research questions: what makes individual brains unique; how the brain's many components orchestrate learning and perform a task; and how to leverage the brain's plasticity to protect and restore brain function. The scientists will meet again in September to further refine the proposal, says neuroscientist Rafael Yuste of Columbia University, who co-organized the meeting and also helped craft the BRAIN initiative. Then, to garner support—and funding—from global leaders, the group aims to present a final proposal to the United Nations General Assembly when it meets in New York City that same month.

If it succeeds, a global brain initiative could inspire China's political leaders to take on "a major role" in international neuroscience, Poo said. U.S. neuroscientists also have a good reason to push for a global project, Yuste said: the upcoming U.S. elections. Anchoring the BRAIN initiative, which President Barack Obama has so visibly championed, in an international collaboration could be a buffer against shifting political winds, he said. ■

FISHERIES SCIENCE

Arctic nations eye fishing ban

As ice recedes in central Arctic Ocean, officials meet to discuss catch moratorium until stocks can be studied

By **Eli Kintisch**

In the late 1980s, hundreds of massive factory trawlers from Japan, the Soviet Union, and other nations swarmed into international waters in the Bering Sea between Russia and the United States, netting millions of tons of pollock. But the lucrative, essentially unregulated fishery quickly came to an ignominious end: In the early 1990s, pollock populations crashed and have not recovered.

Now, researchers and policymakers are working to prevent a repeat of that disaster farther north, in the central Arctic Ocean (CAO), which is increasingly accessible as sea ice melts. Next week, delegates from six of the eight Arctic nations as well as several countries with major fishing industries will meet in Washington, D.C., to discuss a proposal to bar commercial fishing in the CAO until scientists learn more about little-studied stocks and nations agree on catch rules. Fishing shouldn't begin in international waters "until there is adequate scientific information on which to manage such fisheries properly," argues Ambassador David Balton of the U.S. Department of State in Washington, D.C., a major backer of the initiative.

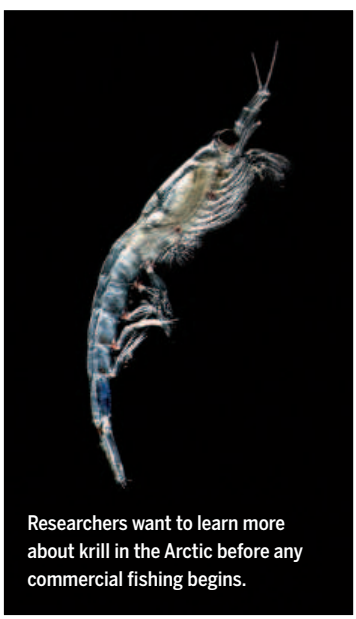

Researchers want to learn more about krill in the Arctic before any commercial fishing begins.

Thick sea ice and doubts about the extent of Arctic fish stocks have kept the CAO's international waters free of commercial fishing. But the area of late winter sea ice has plummeted by 9%, or 1.5 million square kilometers, over the past 3 decades, and the resulting flood of additional sunlight has helped increase primary production by phytoplankton—the base of the marine food web—by 30% since 1998.

Recognizing that such changes might eventually fuel an attractive polar fishery, in 2012 some 2000 scientists called for a fishing moratorium in the CAO. Already, the United States and Canada have basically placed a moratorium on fishing in the exclusive economic zones off their Arctic shores. But those zones extend just 370 km off the coast of each Arctic nation, leaving much of the CAO within a so-called doughnut hole of unprotected international waters. So the United States, Russia, Canada, Norway, and Denmark (representing Greenland) have also pledged to bar their own vessels from fishing in the area until nations agree to sustainably manage CAO fisheries.

Now, the Arctic nations want other countries—particularly Asian nations such as China, Japan, and South Korea that support globe-circling fishing fleets—to join this "precautionary approach." U.S. officials have proposed a binding pact that would put the CAO off-limits to all fishing until researchers learn enough to inform regulations. There is, for example, "a dearth of basic information as to the species (fish and shellfish in particular) found in" the region, an international research team concluded last year. One priority, scientists say, is learning more about Arctic krill, crustaceans that are a key food for fish—and could be one of the first targets of commercial fishers.

To fill some of those data gaps, Arctic nations are meeting with other countries in September in Tromsø, Norway, to shape a science plan. In the meantime, Bolton says next week's talks in Washington represent "the early days" of an effort to put Arctic fishing on a firmer footing. Nations that don't have a direct stake in Arctic territory have said little publicly about the U.S. proposal, but the participation of Asian nations in initial discussions on the issue held last December is viewed as a sign of interest. And many participants vividly remember the Bering Sea pollock disaster. "It's that very experience," Bolton says, "that is driving us in the central Arctic." ■

PHOTO: DR. RUSSELL R. HOPCROFT/INSTITUTE OF MARINE SCIENCE

Published by AAAS

Like other research funded by the Netherlands's main science agency, findings from the Netherlands Institute for Radio Astronomy starting this year are supposed to appear in open-access publications.

PHOTO: © HORIZONS WWP/TRVL/ALAMY STOCK PHOTO

SCIENTIFIC PUBLISHING

Dutch push for a quantum leap in open access

E.U. urged to free all papers by 2020

By **Martin Enserink**, *in Amsterdam*

One of the perks of holding the rotating presidency of the European Union is that it gives a member state a 6-month megaphone to promote its favorite policy ideas. For the Netherlands, which took over the presidency on 1 January, one surprising priority is open access (OA) to the scientific literature. Last week, the Dutch government held a 2-day meeting here in which European policymakers, research funders, librarians, and publishers discussed how to advance OA. The meeting produced an Amsterdam Call to Action that included the ambition to make all new papers published in the European Union freely available by 2020.

Given the slow pace with which OA has gained ground the past 10 years, few believe that's actually possible, but the document is rallying support. Carlos Moedas, the European commissioner for research, science, and innovation, favors an ambitious approach; OA will also be a key discussion point at a meeting of Europe's ministers of research, innovation, industry, and trade in Brussels in late May. "This is an orchestrated push on the European level that we have not seen before," says Ralf Schimmer of the Max Planck Digital Library in Munich, Germany.

Whether all 28 E.U. states are ready to act remains to be seen, and even some OA advocates are critical of the approach that the Netherlands has adopted for its own scientists: an emphatic choice for Gold OA, in which authors pay publishers to make their papers freely available. Many instead prefer Green OA, in which authors post a copy of each published paper in a public repository.

Less than a quarter of newly published papers are immediately available through OA; the rest remain behind a pay wall, some permanently. Many scientists don't care whether their papers are OA, preferring to publish in journals they know or ones with the highest impact factors, and many funding agencies aren't forcing them to change.

Keen to step up the pace, Sander Dekker, the Dutch state secretary for education, culture, and science, announced in 2013 that the government aimed to make the entire Dutch research output available through OA by 2024. The main Dutch funding agency, the Netherlands Organisation for Scientific Research (NWO) in The Hague, joined the movement; it has made OA publishing compulsory for papers resulting from all research projects it funded after 1 January—with a preference for Gold OA.

Meanwhile, the Association of Universities in the Netherlands has pushed for OA in its periodic collective bargaining rounds with big publishers over journal subscriptions. Springer, Wiley, and Sage have all agreed to make research papers on which the corresponding author is from the Netherlands available OA, even if it appears in a non-OA journal; Elsevier has agreed to do the same for 30% of such papers by 2018. The universities and NWO hope that these Big Deals, as they are known, will eventually help foment a Big Flip, in which Gold OA journals supplant subscription journals.

Stevan Harnad, a veteran OA advocate at the University of Québec, Montreal, in Canada, does not think the European Union should embrace that strategy—he calls it "fool's Gold"—because publishers are unlikely to view a flip toward Gold OA as being in their interest. Requiring authors to archive free versions of their papers is a better way to accelerate the pace, he says. But Dekker says Gold OA acknowledges that publishers provide a valuable service—and a problem with Green OA is that many publishers allow authors to self-archive a new paper only after a months-long embargo. "It's like with justice," Dekker says: "Access delayed is access denied."

The Netherlands is attempting a solution to the embargo problem: urging scientists to deposit the "pre-peer review," or submitted, version of a manuscript as soon as the paper appears. "That's a huge mistake," Harnad contends, because that version doesn't include changes, sometimes substantial, made at the journal's behest. NWO Chairman Jos Engelen says the posted version will make that clear; although "less than ideal," the solution is "better than nothing," he says.

Harnad offers another solution. Repositories could post the article immediately behind a wall that opens once the embargo ends; until that time, anyone who wants a copy can press a button to request the paper from the author, who can honor the request with a single click. Many U.K. repositories already have "button-mediated OA," says Harnad, who adds that it's much the same as asking an author for a paper by email.

To the European Commission, Green and Gold both are acceptable, says Robert-Jan Smits, director-general for research and innovation. He hopes the European Union's ministers will adopt the 2020 target when they meet next month, along with other measures to promote data sharing. The meeting "will be like a D-Day" for OA, Smits says. "It will become clear which ministers are really committed." ■

Published by AAAS

ARCHAEOLOGY

Megaproject asks: What drove the Vikings?

Researchers suggest that the nature of pre-Viking society spurred a drive for slaves

By **Andrew Lawler**, *in Orlando, Florida*

On 8 June 793 C.E., a band of foreign warriors attacked the Christian monastery of Lindisfarne on the English coast, wrecking the church, killing the monks, and making off with all the treasure their ships could hold. This brutal attack has long been thought to mark the start of Viking aggression. But archaeologist Neil Price of Sweden's Uppsala University suspects that the roots of the Viking era go back long before this raid.

Armed with a $6 million grant—a princely sum in archaeology—Price and his colleagues want to know the extent to which a need for captive labor and overseas wives helped drive Viking expansion, transforming the provincial Scandinavian sailors and fur traders of the earlier Vendel period into international explorers and marauders. "The social processes are going on long before" the Lindisfarne raid, Price said after his talk at a symposium on Vikings at the annual meeting of the Society for American Archaeology here last week. "We can erase this boundary between the Vendel and Viking eras."

A few kilometers from Price's office at Uppsala, Viking leaders and warriors gathered each spring to plan raids on distant lands. Now, Price plans his own assault, gathering specialists from across Europe to nail down the social and economic forces that spurred the Viking phenomenon. At the meeting, he and his colleagues laid out research plans and discussed preliminary finds. Rather than excavate, the team intends to use the Swedish Research Council's largest ever archaeological grant to reexamine spectacular existing finds using modern methods such as isotopic analysis.

"Price's project goes to the core of the question that all Viking scholars ask: Why the Vikings?" says Jan Bill, an archaeologist at Oslo's Museum of Cultural History. "Just putting some order into the old excavations and publishing them properly will tell us a lot about the background to the Viking age," adds archaeologist Marek Jankowiak of the University of Oxford in the United Kingdom, who specializes in the period but also is not part of the project.

Doubled-edged swords like this one from an Estonian ship burial show that Scandinavians far from their homeland fought fiercely before the accepted start of the Viking era.

The sudden and dramatic breakout by the Vikings has long puzzled scholars. The Lindisfarne raid inaugurated 3 centuries of expansion that led to settlement of Iceland, Greenland, and, briefly, Newfoundland in Canada. To the east, Vikings dominated the rivers of today's western Russia and Ukraine, sent diplomats to Constantinople, and traded as far afield as Baghdad and North Africa.

But although previous scholars identified the raids as the start of the Viking era, Price stresses that their way of life began long before. In the Vendel period from about 550 C.E. to 790 C.E., Scandinavians exported iron and furs and developed impressive seafaring skills. And between 2008 and 2012, researchers discovered two ship burials on the edge of the Baltic Sea in Estonia, 250 kilometers from the Swedish coast. The burials are "the most significant Viking discovery of the last hundred years," Price says—and they apparently predate the Lindisfarne raid by nearly a century, according to dating by radiocarbon and artifact styles.

Found on the island of Saaremaa in the town of Salme, the two war boats served as graves for 40 men. In one, 33 men were stacked atop one another and covered with wooden shields. Elite soldiers were buried with elaborately decorated double-edged swords, and a man who appeared to be the chieftain clasped a sword with a jeweled hilt and held a gaming piece made of wal-

PHOTOS: (TOP TO BOTTOM) RAILI ALLMÄE; LIINA MALDRE

Published by AAAS

A ceremonial ship burial in Estonia is decades older than the supposed first Viking raid, in 793 C.E.

rus ivory in his mouth.

Working with Estonian collaborators, "we plan to throw massive science" at these ancient vessels to glean everything possible about this period, Price said. He'll also focus on some spectacular ship burials at Valsgärde, just outside of Uppsala, dated from the sixth century to the 11th century. The area includes 60 tombs, including those of women, and hundreds of artifacts yet to be carefully analyzed.

Price and his colleagues wonder whether the burials will yield evidence of slavery, which they increasingly see as a powerful factor driving the Viking expansion. Price said the need for slaves may have begun during the Vendel era, when the fast-growing fleet of ships demanded an enormous number of massive woolen sails. This required transforming land into pasture for sheep, producing wool, and making sails—a labor-intensive craft. A single 90-square-meter sail might take a single person up to 5 years to produce, said Ben Raffield, an archaeologist at Simon Fraser University in Burnaby, Canada, who is involved in the project. Price adds that "each ship needed two sails, and there were hundreds of ships," raising the possibility that slave labor was needed to maintain the fleet.

Historical sources make it clear that the "Vikings were taking, transporting, and selling slaves," Raffield said in his talk. He estimates that slaves comprised as much as 25% of Scandinavia's population. Norse sagas mention slaves—"thralls" in Old Norse—who were often given pejorative names like Stinky, Stumpy, and Stupid. But compelling archaeological evidence has been elusive. Iron manacles and collars hint at slavery, but might have been used for prisoners or dogs. Raffield plans to search for evidence of special vessels designed to carry captives.

Other archaeologists have found tantalizing hints of slavery in existing remains. About one in 25 male Viking burials in Sweden and Norway includes teeth incised with deep grooves. The marks were long thought to indicate a warrior class, but at least some of these men were decapitated and placed in a burial with another man, said Anna Kjellström of Stockholm University, who is also part of the project. "You can make a strong argument that these were special slaves who were ritually killed" upon the death of their master, she said in her talk. "The slaves may have been in front of us all the time." The team plans extensive isotopic analysis to discover whether the victims were local or recent, perhaps involuntary, arrivals.

The research program also will analyze changes in Viking society as shown by land use. For example, by the 10th century, architectural clues to slavery become clear. At a site outside Stockholm near today's Ikea, a small round hut dug into the ground sits on a slope above a large manor house. The hut appears to have been the living quarters for slaves at the height of Viking prosperity, said Charlotte Hedenstierna-Jonson of Stockholm University. At another Swedish site, Sanda, a large house is surrounded by much smaller structures, possible slave quarters. "It's not going too far to see these as the big house on a plantation," Price said.

Other researchers praise the team's integration of details into a fuller picture of Vendel and Viking society. "It is now clear that we cannot fully understand the Vikings without taking into account slave hunting and slave trade," Oxford's Jankowiak said. "The 'business model' of the Baltic Vikings appears to have depended on it."

> *"The 'business model' of the Baltic Vikings appears to have depended on [slavery]."*
> **Marek Jankowiak**, University of Oxford

The team also will tackle the disturbing issue of sexual slavery. There are hints of polygyny in Germanic cultures from this time, though researchers aren't sure of its extent in Viking society or in the Vendel era. But if it were prevalent, Price speculates, poorer men would have been eager to seek wives outside Scandinavia. Researchers hope to understand more by pulling together DNA and other data to determine relations and origins among Viking dead.

The argument that Vikings set out to capture women gets tantalizing support from recent genetic studies of living people in Iceland, which has not experienced a significant migration since the Vikings settled it more than a thousand years ago. About three-quarters of male Icelandic settlers hailed from what is today Norway, although well over half of the women were from the British Isles, according to genetic studies of today's Icelanders. That suggests that Viking men partnered with British women on a massive scale. "We must be talking about some degree of coercion," Price said. His team will emphasize examining the remains of Viking women—long understudied—to understand their origins.

Price adds that much more work is required to understand the emergence of the Vikings' raiding society. "This is just the start of a decade of research," he says. ■

METEOROLOGY

Obsolescence looms for balloon data

United States falls behind Europe in adopting modern data format

By **Eric Hand**

Twice a day, hundreds of hydrogen- or helium-filled balloons lift off from stations around the world, carrying temperature, pressure, and humidity sensors. Each balloon, a meter or two in diameter when it's released, rises more than 30 kilometers, radioing data to ground stations; then it bursts and the instrument box parachutes back to the ground. Balloons, or radiosondes, are still critical to weather forecasting. But the 75-year-old system—or at least its data infrastructure—is showing its age.

The operators of more than three-quarters of the world's 800 weather balloon stations still produce data in an antiquated alphanumeric format, and have failed to meet a 2014 deadline to adopt a new, more powerful binary format. Some weather forecasters and climate modelers who use balloon data have also failed to switch over: The United States's Global Forecast System (GFS), for example, can't read the new binary data. As nations turn off the old alphanumeric data streams, unprepared researchers and agencies are facing data gaps.

"It's going to affect a lot of people who don't even realize it's going to affect them," says Patricia Pauley, a meteorologist at the Naval Research Laboratory in Monterey, California.

Balloon data are shared freely among the world's meteorological agencies, and the on-the-spot observations both supplement and ground-truth the satellite data that are now the mainstay of weather forecasting. "Radiosondes are still very important, for numerical weather prediction and also for climate studies," says Bruce Ingleby, a meteorologist at the European Centre for Medium-Range Weather Forecasts (ECMWF) in Reading, U.K.

But the balloon data themselves have been stuck in the past. The alphanumeric format, called TEMP, dates to 1946, when data trans-

Published by AAAS

Weather balloons are released worldwide, even in Antarctica.

missions were too expensive to provide high resolution. To economize, the format reports temperature in steps of 0.2°C, rounds high altitudes to the nearest 10 meters, and divides the whole atmosphere into just 100 levels. And because TEMP is a fixed format, researchers can't add new types of measurements without changing hardware and software worldwide.

In 1988, the World Meteorological Organization (WMO) approved a new set of codes, called the Binary Universal Form for the Representation of meteorological data (BUFR). This format is now the international standard for satellite data and surface observations. In 2003, WMO ordered all radiosonde operators to switch to BUFR by November 2014. Australia and most European nations have done so, and have reaped benefits. For example, BUFR allows atmospheric readings to be taken as often as every second, leading to thousands of levels per balloon flight, rather than 100. BUFR also is better for tracking the effect of wind on GPS-equipped balloons, which can drift hundreds of kilometers during flight.

But with no way to enforce its mandates, WMO's effort to wean nations from TEMP to BUFR has been like "herding cats," says Yves Pelletier, chief of data, performance, and standards at the Canadian Meteorological Centre in Dorval. For meteorologists, who for three generations were used to reading the alphanumeric codes straight from the balloons without special decoding software, the change marks a major culture shift, he says: "They have a bit of trouble envisioning that things can operate differently." The cost of switching software, hardware, and networks so that a station can accommodate BUFR is another obstacle, Pelletier says. That's why only about half of Canada's 31 weather balloon stations have migrated to BUFR, he says; the holdouts are remote stations in the far north, where the cost of changing infrastructure is higher.

Many nations, such as the United States, India, and China, tried to abide by the WMO mandate by taking a shortcut: packaging TEMP data in a binary wrapper that mimics BUFR data. But experts say this "reformatting" approach leads to errors without tapping into BUFR's innate advantages. "It does not accomplish the migration," Pelletier says. "It accomplishes nothing."

Forecasters who use balloon data in models have also been slow to embrace the new format. Some forecast centers, such as ECMWF, now blend the old TEMP data with data from stations that have switched to the new high-resolution BUFR data. But for others, retooling to decode BUFR hasn't been urgent, because the stations broadcasting BUFR data have simultaneously streamed TEMP data.

As of November 2014, however, TEMP is no longer an officially supported WMO code, which means that stations are free to turn off their TEMP streams. One of the first was a set of about a dozen European cargo ships that release weather balloons as they crisscross the North Atlantic Ocean. The cost of satellite data transmission from these ships is high, and so in 2014 they began transmitting only the new format. That's a major loss for centers that rely on TEMP, because ocean data are so sparse. Then, in January of this year, Spain stopped transmitting TEMP. The Netherlands and Cyprus have also announced plans to turn off their TEMP streams. Ingleby says as the data gaps multiply, forecasters will move more quickly to upgrade their systems. "It is going to be an incentive," he says. "It's more stick than carrot."

The U.S. National Oceanic and Atmospheric Administration (NOAA), which oversees the National Weather Service's GFS, says that it hopes to be capable of using BUFR data in its models by the end of 2016. It also has a plan to upgrade its radiosondes to BUFR by early 2017.

The changeover to BUFR could shake up researchers as well. Larry Oolman, a meteorologist at the University of Wyoming in Laramie, has for 20 years maintained a website from which researchers can download radiosonde data for case studies or regional models. Oolman gets the TEMP data from WMO and translates them to text files. On a slow day, he says, he gets 130,000 requests for data from around the world. But now that the TEMP stream from places like Spain is gone, researchers are contacting him to ask why data are disappearing. Oolman says he, too, is going to have to write some software to translate BUFR data. "I'm going to have to figure out how to redesign everything," he says. ■

Leaden balloons

Most of the world's 827 weather balloon stations still produce data in an antiquated, alphanumeric format that dates to the 1940s. Only 22% of the stations use the modern binary format that was supposed to have been adopted internationally by 2014.

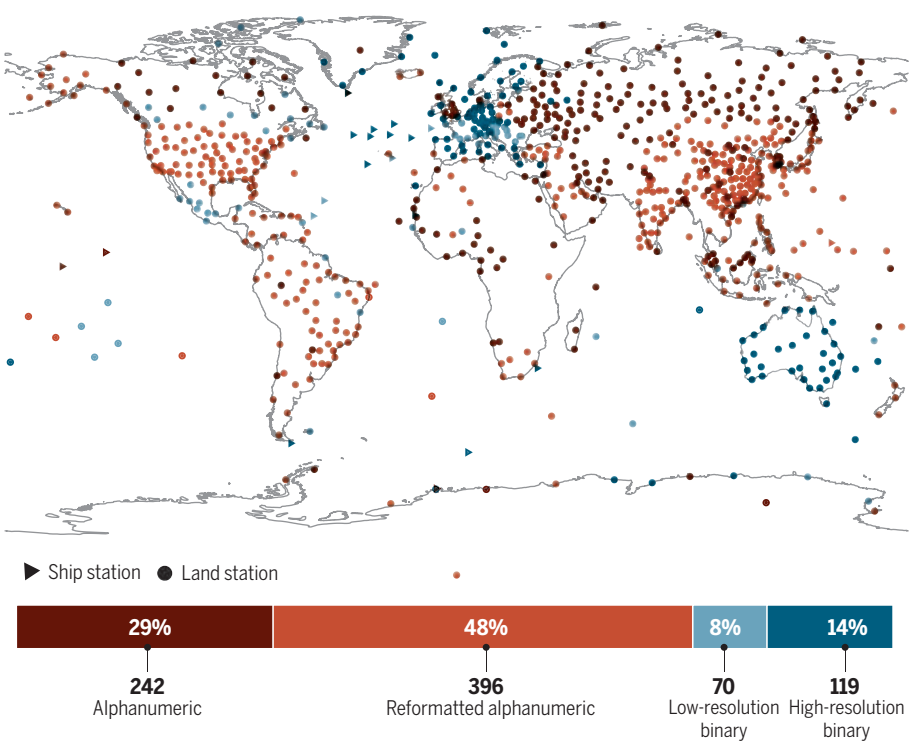

CREDITS: (PHOTO) GRAHAM NEDEN/ECOSCENE/CORBIS; (MAP) V. ALTOUNIAN/*SCIENCE*; (DATA) BRUCE INGLEBY/ECMWF

Published by AAAS

SOCIOLOGY

Rural China is no country for old people

Erosion of families sparks an epidemic of suicides among the elderly

By **Kathleen McLaughlin**, *in Zhangjiajie, China*

Early before breakfast one summer morning in 2014, Xiang Yougyu stepped outside her family home in this bucolic mountain village and hanged herself from an orange tree a few feet from the front door. Xiang, then 74, had some minor health complaints, and was a "sensitive" person, says her husband, Shu Haogui. "She took things too hard." But he never imagined she would take her own life.

The tree where Xiang killed herself has been cut down, and life in the village carries on much as it has for the past few decades. As in other parts of rural China, it's mostly empty-nesters who do the farming here. Young and able-bodied people, like Shu's 20-year-old grandson, migrate to cities for work as China's epic urbanization rolls on. The shift has brought prosperity, but sociologists also blame it for a troubling rise in elderly suicide rates.

"A lot of people say elder suicide is a natural thing. This rate we are seeing is not natural," says Jing Jun of Tsinghua University in Beijing. Worldwide, suicide rates are highest among people over 70, according to the World Health Organization (WHO); in the United States, the rate for people over 65 is about 15 per 100,000. In China's urban areas, suicide rates for people aged 70 to 74 nearly tripled from 13.4 suicides per 100,000 people from 1991 to 1999, to 33.8 per 100,000 from 2002 to 2008, according to data compiled by the Chinese health ministry's disease surveillance network and WHO. But in rural China, Jing says, the suicide rate is about 47 per 100,000—"a situation rarely seen elsewhere in the world." It's "no exaggeration to call this a public health crisis," says Liu Yanwu, a sociologist at Wuhan University.

The epidemic's roots lie in the unraveling of traditional family life in China. In the March issue of the *Journal of Social Issues*, sociologist Xue Bai of Hong Kong Polytechnic University and colleagues describe how elderly Chinese "face a number of challenges with respect to maintaining a positive view of themselves." As economic development and urbanization lure able-bodied young people out of villages and into China's massive migrant workforce, many elderly people are left behind to fend for themselves.

The exodus includes the young women who once helped care for the elderly. In the past, a daughter-in-law was expected to take care of the entire family, including her husband's aging parents. Many women have instead joined the workforce. Greater prosperity has helped lower the suicide rate for all ages, especially among women: China no longer holds claim to being the only country in the world where female suicides outnumber male ones. Overall, China's suicide rate fell from 23.2 per 100,000 in 1999 to 9.8 per 100,000 in 2011, according to a 2013 study from the University of Hong Kong.

Shu Haogui's wife hanged herself from an orange tree when she was 74 years old. She was "sensitive," he says, but he never imagined she would take her own life.

PHOTO: TOM WANG

But the factors behind that positive trend have also isolated the elderly. Rural elderly typically see their children and grandchildren only during Chinese New Year. Neither the government nor the private sector has stepped in to fill a gap in basic care for elderly people. The problem will only worsen: Roughly 15% of China's population today is more than 60 years old; by 2050, that is expected to rise to 39%.

China's new 5-year plan acknowledges that the country's aging population is a paramount concern. Beginning next year, the central government will gradually hike the official retirement age to 55 for women and 60 for men—a move that could help seniors in those age groups feel less isolated and more valuable to society. But those who study China's elderly say much more must be done, such as building more elderly care facilities and filling gaps in the national health insurance program. In Beijing, the waitlist for nursing home facilities is 7 years long, Jing says. In the countryside, nursing homes are even scarcer. "In a culture that plays up filial piety, it just contradicts every cultural expectation we have," Jing says. "There has to be another way of thinking about getting old in China."

Sociologist Zhou Liang of the Xiangya School of Medicine in Hunan is experimenting with ways to engage elderly people and reduce their isolation. Initially, his team tried creating community groups in rural areas. The researchers found, however, that those most at risk of suicide did not participate. Now, Zhou's project works to identify community leaders in villages and tasks them with checking in on older people regularly. Engaging in simple conversation sometimes is enough to ward off depression, he says.

Zhou's group is also conducting extensive interviews with hundreds of families who have lost an elderly member to suicide. The surveys, Zhou hopes, will provide additional clues to how China can tackle the largely unseen epidemic.

"If this was happening among college students, there would be major headlines," Zhou says. "The rural elderly truly are China's invisible people." ■

Kathleen McLaughlin is a writer in Beijing.

Published by AAAS

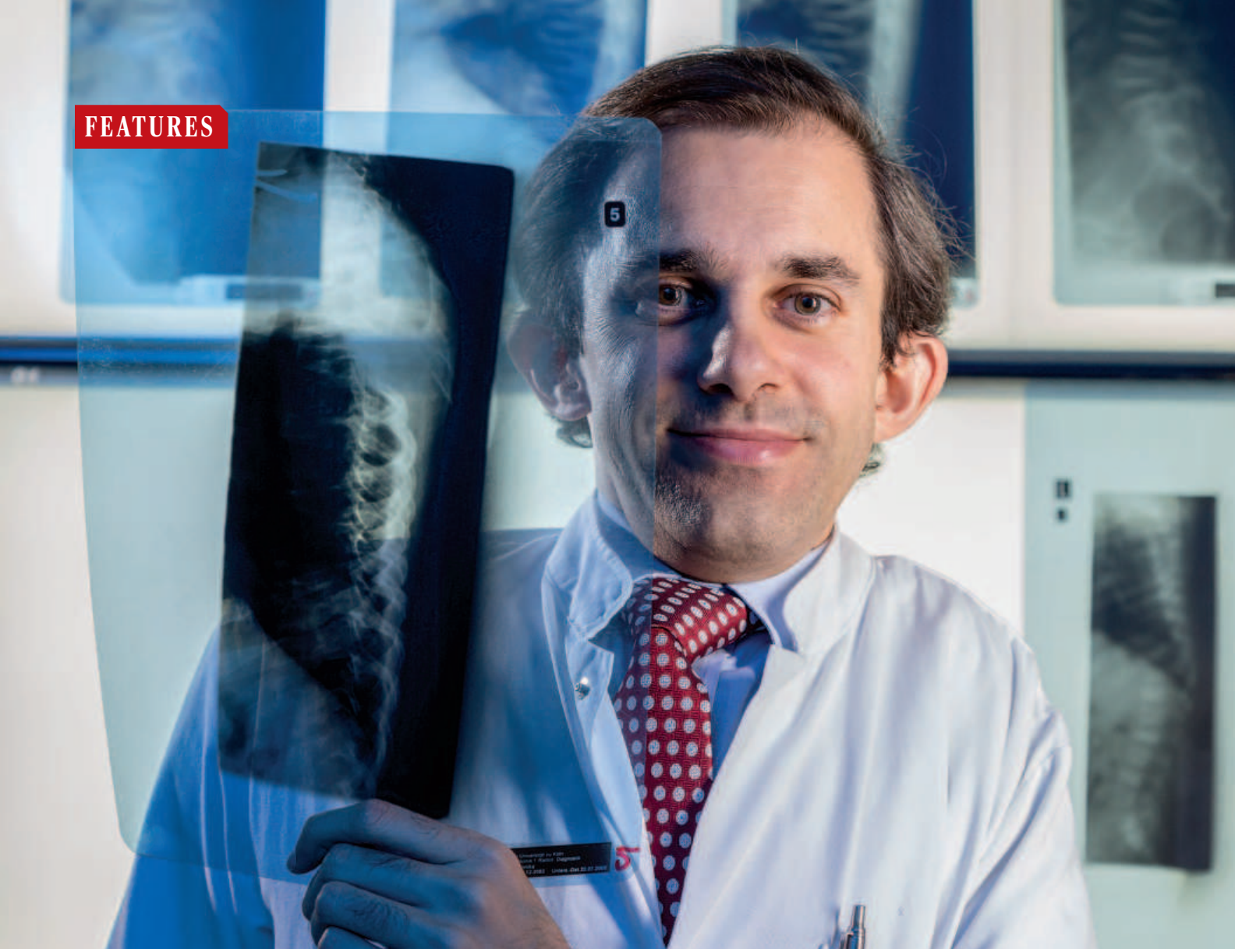

THE SAVIOR CELLS?

After a painstaking journey, researchers are preparing to test stem cell therapy in ailing fetuses

By **Jennifer Couzin-Frankel**

At the time of his birth, 41 years ago in Germany, Oliver Semler had already fractured one bone, a pencil-thin rib. That, his bowed femurs, and a second fracture at 2 days old told doctors he had osteogenesis imperfecta (OI), a debilitating genetic disease in which brittle bones break easily and often—from being jostled at school, for example, or slipping on wet leaves outdoors. Or even, as in Semler's case, from acrobatics in the womb. "I had a cast two or three times a year," says Semler, who's lost count of his fractures but endured 27 surgeries to repair the worst of them. "For my colleagues at school, it was normal. Oliver is not there 2 or 3 days, and he comes back to school with a cast."

Improbably, given the severity of his disease, Semler avoided life in a wheelchair—though his growth was stunted and he stands 4 feet 8 inches tall. He attended medical school and became a pediatrician at the University of Cologne in Germany, where he cares for about 250 children with his condition. Semler is now preparing for a first in OI and well

PHOTO: DAVID KLAMMER

Published by AAAS

Afflicted by a bone disease he now treats, Oliver Semler hopes a new therapy can arrest it before birth.

PHOTO: COURTESY J. OLIVER SEMLER

beyond: a clinical trial of a stem cell treatment for afflicted fetuses, which aims to give them a healthier start to life than he had himself.

The trial, still being planned, is one of a handful being designed in Europe and the United States for arguably the trickiest patient population there is: pregnant women and their fetuses. After decades of hopes raised and dashed, pediatricians, immunologists, and others are cautiously hopeful that new biological insights and a push for treatment from parents-to-be could turn the tide for prenatal stem cell therapy. "I think [there's] a lot more of an understanding about what's feasible, what's safe, what's ethical," says Anna David, who studies fetal therapy at University College London and is collaborating with Semler on the OI trial.

Even trials with just 30 or so mothers, the target for the OI study, require herculean effort: a dozen academic and industry partners, tens of doctors, millions of dollars. A high-profile failure—or worse, injury to the mother or her fetus—could set the field back decades. "That's what keeps me up at night," David says. "Safety, trying to tick all the boxes, thinking as much as possible" about everything that could go wrong. Some fetuses have already been treated on an ad hoc basis, with encouraging results, and that's one factor spurring the trials. But so is the chance that a vial of the right cells, administered at the right moment, could arrest a devastating disease before birth.

BACK IN THE 1980s, when Semler was in elementary school, hopes ran high for treating fetuses with stem cells. Because the fetal immune system is still developing and some of its sentries, such as the T cells, are not fully functional, doctors believed that fetuses would easily accept foreign cells—unlike even a baby, who might need chemotherapy or other toxic treatment to suppress the immune system. The transplanted cells would flourish into healthy blood cells, immune cells, or other elements the fetus lacked, the thinking went, thereby halting damage that a disease was already inflicting in the womb. Maria Grazia Roncarolo, then a young pediatric immunologist, remembers the heady days in Lyon, France, where this theory was put to the test.

In 1988 and 1989 at Edouard Herriot Hospital, two fetuses whose blood cell markers showed they had severe immune disorders became the first ever to receive a cell transplant. Doctors led by Jean-Louis Touraine infused them through the umbilical vein with blood stem cells from 7- to 10-week-old aborted fetuses. Roncarolo helped monitor the first baby after he was born. With a little boy wriggling in front of her, "I was really totally excited," she says. "I thought that I found a way to cure every genetic disease. In my complete young naïveté, I thought I'd found a solution."

A third fetus brought everyone back to Earth. Instead of an immune deficiency, this one had thalassemia, a life-threatening blood disorder. Hoping to treat the fetus when its immune system was especially primitive and the disease in a nascent stage, doctors infused stem cells into the fetus's abdominal cavity at just 12 weeks' gestation. To their shock, the cells were rejected and the transplant failed.

"The assumption we had that the fetus was tolerant [of foreign cells] was wrong," Roncarolo says. Brutally disappointed, she overhauled her career, returned to basic research, and now works at Stanford University in Palo Alto, California, where she studies stem cell transplants and immune tolerance. Meanwhile, the rest of the Lyon team persevered, but outcomes were dismal. Two fetuses died before birth from the treatment; in two others the cells—all from aborted fetuses—didn't engraft. At that point, the doctors halted their efforts.

Outwardly, interest in stem cell therapy for fetuses faded. But behind the scenes, a small cohort of researchers embarked on a years-long journey to understand why it hadn't worked when immunology suggested it should. Pregnancy is a unique setting, with two genetically distinct beings that intertwine without rejecting each other—a setting that, in theory at least, should offer an opening for cell therapy.

As a child, Oliver Semler had repeated fractures.

In the late 2000s came a string of discoveries that helped explain both the successes and the failures. For one thing, researchers learned that fetal T cells are, in fact, able to reject foreign invaders—whether a microbe or a cell transplant—more readily than thought. Later, other researchers found that it probably wasn't just the fetus that had doomed those earlier cell transplants. Maternal immune cells are inevitably circulating through the fetus, and in mouse studies, these cells rebelled against the donor cells.

A group led by Mike McCune at the University of California, San Francisco (UCSF), however, discovered an encouraging phenomenon: Some of the fetus's T cells are primed to convert to so-called T-regulatory cells, which can tolerate outsiders, particularly cells from the mother. In mice, "if you match the transplant to the mom, [nearly] all of the fetuses you transplant can engraft," says Tippi Mackenzie, a pediatric surgeon at UCSF. She began wondering

Published by AAAS

whether donor cells from the mother might be the most likely to get accepted. "It was this eureka moment," she says.

Mackenzie and others also found that in animals, higher doses of donor maternal cells were more effective, and that injecting them into the fetal bloodstream further enhanced success. In humans, this becomes possible after 18 weeks' gestation, by funneling cells through the umbilical vein.

AS SCIENCE PLUGGED ALONG, desperate parents sought drastic solutions. In early 2002, Stefan and Madeleine Karlsson, living in Uppsala, Sweden, and pregnant with their first child, were riding a roller coaster of uncertainty. A 20-week ultrasound had raised red flags, but additional testing turned up nothing. At 25 weeks, doctors "discovered that something was wrong," Stefan Karlsson recalls. "After this we did ultrasounds every week, and the next week all was fine, and the week after that something was wrong again, but no one knew what." At 30 weeks' gestation—a little more than 2 months before normal delivery—doctors shipped off fetal cells for analysis. The results were devastating. The Karlssons learned that their daughter had OI, later diagnosed as the most severe form, type III. Only one other child in the world, in Canada, has been identified with the same mutation. That baby died at 5 months old.

The Karlssons were referred to the Karolinska University Hospital in Stockholm, where physicians proposed a radical strategy: Harvest a specific type of stem cell from the liver of an aborted fetus and infuse it through the umbilical vein into the fetus that Madeleine was carrying. The family agreed.

"We transplanted about 6 million cells," says Cecilia Götherström of Karolinska, who produced the cells. The stem cells used, mesenchymal stem cells (MSCs), are thought to elicit a less vigorous immune reaction than blood stem cells, and MSCs can develop into bone, along with other connective tissues. The hope was that MSCs would take hold and produce new, healthy bone.

The transplanted cells were not a genetic match for the mother or the fetus, whom the Karlssons would name Olivia. Nonetheless, at least some of them engrafted: When Olivia was 9 months old a bone biopsy revealed donor cells mixed in with her own.

At first Olivia did better than the doctors anticipated. But around her sixth birthday she began to deteriorate and suffered a spate of fractures. Eventually, Götherström and her colleagues retransplanted Olivia with more MSCs from the same donor tissue. Olivia's fractures abated, and she has been retransplanted every 4 years since. Now 14 years old, she has not had a fracture in 18 months, surprising her doctors. Olivia's father says she swims for physical therapy, enjoys sewing, arts and crafts, and, like most teenagers, shopping for clothes and spending time with her friends.

Götherström knows that, without a control group, there's no way to be sure that MSCs helped Olivia. Still, heartened by Olivia's experience, she and her colleagues later shipped fetal MSCs to Singapore for another treatment of a fetus with OI, and infused a third whose parents traveled to Sweden from their home in Ireland; that child is now a toddler. And, with others, Götherström began laying the groundwork to test whether in utero therapy really was making a difference. "We've got to do a clinical trial before people do this willy-nilly," says David in the United Kingdom—especially because interest in such treatments could surge as it becomes easier to diagnose serious disorders in utero.

Two years ago, Semler and Götherström met at a conference on OI in Wilmington, Delaware. Until then, Semler hadn't considered stem cell transplants a viable treatment for the disorder. But he knew better than almost anyone that severe OI takes hold before birth, when the skeleton is still forming. On ultrasounds, doctors detect shortened leg bones and even fractures. Supplying MSCs as early as possible, Semler thought, might give a fetus a better chance to build healthy bone, without the side effects of a bone marrow transplant after birth. And Götherström believed that infusing the cells before birth had a better chance of working in part because of differences in fetal circulation: Cells infused into the bloodstream are less likely to get stuck in the lungs and never make it to their destination than they are in a baby.

An OI trial, called BOOSTB4, is now edging toward the starting line. Götherström, David, Semler, and others have secured more than $9 million from the European Union and Swedish Research Council, and are crafting their protocol. Starting later this year, they hope to begin recruiting 15 families across Europe with fetuses shown by ultra-

Gene therapy gets a high-stakes test

By **Jennifer Couzin-Frankel**

At University College London, Anna David is developing a clinical trial even more radical than prenatal stem cell therapy: the first ever test of gene therapy in pregnancy. David cares for mothers and their fetuses suffering from fetal growth restriction (FGR), which affects about 7% of pregnancies. Blood flow to the placenta falters, often for unknown reasons, and many babies are born, and die, far too early.

FGR can be diagnosed by ultrasound, but there's no treatment. So David plans to send a new gene to the placenta via the mother's blood supply. She hopes to begin enrolling pregnant women sometime next year. David, who first proposed the study back in 2008, says it's been a slog to get to this point. "People don't want to test out therapies in pregnancy."

When that treatment is gene therapy, the jitters magnify exponentially. Gene therapy has had a checkered history in children and adults, with side effects including cancer and at least one death. So rather than introduce new genes to the fetus itself, "we've tried to be a little bit more clever," David says, by targeting the uterine arteries.

Working in animals, David has generated evidence that overexpressing the vascular endothelial growth factor (*VEGF*) gene, which promotes blood vessel growth and flow, might help. As a vector for the gene, she's using a well-studied adenovirus that is designed to disappear fairly quickly, and that doesn't cross the placenta to the fetus.

David's team has received nearly $8 million, most of it from the European Medicines Agency, to fund the project, whose acronym aptly spells EVERREST; it also includes a natural history study of FGR and reproductive toxicology work. With a pilot trial she hopes will begin in 2017, David anticipates offering gene therapy to between 15 and 24 women.

In utero gene therapy is "pretty rough going," notes Timothy Crombleholme, a fetal and pediatric surgeon at Children's Hospital Colorado in Denver, who is trying to treat intrauterine growth restriction in animals by transferring a different gene—insulinlike growth factor 1—into the placenta. Ultimately, he believes, "the risk-benefit ratio would swing heavily towards treating in utero as long as we've done our due diligence." For families, that time may already have arrived, especially when the alternative is bleak: doing nothing or delivering the baby—and hoping she survives. ■

Published by AAAS

sound and DNA testing to have severe OI and in the second or third trimester infuse them with MSCs from fetal liver cells, just like those Olivia received. The babies will receive additional infusions after birth. They'll be compared with another cohort of 15, who will receive MSC transplants only after birth, and with historical controls. All the children will be followed for 10 years, to see whether those treated in utero and afterward have fewer fractures, better bone mineral density, better growth, and better quality of life.

"We are not aiming for a cure," cautions Götherström. "It's not that they will get up from a wheelchair and start running." Rather, she hopes that halving the number of fractures, which, along with demonstrating safety, is the trial's goal, will make a major difference to patients and families. And simply pulling off a trial like this one "could open up a wider field of other disorders being treated" before birth, she says.

IN THE UNITED STATES, Mackenzie's group and another have embraced a different approach: treating fetuses with blood stem cells culled from their mothers, the strategy she began exploring in animals almost a decade ago. Last month she filed a request with the U.S. Food and Drug Administration to offer hematopoietic stem cells to fetuses with α thalassemia, a severe form of the disease that is fatal before or soon after birth. Prenatal cell therapy failed for thalassemia nearly 30 years ago, but Mackenzie hopes for a different outcome this time.

Because the cells come from the mother, she expects them to be better tolerated and will infuse a much higher dose into the umbilical vein after 18 weeks' gestation. "If that trial doesn't work, then we would like to go earlier," Mackenzie says, potentially by injecting cells into the fetus's heart.

Alan Flake at The Children's Hospital of Philadelphia (CHOP) in Pennsylvania is planning a similar clinical trial of maternal stem cells in fetuses with sickle cell anemia, a painful, debilitating disease that often shortens life. (Flake led the only known fetal stem cell transplant in the United States. Done in the mid-1990s on a fetus with a severe immune deficiency, it used stem cells donated by the father, and was considered largely successful.) Flake declined to speak with *Science*, citing a hectic schedule and concerns about hyping a treatment not yet in trials, but in a video on CHOP's website he was upbeat. "The research results are absolutely convincing that we can achieve a cure of sickle cell disease," Flake says. The hospital is raising several million dollars to support a trial.

The medical risks of in utero cell transplants are generally considered modest, though they include pregnancy loss. Similar procedures, such as fetal blood transfusions for anemia, are already offered. But some worry about risk that may come after birth. "We are relying on the idea that the stem cells will proliferate and differentiate into what we want," says David Chitayat, a medical geneticist at The Hospital for Sick Children in Toronto, Canada. Chitayat wonders whether proliferation could proceed in unexpected ways, for example leading to tumors—a worry that cuts across many stem cell therapies. (Mackenzie notes that it shouldn't be a problem for her strategy, because she plans to use the same kind of cells as bone marrow transplants, which haven't caused tumors.)

Some also worry that the mother's interests will be subsumed by her fetus's, especially as fetal treatment programs are usually based in children's hospitals, and pediatricians consider the fetus their patient. "There's a person who has that uterus in her body" that needs to be accessed, says Anne Drapkin Lyerly, a bioethicist at the University of North Carolina, Chapel Hill, who has studied fetal surgeries for spina bifida and other conditions. Any treatment will affect not just the fetus, but "the people who are going to be caring for this baby," she says. Lyerly admits she doesn't know exactly how these concerns should be addressed, beyond careful attention to the mother's experience, including how she may react if treatment causes pregnancy loss.

The doctors driving these trials are acutely aware of the risks, but emphasize that the conditions they aim to treat cause lifelong suffering and often early death. If prenatal stem cell therapy proves successful and safe, ethicists and other physicians agree, it could be life-changing. And as Chitayat notes, "if you don't start, you don't know."

Sharing why he embraced cell therapy 14 years ago, when his wife was 7 months pregnant and the field far murkier than it is today, Stefan Karlsson reaches for an answer any parent can appreciate. "For us it was that we did not see any drawbacks in trying stem cells, there were only advantages," he explains. "And that it could help Olivia." ■

A mother's gift of cells

One strategy for fetal stem cell therapy involves using maternal cells as a treatment for fetal blood diseases like thalassemia.

1 The mother undergoes a **bone marrow harvest** so that doctors can collect blood stem cells.

2 The collected cells are **processed for several hours**, and hematopoietic stem cells are separated out from the mix.

3 The stem cells are **injected through the mother's abdomen** into the umbilical vein of her fetus, under ultrasound guidance.

4 The mother's **stem cells begin circulating** through the fetus's bloodstream and develop into different types of blood and immune cells.

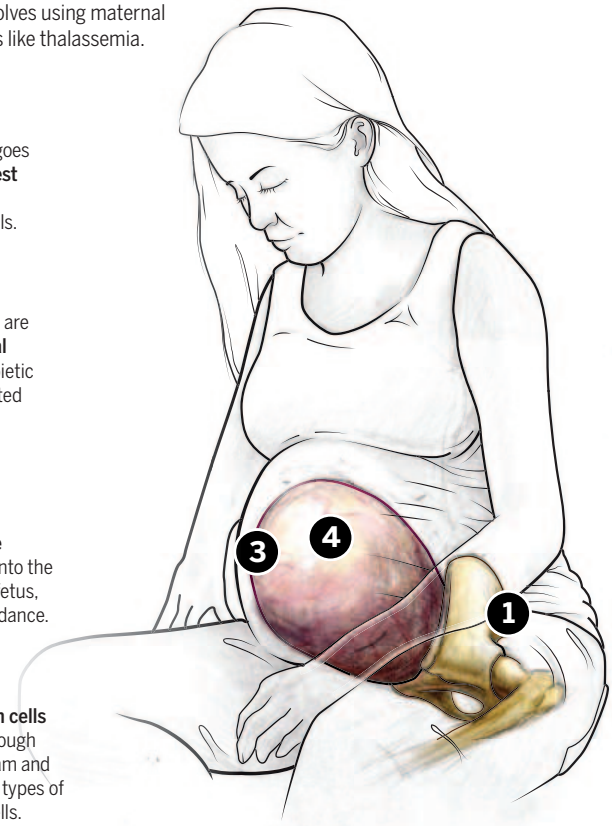

> ***"We've got to do a clinical trial before people do this willy-nilly."***
>
> **Anna David**, University College London

ILLUSTRATION: V. ALTOUNIAN/*SCIENCE*

Published by AAAS

INSIGHTS

PERSPECTIVES

ENVIRONMENT

Tackling mine wastes

Global collaboration is needed to mitigate the environmental impacts of mine wastes

By **Karen Hudson-Edwards**

On 5 November 2015, the Fundão and Santarém mine tailings dams in Minas Gerais, Brazil, failed, releasing 62 million m^3 of sediment and water that destroyed homes, killed at least 17 people, cut off potable water supplies, blanketed more than 650 km of rivers, and flowed into the Atlantic Ocean (see the photo). The tailings dam failure, the largest ever recorded (*1*), demonstrates many of the diverse impacts of mine wastes. How can the potentially severe impacts of mine wastes and the risk of such disasters be reduced?

Mine wastes are unwanted and uneconomic materials (including rock, sediment, tailings, metallurgical wastes, dusts, ash, and processing chemicals) that are found at or near mine sites in virtually every country in the world (*2*). They often contain elevated concentrations of elements such as antimony, arsenic, cadmium, copper, lead, uranium, and zinc. As a result, mine wastes can be toxic, corrosive, or radioactive, or a combination of these. They can therefore pose threats to the health of organisms, plants, and humans if ingested from water, soil, or food grown on the wastes, or inhaled as dust (*3, 4*).

Mine drainage waters are classified as acid, circumneutral, or basic depending on their pH (*5*). Both acidic and basic mine wastes are corrosive and contain potentially toxic or radioactive elements. Globally, acid mine wastes, which arise mainly from the oxidation of iron-sulfide minerals such as pyrite, are the most common. Solid mine wastes often also have a physical as well as chemical impact on the environment. For example, they may cause excessive sedimentation of river systems, altering their natural geomorphological evolution and potentially suffocating aquatic life. Winds can spread these wastes in the form of dust, particularly in arid areas.

Globally, most high-grade ores have already been exploited. Contemporary mining therefore tends to focus on the extraction of lower-grade ores. As a result, current mining operations are associated with higher volumes of waste than previously produced. Historical mine wastes can, however, pose

Department of Earth and Planetary Sciences, Birkbeck, University of London, London WC1E 7HX, UK. E-mail: k.hudson-edwards@bbk.ac.uk

PHOTO: RICARDO MORAES/REUTERS/NEWSCOM

Published by AAAS

Example of the environmental impact of mine wastes. After the 5 November 2015 tailings dam failure in Minas Gerais, Brazil, mine waste flowed through the Doce River into the Atlantic Ocean.

hazards that are potentially just as serious as those resulting from contemporary mining. Mining has occurred since prehistory, and many great empires had active extractive industries. Over time, very large amounts of mining wastes have accumulated. Furthermore, past mining methods were less efficient, environmental protection legislation did not exist, and toxic elements such as mercury were used extensively (as they are in some artisanal mining areas today) to extract ores such as silver and gold (*6*).

There are many examples of historical and contemporary mine wastes posing threats to the environment. For example, in August 2015, waste water and tailings from the Gold Creek Mine flooded into Cement Creek and the Animas River in Colorado, USA, turning them bright yellow. The spill was caused by the attempted remediation of historical mine wastes (*7*).

Contemporary tailings dam spills often affect river basins that have a legacy of historical contamination. On 25 April 1998, the Aznalcóllar spill released ~4 to 5 million m^3 of liquid and tailings bearing arsenic, copper, lead, and zinc to the Río Guadiamar in southwestern Spain (*1*). The tailings from the spill were removed from the floodplain during several cleanup operations, but later research revealed older contaminated alluvium underneath. As the river channel readjusted following the 1998 spill, this historically contaminated sediment was eroded and carried downstream toward Doñana National Park, a UNESCO World Heritage Site (*8*).

Perhaps the most infamous historical mine wastes are those in the Río Tinto Mining District in Andalusia, Spain. Here, more than 5000 years of mining and natural weathering of the sulfide ores have created a strongly acidic (pH < 3) 90-km-long river that bears arsenic, iron, copper, cadmium, nickel, lead, and zinc. Huge piles of waste rock have built up at its headwaters, and red- and yellow-colored alluvium is found along its banks. Gross metal fluxes from historical wastes of the Río Tinto Mining District have a substantial impact on global and local element fluxes: According to calculations by Braungardt *et al.*, 8.1% of the dissolved zinc flux and 1.6% of the dissolved copper flux in global rivers come from the Río Tinto (*9*). Resuspended mine waste dust from the Río Tinto area supplies 32% of the antimony, arsenic, bismuth, cadmium, copper, lead, and zinc to the local atmosphere (*4*), although the mean composition of these elements is below the daily EU limit value of 50 μg m^{-3}.

The global footprint of historical and contemporary mine wastes is clearly substantial. Jones *et al.* (*10*) estimated that 6% of English and Welsh rivers are affected by cadmium-, lead-, and zinc-contaminated discharges from historical mines and weathering of historical mining–contaminated sediments. In Bolivia, 35 km^2 of the Pilcomayo floodplain is covered with heavy metal–contaminated sediments that have been discharged as mining waste over the past 500 years (*11*). Lottermoser (*2*) suggested that ~1 million km^2 globally are covered with mine waste, amounting to several hundred thousand million tons of waste. Although this is a small percentage of Earth's surface, much of it is in inhabited areas or areas of important biodiversity and natural beauty.

Historically, the mining industry has been a vital economic driver, and the industry remains necessary for the global economy as it contributes jobs, social benefits, infrastructure, wealth, and the vast array of goods that are part of everyday modern life. Mine wastes, too, can bring positive benefits. The Río Tinto Mining District is used as a martian analog field site. Along with other mine sites, the district is also a niche host to a large number of species of acid-tolerant microorganisms (*12*) and metal-tolerant plants and organisms. Historical and contemporary wastes can also be recycled or remined to extract their economic commodities.

Overall, however, the environmental impacts of mine wastes are negative. Around the globe, tailings dam accidents, physical weathering, and biogeochemical reactions lead to the remobilization of mine wastes from mine sites to the atmosphere, soils, water, and biosphere, posing risks to global ecosystem and human health. We lack knowledge of many of these environmentally critical reactions. For example, we do not fully understand the biogeochemical behavior of many elements in mine wastes, including the elements bismuth, lithium, and tantalum, which are extensively mined today for use in modern technologies such as solar panels, batteries, and mobile phones. To predict future impacts, we also need to build knowledge of the influence of climate change on the rates of mine waste remobilization.

Many modern mining operations manage mine wastes at their source, thus preventing their remobilization. In these operations,

Published by AAAS

funds are also put in place at the start of, and throughout, mining to pay for eventual closure and remediation. Should such practices continue, the global impacts of mine waste remobilization could be reduced in the future. Nevertheless, the amounts of mine wastes are still rising substantially, and it is now time to make a concerted global effort to predict and mitigate the potentially negative impacts of their remobilization.

Consolidated databases and inventories for mine waste sites have been created for some countries, such as Ireland (*13*). Such efforts need to be extended to the whole world to determine the impacts of global mining on biogeochemical cycles and on human and ecosystem health. Information is required on the locations, sizes, geochemistry, mineralogy, type of mining and processing, and other factors that will enable the global-scale sources, sinks, pathways, and fluxes of mine wastes to be quantified and their hazards identified. Such databases and research can be developed using existing information from academic studies, mining companies, and governmental surveys. However, ultimately they require the sponsorship and participation of funding agencies, governments and nongovernmental organizations, and international bodies such as the United Nations Environment Programme (UNEP), the World Business Council for Sustainable Development (WBCSD), and the Global Environment Facility to help with funding, data acquisition, implementing solutions, and raising global awareness of mine waste impacts and their remediation. ■

REFERENCES AND NOTES

1. WISE (World Information Service on Energy) Uranium Project, Chronology of Major Tailings Dam Failures; www.wise-uranium.org/mdaf.html.
2. B. G. Lottermoser, *Mine Wastes: Characterization, Treatment and Environmental Impacts* (Springer, ed. 3, 2010).
3. O. Morton-Bermea *et al.*, *Environ. Earth Sci.* **74**, 1161 (2015).
4. A. M. Sanchez de la Campa *et al.*, *Environ. Res.* **111**, 1018 (2011).
5. D. K. Nordstrom *et al.*, *Appl. Geochem.* **57**, 3 (2015).
6. C. A. Cooke *et al.*, *Ambio* **40**, 18 (2011).
7. U.S. Environmental Protection Agency, Emergency Response to August 2015 Release from Gold King Mine; www.epa.gov/goldkingmine.
8. P. A. Brewer *et al.*, in *Proceedings from the International Symposium on Major Challenge in Tailings Dams, 71st Annual Meeting of the International Commission on Large Dams (ICOLD), Montréal, Canada*, pp. 46–56 (2003).
9. C. B. Braungardt *et al.*, *Appl. Geochem.* **18**, 1757 (2003).
10. A. Jones *et al.*, *Environ. Sci. Pollut. Res.* **20**, 7570 (2013).
11. S. Balaban *et al.*, *Environ. Earth Sci.* **74**, 4685 (2015).
12. R. Amils, D. Fernandez-Remolar, *Life* **4**, 511 (2014).
13. Geological Survey of Ireland, Inventory of Mine Waste Sites; www.gsi.ie/Programmes/Minerals/Databases/Inventory+Of+Mine+Waste+Sites.htm.

ACKNOWLEDGMENTS

I thank D. Kossoff for insightful comments.

10.1126/science.aaf3354

Mycorrhizal associates. Trees allocate carbon to ectomycorrhizal fungi such as *Amanita muscaria*.

PHOTO: MARCEL VAN DER HEIJDEN

ECOLOGY

Underground networking

Fungal networks transfer carbon between forest trees

By **Marcel G. A. van der Heijden**[1,2,3]

Almost all land plants, including most trees, shrubs, and herbs, form symbiotic associations with mycorrhizal fungi (*1*). These soil fungi acquire nutrients that they transfer to their plant hosts in exchange for carbon (see the photo). Plants in natural vegetation can acquire up to 80% of nitrogen and phosphorus from their mycorrhizal associates (*2*). Individual mycorrhizal fungi can simultaneously colonize many plant hosts of the same species or different species. As a result, plants in natural communities are interconnected by mycorrhizal networks. Earlier studies with small tree seedlings revealed that carbon is transferred from one plant to another through these under-

[1]*Plant-Soil-Interactions, Agroscope, Institute for Sustainability Sciences, 8046 Zurich, Switzerland.* [2]*Department of Evolutionary Biology and Environmental Studies, University of Zurich, 8057 Zurich, Switzerland.* [3]*Plant-Microbe Interactions, Institute of Environmental Biology, Faculty of Science, Utrecht University, 3584 CH Utrecht, Netherlands. E-mail: marcel.vanderheijden@agroscope.admin.ch*

Published by AAAS

ground mycorrhizal pipelines (*3*). On page 342 of this issue, Klein *et al.* (*4*) show that interplant carbon transfer is not confined to tree seedlings.

The authors report forest-scale evidence for substantial tree-to-tree carbon transfer. Their results, obtained from 40-m-tall trees in a mixed forest in Switzerland, show that the equivalent of 280 kg carbon per hectare is transferred yearly between tree roots of different tree species. This is equivalent to 4% of the forest's net carbon uptake (also called its net primary productivity). Furthermore, the results indicate that underground mycorrhizal networks connecting the different tree species are, most likely, responsible for this carbon transfer.

Klein *et al.* use a highly sophisticated system to study carbon cycling in forests. Over a 5-year period, they labeled 40-m-tall Norway spruce trees with isotopically depleted CO_2, using a tall canopy crane and many porous tubes that released the labeled CO_2 near the branches of the trees (*5*). They then measured the carbon isotope signature in fine roots of neighboring unlabeled trees belonging to different taxa and also in unlabeled control trees that were not near labeled trees. The authors also measured the carbon signature in fruiting bodies (mushrooms) of mycorrhizal fungi that associate with the trees (called ectomycorrhizal fungi) and in fruiting bodies of litter-degrading saprotrophic fungi that do not form mycorrhizal associations. They found depleted carbon in ectomycorrhizal fungal fruiting bodies near the labeled Norway spruce trees but not in the nonmycorrhizal saprotrophic fungi, nor in herbs that associated with a different type of mycorrhizal fungi (called arbuscular mycorrhizal fungi). These latter measurements acted as controls and provide evidence that ectomycorrhizal fungi act as carbon conducts.

The total amount of carbon that trees allocate to mycorrhizal fungi can be substantial; Wallander *et al.* have published estimates of 700 to 900 kg per hectare of forest (*6*). A proportion of this (~150 kg per hectare) can be found in mycorrhizal root tips. Part of the carbon found in neighboring tree roots by Klein *et al.* may have remained in the fungal tissue of mycorrhizal structures (the fungal mantle surrounding tree roots and the fungal structures inside the roots) and was not transferred to the tree tissue (*7*). However, a substantial fraction of carbon was also acquired by the neighboring trees, as evidenced by enhanced isotope signal in the stems. This carbon may either have come directly from mycorrhizal fungi or some of it was acquired from the surrounding soil, e.g., through recapture of carbon from root exudates or root remains (*8*).

Overall, the results imply that large mature forest trees jointly maintain a common mycorrhizal network and that carbon can move freely from one tree to another tree through these belowground fungal highways (see the figure). These underground networks can be highly complex because each individual tree and fungus has its own network and can associate with different partners.

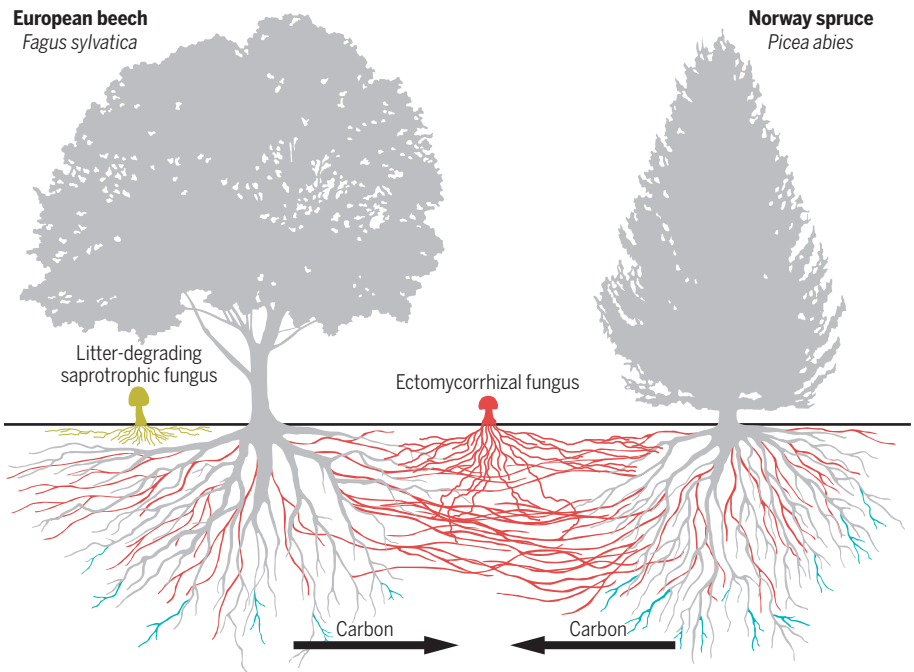

Underground networks. Forest trees are interconnected through extensive mycorrhizal fungal networks that can interlink different tree species. Carbon can move from one three to another through these hyphal networks.

ILLUSTRATION: MODIFIED AFTER (*2*) BY P. HUEY/*SCIENCE*

The results reported by Klein *et al.* also have implications for key questions in mycorrhizal research: Why is this symbiosis so widespread and why has it evolved so successfully? The observation that 4% of net primary productivity is transferred to neighboring trees suggests that carbon is a nonlimiting resource, and not growth-limiting for these large trees (*9*). Thus, carbon allocation and loss to mycorrhizal fungi does not necessarily impair plant fitness. The exchange of "nonlimiting" carbon for nutrients may be one of the key factors responsible for the evolutionary stability of the mycorrhizal symbiosis (*10*).

Klein *et al.* (*4*) measured 17 trees, 5 of which were the labeled trees that grew close to each other and were not randomly dispersed. As a result, replication is low. Further work in different forest ecosystems is needed to confirm the findings and their general validity. An interesting further question is which fraction of the carbon transferred between trees actually leaves the fungal tissue and is transferred to the tree.

An increasing number of studies show that belowground ecosystems are highly complex and diverse (*11*, *12*). Klein *et al.*'s study adds a new dimension to this, revealing that substantial amounts of carbon can move from one tree root system to another. Further work now needs to investigate whether trees benefit from this resource sharing and whether being interconnected through such mycorrhizal fungal networks enhances plant fitness and forest stability over evolutionary time. ■

REFERENCES AND NOTES

1. S. E. Smith, D. J. Read, *Mycorrhizal Symbiosis* (Academic Press, Cambridge, UK, ed. 3, 2008).
2. M. G. A. van der Heijden, F. Martin, M. A. Selosse, I. R. Sanders, *New Phyt.* **205**, 1406 (2015).
3. S. W. Simard, D. A. Perry, M. D. Jones, D. D. Myrold, D. M. Durall, R. Molina, *Nature* **388**, 579 (1997).
4. T. Klein, R. T. W. Siegwolf, C. Körner, *Science* **352**, 342 (2016).
5. C. Körner *et al.*, *Science* **309**, 1360 (2005).
6. H. Wallander, L. O. Nilsson, D. Hagerberg, E. Bååth, *New Phyt.* **151**, 753 (2001).
7. A. H. Fitter, J. D. Graves, N. K. Watkins, D. Robinson, C. Scrimgeour, *Func. Ecol.* **12**, 406 (1998).
8. D. L. Jones, C. Nguyen, R. D. Finlay, *Plant Soil* **321**, 5 (2009).
9. C. Körner, *J. Ecol.* **91**, 4 (2003).
10. F. Walder, M. G. A. van der Heijden, *Nat. Plants* **1**, 15159 (2015).
11. L. Tedersoo *et al.*, *Science* **346**, 1256688 (2014).
12. F. T. de Vries *et al.*, *Proc. Nat. Acad. Sci. USA* **110**, 14296 (2014).

ACKNOWLEDGMENTS

M.H. thanks F. Walder and K. Hartman for helpful comments, U. Kaufmann for artwork, and the national research program "soil as a resource" of the Swiss National Science Foundation (grant 143065) for funding.

10.1126/science.aaf4694

Published by AAAS

CLIMATE ECONOMICS

Opportunities for advances in climate change economics

Target carbon's costs, policy designs, and developing countries

By **M. Burke,[1] M. Craxton,[1] C. D. Kolstad,[1*] C. Onda,[1] H. Allcott,[2] E. Baker,[3] L. Barrage,[4] R. Carson,[5] K. Gillingham,[6] J. Graff-Zivin,[5] M. Greenstone,[7] S. Hallegatte,[8] W. M. Hanemann,[9] G. Heal,[10] S. Hsiang,[11] B. Jones,[12] D. L. Kelly,[13] R. Kopp,[14] M. Kotchen,[6] R. Mendelsohn,[6] K. Meng,[15] G. Metcalf,[16] J. Moreno-Cruz,[17] R. Pindyck,[18] S. Rose,[19] I. Rudik,[20] J. Stock,[21] R. S. J. Tol[22]**

There have been dramatic advances in understanding the physical science of climate change, facilitated by substantial and reliable research support. The social value of these advances depends on understanding their implications for society, an arena where research support has been more modest and research progress slower. Some advances have been made in understanding and formalizing climate-economy linkages, but knowledge gaps remain [e.g., as discussed in (*1*, *2*)]. We outline three areas where we believe research progress on climate economics is both sorely needed, in light of policy relevance, and possible within the next few years given appropriate funding: (i) refining the social cost of carbon (SCC), (ii) improving understanding of the consequences of particular policies, and (iii) better understanding of the economic impacts and policy choices in developing economies.

POLICY

REFINING THE SCC. The SCC is an estimate of the damages caused by emitting carbon. Formally, the SCC estimates the monetized change in social welfare over all future time from emitting one more tonne of carbon today, conditional on a specific trajectory of future global emissions and economic and demographic growth. An understanding of the SCC is used in developing regulations directly or indirectly linked to climate change and is vital to building political support for domestic climate policies worldwide (*3*, *4*). The SCC is usually estimated using an integrated assessment model (IAM), although other methods, such as expert elicitation, are being explored. Widely used values for the SCC have been criticized, with particular skepticism surrounding the empirical basis used by IAMs to project climate damages and, thus, the SCC (*5*). We highlight five promising research directions to refine SCC estimates, which might then improve how they are used in policy (*6*).

First, a better understanding of the economic impact of extreme climatic events is required. Economists can build on advances in our physical understanding of these low-probability, high-damage events (*7*) to study how changing likelihoods could affect damage estimates.

Second, research is needed on how to represent potential damages that are poorly captured in typical economic output measures. Such "nonmarket" damages, which include potential costs of increased civil conflict, changes in human health, and biodiversity loss, could be sizeable (*8*) but are omitted from current damage estimates or are represented in an ad hoc way (e.g., as a simple multiple of market damages). Research should explore new methods for measuring key nonmarket outcomes [e.g., (*9*)], and should clarify how to incorporate accumulating evidence into IAMs.

Third, work is required on how aggregate economic output is affected by changes in climate (*10*). How climate change or the rate of change affect the level of output, the growth rate of output, the stock of capital, or some other metric, can have a major impact on the SCC, because it is a measure of accumulated damage over time. Current evidence is mixed, and resolving the debate will be crucial.

The fourth area for research is adaptation, which has the potential to drastically change the gross damages from climate change. It is one of the least explored areas of climate economics, and little guidance is available on how to build adaptation into damage functions. For example, how farmers may adapt agricultural practices dampens agronomic estimates of damage from a change in climate. A frontier for research is how to con-

[1]Stanford University, Stanford, CA, USA. [2]New York University, New York, NY, USA. [3]University of Massachusetts, Amherst, MA, USA. [4]Brown University, Providence, RI, USA. [5]University of California, San Diego, CA, USA. [6]Yale University, New Haven, CT, USA. [7]University of Chicago, Chicago, IL, USA. [8]World Bank, Washington, DC, USA. [9]Arizona State University, Tempe, AZ, USA. [10]Columbia University, New York, NY, USA. [11]University of California, Berkeley, CA, USA. [12]Northwestern University, Evanston, IL, USA. [13]University of Miami, Coral Gables, FL, USA. [14]Resources for the Future, Washington, DC, USA. [15]University of California, Santa Barbara, CA, USA. [16]Tufts University, Medford, MA, USA. [17]Georgia Institute of Technology, Atlanta, GA, USA. [18]Massachusetts Institute of Technology, Cambridge, MA, USA. [19]Electric Power Research Institute, Palo Alto, CA, USA. [20]Iowa State University, Ames, IA, USA. [21]Harvard University, Cambridge, MA, USA. [22]University of Sussex, Falmer, UK, and Vrije Universiteit Amsterdam, Netherlands. *E-mail: ckolstad@stanford.edu

ILLUSTRATION: DAVIDE/BONAZZI/@SALZMANART

Published by AAAS

nect impact estimates derived from historical short-run fluctuations in weather to potential future impacts from longer-run changes (incorporating adaptation) in climate. Rigorous methods for doing this are in their infancy and urgently need improvement (*11*).

Finally, SCC-focused IAMs, the main tools for aggregating economic costs of mitigation and adaptation, as well as economic damage from changed climate to produce SCC estimates, need a more structured way of incorporating new information. Damage functions in IAMs can rely in part on studies completed more than 20 years ago (*12*). The treatment of uncertainty in IAMs needs improvement, with research needed on the computational challenges of explicitly including decision-making under uncertainty (*13*). Last, the choice in most existing IAMs to examine the well-being (utility) of a representative agent may be inappropriate if impacts differ greatly by region or by type of agent. Understanding nuances of how these models aggregate costs and benefits across disparate regions and populations is of particular importance.

IMPROVING POLICY DESIGN. Political resistance to carbon pricing in many jurisdictions, as well as the emergence of a piecemeal approach to domestic and international climate policy-making, means that it is insufficient to study merely how to price the climate externality in a "first-best" world with no other economic distortions. Although many existing "second-best" policies, such as efficiency standards and support for renewables, are cost-ineffective relative to carbon pricing (*14*), they continue to be implemented for political, distributional, or other reasons.

Research must consider practical dimensions of optimally designing and implementing such policies. First, more rigorous ex post empirical analysis of energy and environmental policies will be critical (*15*). Policies such as carbon pricing schemes, tradable obligations, fuel taxes, renewable portfolio standards, and energy efficiency standards are already in use in different countries and will become more common as countries try to operationalize their pledges in the United Nations Framework Convention on Climate Change process. But there is often little empirical evidence on individual- or market-level responses to these policies. Existing evidence suggests that behavioral responses to a given policy can drive a wedge between ex ante engineering estimates of program costs and benefits and ex post estimates of true costs and benefits (*16*). More evidence with rigorous analysis is sorely needed on a range of mitigation and adaptation policies.

In the long term, the costs of addressing climate change using current technologies could be very large, which makes technological progress critical. A large body of work on the rate and direction of innovation exists, but research is needed on what combinations of R&D and climate policies shape innovation and diffusion of low-carbon technologies (*17*).

BEYOND ADVANCED ECONOMIES. Much of the existing research on climate damages or policies has focused on the developed world. This is problematic, both because developing countries currently represent the majority of the world's population and greenhouse gas emissions and because the nature of impacts and context for policy choice could differ greatly relative to developed regions.

A first key research need is to rigorously quantify how vulnerability to climate change shifts as countries develop and the structure of their economies changes, a question on which evidence is mixed (*10*, *11*). Attention to the burden borne by low-income households will be important, as little is known about how changes in climate and climate policy affect these households' productivity and livelihoods. Growing availability of expenditure surveys in these countries, potentially combined with remotely sensed measures of livelihoods (*18*), could allow rapid progress.

"...what combinations of R&D and climate policies shape innovation and diffusion of low-carbon technologies [?]..."

Emerging economies will play an essential role in the success of mitigation efforts, given their projected demographic and economic growth. Thus, a second key research agenda will be to better understand climate mitigation options in the developing world. Carbon mitigation proposals have faced opposition in many developing countries because of concern that they could hamper growth by constraining energy supply and increasing costs (although a few middle-income countries are experimenting with carbon pricing). Yet, because tax evasion rates are lower for energy taxes compared with income taxes (19), implementing a carbon tax may allow developing-country governments to simultaneously achieve climate-policy goals and raise revenue. Research is needed on the feasibility of different policy tools in different political and institutional contexts, because the appropriateness of policies may differ in countries with heavily subsidized fossil fuels, high rates of tax evasion, and large informal and state-owned sectors. An understanding of how innovation policy can be effective and, more broadly, of how to make low-carbon technologies adoptable in the developing world, is also essential.

Our list of research priorities is not comprehensive and likely debatable. Others, including some of the authors, might emphasize other priorities (e.g., research on temporal discounting, international policy cooperation and coordination, and political economy). But what is crystal clear is that society is hampered in using natural science knowledge of climate change because of gaps in the knowledge of economic and social dimensions of climate change. A much more substantive research program on the economics of climate change is essential; otherwise, effective policy solutions with broad societal support will remain elusive. Future research must continue to include data-intensive empirical work to strengthen the foundations upon which policy-relevant "end products" (such as the SCC) are based, along with research aimed at defining and reframing key questions. ■

REFERENCES AND NOTES

1. O. R. Edenhofer *et al.*, Eds., *Climate Change 2014: Mitigation of Climate Change: Contribution of Working Group III to the Fifth Assessment Report of the Intergovernmental Panel on Climate Change* (Cambridge Univ. Press, New York, 2014).
2. National Research Council, *Hidden Costs of Energy: Unpriced Consequences of Energy Production and Use* (National Academies Press, Washington, DC, 2010).
3. M. Greenstone, E. Kopits, A. Wolverton, *Rev. Environ. Econ. Policy* **7**, 23 (2013).
4. Committee on Assessing Approaches to Updating the Social Cost of Carbon, *Assessment of Approaches to Updating the Social Cost of Carbon: Phase 1 Report on a Near-Term Update* (National Academies Press, Washington, DC, 2016).
5. R. S. Pindyck, *J. Econ. Lit.* **51**, 860 (2013).
6. W. Pizer *et al.*, *Science* **346**, 1189 (2014).
7. Committee on Extreme Weather Events and Climate Change Attribution, *Attribution of Extreme Weather Events in the Context of Climate Change* (National Academies Press, Washington, DC, 2016).
8. S. Hsiang, M. Burke, E. Miguel, *Science* **341**, 1235367 (2013).
9. D. J. Benjamin *et al.*, *Am. Econ. Rev.* **102**, 2083 (2012).
10. M. Burke, S. M. Hsiang, E. Miguel, *Nature* **527**, 235 (2015).
11. M. Dell, B. F. Jones, B. A. Olken, *J. Econ. Lit.* **52**, 740 (2014).
12. S. K. Rose *et al.*, *Understanding the Social Cost of Carbon: A Technical Assessment* (Report 3002004657, Electric Power Research Institute, Palo Alto, CA, 2014)
13. D. L. Kelly, C. D. Kolstad, *J. Econ. Dyn. Control* **23**, 491 (1999).
14. S. Borenstein, *J. Econ. Perspect.* **26**, 67 (2012).
15. M. Greenstone, in *New Perspectives on Regulation*, D. Moss, and J. Cisternino, Eds. (The Tobin Project, Cambridge, MA, 2009).
16. K. Gillingham, K. K. Palmer, *Rev. Environ. Econ. Policy* **8**, 18 (2014).
17. D. Popp, R. G. Newell, A. B. Jaffe, in *Handbook of the Economics of Innovation*, vol. 2, B. H. Hall, N. Rosenberg, Eds. (Elsevier–North Holland, Amsterdam, 2010).
18. J. V. Henderson, A. Storeygard, D. N. Weil, *Am. Econ. Rev.* **102**, 994 (2012).
19. A. A. Liu, *J. Environ. Econ. Manage.* **66**, 656 (2013).

ACKNOWLEDGMENTS

This article is based on discussions at a conference at Stanford University 9 and 10 October 2015. The conference organizers acknowledge support from the U.S. Department of Energy (Climate and Environmental Sciences Division, Office of Science) and from Stanford University (Stanford Environmental and Energy Policy Analysis Center, Stanford Institute for Economic Policy Research, and Precourt Institute for Energy). The views articulated here should not be ascribed to the funding organizations.

10.1126/science.aad9634

Published by AAAS

SYNTHETIC CHEMISTRY

The straight dope on the scope of chemical reactions

Complementary strategies are needed for the analysis and reporting of synthetic methods

By **T. Gensch** *and* **F. Glorius**

More than 100 million molecular compounds have been reported, and the many synthetic methods that have been developed are the source of this diversity. Reports of new synthetic reactions often include substrate scope—that is, how reactivity varied for molecules with the same main reaction center and a variety of different substituents at secondary positions (see the figure, panel A). However, chemists often pursue very complex target molecules (e.g., natural products), and most steps involve reactants bearing many substituents whose presence can adversely affect the outcome. We highlight different tools that are emerging to help chemists determine, "Will this reaction work for my molecule?"

Steric and electronic influences on the reaction center are generally evaluated by varying each of these parameters systematically with different substituents (see the figure, panel B). Predictions can be made by using computationally aided substrate-scope design and statistical analysis of reaction outcomes that can even reach quantitative agreement with experiment (*1*). However, it can be difficult to discretely evaluate the tolerance of a functional group independently of its electronic and steric impact on a reaction center. Synthetic availability of complex starting materials can be a further limiting factor.

A recently introduced complementary approach to this traditional substrate scope is intermolecular reaction screening, where functional-group tolerance is assessed with additives carrying specific functional groups added to reactions of the standard substrate. This easy-to-use formalized protocol, termed "robustness screen" (see the figure, panel C), enables the expedient evaluation of inhibition and decomposition involving individual functional groups independent of interfering steric or electronic effects and requires very little extra synthetic work (*2*–*4*).

Organisch-Chemisches Institut, Westfälische Wilhelms-Universität Münster, Corrensstrasse 40, 48149 Münster, Germany. E-mail: glorius@uni-muenster.de

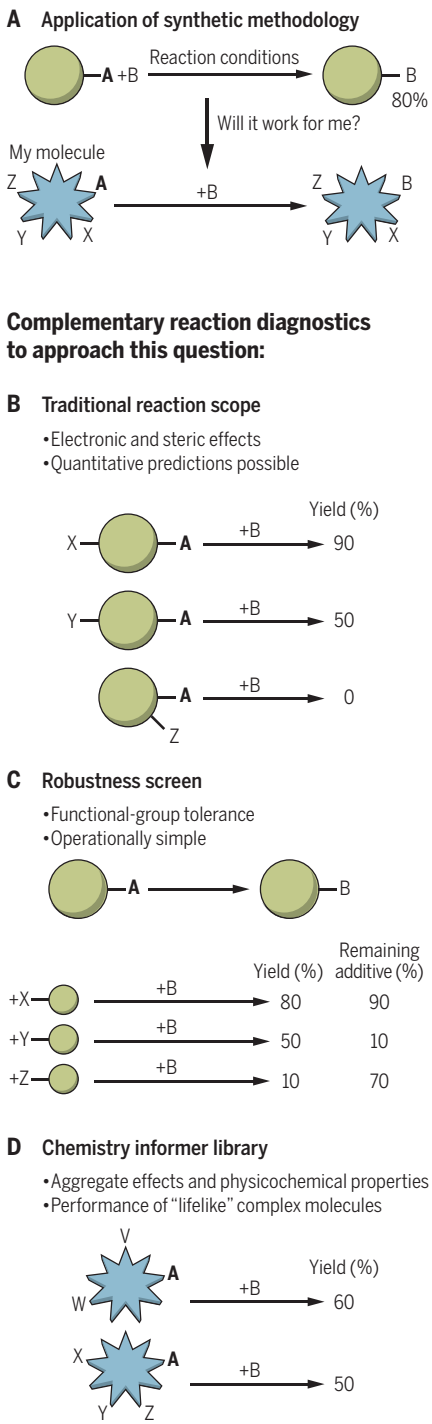

However, the consideration of separated influences of electronic, steric, and functional factors alone may not be adequate in predicting a complex molecule's performance in a reaction. Compound properties emerge from the entirety of molecular features, such as solubility, aggregation behavior, and other physicochemical properties. Krska, Dreher, and co-workers (*5*) now note that the examples reported in methodology publications often bear little resemblance to pharmaceutically relevant molecules, as demonstrated by a comparison of molecular properties of clinically approved drugs with scope examples from reports of relevant synthetic methods.

Guided by a technique from chemoinformatics, the "chemical space" encompassing druglike molecules can be described and visualized in terms of such properties. Sets of complex, druglike molecules were next used as substrates for three test case transformations. These so-called chemistry informer libraries (see the figure, panel D) were selected in such a way that the corresponding reaction products of a set would cover large parts of the chemical space. The widely varying yields obtained by this complex substrate approach show that the diversity of physicochemical properties and whole-molecule effects must be considered in method optimization.

This strategy presents a reaction diagnostic applicable to any reaction type. It raises an awareness of compound properties not present in the simple molecules constituting traditional scope tables of published methodology. The approach is, in principle, amenable to statistical analysis of reaction outcomes in terms of substrate properties if sufficiently large data sets are obtained. To establish a widespread use of chemistry informer library analysis, the availability of appropriate medium- to high-complexity starting materials should be addressed, especially for applications in academic groups that do not have access to extensive libraries of intermediates from drug development.

An ideal report of a new synthetic method should display information on trends regarding steric and electronic effects on the reaction center. In addition, a broad under-

Making assessments. (**A**) Judging the utility of a reported method for a specific synthetic problem requires evaluating the reactivity of substrates that have been reported; here, the reaction center group is denoted "A" and other letters depict various substituents. (**B** to **D**) Complementary reaction diagnostics that can be used for assessing different aspects of chemical reactivity include (B) traditional reaction scope, (C) robustness screens, and (D) chemistry informer libraries.

GRAPHIC: P. HUEY/*SCIENCE*

Published by AAAS

standing of functional-group tolerance and protecting-group stability would be desirable, although the synthetic effort required in a traditional scope is a limiting factor. Thus, approaches like the robustness screen or chemistry informer libraries can expedite additional insight into the functional-group tolerance and performance of more complex molecules with a range of physicochemical properties. Currently, practices range from, on one end, demonstrating some hundreds of examples with functional and protecting groups, systematic trends on electronic factors, and the inclusion of low-yielding and failed substrates. On the other end, a handful of results with the best yields are selected, offering very basic substituent variation and no systematic investigation of reactivity trends.

In a competitive field, the pressure to publish a new method quickly and the notion that low yields in the scope table might decrease the value of a manuscript to a reviewer can lead to a selection bias. Substrates are made and tried that will most likely react in a good yield and avoid suboptimal results; any failures are not reported. However, for any potential user, knowing the limits of a reaction is helpful, and, ironically, a reader might infer that any substrate not shown will not provide a satisfactory outcome in the reaction. Knowing the limitations of an otherwise useful transformation can even stimulate research to improve the reaction system and help expand the set of widely useful synthetic methods. Finally, we encourage a discussion in the community on these matters and hope that along with the robustness screen and chemistry informer libraries, innovative concepts will be advanced. ■

"...the robustness screen or chemistry informer libraries can expedite additional insight into the functional-group tolerance..."

REFERENCES AND NOTES

1. E. N. Bess, A. J. Bischoff, M. S. Sigman, *Proc. Natl. Acad. Sci. U.S.A.* **111**, 14698 (2014).
2. K. D. Collins, F. Glorius, *Nat. Chem.* **5**, 597 (2013).
3. K. D. Collins, A. Rühling, F. Glorius, *Nat. Protoc.* **9**, 1348 (2014).
4. K. D. Collins, F. Glorius, *Acc. Chem. Res.* **48**, 619 (2015).
5. P. S. Kutchukian *et al.*, *Chem. Sci.* **7**, 2604 (2016).

ACKNOWLEDGMENTS

We thank K. D. Collins and E. A. Standley for fruitful discussions.

10.1126/science.aaf3539

CELL BIOLOGY

When cells push the envelope

Nuclear integrity is temporarily compromised to accommodate cell migration

By **Brian Burke**

By enclosing chromosomes within a nuclear envelope (NE), eukaryotic cells are able to segregate transcription and translation, key activities involved in gene expression (*1*). The implication is that maintenance of the NE as a selective barrier represents an essential aspect of normal cellular physiology. However, it also presents the cell with the predicament of how to accommodate a membrane-limited organelle that might occupy a substantial portion of the cell volume. On pages 353 and 359 of this issue, Denais *et al.* (*2*) and Raab *et al.* (*3*), respectively, report that the physical size and mechanical properties of the nucleus may have dramatic effects on the behavior of motile cells.

The most prominent features of the NE are inner and outer nuclear membranes (INM and ONM) that are separated by a perinuclear space. The NE is periodically traversed by nuclear pore complexes that regulate the trafficking of macromolecules between the nucleus and cytoplasm. The other major component of the NE is the nuclear lamina. In most mammalian cells, this is a relatively thin (10 to 30 nm) protein meshwork that lines the nuclear face of the INM and is associated with a variety of INM proteins. The lamina also provides anchoring sites at the nuclear periphery for higher-order chromatin domains.

The major building blocks of the nuclear lamina are the A- and B-type lamins (*4*). In mammalian somatic cells, the former are represented primarily by lamin A and lamin C. B-type lamins, B1 and B2, are expressed in all nucleated cells. A-type lamins, by contrast, are absent from early embryonic cells (*5*). Even in adults, certain cell types do not express A-type lamins. Some cancer cells also display reduced A-type lamin expression, a characteristic that has been linked to increased invasiveness (*6*).

Recent studies have revealed that A-type lamin expression may be influenced by mechanical properties of the extracellular environment (*7*). For instance, fibroblasts grown on stiff substrates display higher lamin A/C expression than those grown on softer or more deformable substrates. In softer tissues, such as brain and fat, lamin A/C expression is substantially lower than in stiffer tissues such as bone and muscle. Such differences in lamin A/C expression are reflected in altered nuclear plasticity. Indeed, fibroblasts derived from mice lacking a functional *Lmna* gene (which encodes lamin A/C) display misshapen nuclei (*5*) that are prone to rupture during cell migration. Thus, the lamina plays an important role in the maintenance of NE integrity as well as in the organization of the nucleus as a whole.

In higher cells, the barrier function of the NE is transiently breached during each cell division to allow the condensed chromosomes access to the mitotic spindle. During interphase, however, loss of NE integrity has been documented only in certain pathological states. For example, transient NE ruptures have been observed in cells harboring *LMNA* mutations (*8*) as well as in cells expressing the HIV Vpr protein (*9*). A similar phenomenon has been reported in several cancer cell lines (*10*). Denais *et al.* and Raab *et al.* document transient NE ruptures in cells migrating in confined environments (see the figure). The implication is that this may be a far more common phenomenon than is currently appreciated and that organisms must have mechanisms to deal with this nuclear wear and tear.

Both Denais *et al.* and Raab *et al.* took advantage of microfabricated substrates on which cells can migrate through channels or constrictions of various dimensions. Denais *et al.*, using a variety of tumor cell lines, found that constrictions with a cross-sectional area below a critical value of ~20 μm^2 caused a factor of 10 increase in the number of cells displaying NE ruptures. Raab *et al.*, using human dendritic cells as well as a human cell line, came to very similar conclusions. Both groups also documented related phenomena in intact mouse tissues.

What happens at the rupture site? NE ruptures always occur at the leading tip of the nucleus as it traverses the constriction and invariably feature the localized loss of nuclear lamins and nuclear pore complexes. The occurrence of NE ruptures appears to mirror increased nuclear pressure, with chromatin often being extruded into the cytoplasm. It is also apparent that the fre-

Institute of Medical Biology, 8A Biomedical Grove, 06-06 Immunos, 138648 Singapore. E-mail: brian.burke@imb.a-star.edu.sg

Published by AAAS

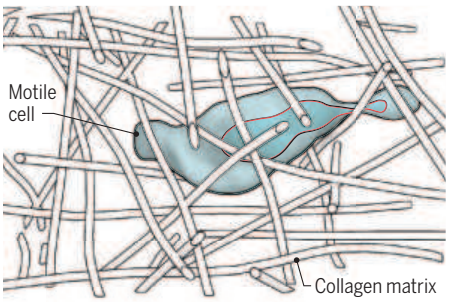

Cell migration blocked

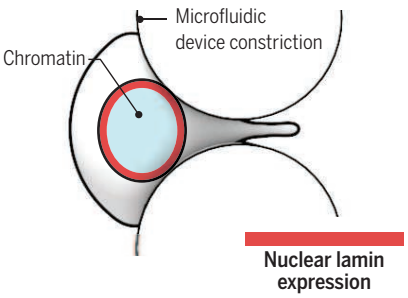

Cell migration proceeds

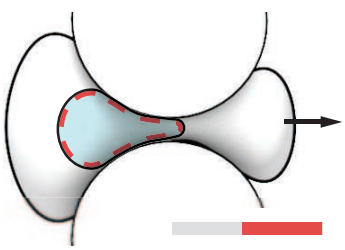

Cell migration proceeds with nuclear rupture

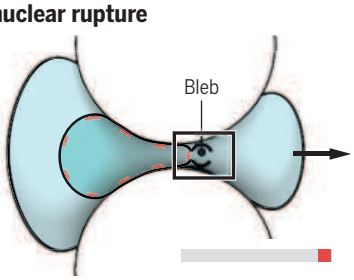

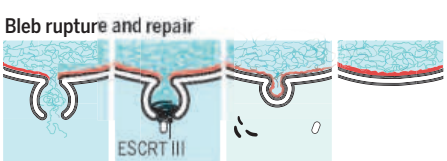

Nuclear wear and tear. As a cell moves within a confined environment, its nuclear membrane will temporarily rupture and then get repaired. Reduced structural stability of the nucleus facilitates cell motility. This is particularly the case with cells that have decreased A-type lamins. ESCRT III machinery is recruited to the lesion to reseal the nuclear envelope.

quency of these events increases in response to reduced expression of lamins A/C and B2. Conversely, as previously reported (*11*), increased A-type lamin expression restricts nuclear deformation and prevents cell migration through constrictions. Evidently, the composition of the lamina must be fine-tuned in such a way as to limit NE rupture without constraining migration.

Denais *et al.* and Raab *et al.* documented the cellular reaction to NE ruptures. Although the nature of any DNA damage is uncertain, mechanical shearing of the DNA might trigger the DNA damage response, as could DNA exposure to cytoplasmic factors. At the same time, ESCRT III (endosomal sorting complex required for transport III) (*12*) components are recruited to the nuclear membrane lesion. ESCRT III is required in the formation of multivesicular endosomes, for the separation of daughter cells (abscission) after cytokinesis, and for the budding of enveloped viruses from the surface of an infected cell. ESCRT III also mediates resealing of the nuclear membranes at the end of mitosis (*13*, *14*). What all of these processes have in common is a requirement for annular fusion at the cytoplasmic surface of various membranes. Clearly, resealing of the nuclear membranes after NE rupture would be predicted to entail exactly this type of activity.

It is clear from Denais *et al.* and Raab *et al.* why lower A-type lamin levels would be associated with increased cell invasiveness. At the same time, such cells display greater susceptibility to NE rupture, with increased genome instability potentially promoting further cancer progression. However, NE rupture could also be the Achilles' heel in these cells because the repair processes, either of the DNA or of the nuclear membranes, might represent viable therapeutic targets. In any event, Denais *et al.* and Raab *et al.* have opened a new window on the dynamics of the NE and nuclear lamina and provide a foundation for new basic and translational research efforts. ■

REFERENCES

1. K. L. Wilson, S. C. Dawson, *J. Cell Biol.* **195**, 171 (2011).
2. C. M. Denais *et al.*, *Science* **352**, 353 (2016).
3. M. Raab *et al.*, *Science* **352**, 359 (2016).
4. B. Burke, C. L. Stewart, *Nat. Rev. Mol. Cell Biol.* **14**, 13 (2013).
5. T. Sullivan *et al.*, *J. Cell Biol.* **147**, 913 (1999).
6. T. Harada *et al.*, *J. Cell Biol.* **204**, 669 (2014).
7. J. Swift *et al.*, *Science* **341**, 1240104 (2013).
8. C. Tamiello *et al.*, *Nucleus* **4**, 61 (2013).
9. C. M. de Noronha *et al.*, *Science* **294**, 1105 (2001).
10. J. D. Vargas *et al.*, *Nucleus* **3**, 88 (2012).
11. A. C. Rowat *et al.*, *J. Biol. Chem.* **288**, 8610 (2013).
12. W. M. Henne *et al.*, *Cold Spring Harb. Perspect. Biol.* **5**, a016766 (2013).
13. Y. Olmos *et al.*, *Nature* **522**, 236 (2015).
14. M. Vietri *et al.*, *Nature* **522**, 231 (2015).

10.1126/science.aaf7735

PHYSICS

Toward single-atom memory

Single holmium atoms can be used as a stable magnetic memory

By **Alexander Ako Khajetoorians**[1] *and* **Andreas J. Heinrich**[2]

Storing information in an ensemble of single-atom magnets represents the ultimate miniaturization of data storage technology, in which two specific orientations of each atomic magnetic moment represent a bit (a 0 or 1) of information (see the figure, panel A). The inherent dilemma in using a single-atom magnet is keeping it magnetized—or, in other words, being able to hold the information in one of the bit states without an external magnetic field for a useful amount of time and at practical temperatures (*1*, *2*). This phenomenon of magnetic remanence is difficult to realize from a single atom, in part because diminished robustness against fluctuations from the environment can unintentionally flip the magnetic state, thus wiping out the magnetic memory. A recent attempt to observe remanence in a single atom (*3*) proved premature, as the results were incompatible with the magnetic ground state of that system (*4*) and could not be reproduced (*4*, *5*). Hence, the question of whether this defining property of a single-atom magnet can actually be achieved has remained an open question until now. On page 318 of this issue, Donati *et al.* (*6*) demonstrate that single holmium atoms exhibit magnetic remanence up to temperatures of 40 K, much higher than previous records of atomic-scale magnets composed of 3 to 12 atoms (*1*, *2*, *5*)—a record in both size and stability for any magnet.

> *"The inherent dilemma in using a single-atom magnet is keeping it magnetized..."*

A requirement for remanence in an atom

[1]Radboud University, 6525 AJ Nijmegen, Netherlands.
[2]IBM, Almaden Research Center, San Jose, CA 95120, USA.
E-mail: a.khajetoorians@science.ru.nl

ILLUSTRATION: V. ALTOUNIAN/SCIENCE

Published by AAAS

adsorbed on a single surface is a large energy barrier that separates two distinct magnetic ground states. This so-called magnetic anisotropy energy (MAE) (see the figure, panel B) was shown to be large for single Co atoms, relative to the bulk, adsorbed on a Pt surface (*7*). At a temperature on the order of the MAE, the magnetic moment should "freeze" on one side of the barrier. This discovery paved a decade-long path, based on x-ray absorption spectroscopy (XAS) and spin-resolved scanning tunneling microscopy (STM), toward realizing magnetic remanence at sufficiently low temperatures (*8*). Although the MAE of a single Co atom has been boosted to the theoretical limit (*9*), the observation of remanence in a single-atom magnet has remained elusive because of the pronounced quantum nature of single-atom spins.

Quantum mechanics restricts the magnetic moment to discrete orientations related to the quantum number J_z, and the energy of each discrete state (see the figure, panel B) is dictated by the local environment or crystal field. In certain cases where the crystal field symmetry is relatively low, shortcuts can be made through the barrier (dashed blue arrow in the figure). This makes the magnetic moment exquisitely sensitive to interactions with electrons and phonons (lattice vibrations), which can exchange angular momentum and connect a ground state with J_z states on the other side of the MAE barrier. For two-fold symmetry (*1*, *2*, *10*), ground-state reversal can occur with just one electron, even in the presence of a large MAE. Therefore, in addition to decoupling the atomic moment from electron and phonon reservoirs, it is necessary to engineer an energy landscape where the magnetic ground states are insensitive to such electron processes (*10*).

"...arrays of single-atom magnets may be used for future memory devices."

Donati *et al.* create such an energy landscape in the form of a four-fold symmetric environment for Ho atoms on MgO. By using circularly polarized XAS and magnetic circular dichroism (XMCD), which is sensitive to the magnetic orientation of the spins in a given magnetic field, they observe a magnetic hysteresis and remanence of an ensemble of Ho atoms. In combination with calculations, they convincingly demonstrate that the observed remanence results from the protection of the Ho ground states from single-electron processes by the four-fold symmetry (see the figure, panel B), which only allows for higher-order processes involving two or more electrons—an observation that they corroborate with measurements on varying thicknesses of the MgO insulating layer. The localized nature of its 4*f* orbitals and a few atomic layers of MgO are sufficient to decouple the Ho moment from the silver metallic electrode, making electron scattering processes as well as phonon excitations highly improbable and thereby establishing a single-atom magnet.

The stability of a single Ho atom on MgO is more robust than one of the best-known molecular magnets (*11*). Theoretically, the symmetry protection shown here is not element-specific, necessitating further investigations with both XMCD and down to an individual atom with spin-resolved STM. It will be imperative to investigate whether remanence can be seen at higher temperatures for viable application, and whether single atoms can be read and written one at a time with electrical current (*1*, *2*). Toward this end, experiments focusing on the dynamical manipulation of an individual atomic spin will be central to efforts to develop single-atom magnets for quantum memory and processing technology (*12*). The present work strongly suggests that arrays of single-atom magnets may be used for future memory devices. Such work could also be extended to spin-logic operations with single atoms (*13*), provided that a suitable route toward magnetic coupling between such spin centers can be engineered. ■

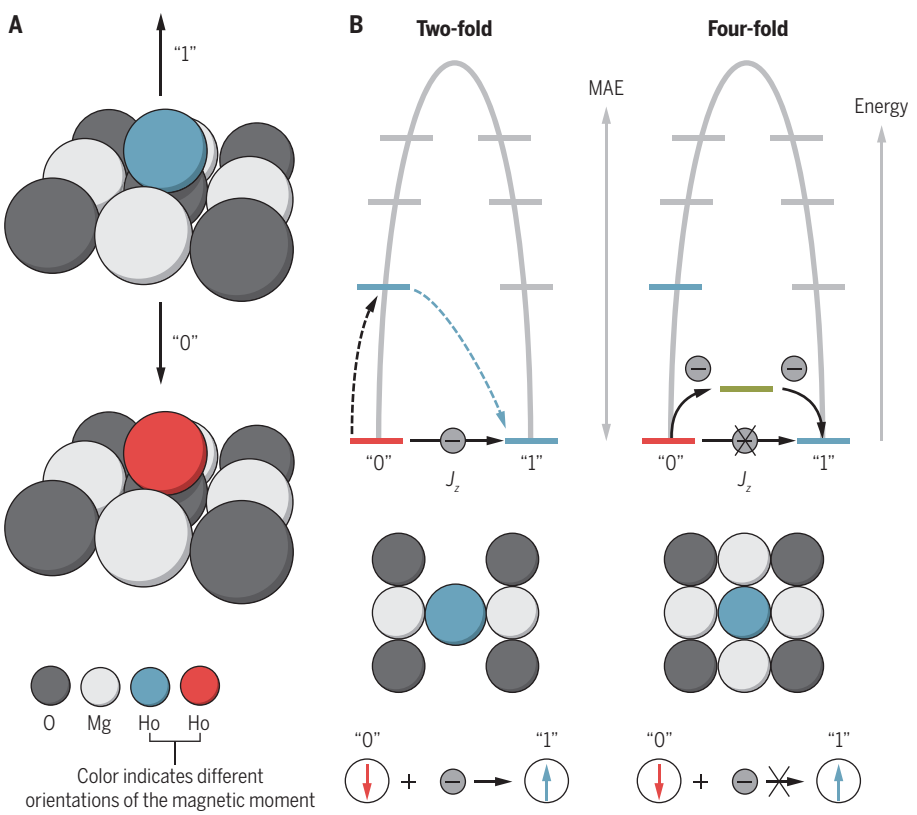

ILLUSTRATION: P. HUEY/*SCIENCE*

A single-atom memory. (**A**) The orientation of the magnetic moment is represented at a 0 or 1 state. (**B**) The energy barriers, defined by the magnetic anisotropy energy (MAE) for a single magnetic atom in a two-fold and four-fold symmetric environment. For a two-fold environment, a single electron can induce a reversal of the magnetic state bypassing the barrier, whereas the four-fold environment protects against such reversal because two or more electrons are needed.

REFERENCES

1. A. A. Khajetoorians *et al.*, *Science* **339**, 55 (2013).
2. S. Loth, S. Baumann, C. P. Lutz, D. M. Eigler, A. J. Heinrich, *Science* **335**, 196 (2012).
3. T. Miyamachi *et al.*, *Nature* **503**, 242 (2013).
4. F. Donati *et al.*, *Phys. Rev. Lett.* **113**, 237201 (2014).
5. M. Steinbrecher *et al.*, *Nat. Commun.* 10.1038/ncomms10454 (2016).
6. F. Donati *et al.*, *Science* **352**, 318 (2016).
7. P. Gambardella *et al.*, *Science* **300**, 1130 (2003).
8. F. Meier, L. Zhou, J. Wiebe, R. Wiesendanger, *Science* **320**, 82 (2008).
9. I. G. Rau *et al.*, *Science* **344**, 988 (2014).
10. C. Hübner, B. Baxevanis, A. A. Khajetoorians, D. Pfannkuche, *Phys. Rev. B* **90**, 155134 (2014).
11. K. R. Meihaus, J. R. Long, *J. Am. Chem. Soc.* **135**, 17952 (2013).
12. S. Baumann *et al.*, *Science* **350**, 417 (2015).
13. A. A. Khajetoorians, J. Wiebe, B. Chilian, R. Wiesendanger, *Science* **332**, 1062 (2011).

10.1126/science.aaf2481

Published by AAAS

TISSUE REGENERATION

A scaffold immune microenvironment

Local immune cells create conditions that support tissue regeneration

By **Stephen F. Badylak**[1,2,3]

The immune system plays a critical role in wound healing, in both host defense and tissue repair. Strategies that use biologic scaffolds to support tissue reconstruction emphasize this essential contribution of representative immune cells. The findings by Sadtler *et al.* (*1*) on page *366* in this issue highlight how the plasticity and diversity of macrophages and lymphocytes support this approach to tissue repair.

Macrophages and T cells have generally been considered only in the context of mammalian defense against pathogens or response to foreign materials. Although recognized as essential for survival and protection against the daily onslaught of ubiquitous pathogens, most attempts at designing and manufacturing implantable devices have focused on strategies to circumvent the body's immune surveillance and response mechanisms, or suppress the "inflammatory" events associated with their presence.

Cell-based mediators of inflammation, rejection, and fibrosis, although previously considered undesirable, are essential components of normal mammalian tissue and organ development (*2, 3*), homeostasis (*4*, *5*), and, ironically, resolution of the proinflammatory process *(6–8)*. These same cells are required participants for true regeneration in species such as the axolotyl (*9*). Even more remarkable is that cells once considered as terminally differentiated mononuclear leukocytes can actually proliferate and function as regulators of the intensity and duration of inflammation and healing (*10*, *11*). Further, the cross-talk that occurs between cells of the innate and adaptive immune system and stem or progenitor cells serves to emphasize the highly orchestrated fashion in which the human body conducts the daily business of survival (*12*, *13*).

The field of stem cell biology has heightened our appreciation of the role of the microenvironment in determining cell fate (*14*, *15*). It has long been recognized that the microenvironment influences more than stem and progenitor cells, and Sadtler *et al.* nicely demonstrate the effect of an extracellular matrix scaffold microenvironment on cells of the immune system. The authors show that in the experimental context of muscle injury in a mouse, bioscaffolds composed of natural extracellular matrix (derived from porcine tissue) induce a cascade of immune cell events that creates a microenvironmental niche conducive to repair (see the figure). This scaffold immune microenvironment involves T helper 2 (T_H2) cells that depend on signaling by mammalian target of rapamycin complex 2 (mTORC2), which drives the activation of T cells to the T_H2 phenotype. The T_H2 cells release anti-inflammatory cytokines and also activate local macrophages toward an "M2" phenotype, which mitigates inflammatory processes. The findings of Sadtler *et al.* provide a new view of how the immune response to biomaterials should be considered in the development of scaffolds for tissue regeneration, and how modulation of the immune response may be part of regenerative therapies.

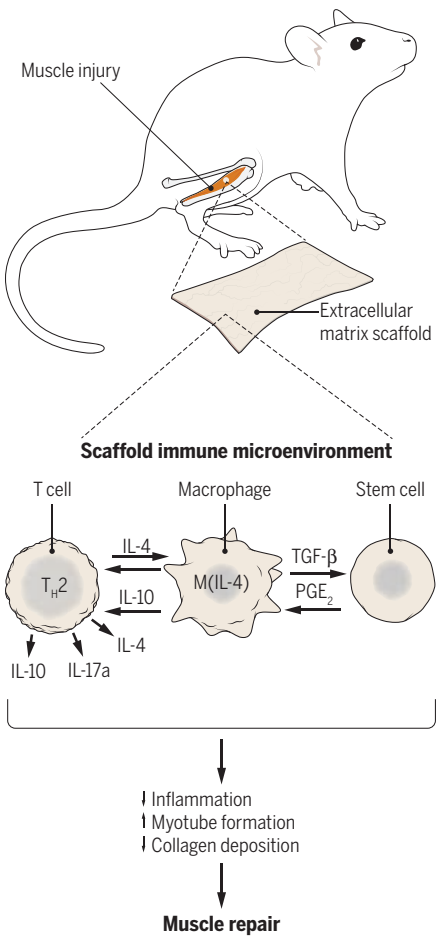

Immune cell support. An implanted scaffold can support muscle regeneration when specific T cells and macrophages locally modify the microenvironment to reduce inflammation and support myotube development. IL, interleukin; PGE_2, prostaglandin E2; TGF-β, transforming growth factor–β.

The emergence and popularity of biomedical engineering is arguably the best example of the benefits of breaking down artificial barriers between developmental biology, immunology, biomaterials science, medicine, molecular biology, and biomedical engineering. Such silos only serve to hinder inevitable discovery that occurs when alternative perspectives are provided. Application of the quantitative principles of engineering to the more qualitative aspects of medicine and biology has given birth to not only new degree-granting programs at academic institutions but a new generation of medical device companies. With long-held beliefs in biology continuing to be challenged—such as the singular role for macrophages in chronic inflammation—and the ever-expanding availability of tools to interrogate the structure and function of cells, tissues, and organs, it seems inevitable that our understanding of biology, health, and disease will be remarkably different within the next decade. ■

[1]McGowan Institute for Regenerative Medicine, University of Pittsburgh, Pittsburgh, PA, USA. [2]Department of Surgery, University of Pittsburgh, PA, USA. [3]Department of Bioengineering, University of Pittsburgh, Pittsburgh, PA, USA. E-mail: badylaks@upmc.edu

REFERENCES

1. K. Sadtler *et al.*, *Science* **352**, 366 (2016).
2. J. M. Leid *et al.*, *Circ. Res.* 10.1161/CIRCRESAHA.115.308270 (2016).
3. T. A. Wynn, A. Chawla, J. W. Pollard, *Nature* **496**, 445 (2013).
4. C. C. Bain, A. M. Mowat, *Immunol. Rev.* **260**, 102 (2014).
5. F. Ginhoux, S. Jung, *Nat. Rev. Immunol.* **14**, 392 (2014).
6. D. P. Vasconcelos *et al.*, *Biomaterials* **37**, 116 (2015).
7. M. C. Little, R. J. Hurst, K. J. Else, *J. Immunol.* **193**, 4684 (2014).
8. N. R. Aggarwal, L. S. King, F. R. D'Alessio, *Am. J. Physiol. Lung Cell. Mol. Physiol.* **306**, L709 (2014).
9. J. W. Godwin, A. R. Pinto, N. A. Rosenthal, *Proc. Natl. Acad. Sci. U.S.A.* **110**, 9415 (2013).
10. C. S. Robbins *et al.*, *Nat. Med.* **19**, 1166 (2013).
11. M. H. Sieweke, J. E. Allen, *Science* **342**, 1242974 (2013).
12. M. Wang *et al.*, *Int. J. Biochem. Cell Biol.* **58**, 53 (2015).
13. A. B. Bloom, M. H. Zaman, *Physiol. Genomics* **46**, 309 (2014).
14. F. Gattazzo, A. Urciuolo, P. Bonaldo, *Biochim. Biophys. Acta* **1840**, 2506 (2014).
15. J. L. Inman, C. Robertson, J. D. Mott, M. J. Bissell, *Development* **142**, 1028 (2015).

10.1126/science.aaf7587

ILLUSTRATION: P. HUEY/*SCIENCE*

Published by AAAS

BOOKS *et al.*

ECONOMICS

Banking on balance

Getting ahead at work shouldn't have to mean falling behind at home

By **Janet Gornick**

From the New Deal through the Reagan era, most policy-makers, employers, and labor economists shared a common assumption: Workers (and potential workers) were men—literally, men—who brought to the table their skills and preferences, largely untouched by external distractions. These men had wives who cleaned their homes, cooked their meals, raised their children, and cared for their elderly parents, leaving them free to work for pay, continuously and productively.

The real world, of course, was never that simple or uniform. Today, in most households headed by couples, both partners work for pay. Nearly half of children in the United States are being raised by a sole female breadwinner. So it is remarkable—stunning, in fact—that federal policy-makers, employers, and the economics discipline (feminist economists aside) have largely failed to adapt their theories or practices to acknowledge a world in which most workers must reconcile employment with pressing needs at home.

New employment practices, such as just-in-time scheduling and round-the-clock e-mailing, compounded by changing family demography (especially the rise of single parenting and the increased longevity of elderly family members) have left millions of working Americans perpetually stressed, conflicted, economically insecure, and time-poor. Yet, on the whole, American social and labor market policies, while changing (especially at the subnational level), remain dangerously inadequate and blatantly irrational.

In this ambitious, fast-paced, fact-filled, and accessible book, Heather Boushey hopes to hit the reset button. She aims to do this by offering a thorough, systematic, evidence-based case for a comprehensive package of institutional reforms. These reforms would include expanding rights to paid family and medical leave, extending workers' options for flexible working time, and increasing investments in high-quality nonfamily care. She has a masterful understanding of the nuts and bolts of policy design and has impressively cataloged an array of promising state and local examples.

The reviewer is at the Graduate Center of the City University of New York, New York, NY 10016, USA. E-mail: jgornick@gc.cuny.edu

Paid time off, access to childcare, and flexible scheduling make economic sense, argues Boushey.

Finding Time
The Economics of Work-Life Conflict
Heather Boushey
Harvard University Press, 2016. 357 pp.

Her policy proposals are not off the beaten path, but her overall argument—simple as it sounds—is a fresh one. Boushey aims to recast these reforms as constituting good economics: "The current, tired debate gets stuck on the question of who deserves a handout—a values question—when really we need to be thinking about how keeping people gainfully employed while they care for their families benefits the economy overall. By looking at these questions through the lens of hard-nosed economics, we can chart a new path."

For several years, Boushey has been a leading scholar of the economics of work and family in the United States, always incorporating a strong policy angle into her work. Based in Washington, she has rare expertise in both policy architecture and the mechanics of the American policy-making process.

As Boushey tackles the complexities of work-family policies (she prefers the term "work-life policies" to stress their economy-wide effects), concerns about inequality inform nearly all of her arguments. Drawing on earlier work that she did with lawyer-scholar-activist Joan Williams, *Finding Time* is framed around the insight that the challenge of reconciling employment and family needs affects workers and families differently, depending on (for the most part) their household income level. She separately assesses the hardships and policy needs of low-income families (whom she describes as "stuck"), middle-class families ("stalled"), and professional families ("soaring above and sounding the alarm").

Boushey's voice is a steady one—steely and critical but optimistic and generous. Despite her demonstrable sympathy for lower-earning families (she grew up in one), she refrains from trivializing the needs of highly paid workers or denying the hardships of their affluent families.

Although she is intensely critical of a multitude of harmful employment practices, Boushey seeks institutional explanations rather than demonizing individual employers. And she tends to blame inadequate policy outcomes on poor thinking, insufficient information, timidity, and bad habits—more than on nefarious or hateful political forces.

The book has one notable weakness. By mostly restricting her discussion to U.S. programs and policies, Boushey misses an opportunity to drill down on successful practices in other countries. National-level leave provisions, working time protections, and generous public care services are not the stuff of science fiction. They have been developed and successfully implemented in many other countries.

As another long-time observer of U.S. work-family policy, it is not clear to me that Boushey's profoundly reasonable book will be able to effectively push back against a political landscape that is hostile to government, conflicted about gender equality, and resistant to compromise. For all of our sakes, I hope that I'm wrong.

10.1126/science.aaf3924

PHOTO: DGLIMAGES/ISTOCKPHOTO

Published by AAAS

ASTROPHYSICS

Fear and loathing in the hunt for gravitational waves

One physicist hits the road to explore LIGO's history and the hard feelings that nearly derailed the entire project

By **Adrian Cho**

On 14 September 2015, at 9:50:45 universal time, humans detected for the first time a gravitational wave—a rippling, infinitesimal stretching of spacetime itself set off when two black holes spiraled into each other. That mind-boggling discovery was made by the 1000 physicists working with the Laser Interferometer Gravitational-Wave Observatory (LIGO), a duo of enormous optical instruments in Livingston, Louisiana, and Hanford, Washington. *Black Hole Blues* provides a lively, if not wholly satisfying, account of the 40-year quest to build LIGO.

Black Hole Blues could hardly be timelier, as LIGO researchers announced their discovery on 11 February. However, Janna Levin, a theoretical physicist at Barnard College in New York City, had been working on the book for 4 years. She tells the tale not of the discovery but primarily of building the machines. It's a story worth telling, as even in retrospect it seems nearly miraculous that the National Science Foundation (NSF) would gamble $1.1 billion on the risky experiment, which requires physicists to compare the lengths of each L-shaped interferometer's 4-kilometer-long arms to within 1/10,000 the width of a proton.

The idea behind LIGO sprang from the mind of Rainer Weiss, an experimentalist at the Massachusetts Institute of Technology (MIT) in Cambridge in the late 1960s. It didn't go far until Kip Thorne, a theorist at the California Institute of Technology (Caltech) in Pasadena, took an interest in the 1970s. In 1979, Thorne brought in Ronald Drever, a notoriously difficult Scot, to run Caltech's efforts, as research stalled at MIT. The imperious Rochus "Robbie" Vogt, freshly fired as Caltech provost, took over as director of the project in 1987, after NSF demanded that MIT and Caltech merge efforts.

The infighting within the founding group is legendary. Drever and Weiss couldn't see eye to eye. Vogt fired Drever for giving an unauthorized talk on work related to LIGO and changed the locks on his office. None of this is new. However, in *Black Hole Blues*, Levin gives the principals room to reflect on their problematic history, and it's poignant, for example, to hear Vogt vacillate between defiance and regret as he talks about losing control of the project. "The mistakes I made were because of the information I had at the time," he says. "And because of my temperament." (Drever now suffers from dementia, so Levin relies on interviews recorded by others in 1997 for his side of the story.)

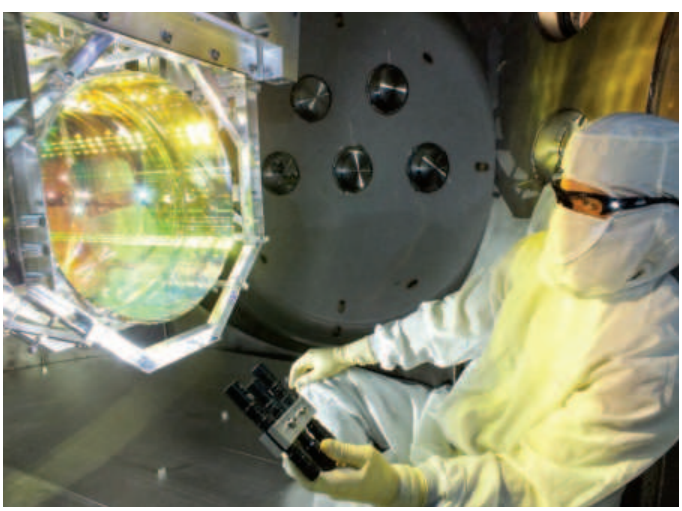

Ninety-nine years after Albert Einstein predicted their existence, LIGO researchers detected the presence of gravitational waves in the fall of 2015.

The book could have gone deeper in several places. For example, Levin recounts how Caltech particle physicist Barry Barish replaced Vogt in 1994, at a time when NSF was about to pull the plug on the project. Barish managed to right the ship and convince NSF to follow through with $300 million for construction. But Levin doesn't explain how Barish did it, even though his overhaul of the project's management may be the real story of LIGO's success. Similarly, she never explains why NSF backed a project that had so many vociferous doubters in the first place.

Black Hole Blues is also a story of Levin's personal introduction to LIGO. She gives first-person accounts of her meetings with the principals and her visits to the LIGO instruments, presenting herself as a stranger in a (somewhat) strange land—she is, after all, a theorist. She refers to her subjects by first names and nicknames: Rai, Kip, Ron, Robbie. Her approach hints at the gonzo journalism of the 1970s.

This tack isn't entirely successful. Instead of so much atmosphere, the book could have used an early chapter explaining how, according to Einstein's general theory of relativity, gravity arises from the warping of spacetime. Without one, the concepts of gravitational waves and black holes may never come into focus for the average reader. Similarly, the book could use a better explanation—and a diagram—of an interferometer.

Moreover, Levin doesn't quite have the chops to write herself into the story. The reader may chuckle at her account of being stuck in a hot car at the Hanford site, afraid to so much as open a window for fear of upsetting a test going on nearby. Often, however, Levin simply gets in the way of the narrative. "I'm using convoluted double negatives because I don't feel myself in a position to more precisely define [John] Wheeler's state of mind," she writes. It's as if you're trying to watch a parade and she keeps stepping in front of you.

Still, *Black Hole Blues* makes an engaging read. It hits all the highlights in the hunt for gravitational waves, including the efforts of Joseph Weber, an electrical engineer at the University of Maryland, College Park, who in 1969 claimed to have spotted the waves as they set massive aluminum cylinders aquiver. When others couldn't reproduce Weber's results, he refused to reconsider and eventually ruined his own reputation. Levin tells that all-too-human story simply, and that's when she is at her best.

The reviewer is at Science, *AAAS, Washington, DC 20005, USA. E-mail: acho@aaas.org*

Black Hole Blues
And Other Songs from Outer Space
Janna Levin
Knopf, 2016. 252 pp.

10.1126/science.aaf5109

PHOTO: ©CALTECH/MIT/LIGO LAB/XINHUA PRESS/CORBIS

Published by AAAS

LETTERS

Edited by **Jennifer Sills**

Financial complexity: Regulating regulation

IN THEIR POLICY FORUM "Complexity theory and financial regulation" (19 February, p. 818), S. Battiston *et al.* present a compelling case that complexity theory—the science of complex adaptive systems—offers insights into how the interconnected economic and financial macrosystem works and, more important, how it fails. They argue that, just as complexity theory has been applied in ecology, so too will these insights lead to better understanding of how the interconnectedness between banks and positive feedback channels move information through the system, which in turn will provide a better understanding of system stability, robustness, and resilience. However, they recognize that this improved model of the financial system will require substantial advancements in the availability of data and the development of quantifiable metrics, and therefore call for such an effort to build a "policy dashboard" that monitors systemic risk and stress-tests the global financial system in real time as we do for the weather. Putting aside how far off it will be before that quantitative modeling project bears fruit, it will be important that it launches with sound premises and foundations.

First, many legal researchers have used complexity theory to shine light on the challenges that regulatory systems face when managing, for example, intellectual property (*1*), the Internet (*2*), the environment (*3*), health care (*4*), and telecommunications (*5*). These efforts, while no further along than those the authors propose for the financial system, nonetheless suggest that legal expertise should be a part of the interdisciplinary team designing the quantitative research project.

Second, there is as much reason to believe that regulatory systems—as highly structured, heterogeneous social systems—are complex adaptive systems as there is to believe that the financial system (and the Internet, environment, and health care) is a complex adaptive system (*6*). Regulatory systems and the socioeconomic systems they are intended to control thus comprise systems of coevolving systems. To be of value, therefore, a "policy dashboard" for the financial system must include a way to monitor the financial regulatory system itself, detect its systemic risk, stress-test its resilience capacity, and understand how it coevolves with banking and other financial system component behaviors. Legal researchers have begun exploring such policy dashboards for policy (*7*), and have also begun quantitative studies of the regulatory system's complex adaptive system behaviors (*8*, *9*).

Third, some answers may be staring us in the face without the need for a full policy dashboard. It does not take complexity theory to know that pollution is bad for the environment. Likewise, some financial system experts have identified low-hanging policy fruit that could lead to substantial stability gains for the system (*10*).

J. B. Ruhl

Vanderbilt University Law School, Nashville, TN 37203, USA. E-mail: jb.ruhl@vanderbilt.edu

REFERENCES

1. D. Tussey, *Loyola U. Chi. Law J.* **37**, 147 (2005).
2. S. Crawford, *Fordham Law Rev.* **74**, 695 (2005).
3. G. Emison, *Duke Env. Law Pol. Forum* **7**, 167 (1996).
4. M. Bloche, *So. Cal. Law Rev.* **82**, 389 (2009).
5. B. Cherry, *Fed. Commerce Law J.* **59**, 369 (2007).
6. J. Ruhl, *Ga. St. Law Rev.* **24**, 885 (2008).
7. J. Ruhl, D. Katz, *Iowa Law Rev.* **101**, 191 (2015).
8. M. Bommarito, D. Katz, *Physica A* **389**, 4195 (2010).
9. R. Boulet *et al.*, in *AI Approaches to the Complexity of Legal Systems* (Springer, 2010), pp. 39–53.
10. M. Ricks, *The Money Problem: Rethinking Financial Regulation* (Univ. of Chicago Press, 2015).

Understanding how the financial system and financial regulation interact could help prevent market failures.

PHOTO: ASSOCIATED PRESS

Financial complexity: Accounting for fraud

THE POLICY FORUM "Complexity theory and financial regulation" (S. Battiston *et al.*, 19 February, p. 818) offers some interesting suggestions regarding the complex dynamics of markets, but it does not address fraud.

How does "traditional economic theory" account for fraud? The role of fraud seems to be rampant at all levels in the case of the 2008 financial crisis in the United States: There was fraud in real estate appraisals (*1*), fraud among accounting firms (*2*), fraud in how the risks associated with novel financial instruments were presented to investors (*3*), and fraud in interbank lending (*4*).

Economist James Galbraith has argued that the existence of a bubble in a stable, regulated market like housing is prima facie evidence of fraud (*5*). William Black, another economist, has asked why neither the U.S. Securities and Exchange Commission nor the Federal Reserve employs a criminologist (*6*).

Explaining the 2008 market failure, and market failures in general, is not a scientific problem so much as a regulatory and enforcement problem. Rather than develop more elaborate models to analyze markets, one simple place to start may be to reinstate regulation like the Glass-Steagall Act (*7*) and to investigate fraud more aggressively.

David Witzling

University of Wisconsin–Milwaukee, Milwaukee, WI 53212, USA. E-mail: drw@frametheweb.com

REFERENCES

1. J. Eaton, "The appraisal bubble," The Center for Public Integrity (2009); www.publicintegrity.org/2009/04/14/2895/appraisal-bubble.
2. R. Wolff, "Lehman Brothers: Financially and morally bankrupt," *The Guardian* (2011); www.theguardian.com/commentisfree/cifamerica/2011/dec/12/lehman-brothers-bankrupt.
3. U.S. Securities and Exchange Commission, "SEC enforcement actions: Addressing misconduct that led to or arose from the financial crisis" (www.sec.gov/spotlight/enf-actions-fc.shtml).
4. "Tracking the libor scandal," *New York Times* (www.nytimes.com/interactive/2015/04/23/business/dealbook/db-libor-timeline.html?_r=0#/#time370_10903).

Published by AAAS

5. A. Sherter, "One word explains what caused the financial crisis: Fraud," CBS MoneyWatch (2010); www.cbsnews.com/news/one-word-explains-what-caused-the-financial-crisis-fraud/.
6. W. K. Black, Levy Institute's Annual Minsky Conference (2009); www.levyinstitute.org/pubs/conf_april09/18th_Minsky_ppt/session1_Black.pdf.
7. N. Irwin, "What is Glass-Steagall? The 82-year-old banking law that stirred the debate," *New York Times* (2015); www.nytimes.com/2015/10/15/upshot/what-is-glass-steagall-the-82-year-old-banking-law-that-stirred-the-debate.html.

Response

IN OUR POLICY FORUM, we argued for the development of a policy dashboard to manage complex financial-economic systems based on an interdisciplinary network analysis and behavioral modeling approach.

Ruhl's first point is that legal expertise should be included in the research design. We agree that this may be useful for developing models. In fact, behavioral agent-based models should incorporate legal regulation and market institutional details.

Protesters accuse CEO Richard S. Fuld Jr. of fraud as he leaves the U.S. Capitol after testifying on the collapse of Lehman Brothers.

Ruhl's second point is that the regulatory system itself should be part of the research and model building. We also agree that the regulatory system and the financial system are coevolving and that ideas from complex systems can be useful to think about this relationship. This is reminiscent of the Lucas critique: Regulation itself affects human behavior through mutual adaptive feedback between individual behavior and regulation (*1*).

However, incorporating the evolution of the regulatory system is more difficult than managing the economic-financial system alone. Research on these coevolving complex systems so far has been mainly qualitative. Haldane's "microscopes and telescopes" (*2*) stresses that the financial-economic system is a complex adaptive "system of systems," including a policy architecture with a layer of national financial systems and economies, a layer of monetary policy, and a layer of global financial architecture.

Even if we do not understand how the regulatory system will evolve, we can test its possible effects and assess plausible alternatives that might improve it. What we advocate should contribute to making evolution of the regulatory system more effective in relation to systemic risk. We can do this even without understanding the long-term evolutionary dynamics of regulation. Complex system models will be not only useful, but essential to gauge effects of regulations.

Finally, Ruhl argues that effective reform measures can already be taken before model building. This may be true, but the point of complexity modeling is to identify possible unintended consequences of regulations. A realistic complexity-based policy dashboard can help to empirically assess reforms before implementing them in real markets. The policy dashboard we propose provides a test bed for such potentially stabilizing regulatory policies.

Witzling argues that fraud played an important role in the financial crisis of 2008. Of course, society has to fight fraud, but removing fraud would not solve the problem. The threat exists already within what is legally possible at the moment. Witzling refers to James Galbraith when he says that "the existence of a bubble in a stable, regulated market like housing is prima facie evidence of fraud." However, one of the essential insights from complex systems is that the bubble and crisis would have occurred without any fraud at all. For example, simple agent-based models of the housing markets, calibrated to U.S. data, generate housing bubbles as soon as leverage levels are turned up to levels that were actually used, and were perfectly legal (*3*, *4*). Furthermore, bubbles and crashes have been frequently observed in controlled laboratory experimental asset markets as the emergent outcome of positive feedback environments (*5*, *6*). The problems that caused the financial crisis of 2008 came from the legal use of excessively high leverage, which generated systemic risk. A model of the reforms developed by the Basel Committee on Bank Supervision illustrates this dramatically (*7*). As soon as the banking sector grows to a certain size, and as soon as it exceeds a leverage threshold that is considerably smaller than that actually used, 10- to 15-year oscillations arise that resemble the Great Moderation (the reduction in economic volatility that began in the 1980s) and subsequent crises, both in magnitude and time scale. Fraud may, of course, amplify these instabilities or may push the system beyond a tipping point, but it is not the primary driving force, as these instabilities are an emergent outcome of complex financial networks (*8*).

The argument about fraud is not one against models or our complexity approach, and economic theory offers ways to investigate what fraud and breaching of trust would do to a system. For example, methods and insight from the theory of evolutionary biology and evolutionary game theory can be used to include agents that "cheat" the system by not following accepted sets of rules in their behavior (*9*, *10*).

Stefano Battiston,[1] Doyne Farmer,[2,3] Andreas Flache,[4] Diego Garlaschelli,[5] Andy Haldane,[6] Hans Heesterbeek,[7] Cars Hommes,[8,9]* Carlo Jaeger,[10,11,12] Robert May,[13] Marten Scheffer[14]

[1]Department of Banking and Finance, University of Zurich, 8032 Zürich, Switzerland. [2]Institute for New Economic Thinking, Oxford Martin School, and Mathematical Institute, University of Oxford, Oxford OX1 2JD, UK. [3]Santa Fe Institute, Santa Fe, NM 87501, USA. [4]Department of Sociology, University of Groningen, 9712 TG Groningen, Netherlands. [5]Lorentz Institute for Theoretical Physics, University of Leiden, 2333 CA Leiden, Netherlands. [6]Bank of England, London, EC2R 8AH, UK. [7]Faculty of Veterinary Medicine, University of Utrecht, 3512 JE Utrecht, Netherlands. [8]Amsterdam School of Economics, University of Amsterdam, 1018 WB Amsterdam, Netherlands. [9]Tinbergen Institute, 1082 MS Amsterdam, Netherlands. [10]Beijing Normal University, Beijing, 100875 China. [11]Potsdam University, 14469 Potsdam, Germany. [12]Global Climate Forum 10178 Berlin, Germany. [13]Department of Zoology, University of Oxford, Oxford OX1 2JD, UK. [14]Environmental Sciences, Wageningen University 6708 PB Wageningen, Netherlands.

*Corresponding author. E-mail: c.h.hommes@uva.nl

REFERENCES

1. R. E. Lucas Jr., *Carnegie-Rochester Conf. Ser. Public Pol.* **1**, 19 (1976).
2. A. G. Haldane, "On microscopes and telescopes" (Workshop Socio-Economic Complexity, Lorentz Center, Leiden, 2015); www.bankofengland.co.uk/publications/Pages/speeches/2015/812.aspx.
3. J. Geanakoplos *et al.*, *Am. Econ. Rev.* **102**, 53 (2012).
4. W. Bolt, M. Demertzis, C. Diks, C. Hommes, M. van der Leij, "Identifying booms and busts in house prices under heterogeneous expectations" (CeNDEF Working Paper, University of Amsterdam, 2015).
5. V. L. Smith, G. L. Suchanek, A. W. Williams, *Econometrica* **56**, 1119 (1988).
6. C. H. Hommes, J. Sonnemans, J. Tuinstra, H. van de Velden, *Rev. Econ. Stud.* **18**, 955 (2005).
7. P. Klimek, S. Poledna, J. D. Farmer, S. Thurner, *J. Econ. Dynam. Control* **50**, 144 (2015).
8. M. Bardoscia, S. Battiston, F. Caccioli, F. Caldarelli, "Pathways towards instability in financial networks" (2016); http://arxiv.org/abs/1602.05883.
9. S.D. Ramchurn, Dong Huynh, N.R. Jennings, *Knowl. Eng. Rev.* **19**, 1 (2004).
10. C. Riehl, M. E. Frederickson, *Philos. Trans. R. Soc. London Ser. B* **371**, 20150090 (2016).

PHOTO: ASSOCIATED PRESS

Published by AAAS

REVIEW SUMMARY

PHOTOVOLTAICS

Photovoltaic materials: Present efficiencies and future challenges

Albert Polman,* Mark Knight, Erik C. Garnett, Bruno Ehrler, Wim C. Sinke

BACKGROUND: Photovoltaics, which directly convert solar energy into electricity, offer a practical and sustainable solution to the challenge of meeting the increasing global energy demand. According to the Shockley-Queisser (S-Q) detailed-balance model, the limiting photovoltaic energy conversion efficiency for a single-junction solar cell is 33.7%, for an optimum semiconductor band gap of 1.34 eV. Parallel to the development of wafer-based Si solar cells, for which the record efficiency has continually increased during recent decades, a large range of thin-film materials have been developed with the aim to approach the S-Q limit. These materials can potentially be deposited at low cost, in flexible geometries, and using relatively small material quantities.

ADVANCES: We review the electrical characteristics of record-efficiency cells made from 16 widely studied photovoltaic material geometries and illuminated under the standard AM1.5 solar spectrum, and compare these to the fundamental limits based on the S-Q model. Cells that show a short-circuit current (J_{sc}) lower than the S-Q limit suffer from incomplete light absorption or incomplete collection of generated carriers, whereas a reduced open-circuit voltage (V_{oc}) or fill factor (FF) reflects unwanted bulk or interfacial carrier recombination, parasitic resistance, or other electrical nonidealities. The figure shows the experimental values for J_{sc} and the $V_{oc} \times FF$ product relative to the S-Q limiting values for the different materials. This graph enables a direct identification of each material in terms of unoptimized light management and carrier collection ($J_{sc}/J_{SQ} < 1$) or carrier management ($V_{oc} \times FF/V_{SQ} \times FF_{SQ} < 1$).

Monocrystalline Si cells (record efficiency 25.6%) have reached near-complete light trapping and carrier collection and are mostly limited by remaining carrier recombination losses. In contrast, thin-film single-crystalline GaAs cells (28.8%) show only minimal recombination losses but can be improved by better light management. Polycrystalline CdTe thin-film cells (21.5%) offer excellent light absorption but have relatively high recombination losses; perovskite cells (21.0%) and $Cu(In,Ga)(Se,S)_2$ (CIGS) cells (21.7%) have poorer light management, although CIGS displays higher electrical quality.

Aside from these five materials (Si, GaAs, CdTe, CIGS, perovskite) with efficiencies of >20%, a broad range of other thin-film materials have been developed with efficiencies of 10 to 12%: micro/nanocrystalline and amorphous Si, $Cu(Zn,Sn)(Se,S)_2$ (CZTS), dye-sensitized TiO_2, organic polymer materials, and quantum dot solids. So far, cell designs based on these materials all suffer from both light management and carrier management problems. Organic and quantum dot solar cells have shown substantial efficiency improvements in recent years.

OUTLOOK: The record-efficiency single-crystalline materials (Si, GaAs) have room for efficiency improvements by a few absolute percent. The future will tell whether the high-efficiency polycrystalline thin films (CdTe, CIGS, perovskite) can rival the efficiencies of Si and GaAs. Because the cost of photovoltaic systems is only partly determined by the cost of the solar cells, efficiency is a key driver to reduce the cost of solar energy, and therefore large-area photovoltaic systems require high-efficiency (>20%), low-cost solar cells. The lower-efficiency (flexible) materials can find applications in building-integrated PV systems, flexible electronics, flexible power generation systems, and many other (sometimes niche) markets. High-efficiency (>20%) materials find applications in large-area photovoltaic power generation for the utility grid as well as in small and medium-sized systems for the built environment. They will enable very large-scale penetration into our energy system, starting now and growing as the cost per kilowatt-hour is reduced further by a factor of 2 to 3. This can be achieved by nanophotonic cell designs, in which optically resonant and nonresonant structures are integrated with the solar cell architecture to enhance light coupling and trapping, in combination with continued materials engineering to further optimize cell voltage. Making big steps forward in these areas will require a coordinated international materials science and engineering effort. ■

ON OUR WEBSITE

Read the full article at http://dx.doi.org/10.1126/science.aad4424

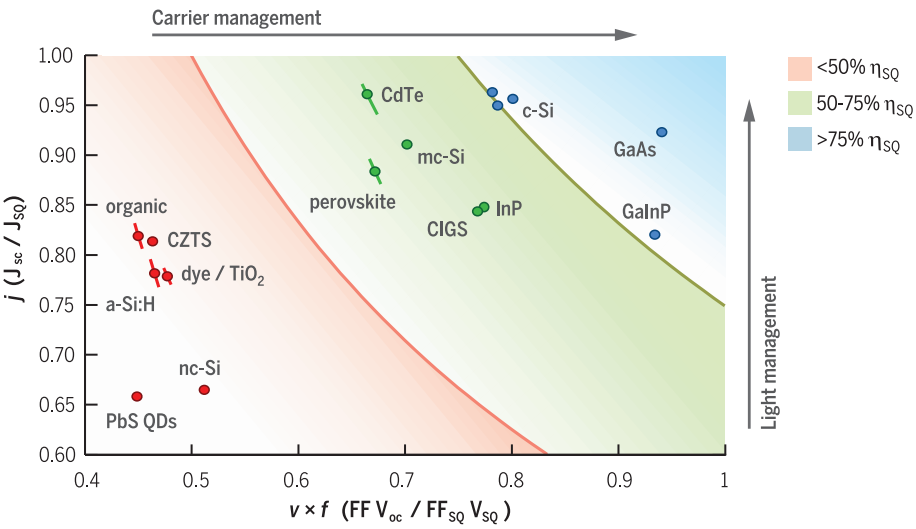

Limiting processes in photovoltaic materials. An efficient solar cell captures and traps all incident light ("light management") and converts it to electrical carriers that are efficiently collected ("carrier management"). The plot shows the short-circuit current and product of open-circuit voltage and fill factor relative to the maximum achievable values, based on the Shockley-Queisser detailed-balance limit, for the most efficient solar cell made with each photovoltaic material. The data indicate whether a particular material requires better light management, carrier management, or both. Colors correspond to cells achieving <50% of their S-Q efficiency limit η_{SQ} (red), 50 to 75% (green), or >75% (blue).

The list of author affiliations is available in the full article online.
*Corresponding author. E-mail: a.polman@amolf.nl
Cite this article as A. Polman *et al.*, *Science* 352, aad4424 (2016). DOI: 10.1126/science.aad4424

REVIEW

PHOTOVOLTAICS

Photovoltaic materials: Present efficiencies and future challenges

Albert Polman,[1]* Mark Knight,[1] Erik C. Garnett,[1] Bruno Ehrler,[1] Wim C. Sinke[1,2]

Recent developments in photovoltaic materials have led to continual improvements in their efficiency. We review the electrical characteristics of 16 widely studied geometries of photovoltaic materials with efficiencies of 10 to 29%. Comparison of these characteristics to the fundamental limits based on the Shockley-Queisser detailed-balance model provides a basis for identifying the key limiting factors, related to efficient light management and charge carrier collection, for these materials. Prospects for practical application and large-area fabrication are discussed for each material.

Photovoltaics (PV), which directly convert solar energy into electricity, offer a practical and sustainable solution to the challenge of meeting the increasing global energy demand. In recent years, the decreasing price of PV systems has levelized the cost of PV-produced electricity to the point that it can now compete with the variable portion of consumer electricity prices in many countries worldwide: The point of "socket parity" has been reached (*1*). Substantial further cost reduction is needed, however, to allow PV to compete in more electricity markets and to enter the multi-terawatt regime. Aside from the solar cell and module fabrication costs, a major and increasing fraction of the cost of PV generation (typically 50%) is related to component and installation requirements such as inverters, cabling, mounting structures, and labor (*1*). As a result, solar cell efficiency is a key lever for PV cost reduction: For a given output power, a higher cell efficiency directly translates into a smaller and therefore less expensive PV system, reducing the levelized cost of electricity. A higher power generation rate per unit area is also important in urban environments where space is limited. The development of PV materials is experiencing an enormous growth, and efficiency records are continually broken. Below, we systematically compare the state of the art of the 16 most studied geometries of PV materials, with emphasis on the limitations of each material and its potential for further improvement and large-scale application.

Solar cells are made of semiconductor materials; given the broad solar spectrum, their fundamental efficiency limit is determined by several factors (Fig. 1). Photons with energies below the band gap are not absorbed, whereas photons with energies above the band gap are not fully converted to electrical energy because of thermalization of charge carriers (Fig. 1A, inset). Taking these two factors into account, ~45% of the incident spectrum-integrated solar power remains for semiconductors with a band gap of 1.1 to 1.4 eV. This is the maximum power that would be generated if the cell were operated at a voltage corresponding to the band gap energy and a current corresponding to full capture of all photons with energy above the band gap, followed by full collection of all generated carriers.

Even in an ideal case, however, the open-circuit voltage V_{oc} is always lower than the band gap energy because thermodynamic detailed balance requires the cell to be in equilibrium with its environment, which implies that there is spontaneous light emission from the cell. The corresponding radiative carrier recombination represents a dark current that causes V_{oc} to be well below the band gap voltage V_g (Fig. 1A, inset). Furthermore, under maximum-power operation (at maximum $J \times V$), the voltage V_{mp} is lower than V_{oc} and the current density J_{mp} is lower than the maximum (short-circuit) current density J_{sc} (Fig. 2A, inset). The efficiency limit that takes all these factors into account was first derived by Shockley and Queisser (S-Q) in 1961 (*2*). Figure 1B shows this limiting efficiency for a single-junction solar cell under "one-sun" illumination with the standard AM1.5 solar spectrum as a function of band gap; the maximum efficiency occurs for a semiconductor with a band gap of 1.34 eV and is 33.7%.

In practical solar cells, not all incident light is absorbed in the active layer(s) and not all generated carriers are collected; hence, J_{sc} is below the maximum value that can be achieved for a given band gap, E_g. The achievable V_{oc} is also reduced below the S-Q value by such phenomena as Auger recombination, band tail recombination, and recombination at bulk, interface, and surface defects (*3*–*5*). Furthermore, resistance and contact losses and other nonidealities reduce the fill factor $FF = (J_{mp}V_{mp})/(V_{oc}J_{sc})$. Combined, these factors lead to practical efficiencies that are often substantially lower than the S-Q limit for a given band gap.

Ideal and record-efficiency solar cells compared

We distinguish three classes of PV materials: (i) ultrahigh-efficiency monocrystalline materials with efficiencies of >75% of the S-Q limit for the corresponding band gap: Si (homojunction and heterojunction), GaAs, and GaInP; (ii) high-efficiency multi- and polycrystalline materials (50 to 75% of the S-Q limit): Si, $Cu(In,Ga)(Se,S)_2$ ("CIGS"), CdTe, methyl ammonium lead halide perovskite [$CH_3NH_3Pd(I,Cl,Br)_3$], and InP; and (iii) low-efficiency materials (<50% of the S-Q limit): micro- or nanocrystalline and amorphous Si, $Cu(Zn,Sn)(Se,S)_2$ ("CZTS"), dye-sensitized TiO_2, organic and polymer materials, and quantum dot materials.

The record efficiency for each of these materials is plotted in Fig. 1B (see also table S1). The experimental values for J_{sc}, V_{oc}, and FF for the record-efficiency cell reported for each individual material are shown in Fig. 2, A to C, together with the limiting values calculated using the S-Q model (*2*). The experimental values for J_{sc} generally follow the trend given by the S-Q limit, with some materials closely approaching this limit. Values for V_{oc} and FF are much more scattered, with only a few materials approaching the S-Q limit. To analyze these trends, we evaluated two characteristic parameters for each material: (i) the current ratio $j = J_{sc}/J_{SQ}$, which indicates the degree of light coupling, absorption, and trapping in the active layer(s) of the cell, and also depends on the carrier collection efficiency; and (ii) the voltage ratio $v = V_{oc}/V_{SQ}$, which is primarily related to the degree of recombination of carriers in the bulk, surfaces, and interfaces. Together, the voltage ratio v and fill factor ratio $f = FF/FF_{SQ}$ indicate the total electrical limitations of a cell (*6*). A plot of j versus $v \times f$ for all evaluated materials (Fig. 3) directly indicates to what degree the cell efficiency is limited by light management or charge carrier management. Next, we describe these data for all materials.

Silicon (efficiency 25.0 to 25.6%)

Silicon has a nearly ideal band gap (E_g = 1.12 eV) for reaching high efficiency (Fig. 1). Si homojunction cells are based on a p-n junction made into either p-type or n-type Si(100) substrates. Several advanced device architectures and contacting schemes have been developed for Si solar cells. Contact recombination represents a major source of loss, so the most successful approaches minimize contact area (e.g., by localized heavy doping or metal deposition), implement passivated contacts, or use a combination of these approaches. In parallel, surface passivation of Si using Si_3N_4, Al_2O_3, SiO_2, or combinations of these materials has been developed to great perfection. The record efficiency for a monocrystalline Si homojunction cell was recently set at 25.1% (*7*) for a cell with a full-area tunnel oxide passivated rear contact and high-quality top surface passivation (the TOPCon design; Fig. 4A), slightly higher than the value of 25.0% (*8*, *9*) reported in 1998 for a cell

[1]Center for Nanophotonics, FOM Institute AMOLF, Science Park 104, 1098 XG Amsterdam, Netherlands. [2]Energy Research Center of the Netherlands (ECN), P.O. Box 1, Petten, Netherlands.
*Corresponding author. E-mail: a.polman@amolf.nl

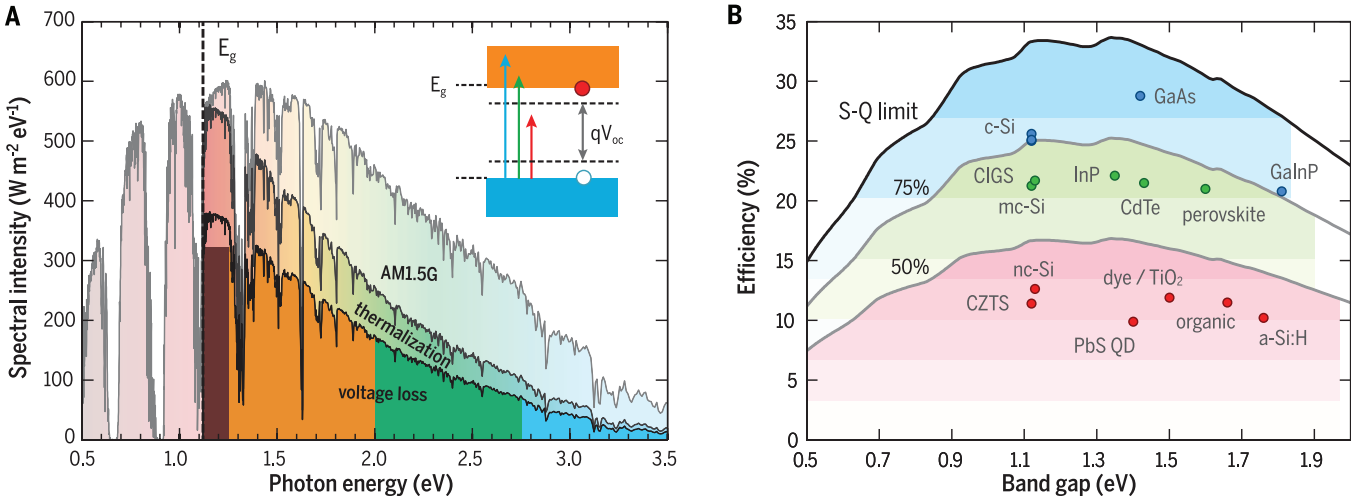

Fig. 1. Fundamental solar cell efficiency limits and present-day records. (**A**) AM1.5 solar spectrum with distinct dips due to molecular absorption in Earth's atmosphere. Photons with energies below the band gap (E_g, dashed black line corresponds to the band gap of Si) are not absorbed, whereas photons with energies above the band gap are not fully converted to electrical energy because of thermalization of charge carriers. The maximum power generated by the cell is limited by voltage loss relative to the band gap voltage. Inset: Electronic band structure with the separation of the quasi-Fermi levels determining the open-circuit voltage V_{oc}. (**B**) Theoretical Shockley-Queisser detailed-balance efficiency limit as a function of band gap (black line) and 75% and 50% of the limit (gray lines). The record efficiencies for different materials are plotted for the corresponding band gaps.

that used local contacts and high-quality surface passivation [the passivated emitter rear localized diffused (PERL) design].

The TOPCon cell has excellent current generation and collection (j = 0.96), similar to the value achieved for two other record-efficiency Si solar cell designs (table S1). This results from a combination of very low surface reflection [achieved by a pyramidal (111)-faceted surface texture combined with an anti-reflection coating (ARC)] and very low recombination losses in the Si wafer and at the surfaces and contact interfaces. Low recombination is also reflected in the relatively high voltage of the TOPCon cell (v = 0.82).

In a radically different design, both the p-n junction and the contacts are placed at the rear of the cell. This interdigitated back-contact (IBC) design features alternating p-type and n-type contact regions (Fig. 4B). The IBC design eliminates front contact shading losses and reduces series resistance by allowing more metal to be used for current collection and transport. This comes at the cost of more challenging carrier transport in the device (carriers generated near the surface must be collected at the back) and requires the use of very high-quality material. Overall current generation and collection in the IBC cell is slightly lower than in the TOPCon cell (j = 0.95 versus 0.96), as is the record efficiency (25.0% versus 25.1%) (*9*–*11*). Note that the IBC cell has an area of 120 cm^2, whereas the TOPCon cell measures 4 cm^2. The IBC cell uses a doped surface layer, which creates a front surface field that repels carriers from the surface, and has a Si_3N_4 top layer that serves as both an ARC and a high-quality passivation layer for the Si surface. The lower surface and bulk recombination rates lead to a slightly higher voltage (v = 0.83) for the IBC cell relative to the TOPCon cell.

An efficiency record of 25.6% was recently reported for an IBC Si solar cell that uses silicon heterojunctions (SHJs) rather than homojunctions for carrier collection (*9*, *12*). In this approach, a thin stack of doped and intrinsic hydrogenated amorphous Si (a-Si:H) layers is deposited onto a crystalline Si surface to form a junction, replacing the process of junction formation by high-temperature dopant diffusion (Fig. 4C). The SHJ design avoids carrier recombination in highly doped p-type and n-type regions and is made using a low-temperature process, which better preserves the minority carrier lifetime of the Si wafer. The surface of the record SHJ cell is passivated with a-Si:H. This design led to the highest voltage observed for a Si solar cell (v = 0.84). The overall result of carrier generation and collection is similar to that of the TOPCon cell (j = 0.96). The origins of the small remaining losses in these high-efficiency Si cells are quite different because of their different design and mode of operation.

As a result of the indirect band gap of Si, the absorption coefficient is relatively low and varies only gradually around the band gap energy, so that a relatively thick wafer is required to absorb all light with photon energies above the band gap. This, however, leads to higher bulk (Auger) recombination and thus reduces V_{oc}. Moreover, it increases the material costs. The present tradeoff among cost, manufacturability, and performance leads to an optimum Si wafer thickness of 100 to 200 μm for commercial cells. These wafers are made by diamond wire sawing from monocrystalline Si rods produced by Czochralski crystal growth.

Multicrystalline Si wafers are cut from cast ingots produced using directional (unseeded or seeded) crystallization, and their fabrication cost is lower than that of monocrystalline wafers. The typical grain size depends on the growth method and can be as large as several centimeters. Multicrystalline Si has a lower electronic quality, due to crystal grain boundaries and intragrain defects, as well as a higher concentration of impurities. As a result, the record-efficiency multicrystalline Si cell has large voltage loss (v = 0.76). Light trapping in these cells is less efficient because the ideal pyramidal surface texture normally formed by alkaline-etching Si(100) to the (111) surface facets cannot be realized on a multicrystalline surface. This, together with incomplete carrier collection due to recombination, leads to a reduced current (j = 0.91). Together, these voltage and current losses yield a lower efficiency (20.8%) (*9*, *13*) than for monocrystalline Si cells. The record-efficiency multicrystalline Si cell has a passivated emitter and rear cell (PERC) p-n junction design (Fig. 4D).

According to the S-Q model, the efficiency limit for Si solar cells is 33.3%, far above the experimental record of 25.6%. A key limiting factor that is not accounted for in the S-Q model is Auger recombination of free carriers that occurs under illumination. Taking this into account for Si, the efficiency limit for an undoped (monocrystalline) Si cell with optimized thickness (110 μm) was calculated to be 29.4% (*14*), leaving room for further development of existing technologies in the coming years.

Today the global PV market is dominated by wafer-based crystalline Si solar modules, with a total market share of >90%. Multicrystalline Si represents ~65% and monocrystalline Si ~35% of this market segment (*15*). PV systems based on Si solar cells installed in the field have been shown to offer high reliability and very limited efficiency degradation over a period longer than 25 years.

GaAs (efficiency 28.8%)

The record efficiency for a single-junction solar cell under one-sun illumination has been achieved using GaAs (28.8%) (*9*, *16*). This material has a direct band gap close to the optimum (1.42 eV; Fig. 1). Because of the high optical absorption coefficient of GaAs, the cell thickness can be kept relatively small (~2 μm) to harvest the solar spectrum

up to the band gap. The record-efficiency cell design has a n-GaAs/p-$Al_{0.3}Ga_{0.7}As$ junction geometry with high–band gap window layers that serve to retain minority carriers in the GaAs active layer (Fig. 4E). The GaAs heterostructure is epitaxially grown using chemical vapor deposition, which is a relatively energy-intensive process. Interestingly, the record efficiency was achieved using a lift-off process, in which a GaAs foil ~2 μm thick was exfoliated from the substrate (by chemical etching of an AlAs buffer layer) and laminated onto a Cu substrate. The voltage of the record-efficiency cell is very high (v = 0.97). Light reflection, top-finger shadowing, incomplete light trapping, and absorption in the metal back contact result in some current loss (j = 0.92), leaving room for improvement. Application of an IBC geometry, for example, could potentially further increase j. An intermediate dielectric back-reflecting geometry can reduce parasitic absorption in the metal back contact. The fill factor in these cells is very high (f = 0.97). Taking into account Auger recombination, the maximum efficiency that can be achieved for a practical single-junction GaAs cell is ~32% (*17*), substantially greater than the current record value.

Whereas III-V solar cells have traditionally been used in niche markets requiring high efficiency on a small area, such as space technology, the newly developed layer-transfer technology enables fabrication of large-area flexible (single-junction) GaAs technology at reduced cost for a much broader range of applications. Encapsulation and recycling of commercial GaAs modules is important because of the use of the toxic element As.

InP (efficiency 22.1%) and GaInP (efficiency 20.8%)

Two other III-V compound semiconductors that have achieved high efficiencies are InP and GaInP. InP (E_g = 1.35 eV) has a band gap similar to that of GaAs, but the maximum reported efficiency of 22.1% (*9*, *18*) is much lower than for GaAs; this difference is due to both lower voltage and lower current (v = 0.81, j = 0.85). Because of the existing high-efficiency GaAs alternative and the scarcity and associated high cost of In, developments on InP cells have been minimal in the past decade. GaInP has a relatively high band gap (1.81 eV), for which the S-Q limit efficiency is 25.2%. The record efficiency achieved for a GaInP cell is 20.8% (*9*, *19*). The voltage loss on the record cell is extremely small (v = 0.96), but current collection (j = 0.82) in these cells leaves much room for improvement. The record-efficiency GaInP cell has the highest fill factor achieved for any material (FF = 0.89; f = 0.98), which is partly related to the high band gap (Fig. 2C). Because of its large band gap, GaInP is used in III-V multijunction solar cell geometries. Recently, a mechanically stacked tandem composed of a GaInP top cell and a Si heterojunction base cell was reported with an efficiency of 29.8% (*11*).

CIGS (efficiency 21.7%)

The record efficiency of $Cu(In,Ga)(Se,S)_2$ (CIGS) thin-film solar cells has steadily increased over the past 20 years, with the present record value at 21.7% (*9*, *20*), making it the highest-efficiency thin-film solar cell material to date, very closely followed by CdTe at 21.5% (*9*, *21*). CIGS has a chalcopyrite crystal structure and its band gap can be continuously tuned between ~1.0 and 2.4 eV by varying the In/Ga and Se/S ratios, with the low–band gap compositions so far always giving the best performance. Polycrystalline films of CIGS are made using sputtering or evaporation from the constituent elements and are typically deposited onto a Mo film that is sputtered on a soda-lime glass substrate. The typical active layer thickness is ~2 to 3 μm. Sodium diffusing from the glass substrate into the CIGS layer has been found to play a key role in passivating defects in the CIGS layer; the record cell also incorporated traces of K. The CIGS composition is typically graded to form an electric field that repels minority carriers from the Mo back contact, which is a strong recombination sink. The cell is finalized by the chemical-bath deposition of CdS to form a heterojunction followed by an intrinsic ZnO buffer layer, a transparent ZnO:Al conducting layer (TCL), and a MgF_2 ARC (Fig. 4F). In some recent high-efficiency devices, the CdS layer is replaced by the more transparent ZnO_xS_{1-x}. Indium is a key element in CIGS, and its scarcity is a concern for scaling up CIGS module production to the terawatt level.

The voltage for the record-efficiency CIGS cells (E_g = 1.13 eV) is very high, with v = 0.84, equal to the best monocrystalline Si cells. Given the polycrystalline nature of the material, this implies that grain boundaries in this material do not act as strong carrier recombination sites. There is substantial current loss (j = 0.84) due to light reflection, incomplete light trapping, absorption in the Mo back contact, and parasitic absorption in the CdS and ZnO:Al layers. The absorption spectrum of CIGS shows a rather gradual variation with energy around the band gap, which leads to unavoidable current loss in the near–band gap spectral range. As with all polycrystalline materials, improving material quality is a complex process that requires optimization of many different parameters such as deposition conditions, (post-)annealing procedures, and ambients. Because of the complex stoichiometry of CIGS, many secondary phases are possible, and much of the progress in efficiency has been achieved by optimizing the deposition and annealing process to avoid such detrimental by-products. Creating a good ohmic electrical contact between Mo and CIGS (via a $MoSe_2$ interfacial layer) is another important factor. Replacing the CdS buffer layer with a nontoxic and more transparent material is also a key research area.

The possibility of band gap tuning makes CIGS an interesting material in tandem solar cells, either by combining CIGS layers with different band gaps or by using a high–band gap CIGS top cell on top of a Si base cell. So far, however, high–band gap (Ga-rich) CIGS cells have not yielded sufficient efficiencies for a CIGS/Si tandem to beat the record-efficiency Si cell.

CdTe (efficiency 21.5%)

CdTe is a binary semiconductor with a cubic zincblende crystal structure and a near-ideal band gap of 1.43 eV. It can be deposited at relatively low temperature using evaporation from CdTe powder. Cells are typically grown in a superstrate configuration starting from a glass substrate coated with fluorine-doped tin oxide (FTO). The subsequent layer stack usually consists of CdS (generally deposited by chemical bath deposition), followed by evaporated CdTe (thickness typically 2 to 3 μm)

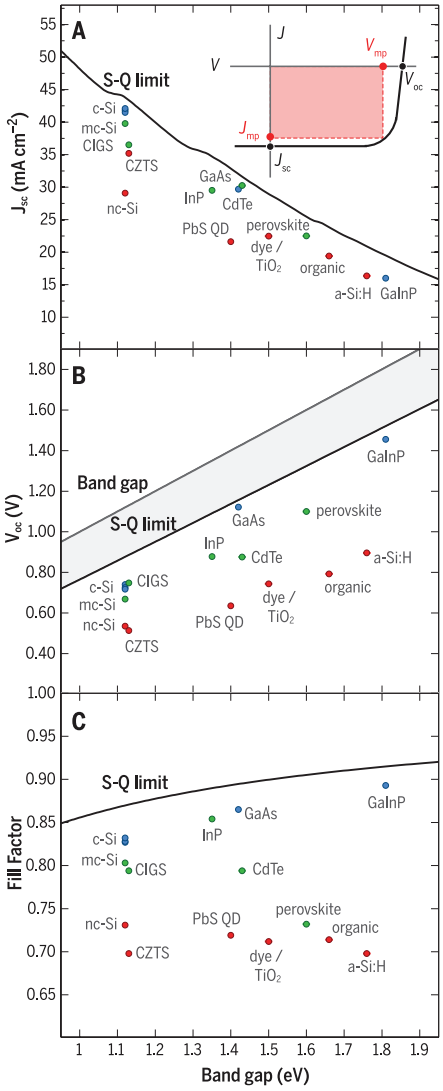

Fig. 2. Record-efficiency cell parameters compared to the detailed-balance limit. Single-junction solar cell parameters are shown as a function of band gap energy according to the Shockley-Queisser limit (solid lines) and experimental values for record-efficiency cells. (**A**) Short-circuit current J_{sc}. Inset: A typical current-voltage $J(V)$ curve, with V_{oc}, J_{sc}, V_{mp}, and J_{mp} indicated. The product of current and voltage is highest at the maximum power point ($J_{mp}V_{mp}$). (**B**) Open-circuit voltage V_{oc}. The voltage corresponding to the band gap is shown for reference, with the voltage gap V_g-V_{SQ} indicated by the gray shaded region. (**C**) Fill factor $FF = (J_{mp}V_{mp})/(V_{oc}J_{sc})$. All data are for standard AM1.5 illumination at 1000 W/m^2.

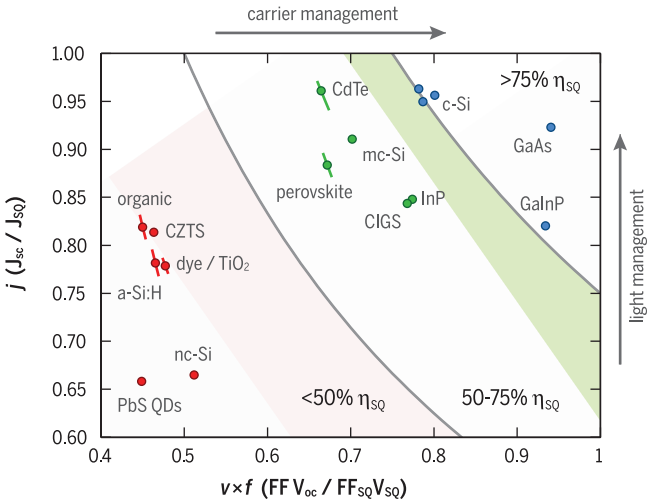

Fig. 3. Fraction of Shockley-Queisser detailed-balance limit for voltage and current achieved by record cells. The current ratio $j = J_{sc}/J_{SQ}$ is plotted versus the product of the voltage and fill factor fractions ($v \times f = FF\ V_{oc}/FF_{SQ}V_{SQ}$) for the record-efficiency cells of all evaluated materials. The lines around some data points correspond to a range of band gaps taken in the S-Q calculations according to uncertainty in the band gap of the record cell. Arrows on top and right axes indicate how improved light management and charge carrier collection improve the cell efficiency. η_{SQ} denotes maximum achievable efficiency according to the SQ model.

and a metal back contact such as Al or Ti, in some cases with a CuZnTe interfacial layer between the metal and the CdTe (Fig. 4G).

The highest reported certified efficiency for CdTe is 21.5% (*9*, *21*), although for the purpose of this review we analyze cells with the previous record of 21.0% (*22*) because detailed data for the new record-efficiency cell are not yet available. The steep absorption coefficient versus energy for CdTe enables very good current collection in CdTe cells (j = 0.96), far superior to any other thin-film technology and equal to that of the record-efficiency monocrystalline Si cells. The high voltage loss in CdTe cells (v = 0.75) is attributed to recombination losses in the crystal grains and at interfaces in the polycrystalline material; the exact nature of this recombination is still unclear.

CdTe solar modules are commercially produced by several companies and have the largest market share among present thin-film technologies, which are dominated by CdTe, CIGS, and thin-film Si. Recycling systems have been set up for commercial CdTe modules, which is particularly important because of the use of the toxic element Cd; the scarcity of Te is also a concern.

Methyl ammonium lead halide perovskite (efficiency 21.0%)

Hybrid organic-inorganic perovskite solar cells have recently taken the PV research world by storm, with efficiencies above 20% achieved after only 5 years of substantial work. These materials have the general formula ABX_3, where A is an organic cation (most often methylammonium, CH_3NH_3), B is an inorganic cation (usually Pb), and X is a halide [typically I, often with a small fraction of Cl or Br: $CH_3NH_3Pb(I,Cl,Br)_3$]. Depending on the halide used, the band gap can be continuously tuned from ~1.6 eV (pure I) to 3.2 eV (pure Cl), with the smaller–band gap materials providing better solar cell efficiencies (*23*). Even smaller band gaps can be achieved using a different organic cation (e.g., formamidinium, H_2NCHNH_2) or inorganic cation (e.g., Sn), and such compounds are desirable as they have a higher efficiency limit (Fig. 1B).

The perovskite salts form polycrystalline films with a perovskite structure at or near room temperature by precipitation from a variety of polar solvents (commonly dimethyl formamide or dimethyl sulfoxide). The device geometry is usually very similar to, and inspired by, those used for solid-state dye-sensitized or polymer bulk heterojunction solar cells. Typically, an FTO-coated glass substrate is coated with an electron-selective contact (usually TiO_2). Subsequently, the perovskite is deposited either by spin-coating the soluble precursors (methyl ammonium iodide and lead iodide, bromide, or chloride) or evaporating the constituent powders. A low-temperature annealing process (<150°C) often helps to improve crystallinity, film morphology, and device performance. Finally, the hole-selective top contact (usually Spiro-OMeTAD, $C_{81}H_{68}N_4O_8$) is spin-coated on top, and the back contact (usually gold) is evaporated to finish the device (Fig. 4H).

The record perovskite solar cell efficiency is 21.0% (*9*, *24*), although for the purpose of this review we analyze cells with the previous record of 20.1% (*9*, *24*) because detailed data for the new record cell are not yet available. This cell has a very small area and exhibits a relatively small voltage loss (v = 0.83), even better than the record-efficiency monocrystalline Si homojunction cells, which is remarkable for a solution-processed semiconductor. Even though the absorption spectrum of perovskites shows a very sharp onset, comparable to that of the best semiconductor absorbers (CdTe and GaAs), the photocurrent loss is still substantial (j = 0.88). This loss comes primarily from parasitic absorption in the hole-conducting layer and the back reflector. The fill factor in these cells (FF = 0.73; f = 0.81) is the lowest of all cells with efficiencies greater than 20%, most likely because of a combination of nonuniformity in the absorber (e.g., pinholes) and carrier-selective contacts that lead to carrier shunting, along with resistive losses associated with nonideal carrier-selective contacts. The fill factor (and thus the efficiency) is expected to continue to increase as these factors are optimized further.

Despite their excellent initial performance, hybrid perovskite solar cells are known to degrade within a few hours to days under standard operating conditions; at present this is the greatest barrier to commercial implementation. The origins of perovskite cell instability are currently a topic of active research, although photoreduction by ultraviolet light and reactions with water have already been identified as likely candidates. Also, measurements of the current-voltage characteristics can suffer from hysteresis, making efficiency analysis complex. The origin of this hysteresis is still unclear, but the leading hypothesis involves ion (or vacancy) migration under operating conditions. The perovskite salts are partially soluble in water, so the cells are sensitive to humidity. Because of Pb toxicity, encapsulation and recycling are important for this technology to become viable for large-scale application. The toxicity challenge is greater for this material than for CdTe and GaAs because the much higher water solubility and lower vaporization temperature make environmental exposure during module encapsulation failure (breakage, fire) more dangerous. Large–band gap perovskites may serve as a top cell in Si/perovskite tandem solar cells that have a potential efficiency above 30%; such an application provides a possible entry point to the market for the perovskite technology and is currently under intense research.

CZTS (efficiency 12.6%)

$Cu(Zn,Sn)(S,Se)_2$ (CZTS) is a solar cell material similar to CIGS, but with the scarce element In replaced by Zn and Ga replaced by Sn. CZTS can crystallize to form either a kesterite or stannite crystal structure, with kesterite being preferable for PV applications. As in CIGS, the band gap of CZTS can be tuned over a substantial range (1.0 to 1.6 eV); the best results have been achieved for a Cu-poor, Zn-rich stoichiometry with the band gap controlled by the S/Se ratio (*25*). The cell structure is nearly identical to what is used for CIGS. Cell fabrication can also follow a similar process, although the record-efficiency CZTS cells have been made using solution deposition of chalcogenides dissolved in hydrazine followed by annealing in selenium vapor. The record CZTS cell has an efficiency of 12.6% (*9*, *26*) and suffers from large voltage loss (v = 0.58) due to recombination at defects in the bulk material and at the charge extraction interfaces. As with CIGS, the complex nature of the material requires study of many different types of defects and careful engineering of the fabrication and device processing to minimize the most detrimental defects. Controlling interfacial reactions at the Mo metal contact is crucial for reducing interfacial recombination and minimizing series resistance. Current loss in CZTS cells is comparable to that of CIGS (j = 0.81). Finding an alternative back contact with lower optical loss (higher reflectivity) that can withstand the full device processing and maintain low series resistance would be a major breakthrough in the development

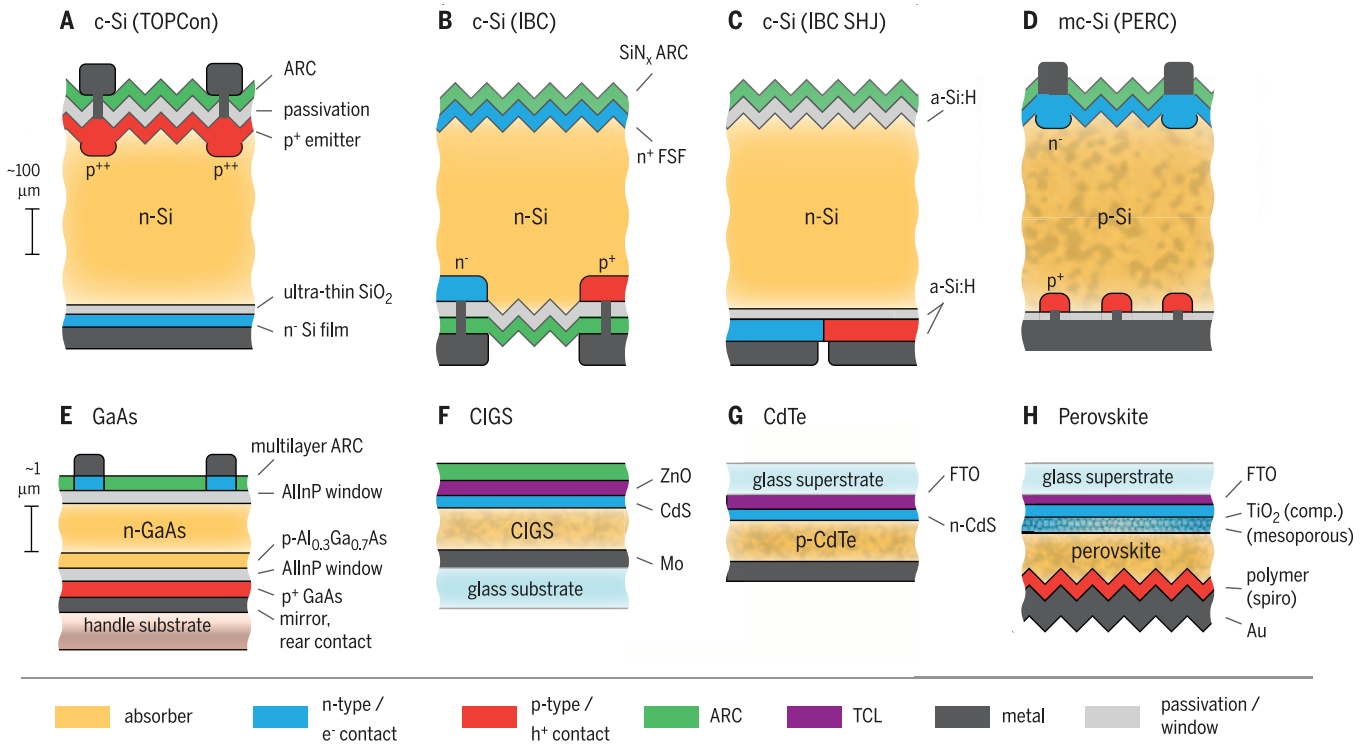

Fig. 4. Layer and contact geometry for solar cells with record efficiencies above 20%. (**A**) TOPCon crystalline Si (Fraunhofer). (**B**) IBC crystalline Si (SunPower). (**C**) Heterojunction IBC crystalline Si (Panasonic). (**D**) Multicrystalline Si (Trina Solar). (**E**) GaAs thin film (Alta Devices). (**F**) CIGS thin film (ZSW Stuttgart). (**G**) CdTe thin film (First Solar). (**H**) Perovskite thin film (KRICT). For industrial cells, the exact geometry is not publicly available.

of CZTS solar cells, although the biggest factor limiting efficiency is the low V_{oc}, a consequence of the relatively poor material quality.

Dye-sensitized solar cells (efficiency 11.9%)

Dye-sensitized solar cells are a special class of devices, as they involve an electrochemical power generation process. In these cells, the absorber is not an extended solid semiconductor but a molecular dye (typically a ruthenium organometallic complex, although zinc porphyrin and even purely organic dyes have also given very high efficiencies) that is coated onto a highly porous nanostructured electrode (typically TiO_2). The photoexcited dye injects electrons into the conduction band of the TiO_2 and accepts electrons from a redox couple (typically I^-/I^{3-}, although higher voltages have been reached with Co-based redox couples) in a nonaqueous electrolyte. The redox active species must then diffuse to the counter electrode (usually Pt or graphite) to be regenerated and complete the current circuit. Dye-sensitized solar cells are made by depositing a very thin compact TiO_2 layer typically on FTO, followed by formation of mesoporous TiO_2 by printing a TiO_2 nanoparticle paste, annealing, $TiCl_4$ treatment to passivate surface traps, and finally dye adsorption by immersion in solution. A glass plate covered with the counter electrode is brought very close to the substrate using spacers, and the cell is filled with electrolyte and sealed. Here, we analyze these cells according to the S-Q model, which assumes a semiconductor absorber with an absorption band edge; although this is not the case for dye-sensitized cells, the numbers for v and j then provide a reference relative to a conventional semiconductor with a band gap equal to the peak of the dye absorption spectrum (1.50 eV).

The record dye-sensitized cell has an efficiency of 11.9% (*9*, *27*) with a large voltage loss (v = 0.60) due to the relatively low potential of the standard I^-/I^{3-} redox couple, which introduces a large energy loss when transferring electrons to the dye. No better dye-based alternatives have been found despite intense research over the past several years: Redox couples with higher potentials either react too quickly with electrons injected into the TiO_2 (leading to recombination) or are too bulky for rapid ionic diffusion through the electrolyte (leading to strong losses in the fill factor at high light levels).

An additional challenge for dye-sensitized solar cells is the relatively high energy and narrow bandwidth associated with molecular absorption, which makes it difficult to harvest a wide range of the solar spectrum (j = 0.78). Using multiple dyes introduces complications with the redox chemistry, whereas using dyes with broader spectra reduces oscillator strength and requires porous electrodes to become too thick for efficient charge extraction. Despite these difficulties, dye-sensitized solar cells have already been commercialized because of their relatively simple fabrication, low-cost materials, and availability in a variety of colors and opacities that are useful when aesthetics are important. Moreover, dye-sensitized solar cells have served as a model system or inspiration for the development of a new class of nanostructured device architectures for PV solar energy conversion and solar fuel generation.

Organic solar cells (efficiency 11.5%)

Organic solar cells offer inexpensive roll-to-roll fabrication on flexible substrates and a wide choice of materials for applications where flexibility and color are important. Organic solar cells come in two varieties: sublimed small-molecule solar cells and solution-processed polymer/fullerene solar cells. The highest reported certified efficiency for a single-junction organic solar cell is 11.5% (*28*, *29*), although for the purpose of this review we analyze cells with the previous record of 11.0% (*9*, *30*) because detailed data for the new record-efficiency cell are not yet available. The previous record was achieved using a polymer with a 1.66-eV band gap.

Polymer solar cells are typically prepared on ITO-coated glass or foil with the active polymer donor–fullerene acceptor blend sandwiched between a hole-selective layer [typically poly(3,4-ethylenedioxythiophene) polystyrene sulfonate (PEDOT:PSS) or MoO_3] and an electron-selective layer such as ZnO, TiO_2, or a low–work function material such as Ca. The typical active layer thickness is ~100 nm.

Because of the low dielectric constant of organic materials, photogenerated electron-hole pairs remain tightly bound, necessitating the use of dedicated architectures such as bulk heterojunctions to achieve efficient charge separation and extraction. The energy offsets needed for the heterojunction to ensure efficient exciton dissociation lead to a voltage loss of ~0.3 eV in practice, which lowers the efficiency by about 2% absolute (*31*). Currently,

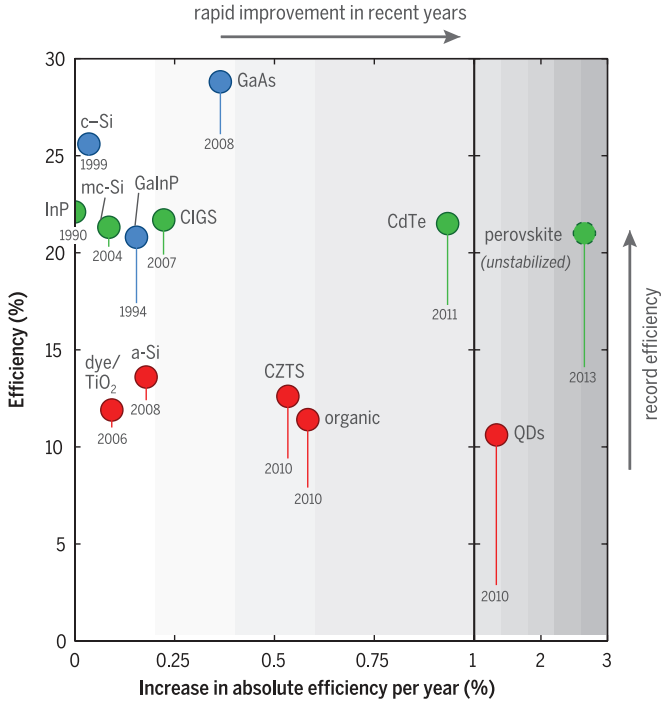

Fig. 5. Rates of improvement in solar cell efficiency over recent years. Average improvements were calculated over a period ending 1 January 2016 and starting with the date of the last record preceding 2010 [with two exceptions: perovskites (starting 2013, when the first certified efficiency was reported) and CdTe (starting 2011, as no recent record before 2010 was available and much progress occurred after 2010)]. Progress in efficiency from the pre-2010 record to the current values is indicated by the vertical lines. Colors correspond to cells achieving <50% of their S-Q efficiency limit (red), 50 to 75% (green), or >75% (blue). This analysis is based on data from the National Renewable Energy Laboratory efficiency chart, Green's tables, and publications (*11*, *19*, *29*).

the limiting problems for organic solar cells are the high rate of nonradiative recombination (via trap states or triplet excited states) and the large degree of static and dynamic disorder, together yielding very large voltage loss (v = 0.57). To a large extent, this voltage loss could be overcome by direct optical excitation of the charge-transfer state between electron donor and electron acceptor. So far, common material combinations show a very low oscillator strength of these charge-transfer states, rendering direct optical excitation nearly absent. Substantial current loss (j = 0.82) is due to parasitic absorption by the selective contacts, incomplete absorption by the polymer, and incomplete carrier collection resulting from nonradiative recombination (low mobility and diffusion length).

As with thin-film Si solar cells, organic PV technology is suffering from the fact that efficiency is becoming an increasingly important driver to reduce the cost of large-area PV systems. Also, organic cells often show degradation under illumination. At the same time, a variety of attributes—relative ease of processing, nontoxicity, low weight, potential for low cost, and possibility of forming flexible modules of many different shapes, colors, and transparencies—enables applications that may not be achievable with thin-film flexible CIGS, CdTe, or perovskite cells that have much higher efficiency.

Thin-film silicon (efficiency 10.1 to 11.4%)

Thin-film microcrystalline or nanocrystalline Si solar cells can be made on a wide range of (flexible) substrates by means of chemical vapor deposition. Typically, a p-i-n geometry is grown on a ZnO:Al-coated textured glass substrate, followed by a ZnO:Al buffer layer and Ag back contact. The record efficiency is 11.4% (*9*, *32*). The relatively slow deposition rate of crystalline Si limits the cell thicknesses that can be practically achieved to 2 to 5 μm, and the textured substrate often leads to defected growth of the microcrystalline film. As a result of this thickness limitation, light with energies near the band gap is not fully absorbed, leading to a very strong current penalty with j = 0.67, the lowest value of all cells reviewed here. Crystal grain boundaries and other defects in deposited micro- or nanocrystalline Si cells are strong sinks for minority carriers, leading to a large voltage loss as well (v = 0.61).

Amorphous Si (a-Si:H) is a semiconductor with much stronger optical absorption than crystalline Si, but with a band gap well above the optimum (1.7 to 1.8 eV). It is made using vacuum deposition techniques, typically at a much higher rate than micro- or nanocrystalline films. Despite the incorporation of hydrogen in these films to passivate bulk defects, the electronic quality of this material is rather low, with a correspondingly large voltage loss (v = 0.61) for the record-efficiency single-junction cell (10.2%) (*9*, *33*). In a-Si:H cells, the optimum efficiency is strongly determined by the trade-off between cell thickness and carrier collection efficiency: A large thickness is required to optimize the capture of incident light, but this reduces the carrier collection efficiency if the cell is thicker than the carrier drift/diffusion length, which is typically a few hundred nanometers; for the record-efficiency cell, j = 0.78. Amorphous Si cells are most often fabricated in a superstrate configuration using a textured glass substrate coated with ITO as a transparent conductor. This then forms the starting point for the subsequent growth of a-Si:H, ZnO:Al buffer layer, and Ag back contact.

As cell efficiency becomes an increasingly important factor in PV cost reduction, the progress of thin-film Si technology has slowed in recent years. Yet the possibility of fabricating flexible modules using a roll-to-roll process provides unique application potential—for example, in building architecture. Thin-film Si triple-junction cells in which amorphous and microcrystalline Si cells are stacked together have shown a record efficiency of 13.4% (*34*).

Quantum dot solar cells (efficiency 9.9%)

Quantum dot (QD) solar cells take advantage of the fact that semiconductor quantum dots can be synthesized using (low-temperature) solution processing, with their band gap tunable by composition and size. The best QD solar cells so far are made using PbS or PbSe QDs as the active layer. The QDs are deposited by spin coating or dip coating and then passivated and functionalized using organic molecules or halide salts. A p-n junction is made in the QD layer using a combination of surface ligands. QD cells are typically made on ITO- or FTO-coated glass, using a metal oxide (typically ZnO or TiO_2) as an electron-selective contact. Molybdenum oxide and Au or Ag are typically used as the back contact.

The record published efficiency for QD solar cells is 9.9% using PbS QDs with a band gap of 1.4 eV, with an architecture similar to previous work (*35*). The 9.9% cells have very large voltage loss (v = 0.56), the largest loss of all cells reviewed here, which is attributed to the fact that the QDs have a distribution of sizes that results in a distribution of band gap energies. In addition, a high density of radiative sub–band gap states and strong nonradiative surface recombination due to the large surface-to-volume ratio in the quantum dots (diameter ~5 nm) leads to recombination. Inefficient transport of carriers by hopping through the QD film limits the QD film thickness that can be practically used. Together, incomplete absorption and strong recombination contribute to a high current loss (j = 0.66). (Note that in the analysis we use the first excitonic peak in the absorption spectrum as the band gap of the quantum dots; taking a smaller electronic band gap correspondingly increases v and decreases j.)

Beyond the Shockley-Queisser limit

The S-Q detailed-balance model describes the efficiency limit for a single-junction solar cell under one-sun illumination. Efficiencies beyond the S-Q limit can potentially be achieved for a single-junction cell by using the process of multiple exciton generation (converting a single photon to multiple excitons, e.g., in quantum dots), by up- or down-conversion of incident light (to make the incident spectral range better match the semiconductor absorption spectrum), or by limiting the range of radiative emission angles (raising the cell voltage). So far, none of these "third-generation" PV concepts has led to an enhanced efficiency record for one of the PV materials described above.

Multijunction solar cells constitute a very broad field of research and are beyond the scope of this review (36). The highest reported efficiency under one-sun illumination is 38.8% for a GaInAs/GaInP/GaAs/AlGaInAs/AlGaInP five-junction tandem geometry (37). However, the manufacturing cost of such a complex cell architecture is very high.

Concentrating PV—that is, increasing the solar flux by focusing light on a solar cell—can (linearly) increase J_{sc} and (logarithmically) increase V_{oc}, leading to a higher efficiency. This concept is being applied in PV systems using macroscale lenses or parabolic mirrors in combination with ultrahigh-efficiency tandem cells. A record cell efficiency of 46.0% was measured using a GaInP/GaAs/GaInAsP/GaInAs tandem cell under 508× concentrated light. Concentrating PV requires a tracking system to follow the Sun and requires direct (rather than diffuse) sunlight.

Historical efficiency trends

There are large differences in the rate of efficiency improvement for the different materials discussed above. For example, after more than 60 years of research, single-crystalline Si is a mature technology, and the efficiency improvements that have been achieved in recent years have been relatively small and gradual. In contrast, the record efficiency for the new perovskite materials has climbed rapidly since the first cells were demonstrated, although cells with these record efficiencies are not yet stable in efficiency.

To illustrate recent trends in cell development, Fig. 5 compares present efficiencies with the average annual increase in absolute efficiency over recent years. Crystalline and multicrystalline Si have recently shown only gradual absolute efficiency improvements in the range of 0.04 to 0.09% per year; the increase in crystalline Si efficiencies results from progress in Si heterojunction cells. The high-efficiency thin-film materials perovskite (2.7% per year), CdTe (0.9% per year), and CIGS (0.2% per year) have made important steps forward over the past few years.

Although these recently demonstrated efficiency increases are no guarantee of improvements in the future, the realization of large yearly increases in materials with remaining room for growth in v, j, and f hints that research efforts have not yet become constrained by fundamental limits. Additional research will tell whether the record efficiency of CIGS, CdTe, or perovskite cells (now 4 to 5% below that of Si IBC cells) can exceed that of Si cells. The efficiency record for thin-film GaAs cells has not been broken since 2012; a more recent record is for thin-film III-V dual-junction cells (31.6%) (29). In the low-efficiency (10 to 12%) category, quantum dot solar cells (1.3% per year) and organic solar cells (0.6% per year) continue to make strong progress. Dye-sensitized cells and CZTS have not reported efficiency improvements since 2012 and 2013, respectively. We note that historically, when materials are developed to the level of commercialization, further efficiency increases are often observed beyond the records first achieved in a research laboratory. For example, the present efficiency records for Si IBC, GaAs, and CdTe cells are realized in manufacturing laboratories.

Solar module efficiencies

Two important factors create a gap between the record efficiency of laboratory solar cells and the record efficiency of laboratory modules or average efficiency of commercial modules, respectively. First, record-efficiency cells are often small-area devices made using specialized laboratory techniques that may be too expensive for large-scale production. For example, thin-film vacuum deposition of metal contacts may be used in the lab, while screen printing of contacts, leading to much lower metal conductivity, is used in industrial fabrication facilities. Second, modules are made of a number of larger-area cells connected in series and encapsulated. In the case of wafer-based technologies, incorporation of cells in a module inevitably leads to current loss (due to incomplete filling of the module area) and fill factor loss (due to additional resistance in cell interconnects and the use of larger cells). Optical effects upon encapsulation may decrease or increase efficiency, depending on the specifics of module design. Efficiencies of typical thin-film modules are lower than those of corresponding record cells because of the "dead area" associated with monolithic interconnection of strip-like cells, inhomogeneities or imperfections in the larger areas of the cells, and series resistance because of larger current transport distances.

Furthermore, in practice, solar modules never operate under conditions equal to the standard test conditions (STC). The solar spectrum and intensity change during the day and vary with the time of year. The dependence of efficiency on incident power is generally lowest for cells with high FF. Here the high-efficiency (mono)crystalline materials as well as thin-film CIGS and CdTe (all with $FF > 0.79$) have an advantage over perovskites and the lower-efficiency thin-film materials ($FF < 0.73$). Also, solar modules heat up under solar irradiation, sometimes reducing the efficiency by 1 to 2% (absolute) relative to their STC value defined at 25°C. The temperature coefficient of efficiency depends strongly on material and is lower for Si heterojunction cells, CdTe, and CIGS than for other materials (38, 39). Another difference between practical, average module efficiency and STC efficiency is related to the fact that in practice modules receive light from a wide range of angles rather than perpendicularly incident light only. This leads to additional reflection losses. Finally, we note that nearly all cell/module combinations show reduction in efficiency over time. This is attributable to factors including degradation of the cells, oxidation of metallic cell interconnects, and photodegradation of polymer encapsulating layers; the magnitude of these effects depends on the cell/module combination (40). Understanding these degradation mechanisms in different climates is a complex but very important research challenge.

On the basis of their share in the market for PV systems, which had an estimated value of $96 billion in 2013 (1), it can be said that monocrystalline Si, multicrystalline Si, CdTe, and CIGS have evolved into mature high-efficiency technologies, with Si technology having >90% of the market share. Record efficiencies for large-area (>800 cm^2) modules are 22.4% for monocrystalline Si (9, 41), 18.5% for multicrystalline Si (9), 18.6% for CdTe, and 17.5% for CIGS (9, 42). These materials all belong to the >75% S-Q limit (for monocrystalline Si) or 50 to 75% S-Q limit (for multicrystalline Si, CIGS, CdTe) classes in Fig. 1B, directly demonstrating the importance of efficiency as a lever for large-scale application.

A recent development is the demonstration of single-junction GaAs solar modules with a record efficiency of 24.1% that are fabricated on an industrial scale and are now on their way to commercial exploitation (43). It will be interesting to see how the manufacturing costs for each of the >20% module technologies will decrease in the coming years. Thin-film solar cells deposited on thin foils are also expected to find new applications in areas where low weight-specific power (in terms of watts per gram) is desired, and in novel forms of building-integrated PV where flexible form factors or partial transparency for visible light are desired.

Thin-film amorphous and crystalline Si modules and flexible foils have also been developed to a commercial level but are applied on a much smaller scale because of their lower efficiency (12.2% for a module based on a tandem geometry) and higher manufacturing costs (44). Furthermore, small-area modules of dye-sensitized solar cells (efficiency 10.0%) (45, 46) and organic solar cells (9.5%) (30) are commercially available but thus far represent a small market. Thin-film perovskite, CZTS, and quantum dot solar cells have been demonstrated in the lab, but modules have not yet been demonstrated on an industrial scale. For perovskites, long-term stability and manufacturability have not yet been demonstrated; for CZTS and quantum dot solar cells, the low efficiency limits its commercial development. Table 1 summarizes technological strengths and selected research technology opportunities for all reviewed materials.

Large-scale application of PV

The present worldwide primary energy supply through all sources (fossil, nuclear, and renewable) amounts to 18.0 TW; final consumption is 12.3 TW (47). In principle, this energy need can be fully met using PV, in combination with proper energy transport and storage systems and secondary conversion into heat and fuels. Assuming a modest module efficiency of 20%, a system capacity factor of 15%, an average ground cover ratio of 50%, and 50% losses related to storage and secondary conversion, 1.6% of Earth's land area would be required to produce an amount of energy equal to the current primary supply. Although in absolute terms this is a very large number, it is not unrealistic. To put this in perspective, this area is less than 5% of the area used for agriculture worldwide. Also, note that substantial land areas are already used today for production of fossil fuels and various types of biofuel. Finally, by drastically increasing the efficiency of solar modules,

Table 1. Technology strengths and key research opportunities for photovoltaic materials. Materials are grouped by degree of technological development. Record cell and module efficiencies are indicated, based on certified measurements. GaInP and InP are not included as no significant development toward commercial technology exists; n.a., not available.

Material	Cell efficiency (%)	Module efficiency (%)	Technology strengths and options	Selected research/technology opportunities
Mature technologies deployed at large scale				
Monocrystalline Si	25.6	22.4	Earth-abundant material; >25-year track record	Further reduce recombination losses, in combination with new metallization schemes; improve light management in thinner wafers; improve IBC and SHJ cell designs
Multicrystalline Si	21.3	18.5	Earth-abundant material; >25-year track record	Improve wafer quality (minimize or passivate defects) to reduce recombination losses
CIGS	21.7	17.5	Flexible substrates	Improve light management; increase efficiency for large band gaps (tandem cells); reduce recombination losses, solution processing
CdTe	21.5	18.6	Flexible substrates; short energy payback time	Reduce recombination losses; develop thinner cell designs using light management
Emerging technologies deployed at smaller scale				
Dye-sensitized TiO_2	11.9	10.0	Tunable colors	Improve redox couple; reduce recombination losses; increase band gap; increase stability
Thin-film Si	11.4	12.2*	Flexible modules	Reduce recombination losses; improve light management
Organic	11.5	9.5	Flexible modules, semitransparent modules	Improve light management; increase band gap; increase stability; reduce recombination losses
Technology at the manufacturing level				
GaAs	28.8	24.1	Very high efficiency; flexible modules	Improve light management; develop IBC geometry; further develop thin-film multijunction cells by layer transfer
Technologies under development				
Perovskite	21.0	n.a.	Solution processing; flexible modules	Reduce recombination losses; improve cell stability; avoid use of Pb; increase efficiency for high–band gap materials (tandem cells); develop Si/perovskite tandems
CZTS	12.6	n.a.	Flexible modules	Reduce recombination losses; improve light management
Quantum dots	9.9	n.a.	Solution processing; flexible modules	Reduce recombination losses; improve light management; avoid use of Pb

*Microcrystalline Si/a-Si tandem geometry.

by integrating PV into buildings and other objects, and by combining PV technology with other renewable sources such as solar thermal energy and wind energy, a much smaller land area would be needed.

For PV to break through at such a large scale, a further reduction in costs of PV technology is required. As stated above, increasing cell efficiency is a key driver for reducing costs, as the costs of the solar cells themselves constitute only part (<50%) of the costs of a full PV system. Furthermore, the overall cost of PV systems will decrease by economy of scale as production capacity and installation volumes are further increased. Scalability of technology and availability of raw materials are essential parameters, as are the energy costs of fabricating PV systems at a large scale. Long lifetime and stable operation are additional crucial parameters, as is design-for-recycling, which allows valuable or toxic materials to be recovered in a practical way.

Future research directions: Light management and carrier management

We have categorized the architectures of 16 PV materials in terms of their current and voltage losses relative to the S-Q limiting values. To further increase the photocurrent in a particular cell design typically requires better management of light in order to reduce reflection, reduce parasitic absorption, and enhance light trapping in the active area of the cell. Nanophotonic concepts, in which nanostructures with typical length scales equal to or smaller than the wavelength of light are incorporated in the solar cell, can serve to reach these goals (*5*, *48*–*50*). Such structures can preferentially scatter and confine light so that it is better absorbed in the cell. Nanophotonic concepts leading to enhanced light trapping can also

reduce the required material thickness, thereby reducing bulk recombination (which enhances the voltage) and reducing costs. Nanophotonic control can also enhance the voltage by reducing entropic losses via control of the angular distribution of light emission from the cell. Large-area engineered nanopatterns integrated in solar cells can be made using soft-imprint technology that can be scaled up to the square-kilometer areas required for large-area production. We predict that further advances in nanophotovoltaics will lead to enhanced photocurrents, and thus enhanced efficiency, in several different PV materials and architectures. Nanophotonic concepts can also be used to engineer the color of solar panels, providing many new opportunities for building-integrated PV.

Improving the cell voltage and fill factor requires detailed understanding of and control over carrier recombination mechanisms in the cell. Making advances in the quality of electrical materials constitutes a major engineering research effort that involves identification of bulk, interface, and surface defects, as well as measurement of their density, energy levels, formation energy, annealing characteristics, passivation behavior, dopant diffusion, contact formation, and many other properties. The realization of high-quality PV materials that enable low-cost manufacturing of solar cells with efficiencies approaching the S-Q limit will require a coordinated international materials science and engineering approach.

Conclusions and outlook

The record efficiency of single-junction solar cells has continually increased over the years, but so far no PV material has closely approached the theoretical S-Q efficiency limit. Monocrystalline Si and GaAs have reached efficiencies of 26 to 29%; several polycrystalline materials (Si, CIGS, CdTe, perovskite) are in the 20 to 22% range; and all other common thin-film materials have efficiencies in the 10 to 13% range. There is much room for improvement in all of the materials discussed, and there is no doubt that efficiency records will continue to be broken in the future (*28*). The lower-efficiency (flexible) materials can find applications in building-integrated PV systems, flexible electronics, flexible power generation systems, and many other (sometimes niche) markets. High-efficiency (>20%) materials can find applications in large-area PV power generation for the utility grid, as well as in small and medium-sized systems for the built environment. They will enable very large-scale penetration into our energy system, starting now and growing as the cost per kilowatt-hour is reduced further by a factor of 2 to 3. This can be achieved by advanced (nanophotonic) cell designs in combination with an extensive materials science and engineering effort to further enhance PV material quality.

REFERENCES AND NOTES

1. *Technology Roadmap: Solar Photovoltaic Energy (2014 Edition)* (International Energy Agency, Paris, 2014).
2. W. Shockley, H. J. Queisser, Detailed balance limit of efficiency of p-n junction solar cells. *J. Appl. Phys.* **32**, 510–519 (1961). doi: 10.1063/1.1736034
3. T. Tiedje, Band tail recombination limit to the output voltage of amorphous silicon solar cells. *Appl. Phys. Lett.* **40**, 627–629 (1982). doi: 10.1063/1.93168
4. U. Rau, J. H. Werner, Radiative efficiency limits of solar cells with lateral band-gap fluctuations. *Appl. Phys. Lett.* **84**, 3735–3737 (2004). doi: 10.1063/1.1737071
5. U. Rau, U. W. Paetzold, T. Kirchartz, Thermodynamics of light management in photovoltaic devices. *Phys. Rev. B* **90**, 035211 (2014). doi: 10.1103/PhysRevB.90.035211
6. M. Topic, R. M. Geisthardt, J. R. Sites, Performance limits and status of single-junction solar cells with emphasis on CIGS. *IEEE J. Photovolt.* **5**, 360–365 (2015). doi: 10.1109/JPHOTOV.2014.2359135
7. S. W. Glunz *et al.*, The irresistible charm of a simple current flow pattern — 25% with a solar cell featuring a full-area back contact. In *Proceedings of the 31st European Photovoltaic Solar Energy Conference and Exhibition*, 259–263 (2015). doi: 10.4229/EUPVSEC20152015-2BP.1.1
8. J. Zhao, A. Wang, M. A. Green, F. Ferrazza, 19.8% efficient "honeycomb" textured multicrystalline and 24.4% monocrystalline silicon solar cells. *Appl. Phys. Lett.* **73**, 1991–1993 (1998). doi: 10.1063/1.122345
9. M. A. Green, K. Emery, Y. Hishikawa, W. Warta, E. D. Dunlop, Solar cell efficiency tables (version 45). *Prog. Photovolt. Res. Appl.* **23**, 1–9 (2015). doi: 10.1002/pip.2573
10. P. J. Cousins *et al.*, Gen III: Improved performance at lower cost. In *Proceedings of the IEEE Photovoltaic Specialists Conference (PVSC)*, 275–278 (2010). doi: 10.1109/PVSC.2010.5615850
11. M. A. Green, K. Emery, Y. Hishikawa, W. Warta, E. D. Dunlop, Solar cell efficiency tables (version 47). *Prog. Photovolt. Res. Appl.* **24**, 3–11 (2016). doi: 10.1002/pip.2728
12. Panasonic press release: Panasonic HIT® solar cell achieves world's highest energy conversion efficiency of 25.6% at research level (10 April 2014); http://news.panasonic.com/press/news/official.data/data.dir/2014/04/en140410-4/en140410-4.html.
13. P. J. Verlinden *et al.*, "Strategy, development and mass production of high-efficiency crystalline Si PV modules." Presented at 6th World Conference on PV Energy Conversion, Kyoto, November 2014.
14. A. Richter, M. Hermle, S. W. Glunz, Reassessment of the limiting efficiency for crystalline silicon solar cells. *IEEE J. Photovolt.* **3**, 1184–1191 (2013). doi: 10.1109/JPHOTOV.2013.2270351
15. D. D. Smith *et al.*, Generation III high efficiency lower cost technology: Transition to full scale manufacturing. In *Proceedings of the 38th IEEE Photovoltaic Specialists Conference (PVSC)*, 1594–1597 (2012). doi: 10.1109/PVSC.2012.6317899
16. B. M. Kayes *et al.*, 27.6% conversion efficiency, a new record for single-junction solar cells under 1 sun illumination. In *Proceedings of the 37th IEEE Photovoltaic Specialists Conference (PVSC)*, 4–8 (2011). doi: 10.1109/PVSC.2011.6185831
17. E. D. Kosten, J. H. Atwater, J. Parsons, A. Polman, H. A. Atwater, Highly efficient GaAs solar cells by limiting light emission angle. *Light Sci. Appl.* **2**, e45 (2013). doi: 10.1038/lsa.2013.1
18. C. J. Keavney, V. E. Haven, S. M. Vernon, Emitter structures in MOCVD InP solar cells. In *Conference Record of the 21st IEEE Photovoltaic Specialists Conference (PVSC)* **1**, 141–144 (1990). doi: 10.1109/PVSC.1990.111606
19. J. F. Geisz, M. A. Steiner, I. Garcia, S. R. Kurtz, D. J. Friedman, Enhanced external radiative efficiency for 20.8% efficient single-junction GaInP solar cells. *Appl. Phys. Lett.* **103**, 041118 (2013). doi: 10.1063/1.4816837
20. P. Jackson *et al.*, Properties of Cu(In,Ga)Se_2 solar cells with new record efficiencies up to 21.7%. *Phys. Status Solidi RRL* **9**, 28–31 (2015). doi: 10.1002/pssr.201409520
21. First Solar press release: "First Solar achieves efficiency, durability milestones" (5 February 2015); http://investor.firstsolar.com/releasedetail.cfm?ReleaseID=895118.
22. First Solar press release: "First Solar builds the highest efficiency thin film PV cell on record" (5 August 2014); http://investor.firstsolar.com/releasedetail.cfm?ReleaseID=864426.
23. G. Xing *et al.*, Low-temperature solution-processed wavelength-tunable perovskites for lasing. *Nat. Mater.* **13**, 476–480 (2014). doi: 10.1038/nmat3911; pmid: 24633346
24. N. J. Jeon *et al.*, Compositional engineering of perovskite materials for high-performance solar cells. *Nature* **517**, 476–480 (2015). doi: 10.1038/nature14133; pmid: 25561177
25. T. K. Todorov, K. B. Reuter, D. B. Mitzi, High-efficiency solar cell with Earth-abundant liquid-processed absorber. *Adv. Mater.* **22**, E156–E159 (2010). doi: 10.1002/adma.200904155; pmid: 20641095
26. W. Wang *et al.*, Device characteristics of CZTSSe thin-film solar cells with 12.6% efficiency. *Adv. Energy Mater.* **4**, 1301465 (2014). doi: 10.1002/aenm.201301465
27. R. Komiya *et al.*, Improvement of the conversion efficiency of a monolithic type dye-sensitized solar cell module. *Technical Digest, 21st International Photovoltaic Science and Engineering Conference, Fukuoka, Japan* **2**, C-5O-08 (2011).
28. An overview of all records with updated values for current and voltage relative to the S-Q limits (table S1) is kept up to date on http://lmpv.amolf.nl/SQ.
29. National Renewable Energy Laboratory, Best Research-Cell Efficiencies; www.nrel.gov/ncpv/images/efficiency_chart.jpg (2016).
30. M. Hosoya *et al.*, "Module development for polymer solar cells (abstract O-Pv-6-2)." Presented at the Grand Renewable Energy Conference, Tokyo, July 2014.
31. T. Kirchartz, K. Taretto, U. Rau, Efficiency limits of organic bulk heterojunction solar cells. *J. Phys. Chem. C* **113**, 17958–17966 (2009). doi: 10.1021/jp906292h
32. H. Sai, T. Matsui, K. Matsubara, M. Kondo, I. Yoshida, 11.0%-efficient thin-film microcrystalline silicon solar cells with honeycomb textured substrates. *IEEE J. Photovolt.* **4**, 1349–1353 (2014). doi: 10.1109/JPHOTOV.2014.2355037
33. T. Matsui *et al.*, Development of highly stable and efficient amorphous silicon based solar cells. In *Proceedings of the 28th European Photovoltaic Solar Energy Conference and Exhibition*, 2213–2217 (2013). doi: 10.4229/28thEUPVSEC2013-3DO.7.2
34. S.-W. Ahn, S.-E. Lee, H. M. Lee, "Toward commercialization of triple-junction thin-film silicon solar panel with >12% efficiency." Presented at the 37th PVSEC Conference, Frankfurt, September 2012.
35. C.-H. M. Chuang, P. R. Brown, V. Bulović, M. G. Bawendi, Improved performance and stability in quantum dot solar cells through band alignment engineering. *Nat. Mater.* **13**, 796–801 (2014). doi: 10.1038/nmat3984; pmid: 24859641
36. K. Tanabe, A review of ultrahigh efficiency III-V semiconductor compound solar cells: Multijunction tandem, lower dimensional, photonic up/down conversion and plasmonic nanometallic structures. *Energies* **2**, 504–530 (2009). doi: 10.3390/en20300504
37. P. T. Chiu *et al.*, 35.8% space and 38.8% terrestrial 5j direct bonded cells. In *Proceedings of the 40th IEEE Photovoltaic Specialist Conference (PVSC)*, 11–13 (2014). doi: 10.1109/PVSC.2014.6924957
38. A. Virtuani, D. Pavanello, G. Friesen, Overview of temperature coefficients of different thin film photovoltaic materials. In *Proceedings of the 25th European Photovoltaic Solar Energy Conference and Exhibition*, 4248–4252 (2010). doi: 10.4229/25thEUPVSEC2010-4AV.3.83
39. T. Mishima, M. Taguchi, H. Sakata, E. Maruyama, Development status of high-efficiency HIT solar cells. *Sol. Energy Mater. Sol. Cells* **95**, 18–21 (2011). doi: 10.1016/j.solmat.2010.04.030
40. R. Jones-Albertus, D. Feldman, R. Fu, K. Horowitz, M. Woodhouse, "Technology advances needed for photovoltaics to achieve widespread grid price parity" (2016); http://energy.gov/eere/sunshot/downloads/technology-advances-needed-photovoltaics-achieve-widespread-grid-price-parity.
41. R. Swanson, "The role of modeling in SunPower's commercialisation efforts." Presented at the Workshop on Challenges in PV Science, Technology, and Manufacturing, West Lafayette, IN, August 2012.
42. H. Sugimoto, High efficiency and large volume production of CIS-based modules. In *Proceedings of the 40th IEEE Photovoltaic Specialist Conference (PVSC)*, 2767–2770 (2014). doi: 10.1109/PVSC.2014.6925503
43. H. Sai *et al.*, Microcrystalline silicon solar cells with 10.5% efficiency realized by improved photon absorption via periodic textures and highly transparent conductive oxide. *Appl. Phys. Express* **6**, 104101 (2013). doi: 10.7567/APEX.6.104101
44. Tel Solar press release: "New record-breaking PV module efficiency has been achieved" (9 July 2014); www.solar.tel.com.
45. H. Ozawa, Y. Okuyama, H. Arakawa, Dependence of the efficiency improvement of black-dye-based dye-sensitized solar cells on alkyl chain length of quaternary ammonium cations in electrolyte solutions. *ChemPhysChem* **15**, 1201–1206 (2014). doi: 10.1002/cphc.201301025; pmid: 24482147

46. N. Tanabe, Dye sensitized solar cell for energy harvesting applications. *Fujikura Tech. Rev.* **42**, 109–113 (2013); www.fujikura.co.jp/eng/rd/gihou/2048261_11754.html.
47. International Energy Agency, Key World Energy Statistics (2015); www.iea.org/publications/freepublications/publication/key-world-energy-statistics-2015.html.
48. H. A. Atwater, A. Polman, Plasmonics for improved photovoltaic devices. *Nat. Mater.* **9**, 205–213 (2010). doi: 10.1038/nmat2629; pmid: 20168344
49. M. L. Brongersma, Y. Cui, S. Fan, Light management for photovoltaics using high-index nanostructures. *Nat. Mater.* **13**, 451–460 (2014). doi: 10.1038/nmat3921; pmid: 24751773
50. A. Polman, H. A. Atwater, Photonic design principles for ultrahigh-efficiency photovoltaics. *Nat. Mater.* **11**, 174–177 (2012). doi: 10.1038/nmat3263; pmid: 22349847

ACKNOWLEDGMENTS

This work is part of the research program of the Foundation for Fundamental Research on Matter (FOM), which is part of the Netherlands Organisation for Scientific Research (NWO). It is also supported by NanoNextNL, a nanotechnology program of the Dutch ministry of economic affairs, the European Research Council, and the Global Climate and Energy Project. The authors declare no competing financial interests. The data are archived in the laboratory of A.P. The data in table S1 will be continuously updated and made available on http://lmpv.amolf.nl/SQ.

SUPPLEMENTARY MATERIALS

www.sciencemag.org/content/352/6283/aad4424/suppl/DC1
Table S1
References (*51*–*56*)

10.1126/science.aad4424

RESEARCH ARTICLE SUMMARY

STRUCTURAL BIOLOGY

Architecture of the symmetric core of the nuclear pore

Daniel H. Lin,* Tobias Stuwe,* Sandra Schilbach, Emily J. Rundlet, Thibaud Perriches, George Mobbs, Yanbin Fan, Karsten Thierbach, Ferdinand M. Huber, Leslie N. Collins, Andrew M. Davenport, Young E. Jeon, André Hoelz†

INTRODUCTION: The nuclear pore complex (NPC) is the primary gateway for the transport of macromolecules between the nucleus and cytoplasm, serving as both a critical mediator and regulator of gene expression. NPCs are very large (~120 MDa) macromolecular machines embedded in the nuclear envelope, each containing ~1000 protein subunits, termed nucleoporins. Despite substantial progress in visualizing the overall shape of the NPC by means of cryo-electron tomography (cryo-ET) and in determining atomic-resolution crystal structures of nucleoporins, the molecular architecture of the assembled NPC has thus far remained poorly understood, hindering the design of mechanistic studies that could investigate its many roles in cell biology.

RATIONALE: Existing cryo-ET reconstructions of the NPC are too low in resolution to allow for de novo structure determination of the NPC or unbiased docking of nucleoporin fragment crystal structures. We sought to bridge this resolution gap by first defining the interaction network of the NPC, focusing on the evolutionarily conserved symmetric core. We developed protocols to reconstitute NPC protomers from purified recombinant proteins, which enabled the generation of a high-resolution biochemical interaction map of the NPC symmetric core. We next determined high-resolution crystal structures of key nucleoporin interactions, providing spatial restraints for their relative orientation. By superposing crystal structures that overlapped in sequence, we generated accurate full-length structures of the large scaffold nucleoporins. Lastly, we used sequential unbiased searches, supported by the biochemical data, to place the nucleoporin crystal structures into a previously determined cryo-ET reconstruction of the intact human NPC, thus generating a composite structure of the entire NPC symmetric core.

ON OUR WEBSITE

Read the full article at http://dx.doi.org/10.1126/science.aaf1015

RESULTS: Our analysis revealed that the inner and outer rings of the NPC use disparate mechanisms of interaction. Whereas the structured coat nucleoporins of the outer ring form extensive surface contacts, the scaffold proteins of the inner ring are bridged by flexible sequences in linker nucleoporins. Our composite structure revealed a defined spoke architecture in which each of the eight spokes spans the nuclear envelope, with limited cross-spoke interactions. Most nucleoporins are present in 32 copies, with the exceptions of Nup170 and Nup188, which are present in 48 and 16 copies, respectively. Lastly, we observed the arrangement of the channel nucleoporins, which orient their N termini into two 16-membered rings, thus ensuring that their N-terminal FG repeats project evenly into the central transport channel.

CONCLUSION: Our composite structure of the NPC symmetric core can be used as a platform for the rational design of experiments to investigate NPC structure and function. Each nucleoporin occupies multiple distinct biochemical environments, explaining how such a large macromolecular complex can be assembled from a relatively small number of genes. Our integrated, bottom-up approach provides a paradigm for the biochemical and structural characterization of similarly large biological mega-assemblies. ■

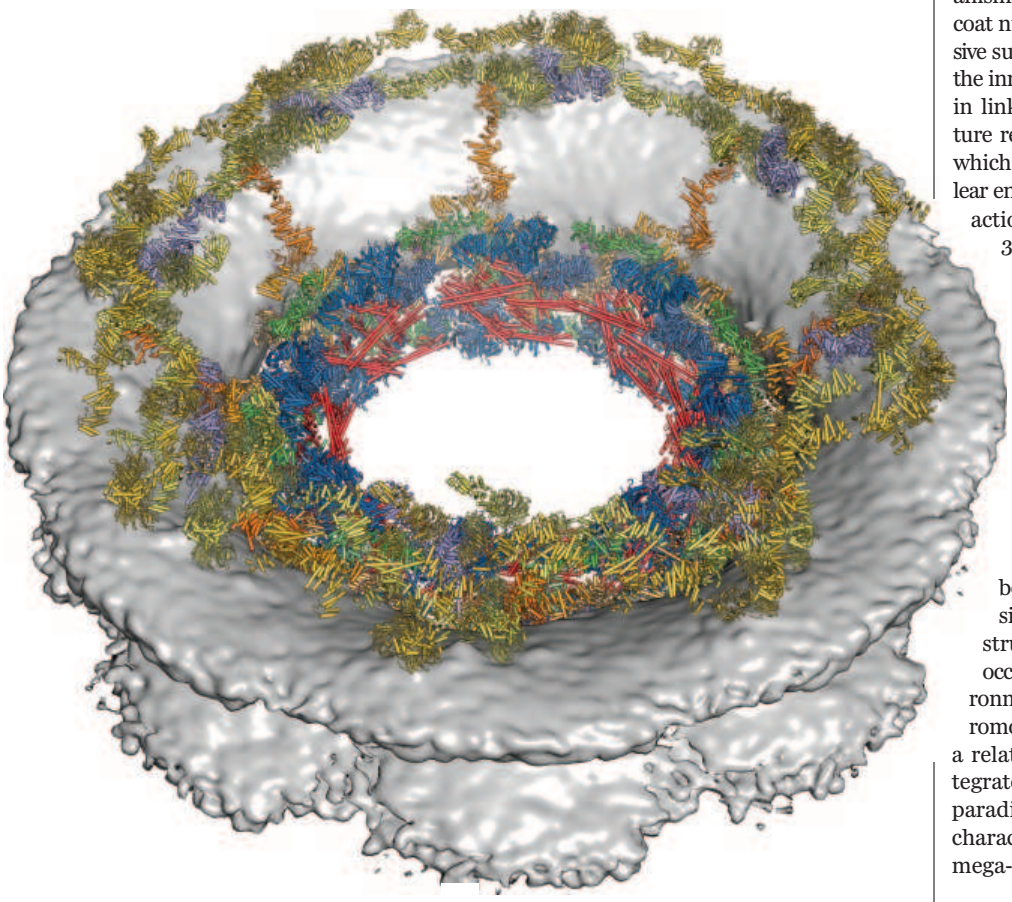

Composite structure of the NPC symmetric core. The composite structure shown here, viewed from above the cytoplasmic face, was generated by means of sequential unbiased docking of nucleoporin and nucleoporin complex crystal structures into a previously reported cryo-ET reconstruction of the intact human NPC. Nucleoporin structures are shown as colored cartoons, and the nuclear envelope density is shown as a gray surface.

The list of author affiliations is available in the full article online.
*These authors contributed equally to this work.
†Corresponding author. E-mail: hoelz@caltech.edu
Cite this article as D. H. Lin *et al.*, *Science* 352, aaf1015 (2016). DOI: 10.1126/science.aaf1015

RESEARCH ARTICLE

STRUCTURAL BIOLOGY

Architecture of the symmetric core of the nuclear pore

Daniel H. Lin,* Tobias Stuwe,* Sandra Schilbach, Emily J. Rundlet, Thibaud Perriches, George Mobbs, Yanbin Fan, Karsten Thierbach, Ferdinand M. Huber, Leslie N. Collins, Andrew M. Davenport, Young E. Jeon, André Hoelz†

The nuclear pore complex (NPC) controls the transport of macromolecules between the nucleus and cytoplasm, but its molecular architecture has thus far remained poorly defined. We biochemically reconstituted NPC core protomers and elucidated the underlying protein-protein interaction network. Flexible linker sequences, rather than interactions between the structured core scaffold nucleoporins, mediate the assembly of the inner ring complex and its attachment to the NPC coat. X-ray crystallographic analysis of these scaffold nucleoporins revealed the molecular details of their interactions with the flexible linker sequences and enabled construction of full-length atomic structures. By docking these structures into the cryoelectron tomographic reconstruction of the intact human NPC and validating their placement with our nucleoporin interactome, we built a composite structure of the NPC symmetric core that contains ~320,000 residues and accounts for ~56 megadaltons of the NPC's structured mass. Our approach provides a paradigm for the structure determination of similarly complex macromolecular assemblies.

The nuclear pore complex (NPC) is a massive molecular transport channel embedded in the nuclear envelope (*1*). In addition to its role as the sole mediator of bidirectional nucleocytoplasmic transport, the NPC is also involved in diverse cellular processes, including transcription, mRNA maturation, and genome organization (*1*, *2*). Despite their very large size (~120 MDa), NPCs are only composed of 34 different proteins (nucleoporins), which assemble into eightfold-symmetric, ~1000 Å–diameter pores that fuse the inner and outer nuclear membranes (Fig. 1, A and B) (*1*). Given their central role in cell biology, nucleoporins have been linked to a wide range of human diseases, including viral infection, cancer, and neurodegenerative disease (*1*, *3*–*9*). However, the structure of the NPC and the mechanisms by which it influences cellular processes have long been enigmatic.

Most nucleoporins are symmetrically distributed in the NPC, forming a symmetric core that in turn recruits asymmetric nucleoporins on the nuclear and cytoplasmic faces (Fig. 1, A and B). Many nucleoporins contain disordered repetitive sequences that are enriched in phenylalanine and glycine residues called FG repeats, which collectively form a central diffusion barrier that prevents passive diffusion of macromolecules with masses greater than ~40 kDa (Fig. 1, A and B). Larger macromolecules can only traffic through the NPC with the assistance of specialized karyopherin transport factors (*10*).

Division of Chemistry and Chemical Engineering, California Institute of Technology, 1200 East California Boulevard, Pasadena, CA 91125, USA.
*These authors contributed equally to this work. †Corresponding author. E-mail: hoelz@caltech.edu

Despite extensive efforts, the protein-protein interaction network within the NPC has remained incompletely characterized, presenting a fundamental limitation to our understanding of NPC architecture. Copurification and mass spectrometry approaches have revealed some of the strongest interactions, but they provide only general spatial restraints because of their limited resolution. The most well-characterized nucleoporin interactions are those within the coat nucleoporin complex (CNC), which makes up about half the mass of the symmetric core and contains Nup120, Nup85, Sec13, Nup145C, Nup84, Nup133, and, in some species, Seh1, Nup37, Nup43, and ELYS (*1*). Structural and biochemical analyses of CNCs from multiple species have revealed a highly conserved architecture in which α-helical domains form extensive interaction surfaces to assemble a large Y-shaped complex (*11*–*14*). Recent advances have dramatically increased the resolution of cryoelectron tomographic (cryo-ET) reconstructions of intact NPCs, facilitating the unbiased placement of 32 copies of a ~400-kDa crystal structure of the yeast CNC into the intact human NPC (*13*, *14*). The CNCs are arranged in pairs of concentric eight-membered rings on both the nuclear and cytoplasmic faces of the NPC, accounting for the majority of the observed protein density in the outer rings of the NPC (*13*, *14*).

Although the organization of the CNC in the intact NPC is well understood, relatively little has been known about the molecular architecture of the inner ring that lines the central channel. The disordered N-terminal FG repeats of the channel nucleoporins Nup49, Nup57, and Nsp1 project into the central channel, and their structured coiled-coil domains form a stable complex, termed the channel nucleoporin heterotrimer (CNT) (*15*, *16*). The CNT, Nic96, Nup192, and Nup145N collectively form a stable subcomplex called the inner ring complex (IRC) (*15*, *17*). The remaining components of the symmetric core, Nup170 and Nup53, are thought to mediate interactions with the nuclear envelope, but the details of the interaction network that assembles these proteins and links them to the CNCs have heretofore been poorly defined (*18*, *19*).

Crystal structures of many nucleoporin fragments from the symmetric NPC core have been determined, including the N-terminal domains (NTDs) of Nup192, Nup188, and Nup157; the C-terminal domain (CTD) of Nup170; the C-terminal tail domains (TAIL) of Nup192 and Nup188; the α-helical solenoid of Nic96, $Nic96^{SOL}$; and the CNT bound to helical region 1 of Nic96, CNT•$Nic96^{R1}$ (*15*, *20*–*26*). However, structures of full-length Nup192, Nup188, and Nup170 have remained elusive. Accurate placement of the existing structures into the intact NPC is limited by both their relatively small size and the resolution of available cryo-ET reconstructions. We used an integrated approach to obtain complete atomic structures and accurate, high-resolution biochemical restraints for determining the near-atomic architecture of the NPC symmetric core.

A major barrier preventing complete biochemical characterization of the NPC has been the difficulty of purifying large quantities of full-length nucleoporins from a single species. To overcome this hurdle, we developed expression and purification protocols for all symmetric core nucleoporins from the thermophilic fungus *Chaetomium thermophilum*, which exhibit superior biochemical stability (*27*). By reconstituting NPC symmetric core protomers from purified proteins, we were able to determine that the interactions between flexible linker sequences and large scaffold nucleoporins drive NPC assembly. We generated a high-resolution biochemical map for these interactions and determined a series of crystal structures that revealed the structural basis for the recognition of flexible linker sequences by the large scaffold nucleoporins. These crystal structures enabled the construction of complete atomic structures for the ordered scaffolds of Nup170, Nup192, and Nic96. Using our biochemical restraints for validation, we performed unbiased searches to dock the atomic structures into a cryo-ET reconstruction of the intact human NPC with high confidence (*28*), thus determining a composite structure of the NPC symmetric core.

Reconstitution of NPC symmetric core protomers

Using nucleoporins from *C. thermophilum*, we first directed our efforts toward reconstituting a soluble protomer that could recapitulate the interaction network within the assembled NPC. We used full-length proteins when possible, but FG repeats, disordered N- or C-terminal regions, or other sequences that prevented soluble protein expression were omitted (Fig. 1B, fig. S1, and tables S1 and S2). We first reconstituted a heterohexameric core CNC containing Nup120, Nup37, ELYS, Nup85, Sec13, and Nup145C, a complex analogous

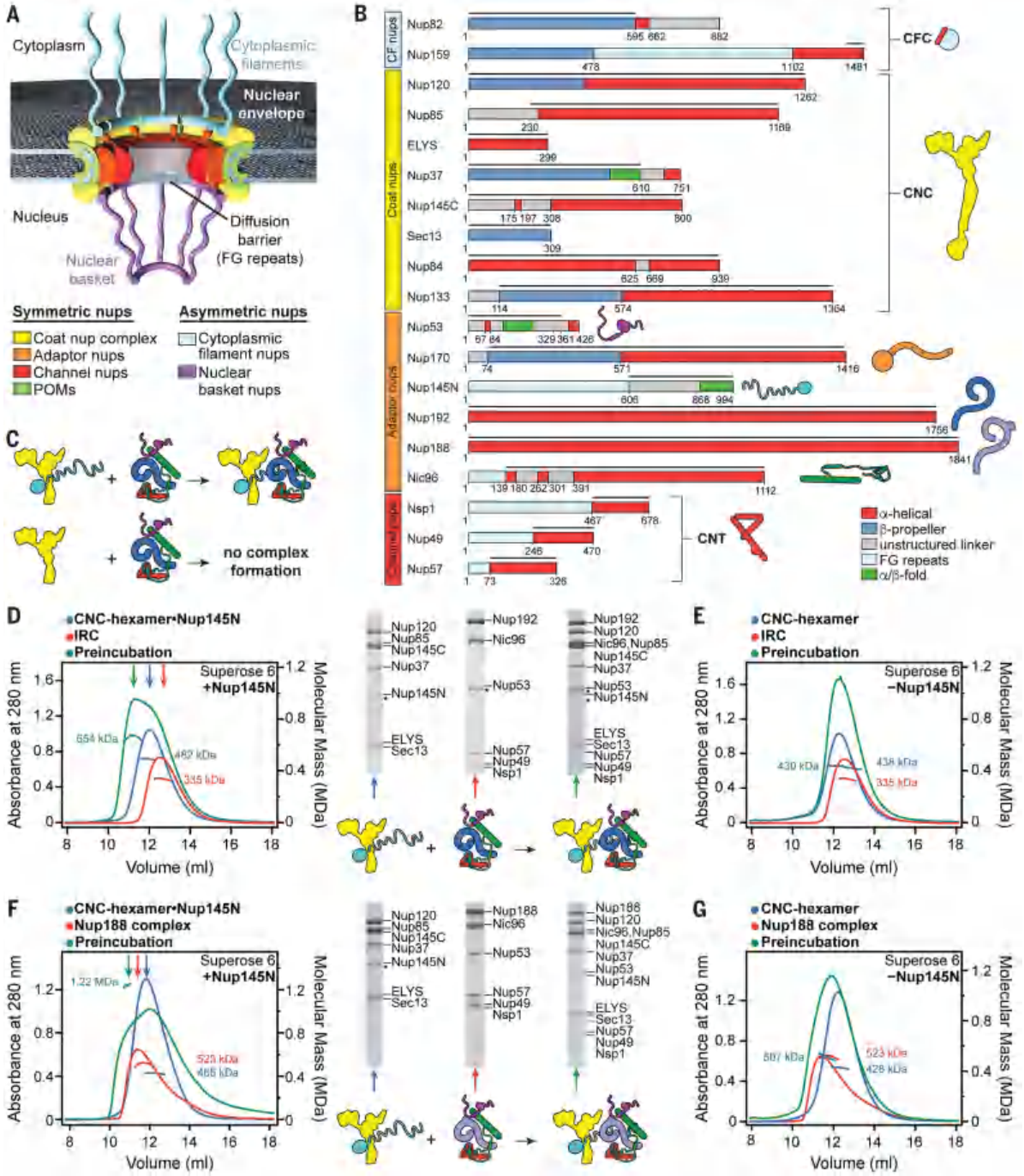

Fig. 1. Reconstitution of NPC symmetric core protomers. (**A**) Cross-sectional conceptual schematic of the NPC. CNCs, colored yellow, form outer rings above the membrane on the nuclear and cytoplasmic faces. Adaptor and channel nucleoporins, respectively colored orange and red, form concentric cylinders in the inner ring. Asymmetric nucleoporins are present on the cytoplasmic and nuclear faces of the NPC. (**B**) Domain organization of nucleoporins used in biochemical reconstitution experiments. Black lines indicate the construct boundaries used. Domains are drawn as horizontal boxes with residue numbers indicated below and are colored according to the legend (bottom right) for observed or predicted folds. Cartoons to the right are used throughout the figures to represent the nucleoporins. Some nucleoporins form stable complexes [CNC, CFC (cytoplasmic filament nucleoporin complex), and CNT) and are drawn as units. (**C**) Cartoon of the experimental setup of (D) to (G). The CNC was preincubated with the IRC or Nup188 complex in the presence or absence of Nup145N. Complex formation was only observed in the presence of Nup145N. (**D** and **E**) The reconstitution of NPC symmetric core protomers containing the CNC hexamer and IRC is dependent on Nup145N. Identical experiments were performed in (D) the presence or (E) the absence of Nup145N. Size-exclusion chromatography (SEC) coupled to MALS profiles of the complexes in isolation (red and blue) and after preincubation (green) are shown. Colored arrows above the chromatogram indicate the resolved peak fractions. Measured molecular masses are indicated for each peak. Representative Coomassie-stained SDS-PAGE gel slices for the peak fractions are shown in the center. Cartoons below the gel slices illustrate the respective complexes. (**F** and **G**) The reconstitution of NPC symmetric core protomers containing the CNC hexamer and Nup188 complex is dependent on Nup145N. Identical experiments were performed in (F) the presence or (G) the absence of Nup145N. Complete SDS-PAGE gels for all panels are shown in fig. S4.

to the yeast CNC that we previously crystallized (fig. S2, A and B) (*14*). This CNC heterohexamer was assembled with Nup84 and Nup133 to form a heterooctameric CNC (fig. S2C). Because of the poor solubility of the intact heterooctameric CNC, we focused our analysis on its heterohexameric core. Similarly, we extended our previous reconstitution of an IRC containing Nup192, Nic96, Nup145N, and the CNT by also incorporating Nup53 (fig. S3A and table S3) (*15*). We found that Nup188, which is evolutionarily related to Nup192, failed to incorporate into the IRC (fig. S3B). Rather, an analogous Nup188 complex formed in the absence of Nup192 (Fig. 1F). By preincubating the core CNC hexamer with either the IRC or the Nup188 complex, we reconstituted two distinct 13-protein complexes that are representative of NPC symmetric core protomers (Fig. 1, C, D, and F, and fig. S4, A and C).

Thus equipped with the ability to reconstitute NPC protomers, we sought to identify the interactions that link the IRC or the analogous Nup188 complex to the CNC. Nup145N is a component of the IRC and Nup188 complex, and Nup145C is a component of the CNC. They originate from the same polypeptide chain after posttranslational cleavage mediated by the Nup145N autoproteolytic domain (APD), which is located in the middle of the Nup145 precursor polypeptide (Fig. 1B) (*29*). Nup145C is composed of a U-bend α-helical solenoid, which is a core component of the CNC, and a disordered ~300-residue N-terminal extension (NTE) (*14*). Previous studies indicate that $Nup145N^{APD}$ can still bind the first six N-terminal residues of Nup145C after cleavage, thus offering a possible mechanism for linking the IRC to the CNC (*30*). The complexes did not interact in the absence of Nup145N (Fig. 1, E and G, and fig. S4, B and D). Moreover, $Nup145N^{APD}$ alone could be incorporated into the CNC (fig. S5). These results indicate that the IRC and CNC are flexibly attached via the long, intrinsically disordered sequences of Nup145N and Nup145C. $Nup145N^{APD}$ also binds to the β-propeller domain of the cytoplasmic filament nucleoporin Nup82 (*15*). However, given that this interaction was outcompeted by CNC binding (fig. S6), another interaction must play a role in retaining the cytoplasmic filaments at the cytoplasmic face of the NPC.

Symmetric core assembly is driven by flexible linkers

We next performed a systematic analysis of the molecular interaction network within the IRC and Nup188 complex, extending our previous work and additionally including Nup170 in our analysis (*15*). These complexes contain large scaffold domains in Nic96, Nup170, Nup188, and Nup192, as well as long, intrinsically disordered sequences in the linker nucleoporins Nup53 and Nup145N (Fig. 1B). The CNC is primarily held together by extensive interfaces between large α-helical solenoid domains (*1*, *14*), but recent studies have hinted that the architectural principles of the remaining symmetric core nucleoporins are different (*15*, *17*, *27*). For example, the scaffold nucleoporin Nic96 possesses a largely unstructured NTE containing two short helical regions, $Nic96^{R1}$ and $Nic96^{R2}$, that are essential for IRC assembly: $Nic96^{R1}$ recruits the CNT to the NPC, and $Nic96^{R2}$ binds Nup192 or Nup188 (*15*). To determine whether the structured domains of the scaffold nucleoporins interact with each other to drive symmetric core assembly, we tested whether $Nic96^{SOL}$, Nup170, Nup192, and Nup188 could form a complex; however, we observed no interaction (Fig. 2A and fig. S7A). Instead, complex formation was achieved only in the presence of the linker nucleoporins Nup53 and Nup145N (Fig. 2, B and C, and fig. S7, B and C). Thus, together with $Nic96^{NTE}$, the flexible linker nucleoporins Nup53 and Nup145N are the primary driving force of IRC and Nup188 complex assembly (*15*).

To further analyze the interaction network between the scaffold and linker nucleoporins, we tested which scaffolds interact with Nup53 or Nup145N to form heterodimers, focusing first on the interactions within the IRC and with Nup170. Nup53 formed robust complexes with Nup192, $Nic96^{SOL}$, and Nup170 (Fig. 2D and fig. S8). We previously reported that Nup145N interacts weakly with $Nic96^{SOL}$ (*15*); in this study, we found that Nup145N also binds to Nup192 and Nup170 (Fig. 2E and fig. S9). All of these scaffold-linker interactions are compatible, as demonstrated by the formation of heterotrimeric complexes (Fig. 2, D and E, and figs. S10 and S11). Nup192 and Nup170 can also bind to both linker nucleoporins simultaneously, indicating that the binding sites on the scaffolds are distinct (fig. S12, A and B). We were able to reconstitute a stoichiometric heterotetramer composed of Nup192, Nup170, Nup53, and Nup145N (fig. S12C).

To improve the biochemical resolution of our interaction map, we next identified the minimal sequence fragments of Nup53 and Nup145N that would be sufficient for scaffold recognition. We previously mapped an interaction between a Nup53 fragment, encompassing residues 31 to 67 ($Nup53^{R1}$), with $Nup192^{NTD}$ (Fig. 2F and fig. S13) (*20*). In this work, we found an adjacent fragment containing residues 69 to 90 ($Nup53^{R2}$) that was recognized by $Nic96^{SOL}$ (Fig. 2F and fig. S14, A and B). A Nup53 fragment including both of these binding sites (residues 1 to 90) was sufficient to link the two scaffolds into a heterotrimeric complex (fig. S14C). We also identified a C-terminal Nup53 fragment containing residues 329 to 361 ($Nup53^{R3}$) that interacted specifically with $Nup170^{NTD}$ (Fig. 2F and fig. S15). Conversely, the association between Nup170 and Nup145N mapped to Nup145N residues 729 to 750 ($Nup145N^{R3}$) and $Nup170^{CTD}$ (Fig. 2F and fig. S16). Nup192 recognized a fragment of Nup145N that spans residues 606 to 683 (Fig. 2F and fig. S17, A and B). $Nup192^{NTD}$ was sufficient for Nup145N binding (fig. S17C), but we also detected a weak interaction with $Nup192^{CTD}$ (fig. S17, D and E), suggesting that binding sites for Nup145N were distributed throughout Nup192. These minimal sequence fragments were specific for their binding partners (fig. S18).

Whereas preincubation of the two linker nucleoporins with Nup192, Nup170, and $Nic96^{SOL}$ produced a robust pentameric complex, the analogous preincubation with Nup188 in place of Nup192 produced a mixture of species (Fig. 2, B and C, and fig. S7, B and C). To understand this difference in behavior, we repeated the above analysis with Nup188 and identified a robust interaction with Nup145N, whereas Nup53 binding was barely detectible (Fig. 2, D and E, and figs. S8C and S9B). In contrast to our above results, however, Nup188 did not strongly bind Nup145N in the presence of Nup192 or Nup170 (Fig. 2, D and E, and fig. S11). Similar to $Nup192^{NTD}$, $Nup188^{NTD}$ was sufficient for Nup145N binding (fig. S19, A and B). However, the minimal Nup192-binding fragment of Nup145N was not sufficient for Nup188 binding (fig. S19, D and E). Instead, we only detected robust complex formation with a much longer fragment encompassing both the Nup192- and Nup170-binding sites (residues 606 to 750), which explains the exclusivity of their interactions (Fig. 2F and fig. S19C). We found a similar architecture for the Nup192- and Nup188-binding sites in $Nic96^{R2}$. The Nup192 minimal binding fragment (residues 286 to 301) again was insufficient for Nup188 binding (fig. S20, A to C), which instead required a larger fragment (residues 274 to 301) (Fig. 2F and fig. S20D). Consistent with these findings, several mutations in the N-terminal region of $Nic96^{R2}$ ablated Nup188 binding but had no effect on Nup192 binding (fig. S20, E to G) (*15*). Thus, Nup192 and Nup188 bind competitively to directly overlapping sequences in Nic96 and Nup145N, establishing the existence of a distinct Nup188 complex with an architecture analogous to the IRC.

In summary, we found that interactions between the large ordered scaffold nucleoporins and flexible interaction motifs in Nup53, Nup145N, and $Nic96^{NTE}$ were the dominant driving force for assembly of the NPC symmetric core outside of the CNCs. We built a biochemical map of these interactions by identifying minimal interaction motifs, revealing that the binding sites were spatially distributed throughout the scaffold nucleoporins, but that many of the binding sites on the linker nucleoporins were adjacent or overlapping in sequence (Fig. 2F). In doing so, we identified the exclusive interactions that provide a molecular basis for the formation of two distinct complexes, the Nup192-harboring IRC and an analogous Nup188 complex. Because existing crystal structures have not captured interactions between scaffold and linker nucleoporins, we used these results to identify important structural targets for determining the structural basis for this mode of interaction.

Atomic architecture of the Nup170 interaction network

We determined a crystal structure of the $Nup170^{NTD}$•$Nup53^{R3}$ complex at 2.1 Å resolution (Fig. 3, A and B, and tables S4 and S5). To obtain high-resolution diffraction, we deleted residues 293 to 305 from the 3D4A loop of $Nup170^{NTD}$ (fig. S21). $Nup170^{NTD}$ is composed of a seven-bladed β-propeller and a C-terminal α-helical domain (Fig. 3B). An N-terminal α-helix packs against the C-terminal

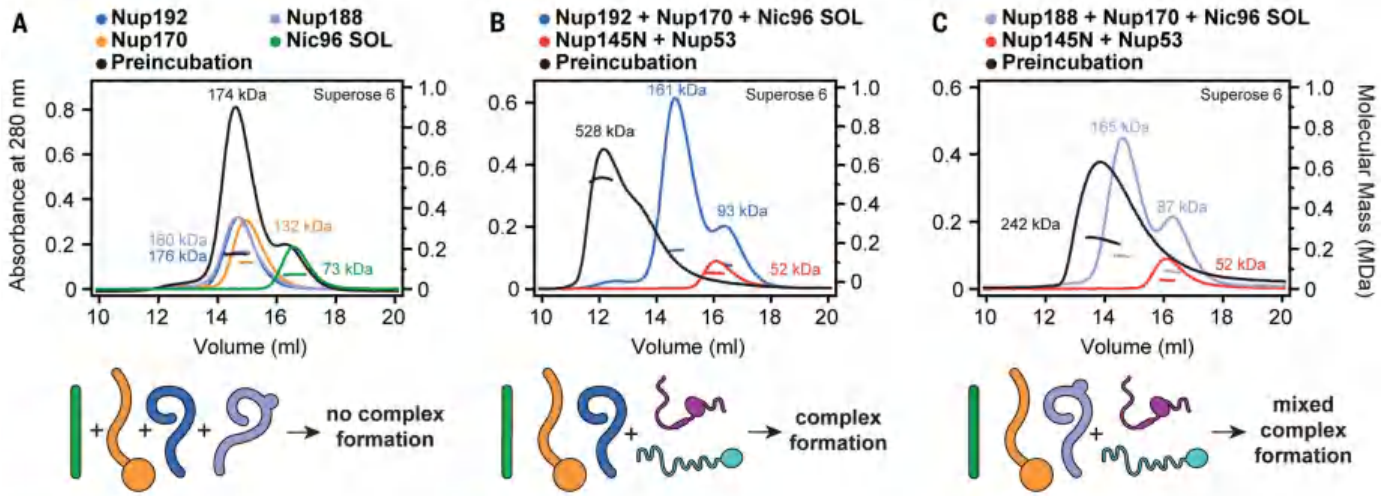

Fig. 2. Biochemical analysis of the interactions mediating NPC symmetric core assembly. (**A**) Scaffold domains of Nup192, Nup188, Nup170, and Nic96^{SOL} do not interact with each other. SEC-MALS profiles of the individual scaffolds alone (blue, purple, orange, and green) and after their preincubation with each other (black) are shown. Measured molecular masses are indicated for each peak. (**B** and **C**) Linker nucleoporins Nup53 and Nup145N mediate scaffold nucleoporin assembly. SEC-MALS profiles of a scaffold nucleoporin mixture (blue or purple), a linker nucleoporin mixture (red), and these complexes after their preincubation with each other (black) are shown. Mixtures of scaffold nucleoporins contained either (B) Nup192 or (C) Nup188. Complete SDS-PAGE gels for all chromatograms are shown in fig. S7. (**D** and **E**) Interaction network between scaffold nucleoporins and (D) Nup53 or (E) Nup145N. Scaffold nucleoporins were tested in SEC-MALS interaction experiments for their ability to form heterodimeric complexes with Nup53 or Nup145N and their compatibility for also forming heterotrimeric complexes. Check marks indicate complexes that can form in SEC-MALS experiments, x's indicate complexes that do not form, and dashes indicate complexes that were not tested. Complete SEC-MALS chromatograms and SDS-PAGE gels are shown in figs. S8 to S11. (**F**) Biochemical interaction map determined from SEC-MALS interaction experiments. Minimal regions of Nup145N and Nup53 sufficient for binding to components of the NPC are depicted by colored bars and dashed lines between interacting regions. Interactions that map to the same regions on Nup145N and Nup53 do not occur simultaneously. Complete SEC-MALS chromatograms and SDS-PAGE gels are shown in figs. S13 to S20. The nucleoporin cartoons are according to Fig. 1B.

D

	Nup53	Nup170•Nup53	Nup192•Nup53
Nic96 SOL	✓	✓	✓
Nup170	✓	–	–
Nup188	×	×	–
Nup192	✓	✓	–

E

	Nup145N	Nup170•Nup145N	Nup192•Nup145N	Nup188•Nup145N
Nic96 SOL	×	–	–	–
Nup170	✓	–	✓	×
Nup188	✓	×	×	–
Nup192	✓	✓	–	×

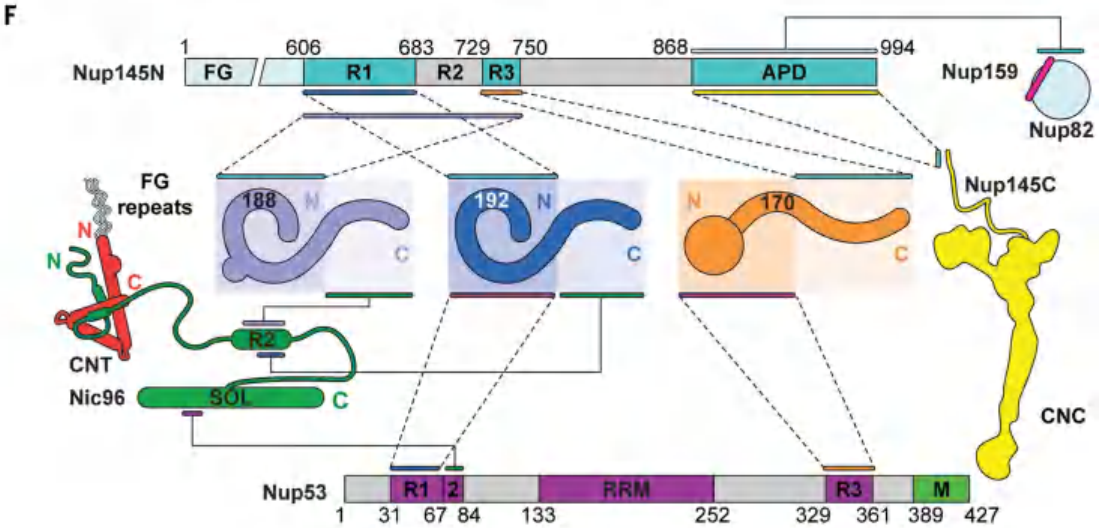

α-helical domain and is followed by three β-strands that form a triple "Velcro closure" against the β-propeller (Fig. 3B). Nup53 adopts an extended conformation and binds atypically to the side of the β-propeller, rather than the top, at blades 1 and 2 (Fig. 3B). The crystallized Nup53 fragment contained residues 329 to 361, but clear density was only observed for residues 342 to 355. Blade 2 of the Nup170 β-propeller deviates substantially from a canonical β-propeller blade to generate two hydrophobic pockets that accommodate Nup53 residues L346, L347, L353, and L354 (Fig. 3C). We identified several mutations in Nup170 and Nup53 that could disrupt their interaction (Fig. 3, D and E, and fig. S22, A and B). We observed a complete loss of binding with mutations to Nup170 residues that are evolutionary conserved—F199, I203, and Y235—suggesting that the binding interface is evolutionarily conserved (Fig. 3, D and E; fig. S21; and fig. S22, A and B).

Nup53 is anchored to the nuclear envelope by its C-terminal amphipathic helix, either directly or through an interaction with NDC1 (*18*, *19*). We found that Nup170 binds to Nup53^{R3}, which is directly adjacent to this C-terminal helix, prompting us to look for features in Nup170 that could also contribute to nuclear envelope binding. We

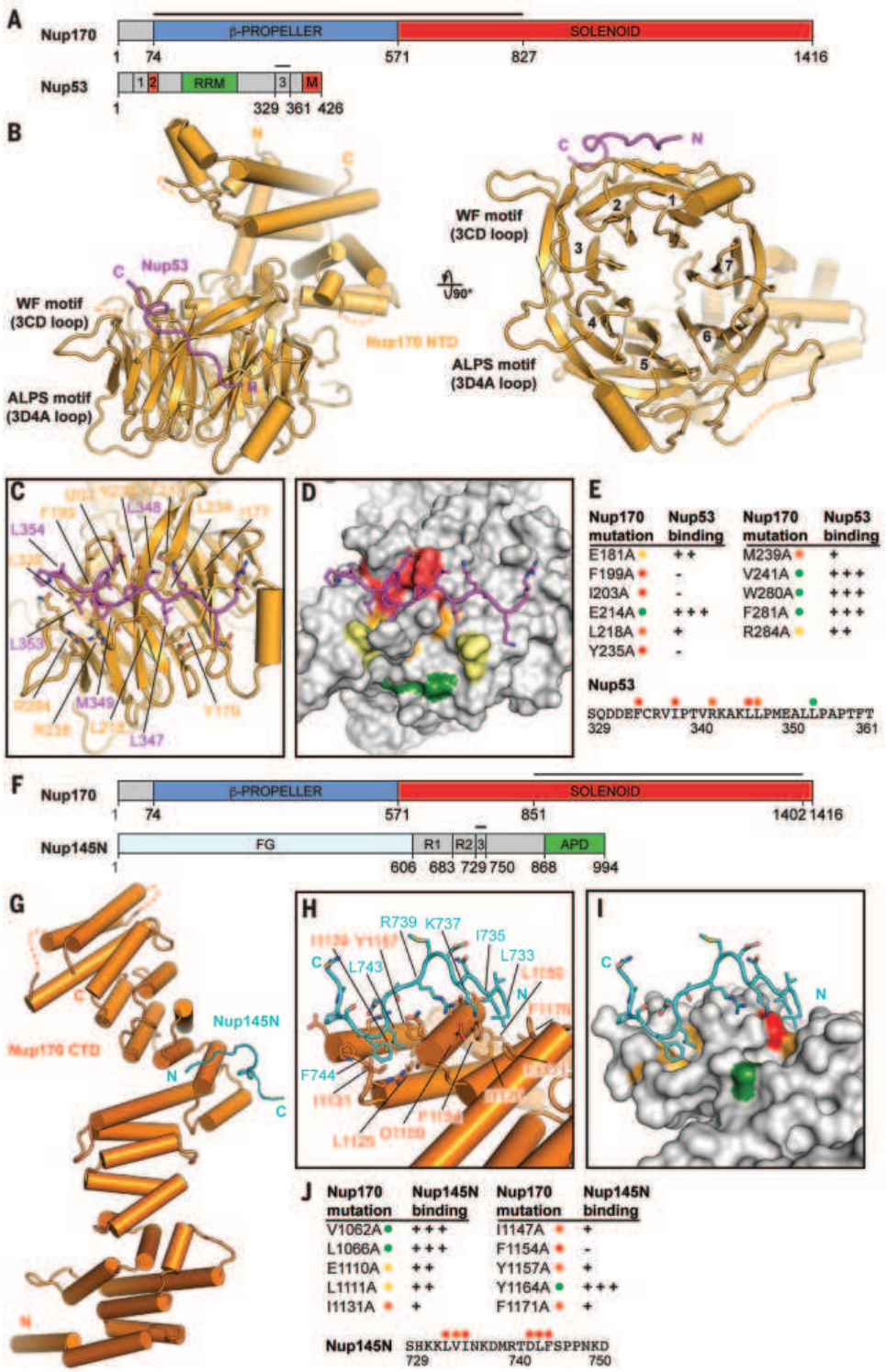

Fig. 3. Structural and biochemical analyses of the Nup170 interaction network. (**A**) Domain structures of Nup170 and Nup53. Black lines indicate fragments used for crystallization. (**B**) Cartoon of the crystal structure of the Nup170^{NTD}•Nup53^{R3} complex. A 90°-rotated view is shown on the right. The potential WF and ALPS membrane interaction motifs are indicated. (**C**) Close-up view of the interaction between Nup170 and Nup53. Nup170 and Nup53 residues involved in the interaction are labeled in orange and purple, respectively. (**D**) Graphic summary of mutational analysis of the Nup170^{NTD}-Nup53^{R3} interaction. Nup170 is shown in surface representation from the same view as in (C). Residues are colored in red, orange, yellow, or green to indicate mutations that had a strong, moderate, weak, or nonexistent effect on binding, respectively. (**E**) Tabular summary of tested Nup170 mutants and their effect on Nup53 binding. Three plus signs indicate wild-type binding, two plus signs indicate moderately weakened binding, one plus sign indicates weak binding, and a dash indicates no binding. Mutations in Nup53 that were tested for binding are indicated by dots above the sequence, following the same color code as in (D). Chromatograms and representative SDS-PAGE gels are shown in fig. S22. (**F**) Domain structures of Nup170 and Nup145N. Black lines indicate fragments used for crystallization. (**G**) Cartoon of the crystal structure of the Nup170^{CTD}•Nup145N^{R3} complex. (**H**) Close-up view of the interaction between Nup170 and Nup145N. Nup170 and Nup145N residues involved in the interaction are labeled in orange and cyan, respectively. (**I**) Graphic summary of mutational analysis of the Nup170^{CTD}-Nup145N^{R3} interaction. Nup170 is shown in surface representation from the same view as in (H). Coloring is according to (D). (**J**) Tabular summary of mutational analysis of the Nup170^{CTD}-Nup145N^{R3} interaction, with the same symbols and coloring as in (E). Chromatograms and representative SDS-PAGE gels are shown in fig. S23. Single-letter abbreviations for the amino acid residues are as follows: A, Ala; C, Cys; D, Asp; E, Glu; F, Phe; G, Gly; H, His; I, Ile; K, Lys; L, Leu; M, Met; N, Asn; P, Pro; Q, Gln; R, Arg; S, Ser; T, Thr; V, Val; W, Trp; and Y, Tyr.

identified two motifs next to the C terminus of Nup53^{R3} that would be juxtaposed with the nuclear envelope. The first was a WF motif composed of solvent-exposed, evolutionarily conserved tryptophan and phenylalanine residues in the 3CD loop (Fig. 3B and fig. S22C). Because tryptophan residues are enriched at membrane interfaces, the WF motif may reinforce membrane binding (*31*). The second motif, residing in the 3D4A loop that we deleted for crystallization, is predicted to form an amphipathic helix with an evolutionarily conserved absence of charged residues; this feature is characteristic of amphipathic lipid packing sensing (ALPS) motifs, which are also present in Nup120 and Nup133 (fig. S22, C and D) (*32*, *33*). The Nup170 ALPS motif contains a universally conserved proline residue on the polar face of the helix, a feature reminiscent of antimicrobial membrane destabilizing peptides (fig. S22D) (*34*). We propose that these additional features on Nup170 act synergistically with the binding of Nup53 to the nuclear envelope to help maintain the extreme membrane curvature in nuclear pores.

We next determined a crystal structure of the Nup170^{CTD}•Nup145N^{R3} complex at 3.5 Å resolution, using a 2.1 Å–resolution structure of Nup170^{CTD} in the apo state as a search model

(Fig. 3, F and G, and tables S4 and S6). Nup170^{CTD} forms an elongated α-helical solenoid containing two stacks of irregular helical pairs, arranged in a zig-zag fashion (Fig. 3G). The two stacks share a long helix (α31) that caps the first stack and initiates the second stack. Nup145N^{R3} binds to a pair of deep hydrophobic pockets on either side of the first two helices of the second helical stack, inserting residues L733 and I735 into the first pocket and L743 and F744 into the second pocket (Fig. 3, G and H). Mutation of any of these residues completely abolished binding to Nup170 (Fig. 3, I and J, and fig. S23B). Similarly, mutation of the residues that formed the hydrophobic pockets (F1171, F1154, I1131, and Y1157) strongly affected binding (Fig. 3, I and J, and fig. S23A). The hydrophobic nature of both binding pockets is retained throughout eukaryotes (fig. S21), suggesting the evolutionary conservation of this interaction. Only minimal rearrangements of the binding pocket occur upon Nup145N binding (fig. S23C).

The Nup145N sequence that binds to Nup170 is also highly conserved throughout eukaryotes, and the homologous residues that are critical for Nup170 binding are conserved in humans (fig. S24A). During mitosis, extensive phosphorylation of *hs*Nup98 (*hs, Homo sapiens*), the human homolog of Nup145N, leads to NPC and nuclear envelope disassembly (*35*). The most abundant mitotic phosphorylation sites in *hs*Nup98 are at residues S608 and S612 (S741 and S745 in *C. thermophilum*), which flank L610 and F611 (L743 and F744 in *C. thermophilum*—residues that we found to be critical for Nup170 binding; fig. S24, A and B) (*35*). To test the possibility that the interaction between Nup170 and Nup145N could be regulated by phosphorylation, we reconstituted a *hs*Nup155•*hs*Nup98 heterodimer that was homologous to our crystallized complex. We observed a robust interaction between *hs*Nup155^{CTD} and the corresponding minimal *hs*Nup98 fragment, which was partially disrupted by a double phosphomimetic mutation (S608E and S612E) (fig. S24C). As revealed by the Nup170^{CTD}•Nup145N^{R3} structure, S612 (S745 in *C. thermophilum*) forms a hydrogen bond with N609 (D743 in *C. thermophilum*). Phosphorylation would therefore destabilize the conformation required to insert the critical hydrophobic residues into the binding pocket in Nup170 (fig. S24B). Disruption of this hydrogen bond by mutagenesis also completely abolished binding (Fig. 3J and fig. S23B). Thus, the Nup170-Nup145N interaction is not only highly conserved, but its disruption is also a key step in mitotic NPC disassembly in humans.

Our structures of Nup170^{NTD} and Nup170^{CTD} did not overlap in sequence, preventing accurate modeling of the full-length protein. Therefore, we crystallized a larger fragment of Nup170 that contained the α-helical solenoids of both domains (Nup170^{SOL}, residues 575 to 1402), and determined the crystal structure at 4.0 Å resolution (fig. S25A, tables S4 and S5, and Movie 1). Whereas we observed no conformational variability for the helices present in Nup170^{NTD}, the Nup170^{CTD} solenoid exhibited a ~20° rotation resulting from a minor rearrangement of helix α27 (fig. S25A). We observed a similar conformational variability in the Nup170^{CTD}•Nup145N^{R3} complex structure, where all four molecules in the asymmetric unit adopted different conformations (fig. S25B). With the structure of Nup170^{SOL} as a template, we superposed the structures of Nup170^{NTD} and Nup170^{CTD}, obtaining a total of eight different conformations for full-length Nup170 (figs. S25B and S26 and Movie 2).

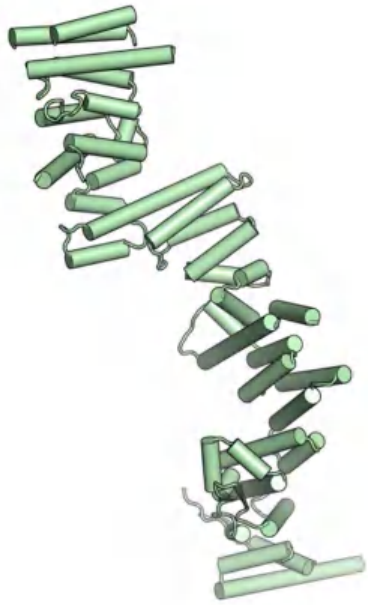

Movie 1. Generation of the Nup170•Nup53^{R3}•Nup145N^{R3} complex structure by superposition. A 360° rotation of the crystal structure of Nup170^{SOL} is shown, followed by a demonstration of the process used for generating the full-length structure by superposition. Colors are the same as in fig. S25.

Movie 2. Morph animation of observed Nup170 conformations. The eight different conformations observed in the superposition-generated structures of full-length Nup170 are animated. The animation pauses at each of the eight experimentally observed conformations of Nup170, which are colored the same as in fig. S25.

Molecular basis for recognition of Nup53 by Nic96

We determined crystal structures of apo Nic96^{SOL} and a Nic96^{SOL}•Nup53^{R2} complex at 3.3 and 2.65 Å resolution, respectively (Fig. 4, A and B; fig. S27; tables S4 and S7; and Movie 3). Nic96^{SOL} forms a rod-shaped molecule consisting of a U-bend α-helical solenoid with the N terminus situated in the middle of the rod. Although residues 31 to 84 of Nup53 were included in the crystallization construct, only residues 67 to 84 were visible in the electron density. Residues 67 to 84 of Nup53 form an amphipathic helix that buries its hydrophobic face into a hydrophobic groove formed by helices α14, α15, and α16 near the U-bend end of the Nic96 solenoid (Fig. 4, B and C). Consistent with our crystal structure, we found that mutations to the hydrophobic residues in this pocket disrupted binding (figs. S28 and S29). Similar to the interaction between Nup170 and Nup145N, we observed minimal conformational rearrangements upon Nup53 binding (Fig. 4D).

Structure of Nup192

Nup192, the largest symmetric core nucleoporin, appears to be shaped like a question-mark at low resolution (*26*). Crystal structures exist for Nup192^{NTD} (residues 1 to 958) and Nup192^{TAIL} (residues 1397 to 1756), but the atomic structure of the entire molecule has thus far remained unresolved (*15*, *20*, *26*). To determine the complete atomic structure of Nup192, we obtained crystals of an engineered Nup192 truncation mutant, Nup192$^{\Delta HEAD}$, from which we had deleted (Δ) the N-terminal head domain (HEAD; residues 1 to 152) and replaced a loop encompassing residues 167 to 184 with a short glycine-serine linker. We determined the crystal structure of Nup192$^{\Delta HEAD}$ at 3.2 Å resolution (Fig. 4, E and F; fig. S30; and tables S4 and S7).

The N-terminal portion of the previously unresolved middle domain of Nup192 (Nup192^{MID}) contains three additional ARM repeats (α46 to α53, residues 959 to 1154) that continue the superhelical solenoid that we previously observed in Nup192^{NTD} (Fig. 4F) (*20*). Similarly, the C-terminal portion of Nup192^{MID} contains a HEAT repeat (α60 to α61, residues 1330 to 1376) that extends the Nup192^{TAIL} solenoid, so that the entire protein forms a continuous HEAT-ARM repeat solenoid (Fig. 4F) (*15*). However, we observed an unusual insertion (residues 1155 to 1329) between the ARM repeats and the HEAT repeat in Nup192^{MID}, containing a ~50-residue helix, α58, that reaches ~75 Å from the beginning of Nup192^{TAIL} to the C terminus of Nup192^{NTD} (Fig. 4F). This insertion,

which we termed the Tower helix, buries several hydrophobic residues against the bottom of Nup192^{NTD}, inducing minor rearrangements that facilitate packing of the Tower helix. Although the Tower helix has only a moderate signature in secondary structure predictions, the evolutionarily related Nup188 is also predicted to contain a similarly long ~40-residue helix at the same location. However, previous models of full-length Nup188 and Nup192 did not anticipate the existence of the Tower helix, highlighting the importance of experimentally determining atomic-resolution structures (*22*, *36*).

Taking advantage of the extensive overlap between our crystal structure of Nup192$^{\Delta HEAD}$ and the existing structures of Nup192^{NTD} and Nup192^{TAIL}, we generated the structure of full-length Nup192 by superposition (Fig. 4G, fig S31, and Movie 4). Inspection of the full-length protein revealed that the first loop in the HEAD domain between α1 and α2 is close enough to contact loops in the MID domain, predominantly with polar and charged residues (Fig. 4G and fig. S31). The binding sites on Nup192 for Nup53 and Nic96, which we previously identified via mutagenesis, are respectively located at the top and bottom of the molecule, ~140 Å apart from each other (fig. S32) (*15*, *20*).

Architecture of the NPC symmetric core

Recent advances in cryo-ET have produced rapidly improving reconstructions of intact NPCs, with the most recent reconstructions reporting average resolutions up to ~20 Å in the best-resolved regions (*13*, *28*, *37*). We previously docked 32 copies of the yeast CNC into a ~34 Å reconstruction of the intact human NPC, taking advantage of the distinctive shape and large size of the complex (*14*). With the addition of the Nic96^{SOL}•Nup53^{R2} structure and the full-length superposition-generated structures of Nup192 and Nup170•Nup53^{R3}•Nup145N^{R3} reported here, as well as our recently reported crystal structure of the CNT•Nic96^{R1} complex, accurate structures were available for essentially the entire ordered mass of the NPC symmetric core (*15*). The domain architectures of the symmetric core nucleoporins are highly conserved from fungi to humans (fig. S33). We successfully located these structures in the recently reported ~23 Å reconstruction of the human NPC, and the arrangement of nucleoporins was validated by our biochemical restraints (*28*). We used an incremental approach to confidently place the crystal structures, starting with the largest structures with the most distinctive shapes and iteratively removing the occupied density to search for other structures (fig. S34). Because the cryo-ET map possesses eightfold rotational symmetry, each solution defined the location and orientation of eight copies of each molecule. We first tested our approach with the yeast CNC crystal structure and found four distinct placements with exceptional scores compared with 50,000 other refined placements, which is in excellent agreement with our previous results (fig. S35A) (*14*). We also readily identified the location and orientation of human Nup84^{CTD}•Nup133^{CTD} in unbiased searches (fig. S35B) (*38*). Based on previously reported biochemical data, we manually docked the Nup37, Nup43, and Nup133 β-propellers and locally optimized their fit (fig. S35C) (*13*, *39*–*41*).

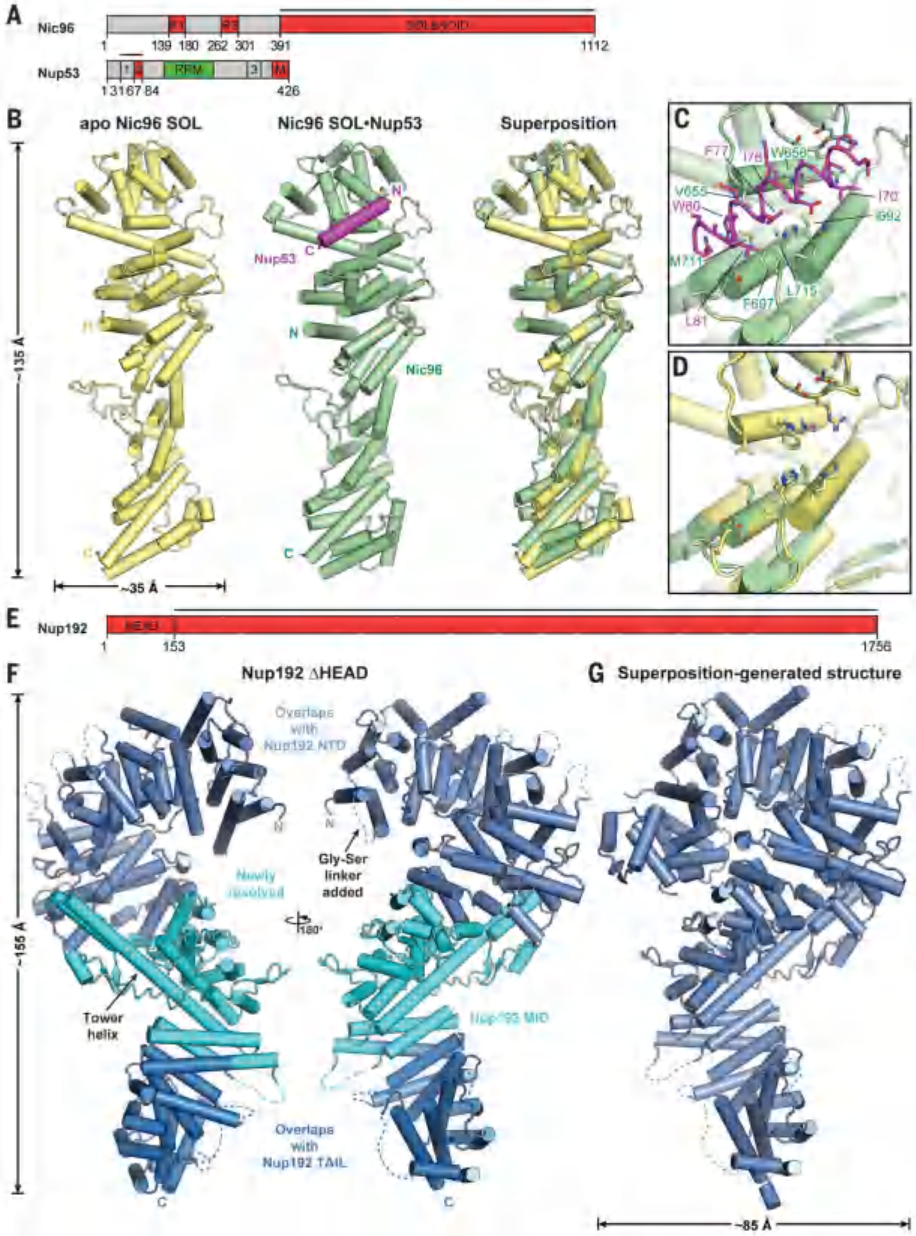

Fig. 4. Structural analysis of the IRC nucleoporins Nic96 and Nup192. (**A**) Domain structures of Nic96 and Nup53. Black lines indicate fragments used for crystallization. (**B**) Cartoons of the crystal structures of apo Nic96^{SOL} (yellow), the Nic96^{SOL}•Nup53^{R2} complex (green and purple), and their superposition (see also Movie 3). (**C**) Close-up view of the Nup53^{R2}-binding site in Nic96^{SOL}. For clarity, Nup53 is shown in ribbon representation. Nic96 and Nup53 residues involved in the interaction are labeled in green and purple, respectively. (**D**) Close-up view of the superposition of apo and Nup53-bound structures of Nic96^{SOL}, revealing minimal conformational changes. (**E**) Domain structure of Nup192. The black line indicates the fragment used for crystallization. (**F**) Cartoon of the crystal structure of Nup192$^{\Delta HEAD}$. A 180°-rotated view is shown on the right. Regions of Nup192 that were resolved in previous crystal structures are colored in shades of blue; the region of the protein that was not included in previous crystallographic analyses is shaded cyan. (**G**) Cartoon of the structure of full-length Nup192, generated by superposing fragment crystal structures (see also fig. S31 and Movie 4).

We next performed unbiased searches for Nup170 and Nup192 by using a map from which any density corresponding to the CNCs had been removed (fig. S36). Because our crystallographic data indicated considerable flexibility in the Nup170 solenoid, we performed searches with the eight different conformations of Nup170. These searches identified two conformations that each yielded two distinct top-scoring solutions (fig. S36, A and B). Searches with full-length Nup192 revealed six solutions, but because Nup192 and Nup188 could

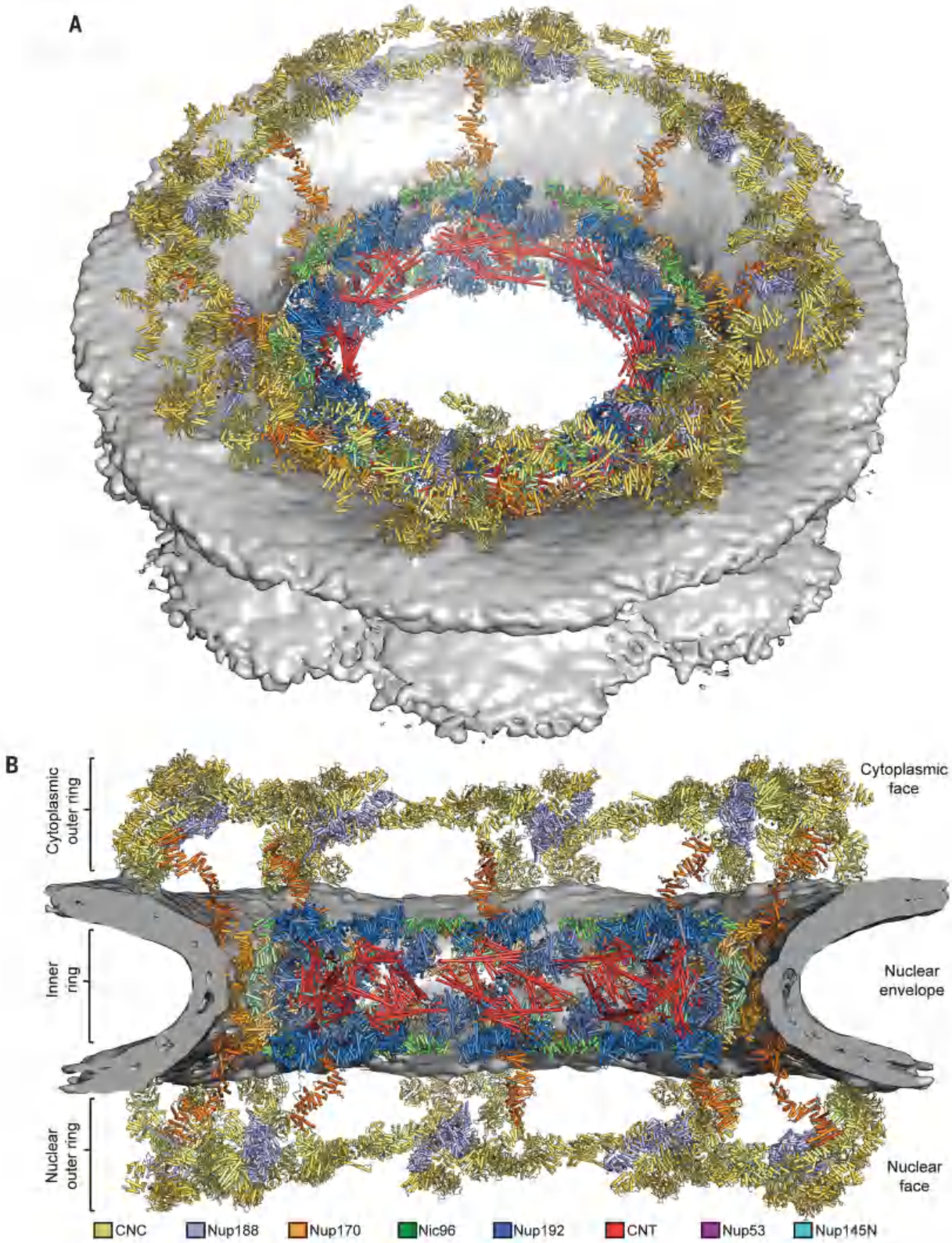

Fig. 5. Architecture of the NPC symmetric core. The composite structure of the NPC symmetric core was generated by docking nucleoporin and nucleoporin complex crystal structures into the cryo-ET reconstruction of the intact human NPC (Electron Microscopy Data Bank entry number EMD-3103). The density corresponding to the nuclear envelope is shown as a gray surface. Proteins are color-coded according to the legend at the bottom. (**A**) View from above the cytoplasmic face and (**B**) a cross-sectional view from within the transport channel (see also figs. S34 to S37 and S40 and Movie 5).

not be distinguished at this resolution, we assigned two of these as Nup188 based on our biochemical results and previously reported cross-linking data, as detailed in the methods (fig. S36C) (*13*, *42*). After removing the density assigned to Nup170, Nup192, and Nup188, we successfully located four distinct copies of the Nic96^{SOL}•Nup53^{R2} and CNT•Nic96^{R1} complexes (fig. S37, A and B). Lastly, we inspected the remaining density in the inner ring in an attempt to locate the ordered domains of Nup53 and Nup145N. We determined crystal structures of Nup53^{RRM} (RRM, RNA recognition motif domain) and Nup145N^{APD}•Nup145C^{N} (where the superscript N denotes residues 1 to 6) at 0.8 and 1.3 Å resolution, respectively, but we could not unambiguously place them because of their small size and globular shape (fig. S38 and tables S4, S8, and S9). We attempted to generate biochemical restraints to confidently dock Nup53^{RRM}, but we were unable to find any binding partners (fig. S39). However, we did find a pair of continuous densities that readily accommodated two additional Nup170 molecules in a third distinct conformation (fig. S40A). These placements were buried in our original global search, but the conformation of this Nup170 structure nevertheless differed slightly from the remaining map density, suggesting that our crystal structures did not capture the full conformational range of Nup170 (fig. S40, B and C).

Having placed the structures of the CNC hexamer, Nup84^{CTD}•Nup133^{CTD}, Nup133^{NTD}, Nup37^{NTD}, Nup43, Nup188^{NTD}, Nup188^{TAIL}, Nup192, Nup170•Nup53^{R3}•Nup145N^{R3}, Nic96^{SOL}•Nup53^{R2}, and CNT•Nic96^{R1}, we acquired a composite structure that accounts for nearly all of the density in the NPC symmetric core, corresponding to ~56 MDa of protein mass, or ~320,000 ordered residues (Fig. 5, fig. S41, table S10, and Movie 5). In total, the composite structure contains a stoichiometry of 16 copies of Nup188; 32 copies of the CNC, Nup192, Nic96, and CNT; and 48 copies of Nup170, Nup53, and Nup145N. Overall, this stoichiometry is in good agreement with a previous study that used mass spectrometry to measure the relative abundances of nucleoporins in the human NPC (*43*).

Spoke architecture

The symmetric core of the NPC consists of eight spokes related by an eightfold rotational axis of symmetry that is perpendicular to the nuclear envelope (Fig. 5A). Outer rings reside above the nuclear and cytoplasmic faces of the nuclear envelope, and an inner ring is embedded in the pore and spans the nuclear envelope (Fig. 5B). When viewed from the cytoplasm, the nucleoporins form distinct cylinders, with the CNTs lining the transport channel, surrounded by successive cylinders formed by Nup192, Nic96, Nup170, and the CNCs (Fig. 5A). Nic96^{NTE} and the linker nucleoporins Nup53 and Nup145N span these cylinders. Only C_8 rotational symmetry was applied to generate the cryo-ET reconstruction, yet we observed an additional twofold axis of symmetry in our composite structure that relates the nuclear and cytoplasmic sides within each spoke (Fig. 6, A to D) (*28*).

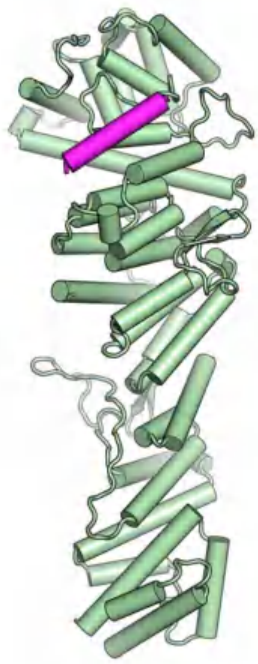

Movie 3. Structure of the Nic96^{SOL}•Nup53^{R2} complex. A 360° rotation of the crystal structure of Nic96^{SOL} •Nup53^{R2} is shown. Colors are the same as in Fig. 4.

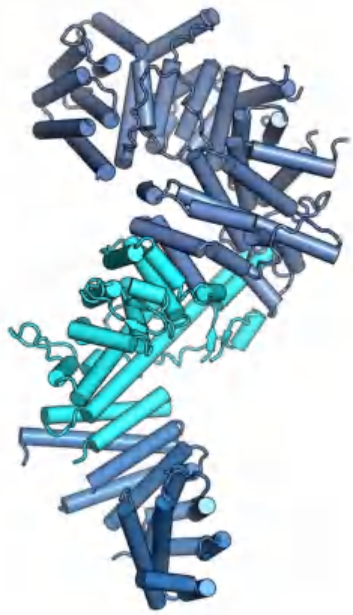

Movie 4. Generation of the structure of full-length Nup192 by superposition. A 360° rotation of the crystal structure of Nup192$^{\Delta HEAD}$ is shown, followed by a demonstration of the process used for generating the full-length structure by superposition. Colors are the same as in fig. S31.

Our results provided spatial restraints for Nic96^{R1} and Nic96^{R2}, allowing us to trace the path of Nic96^{NTE}, which emerges from the middle of Nic96^{SOL}, to its binding sites on Nup192 and the CNT. Each inner ring spoke contains four copies of the IRC, which we defined based on this connectivity (Fig. 6B and Movie 6). Here we refer to these four distinct IRCs as nuclear peripheral, nuclear equatorial, cytoplasmic peripheral, and cytoplasmic equatorial IRCs (Fig. 6B). The nuclear and cytoplasmic equatorial IRCs are related to each other directly by the twofold rotational axis of symmetry, as are the nuclear and cytoplasmic peripheral IRCs. Unexpectedly, the subunits in the equatorial and peripheral IRCs are in approximately the same relative orientation, which was readily apparent upon superposition (Fig. 6E). Because the subunits were placed independently, this unexpected symmetry is an emergent property of the composite structure. In the composite structure, the CNT and Nup192 are in close proximity, suggesting that additional weaker interactions orient the CNTs in the fully assembled NPC. We observed additional knobs of density adjacent to the Nup57 α/β domains of each CNT, which were unexplained by our composite structure (fig. S37D). When we superposed structures of CNT fragments from *Xenopus laevis* onto our docked CNT molecules (*16*), we found that the metazoan-specific ferredoxin-like domain of Nup57 accounts for these extra knobs of density (fig. S37, C and D), further validating our composite structure.

The mechanism by which FG repeats in the central transport channel form a diffusion barrier and facilitate transport is controversial, partly because the stoichiometry and orientation of the FG repeats were previously unknown. Our composite structure revealed a total of 32 CNTs in the inner ring, which would project 96 distinct polypeptide chains in clusters of three into the central channel (Fig. 6F). The orientation of the CNTs suggests that the FG repeats would emanate circumferentially toward the adjacent spoke, rather than pointing radially toward the center of the channel. Unexpectedly, the N termini of the peripheral and equatorial CNTs were evenly spaced and roughly planar, so that they approximately formed two 16-membered rings (Fig. 6F).

In the outer rings, each spoke contains two CNCs on either face, which we refer to as proximal and distal CNCs, based on their distance from the inner ring. The orientations of Nup133 relative to the CNC core differ slightly between the distal and proximal CNCs but create the same overall architecture: Each pair of distal and proximal CNCs forms an arch over the nuclear envelope (fig. S42). The outer rings also contain a Nup188 molecule on either face (fig. S43). The majority of the CNC components are ~100 Å above the membrane, and the only contacts with the membrane are made by the β-propeller domains of Nup120 and Nup133 through their ALPS motifs (Fig. 6C). Similarly, the IRCs do not make direct contacts with the membrane but instead are surrounded by a network of Nup170 molecules that form the outermost layer of the inner ring (Fig. 6C). Each spoke contains three

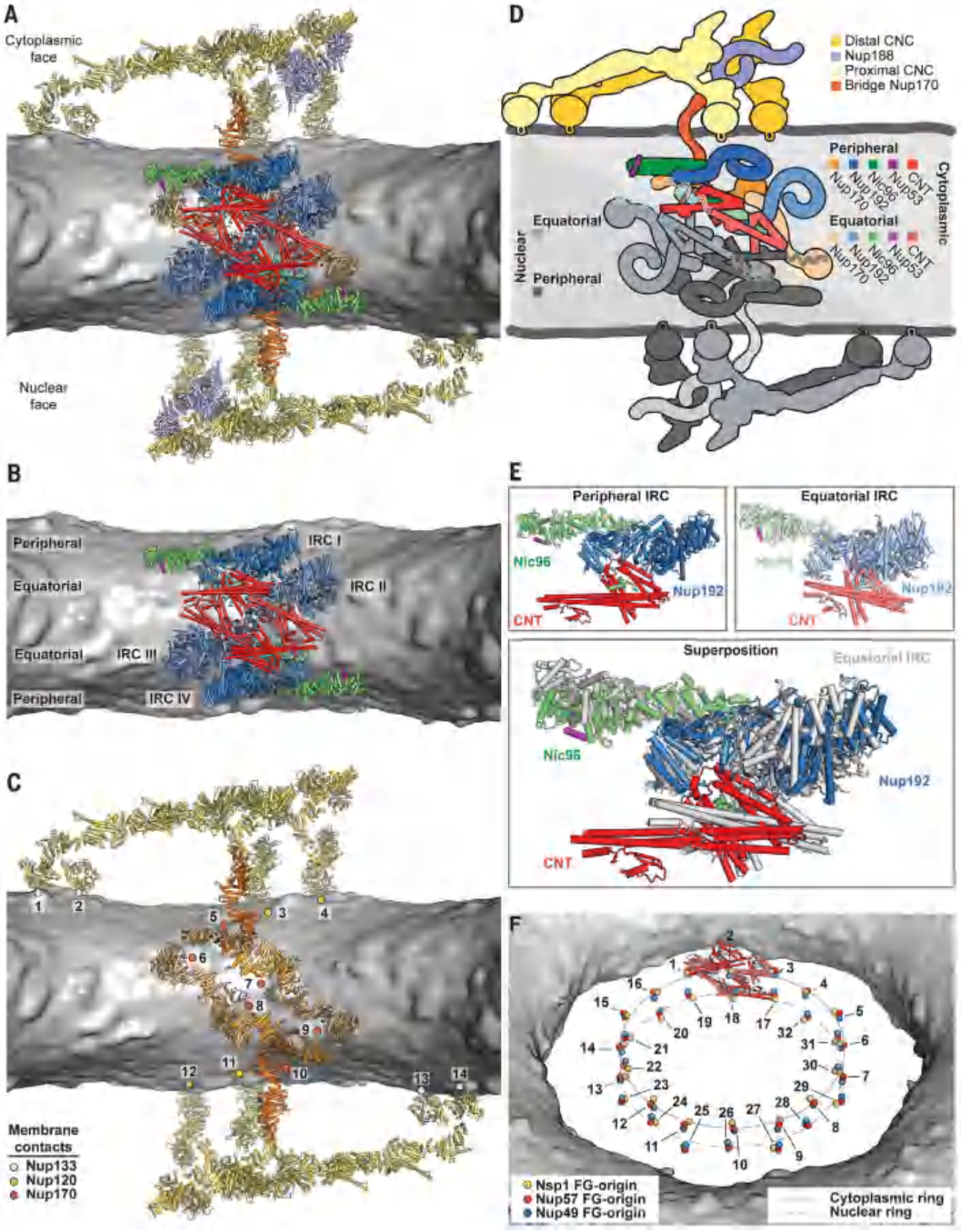

Fig. 6. Architecture of the NPC spoke. (**A**) A cartoon of a single spoke of the NPC symmetric core is shown from the same cross-sectional view as in Fig. 5B. Different shades of colors are used to indicate biochemically distinct dockings of the same protein (see also Movie 6). (**B**) The same view as in (A), but with Nup170 and the nucleoporins from the outer ring removed to highlight the organization of the four IRCs. (**C**) The membrane coat of the NPC. Nup192 and Nic96 molecules and CNTs have been removed for clarity. Contacts between the nuclear envelope and the ALPS motifs in Nup120, Nup133, and Nup170 are indicated by dots (numbered as a guide to the eye). (**D**) Schematic of the NPC spoke. The proteins corresponding to the nuclear side of the spoke are colored in gray, demonstrating the twofold rotational symmetry relating the cytoplasmic and nuclear halves of each spoke. (**E**) Equatorial and peripheral IRCs adopt similar conformations. Identical views of the cytoplasmic peripheral IRC, the cytoplasmic equatorial IRCs, and their superposition are shown. For clarity, the equatorial IRC is colored in gray in the superposition. (**F**) Organization of FG repeats in the inner ring. Colored spheres indicate the positions of the N termini of the three channel nucleoporins for all 32 CNT copies in the inner ring. Despite four distinct CNT positions in each spoke, the N termini for the cytoplasmic and nuclear complexes are arranged in approximately the same plane. Thus, though not possessing true 16-fold symmetry, the CNT N termini approximately form two 16-membered rings, which are indicated by a solid and a dashed line. The FG repeats of the 16-membered CNT rings project circumferentially into the central transport channel with opposite directionality (cytoplasmic CNT ring, counterclockwise; nuclear CNT ring, clockwise). Cartoons of the CNT molecules for a single spoke are shown to indicate the directionality of the FG repeats.

distinct pairs of Nup170 molecules, which we refer to as equatorial, peripheral, and bridging Nup170 molecules. The equatorial pair occupies alternating orientations equatorially along the surface of the nuclear envelope (Fig. 6C and fig. S36A). The resolution of the cryo-ET reconstruction of these molecules is high enough that the central holes of the β-propellers are readily visible at higher contour levels (fig. S36A). The bridging pair of Nup170 molecules connect the inner ring to the outer CNC rings through a contact with Nup120 (Fig. 6C and figs. S36B and S43). The peripheral Nup170 molecules, which have a weaker quality of fit and were identified only after placing all other symmetric core components, contact both the equatorial and bridging Nup170 molecules (Fig. 6C and fig. S40). The equatorial Nic96 molecules contact multiple Nup170 molecules, effectively bridging the nuclear and cytoplasmic networks. The ALPS and WF motifs that we identified in Nup170^{NTD} and the C-terminal amphipathic helix of Nup53 are positioned directly adjacent to the nuclear envelope (Fig. 6C). Thus, Nup170 and Nic96 constitute a membrane coat for the inner ring that is analogous to the CNCs in the outer ring.

Inter-spoke interactions

We next searched for interfaces that mediate interactions between spokes. Several potential interactions have been identified in previous studies, including one between Nup133^{NTE} and Nup120^{NTD} (*40*). Our composite structure revealed

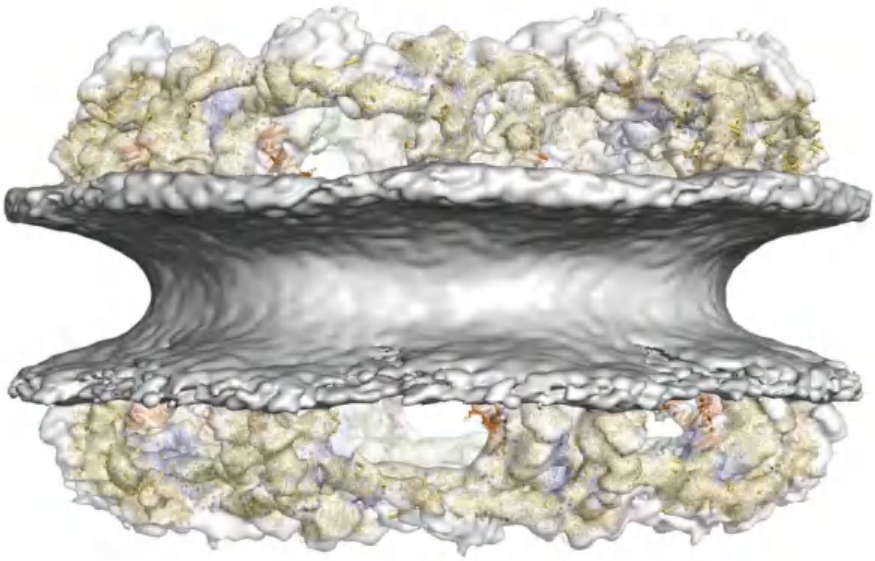

Movie 5. Overview of the composite structure of the NPC symmetric core. The structures are shown as docked into the cryo-ET reconstruction of the intact human NPC, oriented with the cytoplasmic face on top and the nuclear face on the bottom. The nuclear envelope and protein densities are colored in gray and white, respectively. Crystal structures of symmetric core nucleoporins are first shown as cartoons (colored according to Fig. 5), then without the cryo-ET reconstruction density, and finally in surface representation.

four additional interactions between CNC components that could link adjacent spokes: (i) between the neighboring proximal Nup84 and the distal Nup85, (ii) between the proximal Nup133 α-helical solenoid and the distal Nup120 α-helical solenoid, (iii) between the proximal Nup133 β-propeller and the proximal Nup120 β-propeller, and (iv) between the distal Nup133 β-propeller and the distal Nup120 β-propeller (fig. S43, A to C). The space between the proximal and distal CNCs contains a density that readily accommodates a Nup188 molecule. Nup188 recognizes a special niche generated in the CNC inter-spoke interface, bridging four CNC molecules by potentially making contacts with (v) the distal Sec13, (vi) the distal Nup85, (vii) the proximal Nup43, and (viii) the proximal Nup133 of a neighboring spoke (fig. S43, B and C). The Nic96^{R2}-binding site in Nup188^{TAIL} is not occluded by any additional density (fig. S43B). Because of the absence of strong density in this region, we cannot determine whether only Nup188 or an entire Nup188 complex would be anchored to the outer rings at this site. However, any flexibly tethered components of the NPC, including the remainder of the Nup188 complex, may not be clearly visible in cryo-ET reconstructions.

Inspection of the interaction surfaces also provided a molecular explanation for how two CNC rings are assembled. Nup133 and Nup170 bind to distinct Nup120 molecules via overlapping interfaces on the proximal and distal Nup120 molecules, respectively, effectively capping the CNCs on either side (fig. S43, D and E). These results are in agreement with a common evolutionary origin for Nup120, Nup133, and Nup170, which all possess similar domain architectures, contact the nuclear envelope via ALPS motifs, and interact with each other at inter-spoke interfaces. The U-bend solenoid nucleoporins—Nup85, Nup145C, Nup84, and Nic96—bridge these inter-spoke interfaces to form a continuous membrane-bending coat. These results also support the protocoatomer hypothesis of a common evolutionary origin for vesicle coats and the NPC coat, which contends that the extant nucleoporins derive from an ancient membrane coat that contained these protein folds (*44*).

We could only identify a single interaction that would analogously link the inner ring spokes, which would be mediated by an interaction between Nup53^{R1} and Nup192 (Fig. 7). In our composite structure, peripheral Nic96 molecules orient Nup53^{R2} directly adjacent to the Nup53-binding site on equatorial Nup192 molecules from a neighboring spoke (Fig. 7B). Our biochemical mapping experiments identified adjacent binding sites for Nic96 and Nup192 on Nup53 (Fig. 2F) and indicate that a fragment containing both of these binding sites could bridge the two nucleoporins (fig. S14C). Thus, binding of Nup53^{R1} in trans to a Nup192 molecule from a neighboring spoke would link the inner ring spokes.

An open question regarding nucleocytoplasmic transport has been the mechanism of inner nuclear membrane (INM) protein transport through the NPC, particularly for INM proteins with large globular nuclear domains. Peripheral channels on the order of ~100 Å have been proposed as routes for INM transport (*45*), but we observed no such channels through the inner ring in either our composite structure or the cryo-ET reconstruction (Fig. 5). Given the dense packing within each spoke, traffic of INM proteins through a spoke would require considerable disruption of the NPC structure (Fig. 7A). Rather, the most likely path through the inner ring would be at the inter-spoke interfaces where Nup53^{R1} and Nup192 interact (Fig. 7). The CNCs form a ~100 Å arch above this interface, providing an uninterrupted path to the inner ring and possibly explaining the previously observed upper limit for the size of nuclear domains (Fig. 6A) (*46*). However, the channel at the inner ring is much smaller, suggesting that rearrangements at the inter-spoke interface may be necessary to traffic large nuclear domains. Thus, our composite structure of the NPC symmetric core enables rational design of experiments to further understand the mechanism of INM protein import.

A flexible linker mediates CNC oligomerization

While reconstituting the CNCs, we noticed that the assembly of the CNC octamer spontaneously generated a separate solution phase (fig. S44A). Similar phase transitions have previously been observed in other systems with multiple binding valencies, suggesting that the oil droplet formation that we observed resulted from oligomerization of the CNC (*47*). We previously identified an interaction between Nup133^{NTE} and Nup120 that would mediate head-to-tail CNC ring formation, which would be consistent with the composite structure of the NPC (*40*). Removal of the unstructured Nup133^{NTE} completely ablated both oil droplet and complex formation, suggesting that this flexible interaction serves as a driving force for CNC ring formation (fig. S44). We also found that Nup170 could be incorporated into this separate solution phase and that this incorporation was ablated by C-terminal truncation, which is consistent with the interaction between the proximal Nup120 and bridging Nup170 molecules that we observed in our composite structure (fig. S44A).

Conservation of NPC architecture

Our results establish the principles that drive the assembly of nucleoporins in the NPC. Whereas the outer rings assemble largely through structurally rigid interaction surfaces, inner ring assembly is primarily driven by flexible linker sequences within Nup53, Nup145N, and Nic96^{NTE}. This dichotomy may reflect the different roles of the respective complexes. The outer rings provide a structural scaffold for the NPC, and, given their location above the plane of the nuclear envelope, their assembly would not be greatly affected by the dynamic generation of membrane curvature during fusion of the inner and outer nuclear membranes. In contrast, the proteins in the inner

ring occupy an environment that only exists after membrane fusion, probably necessitating conformational flexibility over the course of NPC assembly.

The importance of these flexible interactions in the NPC is highlighted by their evolutionary conservation, despite poor overall sequence conservation in the linker nucleoporins Nup53 and Nup145N. The overall folds of the scaffold proteins are well conserved in *S. cerevisiae* (*sc*) (fig. S45); furthermore, point mutations in the binding pockets of *sc*Nic96, *sc*Nup170, and *sc*Nup157 disrupted their interaction with linker sequences (figs. S46 to S48). A complete understanding of the interaction network in *S. cerevisiae* has been difficult to obtain because of the genetic redundancy that arises from several gene duplications (Nup170 and Nup157; Nup53 and Nup59; and Nup145N, Nup100, and Nup116). We found that the paralogs mostly retained the ability to form these interactions, but we did not detect an interaction between *sc*Nup188 and any of the Nup145N paralogs (figs. S46 to S50).

Our structural data also highlight the evolutionary conservation of the structure and interactions of nucleoporins. Although crystal structures of the human scaffold nucleoporins have not

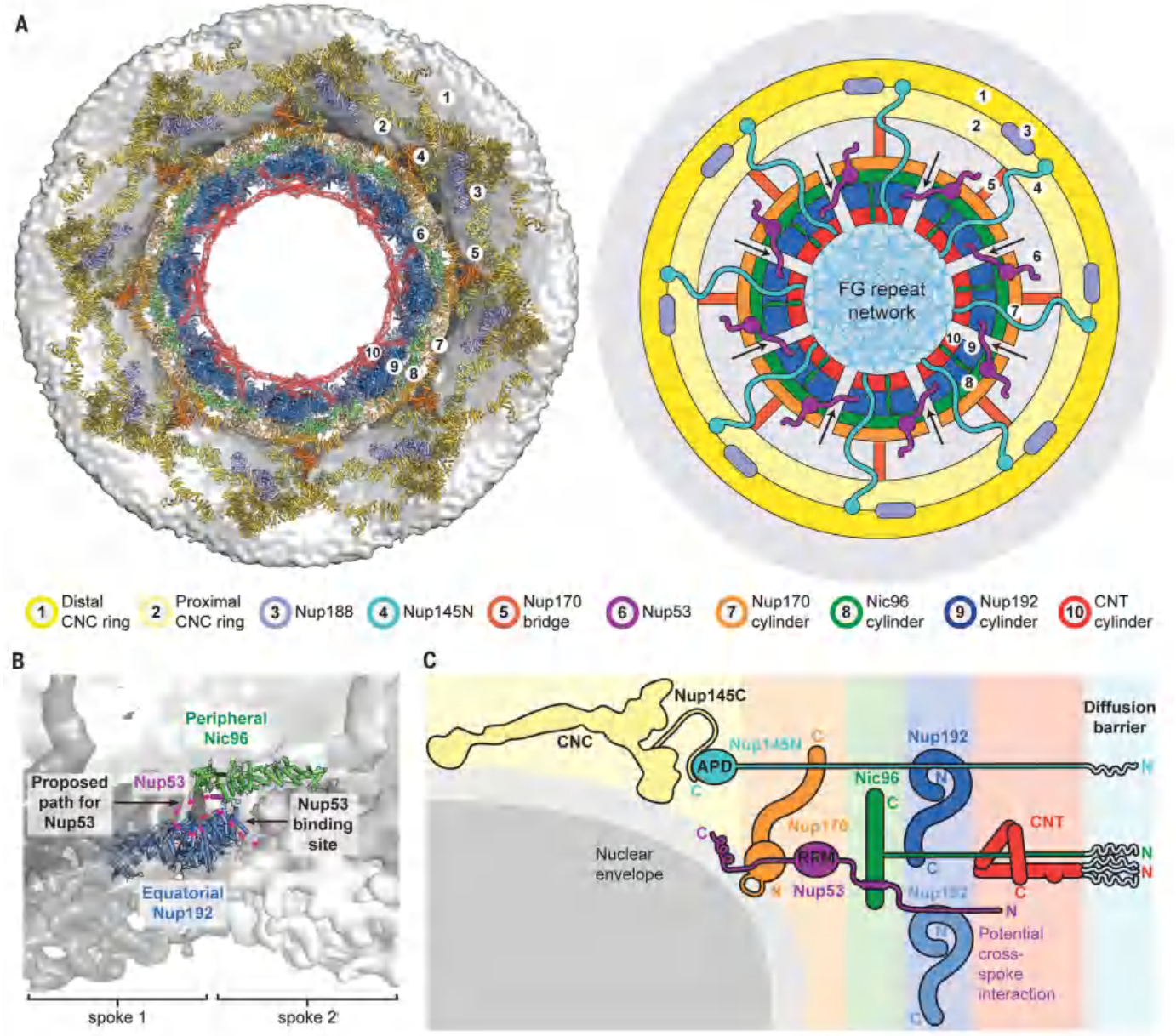

Fig. 7. Cylindrical organization of the NPC. (**A**) Top view of the composite structure of the NPC symmetric core, viewed from the cytoplasm (left). Coloring is according to Fig. 5. The schematic representation on the right illustrates the distinct concentric cylinders observed in the symmetric core. Cartoons of the linker nucleoporins and the unstructured NTE of Nic96 are shown to indicate how they span across multiple cylinders. Arrows indicate gaps between the inner ring spokes, which represent proposed paths for inner nuclear membrane protein transport. (**B**) Only a single contact is observed between two adjacent inner ring spokes. A close-up view of the inter-spoke interface in the inner ring is shown in an orientation similar to Fig. 5A. The two adjacent spokes are depicted as gray and white surfaces on the left and right, respectively. An equatorial Nup192 molecule (spoke 1) and a peripheral Nic96 molecule bound to Nup53 (spoke 2) are shown as cartoons. The Nup53-binding site on Nup192 is labeled, and the proposed path of the peptide is drawn as a purple dashed line. (**C**) Schematic illustrating the concentric cylinder organization of the symmetric core, viewed from the side. The order and arrangement of the binding sites for the linker nucleoporins observed in the composite structure are depicted. The proposed inter-spoke interaction between Nup53 and Nup192 is drawn at the bottom.

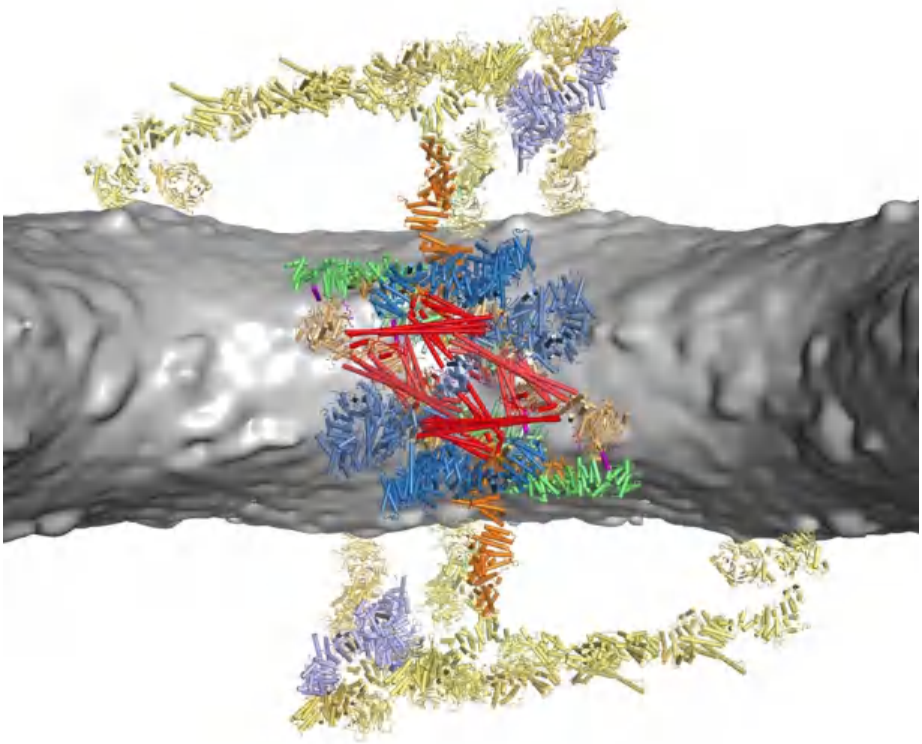

Movie 6. Rotating structure of a single spoke of the NPC symmetric core. The crystal structures are shown as docked into the cryo-ET reconstruction of the intact human NPC, oriented with the cytoplasmic face on top and the nuclear face on the bottom. The nuclear envelope is colored in gray. Crystal structures of symmetric core nucleoporins are shown as cartoons colored according to Fig. 6.

been determined, previous comparisons of the fungal CNC with low-resolution reconstructions of the human CNC suggest a conserved architecture (*13*, *14*). Superposition of the structures of Nup53^{RRM} and Nup145N^{APD} with their human homologs also revealed that their folds are identical (fig. S38) (*30*). In addition, the mechanism of interaction between Nup170 and Nup145N is conserved in humans, and we found that phosphomimetic mutations weakened the interaction between *hs*Nup98 and *hs*Nup155. Several other phosphorylation sites have been identified in Nup98, many of which potentially overlap with scaffold binding sites (*35*). Therefore, phosphorylation could also regulate other key interactions, including those that occur between Nup145N and Nup188, Nup192, and the CNC. Nup53 is similarly phosphorylated in a cell cycle–dependent manner, and phosphorylation of both linker nucleoporins thus would be an effective means to disassemble the entire inner ring of the NPC (*48*).

Conclusions

Determining the molecular details of nucleocytoplasmic transport has been a longstanding challenge, at least in part due to an incomplete understanding of the architecture and biochemistry of the NPC itself. We used purified recombinant proteins to systematically characterize the nucleoporin interaction network and determine atomic-resolution structures of nucleoporin complexes. This approach was crucially complemented by recent advances in cryo-ET reconstructions (*28*). Using the results of our divide-and-conquer approach, we were able to dock the available crystal structures into a cryo-ET reconstruction of the human NPC, yielding a composite structure for the entire NPC symmetric core. This union of bottom-up and top-down approaches offers a paradigm for determining the architectures of similarly complex macromolecular assemblies.

Our composite structure differs dramatically from previously reported computational models, not only in relative and absolute stoichiometry but also in overall architecture (*49*). These discrepancies highlight the complexities that must be accommodated when attempting a holistic, computational approach. We observed a high degree of symmetry in the structure of the NPC, which explains how such a limited vocabulary of proteins can generate such a large macromolecular structure. Most nucleoporins also occupy multiple distinct biochemical environments. Nup170 offers a dramatic example of this property: Biochemically distinct versions of Nup170 are either buried in the inner ring or are exposed in the bridge between the inner and outer rings. Similarly, Nup120 uses overlapping, exclusive interfaces to contact Nup170 and Nup133. Because of this diversification of nucleoporin function, the NPC can be encoded by a relatively small number of genes. The gene duplications of nucleoporins in *S. cerevisiae* may reflect the gradual separation of these distinct functions into several genes. Nup170 appears to also adopt different conformations in each of its distinct biochemical environments, which is consistent with the wide conformational range that we observed in the crystal structures. It is possible that the different conformations are the result of different mechanical forces acting on Nup170 at each position.

Biochemical diversification of proteins within the same protein complex also generates enormous challenges for computationally modeling the structure of the NPC and similar complexes, because distance restraints such as cross-links that are valid in one biochemical environment may be violated in another. This challenge is exacerbated by the possibility of flexibly tethered domains or nucleoporins, such as those in the Nup188 complex. Our results also highlight the confounding effect generated by the flexible linker nucleoporins Nup53 and Nup145N, which occupy binding sites that span the entirety of the inner ring, rather than a single globular volume. The structure of the NPC could be used as a template for the development of methods that can accommodate these additional complexities.

Our composite structure of the NPC provides a rich platform for contextualizing previous results, not all of which can be discussed here. The structure also permits the rational design of new experiments to not only further validate the structure, but also to begin structure-function investigation of the NPC. Our biochemical results led to a map of the strongest and most conserved interactions, but our composite structure indicates that many additional interactions can occur in the context of the assembled NPC. However, a structural understanding of the entire NPC at single-residue resolution still requires several advances. Successful placement of crystal structures of fungal nucleoporins into a cryo-ET reconstruction of the intact human NPC demonstrates not only the evolutionary conservation of NPC structure, but also the need for structural characterization of human nucleoporins and further improvement of the resolution of cryo-ET reconstructions to increase the accuracy of the composite structure of the NPC. Improved resolution in cryo-ET reconstructions in which secondary structure elements can be visualized would enable flexible fitting of high-resolution crystal structures. We were not able to dock any of the asymmetric components of NPC into the composite structure, because of the small size of extant structures and the absence of high-quality restraints (fig. S41). A similar approach to the one used here will be necessary to extend our analysis to the many proteins in the cytoplasmic filaments and nuclear basket that interact directly with transport factors and that are implicated in human disease. Lastly, high-resolution structural characterization of the remaining interactions, especially

those involving flexible linker sequences, remains critical to building a truly complete structure of the NPC, because these interactions may never be resolved in cryo-ET reconstructions.

Materials and methods

Bacterial expression constructs

DNA fragments were amplified by polymerase chain reaction using *C. thermophilum* and *H. sapiens* cDNA. SUMO (small ubiquitin-like modifier)–tagged proteins were cloned into a modified pET28a or pET-MCN vector containing an N-terminal hexahistidine tag followed by a SUMO tag by using BamHI and NotI restriction sites (*50*, *51*). Hexahistidine-tagged proteins were cloned into a modified pET28a vector containing an N-terminal hexahistidine tag followed by a protease cleavage site (PreScission) by using NdeI and NotI restriction sites (*52*). Glutathione *S*-transferase (GST)–tagged proteins were cloned into a pGEX-6P1 vector by using the BamHI and NotI restriction sites. Mutants were generated by QuikChange mutagenesis and confirmed by DNA sequencing. Details of bacterial expression constructs are shown in table S1.

Protein expression and purification

Proteins were expressed in *Escherichia coli* BL21-CodonPlus(DE3)-RIL cells (Stratagene) in Luria-Bertani media and induced at an OD 600 (optical density at 600 nm) of 0.8 with 0.5 mM isopropyl-β-D-thiogalactopyranoside. Details regarding expression times and temperatures are given in table S1. Seleno-L-methionine (SeMet)–labeled proteins were expressed with a methionine pathway inhibition protocol, as previously described (*53*). Cells were harvested by centrifugation and resuspended in a buffer containing 20 mM TRIS [tris (hydroxymethyl)aminomethane, pH 8.0], 500 mM sodium chloride, and 5 mM 2-mercaptoethanol (β-ME) for hexahistidine-tagged proteins, or a buffer containing 20 mM TRIS (pH 8.0), 200 mM sodium chloride, and 4 mM DTT for GST-tagged proteins; both were supplemented with complete EDTA-free protease inhibitor cocktail (Roche), unless otherwise noted. For purification, the cell suspensions of all proteins and protein complexes were supplemented with 1 mg deoxyribonuclease I (Roche) and lysed by using a cell disruptor (Avestin). Cell lysates were cleared by means of centrifugation at 30,000*g* for 1 hour. The supernatants were filtered through a 0.45-μm filter (Millipore) and purified using standard chromatography methods (details are given in table S2). Proteins were concentrated to ~10 to 20 mg/ml for biochemical interaction experiments, complex reconstitution, and crystallization. Representative chromatograms and SDS–polyacrylamide gel electrophoresis (SDS-PAGE) analyses are shown for the purifications for Nup120•Nup37•ELYS•Nup85, Sec13•Nup145C, Nup84•Nup133, Nic96•CNT, Nup192, Nup188, Nup170, Nup53, and Nup145N (figs. S51 to S59).

Reconstitution of Nup120•Nup37•ELYS•Nup85

Purified Nup120•Nup37•ELYS heterotrimer was mixed with a twofold molar excess of purified Nup85, incubated for 30 min on ice, and injected onto a HiLoad Superdex 200 16/60 prep grade (PG) gel filtration column equilibrated in 20 mM TRIS (pH 8.0), 150 mM sodium chloride, 5 mM dithiothreitol (DTT), and 5% (v/v) glycerol. Complex-containing fractions were pooled and concentrated to ~8 mg/ml for biochemical studies and further reconstitutions (see also fig. S51 for alternative copurification).

Reconstitution of Nup120•Nup37•ELYS•Nup85•Sec13•Nup145C (CNC hexamer)

Purified Nup120•Nup37•ELYS•Nup85 heterotetramer was mixed with a twofold molar excess of purified Sec13•Nup145C heterodimer, incubated for 30 min on ice, and injected onto a HiLoad Superdex 200 16/60 PG gel filtration column equilibrated in 20 mM TRIS (pH 8.0), 150 mM sodium chloride, 5 mM DTT, and 5 % (v/v) glycerol. Complex-containing fractions were pooled and concentrated to ~8 mg/ml for biochemical studies and further reconstitutions.

Reconstitution of Nup120•Nup37•ELYS•Nup85•Sec13•Nup145C•Nup84•Nup133$^{\Delta NTE}$ (CNC octamer)

Purified Nup120•Nup37•ELYS•Nup85•Sec13•Nup145C (CNC hexamer) was mixed with a 1.1-fold molar excess of purified Nup84•Nup133$^{\Delta NTE}$ heterodimer, incubated for 30 min on ice, and injected onto a HiLoad Superdex 200 16/60 PG gel filtration column equilibrated in 20 mM TRIS (pH 8.0), 150 mM sodium chloride, 5 mM DTT, and 5 % (v/v) glycerol. Complex-containing fractions were pooled and concentrated to ~8 mg/ml for biochemical studies and further reconstitutions.

Reconstitution of Nic96^{SOL}•SUMO-Nup53$^{1–90}$

Purified Nic96^{SOL} was mixed with a 1.2-fold molar excess of purified SUMO-Nup53$^{1–90}$, incubated on ice for 30 min, and injected over a HiLoad Superdex 200 16/60 PG column equilibrated in a buffer containing 20 mM TRIS (pH 8.0), 100 mM sodium chloride, and 5 mM DTT. Complex-containing fractions were pooled and concentrated at room temperature to ~10 mg/ml for biochemical studies.

Purification of Nic96•CNT

Cells containing Nic96 and CNT were grown individually and resuspended in 50 mM TRIS (pH 8.0), 500 mM sodium chloride, 4 mM β-ME, and 10 % (v/v) glycerol supplemented with complete EDTA-free protease inhibitor cocktail, 2 mM bovine lung aprotinin (Sigma), and 1 mM phenylmethanesulfonyl fluoride (Sigma). Before lysis, cell suspensions containing CNT and Nic96 were mixed in a 3:1 ratio. Clarified lysate was loaded onto a Ni–nitrilotriacetic acid column equilibrated in a buffer containing 25 mM TRIS (pH 8.0), 500 mM sodium chloride, 4 mM β-ME, 20 mM imidazole, and 5 % (v/v) glycerol and eluted with an imidazole gradient. Peak fractions were pooled and desalted using a HiPrep 26/20 Desalting column (GE Healthcare) equilibrated in a buffer containing 20 mM TRIS (pH 8.0), 150 mM sodium chloride, 5 mM DTT, and 5 % (v/v) glycerol in the presence of ULP1 protease. After SUMO cleavage, the protein was loaded onto a MonoQ 5/50 GL column (GE Healthcare) equilibrated in 20 mM TRIS (pH 8.0), 150 mM sodium chloride, 5 mM DTT, and 5 % (v/v) glycerol and eluted with a sodium chloride gradient. Complex-containing fractions were pooled for further biochemical reconstitutions (see also fig. S54).

Reconstitution of Nup192•Nup145N, Nup192•Nup53, and Nup192•Nup145N•Nup53

Purified Nup192 was mixed with a 1.5-fold molar excess of purified Nup53 and/or Nup145N. The mixture was incubated on ice for 30 min before injection onto a HiLoad Superdex 200 16/60 PG column equilibrated in a buffer containing 20 mM TRIS (pH 8.0), 100 mM sodium chloride, and 5 mM DTT. Complex-containing fractions were pooled and concentrated to ~10 mg/ml for biochemical studies and further reconstitutions.

Reconstitution of Nup192•Nic96•Nup53•CNT and Nup192•Nic96•Nup145N•Nup53•CNT (IRC•Nup53)

Purified Nup192•Nup53 heterodimer or Nup192•Nup145N•Nup53 heterotrimer was mixed with a twofold molar excess of purified Nic96•CNT heterotetramer, incubated for 30 min on ice, and injected onto a HiLoad Superdex 200 16/60 PG gel filtration column equilibrated in 20 mM TRIS (pH 8.0), 100 mM sodium chloride, 5 mM DTT, and 2% (v/v) glycerol. Complex-containing fractions were pooled and concentrated to ~5 mg/ml for biochemical studies.

Reconstitution of Nup82^{NTD}•Nup159^{T}•Nup145N

Purified Nup82^{NTD}•Nup159^{T} heterodimer (T, TAIL; residues 1440 to 1481) was mixed with a 1.2-fold molar excess of purified Nup145N, incubated on ice for 30 min, and injected onto a HiLoad Superdex 200 16/60 PG column equilibrated in buffer containing 20 mM TRIS (pH 8.0), 100 mM sodium chloride, and 5 mM DTT. Complex-containing fractions were pooled and concentrated to ~30 mg/ml for biochemical studies.

Reconstitution of Nup170•Nup53, Nup170•Nup145N, and Nup170•Nup53•Nup145N

Purified Nup170 was mixed with a twofold molar excess of purified Nup53 and/or Nup145N. The mixture was incubated on ice for 30 minutes before injection onto a HiLoad Superdex 200 16/60 PG column equilibrated in a buffer containing 20 mM TRIS (pH 8.0), 200 mM sodium chloride, 5 mM DTT, and 5% (v/v) glycerol. Complex-containing fractions were pooled and concentrated to ~10 mg/ml for biochemical studies and further reconstitutions.

Reconstitution of Nup170•Nup53•Nup192

Purified Nup170•Nup53 heterodimer was mixed with a 1.2-fold molar excess of purified Nup192, incubated on ice for 30 min, and injected onto a HiLoad Superdex 200 16/60 PG column equilibrated in a buffer containing 20 mM TRIS (pH 8.0), 150 mM sodium chloride, and 5 mM DTT. Complex-containing fractions were pooled

and concentrated to ~8 mg/ml for biochemical studies.

Reconstitution of Nup188•Nup145N

Purified Nup188 was mixed with a twofold molar excess of purified Nup145N, incubated on ice for 30 min, and injected onto a HiLoad Superdex 200 16/60 PG column equilibrated in a buffer containing 20 mM TRIS (pH 8.0), 100 mM sodium chloride, and 5 mM DTT. Complex-containing fractions were pooled and concentrated to ~10 mg/ml for biochemical studies and further reconstitutions.

Reconstitution of Nup188•Nic96•Nup53•CNT

Purified Nup188 was mixed with twofold molar excess of purified Nup53 and Nic96•CNT heterotetramer, incubated for 30 min on ice, and injected onto a HiLoad Superdex 200 16/60 PG gel filtration column equilibrated in 20 mM TRIS (pH 8.0), 100 mM sodium chloride, 5 mM DTT, and 2% (v/v) glycerol. Complex-containing fractions were pooled and concentrated to ~5 mg/ml for biochemical studies.

Reconstitution of scNup170^{CTD}•scNup145N and scNup157^{CTD}•scNup145N

Purified *sc*Nup170^{CTD} or *sc*Nup157^{CTD} was mixed with a 1.5-fold molar excess of purified *sc*Nup145N. The mixture was incubated on ice for 30 min prior to injection over a HiLoad Superdex 200 16/60 PG column equilibrated in a buffer containing 20 mM TRIS (pH 8.0), 300 mM sodium chloride, 5 mM DTT, and 5% (v/v) glycerol. Complex-containing fractions were pooled and concentrated to ~10 mg/ml for biochemical studies.

Reconstitution of scNup170^{CTD}•scNup100

Purified *sc*Nup170^{CTD} was mixed with a 1.5-fold molar excess of purified *sc*Nup100, incubated on ice for 30 min, and injected onto a HiLoad Superdex 200 16/60 PG column equilibrated in a buffer containing 20 mM TRIS (pH 8.0), 100 mM sodium chloride, 5% (v/v) glycerol, and 5 mM DTT. Complex-containing fractions were pooled and concentrated to ~10 mg/ml for biochemical studies.

Multiangle light scattering coupled to analytical size-exclusion chromatography

Purified proteins and complex formations were characterized by inline multiangle light scattering (MALS) after separation on a Superdex 200 10/300 GL or a Superose 6 10/300 GL column. All experiments conducted using the Superdex 200 10/300 GL column were performed in a buffer containing 20 mM TRIS (pH 8.0), 100 mM sodium chloride, and 5 mM DTT, whereas experiments conducted using the Superose 6 10/300 GL column were performed in a buffer containing 20 mM TRIS (pH 8.0), 150 mM sodium chloride, and 5 mM DTT. The chromatography system was connected in series with an 18-angle light-scattering detector (DAWN HELEOS II, Wyatt Technology), a dynamic light-scattering detector (DynaPro Nanostar, Wyatt Technology), and a refractive index detector (Optilab t-rEX, Wyatt Technology). Data were collected at 21°C every 1 s at a flow rate of 0.4 ml/min and analyzed using ASTRA 6 software, thereby generating molar mass and mass distribution (polydispersity) measurements of the samples (*54*). For interaction studies, proteins were mixed and preincubated on ice for 30 min before being applied to the gel filtration column. Protein-containing fractions were analyzed by SDS-PAGE followed by Coomassie brilliant blue staining. Experimental and theoretical masses of all proteins and complexes are listed in table S10.

Immunoblotting

Protein from peak fractions was resolved on a 12% SDS-PAGE gel, transferred to polyvinylidene difluoride membranes, and immunoblotted with a mouse antibody against the aviTag (Genscript, 1:1000 dilution), followed by an alkaline phosphatase-conjugated goat antibody against mouse immunoglobulin G (Promega, 1:4000 dilution). Blots were developed with SigmaFast bromochloroindolyl phosphate–nitro blue tetrazolium tablets (Sigma) for 2 to 3 min and imaged immediately.

Crystallization and structure determination

Crystallization trials for all proteins were performed at 21°C in hanging drops containing 1 μl of protein and 1 μl of reservoir solution. SeMet-labeled crystals were grown under similar conditions. Details of the crystallization and cryoprotection are given in table S4. X-ray diffraction data were collected at 100 K at beamline 8.2.2 at the Advanced Light Source (ALS) at Lawrence Berkley National Laboratory, beamline BL12-2 at the Stanford Synchrotron Radiation Source (SSRL), and beamline GM/CA-CAT 23ID-D at the Advanced Photon Source (APS). The x-ray diffraction data were processed using XDS (*55*). Structures were phased with Phaser, and maps were improved by density modification with RESOLVE (*56*, *57*). Iterative rounds of model building and refinement were performed using COOT and PHENIX (*58*, *59*). All models had excellent stereochemistry and geometry, as determined by Molprobity (*60*). Details of refinement and data processing are given in tables S5 to S9.

Structure determination of Nup170^{NTD}•Nup53$^{329–361}$

Purified Nup170^{NTD} was mixed with a threefold molar excess of synthesized Nup53$^{329–361}$ peptide (Zhejiang Ontores Biotechnologies). To obtain high-resolution diffraction, residues 293 to 305 of Nup170^{NTD}, which were predicted to reside in a large loop, were deleted. Crystals were grown in 1.0 M sodium potassium phosphate (pH 6.9) and cryoprotected by gradual addition of glycerol to the crystallization drop. The Nup53$^{329–361}$ peptide was added to all cryoprotectant solutions. The structure was determined by single-wavelength anomalous dispersion (SAD) with Phaser, using anomalous x-ray diffraction data collected from a crystal containing SeMet-labeled Nup170^{NTD}.

Structure determination of apo Nup170^{CTD}

A quadruple methionine mutant (Y905M, L1007M, L1183M, and V1292M) was used for crystallization and collection of SeMet SAD data for apo Nup170^{CTD}. Crystals were grown in 0.1 M MES (pH 6.3), 10% (w/v) PEG-20,000 (polyethylene glycol, molecular weight 20,000), 10% (v/v) ethylene glycol, and 0.2 M potassium thiocyanate and cryoprotected by gradual addition of ethylene glycol to the crystallization drop. The four additional methionine positions were introduced as sequence markers for high-confidence sequence assignment. An initial model was used for molecular replacement in Phaser with diffraction data collected from crystals of native apo Nup170^{CTD} that diffracted to 2.1 Å resolution. Crystals of native apo Nup170^{CTD} were grown in 0.1 M Hepes (pH 7.0) and 1.0 M sodium acetate and cryoprotected by gradual addition of ethylene glycol to the crystallization drop.

Structure determination of Nup170^{CTD}•Nup145N$^{729–750}$

Purified Nup170^{CTD} was incubated with a threefold molar excess of synthesized Nup145N$^{729–750}$ peptide (Zhejiang Ontores Biotechnologies). Attempts to obtain crystals with stoichiometric Nup145N incorporation revealed that two regions of Nup170^{CTD} could bind to the Nup145N-binding pocket (1403 to 1416 and 1375 to 1377), blocking the Nup170-Nup145N interaction. To obtain crystals of the complex, both of these regions of Nup170 were deleted. Complex crystals were grown in 0.2 M lithium acetate and 12% (w/v) PEG-3350. Crystals were cryoprotected by gradual addition of ethylene glycol to the crystallization drop. Phasing was performed by means of molecular replacement in Phaser, using the structure of apo Nup170^{CTD} as a search model.

Structure determination of Nup170^{SOL}

Crystals of Nup170^{SOL} were grown in 0.1 M Hepes (pH 7.1) and 0.5 M ammonium sulfate and cryoprotected by gradual addition of ethylene glycol to the crystallization drop. The Nup170^{SOL} structure was determined with the MR-SAD routine in PHENIX, combining molecular replacement phases obtained by using the corresponding fragments of the Nup170^{NTD} and Nup170^{CTD} structures with SAD phases obtained from anomalous x-ray diffraction data that were collected from a crystal containing SeMet-labeled Nup170^{SOL}. The crystals diffracted with a high degree of anisotropy, with diffraction past 3.9 Å for two axes, but diffraction was limited to 4.5 Å for the third axis. Minimal model building was performed after the high-resolution structures were refined as rigid bodies, with the exception of the loops connecting helices α16, α17, and α18, which were not observed in the other structures. The overall correctness of the observed conformation was confirmed by calculating anomalous difference Fourier maps to locate the methionine positions. Refinement was performed with anisotropically truncated data, which yielded more interpretable maps.

Structure determination of apo Nic96^{SOL} and Nic96^{SOL}•Nup53$^{31–84}$

The structure of apo Nic96^{SOL} was determined using SAD x-ray diffraction data collected from crystals grown with SeMet-labeled Nic96^{SOL} in 4% (v/v) tacscimate (pH 7.4) and 14% (w/v) PEG-3350 and cryoprotected by exchanging the

crystallization buffer with paratone-N. Purified Nic96^{SOL}•Nup53$^{31–84}$ was crystallized in 0.1 M TRIS (pH 7.0) and 12% (w/v) PEG-6000, and 1.2 M sodium chloride, and crystals were also cryoprotected by exchanging the crystallization buffer with paratone-N. An initial model of apo Nic96^{SOL} was built using the experimental electron density map and used as a search model in molecular replacement to determine the structure of Nic96^{SOL}• Nup53$^{31–84}$ at 2.65 Å resolution. Residues 31 to 66 of Nup53 are presumed to be disordered, because only residues 67 to 84 were visible in the electron density map.

Structure determination of Nup192$^{\Delta HEAD}$

Despite extensive optimization and screening, crystals of Nup192$^{\Delta HEAD}$ diffracted to ~10 Å resolution at best. Inspection of the crystal structure of Nup192^{NTD} suggested helix α9, which protrudes from the surface of the protein, might be preventing the formation of stable crystal contacts. Thus, we replaced residues 167 to 184 with a GSGS linker. Crystals of this mutant grown in 0.1 M TRIS (pH 7.9), 6% (w/v) PEG-4000, and 5% (v/v) polypropylene glycol displayed improved diffraction to ~5 Å resolution. While screening for heavy metal derivatives, we noticed that the diffraction quality of these crystals was improved further by soaking with 0.2-μl saturated potassium hexachloroosmate (K_2OsCl_6) solution in a total drop volume of 5 μl for 1 min. Crystals were cryoprotected by gradually supplementing the drop with polypropylene glycol in 5% steps. The structure was determined by molecular replacement with Phaser, using the corresponding fragments of Nup192^{NTD} [Protein Data Bank identifier (PDB ID) 4KNH] and Nup192^{TAIL} (PDB ID 5CWV), followed by SAD phasing, using anomalous x-ray diffraction data collected at the osmium L3 edge (*15*, *20*). Although the crystals only grew in the presence of Nup53$^{31–67}$ peptide, no strong electron density was observed for the peptide, probably because of partial occupancy of the peptide in the crystal.

Structure determination of Nup53^{RRM}

Nup53^{RRM} crystallized in two different crystal forms. Crystals grown in 0.1 M Hepes (pH 7.0), 24% (w/v) PEG-3350, and 0.2 M potassium iodide crystallized in the space group $P2_12_12_1$. Crystals were cryoprotected by gradual addition of ethylene glycol to the crystallization drop. The crystal structure was determined by SAD phasing with Phaser, using anomalous x-ray diffraction data from a crystal grown with SeMet-labeled Nup53^{RRM}. Iodide ions were placed in the native structure based on peaks in the anomalous difference Fourier map. These crystals diffracted exceptionally well, with diffraction clearly visible up to 0.7 Å resolution, but the geometry of the beamline did not permit positioning of the detector close enough to measure all spots with very high Bragg angles. As a result, the completeness of the data in the highest-resolution shells is low, but these data were included because they improved the quality of the electron density maps. The second crystal form of Nup53^{RRM} crystallized in the space group $P3_121$ in 4% (v/v) tacsimate (pH 4.1) and 15% (w/v) PEG-3350. The crystals were cryoprotected in 32% (v/v) tacsimate (pH 4.1) and 19% (w/v) PEG-3350. The structure was determined by SAD phasing with Phaser, using anomalous x-ray diffraction data collected from potassium hexachloroosmate–derivatized native crystals.

Structure determination of Nup145N^{APD}•Nup145C^{N}

Crystals of Nup145N^{APD} were grown in 0.1 M citric acid (pH 3.0) and 25% (w/v) PEG-3350 and cryoprotected with mother liquor supplemented with 25% (v/v) ethylene glycol. The structure was determined by molecular replacement with Phaser, using the crystal structure of Nup145N^{APD} (PDB ID 5CWW) as a search model (*15*). We also crystallized a catalytically dead mutant, Nup145N^{APD} T994A, that was fused to the N-terminal six residues of Nup145C. Crystals grew in 0.1 M TRIS (pH 8.8), 32% (w/v) PEG-4000, and 0.2 M lithium sulfate and were cryoprotected with mother liquor supplemented with 10% (v/v) glycerol. The structure was determined by molecular replacement with Phaser, using the crystal structure of Nup145N^{APD} as the search model.

Generation of full-length structures by superposition for docking into cryo-ET reconstructions

Superposition-generated structures of full-length Nup170 and Nup192 were generated by careful superposition of crystal structures of the respective fragments. For Nup170, the crystal structure Nup170^{NTD}•Nup53$^{329–361}$ was superposed onto the crystal structure of Nup170^{SOL}. Minor differences in the conformations of helices were observed at the truncated ends of the structures, but the conformation included in the models always corresponded to the structure in which no truncation was made. The various structures of Nup170^{CTD} were superposed onto the crystal structure of Nup170^{SOL} by using only helices α19 to α24, which displayed only minimal conformation rearrangements. In the superposition-generated full-length Nup170 structure, residues 1 to 808 were derived from the Nup170^{NTD}•Nup53$^{329–361}$ crystal structure, residues 809 to 844 were derived from the Nup170^{SOL} crystal structure, and residues 845 to 1416 were derived from the various Nup170^{CTD} crystal structures (see also fig. S25 and Movie 1). A similar approach was used to superpose the structure of Nup192^{NTD} (PDB ID 4KNH) and Nup192^{TAIL} (PDB ID 5CWV) onto the crystal structure of Nup192$^{\Delta HEAD}$, superposing only helices that had identical conformations in both crystal structures (15, 20). In the full-length Nup192 superposition-generated structure, residues 1 to 253 were derived from the Nup192^{NTD} crystal structure, residues 254 to 1750 from the Nup192$^{\Delta HEAD}$ crystal structure, and residues 1750 to 1756 from the Nup192^{TAIL} crystal structure (see also fig. S31 and Movie 4).

Docking crystal structures into the cryo-ET reconstruction of the intact human NPC

An incremental approach was used to dock available crystal structures and superposition-generated structures into the previously reported ~23 Å cryo-ET reconstruction of the intact human NPC (*28*). For all structures other than Nup37, Nup43, and Nup133^{NTD}, global searches in the cryo-ET reconstruction were performed using the UCSF Chimera Fit Map command (*61*). Searches consisted of 50,000 initial placements that were locally optimized and scored based on correlation between a simulated 20 Å map of the docked model and the cryo-ET reconstruction, taking into account the C_8 rotational symmetry of the latter. The top-scoring solutions for the search were inspected for their agreement with previously published biochemical data and the biochemical data presented here. A flowchart of our incremental docking approach can be found in fig. S34. The average Fourier shell correlation between a single spoke and the map corresponding to the docked spoke was calculated using Refmac5 to a value of 0.79 at the reported resolution of the map (23 Å) (*62*).

Docking of the CNC

Searches for the CNC hexamer (PDB ID 4XMM) and the *hs*Nup84•*hs*Nup133 heterodimer (PDB ID 3CQC) were performed in maps from which the density corresponding to the nuclear envelope had been removed (*14*, *38*). Because of its large size and distinctive shape, the four top-scoring solutions of the CNC hexamer have much higher scores than any other solution. Nup37 was docked by superposing the crystal structure of the *S. pombe* Nup120^{NTD}•Nup37 heterodimer (PDB ID 4FHN) onto the CNC hexamer (*39*). *hs*Nup43 was docked into an unoccupied density next to Nup85, based on a previously identified cross-link and the previously reported interaction (*13*, *41*). *hs*Nup133 (PDB ID 1XKS) was docked in an unoccupied density next to the Nup120 β-propeller, and the fit was optimized locally with the Fit Map command (*63*). Because the resolution of the map cannot distinguish between different orientations of the Nup43 and Nup133 β-propellers, their exact orientation is ambiguous. Details regarding CNC docking can be found in fig. S35.

Docking of Nup170, Nup192, and Nup188

Before performing global searches for Nup170 and Nup192, the density corresponding to the docked CNCs was removed to obtain placements that would not clash with the CNCs. Searches in maps that included the density assigned to the CNCs produce similar results. Searches with Nup170 were performed using multiple conformations. Most conformations produced similar results, referred to as conformation I, and occupied two symmetry-related positions in the inner ring. A different conformation (conformation II), which was derived from the structure of the apo Nup170^{CTD} quadruple methionine mutant, occupied symmetry-related positions bridging the inner and outer rings. For Nup192, we accepted five placements from the global search results, two placements in the inner ring, two placements in the outer rings, and one placement on the nuclear peripheral side of the inner ring. A matching cytoplasmic peripheral

placement was not found in global searches, but the manual placement on the cytoplasmic peripheral side of the inner ring generated a score that would have ranked as the 9th highest. The four molecules placed in the inner ring were assigned as Nup192, and the two molecules placed in the outer rings were assigned as Nup188, based on the following considerations: (i) Nup188 binding to Nup145N was incompatible with both Nup192 and Nup170, making it unlikely that Nup188 is a component of the tightly packed inner ring core; (ii) cross-linking and mass spectrometry data identified cross-links between Nup188 and Nup85 (*13*, *42*); and (iii) Nup188 mislocalization behavior was found to be consistent with other outer ring components upon genetic perturbation (*64*). Details regarding Nup170, Nup192, and Nup188 docking can be found in fig. S36.

Docking of Nic96^{SOL}•Nup53$^{31–84}$ and CNT•Nic96^{R1}

Searches for the Nic96^{SOL}•Nup53$^{31–84}$ complex were performed using a map of the inner ring from which the density corresponding to the placed Nup170, Nup188, and Nup192 molecules had also been removed. Many high-scoring solutions of Nic96^{SOL} were related to each other by rotations along the long axis of the rod-shaped molecule, reflecting the ambiguity of the exact rotational orientation of the molecule at the resolution of the cryo-ET reconstruction. Searches for the CNT•Nic96^{R1} complex (PDB ID 5CWS) were performed in a map from which the density corresponding to the placed Nic96^{SOL} molecules also had been removed (*15*). Superposition of the *X. laevis (xl)* CNT crystal structures (PDB IDs 5C2U and 5C3L) was performed by superposing *xl*Nup54 from the *xl*CNT structure directly onto Nup57 from the CNT structure, and then superposing the ferredoxin-like domain onto the *xl*CNT structure (*16*). Details regarding Nic96^{SOL}•Nup53$^{31–84}$ and CNT• Nic96^{R1}docking can be found in fig. S37.

Manual identification of a third pair of Nup170 molecules

After successful placement of 32 copies each of Nup170, Nup192, Nic96^{SOL}, and the CNT in the inner ring, we continued our analysis by removing the density corresponding to the docked molecules. There were four major distinct densities remaining in the inner ring, each of which appeared on both the nuclear and cytoplasmic sides (fig. S40). The first set of densities corresponded to the ferredoxin-like domain that is only present in metazoan Nup57. The second set corresponded to the density adjacent to the C-terminal TAIL domains of the equatorial Nup192 molecules, which we assume arises from our structure imperfectly capturing the conformation of Nup192 in the assembled NPC. The third major density was adjacent to the equatorial Nup170 β-propellers. We were unable to assign this density confidently to any remaining subunit, such as Nup53^{RRM}, Nup145N^{APD}, or any other nucleoporin of known structure. Lastly, a pair of extended densities was adjacent to the nuclear envelope (fig. S40). These densities were very similar in shape to the Nup170 molecules that we had already placed, but neither of the conformations that we previously placed yielded a high-quality fit. Instead, we found the best fit with a third conformation, although visible differences suggest that even this structure did not perfectly capture the conformation of this third molecule inside the NPC. Details regarding docking for this conformation of Nup170 can be found in fig. S40.

Protein labeling for oligomerization experiments

Proteins were labeled under conditions that were selective for the N-terminal amino group of proteins. Before the labeling reaction, purified CNC hexamer, Nup84•Nup133, and Nup84•Nup133$^{\Delta NTE}$ complexes at concentrations of 10 to 20 μM were dialyzed in a buffer containing 100 mM sodium bicarbonate (pH 8.0), 100 mM sodium chloride, and 5 mM DTT. 20 μM Nup170 and Nup170$^{\Delta C}$ were dialyzed against a buffer containing 100 mM sodium bicarbonate (pH 8.0), 200 mM sodium chloride, and 5 mM DTT. For the labeling reactions, BODIPY (boron-dipyrromethene) FL NHS Ester (succinimidyl ester) or Alexa Fluor 647 NHS Ester (succinimidyl ester) dyes (Molecular Probes) were added at ratios equimolar to the dialyzed protein samples and incubated for 50 min at room temperature. The reaction was subsequently quenched by dialysis against buffers containing 100 mM TRIS (pH 8.0) instead of sodium bicarbonate.

Oligomerization experiments

Oil droplet formation was analyzed by fluorescence microscopy with a Carl Zeiss AxioImagerZ.1 equipped with an AxioCamMRm camera. Experiments performed without Nup170 were performed with BODIPY-labeled CNC hexamer and Alexa Fluor 647–labeled Nup84•Nup133 or Nup84•Nup133$^{\Delta NTE}$. Proteins were mixed at equimolar ratios directly on a cover slide and analyzed immediately. For experiments involving the incorporation of Nup170, BODIPY-labeled CNC hexamer and unlabeled Nup84•Nup133 were first mixed together in equimolar ratios and then subsequently incubated with a 1.5-fold molar excess of Alexa Fluor 647–labeled Nup170 or Nup170$^{\Delta C}$.

Figures and movies

Gel filtration profiles and MALS graphs were generated in IGOR (WaveMetrics) and assembled in Adobe Illustrator. Sequence alignments were generated using MUSCLE and colored with ALSCRIPT (*65*, *66*). Electrostatic potentials were calculated with APBS (Adaptive Poisson-Boltzmann Solver) software (*67*). All structural figures and movies were generated using PyMol (www.pymol.org).

REFERENCES AND NOTES

1. A. Hoelz, E. W. Debler, G. Blobel, The structure of the nuclear pore complex. *Annu. Rev. Biochem.* **80**, 613–643 (2011). doi: 10.1146/annurev-biochem-060109-151030; pmid: 21495847
2. A. Ibarra, M. W. Hetzer, Nuclear pore proteins and the control of genome functions. *Genes Dev.* **29**, 337–349 (2015). doi: 10.1101/gad.256495.114; pmid: 25691464
3. V. Le Sage, A. J. Mouland, Viral subversion of the nuclear pore complex. *Viruses* **5**, 2019–2042 (2013). doi: 10.3390/v5082019; pmid: 23959328
4. A. Köhler, E. Hurt, Gene regulation by nucleoporins and links to cancer. *Mol. Cell* **38**, 6–15 (2010). doi: 10.1016/j.molcel.2010.01.040; pmid: 20385085
5. K. Zhang *et al.*, The C9orf72 repeat expansion disrupts nucleocytoplasmic transport. *Nature* **525**, 56–61 (2015). doi: 10.1038/nature14973; pmid: 26308891
6. A. C. Woerner *et al.*, Cytoplasmic protein aggregates interfere with nucleocytoplasmic transport of protein and RNA. *Science* **351**, 173–176 (2016). doi: 10.1126/science.aad2033; pmid: 26634439
7. H. M. Kaneb *et al.*, Deleterious mutations in the essential mRNA metabolism factor, hGle1, in amyotrophic lateral sclerosis. *Hum. Mol. Genet.* **24**, 1363–1373 (2015). pmid: 25343993
8. B. D. Freibaum *et al.*, GGGGCC repeat expansion in C9orf72 compromises nucleocytoplasmic transport. *Nature* **525**, 129–133 (2015). doi: 10.1038/nature14974; pmid: 26308899
9. A. Jovičić *et al.*, Modifiers of C9orf72 dipeptide repeat toxicity connect nucleocytoplasmic transport defects to FTD/ALS. *Nat. Neurosci.* **18**, 1226–1229 (2015). pmid: 26308983
10. A. Cook, F. Bono, M. Jinek, E. Conti, Structural biology of nucleocytoplasmic transport. *Annu. Rev. Biochem.* **76**, 647–671 (2007). doi: 10.1146/annurev.biochem.76.052705.161529; pmid: 17506639
11. K. Thierbach *et al.*, Protein interfaces of the conserved Nup84 complex from *Chaetomium thermophilum* shown by crosslinking mass spectrometry and electron microscopy. *Structure* **21**, 1672–1682 (2013). doi: 10.1016/j.str.2013.07.004; pmid: 23954503
12. K. Kelley, K. E. Knockenhauer, G. Kabachinski, T. U. Schwartz, Atomic structure of the Y complex of the nuclear pore. *Nat. Struct. Mol. Biol.* **22**, 425–431 (2015). pmid: 25822992
13. K. H. Bui *et al.*, Integrated structural analysis of the human nuclear pore complex scaffold. *Cell* **155**, 1233–1243 (2013). doi: 10.1016/j.cell.2013.10.055; pmid: 24315095
14. T. Stuwe *et al.*, Architecture of the nuclear pore complex coat. *Science* **347**, 1148–1152 (2015). doi: 10.1126/science.aaa4136; pmid: 25745173
15. T. Stuwe *et al.*, Architecture of the fungal nuclear pore inner ring complex. *Science* **350**, 56–64 (2015). doi: 10.1126/science.aac9176; pmid: 26316600
16. H. Chug, S. Trakhanov, B. B. Hülsmann, T. Pleiner, D. Görlich, Crystal structure of the metazoan Nup62•Nup58•Nup54 nucleoporin complex. *Science* **350**, 106–110 (2015). doi: 10.1126/science.aac7420; pmid: 26292704
17. J. Fischer, R. Teimer, S. Amlacher, R. Kunze, E. Hurt, Linker Nups connect the nuclear pore complex inner ring with the outer ring and transport channel. *Nat. Struct. Mol. Biol.* **22**, 774–781 (2015). doi: 10.1038/nsmb.3084; pmid: 26344569
18. N. Eisenhardt, J. Redolfi, W. Antonin, Interaction of Nup53 with Ndc1 and Nup155 is required for nuclear pore complex assembly. *J. Cell Sci.* **127**, 908–921 (2014). doi: 10.1242/jcs.141739; pmid: 24363447
19. E. Onischenko, L. H. Stanton, A. S. Madrid, T. Kieselbach, K. Weis, Role of the Ndc1 interaction network in yeast nuclear pore complex assembly and maintenance. *J. Cell Biol.* **185**, 475–491 (2009). doi: 10.1083/jcb.200810030; pmid: 19414609
20. T. Stuwe, D. H. Lin, L. N. Collins, E. Hurt, A. Hoelz, Evidence for an evolutionary relationship between the large adaptor nucleoporin Nup192 and karyopherins. *Proc. Natl. Acad. Sci. U.S.A.* **111**, 2530–2535 (2014). doi: 10.1073/pnas.1311081111; pmid: 24505056
21. H. S. Seo, B. J. Blus, N. Z. Jankovic, G. Blobel, Structure and nucleic acid binding activity of the nucleoporin Nup157. *Proc. Natl. Acad. Sci. U.S.A.* **110**, 16450–16455 (2013). doi: 10.1073/pnas.1316607110; pmid: 24062435
22. K. R. Andersen *et al.*, Scaffold nucleoporins Nup188 and Nup192 share structural and functional properties with nuclear transport receptors. *eLife* **2**, e00745 (2013). doi: 10.7554/eLife.00745; pmid: 23795296
23. J. R. Whittle, T. U. Schwartz, Architectural nucleoporins Nup157/170 and Nup133 are structurally related and descend from a second ancestral element. *J. Biol. Chem.* **284**, 28442–28452 (2009). doi: 10.1074/jbc.M109.023580 pmid: 19674973
24. N. Schrader *et al.*, Structural basis of the Nic96 subcomplex organization in the nuclear pore channel. *Mol. Cell* **29**, 46–55 (2008). doi: 10.1016/j.molcel.2007.10.022; pmid: 18206968
25. S. Jeudy, T. U. Schwartz, Crystal structure of nucleoporin Nic96 reveals a novel, intricate helical domain architecture. *J. Biol. Chem.* **282**, 34904–34912 (2007). doi: 10.1074/jbc.M705479200; pmid: 17897938

26. P. Sampathkumar *et al*., Structure, dynamics, evolution, and function of a major scaffold component in the nuclear pore complex. *Structure* **21**, 560–571 (2013). doi: 10.1016/j.str.2013.02.005; pmid: 23499021
27. S. Amlacher *et al*., Insight into structure and assembly of the nuclear pore complex by utilizing the genome of a eukaryotic thermophile. *Cell* **146**, 277–289 (2011). doi: 10.1016/j.cell.2011.06.039; pmid: 21784248
28. A. von Appen *et al*., In situ structural analysis of the human nuclear pore complex. *Nature* **526**, 140–143 (2015). doi: 10.1038/nature15381; pmid: 26416747
29. M. T. Teixeira *et al*., Two functionally distinct domains generated by in vivo cleavage of Nup145p: A novel biogenesis pathway for nucleoporins. *EMBO J.* **16**, 5086–5097 (1997). doi: 10.1093/emboj/16.16.5086; pmid: 9305650
30. A. E. Hodel *et al*., The three-dimensional structure of the autoproteolytic, nuclear pore-targeting domain of the human nucleoporin Nup98. *Mol. Cell* **10**, 347–358 (2002). doi: 10.1016/S1097-2765(02)00589-0; pmid: 12191480
31. J. A. Killian, G. von Heijne, How proteins adapt to a membrane-water interface. *Trends Biochem. Sci.* **25**, 429–434 (2000). doi: 10.1016/S0968-0004(00)01626-1; pmid: 10973056
32. G. Drin *et al*., A general amphipathic alpha-helical motif for sensing membrane curvature. *Nat. Struct. Mol. Biol.* **14**, 138–146 (2007). doi: 10.1038/nsmb1194; pmid: 17220896
33. S. J. Kim *et al*., Integrative structure-function mapping of the nucleoporin Nup133 suggests a conserved mechanism for membrane anchoring of the nuclear pore complex. *Mol. Cell. Proteomics* **13**, 2911–2926 (2014). doi: 10.1074/mcp.M114.040915; pmid: 25139911
34. D. I. Fernandez, T. H. Lee, M. A. Sani, M. I. Aguilar, F. Separovic, Proline facilitates membrane insertion of the antimicrobial peptide maculatin 1.1 via surface indentation and subsequent lipid disordering. *Biophys. J.* **104**, 1495–1507 (2013). doi: 10.1016/j.bpj.2013.01.059; pmid: 23561526
35. E. Laurell *et al*., Phosphorylation of Nup98 by multiple kinases is crucial for NPC disassembly during mitotic entry. *Cell* **144**, 539–550 (2011). doi: 10.1016/j.cell.2011.01.012; pmid: 21335236
36. D. Flemming *et al*., Analysis of the yeast nucleoporin Nup188 reveals a conserved S-like structure with similarity to karyopherins. *J. Struct. Biol.* **177**, 99–105 (2012). doi: 10.1016/j.jsb.2011.11.008; pmid: 22138091
37. M. Eibauer *et al*., Structure and gating of the nuclear pore complex. *Nat. Commun.* **6**, 7532 (2015). doi: 10.1038/ncomms8532; pmid: 26112706
38. T. Boehmer, S. Jeudy, I. C. Berke, T. U. Schwartz, Structural and functional studies of Nup107/Nup133 interaction and its implications for the architecture of the nuclear pore complex. *Mol. Cell* **30**, 721–731 (2008). doi: 10.1016/j.molcel.2008.04.022; pmid: 18570875
39. S. Bilokapic, T. U. Schwartz, Molecular basis for Nup37 and ELY5/ELYS recruitment to the nuclear pore complex. *Proc. Natl. Acad. Sci. U.S.A.* **109**, 15241–15246 (2012). doi: 10.1073/pnas.1205151109; pmid: 22955883
40. H. S. Seo *et al*., Structural and functional analysis of Nup120 suggests ring formation of the Nup84 complex. *Proc. Natl. Acad. Sci. U.S.A.* **106**, 14281–14286 (2009). doi: 10.1073/pnas.0907453106; pmid: 19706512
41. C. Xu *et al*., Crystal structure of human nuclear pore complex component NUP43. *FEBS Lett.* **589**, 3247–3253 (2015). pmid: 26391640
42. D. I. Kim *et al*., Probing nuclear pore complex architecture with proximity-dependent biotinylation. *Proc. Natl. Acad. Sci. U.S.A.* **111**, E2453–E2461 (2014). doi: 10.1073/pnas.1406459111; pmid: 24927568
43. A. Ori *et al*., Cell type-specific nuclear pores: A case in point for context-dependent stoichiometry of molecular machines. *Mol. Syst. Biol.* **9**, 648 (2013). doi: 10.1038/msb.2013.4; pmid: 23511206
44. D. Devos *et al*., Components of coated vesicles and nuclear pore complexes share a common molecular architecture. *PLOS Biol.* **2**, e380 (2004). pmid: 15523559
45. S. S. Katta, C. J. Smoyer, S. L. Jaspersen, Destination: Inner nuclear membrane. *Trends Cell Biol.* **24**, 221–229 (2014). doi: 10.1016/j.tcb.2013.10.006; pmid: 24268652
46. R. Ungricht, U. Kutay, Establishment of NE asymmetry—targeting of membrane proteins to the inner nuclear membrane. *Curr. Opin. Cell Biol.* **34**, 135–141 (2015). doi: 10.1016/j.ceb.2015.04.005; pmid: 26112002
47. P. Li *et al*., Phase transitions in the assembly of multivalent signalling proteins. *Nature* **483**, 336–340 (2012). doi: 10.1038/nature10879; pmid: 22398450
48. C. P. Lusk *et al*., Nup53p is a target of two mitotic kinases, Cdk1p and Hrr25p. *Traffic* **8**, 647–660 (2007). doi: 10.1111/j.1600-0854.2007.00559.x; pmid: 17461799
49. F. Alber *et al*., The molecular architecture of the nuclear pore complex. *Nature* **450**, 695–701 (2007). doi: 10.1038/nature06405; pmid: 18046406
50. E. Mossessova, C. D. Lima, Ulp1-SUMO crystal structure and genetic analysis reveal conserved interactions and a regulatory element essential for cell growth in yeast. *Mol. Cell* **5**, 865–876 (2000). doi: 10.1016/S1097-2765(00)80326-3; pmid: 10882122
51. C. Romier *et al*., Co-expression of protein complexes in prokaryotic and eukaryotic hosts: Experimental procedures, database tracking and case studies. *Acta Crystallogr. D Biol. Crystallogr.* **62**, 1232–1242 (2006). pmid: 17001100
52. A. Hoelz, A. C. Nairn, J. Kuriyan, Crystal structure of a tetradecameric assembly of the association domain of Ca^{2+}/calmodulin-dependent kinase II. *Mol. Cell* **11**, 1241–1251 (2003). doi: 10.1016/S1097-2765(03)00171-0; pmid: 12769848
53. S. Doublié, Preparation of selenomethionyl proteins for phase determination. *Methods Enzymol.* **276**, 523–530 (1997). doi: 10.1016/S0076-6879(97)76075-0; pmid: 9048379
54. P. J. Wyatt, Multiangle light scattering: The basic tool for macromolecular characterization. *Instrum. Sci. Technol.* **25**, 1–18 (1997). doi: 10.1080/10739149709351443
55. W. Kabsch, Xds. *Acta Crystallogr. D Biol. Crystallogr.* **66**, 125–132 (2010). doi: 10.1107/S0907444909047337; pmid: 20124692
56. T. C. Terwilliger, Maximum-likelihood density modification. *Acta Crystallogr. D Biol. Crystallogr.* **56**, 965–972 (2000). doi: 10.1107/S0907444900005072; pmid: 10944333
57. A. J. McCoy *et al*., Phaser crystallographic software. *J. Appl. Crystallogr.* **40**, 658–674 (2007). doi: 10.1107/S0021889807021206; pmid: 19461840
58. P. D. Adams *et al*., PHENIX: A comprehensive Python-based system for macromolecular structure solution. *Acta Crystallogr. D Biol. Crystallogr.* **66**, 213–221 (2010). doi: 10.1107/S0907444909052925; pmid: 20124702
59. P. Emsley, K. Cowtan, Coot: Model-building tools for molecular graphics. *Acta Crystallogr. D Biol. Crystallogr.* **60**, 2126–2132 (2004). doi: 10.1107/S0907444904019158; pmid: 15572765
60. I. W. Davis *et al*., MolProbity: All-atom contacts and structure validation for proteins and nucleic acids. *Nucleic Acids Res.* **35**, W375–W383 (2007). doi: 10.1093/nar/gkm216; pmid: 17452350
61. E. F. Pettersen *et al*., UCSF Chimera—a visualization system for exploratory research and analysis. *J. Comput. Chem.* **25**, 1605–1612 (2004). doi: 10.1002/jcc.20084; pmid: 15264254
62. G. N. Murshudov *et al*., REFMAC5 for the refinement of macromolecular crystal structures. *Acta Crystallogr. D Biol. Crystallogr.* **67**, 355–367 (2011). doi: 10.1107/S0907444911001314; pmid: 21460454
63. I. C. Berke, T. Boehmer, G. Blobel, T. U. Schwartz, Structural and functional analysis of Nup133 domains reveals modular building blocks of the nuclear pore complex. *J. Cell Biol.* **167**, 591–597 (2004). doi: 10.1083/jcb.200408109; pmid: 15557116
64. T. Makio *et al*., The nucleoporins Nup170p and Nup157p are essential for nuclear pore complex assembly. *J. Cell Biol.* **185**, 459–473 (2009). doi: 10.1083/jcb.200810029; pmid: 19414608
65. G. J. Barton, ALSCRIPT: A tool to format multiple sequence alignments. *Protein Eng.* **6**, 37–40 (1993). doi: 10.1093/protein/6.1.37; pmid: 8433969
66. R. C. Edgar, MUSCLE: Multiple sequence alignment with high accuracy and high throughput. *Nucleic Acids Res.* **32**, 1792–1797 (2004). doi: 10.1093/nar/gkh340; pmid: 15034147
67. N. A. Baker, D. Sept, S. Joseph, M. J. Holst, J. A. McCammon, Electrostatics of nanosystems: Application to microtubules and the ribosome. *Proc. Natl. Acad. Sci. U.S.A.* **98**, 10037–10041 (2001). doi: 10.1073/pnas.181342398; pmid: 11517324

ACKNOWLEDGMENTS

We thank J.-Y. Mock, S. Petrovic, and A. Patke for critical reading of the manuscript. We thank M. Beck for sharing the cryo-ET reconstruction of the intact human NPC before publication; E. Hurt for providing material and discussions; and C. Bayes, S. Butkovich, C. Frick, A. Koehl, H. Kuberczyk, R. Tran, and S. Zimmerman for experimental support. We also acknowledge J. Kaiser and the scientific staff of the SSRL beamline 12-2, the National Institute of General Medical Sciences and National Cancer Institute Structural Biology Facility (GM/CA) at the APS, and the ALS beamline 8.2.1 for their support with x-ray diffraction measurements. We acknowledge the Gordon and Betty Moore Foundation, the Beckman Institute, and the Sanofi-Aventis Bioengineering Research Program for their support of the Molecular Observatory at the California Institute of Technology (Caltech). The operations at the SSRL, ALS, and APS are supported by the U.S. Department of Energy and the National Institutes of Health (NIH). GM/CA has been funded in whole or in part with federal funds from the National Cancer Institute (grant ACB-12002) and the National Institute of General Medical Sciences (grant AGM-12006). D.H.L and A.M.D. were supported by a NIH Research Service Award (5 T32 GM07616). D.H.L. was also supported by an Amgen Graduate Fellowship through the Caltech-Amgen Research Collaboration. T.S. was supported by a postdoctoral fellowship from the Deutsche Forschungsgemeinschaft. F.M.H. was supported by a doctoral fellowship from the Boehringer Ingelheim Fonds. Y.F. was supported by a visiting doctoral student scholarship from the China Scholarship Council. A.H. was supported by Caltech startup funds, the Albert Wyrick V Scholar Award from the V Foundation for Cancer Research, the 54th Mallinckrodt Scholar Award from the Edward Mallinckrodt Jr. Foundation, a Kimmel Scholar Award from the Sidney Kimmel Foundation for Cancer Research, a Camille-Dreyfus Teacher Scholar Award, and NIH grant R01-GM111461, and he is an inaugural Heritage Principal Investigator of the Heritage Medical Research Institute. The coordinates and structure factors have been deposited in the PDB with accession numbers 5HAX ($Nup170^{NTD}$•$Nup53^{R3}$), 5HAY ($Nup170^{CTD}$), 5HAZ ($Nup170^{CTD}$), 5HB0 ($Nup170^{CTD}$•$Nup145N^{R3}$), 5HB1 ($Nup170^{SOL}$), 5HB2 ($Nic96^{SOL}$), 5HB3 ($Nic96^{SOL}$•$Nup53^{R2}$), 5HB4 ($Nup192^{\Delta HEAD}$), 5HB5 ($Nup145N^{APD}$), 5HB6 ($Nup145N^{APD}$•$Nup145C^{N}$), 5HB7 ($Nup53^{RRM}$, space group $P2_12_12_1$), and 5HB8 ($Nup53^{RRM}$, space group $P3_121$). A PyMol session file containing the composite structure of the NPC symmetric core can be obtained from our webpage (http://ahweb.caltech.edu). The authors declare no financial conflicts of interest. This work is dedicated to the memory of Mandy Hoelz.

SUPPLEMENTARY MATERIALS

www.sciencemag.org/content/352/6283/aaf1015/suppl/DC1
Figs. S1 to S59
Tables S1 to S10

17 December 2015; accepted 19 March 2016
10.1126/science.aaf1015

RESEARCH ARTICLES

STRUCTURAL BIOLOGY

Crystallographic capture of a radical *S*-adenosylmethionine enzyme in the act of modifying tRNA

Erica L. Schwalm,[1*] Tyler L. Grove,[1*] Squire J. Booker,[1,2,3]† Amie K. Boal[1,2]†

RlmN is a dual-specificity RNA methylase that modifies C2 of adenosine 2503 (A2503) in 23*S* rRNA and C2 of adenosine 37 (A37) in several *Escherichia coli* transfer RNAs (tRNAs). A related methylase, Cfr, modifies C8 of A2503 via a similar mechanism, conferring resistance to multiple classes of antibiotics. Here, we report the x-ray structure of a key intermediate in the RlmN reaction, in which a Cys^{118}→Ala variant of the protein is cross-linked to a $tRNA^{Glu}$ substrate through the terminal methylene carbon of a formerly methylcysteinyl residue and C2 of A37. RlmN contacts the entire length of $tRNA^{Glu}$, accessing A37 by using an induced-fit strategy that completely unfolds the tRNA anticodon stem-loop, which is likely critical for recognition of both tRNA and ribosomal RNA substrates.

RlmN is a radical *S*-adenosylmethionine (SAM) enzyme that is best known for catalyzing the methylation of C2 of adenosine 2503 (A2503) (*1*–*3*) in domain V of 23*S* ribosomal RNA (rRNA). A2503, a conserved nucleotide, resides in the peptidyltransferase (PTC) center of the ribosome near the entrance to the exit channel for the nascent polypeptide (*4*–*7*). C2 modification is not essential but has been reported to enhance translational fidelity (*8*, *9*). A2503 is also methylated at C8 by Cfr, which is both evolutionarily and mechanistically related to RlmN (*10*, *11*). The C8 modification, however, confers resistance to more than five classes of antibiotics that target the bacterial ribosome (*12*–*15*). Although methylation of C8 of A2503 is the only known in vivo activity of Cfr, RlmN also installs a C2 methyl group at adenosine 37 (A37) in six *Escherichia coli* tRNAs ($tRNA^{Arg}{}_{ICG}$, $tRNA^{Asp}{}_{QUC}$, $tRNA^{Gln}{}_{cmnm5sUUG}$, $tRNA^{Gln}{}_{CUG}$, $tRNA^{Glu}{}_{mnm5s2UUC}$, and $tRNA^{His}{}_{QUG}$) (*16*). RlmN thus joins a pseudouridine synthase, RluA, as the only known dual-specificity RNA modification enzymes capable of acting both on rRNA and on tRNA (*17*, *18*).

Although SAM is the source of the appended methyl carbon in the reactions catalyzed by RlmN and Cfr, these enzymes operate via a mechanism that is distinctly different from that of typical SAM-dependent methyltransferases (fig. S1), as demanded by the inertness of the C2 and C8 carbons of adenosine to electrophilic attack and the low acidities of their associated protons (*3*, *19*–*23*). As radical SAM (RS) enzymes, RlmN and Cfr use very similar radical-based mechanisms of catalysis, initiated by the abstraction of a hydrogen atom (H•) from a Cys-appended methyl group via a 5′-deoxyadenosyl 5′-radical (5′-dA•) (*20*). Subsequent attack of the resulting methylene radical on the carbon atom undergoing methylation affords a protein/RNA cross-linked intermediate whose resolution requires prior proton abstraction from C2 (RlmN) or C8 (Cfr) of the substrate by an unidentified base. This intermediate has been trapped via mutagenesis of a key Cys residue (C118 in RlmN) in the Cfr and RlmN reactions and characterized by spectroscopic (*21*, *24*), proteomic (*25*), and biochemical methods (*20*, *21*, *24*, *25*). Conversion of the intermediate to the methylated product has also been demonstrated in the Cfr reaction (*21*). Although x-ray structures exist for RlmN in the presence and absence of SAM (*24*, *26*), the large and conformationally flexible nature of its rRNA target has precluded successful structure determination of an enzyme-substrate complex. Here, we take advantage of our current mechanistic understanding of the system to obtain an x-ray crystal structure of a C118A variant of RlmN cross-linked to an RNA substrate. (Single-letter abbreviations for the amino acid residues are as follows: A, Ala; C, Cys; D, Asp; E, Glu; F, Phe; G, Gly; H, His; I, Ile; K, Lys; L, Leu; M, Met; N, Asn; P, Pro; Q, Gln; R, Arg; S, Ser; T, Thr; V, Val; W, Trp; and Y, Tyr. In the mutants, other amino acids were substituted at certain locations; for example, C118A indicates that cysteine at position 118 was replaced by alanine.)

Studies by Grove *et al.* (*20*) and McCusker *et al.* (*25*) showed that the C118A or C118S variants of RlmN are unable to resolve a covalent protein/RNA intermediate during catalysis and become cross-linked to the nucleic acid when overproduced in *E. coli*. Because those studies predated the recognition that RlmN is responsible for methylation of tRNA in *E. coli* (*16*), it was assumed that the protein was cross-linked to a fragment of 23*S* rRNA. However, when the cross-linked enzyme was isolated by means of ion-exchange chromatography (fig. S2), observation of a distinct RNA-containing protein fraction suggested that the enzyme was cross-linked to a homogeneous RNA. Diffraction-quality crystals of the in vivo cross-linked species yielded x-ray data sets to 2.9 Å resolution, and the structure was solved by molecular replacement using a previously published RlmN structure (PDB accession code 3RFA) (table S1). Surprisingly, the electron density most closely resembled $tRNA^{Glu}$ rather than the expected rRNA fragment (fig. S3A) (*16*).

Each of the tRNAs expected to be modified by RlmN (*16*) were generated by means of in vitro transcription, and $tRNA^{Glu}$ and $tRNA^{Arg}$ support the greatest turnover rate in activity assays (fig. S4). The structure of transcribed $tRNA^{Glu}$ cross-linked to purified RlmN C118A (termed the in vitro cross-link) was solved to 2.4 Å resolution (Fig. 1). Positive difference density was observed between the terminal methylene unit of $mCys^{355}$ and C2 of A37 (Fig. 2A), but modeling the interaction as a carbon-carbon bond fully accounts for the electron density, confirming the presence of a covalent adduct. Remarkably, methionine (Met) and 5′-deoxyadenosine (5′-dA) remain visible in the active site, even in the in vivo structure, suggesting that they dissociate after the methylated RNA is released (Fig. 2B). In the absence of the RNA substrate, $mCys^{355}$ resides near the SAM methyl group, cited as ideal for methyl acquisition from the cosubstrate (*26*) but relatively far (~6 Å) from the site of 5′-dA• formation (Fig. 2C). Interaction with tRNA, however, brings the Cys-appended methyl group within 4.1 Å of C-5′ of the SAM cleavage product, which is appropriate for H• abstraction (Fig. 2B). An extended water-mediated hydrogen-bonding network (fig. S5) between the backbone of the loop and A37 of the substrate facilitates the 5 Å shift in the $mCys^{355}$ loop. Structural features specific to adenine, such as N3 and the exocyclic amine (Fig. 2D), provide a basis for selective recognition of the target base. Because these interactions would ensure specificity for reaction with C2, Cfr may use a different strategy to configure the analogous Cys for C8 methylation.

Recent mechanistic studies suggest that resolution of the covalent cross-link requires prior deprotonation at C2, possibly by C118 (fig. S1) (*24*). The cross-linked structure shows A118 pointed directly at C2 of A37, 3.7 Å away, supporting assignment of C118 as the general base (Fig. 2E). Upon deprotonation of C2, radical fragmentation of the C–S bond would generate a thiyl radical and an enamine, which can tautomerize to the methylated product upon return of the C2 proton initially abstracted by C118. Catalysis is then completed through reduction of the thiyl radical by one electron. According to the structure of the cross-linked species, the thiyl radical would be ~9.9 Å away from the nearest iron ion in the cluster, which is consistent with direct electron

[1]Department of Chemistry, Pennsylvania State University, University Park, PA 16802, USA. [2]Department of Biochemistry and Molecular Biology, Pennsylvania State University, University Park, PA 16802, USA. [3]Howard Hughes Medical Institute, Pennsylvania State University, University Park, PA 16802, USA. *These authors contributed equally to this work. †Corresponding author. E-mail: squire@psu.edu (S.J.B.); akb20@psu.edu (A.K.B.)

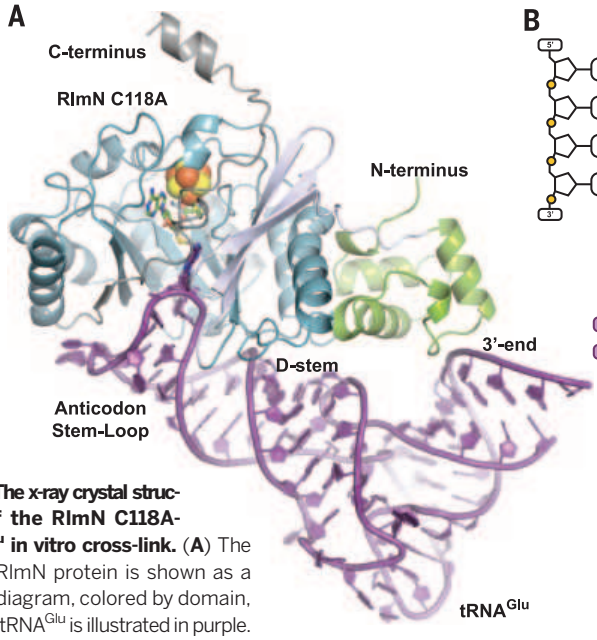

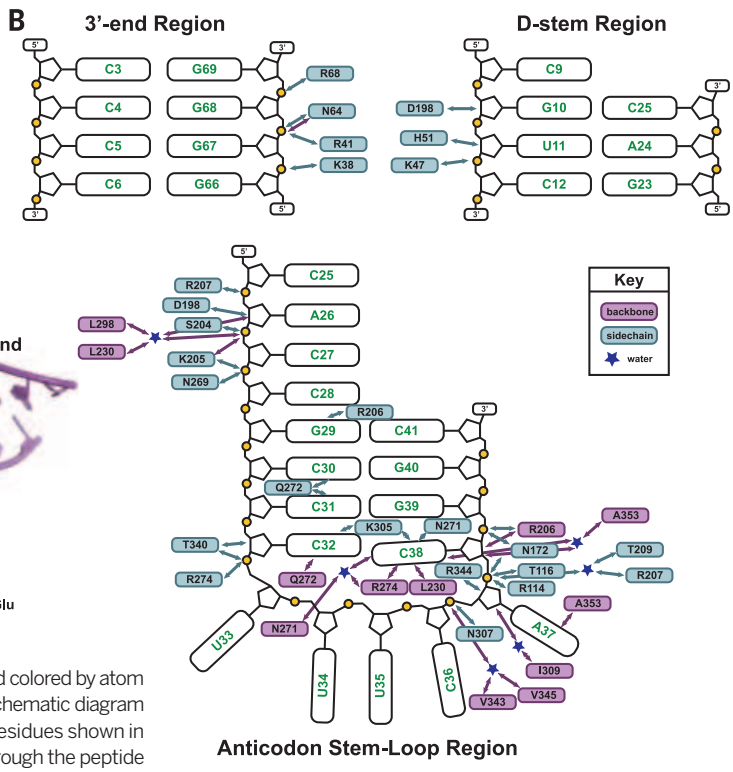

Fig. 1. The x-ray crystal structure of the RlmN C118A-tRNA^{Glu} in vitro cross-link. (**A**) The C118A RlmN protein is shown as a ribbon diagram, colored by domain, and the tRNA^{Glu} is illustrated in purple. The mC355-A37 cross-link and SAM cleavage products, 5′-dA and methionine, are shown in stick format and colored by atom type. The $[4Fe\text{-}4S]^{2+}$ cluster is shown as a space-filling model. (**B**) A schematic diagram of the interactions between RlmN and the tRNA substrate. Protein residues shown in blue interact via the side chain, and those shown in purple interact through the peptide backbone. Blue stars represent water molecules. The RNA is divided into three parts corresponding to the three regions of interaction observed in the complex.

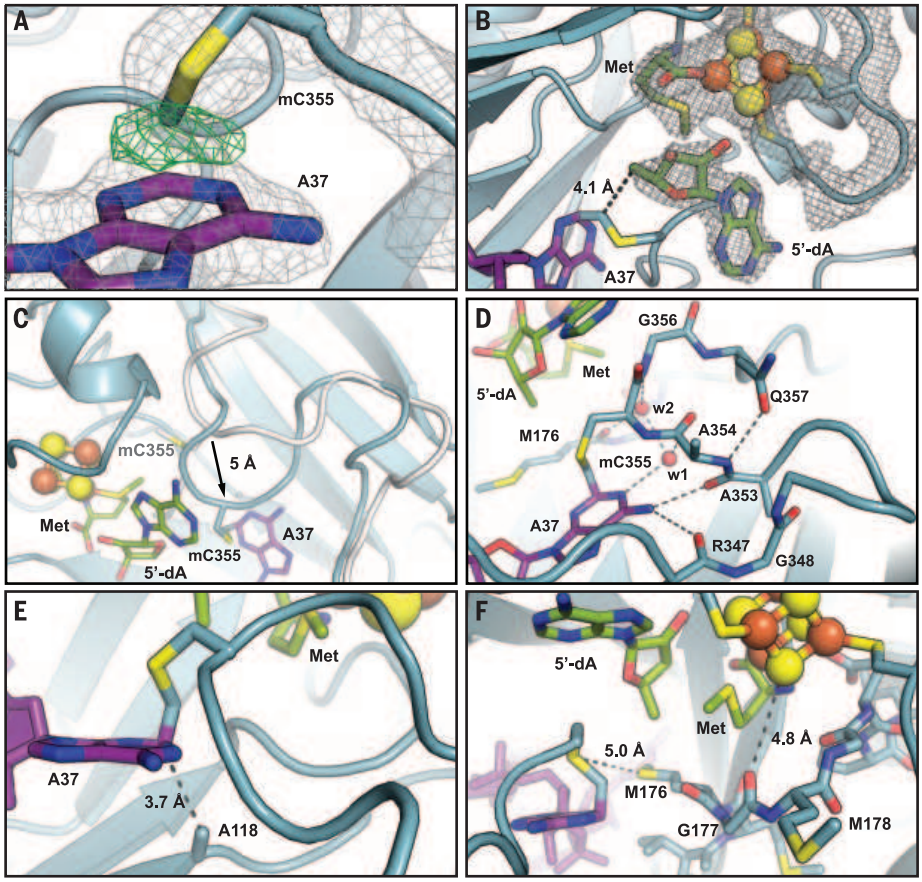

Fig. 2. Views of the active site in the structure of the RlmN C118A-tRNA^{Glu} in vitro cross-link. (**A**) A zoomed-in view of mC355 and A37 with selected residues and cofactors shown in stick format and colored by atom type. A $2F_o$-F_c electron density map (gray mesh, contoured at 2.0σ) and an omit map (green mesh, contoured at 4.0σ) for the covalent bond between A37 C2 and the mCys^{355} Cδ are shown in overlay. (**B**) $2F_o$-F_c electron density map for RlmN residues 125 to 132 (CX_3CX_2C motif, which binds the [4Fe-4S] cluster), the [4Fe-4S] cluster, methionine, and 5′-dA. The distance between the 5′-carbon of 5′-dA to the mC355 Cδ, which is consistent with H• abstraction via a 5′-dA• necessary to initiate cross-link formation, is indicated by a dashed line. (**C**) Overlay of loop from the wild-type RlmN x-ray structure with SAM (white, PDB accession code 3RFA) with the RlmN C118A in vitro cross-link (blue), illustrating the 5 Å shift in position of the loop backbone upon interaction with the tRNA substrate. Selected amino acid side chains, nucleic acid bases, 5′-dA, and methionine are shown in stick format. The [4Fe-4S] cluster is illustrated as a ball-and-stick model. (**D**) A detailed view of the interactions involved in loop repositioning. Hydrogen-bonding interactions are illustrated with dashed lines, and ordered water molecules are shown as red spheres. (**E**) A zoomed-in view of the loop containing mC355 with the covalent cross-link to C2 of A37 shown in sticks. The distance between C2 of A37 and A118, which is consistent with assignment of C118 as a proton acceptor in the wt RlmN reaction, is indicated by a dashed line. (**F**) An alternate view of the active site with the conserved MGMGE motif and other selected amino acids displayed in stick format. Interactions potentially important in thiyl radical stabilization or in electron transfer mediated by the $[4Fe\text{-}4S]^{1+}$ are shown as dashed lines.

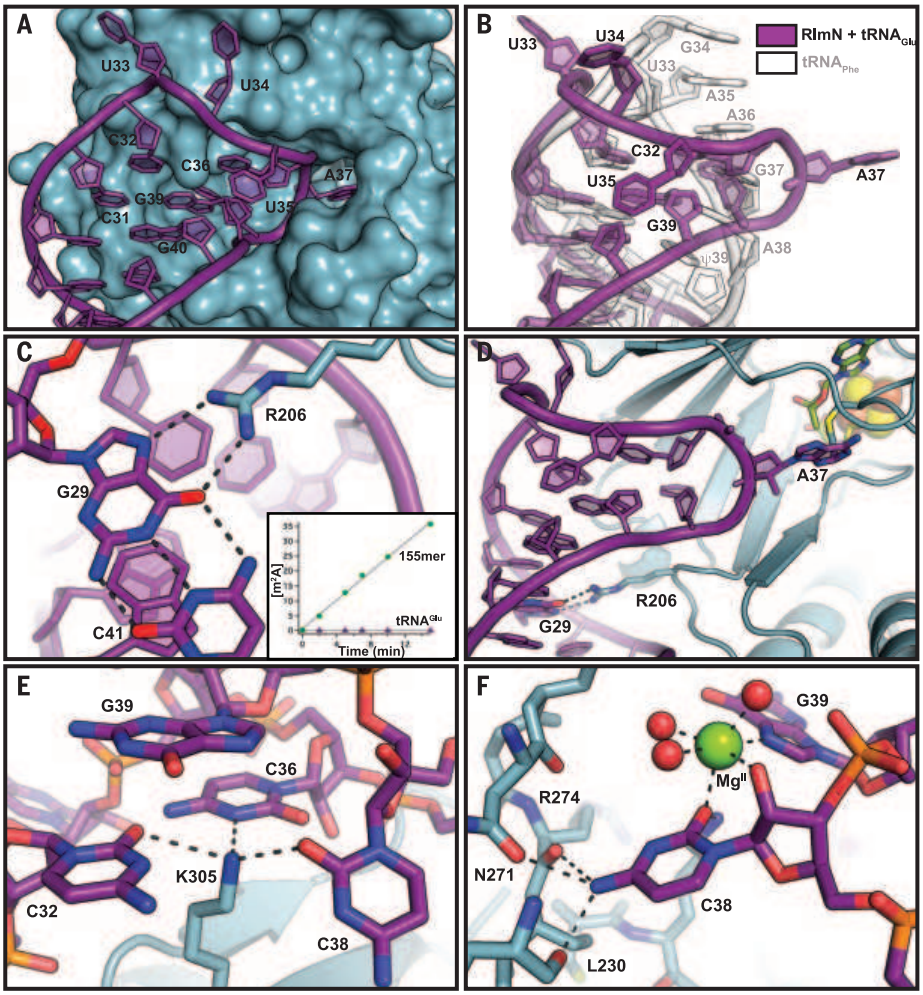

Fig. 3. Selected views of the interactions between RlmN and tRNA^{Glu}. (**A**) An illustration of a surface representation of RlmN showing its interaction with the tRNA anticodon stem-loop (purple). (**B**) A comparison of the structure of the anticodon stem-loop in the C118A RlmN tRNA^{Glu} cross-linked intermediate structure (purple) with the yeast tRNA^{Phe} structure (white, PDB accession code 4TNA). (**C**) A zoomed-in view of R206 with G29 and C41. Selected amino acid residues and nucleic acid bases are shown in stick format. Hydrogen-bonding interactions are displayed as dashed lines. (Inset) The rate of formation of m^{2}adenosine by RlmN R206A using an in vitro–transcribed 155-oligomer rRNA (green circles) or tRNA^{Glu} (purple triangles) as a substrate. (**D**) A zoomed-out view of the position of R206 in relation to the mC355/A37 cross-link and other active site components. The [4Fe-4S] cluster is illustrated as a space-filling model. (**E**) A view of the interactions of K305 with C32, C36, and C38. (**F**) The internal binding pocket of C38. The Mg^{2+} ion is shown as a green sphere, and ordered water molecules are shown as red spheres. Hydrogen-bonding and metal-coordination interactions are shown as dashed lines.

transfer between the two species. The proximity (5.0 Å) of the Cys^{355} side chain (the proposed site of thiyl radical formation) to the sulfur atom of Met^{176} (Fig. 2F), a strictly conserved residue in RlmN and Cfr, might allow formation of a transient thiosulfuranyl radical (*27*). In *E. coli* class III ribonucleotide reductase (RNR), a similar species is proposed to protect a reactive thiyl radical intermediate when reducing equivalents necessary to complete the reaction cycle are scarce (*27*). A similar interaction could be advantageous in RlmN if electron transfer to resolve the cross-linked intermediate is rate-limiting in vivo.

The protein component of the in vitro cross-link changes very little relative to that of the in vivo cross-link, as well as when compared with the previously solved structures of RlmN (Fig. 1A and figs. S3 and S6) (*26*). The protein–nucleic acid interface spans the entire face of tRNA^{Glu} using three separate regions or domains (Fig. 1B and figs. S7 and S8). The N-terminal domain, hypothesized to bind RNA because of its structural similarity with known nucleic acid–binding proteins (*26*), uses only four points of contact to interact with the backbone at the 3′ end of tRNA^{Glu} (fig. S8). The small number of substrate-binding determinants is surprising, although the domain may interact more extensively with the larger rRNA substrate. Additional residues in the N-terminal domain (K47 and H51) and a side chain (D198) contributed by a longer peripheral loop in the radical SAM core bind to the RNA backbone in the major groove of the D-stem of the tRNA (nucleotides 10 to 12) (fig. S8). RlmN binds the concave surface of the substrate, suggesting that it requires full-length L-shaped tRNA for efficient catalysis. Other structurally characterized tRNA-modifying enzymes share the same requirement (*28*), but the overall binding mode and type of RNA recognition elements found in RlmN more closely resemble those of tRNA synthetases (*29*) (fig. S9).

The most extensive RlmN-tRNA interactions involve the anticodon stem-loop (ACSL) of tRNA^{Glu} near A37. The protein binds in the minor groove of the ACSL (Fig. 1A) and interacts more intimately with the nucleobases (Fig. 1B). Only a few sequence-specific contacts are observed—which is typical of ruler or position-specific RNA recognition strategies found in other tRNA modification systems (*28*, *30*)—which would enable RlmN to accommodate the substantial sequence diversity of its tRNA substrates (*16*) in addition to its rRNA substrate (*3*). A strictly conserved arginine (R206) residue and G29 of tRNA^{Glu} (Fig. 3C), found in all six *E. coli* tRNAs containing the m^{2}A modification (*16*), form sequence-specific bidentate hydrogen bonds (H-bonds) between the exocyclic amine and N7 of G29, similar to an interaction found in the discriminating glutamyl-tRNA synthetase, in which a single arginine-cytosine interaction allows the tRNA synthetase to distinguish between tRNA^{Glu} and tRNA^{Gln} (*31*). In R206A RlmN, the ability to methylate tRNA^{Glu} is completely abolished, whereas methylation of a 155-oligomer rRNA substrate remains unaffected (Fig. 3C, inset). R206 may serve as an anchor for the tRNA substrate (Fig. 3D) to initiate base-flipping of A37 into the active site via an unusual mechanism that involves dramatic deformation of the ACSL backbone.

The ACSL conformational change is induced by an RlmN-specific secondary structure element (*26*), a seventh β-strand that forces an outward splay of all of the non–Watson-Crick base-paired residues in the ACSL (Fig. 3, A and B). As a result, A37 is sequestered into an active site pocket using a distinctive base-flipping mechanism (*32*) that completely disrupts the single-strand aromatic base stack in the ACSL. A similar tactic is observed in other tRNA-modifying enzymes, including bacterial adenosine deaminase (TadA) (*33*) and A37 N^6-isopentenyltransferase (MiaA) (fig. S10) (*34*). Apart from A37 (fig. S13), C38 makes the most extensive contacts in the active site (Fig. 3, E and F). The use of distinct complementary binding pockets for multiple bases in the ACSL resembles the substrate recognition strategy used by bacterial Gln tRNA synthetase to read out the sequence in the anticodon and discriminate among potential targets (*35*). However, in RlmN the C38 binding pocket is not base-specific. The observation is consistent with the sequences of the known targets for A37 C2 methylation, which would require accommodation of any nucleobase at position 38 except G (*16*). In RlmN, the additional C38 pocket may simply stabilize the new tRNA conformation in this region and promote extrusion of A37.

The structure of RlmN cross-linked to a tRNA^{Glu} substrate reveals that the protein recognizes the

overall shape of $tRNA^{Glu}$ via interaction with the sugar-phosphate backbone in the D-stem–loop and the 3′ end of the tRNA. The observed analogies to tRNA synthetase structures, coupled with the known dual specificity of the enzyme toward A2503 in the central domain of 23*S* rRNA, provide a link between RlmN and three distinct components of the protein synthesis machinery, suggesting an early origin for A37/A2503 C2 methylation among known RNA modifications. In the ACSL region, the enzyme pries open the tRNA structure to gain access to its A37 nucleobase target. The recognition strategy is fully distinct from that used by RluA, the only other known dual-specificity RNA modification enzyme (*17*). In that system, sequence elements conserved among rRNA and tRNA substrates dictate specificity, although the protein also relies on local RNA refolding for readout of the key motifs. The ability of RlmN to substantially remodel tRNA in the anticodon region may represent a second mechanism to confer dual specificity. The observations here highlight an intriguing structural connection between tRNA and the core of the bacterial ribosome (*36*), a theme that RlmN likely exploits in targeting two distinct substrates that exhibit little sequence similarity but share tertiary features common to evolutionarily ancient components of the protein synthesis machinery.

REFERENCES AND NOTES

1. S.-M. Toh, L. Xiong, T. Bae, A. S. Mankin, *RNA* **14**, 98–106 (2008).
2. J. A. Kowalak, E. Bruenger, J. A. McCloskey, *J. Biol. Chem.* **270**, 17758–17764 (1995).
3. F. Yan *et al.*, *J. Am. Chem. Soc.* **132**, 3953–3964 (2010).
4. N. Ban *et al.*, *Cell* **93**, 1105–1115 (1998).
5. J. Harms *et al.*, *Cell* **107**, 679–688 (2001).
6. B. S. Schuwirth *et al.*, *Science* **310**, 827–834 (2005).
7. M. Selmer *et al.*, *Science* **313**, 1935–1942 (2006).
8. N. Vázquez-Laslop, H. Ramu, D. Klepacki, K. Kannan, A. S. Mankin, *EMBO J.* **29**, 3108–3117 (2010).
9. H. Ramu *et al.*, *Mol. Cell* **41**, 321–330 (2011).
10. G. C. Atkinson *et al.*, *Antimicrob. Agents Chemother.* **57**, 4019–4026 (2013).
11. A. M. B. Giessing *et al.*, *RNA* **15**, 327–336 (2009).
12. K. S. Long, J. Poehlsgaard, C. Kehrenberg, S. Schwarz, B. Vester, *Antimicrob. Agents Chemother.* **50**, 2500–2505 (2006).
13. L. K. Smith, A. S. Mankin, *Antimicrob. Agents Chemother.* **52**, 1703–1712 (2008).
14. C. Kehrenberg, S. Schwarz, L. Jacobsen, L. H. Hansen, B. Vester, *Mol. Microbiol.* **57**, 1064–1073 (2005).
15. G. Morales *et al.*, *Clin. Infect. Dis.* **50**, 821–825 (2010).
16. A. Benítez-Páez, M. Villarroya, M.-E. Armengod, *RNA* **18**, 1783–1795 (2012).
17. C. Hoang *et al.*, *Mol. Cell* **24**, 535–545 (2006).
18. S. Raychaudhuri, L. Niu, J. Conrad, B. G. Lane, J. Ofengand, *J. Biol. Chem.* **274**, 18880–18886 (1999).
19. M. R. Bauerle, E. L. Schwalm, S. J. Booker, *J. Biol. Chem.* **290**, 3995–4002 (2015).
20. T. L. Grove *et al.*, *Science* **332**, 604–607 (2011).
21. T. L. Grove *et al.*, *Nat. Chem. Biol.* **9**, 422–427 (2013).
22. T. L. Grove, M. I. Radle, C. Krebs, S. J. Booker, *J. Am. Chem. Soc.* **133**, 19586–19589 (2011).
23. F. Yan, D. G. Fujimori, *Proc. Natl. Acad. Sci. U.S.A.* **108**, 3930–3934 (2011).
24. A. Silakov *et al.*, *J. Am. Chem. Soc.* **136**, 8221–8228 (2014).
25. K. P. McCusker *et al.*, *J. Am. Chem. Soc.* **134**, 18074–18081 (2012).
26. A. K. Boal *et al.*, *Science* **332**, 1089–1092 (2011).
27. Y. Wei *et al.*, *J. Am. Chem. Soc.* **136**, 9001–9013 (2014).
28. R. Ishitani, S. Yokoyama, O. Nureki, *Curr. Opin. Struct. Biol.* **18**, 330–339 (2008).
29. M. Ibba, D. Söll, *Annu. Rev. Biochem.* **69**, 617–650 (2000).
30. I. J. MacRae *et al.*, *Science* **311**, 195–198 (2006).
31. S. Sekine, O. Nureki, A. Shimada, D. G. Vassylyev, S. Yokoyama, *Nat. Struct. Biol.* **8**, 203–206 (2001).
32. R. J. Roberts, X. Cheng, *Annu. Rev. Biochem.* **67**, 181–198 (1998).
33. H. C. Losey, A. J. Ruthenburg, G. L. Verdine, *Nat. Struct. Mol. Biol.* **13**, 153–159 (2006).
34. S. Chimnaronk *et al.*, *Biochemistry* **48**, 5057–5065 (2009).
35. T. A. Steitz, M. A. Rould, J. J. Perona, *Mol. Biol. Rep.* **14**, 213–214 (1990).
36. S. T. de Farias, T. G. do Rêgo, M. V. José, *Front. Genet.* **5**, 303 (2014).

ACKNOWLEDGMENTS

This work has been supported by NIH grants GM100011 (A.K.B.) and GM101957 (S.J.B.), the Searle Scholars Program (A.K.B.), and Tobacco Settlement Funds (TSF13/14 SAP_4100062216) to S.J.B. Use of the Advanced Photon Source was supported by the U.S. Department of Energy, Office of Science, Office of Basic Energy Sciences, under contract DE-AC02-06CH11357. Use of the LS-CAT Sector 21 was supported by the Michigan Economic Development Corporation and the Michigan Technology Tri-Corridor (grant 085P1000817). GM/CA-CAT has been funded in whole or in part with federal funds from the National Cancer Institute (Y1-CO-1020) and the National Institute of General Medical Science (Y1-GM-1104). Coordinates and structure factors have been deposited in the Protein Data Bank (PDB) with accession codes 5HR6 (C118A RlmN/tRNA in vivo cross-link) and 5HR7(C118A RlmN/tRNA in vitro cross-link).

SUPPLEMENTARY MATERIALS

www.sciencemag.org/content/352/6283/309/suppl/DC1
Materials and Methods
Figs. S1 to S11
Table S1
References (*37–45*)

30 October 2015; accepted 23 February 2016
10.1126/science.aad5367

INTERSTELLAR DUST

Flux and composition of interstellar dust at Saturn from Cassini's Cosmic Dust Analyzer

N. Altobelli,[1]*† F. Postberg,[2,3]† K. Fiege,[2,4]† M. Trieloff,[2,5]† H. Kimura,[6] V. J. Sterken,[7] H.-W. Hsu,[8] J. Hillier,[9] N. Khawaja,[3] G. Moragas-Klostermeyer,[3] J. Blum,[10] M. Burton,[11] R. Srama,[3] S. Kempf,[8] E. Gruen[2,3,8]

Interstellar dust (ISD) is the condensed phase of the interstellar medium. In situ data from the Cosmic Dust Analyzer on board the Cassini spacecraft reveal that the Saturnian system is passed by ISD grains from our immediate interstellar neighborhood, the local interstellar cloud. We determine the mass distribution of 36 interstellar grains, their elemental composition, and a lower limit for the ISD flux at Saturn. Mass spectra and grain dynamics suggest the presence of magnesium-rich grains of silicate and oxide composition, partly with iron inclusions. Major rock-forming elements (magnesium, silicon, iron, and calcium) are present in cosmic abundances, with only small grain-to-grain variations, but sulfur and carbon are depleted. The ISD grains in the solar neighborhood appear to be homogenized, likely by repeated processing in the interstellar medium.

Most of the presolar dust grains, containing the heavy elements from which the planets formed, were destroyed or heavily processed during the first stage of solar system formation. Although a minor population of presolar grains, recognized by their extremely diverse isotopic composition, survived this process in meteorite parent bodies (*1*), it is completely unknown whether those grains are representative of the grain populations in the interstellar medium (ISM) (*2–4*). Interstellar dust (ISD) from the local interstellar cloud (LIC) is injected into the solar system as a highly directional stream nearly aligned with the ecliptic (heliocentric ecliptic longitude/latitude of 79°/−8°) (*2*, *5*). This LIC-ISD flow was first detected in situ by the dust instrument onboard the Ulysses spacecraft (*6*) and has been monitored using a variety of dust detectors at solar distances ranging from 0.3 to 5 astronomical units (AU) (*5*, *7–11*). In situ sampling of the ISD flow was attempted by the Stardust mission, and recent laboratory analyses of the aerogel collectors have revealed three tracks caused by ISD impactors, of which two showed an ISD end particle and the third residuals on the track walls. Elemental residues were also found, probably of ISD origin, in four impact craters in the aluminum foil collectors (*12*). The Cassini spacecraft has been in orbit around Saturn since 2004,

[1]European Space Agency, European Space Astronomy Centre, Madrid, Spain. [2]Institut für Geowissenschaften, University of Heidelberg, Heidelberg, Germany. [3]Institut für Raumfahrtsysteme, University of Stuttgart, Stuttgart, Germany. [4]Georgia Institute of Technology, School of Chemistry and Biochemistry, Atlanta, GA, USA. [5]Klaus-Tschira-Labor für Kosmochemie, University of Heidelberg, Heidelberg, Germany. [6]Kobe University, Kobe, Hyōgo, Japan. [7]International Space Sciences Institute, Bern, Switzerland. [8]University of Boulder, Boulder, CO, USA. [9]University of Kent, Kent, UK. [10]Technische Universität Braunschweig, Institut für Geophysik und Extraterrestrische Physik, Braunschweig, Germany. [11]Jet Propulsion Laboratory, Pasadena, CA, USA.
***Corresponding author. E-mail: nicolas.altobelli@sciops.esa.int**
†These authors contributed equally to this work.

carrying the Cosmic Dust Analyzer (CDA), whose chemical analyzer (CA) subsystem acquires time-of-flight (TOF) mass spectra of dust particles, revealing the grains' elemental composition (*13*). Primarily designed to study the dust populations native to the Saturnian system, Cassini CDA has also proven to be an in situ observatory for dust from beyond Saturn. In this work, we present the result of the analysis of 10 years of Cassini CDA data (mid-2004 until 2013), revealing the faint but distinct signature of LIC-ISD in the largely dominant background of Saturn's E ring water-ice particles originating from Enceladus (*14*).

Flux, mass distribution, direction, and dynamics of ISD grains at Saturn

We identify a total of 36 ISD grains within a distance of 9 to 60 Saturn radii from the planet, characterized by their high entry speed into the Saturnian system, from a direction compatible with the expected LIC-ISD flow at Saturn (Fig. 1). Both the cumulative radial and temporal distribution of the ISD grain detections at Saturn can be reproduced if the ISD grains in the observed mass range account for an average flux of 1.5×10^{-4} m^{-2} s^{-1}, corrected for Saturn's motion (Fig. 2) (see the supplementary materials). The time period covered by our analysis was particularly favorable to ISD detection at Saturn. From 2004 onward, Saturn was moving toward the ISD downstream direction, gradually increasing the relative flux, which peaked in 2010 when Saturn's velocity vector direction was aligned to the ISD upstream direction (*15*). Moreover, in 2010 there was a strong focusing of the smaller particles by the Lorentz force resulting from the relative particle motion with the interplanetary magnetic field (IMF) (*16*). The ISD stream is well collimated around the reference ISD direction, within the uncertainty of the impact direction measurement of 28° (Fig. 2 and supplementary materials). From the measured impact ion charge amplitude and modeling of the grain dynamics, we derived the mass as well as the radiation pressure-to-gravity ratio (β) for each grain (see the supplementary materials). The method used allows for a mass derivation independent of any assumption on β. The mass distribution and β ratio are plotted on Fig. 3. The mass distribution peak is located at ~10^{-17} kg, with a decrease in grain abundance above 10^{-16} kg and a sharp cutoff below 5×10^{-18} kg. The deficit of large grains (above 10^{-16} kg) is due to the lack of sensitivity of our ISD identification methods based on the TOF spectra, preventing us from detecting the largest ISD grains present in the Ulysses data (*17*, *18*).

Composition of ISD grains

Figure 4 (upper panel) shows a typical mass spectrum from an ISD grain. Owing to the high velocity of ISD impacts (typically above 20 km/s), the energy densities upon impact are high enough to totally vaporize the solid grain and yield cation spectra that are clearly dominated by elemental ions rather than molecular ones. The main elemental cation peaks in all ISD spectra (going from lower to higher atomic masses) are carbon, oxygen, sodium/magnesium, potassium/calcium, iron, and rhodium. Rhodium, however, is not indigenous to particles but is excavated from CA target material, as well as a substantial fraction of the observed carbon that is contamination from the Rh target (*19*) (see the supplementary materials). Owing to the relatively low mass resolution of the CDA, signatures of Na/Mg and K/Ca cannot be easily separated in most spectra. However, the positions of the maxima of the respective peaks indicate that Mg^+ and Ca^+ dominate the adjacent species in almost every ISD spectrum. Although not forming individual peaks, Al^+ and Si^+ are visible as an extended flank on the Mg signature. In one individual spectrum, cations of Cr are indicated. The Fe signature is very broad in every ISD spectrum; therefore, although not detectable, minor amounts of Ti, V, Mn, and Ni are possible. We use other nonwater spectra of particles from the ISD direction, which, however, do not fulfill the speed criterion for ISD selection (see Fig. 1), for comparison. These particles are hereafter called the reference group (see the supplementary materials). We compare on Fig. 4 (lower panels) the Mg^+/Fe^+ line amplitude ratios and Mg^+/Ca^+ line amplitude ratios of ISD grains with the reference group. The compositional difference between the ISD and the reference group is apparent at first glance. The ISD grains (i) are clearly compositionally distinct from the reference group and (ii) exhibit a very similar composition within their own group.

To quantify the relative contributions of the major elements Mg, Si, Ca, and Fe in individual ISD particles, we applied the following procedure (for details, see the methods section of the supplementary materials): For each individual mass spectrum, a model spectrum was calculated using a least-square fit procedure to obtain the relative contributions of ions of different elements, particularly to deconvolve the Si peak from the Mg peak tail. Because all elements have a different probability to form cations (e.g., Mg forms cations five times more often than silicon), ion abundances were translated into element abundances by using appropriate relative sensitivity factors (RSFs) (supplementary materials) (*20*). Resulting element composition ratios are shown in Fig. 5 [ratios by weight % (wt %)]. It can be verified that Mg/Si, Fe/Si, Mg/Fe, and Ca/Fe ratios are on average CI chondritic (carbonaceous chondrite of type Ivuna whose composition is considered as a proxy of solar or cosmic element abundances) and similar to a composition inferred for LIC-ISM dust (*21*). For comparison, Fig. 5 (upper panels) shows both the range of elemental compositions for our ISD data and isotopically anomalous presolar stardust grains found in meteorites (*22*–*28*).

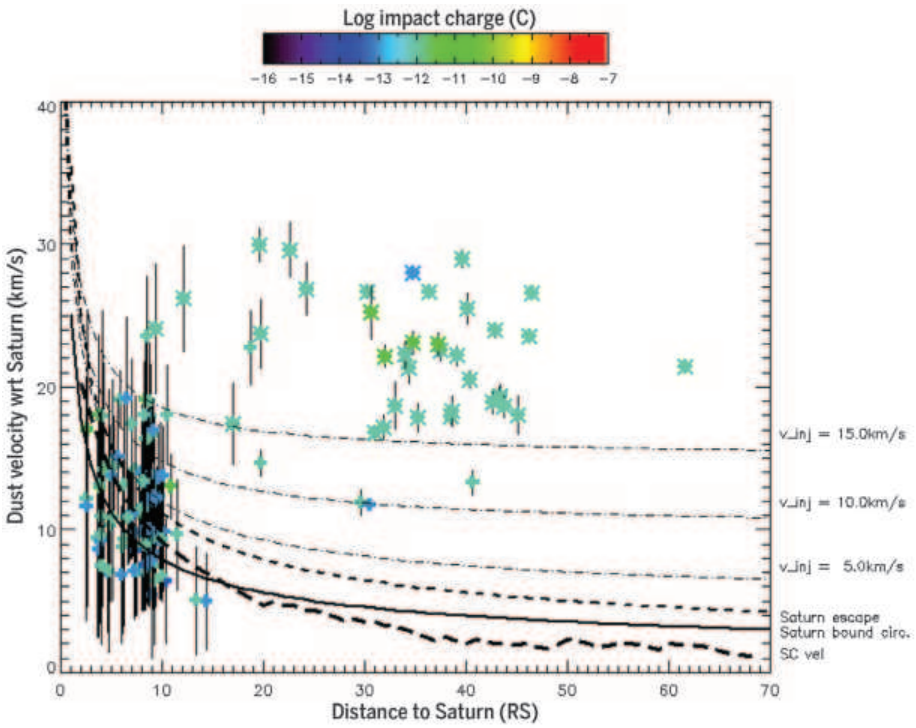

Fig. 1. Minimum speeds inferred from TOF mass spectra. Plotted are the minimum speeds of nonwater dust grains coming from within 50° of the reference ISD direction (see the methods), with respect to Saturn as a function of the radial distance to Saturn. The color code indicates the total charge of the ions (ion yield) generated upon impact. The grains identified as ISD are plotted using an asterisk symbol. The plain and dashed lines in black indicate reference speeds with respect to Saturn as a function of the radial distance: the speed on Keplerian bound circular orbits, the spacecraft speed averaged per distance bins over 2004 to 2013 (SC vel), and the theoretical speed of interplanetary particles, depending on their injection speed at Saturn's Hill sphere (v_{inj}). (For comparison, see fig. S3.)

Those grains condensed in the outflows of asymptotic giant branch (AGB) stars and supernovae and became part of the ISM before they were incorporated into the parental molecular cloud from which our solar system formed.

No mass line in agreement with sulfur can be observed in any of the ISD spectra. Sulfur is considerably harder ionized than most metals, but it forms abundant cations at impact speeds exceeding ~9 km/s (*29*). Ascribing all ions detected between mass 31 and 34 to sulfur (although these ions do not form a distinct peak there; see Fig. 4) and using the minimum RSF of S for impact speeds between 20 km/s and 30 km/s normalized to Fe by (*29*), we calculate an upper limit for the average S/Fe (atomic) ratio of 0.0952 + 0.101/− 0.077. This upper limit is consistent with the value computed for LIC-ISM dust of 0.097 ± 0.058 (*30*). However, it is significantly lower than the CI chondritic ratio of 0.48.

Carbon is another element that appears to be highly depleted in our ISD mass spectra. A significant carbon peak is present in all spectra, but figs. S1 and S2 show that a greater part of it is due to a well-known target contamination of the CDA (*19*). Only if we neglect target contamination and ascribe the entire carbon signal to impacting particles and if we furthermore assume very low detection efficiencies of carbon (see the supplementary materials' section on carbon abundance), a quantification results in an average C/O atomic ratio of 0.32 ± 0.25, which would be consistent with an LIC-ISM dust value of 0.32 ± 0.29 (*3*). This value assumes a higher fraction of carbon in the gas phase, in contrast to an alternative value of 0.81 ± 0.55, which is calculated based on different solar photospheric abundances (*3*). It could well be, however, that only 10% or less of the carbon is indigenous to the particles (figs. S1, S2, and S6) and that we underestimate the carbon detection efficiency by an order of magnitude, which would lower the observed C/O ratio to <0.032—i.e., far below the ISM dust value.

Discussion

Our analysis shows that ISD grains from the local interstellar neighborhood of the solar system can reach the inner Saturnian system. Given the relative insensitivity of the CDA's CA for large grains, it is clear that the mass distribution derived is representative of the smaller grains only up to about 5×10^{-16} kg. For the same reason, our flux value is a lower estimate, and the total flux accounting for the undetected large grains could be up to twice as large (3×10^{-4} m^{-2} s^{-1}). Our measurements suggest, therefore, that the ISD flux at Saturn (10 AU) is larger than the fluxes measured by Ulysses at distances up to 5 AU. It is likely that this larger ISD flux at Saturn is related to a focusing effect predicted for the grains as they interact with the IMF (*16*) during our collection period, confirming that the ISD grains, in the size range covered by our study, have a nonzero charge-to-mass (q/m) ratio.

The deficit of very small grains in our data, despite the sensitivity of our method that enables the detection of grains with masses as low as 10^{-19} kg, can be explained by the filtering of such small grains at the heliopause and inner heliosphere (*15*, *31*, *32*). This phenomenon was also observed in the Ulysses ISD data (*17*). We confirm the existence of grains with β > 1 with a maximum value reached between 10^{-17} and 10^{-16} kg, in good agreement with the β-mass domains inferred from Ulysses data (*3*).

The β-mass curve by itself cannot directly provide the grain composition and structure unambiguously but provides an independent consistency check of the compositional measurements by the CDA mass spectra. The β ratio quantifies the solar photon scattering efficiency and, combined with the grain mass, is a proxy for the grain composition and structure (*3*, *16*). Synthetic β-mass curves were computed using Mie theory for different grain models with bulk composition compatible with the measured TOF spectra and compared with the β-mass curve inferred from the grain dynamics (Fig. 3). All models of grains considered for the β computation are amorphous but compact particles, by opposition to porous structures. For the size regime of less than a few hundred nanometers observed by the CDA, the assumption of compact particles is the most plausible one and is reasonably supported by our observations (see supplementary materials' section on derivation of the β-mass curve). In contrast, larger ISD in the μm regime are likely porous aggregates (*33*). Good agreement is found for silicate particles enriched with metallic Fe. In contrast, the β ratio of pure Fe-Mg silicates without metallic Fe enrichment cannot exceed unity, which is in disagreement with the high β ratio of most grains above 5×10^{-17} kg. As we find no indications for abundant organic material in CDA mass spectra, we conclude that at least some of the iron identified by the CDA has to be in metallic form. However, our upper limit for carbon does not exclude the presence of thin

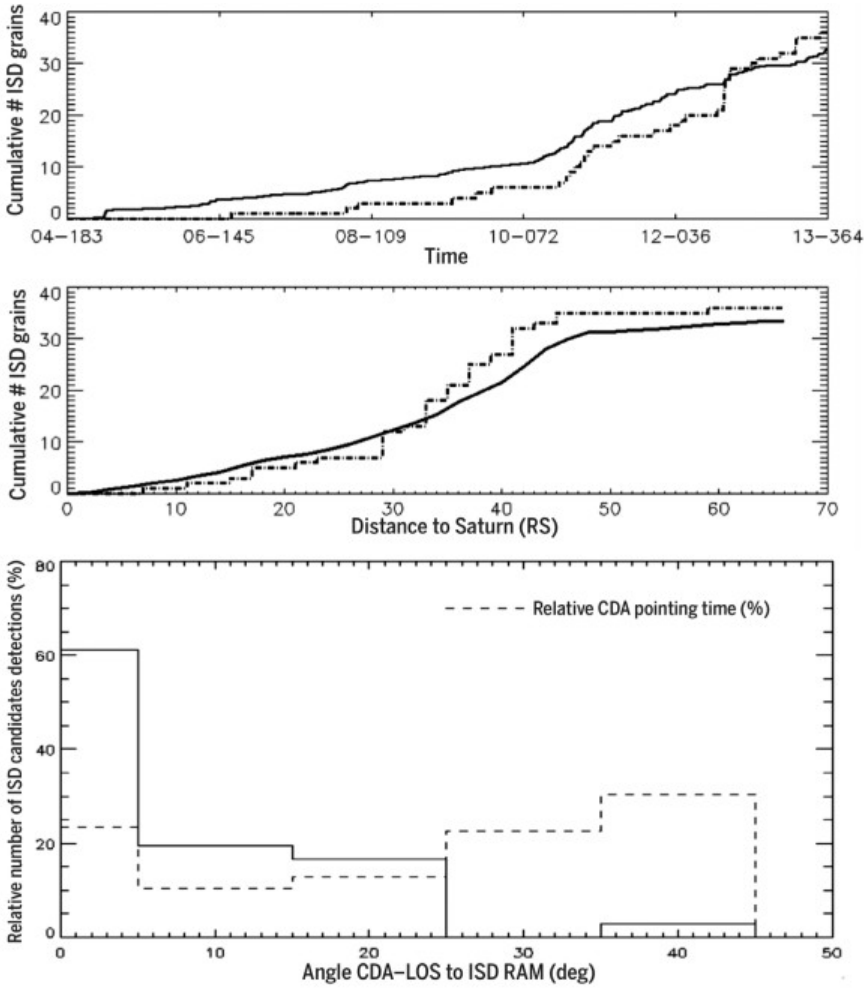

Fig. 2. ISD flux and direction. Cumulative temporal and radial distance distribution of the ISD grain detections (black dotted-dashed lines on the upper and middle panels, respectively). The plain lines are the modeled distributions obtained by computing the number of ISD grains from the reference ISD direction with a flux of 1.5×10^{-4} m^{-2} s^{-1} (see the methods section of the supplementary materials). The lower panel shows the distribution of the angles between the CDA boresight at the time of ISD grain detection and the ISD reference direction. The relative time spent in each angle bin over the time period 2004 to 2013 is indicated by the dashed line. Although the CDA spends most of the time pointing 30 or 40° away from the reference ISD direction, all except one ISD grain were detected within 20° of the reference ISD direction.

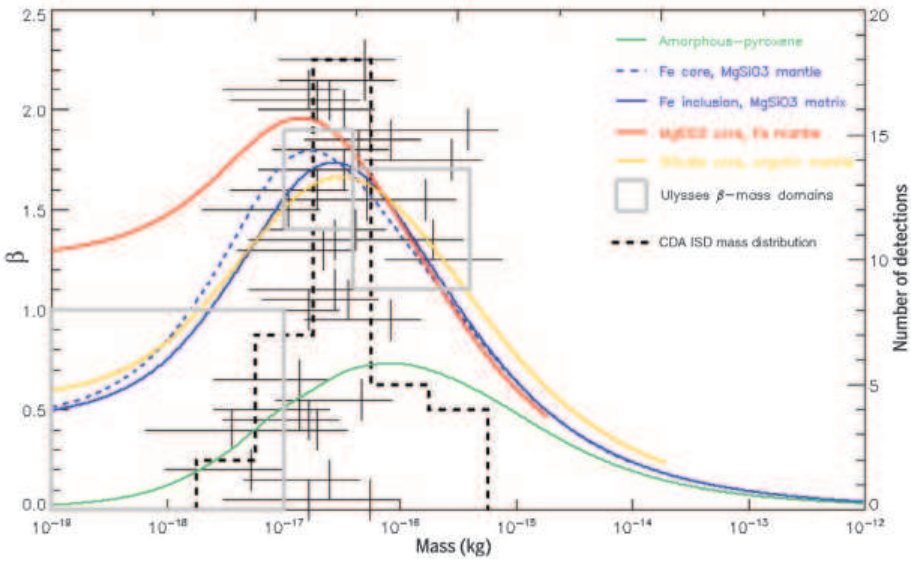

Fig. 3. ISD grain mass distribution and β-mass values. The dashed black line indicates the grain mass distribution. The individual β and mass values inferred for each ISD grain are plotted with error bars. A one order of magnitude error in the mass determination results from the mass-velocity calibration uncertainty (*13*). A maximum error of 0.2 in the determination of β is applied for all grains. This maximum error takes into account a range of possible (β-dependent) velocity values. Theoretical β-mass values obtained using Mie theory computations for amorphous grains with different compositions and structures are indicated as plain and dashed lines. $MgSiO_3$ only refers to composition and does not imply crystallinity. The gray rectangular areas show the range of β-mass values inferred from the Ulysses ISD data (*3*). A structure with heterogeneous distribution of Fe and/or C is needed to explain the relatively high β values.

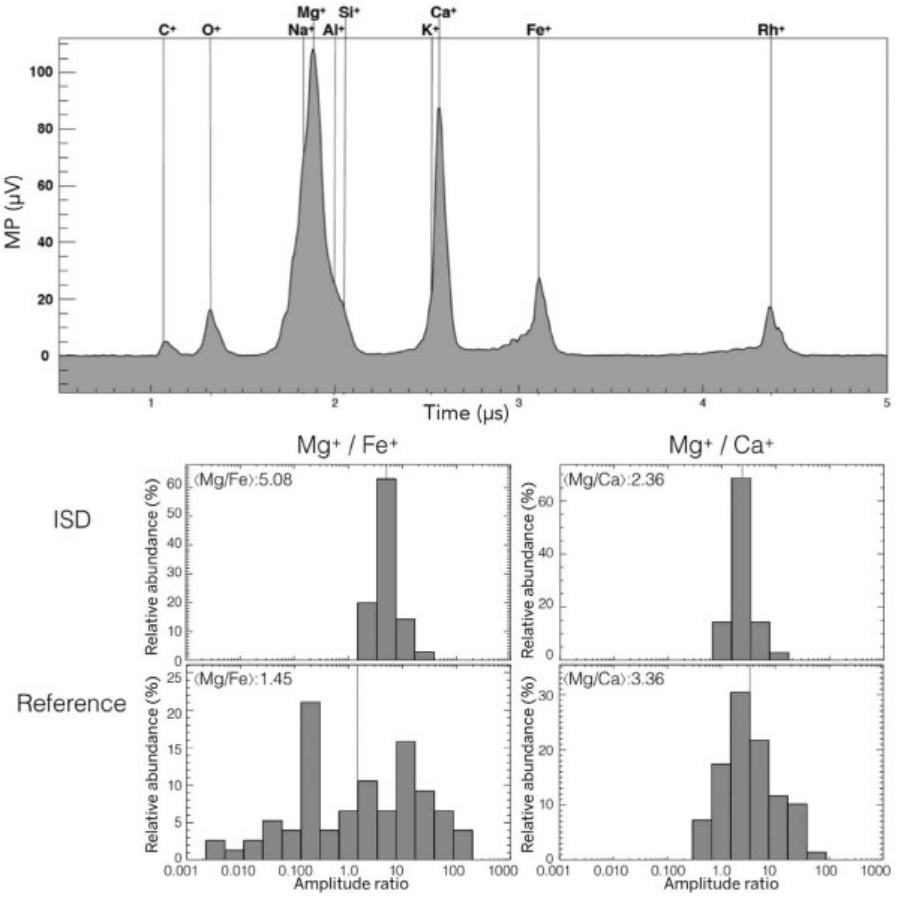

Fig. 4. Typical CDA ISD TOF mass spectrum and comparison of ISD spectra with reference group spectra. The upper panel shows a typical impact ionization mass spectrum from an ISD grain. Vertical lines indicate the positions of relevant cation species. The *x* axis indicates the TOF needed by the cations to reach the ion detector (after triggering the event), from which the ion masses are derived. The *y* axis shows the amplitude of the electrical signal derived from the detected cations, a measure of their abundance. The ions of the main particle constituents form the main peaks: Mg, Fe, Ca, and O. Si and Al are forming a distinct shoulder on the right flank of the Mg signature. The Rh peak is from the CDA's impact target made of rhodium. To convert the ion abundance into elemental abundance, RSFs have to be applied (see the methods). In the lower panel are shown the ratios of cations observed in ISD spectra (upper panels) and spectra of the reference group (lower panels). The narrow distributions observed in ISD spectra suggest that ISD grains have a similar composition.

organic mantles on the ISD grains causing an increase in the β ratio. Collecting ISD grains at Saturn allowed us to sample LIC dust at the largest heliocentric distance yet achieved in situ, reducing the amount of dynamical filtering as compared with former detections performed closer to the Sun. In addition, the relative position of Saturn and the Sun, with respect to the ISD stream over the time period considered in this work, permitted the detection of grains with a wide range of β values (*16*). We are therefore convinced that our compositional results are not significantly affected by a selection bias related to the grain dynamics in the solar system.

All models of LIC-ISD grain composition thus far have been based on the ultraviolet (UV) spectra measurements of absorption lines of C, N, O, Mg, Al, Si, S, and Fe in the gas phase of the LIC along the lines of sight toward nearby stars (*2*, *3*, *34*). These models assume that the element total abundance corresponds to cosmic abundances derived from the solar photosphere composition and that an element depletion in the gas results from its incorporation into dust grains. Most of these

studies suggest dust populations with different compositions: a Mg-rich silicate population, a carbon-rich population, Fe-rich dust (possibly oxides), and an Al-rich group (possibly corundum). A model of ISD grains in the general ISM (*35*, *36*) proposes a core of silicate composition and an organic mantle remaining after UV radiation of ices. A more detailed mineralogical model was proposed (*3*), with grains made of a core of Mg-rich olivine and pyroxene composition and iron-bearing metallic inclusions (like kamacite), coated by an organic refractory mantle containing CHON-bearing material.

Our in situ detection of ISD provides constraints on these models. First of all, the average composition of our Mg, Si, Ca, and Fe data is in general consistent with the observation that these elements are fully condensed from the gas that forms the LIC, resulting in cosmic (CI chondritic) element abundances (Fig. 5), and that particles of silicate composition dominate the LIC-ISD population. More important, our data demonstrate that compositional homogeneity extends down to small spatial scales of 200 nm—i.e., the grain size of the ISD particles observed by the CDA. All grains contain these silicate-forming elements, and individual grain-to-grain variations are limited (see Figs. 5 and 6; note that some, if not most, of the scatter of our data is due to stochastic uncertainties of the impact ionization of the CDA). In the investigated size regime, there are no indications of other, compositionally diverse ISD populations such as pure Fe-O grains or pure carbonaceous particles. The absence of the latter was already suggested by (*34*, *37*). Although we cannot entirely rule out their existence in the LIC, such populations do not appear to represent more than an upper limit of $\frac{1}{2} \times \frac{\sqrt{36}}{36} \approx 10\%$ of the ISD grains observed by the CDA penetrating into the solar system (assuming Poisson statistics for the error on the number of ISD grains detected). The depletion of carbon and sulfur inferred from the gas-absorption spectra of the LIC indicates loss of these compounds from ISD grains. The most plausible explanation is that volatile sulfur and carbon are incompletely condensed under conditions applicable for the LIC. In this respect, it should be noted that Mg/Si and Fe/Si ratios are slightly higher than cosmic abundances and could indicate a small deficit of Si, which is more volatile than the other major rock-forming elements Mg or Fe. The process responsible for the loss of these volatile substances needs further clarification.

Only the Stardust mission has previously provided insights into the composition of contemporary interstellar dust crossing our solar system, with material collected in aerogel and extracted from four impact craters resulting from ISD impacts in the aluminum foil collectors (*12*, *38*, *39*). The sizes of these impact craters between 0.28 and 0.46 μm imply particles of similar sizes as those observed with the CDA (*12*). The inferred bulk particle composition is in agreement with our results, except for the presence of sulfide in three of the four craters (*39*), whereas there is no indication of sulfur in CDA ISD mass spectra. Three particles were collected in aerogel; two of them—Orion and Hylabrook—yielded compositional data (*39*) that allow a comparison in Fig. 5. Although Mg/Fe ratios are within the range of the CDA's ISD particles, the Mg/Si and Fe/Si ratios are significantly higher—i.e., the Stardust ISD particles are depleted in Si with respect to cosmic abundances. It should be kept in mind, however, that Orion and Hylabrook are much larger and perhaps porous particles, so that the formation mechanisms and the particles' chemical

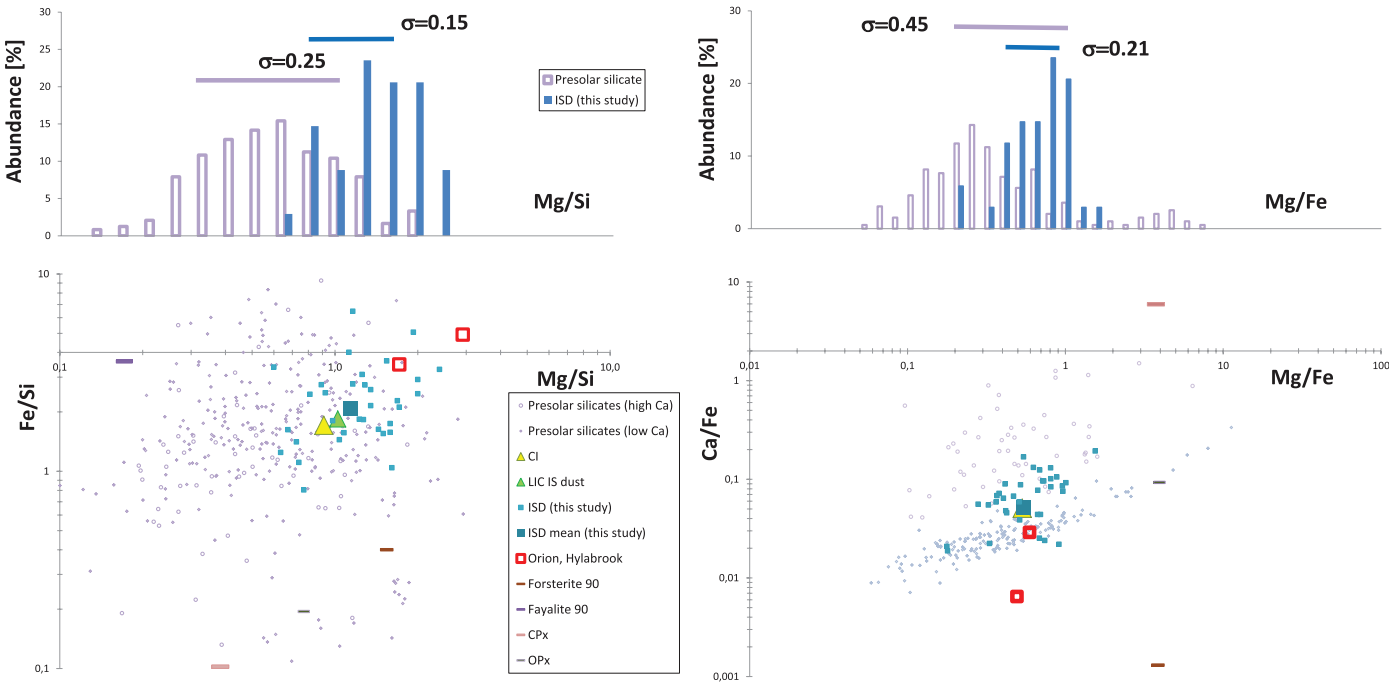

Fig. 5. Comparison of element wt % ratios in CDA ISD grains with chondritic and presolar material. Mg/Si, Fe/Si (lower panel, left side) and Mg/Fe, Ca/Fe ratios (lower panel, right side) are shown for ISD grains (blue squares). The elemental ratios given by the *x* axis of each lower panel also apply to the upper panels. The average composition (large blue square) is compatible with CI chondrites (yellow triangle), indicating average cosmic element abundance ratios, and is also compatible with LIC-ISD composition from astronomical observations (green triangle). Limited compositional variation is possible, but at least part of this scatter is due to the detection method. For comparison, we analyzed compositional data of 388 presolar circumstellar dust grains, which were obtained by Auger spectroscopy (*22*–*28*). Grains of silicate composition [i.e., with atomic ratios of (Fe+Mg+Ca)/Si < 2.2] are shown. Histograms for Mg/Si and Mg/Fe (upper panels) demonstrate their larger scatter and more heterogeneous composition compared with the ISD grains of this study. For low Ca presolar silicate grains (gray diamonds), the Ca/Fe values are upper limits, assuming the detection limit as Ca abundance; hence, the true scatter of the presolar silicate grains in Ca/Fe is actually larger. The smaller scatter of the LIC-ISD grain population in this study indicates that they represent a secondary population that was derived by processing and homogenization in the ISM from a primary, more heterogeneous circumstellar grain population. Also shown are typical compositions of silicates like forsterite (Fo90Fa10), fayalite (Fa90Fo10), and Mg-rich clino- and orthopyroxene (CPx and OPx) from a primitive mantle lherzolite (*20*), again emphasizing that the LIC-ISD grains represent average compositions rather than mineral end-member compositions. Two data points are shown for the Orion and Hylabrook particles returned by the Stardust mission: Although Mg/Fe is largely compatible with our ISD data, Mg/Si is significantly higher.

history might not be directly comparable to our data.

Our results can also be compared with elemental compositions of interstellar grains preserved in 4.6-billion-year-old meteorites (Fig. 5). These interstellar grains survived processing in the protoplanetary disc when our solar system formed and consist of compositionally diverse populations. Their specific isotopic compositions reflect the nucleosynthetic processes of their host stars at the time, when these grains condensed in the outflows of the parental AGB stars or supernovae. Analysis of the inventory of presolar grains in meteorites indicates that the main population is silicates (e.g., olivine and pyroxene), with minor contributions (i.e., a few percent) of oxides (e.g., corundum and hibonite) and carbonaceous grains, mainly silicon carbide (*40*), with an abundance of >20%, possibly up to 50%.

The upper panels of Fig. 5 show histograms of Mg/Si and Mg/Fe ratios of presolar silicate populations and our ISD data. It can be verified that the scatter of elemental compositions of presolar silicates is about a factor of 2 larger (on logarithmic scales) compared with the CDA ISD data. Figure 6 additionally displays (Mg+Fe+Ca)/Si ratios (atom %): Although the presolar grain population has a maximum between pyroxene- and olivine-type silicate composition with values between 1 and 2, our ISD grain population centers between 2 and 3, similar to LIC-ISM dust composition inferred from astronomical observations (*37*). Such values can be explained by the presence of either Mg, Fe, or Ca oxides or metallic Fe. These phases occur also in the Orion and Hylabrook ISD particles, which also have high (Mg+Fe+Ca)/Si ratios. For the Stardust ISD residues on Al foils, only one particle yielded a quantifiable bulk value of 3.3, whereas for the remaining residues, the bulk values could not be constrained because of the uncertain proportions of silicates and Fe metal and sulfide.

These observations indicate that the major population of dust grains in the ISM is different from pristine circumstellar stardust. A more homogeneous composition concerning Mg/Si or Mg/Fe can be explained by destruction, recondensation, and equilibration processes in the ISM that homogenize an initially diverse population that started as circumstellar dust. This could also explain the observation that the high Mg end of the presolar silicate population in Fig. 5 (which are crystalline circumstellar olivine grains) is missing in the Cassini ISD data: Grain destruction and recondensation will wipe out the high Mg tail and result in a very low fraction of crystalline ISM grains. The same conclusion arises from the nondetection of SiC in our ISD population, because SiC is not expected to condense in the ISM. Among presolar grains, SiC—condensed in circumstellar atmospheres—should have a 20 to 50% abundance. The 20% estimate is a lower limit, because many meteorites have a SiC/silicate ratio that is higher than 1:5, although this is ascribed to preferential metamorphic destruction of silicates on meteorite parent bodies. On the other hand, model calculations of circumstellar dust (*4*) also yield relatively high values for the SiC/silicate ratio. The probability of detecting 36 silicates (and no SiC) among a mixture of 80% silicates and 20% SiC is as low as 0.03%, and 5% (i.e., below the 2-sigma confidence level) for an 8% SiC abundance. Destruction and recondensation of grains in the ISM are supported by observations showing that, in the diffuse ISM, the most condensable (atomic mass >23) elements are depleted in the gas phase and hence bound in solids, whereas the average lifetime of interstellar grains against destruction by supernova shocks (about 0.5 billion years) is much shorter than the average residence time of matter in the ISM (2.5 billion years) (*4*). During this residence time, ISD grains frequently cycle between the hot ISM (low-density regions carved by supernovae), the warm diffuse medium (accessible by spectroscopic observations), and cold molecular clouds, which are star-formation regions. Under the assumption that typically 5% of molecular cloud material is consumed by new stars and planetary systems, interstellar grains cycle on time scales of ~125 million years between the hot medium and the cold medium. Although destruction and devolatilization processes prevail in the hot medium due to high grain velocities and supernova shock waves, recondensation can occur in the cold medium.

Our results indicate that a homogeneous population of grains with roughly average cosmic abundances (concerning Mg:Si:Ca:Fe ratios), possibly including metallic nanophase iron, is the primary constituent of the LIC-ISD, emphasizing the importance of recondensation processes (*4*, *37*). A further implication is that searches for presolar interstellar grains in meteorites led by isotopic anomalies are likely to miss a population that recondensed in the ISM, because destruction and recondensation of solids would erase isotopic anomalies. Hence, a considerable fraction of yet unrecognized—isotopically inconspicuous—ISD could reside in meteorites and cometary material awaiting its discovery [see, for example, the discussion in (*41*, *42*)].

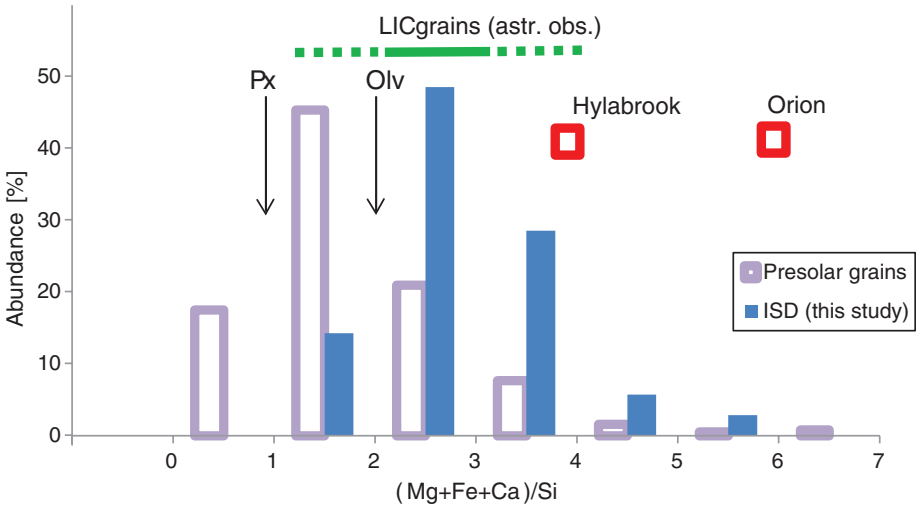

Fig. 6. Comparison of (Mg+Fe+Ca)/Si ratio histograms (in atom %) of CDA ISD grains, presolar circumstellar material, LIC-ISD determined by astronomical observations, and ISD returned by the Stardust mission. Presolar grains have a maximum at a silicate composition intermediate between pyroxene and olivine and a tail to high values caused by a bias (overabundance) of refractory oxides. LIC-ISD values center between 2 and 3. Such high values are caused either by oxides or by metallic Fe, phases that have also been observed in the Stardust particles Orion and Hylabrook. The presolar circumstellar grain population is biased; for example, there is possibly selective loss of amorphous grains or a higher fraction of resistant oxides due to metamorphic destruction on asteroids or comets. Nevertheless, it is highly unlikely that the presolar grain population initially had a distribution similar to our ISD data: In this case, the presolar population should have lost primarily the oxide or metal component, which is, however, unlikely, as oxides are rather more resistant against metamorphic destruction.

REFERENCES AND NOTES

1. E. Zinner *et al.*, *Geochim. Cosmochim. Acta* **71**, 4786–4813 (2007).
2. P. C. Frisch *et al.*, *Astrophys. J.* **525**, 492–516 (1999).
3. H. Kimura, I. Mann, E. K. Jessberger, *Astrophys. J.* **583**, 314–321 (2003).
4. S. Zhukovska, H.-P. Gail, M. Trieloff, *Astron. Astrophys.* **479**, 453–480 (2008).
5. M. Landgraf, *J. Geophys. Res.* **105** (A5), 10303–10316 (2000).
6. E. Grün *et al.*, *Nature* **362**, 428–430 (1993).
7. M. Landgraf, J.-C. Liou, H. A. Zook, E. Grün, *Astrophys. J.* **123**, 2857 (2002).
8. N. Altobelli *et al.*, *J. Geophys. Res.* **108** (A10), 8032 (2003).
9. N. Altobelli *et al.*, *J. Geophys. Res.* **110** (A7), A07102 (2005).
10. N. Altobelli, E. Grün, M. Landgraf, *Astron. Astrophys.* **448**, 243–252 (2006).
11. I. Mann, *Annu. Rev. Astron. Astrophys.* **48**, 173–203 (2010).
12. R. M. Stroud *et al.*, *Meteorit. Planet. Sci.* **49**, 1698–1719 (2014).
13. R. Srama *et al.*, *Space Sci. Rev.* **114**, 465–518 (2004).
14. F. Spahn *et al.*, *Planet. Space Sci.* **54**, 1024–1032 (2006).
15. V. J. Sterken *et al.*, *Astron. Astrophys.* **552**, A130 (2013).
16. V. J. Sterken *et al.*, *Astron. Astrophys.* **538**, A102 (2012).
17. M. Landgraf, W. J. Baggaley, E. Grün, H. Krüger, G. Linkert, *J. Geophys. Res.* **105** (A5), 10343–10352 (2000).
18. H. Krüger, M. Landgraf, N. Altobelli, E. Grün, *Space Sci. Rev.* **130**, 401–408 (2007).
19. F. Postberg *et al.*, *Planet. Space Sci.* **57**, 1359–1374 (2009).
20. K. Fiege *et al.*, *Icarus* **241**, 336–345 (2014).
21. N. Przybilla, M.-F. Nieva, K. Butler, *Astrophys. J.* **688**, L103–L106 (2008).
22. M. Bose, C. Floss, F. J. Stadermann, *Astrophys. J.* **714**, 1624–1636 (2010).

23. M. Bose, C. Floss, F. J. Stadermann, R. M. Stroud, A. K. Speck, *Geochim. Cosmochim. Acta* **93**, 77–101 (2012).
24. A. N. Nguyen, L. R. Nittler, F. J. Stadermann, R. M. Stroud, C. M. O. Alexander, *Astrophys. J.* **719**, 166–189 (2010).
25. C. Vollmer, P. Hoppe, F. J. Stadermann, C. Floss, F. E. Brenker, *Geochim. Cosmochim. Acta* **73**, 7127–7149 (2009).
26. C. Floss, F. J. Stadermann, *Meteorit. Planet. Sci.* **47**, 992–1009 (2012).
27. C. Floss, F. Stadermann, *Geochim. Cosmochim. Acta* **73**, 2415–2440 (2009).
28. X. Zhao, C. Floss, Y. Lin, M. Bose, *Astrophys. J.* **769**, 49 (2013).
29. J. K. Hillier *et al.*, *Planet. Space Sci.* **97**, 9–22 (2014).
30. H. Kimura, *Mon. Not. R. Astron. Soc.* **449**, 2250–2258 (2015).
31. J. Slavin, P. Frisch, J. Heerikhuisen, N. Pogorelov, H. R. Mueller, W. T. Reach, G. Zank, A. Li, 38th COSPAR Scientific Assembly, Plenary Meeting (Bremen, Germany, 18 to 25 July 2010), p. 1618.
32. J. D. Slavin *et al.*, *Astrophys. J.* **760**, 46 (2012).
33. V. J. Sterken, P. Strub, H. Krüger, R. von Steiger, P. Frisch, *Astrophys. J.* **812**, 141 (2015).
34. J. D. Slavin, P. C. Frisch, *Astron. Astrophys.* **491**, 53–68 (2008).
35. J. M. Greenberg, J. I. Hage, *Astrophys. J.* **361**, 260 (1990).
36. H. Kimura, I. Mann, E. K. Jessberger, Meteoroids 2001 Conference, B. Warmbein, ed. (2001), vol. 495 of ESA Special Publication, pp. 633–642.
37. P. C. Frisch, J. D. Slavin, *Earth Planets Space* **65**, 175–182 (2013).
38. A. J. Westphal *et al.*, *Meteorit. Planet. Sci.* **49**, 1720–1733 (2014).
39. A. J. Westphal *et al.*, *Science* **345**, 786–791 (2014).
40. J. Leitner, C. Vollmer, P. Hoppe, J. Zipfel, *Astrophys. J.* **745**, 38 (2012).
41. J. P. Bradley *et al.*, *Science* **285**, 1716–1718 (1999).
42. L. P. Keller, S. Messenger, *Geochim. Cosmochim. Acta* **75**, 5336–5365 (2011).

ACKNOWLEDGMENTS

N.A. and F.P. acknowledge European Space Agency faculty funding for travels and meetings that were necessary for the completion of this work. Funding through Deutsche Forschungsgemeinschaft (DFG) within the priority program 1385 "The First 10 Million Years of the Solar System - A Planetary Materials Approach" is acknowledged by K.F., J.B. (grant BL 298/20-2), and R.S., M.T., E.G., J.H., and F.P. (grants TR333/14 and SR77/1). J.H. has received funding from the People Programme (Marie Curie Actions) of the European Union's Seventh Framework Programme FP7 2013 under Reemployment and Eligibility Assessment (REA) grant agreement number 622856. R.S. and F.P. acknowledge funding through Deutsches Zentrum für Luft- und Raumfahrt (DLR), Germany. V.J.S. acknowledges funding through the International Space Science Institute. N.K. acknowledges funding through the DFG. M.T. acknowledges funding by the Klaus Tschira Foundation. We thank J. Leitner, A. Westphal, R. Stroud, L. Nittler, P. Hoppe, H. Ishii, and H.-P. Gail for helpful discussions. We thank three anonymous reviewers for their thorough review of this paper. All CDA data used for this analysis are archived on the Small Bodies Node of the Planetary Data System (PDS-SBN), at http://sbn.psi.edu/archive/cocda.

SUPPLEMENTARY MATERIALS

www.sciencemag.org/content/352/6283/312/suppl/DC1
Materials and Methods
Figs. S1 to S6
Table S1
References (*43–61*)

3 June 2015; accepted 3 March 2016
10.1126/science.aac6397

REPORTS

MOLECULAR MAGNETISM

Magnetic remanence in single atoms

F. Donati,[1] S. Rusponi,[1] S. Stepanow,[2] C. Wäckerlin,[1] A. Singha,[1] L. Persichetti,[2] R. Baltic,[1] K. Diller,[1] F. Patthey,[1] E. Fernandes,[1] J. Dreiser,[1,3] Ž. Šljivančanin,[4,5] K. Kummer,[6] C. Nistor,[2] P. Gambardella,[2]* H. Brune[1]*

A permanent magnet retains a substantial fraction of its saturation magnetization in the absence of an external magnetic field. Realizing magnetic remanence in a single atom allows for storing and processing information in the smallest unit of matter. We show that individual holmium (Ho) atoms adsorbed on ultrathin MgO(100) layers on Ag(100) exhibit magnetic remanence up to a temperature of 30 kelvin and a relaxation time of 1500 seconds at 10 kelvin. This extraordinary stability is achieved by the realization of a symmetry-protected magnetic ground state and by decoupling the Ho spin from the underlying metal by a tunnel barrier.

The search for the ultimate size limit of magnetic information storage, and the aim of exploring magnetic quantum properties for information processing, have driven fundamental research toward atomic-scale structures that contain fewer and fewer atoms. Benchmarks for such systems are long magnetic relaxation times, i.e., magnetic quantum states that are stable on the time scales required for storage or quantum computation. Single-molecule magnets (*1–6*) are promising candidates as they are chemically robust in ambient conditions and exhibit magnetic bistability at cryogenic temperatures, with a record relaxation time of 100 s at 13.9 K for N_2^{3-} radical-bridged dilanthanide complexes in the bulk phase (*6*). Further reducing the number of constituent atoms in such systems, however, implies removing the organic ligands, thereby bringing the magnetic core in direct contact with a surface. Presently, the smallest magnets are antiferromagnetic Fe_{12} double chains (*7*) and ferromagnetic Fe_5 clusters (*8*) supported on nonmagnetic surfaces. Both exhibit lifetimes of hours below 0.5 K, while supported nanostructures of smaller size retain their magnetic orientation only on a time scale of seconds (*9*, *10*).

Ultimately, the smallest size of a magnet can be reached with a single surface-adsorbed atom. The magnetism of single atoms has become the subject of intense research (*11–17*) since the discovery of a giant magnetic anisotropy for Co atoms adsorbed onto a Pt(111) surface (*18*). However, despite the high magnetic anisotropy originating from the extremely low coordination, all adatom-surface combinations investigated so far are paramagnetic down to 0.3 K, with the longest achieved magnetic lifetime being 230 μs at 0.6 K (*16*, *17*). Thus, in addition to anisotropy, the magnetic states of a quantum magnet need to be protected from quantum tunneling of the magnetization as well as from scattering with electrons and phonons of the substrate. The first condition requires a degenerate ground state doublet with a projected total angular momentum J_z that is protected from mixing with other states by the symmetry of the adsorption sites' ligand field (*19*, *20*). The second requires decoupling the magnetic atom from the phonon and conduction electron baths.

Here, we investigated ensembles of rare-earth atoms, whose spin and orbital moments originate from the strongly localized 4f orbitals and interact weakly with the surrounding environment. Additional decoupling is ensured by choosing an insulating substrate with low phonon density of states, such as MgO. We found that Ho atoms deposited on MgO(100) thin films grown on a Ag(100) surface formed single-atom magnets with a relaxation time that depended on the MgO thickness. Not only did the Ho atoms show magnetic bistability, they also had exceptionally large coercive field and showed magnetic hysteresis up to 30 K, a temperature substantially higher than the blocking temperature of single-molecule magnets on comparable time scales. These exceptional properties originate from a combination of factors—namely, the specific mixing of odd J_z states of Ho in the C_{4v} symmetric ligand field of MgO(100), which protects the magnetization from reversal by tunneling and first-order electron scattering at zero and finite fields, and the weak coupling to the electronic and vibrational degrees of freedom of the substrate, provided by the stiff and insulating MgO buffer layer.

We created a quasi-monodisperse ensemble of individual Ho atoms adsorbed on ultrathin MgO(100) films grown on Ag(100) by depositing minute amounts of Ho at a sample temperature below 10 K, which ensured that the thermal mobility of the adatoms was blocked. Low-temperature scanning tunneling microscopy (STM) images

[1]Institute of Physics, Ecole Polytechnique Fédérale de Lausanne (EPFL), Station 3, CH-1015 Lausanne, Switzerland. [2]Department of Materials, ETH Zürich, Hönggerbergring 64, CH-8093 Zürich, Switzerland. [3]Swiss Light Source, Paul Scherrer Institute, CH-5232 Villigen PSI, Switzerland. [4]Vinča Institute of Nuclear Sciences (020), Post Office Box 522, 11001 Belgrade, Serbia. [5]Texas A&M University at Qatar, Doha, Qatar. [6]European Synchrotron Radiation Facility (ESRF), F-38043 Grenoble, France.
***Corresponding author. E-mail: pietro.gambardella@mat.ethz.ch (P.G.); harald.brune@epfl.ch (H.B.)**

displayed the Ho atoms as localized protrusions with identical apparent heights and widths (Fig. 1A). Ab initio calculations using density functional theory (DFT) in the GGA+U approximation (*21*) identify the O-top as the most favorable adsorption site (Fig. 1B and table S3). Atomic-resolution images of samples with coadsorbed Co or Fe atoms confirmed this assignment (fig. S2). The adatoms were immobile up to 50 K and, therefore, at all temperatures where we characterized their magnetic properties.

X-ray absorption and magnetic circular dichroism spectra (XAS and XMCD) taken at the Ho $M_{4,5}$ edges (3d→4f transitions) with the x-ray beam and magnetic field parallel to the surface normal revealed a pronounced dichroism (Fig. 1D). This magnetic signal indicates the presence of a large localized magnetic moment that aligns along the field direction. Recording the maximum of the XMCD peak as a function of the external field allowed us to measure the magnetization loop of the Ho adatoms. At 6.5 K, we observed a clear hysteresis opening along the out-of-plane direction and a remanent magnetization of 25% of saturation (Fig. 1E). After saturation, the Ho atoms retained their magnetization even in the absence of an external field. In addition, the loop showed a coercive field of 1 T and remains open up to the maximum available field of 8.5 T, indicating a long relaxation time even at extremely high magnetic fields.

This exceptional magnetic stability is related to the symmetry of the Ho quantum states. We identify them by comparing experimental spectra and magnetization curves with multiplet calculations (fig. S6). At zero field, the ground state is a perfectly degenerate doublet. The two states, labeled as $|0\rangle$ and $|1\rangle$, exhibited out-of-plane projections of the total moment $\langle J_z = \pm 4.66\rangle$ (Fig. 1C). This value matches well with the result of the sum rules directly applied to the experimental XAS and XMCD spectra (*22*). In the C_{4v} symmetry of the O adsorption site, this ground state doublet is a superposition of the the quantum states J_z = ±7; ±3; ∓1; and ∓5, with the first two contributing the most (table S2). Thus, it is protected from first-order spin excitations (Δm = 0, ±1) at any external magnetic field (*20*), which prevents magnetization reversal by electron scattering. In addition, the very low density of vibrational modes in the MgO layer (fig. S9) strongly suppresses first-order scattering with phonons (Δm = ±1, ±2). The absence of Ho-MgO vibrational modes in the region of hyperfine level crossing can further slow down relaxation at low fields, as observed for $TbPc_2$ molecules grafted on suspended nanotubes (*23*). Thus, the combination of magnetic ground state, symmetry of the adsorption site, and decoupling from the metal substrate guarantees protection against all first-order scattering and ultimately allows for long magnetic lifetimes.

The first excited state $|2\rangle$ is a $\langle J_z = 0\rangle$ singlet lying 4.5 meV above the ground state. This energy separation is sufficient to prevent electronic level crossings up to more than 10 T (Fig. 1C), hence the absence of quantum tunneling steps in the hysteresis loop (*3*). Further excited states lie at a higher energy and played no role at the temperatures and magnetic fields used here.

To access the magnetic lifetime, we first initialized the ensemble of Ho atoms in the $|0\rangle$ state by applying an external field B = +6.8 T until saturation was reached. We then swept the magnetic field to near zero (B = 0.01 T) and recorded the time needed for the magnetization of the ensemble to vanish—namely, to reach equal occupation of the $|0\rangle$ and $|1\rangle$ states (Fig. 2A). At a temperature of 10 K, we found an exponential decrease in the XMCD signal with a characteristic lifetime of τ = 1586 ± 131 s (Fig. 2C). Notably, we observed comparable magnetic lifetimes down to 2.5 K (fig. S4A), implying that below 10 K, the magnetic relaxation is essentially driven by nonthermal processes.

Measurements at different photon fluxes revealed that the lifetime of Ho atoms is mostly limited by the secondary electron cascade generated by the absorbed photons. The scattering with these hot electrons reduces the magnetic lifetime, as recently reported for endofullerene single-molecule magnets (*24*). The measured lifetimes hence represent a lower bound to the intrinsic magnetic lifetimes. Extrapolation to the zero-flux limit suggests intrinsic lifetimes of the order of 1 hour at 2.5 K (fig. S4B). Increasing the temperature to 20 K activates thermal relaxation processes and results in a slightly decreased magnetic lifetime of 675 ± 77 s (Fig. 2C). The lifetime of the Ho atoms on MgO is much longer than for Ho

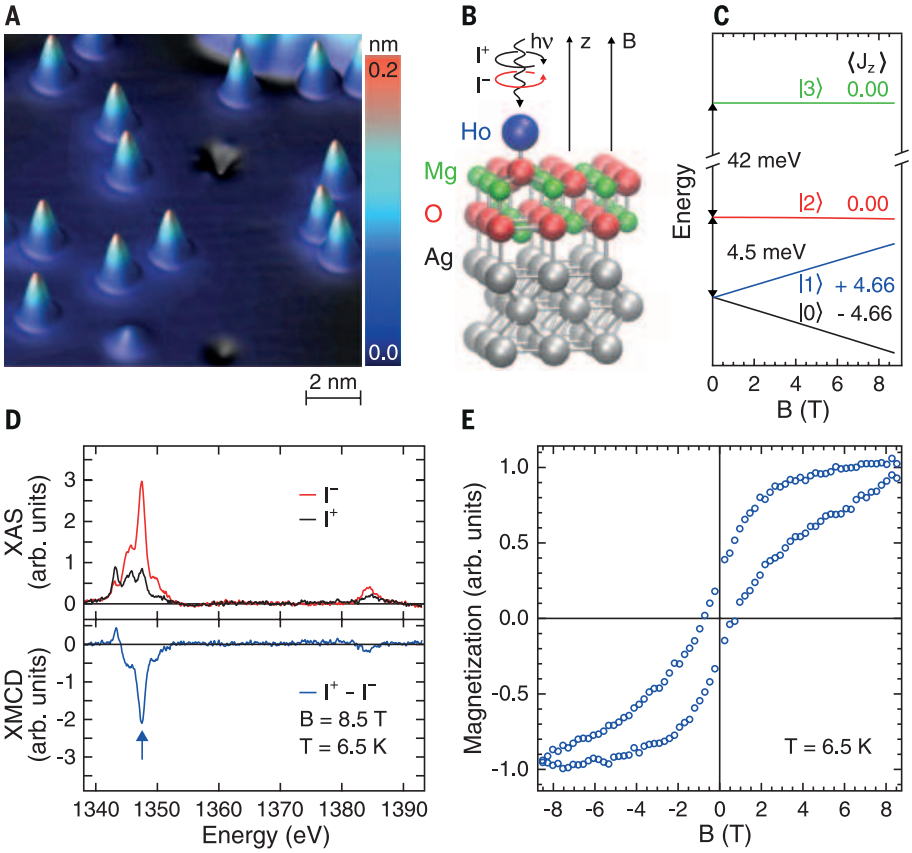

Fig. 1. Ho atoms on MgO films. (**A**) Constant-current STM image of Ho atoms on 2 monolayer (ML) MgO/Ag(100) (tunnel voltage V_t = 100 mV, tunnel current I_t = 20 pA, T = 4.7 K, Ho coverage Θ_{Ho} = 0.005 ± 0.001 ML). (**B**) Adsorption geometry of Ho atoms on top of O on 2-ML MgO/Ag(100) as simulated with DFT, together with a schematic of the XAS experiment. (**C**) Splitting of the lowest quantum levels of Ho atoms from multiplet calculations. Zero-field values of $\langle J_z\rangle$ are reported. (**D**) XAS and XMCD at the $M_{4,5}$ edges for an ensemble of individual Ho adatoms. The arrow points to the maximum of the XMCD signal that is recorded as a function of magnetic field to obtain the magnetization curves shown in (**E**) (field sweep rate *dB/dt*) = 8 mT/s, photon flux $\phi = 1 \times 10^{-2}$ nm^{-2} s^{-1}, T = 6.5 K, Θ_{Ho} = 0.01 ML, MgO coverage Θ_{MgO} = 7.0 ML).

ions in $HoPc_2$ (*25*) and Ho-doped bulk crystals (*26*), possibly because of the larger level splitting and the smaller number of vibration modes allowed for atoms adsorbed on surfaces.

We further characterized the magnetic lifetime at a large magnetic field. We prepared the ensemble in the $|1\rangle$ state at $B = -6.8$ T and measured the time needed to fully reverse to the $|0\rangle$ state at $B = +6.8$ T and $T = 10$ K (Fig. 2B). We observed an exponential increase in the magnetization up to saturation with $\tau_{rev} = 1223 \pm 69$ s (Fig. 2D). Thus, the Ho atoms on MgO retained their long lifetimes even at a very high field where single-molecule magnets typically exhibit faster relaxations because of level crossing, quantum tunneling of the magnetization, or scattering with phonons (*1–5*).

To probe the temperature dependence of the remanence and of the coercive field of Ho atoms, we recorded hysteresis loops in the most favorable experimental conditions, i.e., using the fastest field sweep rate dB/dt and lowest photon flux achievable (Fig. 3A). Under these conditions, the hysteresis opening at 10 K (Fig. 3B) was even wider than the one in Fig. 1E, showing a coercive field of 3.7 ± 0.3 T and a remanent magnetization of 50% of saturation. In addition, the hysteresis remained open up to 30 K, and only at 40 K was the magnetization loop essentially closed (Fig. 3C). These results further show that the magnetic quantum states of Ho atoms were notably protected against scattering with Ag conduction electrons and MgO phonons.

Although the Ho ground state was protected against magnetization reversal via first-order electron-spin excitations, it is possible, in principle, to reverse the magnetization via direct scattering with phonons or by two-electron or -phonon transitions through the first excited state. The reversal processes that are triggered by the scattering with conduction electrons and with the soft phonon modes of the underlying metal are expected to critically depend on the thickness of the MgO layer. Accordingly, we observed that the hysteresis loops of Ho atoms became narrower when the thickness of

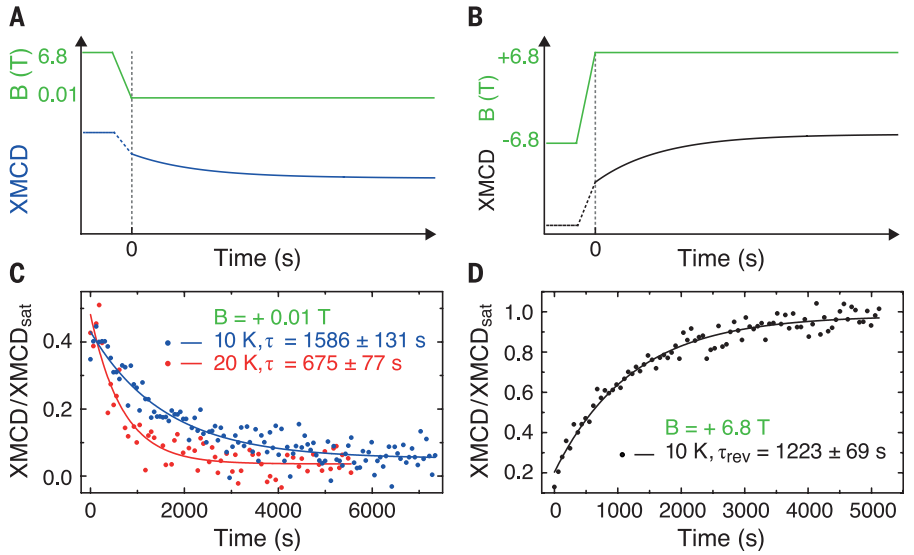

Fig. 2. Magnetization lifetime. (**A** and **B**) Scheme of the measurements. After saturation at $|B_{max}| = 6.8$T, the field was swept to the indicated values. Measurements of XMCD started at the end of the sweep. (**C** and **D**) Time evolution of the maximum XMCD intensity (dots) normalized to the saturation value at $B = +6.8$ T ($\Theta_{Ho} = 0.015$ ML, $\Theta_{MgO} = 6.0$ ML, $\phi = 0.14 \times 10^{-2}$ nm^{-2} s^{-1}, $dB/dt = 33$ mT/s). Exponential fits (solid lines) give the magnetic lifetime τ and reversal time τ_{rev} of the Ho atoms.

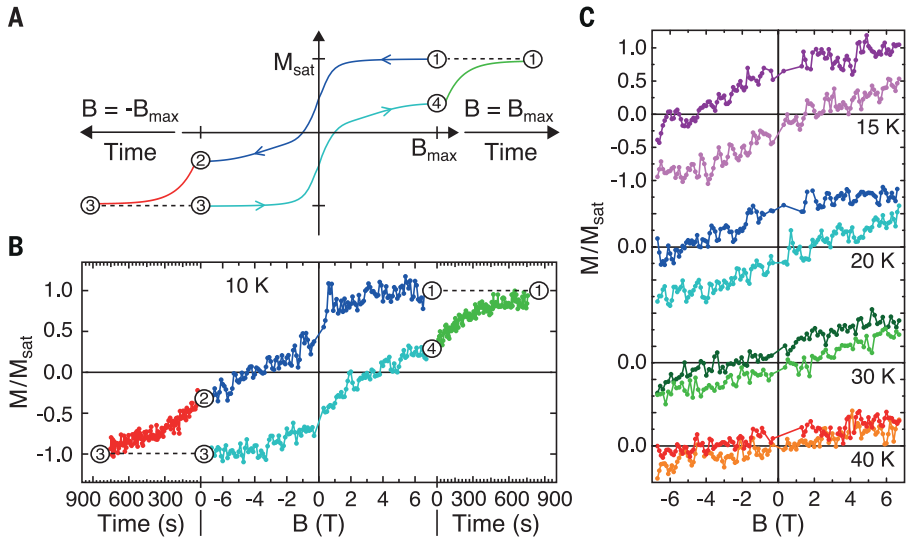

Fig. 3. Magnetic hysteresis at increasing temperatures. (**A**) Scheme for the hysteresis measurements at a fast sweep rate of the magnetic field. We first kept the magnetic field at $+B_{max}$ for sufficient time to reach $+M_{sat}$ (*1*), then measured M while sweeping the field to $-B_{max}$ (*2*). This fast sweep leaves the system out of equilibrium at B_{max}. Thus, we allow the system to relax at constant $B = -B_{max}$ until equilibrium is reached (*3*) before starting the new branch of the loop (3-4-1). (**B**) Hysteresis loop recorded at $T = 10$ K following the scheme described in (A). (**C**) Evolution of the hysteresis loop with the temperature (dark, downsweep; light, upsweep). The relaxation part is not shown ($\Theta_{Ho} = 0.01$ ML, $\Theta_{MgO} = 4.3$ ML, $\phi = 0.55 \times 10^{-2}$ nm^{-2} s^{-1}, $dB/dt = 33$ mT/s).

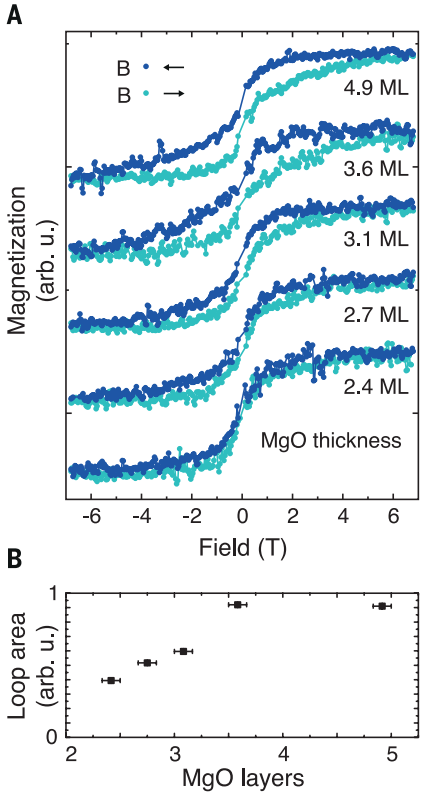

Fig. 4. Effect of the MgO layer thickness. (**A**) Magnetization loops acquired on Ho atoms on MgO films of various thicknesses as indicated close to each loop ($T = 2.5$ K, $dB/dt = 12$ mT/s, $\phi = 2.15 \times 10^{-2}$ nm^{-2} s^{-1}, $\Theta_{Ho} = 0.005$ to 0.010 ML). The curves were rescaled to the corresponding saturation value at $B = +6.8$ T. The reduced loop opening compared to that in Figs. 1 and 3 is a consequence of the higher photon flux and the lower sweep rate used here. (**B**) Loop area as a function of MgO thickness, reaching a constant value at 3.6 ML.

the MgO film was reduced below 3.6 monolayers (ML) and were almost closed for a thickness of 2.4 ML (Fig. 4). We observed essentially no variation in the XAS and XMCD spectra of Ho atoms with the number of MgO layers (fig. S5), hence the Ho ground state was unaffected by the MgO thickness. Thus, protection against first-order reversal is a necessary but not a sufficient condition to prevent magnetization reversal. To obtain long magnetic lifetimes in single atoms, an efficient decoupling from the electron and phonon bath is also required to ultimately suppress higher-order scattering processes that cannot be eliminated by symmetry. This result also suggests that long spin lifetimes are unlikely for single atoms in direct contact with a metal substrate.

The need of a decoupling layer to obtain long lifetimes is in stark contrast with the interpretation of STM experiments on Ho atoms on Pt(111), which reported telegraph noise in the differential conductance with characteristic times of up to 700 s at T = 0.7 K and zero field (*19*). This signal was interpreted as magnetic bistability and ascribed to a J_z = 8 ground state, as calculated by DFT, which would be protected by the C_{3v} symmetry of the adsorption site. However, XMCD measurements revealed that Ho atoms on Pt(111) have a ground state J_z = 6 that is incompatible with long spin lifetimes in a C_{3v}-symmetric crystal field (*27*). In addition, the magnetization curves at 2.5 K are fully reversible. According to these XMCD results, Ho/Pt(111) is a perfect paramagnet, as are all the other single atoms on surfaces previously reported. Moreover, subsequent STM experiments on the same system could reproduce neither telegraph noise nor spin excitations (*10*). Together with further STM observations on other 4f elements (*28*), this questions the interpretation of the results reported in (*19*) as magnetic bistability of Ho/Pt(111).

The relative simplicity of the Ho/MgO system, based on common physical deposition methods, as well as the planar geometry of the system opens the possibility of probing and manipulating the Ho spin and its environment in a controlled way. Using MgO as a decoupling layer could improve the magnetic stability not only of individual atoms but also of surface-supported molecular magnets, paving the road to scalable and robust nanoscale spintronic devices.

REFERENCES AND NOTES

1. R. Sessoli, D. Gatteschi, A. Caneschi, M. A. Novak, *Nature* **365**, 141–143 (1993).
2. N. Ishikawa, M. Sugita, T. Ishikawa, S. Y. Koshihara, Y. Kaizu, *J. Am. Chem. Soc.* **125**, 8694–8695 (2003).
3. M. Mannini *et al.*, *Nature* **468**, 417–421 (2010).
4. J. M. Zadrozny *et al.*, *Nat. Chem.* **5**, 577–581 (2013).
5. L. Ungur, J. J. Le Roy, I. Korobkov, M. Murugesu, L. F. Chibotaru, *Angew. Chem. Int. Ed.* **53**, 4413–4417 (2014).
6. J. D. Rinehart, M. Fang, W. J. Evans, J. R. Long, *J. Am. Chem. Soc.* **133**, 14236–14239 (2011).
7. S. Loth, S. Baumann, C. P. Lutz, D. M. Eigler, A. J. Heinrich, *Science* **335**, 196–199 (2012).
8. A. A. Khajetoorians *et al.*, *Science* **339**, 55–59 (2013).
9. S. Yan, D.-J. Choi, J. A. J. Burgess, S. Rolf-Pissarczyk, S. Loth, *Nat. Nanotechnol.* **10**, 40–45 (2015).
10. M. Steinbrecher *et al.*, *Nat. Commun.* **7**, 10454 (2016).
11. C. F. Hirjibehedin *et al.*, *Science* **317**, 1199–1203 (2007).
12. F. Meier, L. Zhou, J. Wiebe, R. Wiesendanger, *Science* **320**, 82–86 (2008).
13. H. Brune, P. Gambardella, *Surf. Sci.* **603**, 1812–1830 (2009).
14. A. A. Khajetoorians *et al.*, *Phys. Rev. Lett.* **106**, 037205 (2011).
15. F. Donati *et al.*, *Phys. Rev. Lett.* **111**, 236801 (2013).
16. I. G. Rau *et al.*, *Science* **344**, 988–992 (2014).
17. S. Baumann *et al.*, *Science* **350**, 417–420 (2015).
18. P. Gambardella *et al.*, *Science* **300**, 1130–1133 (2003).
19. T. Miyamachi *et al.*, *Nature* **503**, 242–246 (2013).
20. C. Hübner, B. Baxevanis, A. A. Khajetoorians, D. Pfannkuche, *Phys. Rev. B* **90**, 155134 (2014).
21. P. Blaha, K. Schwarz, G. Madsen, D. Kvasnicka, J. Luitz, WIEN2k: An Augmented Plane Wave plus Local Orbitals Program for Calculating Crystal Properties (Karlheinz Schwarz, Techn. Universitat Wien, Austria, 2001).
22. Supplementary materials are available on *Science* Online.
23. M. Ganzhorn, S. Klyatskaya, M. Ruben, W. Wernsdorfer, *Nat. Nanotechnol.* **8**, 165–169 (2013).
24. J. Dreiser *et al.*, *Appl. Phys. Lett.* **105**, 032411 (2014).
25. N. Ishikawa, M. Sugita, W. Wernsdorfer, *J. Am. Chem. Soc.* **127**, 3650–3651 (2005).
26. R. Giraud, W. Wernsdorfer, A. M. Tkachuk, D. Mailly, B. Barbara, *Phys. Rev. Lett.* **87**, 057203 (2001).
27. F. Donati *et al.*, *Phys. Rev. Lett.* **113**, 237201 (2014).
28. D. Coffey *et al.*, *Sci. Rep.* **5**, 13709 (2015).

ACKNOWLEDGMENTS

Funding from the Swiss National Science Foundation (grants 200021-153404, 200020-157081, 200021-146715, PZ00P2 142474, and IZ73Z0-152406) and the Swiss Competence Centre for Materials Science and Technology (CCMX) is gratefully acknowledged. L.P. was supported by an ETH Postdoctoral Fellowship (FEL-42 13-2). K.D. acknowledges support from the "EPFL Fellows" fellowship program cofunded by Marie Curie, FP7 grant agreement no. 291771. Z.S. was supported by the Serbian Ministry of Education and Science under grants ON171033 and ON171017. The DFT calculations were performed at the PARADOX-IV supercomputer at the Scientific Computing Laboratory (SCL) of the Institute of Physics Belgrade. The XMCD experiments were performed at the EPFL-PSI X-Treme beamline of the Swiss Light Source (SLS) and the ID32 beamline of the European Synchrotron Radiation Facility (ESRF). The authors declare that they have no competing financial interests.

SUPPLEMENTARY MATERIALS

www.sciencemag.org/content/352/6283/318/suppl/DC1
Materials and Methods
Figs. S1 to S9
Tables S1 to S3
References (*29–56*)

4 December 2015; accepted 8 March 2016
10.1126/science.aad9898

HYDROGEN BONDING

Nuclear quantum effects of hydrogen bonds probed by tip-enhanced inelastic electron tunneling

Jing Guo,[1]* Jing-Tao Lü,[2]* Yexin Feng,[1,3]* Ji Chen,[1] Jinbo Peng,[1] Zeren Lin,[1] Xiangzhi Meng,[1] Zhichang Wang,[1] Xin-Zheng Li,[4,5]† En-Ge Wang,[1,5]† Ying Jiang[1,5]†

We report the quantitative assessment of nuclear quantum effects on the strength of a single hydrogen bond formed at a water-salt interface, using tip-enhanced inelastic electron tunneling spectroscopy based on a scanning tunneling microscope. The inelastic scattering cross section was resonantly enhanced by "gating" the frontier orbitals of water via a chlorine-terminated tip, so the hydrogen-bonding strength can be determined with high accuracy from the red shift in the oxygen-hydrogen stretching frequency of water. Isotopic substitution experiments combined with quantum simulations reveal that the anharmonic quantum fluctuations of hydrogen nuclei weaken the weak hydrogen bonds and strengthen the relatively strong ones. However, this trend can be completely reversed when a hydrogen bond is strongly coupled to the polar atomic sites of the surface.

In terms of tunneling and zero-point motion, nuclear quantum effects (NQEs) play important roles in the structure, dynamics, and macroscopic properties of hydrogen-bonded (H-bonded) materials (*1–5*). Despite enormous theoretical efforts toward pursuing proper treatment of the nuclear motion at a quantum mechanical level (*5–9*), accurate and quantitative description of NQEs on the H-bonding interaction has proven to be experimentally challenging. Conventional methods for probing the NQEs are based on spectroscopic or diffraction techniques (*4*, *10–14*). However, those techniques have poor spatial resolution and only measure the average properties of many H bonds, which are susceptible to structural inhomogeneity and local environments. The spatial variation and interbond coupling of H bonds lead to spectral broadening that may easily smear out the subtle details of NQEs.

[1]International Center for Quantum Materials, School of Physics, Peking University, Beijing 100871, P. R. China. [2]School of Physics and Wuhan National High Magnetic Field Center, Huazhong University of Science and Technology, Wuhan 430074, P. R. China. [3]School of Physics and Electronics, Hunan University, Changsha 410082, P. R. China. [4]School of Physics, Peking University, Beijing 100871, P. R. China. [5]Collaborative Innovation Center of Quantum Matter, Beijing 100871, P. R. China.
*These authors contributed equally to this work. **†Corresponding author. E-mail: xzli@pku.edu.cn (X.-Z.L.); egwang@pku.edu.cn (E.-G.W.); yjiang@pku.edu.cn (Y.J.)**

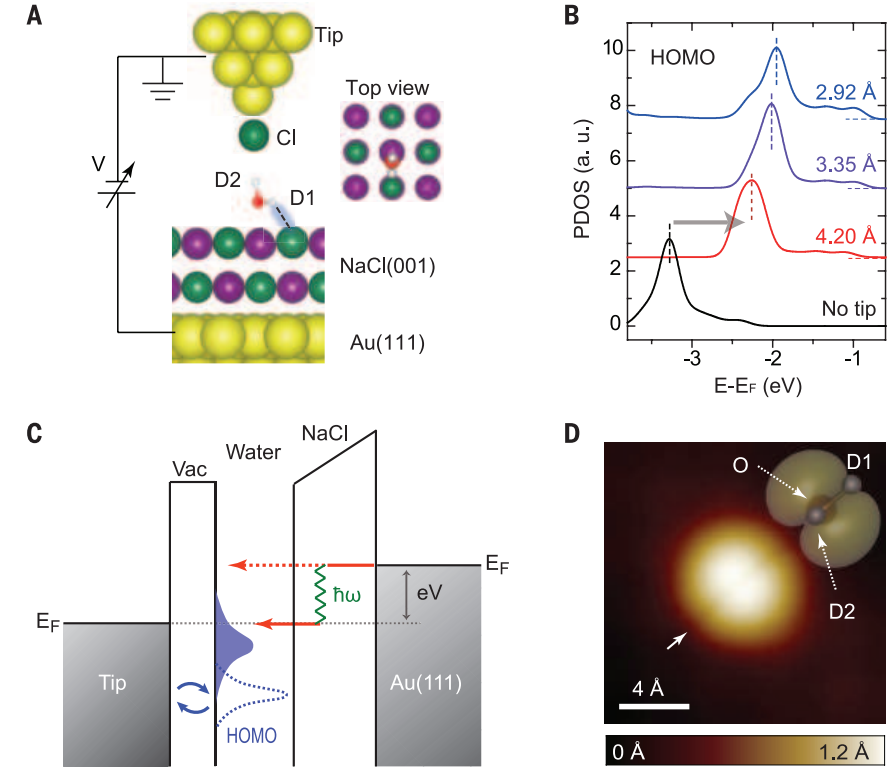

Fig. 1. Experimental setup and orbital gating. (**A**) Schematic of the experimental setup. One OD bond (D2) of the D_2O monomer is free and the other (D1) forms a H bond with Cl^- of NaCl (denoted by a dashed line). O, D, Au, Cl^-, and Na^+ are denoted by red, white, golden, green, and purple spheres, respectively. (**B**) Calculated HOMO states of the water molecule at different tip heights. Dashed lines denote the peak positions of the HOMO states; the arrow indicates the gating of the HOMO toward the Fermi level by the STM tip. *E*, energy; E_F, Fermi level; PDOS, projected density of states; a.u., arbitrary units. (**C**) Schematic of the tip-enhanced IET process. The tip-water coupling "gates" HOMO to the proximity of E_F, thus resonantly enhancing the cross section of the IET process. Vac, vacuum; $\hbar$, Planck's constant divided by 2π; ω; vibrational angular frequency. (**D**) STM topography of a D_2O monomer (V = 100 mV, I = 50 pA). The inset shows the calculated isosurface of charge density of the HOMO.

One promising technique to overcome these challenges is inelastic electron tunneling spectroscopy (IETS) based on a scanning tunneling microscope (STM), which combines sub-ångström spatial resolution and single-bond vibrational sensitivity (*15–18*). In a conventional IETS regime, the electron-vibration coupling is only a weak perturbation on the elastic scattering picture, leading to a very small cross section for vibrational excitation and extraordinarily weak IET signals (*19*, *20*). This limitation particularly affects closed-shell molecules such as water, whose frontier orbitals are located far away from the Fermi level (E_F) (*21*). Thus, it has been very difficult to obtain reliable vibrational spectroscopy of water with conventional IETS. To this end, we developed a tip-enhanced IETS technique to achieve a sufficiently high signal-to-noise ratio for water, which allowed us to quantitatively reveal the quantum component of the H bonds and the important role of the local environment in dictating the NQEs.

The STM-IETS experiments were performed on water monomers adsorbed on a Au-supported NaCl(001) bilayer (*22*) (fig. S1). The water is adsorbed on top of a Na^+ site in a "standing" configuration (*23*). One OD bond (D2) of a D_2O molecule dangles upward, and the other (D1) forms a H bond with the Cl^- of the NaCl surface (Fig. 1A). To enhance the IETS signals, we used a Cl-terminated STM tip to "gate" the highest occupied molecular orbital (HOMO) of water to the proximity of E_F via tuning tip-water coupling (Fig. 1B). Orbital gating with the Cl tip was highly selective and much more effective than gating with the bare tip, owing to the stronger coupling of the HOMO with the Cl p_z orbital (fig. S4). In such a near-resonance case, the HOMO is strongly coupled to the molecular

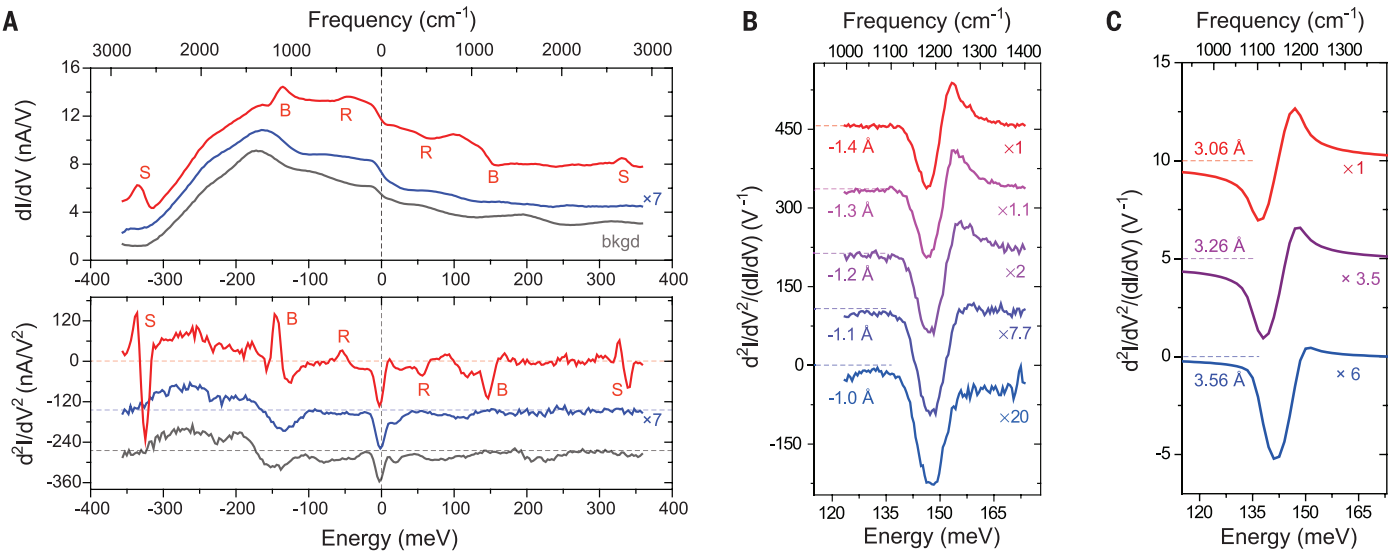

Fig. 2. Tip-enhanced IETS of a D_2O monomer. (**A**) dI/dV and d^2I/dV^2 spectra taken at different tip heights. Red (–1.2 Å) and blue (–0.4 Å) curves were taken on the D_2O monomer. Gray curves (–1.2 Å) were acquired on the NaCl surface (denoted as "bkgd"). The vibrational IET features are denoted as "R" (rotational), "B" (bending), and "S" (stretching). Dashed horizontal lines represent zero levels of the *y* axes for each curve. (**B** and **C**) Experimental (B) and calculated (C) d^2I/dV^2 spectra (normalized by dI/dV) of the bending mode as a function of tip height. For clarity, each curve is scaled properly to ensure the same magnitude. All tip heights in the experiment are referenced to the gap set with V = 100 mV and I = 50 pA. The tip height in (C) is defined in fig. S2.

vibrational modes ($\hbar\omega$, where $\hbar$ is Planck's constant h divided by 2π and ω is the vibrational angular frequency), resulting in a resonantly enhanced IET process (Fig. 1C) (*24–26*). The STM topography of the D_2O monomer near the zero bias exhibited a HOMO-like double-lobe structure with a nodal plane in between the lobes (Fig. 1D and fig. S4).

For typical tip-enhanced IETS of the D_2O monomer (Fig. 2A), the Cl tip was positioned slightly away from the nodal plane of the molecule (fig. S5). At a large tip-water separation, the spectra were featureless (blue), simply following the background (gray). Once the tip-water separation was decreased by ~0.8 Å (red), additional kinks arose in the dI/dV spectrum (I, current; V, voltage). In the corresponding d^2I/dV^2 curve, these kink features are further magnified as prominent peaks and dips that are point-symmetric with respect to the zero bias. Comparison with density functional theory (DFT) calculations allowed us to assign the spectral features ("R," "B," and "S") to the frustrated rotational, bending, and stretching modes, respectively (fig. S6).

High-resolution d^2I/dV^2 spectra of the bending mode (B) (Fig. 2B) show that as the tip height decreased, the normalized IETS intensity was enhanced by more than one order of magnitude, and the line shape changed from a symmetric dip to an asymmetric Fano-shaped feature (*25*). Such behavior was well reproduced by DFT-based transport calculations (Fig. 2C) (*22*), which revealed that the drastic increase of the spectral intensity mainly arose from the enhancement of the HOMO states near the bias window of IETS, whereas the symmetric-to-asymmetric line shape change arose from the competition between two high-order elastic channels controlled by the tip-water coupling (fig. S7). The resonantly enhanced IETS had a very high signal-to-noise ratio (up to 30% in relative conductance change), which is crucial for precisely determining the H-bonding strength.

The frequency shift of the stretching mode (S) is very sensitive to H-bonding strength (*27*, *28*). The adsorbed D_2O has two distinct S modes (denoted as D1 and D2 in Fig. 3A). The energy of D2 nearly coincides with that of the free OD stretching and thus should arise from the upright dangling OD bond (Fig. 1A). We attributed the other mode (D1), which was considerably red-shifted, to the downward OD H-bonded with the NaCl surface. For H_2O, only the red-shifted mode (H1) could be observed; the higher mode (H2) was too weak to produce any detectable signal (Fig. 3A). The spectral intensity of D2 was also much smaller than that of D1. Such a difference can be explained by considering the propensity rules (fig. S8) (*29*, *30*).

Notably, we could continuously modify the H-bonding strength by adjusting the tip height. As the tip height decreased, the water molecule was pushed closer to the substrate by the Pauli repulsion force, which led to a strengthening of the O–D···Cl H bond (fig. S9). Accordingly, the two-dimensional (2D) color map of our IETS results shows that both D1 and D2 shifted to lower energies as the tip height decreased (Fig. 3B). The D2 mode almost vanished around –1.36 Å (marked by two arrows), where the D1 mode underwent a symmetric-to-asymmetric line shape change. The red shifts of the D1 and D2 modes were independent of the bias polarity, thus excluding the origin of the electric field effect. Note that Chiang *et al.* recently observed the vibrational frequency shift of a CO molecule in the STM junction that was not the result of H-bond formation (*31*).

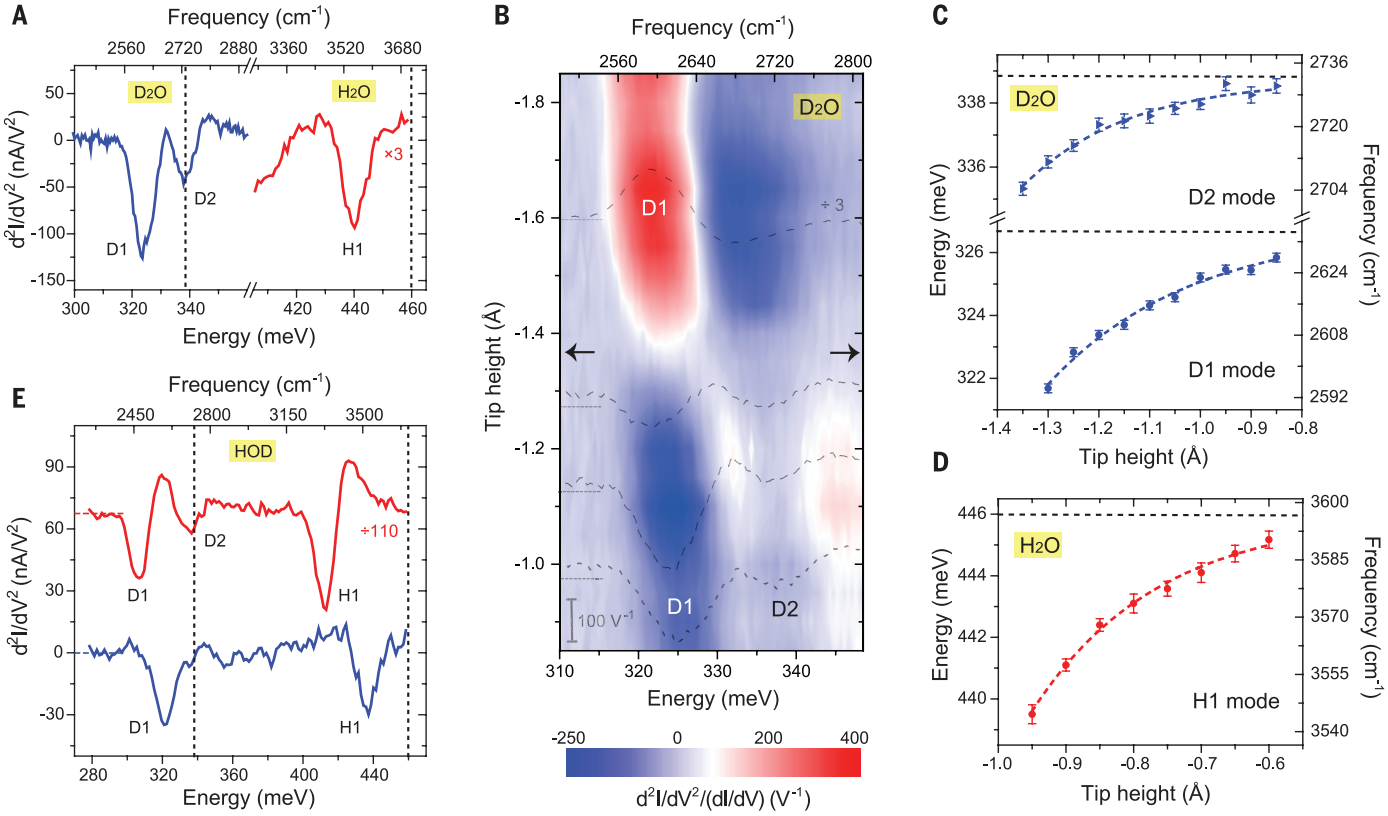

Fig. 3. Tuning the H-bonding strength with the Cl tip. (**A**) High-resolution IETS of D_2O (blue: –1 Å) and H_2O (red: –0.9 Å) monomers, focusing on the stretching modes (marked as D1, D2, and H1). Vertical dashed lines denote the vibrational energies of the free OD and OH stretching modes. (**B**) Two-dimensional (2D) IETS color map of the D_2O monomer as a function of tip height. Four representative IET spectra (dashed curves) at different tip heights are superimposed onto the map. Arrows denote the tip height of –1.36 Å, where the D2 mode nearly vanished and the D1 mode underwent a change in line shape from symmetric to asymmetric. (**C** and **D**) Energies of the D1, D2, and H1 modes as a function of tip height. Each data set can be nicely fitted to an inversed exponential decay. Horizontal dashed lines represent the asymptotic lines of those curves when extrapolated to infinite tip height. Error bars reflect the fitting error and the accuracy of the bias channel (~0.1 meV). (**E**) High-resolution IETS of a HOD monomer (blue: –1.4 Å, red: –2.3 Å).

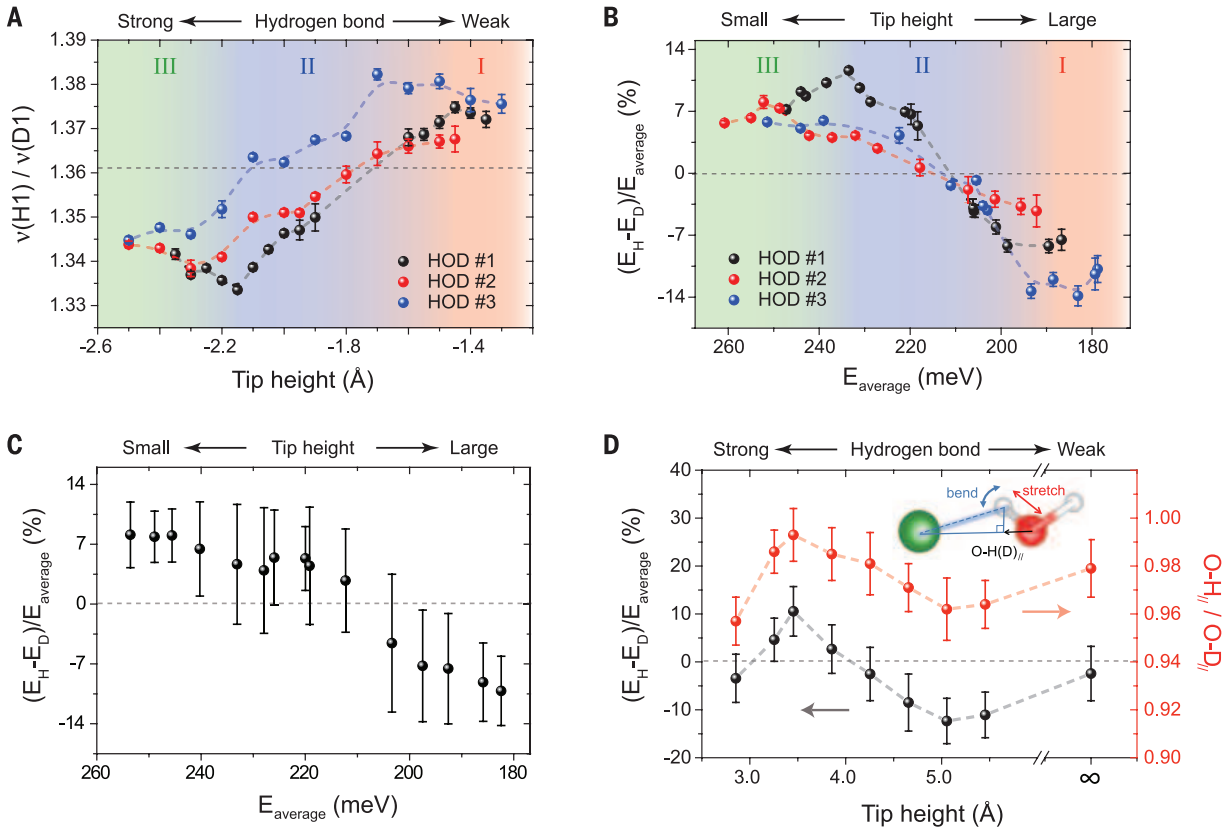

Fig. 4. Nuclear quantum effects on H-bonding strength of HOD monomers. (**A**) Ratio between the frequency (ν) of H1 and D1 as a function of tip height for three different HOD monomers. The ratio (1.361) between the frequency of the free OH and OD stretching modes is denoted by a horizontal dashed line. (**B**) Relative difference between H-bond energies of O–H···Cl (E_H) and O–D···Cl (E_D) as a function of their average [$E_{average} = (E_H + E_D)/2$]. Error bars in (A) and (B) were calculated by the uncertainty propagation formula from the errors of the D1 and H1 modes. (**C**) Same as (B), but the data were averaged for seven different HOD monomers. Error bars in (C) reflect the standard error. (**D**) Calculated H-bonding energy change upon isotope substitution (black) and the ratio between averaged projection of O–H and O–D covalent bonds along the intermolecular axis (red) as a function of tip height. The tip height is defined in fig. S2. The inset illustrates the geometry used for projecting the O–H(D) bond onto the intermolecular axis [O-H(D)$_{//}$]. Error bars in (D) reflect the statistical error in the PIMD simulations.

In Fig. 3, C and D, we plot the energies of the D1, D2, and H1 modes as a function of tip height, which can be fitted to inversed exponential decays (*22*). Extrapolating these curves to infinite tip height eliminated the influence of the STM tip. The resulting energy of D2 (338.7 ± 0.3 meV) is ~1 meV greater than that of the free OD stretching mode (338 meV). Such a blue shift may arise from the vibrational coupling between the D1 and D2 transition dipoles (fig. S6) (*32*). To minimize the contribution of vibrational coupling to the frequency shift, we switched to HOD monomers, in which OH and OD stretching are completely decoupled because of the large energy mismatch. Surprisingly, the OD and OH stretching modes were both red-shifted (blue curve in Fig. 3E), which suggests that they are both H-bonded. Upon decreasing the tip height, the free OD stretching mode (D2) emerged and coexisted with D1 (red). Thus, the HOD monomer must be rapidly flipping on the surface such that OH and OD form H bonds alternatively with the substrate (fig. S10).

This finding provides a rare opportunity to accurately quantify the NQEs on H-bonding strength by comparing the D1 and H1 modes in the same molecule. Figure 4A shows the ratio between the frequency of H1 and D1 (fig. S11) as a function of STM tip height for three different HOD monomers. As the tip approached the water molecule, this ratio decreased as a general trend. But at both large and small tip heights, distinct reversal behaviors appear (regions I and III). These curves differ from each other well beyond the experimental errors, which may arise from the influence of local environments created by the different condition of the tips and the inhomogeneity of the surface resulting from the Au substrate (fig. S1). In region II, these curves cross over the ratio of the free HOD monomer (1.361) (*33*), which is a clear indicator that NQEs affect the H-bonding interaction when isotope substitution occurs. We found that Stark shifts of the D1 and H1 modes are negligible because their dipole moments are almost orthogonal to the electric field of the STM tip (*34*).

To extract the impact of NQEs explicitly, we used an empirical relation to convert the red shifts of D1 and H1 into H-bonding energy (*22*, *27*). Figure 4B shows the relative H-bonding energy difference between H and D as a function of their average energies. In general, the NQEs weakened the weak H bonds and strengthened the relatively strong ones, but the impact of NQEs tended to diminish at the weak- and strong-bond limits (regions I and III). Figure 4C shows averaged data for seven different HOD monomers. Although the crossover still occurs, the turning points at both ends are smeared out after averaging. The quantum component of the H bond can account for up to 14% of the bond strength (Fig. 4B), which is much greater than the thermal energy contribution, even at room temperature.

To understand the behavior of NQEs, we carried out ab initio path integral molecular dynamics (PIMD) simulations (Fig. 4D and fig. S12) (*22*). The simulated results (black curve in Fig. 4D) are in excellent agreement with the experimental observations. To explore the physical basis for these changes, we defined a projection of the OH (OD) covalent bond length along the intermolecular axis of the H bonds (inset of Fig. 4D). The zero-point motion of O–H (O–D) stretching increases the projection, whereas that of H-bond bending decreases the projection, due to the anharmonic nature of the potentials. The ratio between the averaged O–H and O–D projections (red curve) correlates well with the bonding energy difference (black curve). A delicate interplay between covalent bond stretching and H-bond bending determines the bonding energy change upon isotope substitution.

The anharmonic quantum fluctuation of the stretching (bending) mode becomes more (less) pronounced as the H bond gets stronger (*9*), which accounts for the observed crossover behavior in region II. However, the reversal behaviors in regions I and III are not predicted by this simple theoretical picture. At the weak-bond limit (region I), the quantum contributions of these two modes both diminish quickly and tend to cancel each other, resulting in the fade-out of the energy difference. The turning point at the strong-bond limit (region III) is closely related to the unusual noncolinear geometry of the O–H···Cl H bond, which arises from the electric repulsive interaction between the H1 (D1) atom and the Na^+ cation of the NaCl surface (fig. S12). Such an interaction modifies the potential profile along the H-bond bending direction as the water molecule approaches the surface, so anharmonic H-bond bending is greatly enhanced and even dominates over O–H stretching, leading to the reversal behavior of NQEs for strong H bonds. This implies that the NQEs of a H bond are extremely sensitive to coupling with the local environment, which is, at present, inaccessible by macroscopic spectroscopic methods. Not only do these findings substantially advance our understanding of the quantum nature of H bonds, they also open up a new route for spectroscopic studies of H-bonded systems at the single-bond level.

REFERENCES AND NOTES

1. N. Greenwood, A. Earnshaw, *Chemistry of the Elements* (Butterworth Heinemann, 1997).
2. A. Hodgson, S. Haq, *Surf. Sci. Rep.* **64**, 381–451 (2009).
3. M. Benoit, D. Marx, M. Parrinello, *Nature* **392**, 258–261 (1998).
4. A. K. Soper, C. J. Benmore, *Phys. Rev. Lett.* **101**, 065502 (2008).
5. F. Paesani, G. A. Voth, *J. Phys. Chem. B* **113**, 5702–5719 (2009).
6. M. E. Tuckerman, D. Marx, M. L. Klein, M. Parrinello, *Science* **275**, 817–820 (1997).
7. G. A. Voth, D. Chandler, W. H. Miller, *J. Chem. Phys.* **91**, 7749–7760 (1989).
8. J. A. Morrone, R. Car, *Phys. Rev. Lett.* **101**, 017801 (2008).
9. X. Z. Li, B. Walker, A. Michaelides, *Proc. Natl. Acad. Sci. U.S.A.* **108**, 6369–6373 (2011).
10. D. F. Brougham, R. Caciuffo, A. J. Horsewill, *Nature* **397**, 241–243 (1999).
11. C. Andreani, D. Colognesi, J. Mayers, G. F. Reiter, R. Senesi, *Adv. Phys.* **54**, 377–469 (2005).
12. A. Pietropaolo *et al.*, *Phys. Rev. Lett.* **100**, 127802 (2008).
13. Y. Harada *et al.*, *Phys. Rev. Lett.* **111**, 193001 (2013).
14. Y. Nagata, R. E. Pool, E. H. G. Backus, M. Bonn, *Phys. Rev. Lett.* **109**, 226101 (2012).
15. B. C. Stipe, M. A. Rezaei, W. Ho, *Science* **280**, 1732–1735 (1998).
16. Y. Kim, T. Komeda, M. Kawai, *Phys. Rev. Lett.* **89**, 126104 (2002).
17. A. J. Heinrich, C. P. Lutz, J. A. Gupta, D. M. Eigler, *Science* **298**, 1381–1387 (2002).
18. H. Gawronski, M. Mehlhorn, K. Morgenstern, *Science* **319**, 930–933 (2008).
19. N. Lorente, M. Persson, *Phys. Rev. Lett.* **85**, 2997–3000 (2000).
20. M. Galperin, M. A. Ratner, A. Nitzan, A. Troisi, *Science* **319**, 1056–1060 (2008).
21. K. Morgenstern, J. Nieminen, *Phys. Rev. Lett.* **88**, 066102 (2002).
22. Supplementary materials are available on *Science* Online.
23. J. Guo *et al.*, *Nat. Mater.* **13**, 184–189 (2014).
24. B. N. J. Persson, A. Baratoff, *Phys. Rev. Lett.* **59**, 339–342 (1987).
25. M. Galperin, M. A. Ratner, A. Nitzan, *J. Chem. Phys.* **121**, 11965–11979 (2004).
26. H. Song *et al.*, *Nature* **462**, 1039–1043 (2009).
27. M. Rozenberg, A. Loewenschuss, Y. Marcus, *Phys. Chem. Chem. Phys.* **2**, 2699–2702 (2000).
28. T. Steiner, *Angew. Chem. Int. Ed.* **41**, 48–76 (2002).
29. N. Lorente, M. Persson, L. J. Lauhon, W. Ho, *Phys. Rev. Lett.* **86**, 2593–2596 (2001).
30. M. Ohara, Y. Kim, S. Yanagisawa, Y. Morikawa, M. Kawai, *Phys. Rev. Lett.* **100**, 136104 (2008).
31. C. L. Chiang, C. Xu, Z. Han, W. Ho, *Science* **344**, 885–888 (2014).
32. I. V. Stiopkin *et al.*, *Nature* **474**, 192–195 (2011).
33. A. V. Iogansen, *Spectrochim. Acta A* **55**, 1585–1612 (1999).
34. Y. Li *et al.*, *Nano Lett.* **16**, 1104–1109 (2016).

ACKNOWLEDGMENTS

This work was supported by the National Basic Research Programs of China under grant 2012CB921303 and the National Natural Science Foundation of China under grants 91321309, 11290162/A040106, 11304107, 61371015, 11422431, 11275008, 11274002, and 91021007. Y.J. acknowledges support from the National Program for Support of Top-Notch Young Professionals. We are grateful for the computational resources provided by the supercomputer TianHe-1A in Tianjin, China.

SUPPLEMENTARY MATERIALS

www.sciencemag.org/content/352/6283/321/suppl/DC1
Materials and Methods
Supplementary Text
Figs. S1 to S12
References (*35–50*)

6 January 2016; accepted 14 March 2016
10.1126/science.aaf2042

THERMODYNAMICS

A single-atom heat engine

Johannes Roßnagel,[1]* Samuel T. Dawkins,[1] Karl N. Tolazzi,[2] Obinna Abah,[3] Eric Lutz,[3] Ferdinand Schmidt-Kaler,[1] Kilian Singer[1,4]*

Heat engines convert thermal energy into mechanical work and generally involve a large number of particles. We report the experimental realization of a single-atom heat engine. An ion is confined in a linear Paul trap with tapered geometry and driven thermally by coupling it alternately to hot and cold reservoirs. The output power of the engine is used to drive a harmonic oscillation. From direct measurements of the ion dynamics, we were able to determine the thermodynamic cycles for various temperature differences of the reservoirs. We then used these cycles to evaluate the power *P* and efficiency η of the engine, obtaining values up to $P = 3.4 \times 10^{-22}$ joules per second and η = 0.28%, consistent with analytical estimations. Our results demonstrate that thermal machines can be reduced to the limit of single atoms.

Heat engines, which convert thermal energy into mechanical work, have played a central role in society since the industrial revolution and are ubiquitous as generators of motion (*1*). The working fluid of a macroscopic engine typically contains on the order of 10^{24} particles. Experimental progress in the past decade has led to the miniaturization of thermal machines down to the microscale, using microelectromechanical (*2*), piezoresistive (*3*), and cold atom (*4*) systems, as well as single colloidal particles (*5*, *6*) and single molecules (*7*). In his 1959 talk "There is plenty of room at the bottom," Feynman envisioned tiny motors working at the single-atom level (*8*).

Here, we report the realization of a classical single-atom heat engine whose working agent is an ion held within a modified linear Paul trap. We use laser cooling and electric-field noise to engineer cold and hot reservoirs. To determine the temperature of the ion, we make use of fast thermometry methods, which make use of the Doppler broadening of optical resonances (*9*). The thermodynamic cycle of the engine is established for various temperature differences of the reservoirs, from which we deduce work and heat, and thus power output and efficiency. We additionally show that the work produced by the engine can be effectively stored and used to drive a harmonic oscillator against friction.

Trapped ions offer an exceptional degree of control in their preparation and manipulation, great precision in the measurement of their parameters (*10*, *11*), and the capability of coupling to engineered reservoirs (*12*, *13*). Hence, they provide an ideal setup for operating and characterizing a single-particle heat engine (*14*).

In our experiment, a single $^{40}Ca^+$ ion is trapped in a linear Paul trap with a funnel-shaped electrode geometry (Fig. 1A). The electrodes are driven symmetrically at a radio-frequency voltage of 830 V_{pp} at 21 MHz, resulting in a tapered harmonic pseudo-potential (Fig. 1B) of the form $U = (m/2)\sum_i \omega_i^2 i^2$ (*10*), where m is the atomic mass and $i \in \{x, y\}$ denotes the radial trap axes (Fig. 1A). The axial confinement is realized with constant voltages on the two end-cap electrodes, resulting in a trap frequency of $\omega_z/2\pi$ = 81 kHz. The trap angle θ = 10° and the radial extent of the trap r_0 = 1.1 mm at z = 0 characterize the geometry of the funnel. The resulting radial trap frequencies $\omega_{x,y}$ decrease in the axial z-direction as

$$\omega_{x,y} = \frac{\omega_{0x,0y}}{\left(1 + \frac{z \tan\theta}{r_0}\right)^2} \qquad (1)$$

The eigenfrequencies in the radial directions at the

[1]QUANTUM, Institut für Physik, Universität Mainz, D-55128 Mainz, Germany. [2]Max-Planck-Institut für Quantenoptik, D-85748 Garching, Germany. [3]Department of Physics, Friedrich-Alexander-Universität Erlangen-Nürnberg, D-91058 Erlangen, Germany. [4]Experimentalphysik I, Universität Kassel, D-34132 Kassel, Germany.
***Corresponding author. E-mail: j.rossnagel@uni-mainz.de (J.R.); ks@uni-kassel.de (K.S.)**

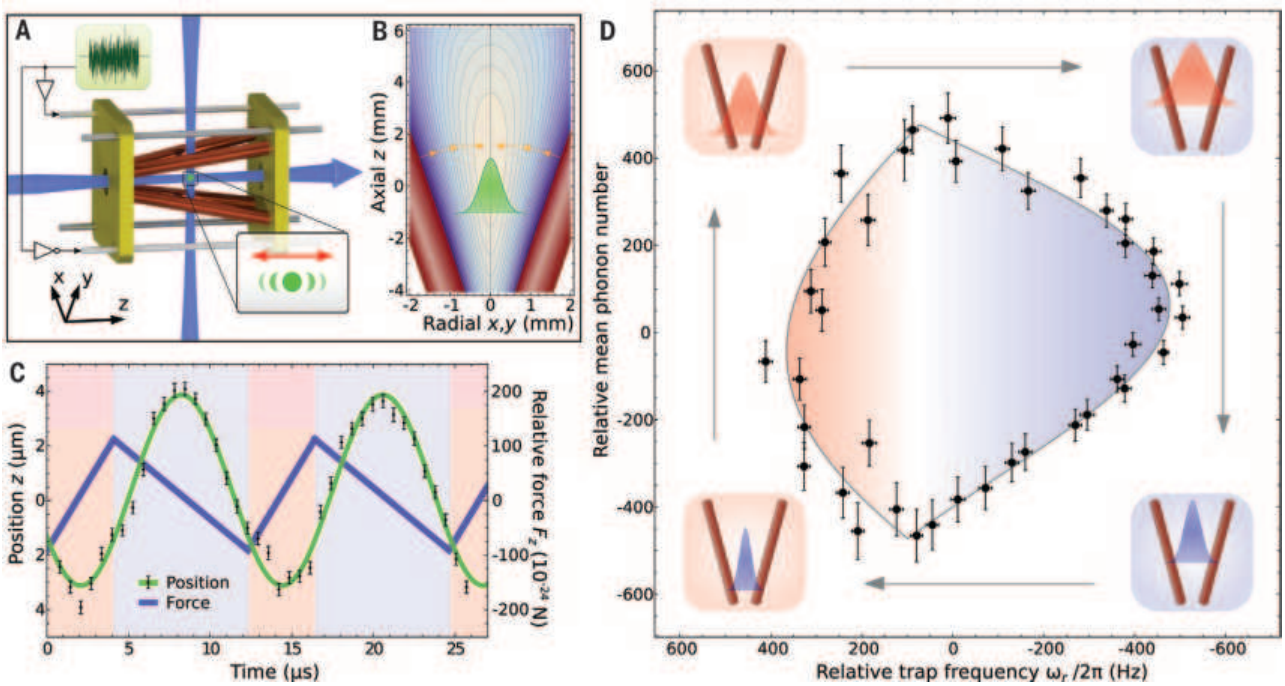

Fig. 1. Single-atom heat engine. (**A**) Experimental setup composed of a single trapped ion (green); lasers for cooling, damping, and observation of the ion (blue); radio-frequency electrodes in funnel geometry (red); end caps (gold); and outer electrodes (gray). The position of the ion is imaged on an ICCD camera. Opposing voltage noise waveforms are additionally supplied to the outer electrodes so as to generate electric-field noise without affecting the trap frequencies. (**B**) Cross section of the funnel-shaped pseudo-potential between the radio-frequency electrodes (red), with a minimum at the center. The gradient of the potential (orange arrows) has an axial component that increases with radial displacement *x* or *y*. A force in the axial direction arises as a function of the finite width of the radial thermal state of the ion (green Gaussian distribution). (**C**) Position of the ion (black symbols) determined from the average of more than 200,000 camera images at each time step. The error bars result from the uncertainty of Gaussian fits to the recorded fluorescence images. The measured positions are described by a sinusoidal fit (green line). Background colors indicate the periodic interaction with the hot (red) and cold (blue) reservoirs, which gives rise to a periodic driving force (blue line) according to Eq. 1, shown relative to its mean value of 5.03×10^{-21} N. (**D**) Thermodynamic cycle of the engine for one radial direction. Trap frequencies in the radial direction ω_r are deduced directly from the measured *z*-positions. The temperature *T* of the radial state of motion, and thus the corresponding mean phonon number $\bar{n}_r$, is determined from separate measurements (see text and Fig. 2). The values of ω_r and $\bar{n}_r$ are given with respect to the center of the cycle at $\omega_{0r}/2\pi = 447.9 \pm 0.2$ kHz and $\bar{n}_{0r} = 2.61\ (\pm 0.04) \times 10^4$ phonons. The shaded area enclosed by the cycle is proportional to the work performed by the engine, where red and blue colors indicate heating and cooling periods, respectively. The black line is the calculated trajectory of the cycle (see text). The pictograms in the corners illustrate the different stages of an idealized cycle.

trap minimum $z = 0$ are $\omega_{0x}/2\pi = 447$ kHz and $\omega_{0y}/2\pi = 450$ kHz, with the degeneracy lifted, but sufficiently close to permit the approximation of cylindrical symmetry with $r^2 = x^2 + y^2$ and a mean radial trap frequency ω_r. An additional set of outer electrodes compensates for stray fields. The trapped ion is cooled by a laser beam at 397 nm, which is red-detuned to the internal electronic $S_{1/2} - P_{1/2}$ transition (*10*); the resulting fluorescence is recorded by a rapidly gated intensified charge-coupled device (ICCD) camera.

The heating and cooling cycle of the ion is designed such that the ion thermalizes as if in contact with a thermal reservoir. A cold bath interaction is realized by exposing the ion to a laser cooling beam, leading to an equilibrium temperature of $T_C = 3.4$ mK (*9*, *15*). A hot reservoir interaction with finite temperature T_H is designed by additionally exposing the ion to white electric-field noise. The interplay of photon scattering and noise leads to a thermal state of the ion at temperature *T* at any given moment (*9*, *16*, *17*).

In our setup, heating and cooling act on the radial degrees of freedom. The resulting time-averaged spatial distribution of the radial thermal state is of the form

$$\xi_r(r, \phi, T) = \frac{1}{2\pi\sigma_r^2(T)} \exp\left[\frac{-(r - r_0)^2}{2\sigma_r^2(T)}\right] \quad (2)$$

with a temperature-dependent time-averaged width $\sigma_r(T) = \sqrt{k_B T / m\omega_r^2}$, where k_B is the Boltzmann constant. Because the thermal energy during the operation of the engine is larger than the energy spacing of the harmonic oscillator ($k_B T >> \hbar\omega_r$), a classical description of the dynamics is appropriate.

The heat engine is driven by alternately heating and cooling the ion in the radial direction by switching the electric noise on and off; the cooling laser is always on. Heating and cooling change the spatial width $\sigma_r(T)$ of the radial thermal state $\xi_r(r, \phi, T)$. Owing to the geometry of the trap, the gradient of the funnel-shaped pseudo-potential *U* has a component in the axial direction *z* that depends on the radial position *r* (Fig. 1B). As a consequence, the finite width of the radial thermal state $\xi_r(r, \phi, T)$ leads to a temperature-dependent average force in the axial direction:

$$F_z(T) = -\int_0^{2\pi}\int_0^{\infty} \xi_r(r, \phi, T) \frac{dU(r)}{dz} r\, dr\, d\phi \quad (3)$$

During the first part of the cycle, the ion is heated and the width $\sigma_r(T)$ increases. As a result, the ion moves along the *z* axis to a weaker radial confinement. We calculate a static displacement of 11 nm for the relative change of $\Delta F_z = 2 \times 10^{-22}$ N, corresponding to Fig. 1C. During this first step, the axial potential energy of the ion increases and work is produced. The second step occurs during exposure to the cold reservoir when the electric-field noise is switched off. Here the radial width σ_r and the corresponding force F_z decrease as the temperature is reduced, and the ion moves back to its initial position owing to the restoring force of the axial potential. The combination of heating and cooling gives rise to a closed thermodynamic cycle and leads to a periodic force $F_z(T)$ in the axial direction (Fig. 1C). We switch between heating and cooling with precise timing, such

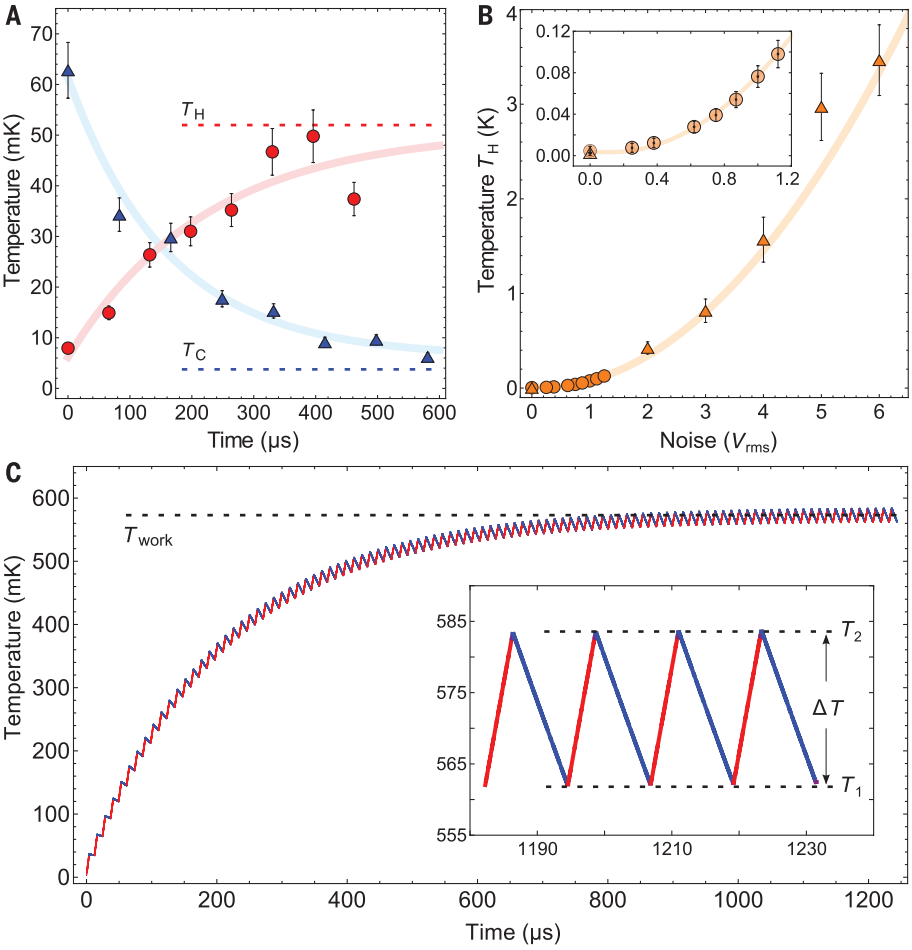

Fig. 2. Temperature dynamics of the engine. (**A**) Thermalization curves derived from dark-state thermometry of the radial thermal state of the ion when heated to T_H = 51 mK (red) and cooled to T_C = 6 mK (blue). Individual errors result from fits to the dark resonances as well as the uncertainty caused by the laser linewidths (*9*). Individual fits reveal thermalization time constants for heating and cooling of t_H = 190 ± 30 μs and t_C = 210 ± 10 μs, respectively. (**B**) Dependence of the hot bath temperature T_H on the root mean square of the electric noise applied to the trap electrodes, measured by dark-state thermometry (circles) (*9*) and spatial thermometry (triangles) (*21*). The inset shows a magnification of the low-temperature values. (**C**) Simulated temperature of the ion as a function of time using the parameters for thermalization. Heating and cooling durations in each cycle are 4.1 μs and 8.2 μs, respectively. With an electric-field noise amplitude of 4 V, we calculate a working point temperature T_{work} = 568 mK and a temperature difference $\Delta T = T_2 - T_1$ = 21.5 mK. The inset shows an enlargement of the cooling and heating processes at steady-state operation.

that the cycle repeats itself at a rate equal to the axial trap frequency ω_z. The engine therefore effectively drives a harmonic oscillation in the axial direction. The work produced in each cycle is thus resonantly transferred to the axial degree of freedom and stored in the amplitude of the oscillation. The essentially frictionless nature of the system leads to an ever-increasing oscillation. The axial motion thus plays a role similar to the flywheel of a mechanical engine.

To contain this oscillation, we provide adjustable damping by introducing an additional cooling laser in the axial direction. Steady-state operation is reached when the work generated by the engine is balanced by the energy dissipated by the damping. We measure the amplitude of the steady-state oscillation of the ion in the *z*-direction by recording fluorescence images with the ICCD camera; the exposure time is 700 ns, which is much shorter than the axial oscillation period. The camera is synchronized with the temperature modulation, allowing for the repetitive recording of images at particular phases of the oscillation. Thus, the position of the ion can be determined precisely as a function of time, thereby revealing the amplitude and phase of the resulting sinusoidal oscillation (*18*) (Fig. 1C). We verified that both are independent to an inversion of the noise signal. To facilitate the position measurement, we use the damping laser to reduce the incoherent, thermal motion in the axial direction, which originates from bath interactions. For efficient cooling while maintaining low damping of the oscillation, the laser is applied only around the turning points of the axial motion (*15*).

The thermodynamic cycle of the single-ion heat engine is shown in Fig. 1D by plotting the

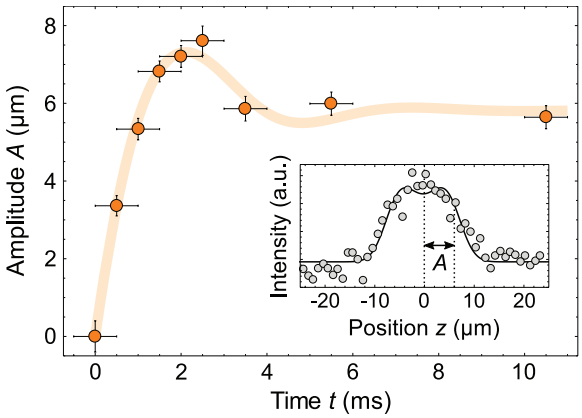

Fig. 3. Determination of the damping coefficient. The effect of the damping coefficient γ is studied by directly driving the ion axially with the end caps in the absence of the thermal reservoir interactions. The step response is observed by determining the amplitude A of the ion's oscillation (orange circles) at time t after switching the end cap drive on. In accord with the dynamics of a driven damped harmonic oscillator, the step response features a rise toward a steady-state amplitude A_0, superposed with a decaying beat frequency at ω_b between the resonance ω_z and drive frequency ω_d according to the relation $A(t) = A_0\sqrt{[\cos(\omega_b t) - (\omega_z/\omega_d)\exp(-\gamma_i t)]^2 + \sin(\omega_b t)^2}$. A fit to the data (orange line) reveals γ_i = 560 ± 100 s^{-1}; the average of four such measurements yielded γ = 480 ± 140 s^{-1}. (**Inset**) Determination of oscillation amplitude at 5.5 ms by fitting a time-integrated sinusoidally modulated Gaussian (black line) to the projections of the corresponding camera images, with exposure time of 1 ms (gray circles). The width of the Gaussian is determined from the image of an ion at rest.

mean phonon number $\overline{n}_r = k_B T/\hbar\omega_r$ of the thermal state of the ion in the radial direction as a function of the corresponding trap frequency ω_r (*19*). The radial trap frequencies $\omega_r(t)$ are obtained from the measured axial positions of the ion $z(t)$ in conjunction with calibration measurements of the tapered confinement described by Eq. 1. The temperature of the ion at any given moment of the cycle is deduced from the interplay of the heating and cooling rates (Fig. 2). We determine these rates via a stroboscopic measurement of the thermal broadening of narrow resonances of dark states caused by coherent population trapping, which are sensitive to the velocity of the ion through the Doppler shift (Fig. 2A). A detailed description of this technique, originally used for cold atoms (*20*), is presented in (*9*). The temperature of the hot reservoir T_H can be adjusted via the applied electric-field noise and has been measured using dark-state thermometry, as well as spatial thermometry (*21*) for higher temperatures (Fig. 2B). The heating and cooling processes are much slower than the internal dynamics of the ion; thus, the cycle can be regarded as quasi-static with negligible losses caused by irreversible processes (*22*). Because the ion is in permanent contact with one of the reservoirs, the dynamics are similar to those of a Stirling engine (*5*, *23*).

We derived the power output during steady-state operation in three independent ways. We first determined the power $P_{cyc} = W_{cyc}/t_{cyc}$, with cycle time $t_{cyc} = 2\pi/\omega_z$, by evaluating the work as the area of the cycles for both radial directions, $W_{cyc} = \hbar\oint 2\overline{n}_r d\omega_r$ (*19*). To assess the performance of the engine, we computed the power for various temperature differences $\Delta T = T_2 - T_1$ between maximum temperature T_2 and minimum temperature T_1 in the cycle, as defined in Fig. 2C. The difference ΔT can be tuned by adjusting either the reservoir temperatures or the relative duration of the reservoir interaction, given by the duty cycle $d = t_H/t_{cyc}$ of the hot bath interaction time t_H per cycle.

We alternatively deduced the power directly from the measurement of the axial oscillation amplitudes A_z of up to 15 μm. The driving power of a driven damped harmonic oscillator at steady state yields $P_{osc} = \gamma m\omega_z^2 A_z^2$ (*24*). The damping parameter $\gamma = 480 \pm 140\ s^{-1}$ was determined separately via observation of the step response of the ion's oscillation to a coherent drive (Fig. 3). Both methods give consistent values of the power, of up to $3.4\ (\pm 0.5) \times 10^{-22}$ J/s, depending on ΔT (Fig. 4A). This represents a power-to-particle ratio of 1.5 kW/kg, comparable to that of a typical car engine, indicating that the power scales approximately with the number of particles of the working agent.

We further calculated analytically the engine output power using the expression for work performed during a single cycle:

$$W_{ana} = -\oint F_z(t)\frac{dz(t)}{dt}dt \qquad (4)$$

The driving force F_z is calculated from Eq. 3, accounting for the temperature variations of the ion determined as shown in Fig. 2C and neglecting the weak z dependence. The resulting motion $z(t)$ is derived assuming expressions of a resonantly driven damped harmonic oscillator. Thus, for the output power, we find

$$P_{ana} = \frac{W_{ana}}{t_{cyc}} = \frac{4k_B^2 \sin^2(\pi d)\tan^2\theta\,\Delta T^2}{m\pi^4\gamma[(d^2-d)r_0]^2}$$

$$= (8.8\times 10^{-20}\ \mathrm{Js^{-1}K^{-2}})\Delta T^2 \qquad (5)$$

This analytical formula is plotted using experimental parameters in Fig. 4A and is in agreement with the measured P_{cyc}.

We further evaluated the efficiency of the engine, $\eta_{cyc} = W_{cyc}/Q_H$, from the measured data by determining the heat absorbed from the hot reservoir, $Q_H = \int_H TdS$, from the *TS* diagram shown in Fig. 4B. Here, S denotes the entropy of a thermal harmonic oscillator, $S = k_B[1 + \ln(k_B T/\hbar\omega_r)]$ (*22*, *25*). To this end, we transformed the measured data of the cycle in Fig. 2B according to $\{\omega_r, \overline{n}_r\} \rightarrow \{S, T\}$. Using the above analytical approach, we find

$$\eta_{ana} = \frac{4k_B \sin^2(\pi d)\tan^2\theta\,\Delta T}{m\pi^3\gamma\omega_z[(d^2-d)r_0]^2} = (0.041\,\mathrm{K}^{-1})\Delta T \qquad (6)$$

The resulting efficiencies (Fig. 4C) reach values up to $\eta_{cyc} = 0.28 \pm 0.07\%$, in agreement with the analytical expectation. A comparison of this value with the corresponding efficiency at maximum

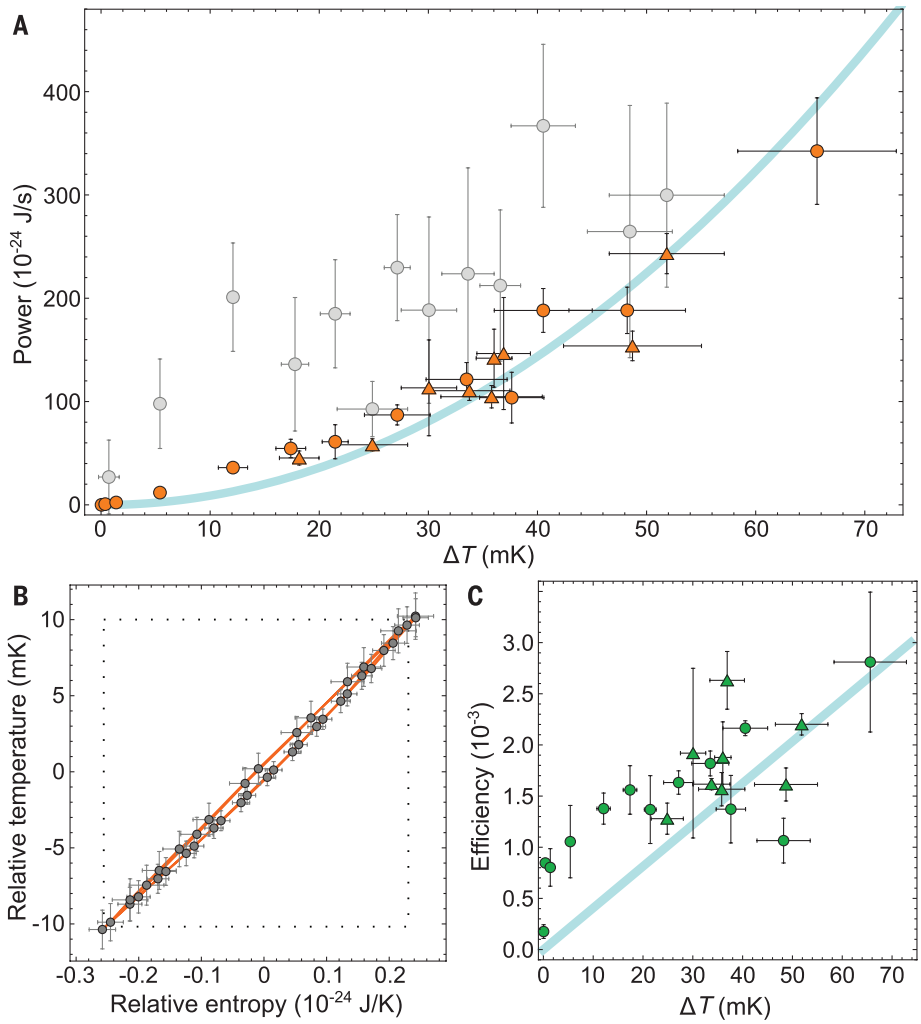

Fig. 4. Power and efficiency of the heat engine. (**A**) Power of the engine, calculated from the measured cycles (orange) and from a direct analysis of the amplitude (gray). The temperature differences ΔT were achieved by varying the electric-field noise (circles) and the duty cycle of heating and cooling (triangles). The measured cycle data are consistent with the expected value from analytical calculations (blue line). The larger error bars of the gray data stem from the uncertainty on the damping coefficient γ. (**B**) The heat engine cycle, corresponding to Fig. 1D; temperature is shown relative to 568 mK and entropy relative to 179.6×10^{-24} J/K. Both work and efficiency can be derived from integrating this cycle. The square (dotted line) represents the equivalent Carnot cycle for the full range of parameters and shows the case of the theoretical maximum efficiency. (**C**) Measured efficiency as a function of ΔT, which was tuned by varying the noise amplitude (circles) or the duty cycle (triangles), compared to the result of the analytical calculation (blue line).

power, given by the Curzon-Ahlborn (*26*) formula $\eta_{CA} = 1 - \sqrt{T_1/T_2} = 1.9\%$, reflects that the current trap parameters do not correspond to the optimal point (*14*). The performance of future single-ion heat engines could be improved by redesigning the geometry of the trap to have cycles with a higher range of frequencies ω_r (see Fig. 4B). This could be achieved by increasing either the angle of the taper or the absolute radial trap frequencies.

We have demonstrated a realization of a heat engine whose working agent is a single atom. This classical device offers a broad platform for future experiments investigating, for instance, machines coupled to nonthermal reservoirs (*27*) or single-ion refrigerators and pumps (*28*). Moreover, the quantum regime ($k_B T \approx \hbar\omega_r$) could be reached by replacing Doppler cooling by electromagnetically induced transparency cooling or side-band cooling (*10*), as in the recent verification of the quantum Jarzynski equality (*29*). In the quantum domain, dark-state thermometry could be replaced by side-band spectroscopy, again allowing for the determination of the cycle of the engine and thus its power and efficiency. Such a system would permit the study of the performance of small quantum machines (*30*, *31*) and the exploration of genuine quantum effects in thermodynamics, such as quantum coherences (*32*) and correlations (*33*), as well as the testing of predictions of quantum resource theory (*34*, *35*).

REFERENCES AND NOTES

1. Y. A. Çengel, M. A. Boles, M. Kanoğlu, *Thermodynamics: An Engineering Approach* (McGraw-Hill, ed. 8, 2014).
2. S. Whalen, M. Thompson, D. Bahr, C. Richards, R. Richards, *Sens. Actuators A* **104**, 290–298 (2003).
3. P. Steeneken *et al.*, *Nat. Phys.* **7**, 354–359 (2011).
4. J.-P. Brantut *et al.*, *Science* **342**, 713–715 (2013).
5. V. Blickle, C. Bechinger, *Nat. Phys.* **8**, 143–146 (2012).
6. I. A. Martínez *et al.*, *Nat. Phys.* **12**, 67–70 (2016).
7. T. Hugel *et al.*, *Science* **296**, 1103–1106 (2002).
8. R. P. Feynman, *Eng. Sci.* **23**, 22 (1960).
9. J. Roßnagel, K. N. Tolazzi, F. Schmidt-Kaler, K. Singer, *New J. Phys.* **17**, 045004 (2015).
10. D. Leibfried, R. Blatt, C. Monroe, D. Wineland, *Rev. Mod. Phys.* **75**, 281–324 (2003).
11. R. Blatt, D. Wineland, *Nature* **453**, 1008–1015 (2008).
12. J. F. Poyatos, J. I. Cirac, P. Zoller, *Phys. Rev. Lett.* **77**, 4728–4731 (1996).
13. C. J. Myatt *et al.*, *Nature* **403**, 269–273 (2000).
14. O. Abah *et al.*, *Phys. Rev. Lett.* **109**, 203006 (2012).
15. H. J. Metcalf, P. van der Straten, *Laser Cooling and Trapping* (Springer, 1999).
16. J. I. Cirac, R. Blatt, P. Zoller, W. D. Phillips, *Phys. Rev. A* **46**, 2668–2681 (1992).
17. J. I. Cirac, M. Lewenstein, P. Zoller, *Phys. Rev. Lett.* **72**, 2977–2980 (1994).
18. H. C. Nägerl, D. Leibfried, F. Schmidt-Kaler, J. Eschner, R. Blatt, *Opt. Express* **3**, 89–96 (1998).
19. B. Lin, J. Chen, *Phys. Rev. E* **67**, 046105 (2003).
20. T. Peters, B. Wittrock, F. Blatt, T. Halfmann, L. P. Yatsenko, *Phys. Rev. A* **85**, 063416 (2012).
21. S. Knünz *et al.*, *Phys. Rev. A* **85**, 023427 (2012).
22. G. S. Agarwal, S. Chaturvedi, *Phys. Rev. E* **88**, 012130 (2013).
23. K. Brandner, K. Saito, U. Seifert, *Phys. Rev. X* **5**, 031019 (2015).
24. J. R. Taylor, *Classical Mechanics* (University Science, Sausalito, CA, 2005).
25. L. D. Landau, E. M. Lifschitz, *Statistical Physics* (Elsevier, 1980).
26. F. Curzon, B. Ahlborn, *Am. J. Phys.* **43**, 22 (1975).
27. J. Roßnagel, O. Abah, F. Schmidt-Kaler, K. Singer, E. Lutz, *Phys. Rev. Lett.* **112**, 030602 (2014).
28. B. Lin, J. Chen, *Phys. Rev. E* **68**, 056117 (2003).
29. S. An *et al.*, *Nat. Phys.* **11**, 193–199 (2014).
30. N. Linden, S. Popescu, P. Skrzypczyk, *Phys. Rev. Lett.* **105**, 130401 (2010).
31. R. Kosloff, A. Levy, *Annu. Rev. Phys. Chem.* **65**, 365–393 (2014).
32. M. O. Scully, M. S. Zubairy, G. S. Agarwal, H. Walther, *Science* **299**, 862–864 (2003).
33. R. Dillenschneider, E. Lutz, *Europhys. Lett.* **88**, 50003 (2009).
34. F. G. Brandão, M. Horodecki, J. Oppenheim, J. M. Renes, R. W. Spekkens, *Phys. Rev. Lett.* **111**, 250404 (2013).
35. M. Horodecki, J. Oppenheim, *Nat. Commun.* **4**, 2059 (2013).

ACKNOWLEDGMENTS

We thank Princeton Instruments for the loan of the ICCD camera and S. Deffner for fruitful discussions. Supported by the German Research Foundation (grant "Einzelionenwärmekraftmaschine"), the Volkswagen Foundation (grant "Atomic Nano-Assembler"), European Union (EU) COST action MP1209, and the EU Collaborative Project TherMiQ (grant agreement 618074). The data presented in this report are available upon request to K.S.

14 October 2015; accepted 4 March 2016
10.1126/science.aad6320

ORGANOMETALLICS

Pre-transmetalation intermediates in the Suzuki-Miyaura reaction revealed: The missing link

Andy A. Thomas and Scott E. Denmark*

Despite the widespread application of Suzuki-Miyaura cross-coupling to forge carbon-carbon bonds, the structure of the reactive intermediates underlying the key transmetalation step from the boron reagent to the palladium catalyst remains uncertain. Here we report the use of low-temperature rapid injection nuclear magnetic resonance spectroscopy and kinetic studies to generate, observe, and characterize these previously elusive complexes. Specifically, this work establishes the identity of three different species containing palladium-oxygen-boron linkages, a tricoordinate boronic acid complex, and two tetracoordinate boronate complexes with 2:1 and 1:1 stoichiometry with respect to palladium. All of these species transfer their boron-bearing aryl groups to a coordinatively unsaturated palladium center in the critical transmetalation event.

Palladium-catalyzed cross-coupling reactions have fundamentally changed the practice of organic synthesis. These reactions forge carbon-carbon bonds through the migration of a carbon-based substituent from a main group element to palladium, as exemplified by the Kumada-Tamao-Corriu (Mg) (*1*), Suzuki-Miyaura (B) (*2*), Stille-Migita-Kosugi (Sn) (*3*), Negishi (Zn) (*4*), and Hiyama-Denmark (Si) (*5*) reactions. The Nobel Prize–sharing Suzuki-Miyaura reaction (*6*) is currently the premier cross-coupling process and has been widely applied in organic (*7*), medicinal (*8*), and materials (*9*) chemistry. It is also frequently used in the industrial syntheses of fine chemicals (*10*) and pharmaceuticals (*11*) because of its demonstrated reliability, its functional group compatibility, and the low cost and ease of handling of a wide variety of commercially available boron-based reagents.

Despite the preeminent status of the Suzuki-Miyaura reaction, a fundamental understanding of the critical migratory transmetalation event from boron to palladium has thus far been lacking (*12*–*18*). For decades, chemists have considered two pathways (path A and path B in Fig. 1) that differ in the role that the hydroxide ion plays in initiating the transmetalation event. Path A proceeds through the combination of a negatively charged aryltrihydroxyboronate (compound **1**) and a palladium halide complex (**2**), which form a hypothetical intermediate containing a Pd-O-B unit (**3**). The alternative path B proceeds through the combination of a neutral arylboronic acid (**4**) and a palladium hydroxide complex (formed through the displacement of the organopalladium halide by hydroxide; **5**), ultimately converging to the same intermediate **3**, which is then poised to transfer the aryl group to palladium in an intramolecular β-aryl elimination step, followed by reductive elimination (Fig. 1). Species such as **3** represent the missing link between the starting organoboron reagents and the diorganopalladium intermediates that are known to afford cross-coupling products.

The role of the base in the Suzuki-Miyaura reaction was investigated initially by the Soderquist laboratory (*12*) and, more recently, by the laboratories of Hartwig (*13*), Amatore and Jutand (*14*–*16*), and Schmidt (*17*, *18*). The kinetic analysis in (*13*) established that path B is favored over path A by more than four orders of magnitude, a conclusion that is reinforced by the extensive kinetic studies in (*14*–*16*), which clearly identified multiple antagonistic roles for the hydroxide ion. Although nuclear magnetic resonance (NMR) spectroscopic and kinetic studies have

Roger Adams Laboratory, Department of Chemistry, University of Illinois, Urbana, IL 61801, USA.
***Corresponding author. E-mail: sdenmark@illinois.edu**

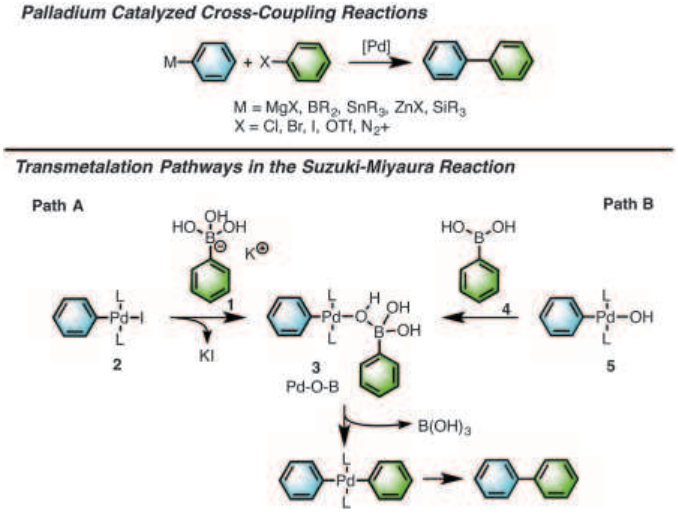

Fig. 1. Palladium-catalyzed cross-coupling reactions and proposed transmetalation pathways in the Suzuki-Miyaura process. R indicates an organic group. Compound numbers are shown in bold in the lower panel.

provided independent evidence for these pathways, the actual composition and structure of the transmetalation precursors have not been unambiguously defined, despite being widely assumed. Because of the transient nature of these intermediates, traditional methods (e.g., electrospray mass spectrometry and traditional NMR spectroscopy) have proven incapable of characterizing highly reactive intermediates such as **3** (*19*, *20*). Although the intermediacy of a species containing a Pd-O-B linkage has been proposed, its observation and characterization have eluded chemists for over 30 years (*21*). A recent review by Lennox and Lloyd-Jones (*22*) states that "[t]he barrier of this process was predicted computationally to be low (14–22 kcal mol^{-1}), suggesting specialist techniques will need to be applied to detect and confirm the identity of [**3**] experimentally." One such technique that has proven valuable for providing structural and kinetic data in similar mechanistic studies is rapid injection NMR (RI-NMR) (*23*).

Aided by the RI-NMR apparatus developed in our laboratories (*24*), we have undertaken the generation and structural and kinetic characterization of these elusive intermediates. We hypothesized that combining stoichiometric amounts of arylpalladium complex *trans*-(*i*-$Pr_3P)_2$(4-FC_6H_4)Pd(OH) (**6**) with 4-fluorophenylboronic acid (**7**) (Fig. 2, route 1), or *trans*-(*i*-$Pr_3P)_2$(4-FC_6H_4)Pd(I) (**8**) with thallium 4-fluorophenylboronate (**10**) (Fig. 2, route 2), should converge on a species whose structure and kinetic competence can be examined. The choice of triisopropylphosphine (*i*-Pr_3P) was critical to allow the preparation of discrete, stable precursors and also to facilitate structural assignments (*25*, *26*).

The synthesis in route 1 involved the addition of a tetrahydrofuran-d_8 (THF-d_8) solution of 4-fluorophenylboronic acid (**7**) to a THF-d_8 solution of *trans*-(*i*-$Pr_3P)_2$(4-FC_6H_4)Pd(OH) (**6**), together with 2.0 equivalents of *i*-Pr_3P, at −78°C (Fig. 2). Although no new species were observed at −60°C, warming the solution to −30°C resulted in the quantitative conversion of compounds **6** and **7** to a new species. The combination of one- and two-dimensional NMR spectroscopic techniques executed at −30°C led to the structural elucidation of the newly formed species as complex **11**, containing a Pd-O-B linkage (supplementary materials, figs. S1 to S10).

The coordination geometry was assigned to a *trans*-bisphosphino square planar palladium complex. This assignment was based on the observation of the ^{13}C NMR signal (PCH) at 25.38 parts per million (ppm) as an apparent triplet ($J_{P\text{-}C}$ = 10 Hz; *J* is the coupling constant between the phosphorus and carbon atoms) attributable to virtual coupling (*27*) and the ^{31}P NMR signal at 29.98 ppm (a solitary singlet), which is shifted slightly upfield compared with the corresponding resonance of **6** at 33.00 ppm (figs. S2 and S4).

The bonding connectivity of complex **11** was established by the observation of strong through-space interactions [nuclear Overhauser effect (NOE) spectroscopy] of both H_b and H_d (hydrogens in the b and d positions) with the methyl hydrogens on the *i*-Pr_3P group (Fig. 2, blue arrows, and fig. S10). In addition, cross peaks between the B-OH group and the *ipso*-carbon [C(1)]–bearing boron ($^3J_{BOH\text{-}C(1)}$) were observed in the heteronuclear multiple-bond correlation (HMBC) spectrum (Fig. 2, red bonds, and fig. S9). The resonances for H_a and H_b (Fig. 2, blue aryl) and H_c and H_d (green aryl) are shifted slightly downfield (+0.07 to +0.16 ppm) in complex **11**, compared with substrates **6** and **7** (table S1). The resonances for the fluorine atoms in **11** [F_a (blue aryl) and F_b (green aryl)] are both shifted upfield relative to those associated with **6** and **7**, but the change was much more pronounced for F_b (−4.54 to −0.91 ppm), which facilitated their identification.

Most importantly, the boron atom in complex **11** was assigned to a tricoordinate geometry [6-B-3 (*28*)] on the basis of the ^{11}B NMR signal, which appeared as a broad singlet at 29 ppm (table S1)—well within the chemical shift regime for 6-B-3 boron compounds (*29*). Related 6-B-3 complexes of arylboronic and diarylborinic acids with Pt and Rh have been synthesized and exhibit ^{11}B NMR resonances similar to that of **11** (*30*, *31*).

To provide additional evidence for the structure of **11**, an independent synthesis was carried out (route 2). This synthesis involved combining *trans*-(*i*-$Pr_3P)_2$(4-FC_6H_4)Pd(I) (**8**) with 3.0 equivalents of thallium 4-fluorophenylboronate (**10**) in the presence of dibenzo-22-crown-6 (*32*), together with 1.0 equivalent of *i*-Pr_3P in THF, at −78°C; this was followed by warming to −30°C in the NMR spectrometer (Fig. 2). A small amount of conversion (~10%) to complex **11** was observed, together with cross-coupling product **13** (~30%), by ^{31}P and ^{19}F NMR spectroscopy, demonstrating that intermediate **11** can be formed without the intermediacy of arylpalladium hydroxide complexes (*33*).

To support the assertion that the boron atom in **11** is tricoordinate (6-B-3), a second independent synthesis of **11** was undertaken (route 3). A solution of arylpalladium hydroxide complex **6** and 4-fluorophenylboroxine **12** (0.33 equivalents) in THF-d_8 was combined with 2.0 equivalents of *i*-Pr_3P at −78°C in an NMR tube, which was quickly inserted into the NMR spectrometer that had been pre-cooled to −60°C, whereupon complex **11** was observed (Fig. 2, route 3). A ~50% conversion to **11** was observed at −60°C over 36 hours, along with cross-coupling product **13**. The similarity of the spectroscopic data (including the NOE spectroscopy cross peaks and the ^{11}B NMR chemical shifts; figs. S13 to S21) for the species generated from the three independent syntheses provides compelling support for the structural assignment of **11** as a 6-B-3 palladium(II) complex containing a Pd-O-B linkage.

The formation of 6-B-3 complex **11** must proceed via an 8-B-4 complex (such as **3**; Fig. 1) that is formed initially which then suffers by the rapid loss of a molecule of water. We attempted to shift the equilibrium toward such a complex by generating **11** in mixtures of THF and H_2O (99:1), but we observed no change in the ^{31}P, ^{19}F, or ^{11}B NMR spectra. We considered exploring more strongly coordinating hydroxide sources that are often used in Suzuki-Miyaura reactions, but the addition of inorganic bases to THF-H_2O blends is known to form biphasic mixtures (*13*). Fortunately, CsOH•H_2O dissolves readily at −30°C in mixtures of THF and CH_3OH (12:1). A freshly generated sample of 6-B-3 complex **11** (from **6** and **7;** vide supra) at 0.034 M in THF was cooled to −78°C; this was followed by the addition of 50 μl of a 2 M solution (5.0 equivalents) of CsOH•H_2O in methanol. The sample was monitored by NMR spectroscopy at −30°C, but again, no change in the ^{19}F, ^{31}P, or ^{11}B NMR spectra was observed.

The resistance of the boron atom in complex **11** to adopt a tetracoordinate geometry is probably caused by the steric hindrance that results from the presence of two *i*-Pr_3P ligands on the palladium atom (F- and B-strain) (*34*). Thus, to enable saturation of the boron valences would require a decrease in steric congestion, achieved by

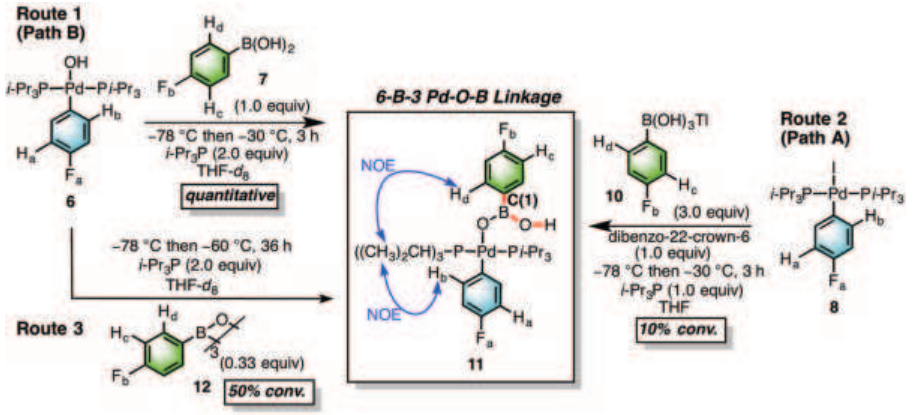

Fig. 2. Formation of a 6-B-3 complex containing a Pd-O-B linkage. The crossing lines for compound **12** signify a cyclic trimer. In the middle panel, the red bonds indicate HMBC cross peaks. Throughout, h indicates hours; equiv, equivalents; conv., conversion; quantitative, 100% conv.

removing a i-Pr_3P ligand from arylpalladium hydroxide complex **6**. This hypothesis led to the investigation of monoligated arylpalladium hydroxy complex, $[(i\text{-}Pr_3P)(4\text{-}FC_6H_4)Pd(OH)]_2$ (**17**), which exists in dimeric form in both solution and solid states (*35*).

The addition of a THF-d_8 solution of **7** (2.0 equivalents) to a THF-d_8 solution of **17** (1.0 equivalent) at −78°C, followed by warming to −60°C, produced no new complexes. However, upon cooling the solution to −100°C, a new species emerged, with complete consumption of **17** and with 50% of **7** remaining (Fig. 3, route 4). The structure of this species could be assigned as the bridged *bis*-arylpalladium arylboronate complex (**18**), which is reminiscent of other palladium acetate and carbonate complexes (*36*, *37*). The stoichiometry of complex **18** was determined by adding a THF-d_8 solution of **7** (1.0 equivalent) to a THF-d_8 solution of **17** (1.0 equivalent) at −60°C, followed by cooling to −100°C, where a quantitative conversion was observed. This dinuclear complex did not incorporate another molecule of **7**, even in the presence of 3 additional equivalents of **7** at −100°C. However, exchange spectroscopy showed cross peaks between **18** and unbound **7** at −100°C, demonstrating that the system was in equilibrium even at this temperature. This stoichiometry (1B:2Pd) is attributed to the thermochemical preference for Pd-(μ-OH)-Pd moieties, which is observed in other bridged mixed-hydroxide complexes (*38*).

The connectivity of the Pd-O-B linkage in **18** was confirmed by the observation of NOEs between H_b, H_d, and the bridging OH group with the methyl hydrogens on the i-Pr_3P group. The observation of NOE cross peaks, along with HMBC ($^3J_{BOH\text{-}C(1)}$) cross peaks between the BOH and the *ipso*-carbon–bearing boron (red bonds), indicates that the arylboronic acid and arylpalladium hydroxide are connected. The ^{11}B NMR chemical shift of **18** was too broad to determine accurately. The broadening of the ^{11}B NMR signal in complex **18** is probably attributable to the chemical exchange between **7** and **18**.

To further aid in the structure determination of **18**, we combined 3.0 equivalents of thallium arylboronate **10** with $[(i\text{-}Pr_3P)(4\text{-}FC_6H_4)Pd(I)]_2$ (**19**) in THF-d_8 at −78°C and then warmed the sample to −50°C (Fig. 3, route 5). Cooling the mixture to −100°C resulted in the observation of complex **18** (~50%) by ^1H NMR spectroscopy. The ability to forge the Pd-O-B linkage in **18** by two routes provides compelling support for the structural assignment.

In an attempt to arrive at a different stoichiometry (1B:1Pd), 60 μl of CH_3OH was injected into a THF-d_8 solution of **18** with 1.0 equivalent of **7** (from **17** and **7**; vide supra), which resulted in the quantitative formation of a new species (**20**) (Fig. 3). The presence of a Pd-O-B linkage in **20** was established by the observation of NOE cross peaks between the methyl hydrogens on the i-Pr_3P and both H_b and H_d (Fig. 3, blue arrows, and fig. S57). The ^{11}B NMR chemical shift of **20** at 9 ppm is well within the characteristic chemical shift regime of tetracoordinate (8-B-4) complexes (*12*, *13*, *39*). The proposed Pd-O-B-O core can be found in an analogous bridging arylpalladium acetate complex (*40*, *41*).

The ability to generate intermediate species containing Pd-O-B linkages provided a singular opportunity to examine the kinetic aspects of the transmetalation event in the Suzuki-Miyaura cross-coupling reaction. The transfer of the aryl group from boron to palladium was investigated by using NMR spectroscopy to follow the decay of complex **20** and the concomitant formation of cross-coupling product **13**.

The addition of CH_3OH into a THF solution of **18** and **7** at −55°C led to the generation of **20**. The subsequent formation of cross-coupling product **13** was monitored by ^{19}F NMR spectroscopy at −30°C (to expedite data collection). First-order plots of [**20**] and [**13**] versus time (figs. S62 to S64) were fitted by using the functions $[A] = [A]_0e^{-kt}$ and $[P] = [A]_0(1 - e^{-kt})$, respectively, where [A] is the concentration of **20**, $[A]_0$ is the initial concentration of **20**, [P] is the concentration of **13**, k is the rate constant, and t is time. These functions provided accurate values for k_{obs} (the observed kinetic constant) for the decay of **20** [$(1.41 \pm 0.02) \times 10^{-3}\ s^{-1}$] and the formation of **13** [$(1.55 \pm 0.09) \times 10^{-3}\ s^{-1}$; Fig. 4A].

A similar kinetic analysis was performed in pure THF by combining a THF solution of **7** (2.0 equivalents) with a THF solution of **17** (1.0 equivalent) at −78°C, followed by warming the sample to −30°C. First-order decay of arylpalladium complex **18** and the formation of **13** were observed with k_{obs} values of $(7.59 \pm 0.58) \times 10^{-4}\ s^{-1}$ and $(5.78 \pm 0.13) \times 10^{-4}\ s^{-1}$, respectively (figs. S65 to S67), indicating that the decay of **18** and the formation of **13** coincide. The correspondence of these rate constants and the clean first-order behavior suggests that at −30°C, **18** is largely converted to **20** (sufficient **7** is present to allow this) (*42*). Moreover, the similarity of the rate constants in THF and the THF-CH_3OH mixture further supports the conclusion that **18** is converted to **20** before transmetalation (Fig. 4A) (*43*).

The generation of 6-B-3 complex **11**, with its Pd-O-B linkage, raised the question of whether this complex is a competent intermediate in the Suzuki-Miyaura reaction. Complex **11** was thermally stable at −30°C in the presence of an excess of i-Pr_3P for over 24 hours, indicating that added phosphine attenuates the rate of the transmetalation process. A THF solution of this complex was warmed from −30°C in 10°C intervals, whereupon a

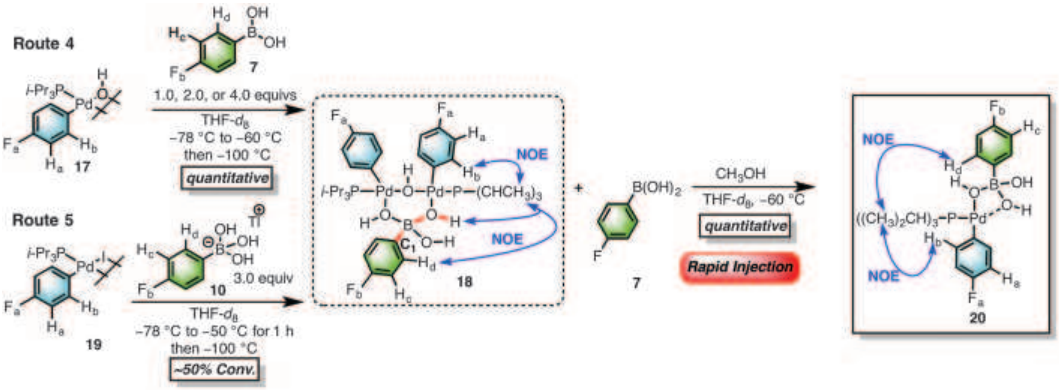

Fig. 3. Formation of 8-B-4 complexes containing Pd-O-B linkages.

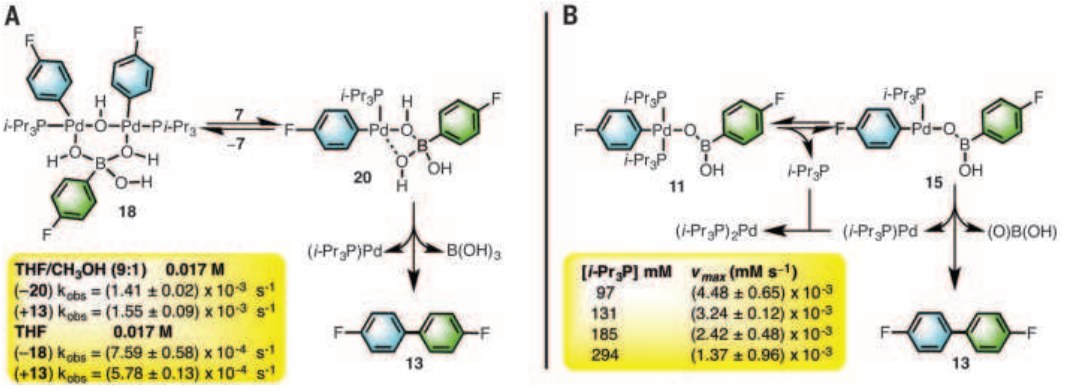

Fig. 4. Kinetic data. (**A**) Formation of **13** from 8-B-4 complexes **18** and **20** (negative signs indicate consumption of starting material). (**B**) Inverse order dependence on [*i*-Pr_3P] for the formation of **13** from 6-B-3 complex **11**.

considerable amount of cross-coupling product **13** was observed by means of ^{19}F NMR spectroscopy at 20°C over the course of 3 to 12 hours. A plot of [**11**] versus time displayed s-shaped curves (figs. S68 to S91), signifying that the k_{obs} increases during the course of the reaction (which is indicative of autocatalysis) (*44*).

To confirm the kinetic requirement for phosphine dissociation in the cross-coupling of **11**, the kinetic order in phosphine was determined by adding a THF solution of **7** to a solution of **6** with increasing amounts of *i*-Pr_3P, ranging from 97 to 294 mM, at 20°C (Fig. 4B). The s-shaped kinetic profiles were fitted, and a v_{max} (maximum rate) was extracted from the data (*45*). A plot of log[v_{max}] versus log[*i*-Pr_3P] gave a slope of −1.05 ± 0.05 (fig. S92), which is consistent with an inverse dependence on phosphine, indicating that dissociation of a phosphine is a pre-equilibrium process that leads to the hypothetical 14-electron palladium complex **15**. Because **15** is formed in such a low-equilibrium concentration, it is not possible to determine whether transmetalation occurs directly from this 6-B-3 species or whether it requires the coordination of another group on boron to form species related to **20**. Although very low levels of halide and water are present, the coordination state of boron in the transmetalation event cannot be unambiguously established.

Through the combination of three methods of investigation (spectroscopic analyses, independent syntheses, and kinetic measurements), we have unambiguously identified and characterized three pre-transmetalation species containing Pd-O-B linkages that undergo the Suzuki-Miyaura cross-coupling reaction. Despite the long-held assumption that these types of intermediates are involved in the transmetalation event, our study provides the first definitive evidence for their involvement. We have demonstrated that both tetracoordinate (**18** and **20**) and tricoordinate (**11**) boron complexes containing the critical Pd-O-B moieties are able to transfer their B-aryl groups to palladium. Moreover, our investigations establish that an empty coordination site on the palladium atom is needed for the transmetalation event to take place from all three Pd-O-B–containing species. We foresee these results serving as a platform for further investigations of the venerable Suzuki-Miyaura cross-coupling process.

REFERENCES AND NOTES

1. F. Chemla, F. Ferriera, A. Perez-Luna, L. Micouin, O. Jackowski, in *Metal-Catalyzed Cross-Coupling Reactions and More*, A. de Meijere, S. Bräse, M. Oestreich, Eds. (Wiley-VCH, ed. 3, vol. 1, 2014), chap. 5, pp. 365–422.
2. J. C. H. Lee, D. G. Hall, in *Metal-Catalyzed Cross-Coupling Reactions and More*, A. de Meijere, S. Bräse, M. Oesteich, Eds. (Wiley-VCH, ed. 3, vol. 1, 2014), chap. 2, pp. 65–132.
3. B. Martín-Matute, K. J. Szabó, T. N. Mitchell, in *Metal-Catalyzed Cross-Coupling Reactions and More,* A. de Meijere, S. Bräse, M. Oestreich, Eds. (Wiley-VCH, Weinheim, ed. 3, vol. 1, 2014), chap. 6, pp. 423–465.
4. S. Xu, H. Kamada, E. H. Kim, A. Oda, E. Negishi, in *Metal-Catalyzed Cross-Coupling Reactions and More,* A. de Meijere, S. Bräse, M. Oestreich, Eds. (Wiley-VCH, Weinheim, ed. 3, vol. 1, 2014), chap. 3, pp. 133–278.
5. W. T. T. Chang *et al*., *Org. React.* **75**, 213–746 (2011).
6. A. Suzuki, *Angew. Chem. Int. Ed.* **50**, 6722–6737 (2011).
7. A. Suzuki, *J. Organomet. Chem.* **576**, 147–168 (1999).
8. C. Valente, M. Organ, in *Boronic Acids: Preparation and Applications in Organic Synthesis and Medicine*, D. G. Hall, Ed. (Wiley-VCH, vol. 2, 2005), chap. 4, pp. 213–262.
9. J. Liu, J. J. Lavigne, in *Boronic Acids: Preparation and Applications in Organic Synthesis and Medicine*, D. G. Hall, Ed. (Wiley-VCH, vol. 2, 2005), chap. 14, pp. 612–676.
10. B. Matthias, H. U. Blaser, Eds., *Organometallics as Catalysts in the Fine Chemical Industry*, vol. 42 of *Topics in Organometallic Chemistry* (Springer-Berlin, 2013).
11. J. Magano, J. R. Dunetz, *Chem. Rev.* **111**, 2177–2250 (2011).
12. K. Matos, J. A. Soderquist, *J. Org. Chem.* **63**, 461–470 (1998).
13. B. P. Carrow, J. F. Hartwig, *J. Am. Chem. Soc.* **133**, 2116–2119 (2011).
14. C. Amatore *et al*., *Chemistry* **17**, 2492–2503 (2011).
15. C. Amatore *et al*., *Chemistry* **18**, 6616–6625 (2012).
16. C. Amatore *et al*., *Chemistry* **19**, 10082–10093 (2013).
17. A. F. Schmidt *et al*., *Russ. J. Gen. Chem.* **81**, 1573 (2011).
18. A. F. Schmidt, A. A. Kurokhtina, *Kinet. Catal.* **53**, 714–730 (2012).
19. A. O. Aliprantis, J. W. Canary, *J. Am. Chem. Soc.* **116**, 6985–6986 (1994).
20. C. Sicre *et al*., *Tetrahedron* **64**, 7437–7443 (2008).
21. N. Miyaura, A. Suzuki, *J. Chem. Soc. Chem. Commun.* **1979**, 866–867 (1979).
22. A. J. J. Lennox, G. C. Lloyd-Jones, *Angew. Chem. Int. Ed.* **52**, 7362–7370 (2013).
23. J. F. McGarrity, J. Prodolliet, *J. Org. Chem.* **49**, 4465–4470 (1984).
24. S. E. Denmark, B. J. Williams, B. M. Eklov, S. M. Pham, G. L. Beutner, *J. Org. Chem.* **75**, 5558–5572 (2010).
25. Although *i*-Pr_3P is not commonly used in Suzuki-Miyaura reactions, it is structurally similar to *c*-Hex_3P (*c*-Hex, cyclohexyl), which has widespread application (*2, 26*).
26. G. C. Fu, *Acc. Chem. Res.* **41**, 1555–1564 (2008).
27. Y. Nishihara, H. Onodera, K. Osakada, *Chem. Commun. (Camb.)* **2004**, 192–193 (2004).
28. This nomenclature designates an N-X-L species, where N is the number of formally valence-shell electrons around atom X that are involved in bonding L ligands to X (*29*).
29. C. W. Perkins *et al*., *J. Am. Chem. Soc.* **102**, 7753–7759 (1980).
30. K. Osakada, H. Onodera, Y. Nishihara, *Organometallics* **24**, 3815–3817 (2005).
31. P. Zhao, C. D. Incarvito, J. F. Hartwig, *J. Am. Chem. Soc.* **129**, 1876–1877 (2007).
32. E. Weber, K. Skobridis, M. Ouchi, T. Hakushi, Y. Inoue, *Bull. Chem. Soc. Jpn.* **63**, 3670–3677 (1990).
33. We cannot unambiguously exclude the possibility that thallium hydroxide dissociates to a minor extent, forming the palladium hydroxide complex **6**. These results do not contradict the conclusions of the studies led by Hartwig (*13*) and Amatore and Jutand (*14–16*). The kinetic incompetence of sodium or potassium boronates in aqueous-organic solutions need not carry over to organic-only solutions of thallium boronates.
34. H. C. Brown, *J. Am. Chem. Soc.* **67**, 374–378 (1945).
35. V. V. Grushin, H. Alper, *Organometallics* **15**, 5242–5245 (1996).
36. T. A. Stephenson, S. M. Morehouse, A. R. Powell, J. P. Heffer, G. Wilkinson, *J. Chem. Soc.* 3632–3640 (1965).
37. C. S. Wei *et al*., *Angew. Chem. Int. Ed.* **52**, 5822–5826 (2013).
38. M. S. Driver, J. F. Hartwig, *Organometallics* **16**, 5706–5715 (1997).
39. H. Nöth, B. Wrackmeyer, in *Nuclear Magnetic Resonance Spectroscopy of Boron Compounds*, P. Diehl, E. Fluck, R. Kosfeld, Eds., vol. 14 of *NMR Basic Principles and Progress* (Springer-Verlag, 1978), chap. 7, pp. 74–100.
40. Y. Tan, F. Barrios-Landeros, J. F. Hartwig, *J. Am. Chem. Soc.* **134**, 3683–3686 (2012).
41. We cannot unambiguously exclude the possibility that methanol has incorporated into complex **20**.
42. Although **18** and **7** are both observed at −100°C, at −30°C, these species converge, thus preventing a definitive assignment of whether **18** or **20** is the actual species undergoing decay in the kinetic analysis.
43. M. Wakioka, Y. Nakamura, Q. Wang, F. Ozawa, *Organometallics* **31**, 4810–4816 (2012).
44. The identity of the species that is inducing autocatalysis has not been determined at this time.
45. R. Schmid, V. N. Sapunov, *Non-Formal Kinetics: In Search for Chemical Reaction Pathways*, vol. 14 of *Monographs in Modern Chemistry*, H. F. Ebel, Ed. (Verlag Chemie, 1982).

ACKNOWLEDGMENTS

We are grateful for generous financial support from the NSF (CHE-1012663 and CHE-1151566). A.A.T. is grateful to the University of Illinois for graduate fellowships. We thank L. Zhu for helpful suggestions regarding NMR spectroscopy. Some of the data presented here were collected in the Core Facilities of the Carl R. Woese Institute for Genomic Biology on a 600-MHz NMR instrument (funded by NIH grant S10-RR028833) or at the Integrated Molecular Structure Education and Research Center at Northwestern University. Full experimental procedures, characterization and kinetic data, and copies of the ^{1}H, ^{13}C, ^{31}P, ^{19}F, ^{11}B, NOE, and exchange spectra can be found in the supplementary materials.

SUPPLEMENTARY MATERIALS

www.sciencemag.org/content/352/6283/329/suppl/DC1
Materials and Methods
Figs. S1 to S118
Tables S1 to S26
References (*46–51*)

28 October 2015; accepted 23 February 2016
10.1126/science.aad6981

ELECTROCHEMISTRY

Homogeneously dispersed multimetal oxygen-evolving catalysts

Bo Zhang,[1,2]* Xueli Zheng,[1,3]* Oleksandr Voznyy,[1]* Riccardo Comin,[1] Michal Bajdich,[4,5] Max García-Melchor,[4,5] Lili Han,[3,6] Jixian Xu,[1] Min Liu,[1] Lirong Zheng,[7] F. Pelayo García de Arquer,[1] Cao Thang Dinh,[1] Fengjia Fan,[1] Mingjian Yuan,[1] Emre Yassitepe,[1] Ning Chen,[8] Tom Regier,[8] Pengfei Liu,[9] Yuhang Li,[9] Phil De Luna,[1] Alyf Janmohamed,[1] Huolin L. Xin,[6] Huagui Yang,[9] Aleksandra Vojvodic,[4,5]† Edward H. Sargent[1]†

Earth-abundant first-row (3d) transition metal–based catalysts have been developed for the oxygen-evolution reaction (OER); however, they operate at overpotentials substantially above thermodynamic requirements. Density functional theory suggested that non-3d high-valency metals such as tungsten can modulate 3d metal oxides, providing near-optimal adsorption energies for OER intermediates. We developed a room-temperature synthesis to produce gelled oxyhydroxides materials with an atomically homogeneous metal distribution. These gelled FeCoW oxyhydroxides exhibit the lowest overpotential (191 millivolts) reported at 10 milliamperes per square centimeter in alkaline electrolyte. The catalyst shows no evidence of degradation after more than 500 hours of operation. X-ray absorption and computational studies reveal a synergistic interplay between tungsten, iron, and cobalt in producing a favorable local coordination environment and electronic structure that enhance the energetics for OER.

Efficient, cost-effective, and long-lived electrolysers are a crucial missing piece along the path to fuels synthesized with renewable electricity (*1*, *2*). The bottleneck in improving water-splitting technologies is the oxygen-evolving reaction (OER), in which even the most efficient precious-metal catalysts require a substantial overpotential (η) to reach the desired current densities of ≥10 mA cm^{-2} (*2*, *3*). Researchers have explored earth-abundant first-row (3d) transition-metal oxides (*4*–*9*), including 3d metal oxyhydroxides (*4*, *5*), oxide perovskites (*7*), cobalt phosphate composites (*6*), nickel borate composites (*10*), and molecular complexes (*9*, *11*). The OER performance of multimetal oxides based on iron (Fe), cobalt (Co), and nickel (Ni) is particularly promising, and OER activity often outperforms that of the corresponding single-metal oxides (*5*, *12*–*15*).

[1]Department of Electrical and Computer Engineering, University of Toronto, 35 St George Street, Toronto, Ontario M5S 1A4, Canada. [2]Department of Physics, East China University of Science and Technology, 130 Meilong Road, Shanghai 200237, China. [3]Tianjin Key Laboratory of Composite and Functional Materials, School of Materials Science and Engineering, Tianjin University, Tianjin 300072, China. [4]SUNCAT Center for Interface Science and Catalysis, Department of Chemical Engineering, Stanford University, Stanford, CA 94305, USA. [5]SLAC National Accelerator Laboratory, 2575 Sand Hill Road, Menlo Park, CA 94025, USA. [6]Center for Functional Nanomaterials, Brookhaven National Laboratory, Upton, New York 11973, USA. [7]Beijing Synchrotron Radiation Facility, Institute of High Energy Physics, Chinese Academy of Sciences, Beijing 100049, China. [8]Canadian Light Source (CLS), 44 Innovation Boulevard, Saskatoon, SK, S7N 2V3, Canada. [9]Key Laboratory for Ultrafine Materials of Ministry of Education, School of Materials Science and Engineering, East China University of Science and Technology, 130 Meilong Road, Shanghai 200237, China. *These authors contributed equally to this work. **†Corresponding author. E-mail: ted.sargent@utoronto.ca (E.H.S); alevoj@stanford.edu (A.V.)**

We examined whether multimetal oxide OER catalysts could be improved by systematically modulating their 3d electronic structure. Prior results suggest that the introduction of additional metals has a limited impact on the behavior of the 3d metals, likely because of their undesired separation into two noninteracting metal oxide phases (*16*, *17*). For modulation, we focus in particular on tungsten (W), which in its highest oxidation state is a structurally versatile coordination host (*9*, *11*). We began with computational studies aimed at identifying effects of W-modulation of the local coordination environment and the impacts on the resulting electronic structure and on the consequent energetics of the OER. The OER performance of unary Co, Fe, and Ni oxides has been well established both from theory and experiment (*14*, *15*, *18*). Previous computational studies show that the OER activity is mainly driven by the energetics of the OER intermediates (*OH, *O, and *OOH) on the surfaces, with the O to OH adsorption energy difference being the main descriptor for the observed activity trends among these materials (*14*, *15*, *18*). Binary metal oxides such as Ni-Fe and Co-Fe, as well as doped unary oxides, have also been investigated, and their activity can also be predicted by using the above-mentioned descriptor-based approach (*5*, *12*, *13*). Theoretical studies suggest that for a given unary metal oxide, the energetics of OER intermediates can be modulated by incorporating metal elements, and that in turn these tune the catalytic activity of these materials.

Theoretical calculations of ternary and higher mixtures of oxides have been hindered by the complexity of these materials and the associated computational cost. We simplified our approach by starting from the calculated OER energetics for the pure β-CoOOH, γ-FeOOH, and WO_3 phases and estimating the effect of alloying on the energetics of OER intermediates via simple linear interpolation arguments. Our density functional theory plus U (DFT+U) calculations revealed that the adsorption energy of OH is too strong on the FeOOH(010) surface, whereas it is too weak on the CoOOH(01-12) and WO_3(001) surfaces (Fig. 1A) (*19*). To test the interpolation principle, we next calculated the OH adsorption energy on the Fe-doped CoOOH(01-12) surface: This energy falls approximately halfway between the one obtained for the unary CoOOH(01-12) and FeOOH(010) surfaces. Similarly, adding Co into WO_3(001) or adding W into CoOOH(01-12) led to an averaged OH adsorption energy for the $CoWO_4$ system (*20*) and W-doped CoOOH(01-12). By extending this scheme to ternary Co-Fe-W metal-oxide systems, we estimate that FeW-doped CoOOH(01-12) should result in near-optimal *OH energetics for OER.

Next, we proceeded to calculate the energetics of all intermediates (*OH, *O, and *OOH) and extracted overpotentials for the set of unary and Fe- and W-doped surfaces mentioned above [computational methodology is provided (*19*)]. Given the plethora of possible ternary Co-Fe-W oxide alloys, we limited our computational study to the investigation of the above active site motifs, which are also expected to benefit from the interpolation scheme of Fig. 1A. We chose to study only the chemistry of substitutionally metal-doped surface sites. All calculated theoretical OER overpotentials shown in the two-dimensional (2D) volcano plot of Fig. 1B support the general validity of the interpolation scheme not just for *OH energetics, but also for the O to OH adsorption energy difference, denoted as ΔG_O-ΔG_{OH}. The potential limiting kinetic barriers for the reaction were also experimentally determined and found to be small compared with thermodynamics (*19*). The tunability of adsorption energies upon alloying would hence allow for substantial improvement in OER activity.

We found that the OER activity of the unary pure CoOOH(01-12) surface can be improved via single-site doping with subsurface Fe atoms. This improvement can be attributed to the change in ΔG_{OH} and also in ΔG_O-ΔG_{OH} at the Co-site and can be rationalized by the difference in electron affinity between Co^{4+} (at the surface) and Fe^{3+} (subsurface) sites. Furthermore, adding a W dopant in the vicinity of the Co active site of the Fe-doped CoOOH surface (Fig. 1B, inset) further improves the energetics for OER. The substitution of a W dopant at a Co^{4+} site results in (i) migration of protons away from W, which prefers the W^{6+} formal oxidation state, toward oxygen at Co sites, and (ii) compressive strain of larger W atoms on the surrounding Co sites. As a result of these geometric and electronic changes, we identified a favorable direct O_2 mechanism for OER with a theoretical overpotential of only 0.4 V compared with the standard electrochemical OOH mechanism [computational methodology details are provided in (*19*)].

In light of these findings, we sought to devise a controlled process to incorporate W^{6+} into FeCo

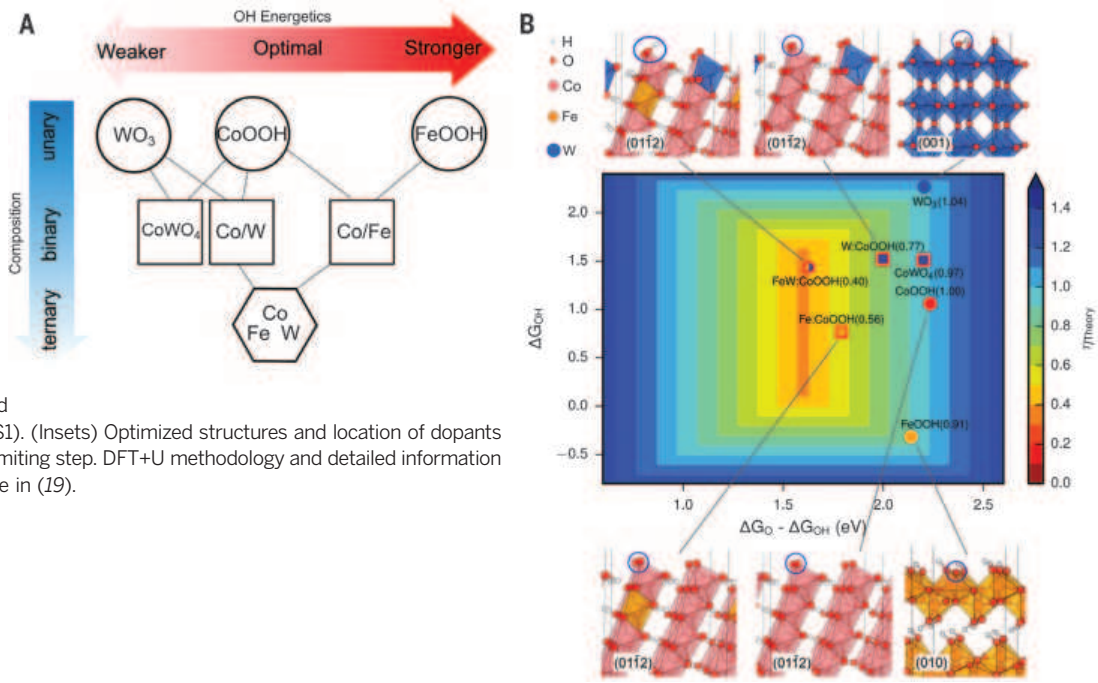

Fig. 1. Tuning the energetics of OER intermediates via alloying. (**A**) Change in OH adsorption energetics (ΔG_{OH}) as a function of increasing composition obtained by interpolation between the calculated pure phases: WO_3 (001), CoOOH (01-12), FeOOH (010), and $CoWO_4$ (010) (*20*). (**B**) OER activities of pure Fe,Co oxyhydroxides and W,Fe-doped Co oxyhydroxides, cobalt tungstate, and W oxides calculated with DFT+U. The optimum is obtained for WFe-doped β-CoOOH (table S1). (Insets) Optimized structures and location of dopants and active sites at the potential limiting step. DFT+U methodology and detailed information about these systems are available in (*19*).

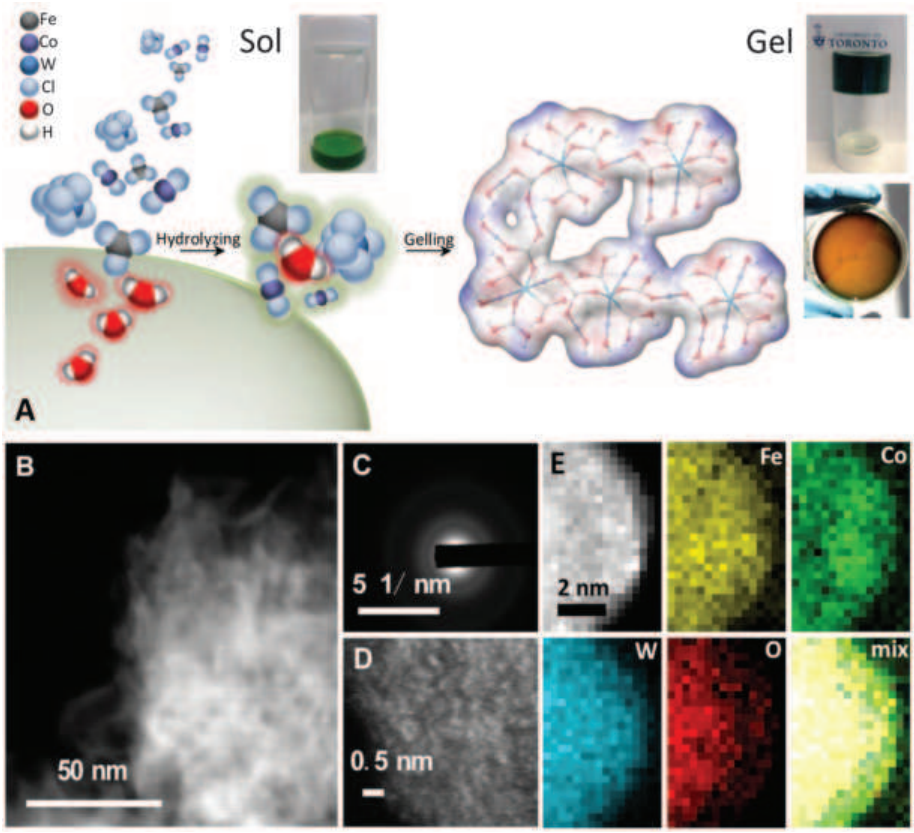

Fig. 2. Preparation of G-FeCoW oxyhydroxides catalysts. (**A**) Schematic illustration of the preparation process for the gelled structure and pictures of the corresponding sol, gel, and gelled film. (**B**) HAADF-STEM image of nanoporous structure of G-FeCoW. (**C**) SAED pattern. (**D**) Atomic-resolution HAADF-STEM image. (**E**) EELS elemental mapping from the G-FeCoW oxyhydroxides sample.

oxyhydroxides in an atomically homogeneous manner. We explored a room-temperature sol-gel procedure that would feature precursors mixed in a homogeneous manner that would be hydrolyzed at a controlled rate so as to achieve atomic homogeneity. First, we dissolved inorganic metal chloride precursors in ethanol. These were controllably hydrolyzed in order to produce a multimetal oxyhydroxide gel via a room-temperature sol-gel process (Fig. 2A) (*21*). The hydrolysis rates of $CoCl_2$, $FeCl_3$, and WCl_6 vary greatly, so very low concentrations of water and propylene oxide were used to tune their hydrolysis independently—a strategy that we anticipated could lead to the desired homogeneous spatial distribution of the three metallic elements (*19*).

After supercritical drying with CO_2, the gel transformed into amorphous metal oxyhydroxides powders. From inductively coupled plasma optical emission spectrometry (ICP-OES) analysis, we determined the molar ratio of Fe:Co:W to be 1:1.02:0.70. Atomic-resolution scanning transmission electron microscopy (STEM) performed in high-angle annular dark field (HAADF) mode (Fig. 2D and fig. S5A), combined with selected-area electron diffraction (SAED) analysis (Fig. 2C), revealed the absence of a crystalline phase. X-ray diffraction (XRD) (fig. S2A) further confirmed that the gelled FeCoW is an amorphous phase (*19*). The STEM measurements show a crumpled and entangled structure composed of nanosheets and nanopores (Fig. 2B). Electron energy loss spectroscopy (EELS) elemental maps with subnanometer resolution (Fig. 2E) showed a uniform, uncorrelated spatial distribution of Fe, Co, and W. The statistics of the atom-pair separation distances, obtained from the STEM elemental maps, show that the nearest-neighbor separations of all

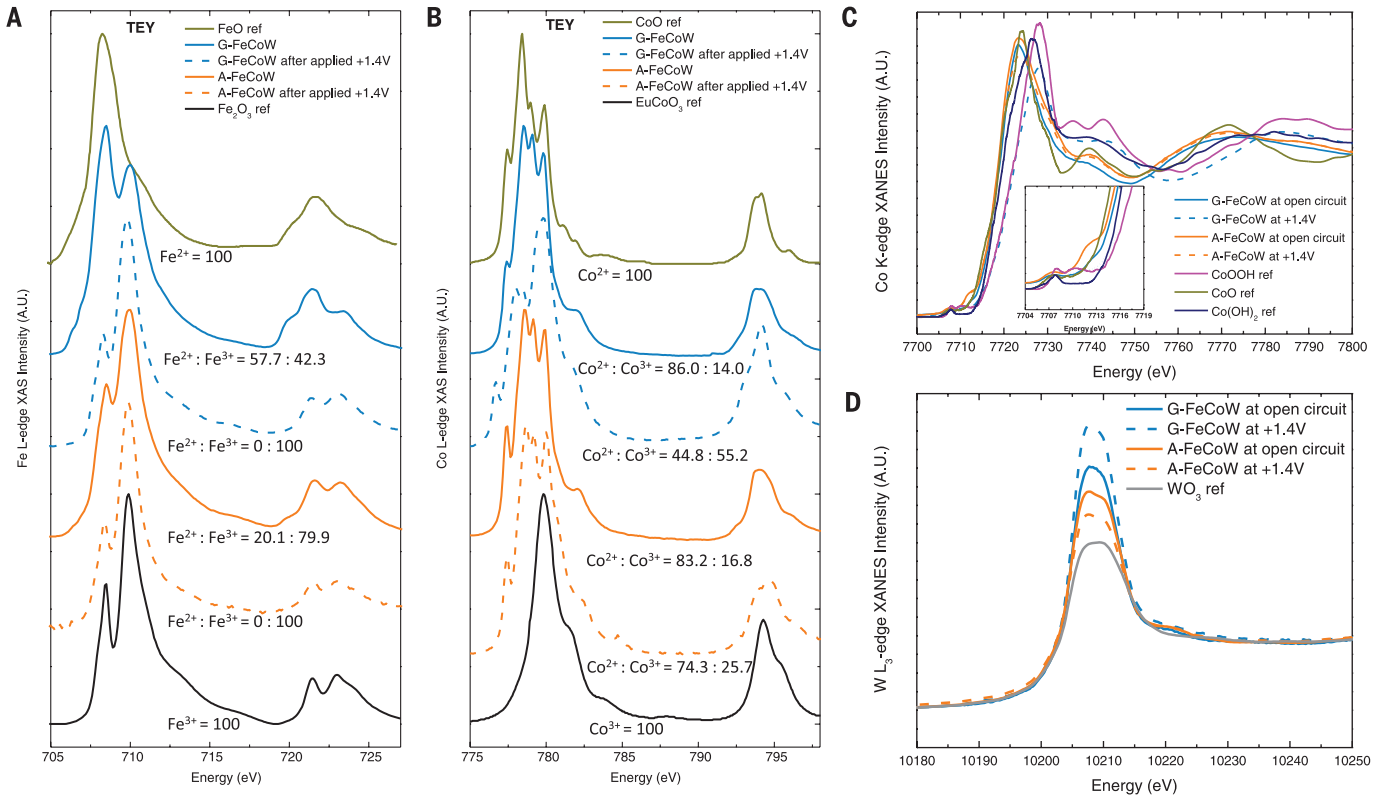

Fig. 3. Surface and bulk x-ray absorption spectra of G-FeCoW oxyhydroxide catalysts and A-FeCoW controls. (**A**) Surface-sensitive TEY XAS scans at the Fe L-edge before and after OER at +1.4 V (versus RHE), with the corresponding molar ratio of Fe^{2+} and Fe^{3+} species. (**B**) Surface-sensitive TEY XAS scans at the Co L-edge before and after OER at +1.4 V (versus RHE). (**C**) Bulk Co K-edge XANES spectra before and after OER at +1.4 V (versus RHE). (Inset) The zoomed in pre-edge profiles. The Co K-edge data of $Co(OH)_2$ and CoOOH are from (*30*). (**D**) Bulk W L3-edge XANES spectra before and after OER at +1.4 V (versus RHE).

Table 1. Comparison of catalytic parameters of G-FeCoW and controls.

Samples	On gold foam	On glassy carbon electrode (GCE)		On Au(111)		References
	Overpotential* (mV)	Overpotential* (mV)	TOF† (s^{-1})	Overpotential* (mV)	ΔH (kJ mol^{-1}) at η=300 mV	
LDH FeCo	279 (±8)	331 (±3)	0.0085	429 (±4)	81	This work
G-FeCo	215 (±6)	277 (±3)	0.043	346 (±4)	60	This work
G-FeCoW	191 (±3)	223 (±2)	0.46 (±0.08)	315 (±5)	49	This work
A-FeCoW	232 (±4)	301 (±4)	0.17	405 (±2)	80	This work
Amorphous-$FeCoO_x$‡	–	300	–	–	–	(*4*)
LDH NiFe	–	300	0.07	–	–	(*25*)
CoOOH	–	–	–	550	–	(*23*)
IrO_2	–	260	0.05	–	–	(*25*)
NiFeOOH	–	340	–	–	66 (-/+5)	(*27*)
$Ni_{60}Co_{40}$ oxides	–	263	–	–	72.6§	(*29*)
NiFe LDH/ GO	–	210	0.1	–	–	(*22*)

*Obtained at the current density of 10 mA cm^{-2}, without *iR* correction. †Obtained at 95% *iR* corrected η = 300 mV, assuming all loaded 3d-metal atoms as active sites. ‡Obtained from the LSV plots at the current density of 4 mA cm^{-2} in 0.1 M KOH aqueous solution. §Obtained at 280 mV in 1M NaOH aqueous solution.

two-metal atom pairs are highly consistent (figs. S3, S4, and S6, A to E) (*19*). This homogeneity results from (i) the homogeneous dispersion of three precursors in solution and (ii) controlled hydrolysis, the latter enabling the maintenance of the homogeneous phase in the final gel state without phase separation of different metals caused by precipitation. In contrast, conventional processes (*17*), even when their precursors are homogeneously mixed, result in crystalline products formed heterogeneously during the annealing process leading to phase separation caused by lattice mismatch. For structural comparison with prior sol-gel reports that used an annealing step (*17*), we annealed the samples at 500°C and

then found crystalline phases (figs. S5B, high-resolution TEM images, and S2B, XRD) that included separated Fe_3O_4, Co_3O_4, and $CoWO_4$. Elemental mapping of this sample (fig. S6, A1 to E1) further confirmed the phase separation of Fe from Co and W atoms (*19*).

We investigated the influence of incorporating W (with its high oxidation state) on the electronic and coordination structures of Fe and Co using x-ray absorption spectroscopy (XAS). We examined (i) conventionally layered double hydroxides of FeCo (LDH FeCo) that have the same structure as the state-of-the-art OER catalysts (LDH NiFe) (*22*), (ii) FeCo oxyhydroxides (without W) prepared via the annealing-free sol-gel process (gelled FeCo, labeled G-FeCo), (iii) gelled FeCoW oxyhydroxides (G-FeCoW), and (iv) annealed G-FeCoW at 500°C (A-FeCoW).

To evaluate the change of oxidation states of metal elements during OER, we performed XAS on the G-FeCoW and A-FeCoW samples before and after OER; the latter condition was realized by oxidizing samples at +1.4 V versus the reversible hydrogen electrode (RHE) in the OER region. XAS in total electron yield (TEY) mode provides information on the near-surface chemistry (below 10 nm). We acquired TEY data at the Fe and Co L-edges on samples prepared ex situ. For comparison, on the same samples we also measured in situ XAS (during OER) at the Fe and Co K-edges via fluorescent yield, a measurement that mainly probes chemical changes in the bulk. TEY XAS spectra in Fig. 3A revealed that the surface Fe^{2+} ions in G-FeCoW had been oxidized to Fe^{3+} at +1.4 V, which is in agreement with thermodynamic data for Fe. However, the oxidation states of Co in G-FeCoW and A-FeCoW samples were appreciably different at +1.4 V. In G-FeCoW, the valence states of both surface (Fig. 3B) and bulk (Fig. 3C) Co were similar to pure Co^{3+}, including only a modest admixture with Co^{2+} (fig. S12); in particular, the Co-K edge profile closely resembled CoOOH (*23*), which is consistent with our DFT model. In contrast, in A-FeCoW (in which W is phase-separated), even after a potential of +1.4 V was applied, the surface (Fig. 3B) and bulk (Fig. 3C) manifested a substantially higher Co^{2+} content (fig. S12), which is consistent with the Co_3O_4 and $CoWO_4$ phases. These oxides had been found to be much less reactive in DFT simulations (*14*, *20*). The bulk and surface Fe and Co edge profiles are shown in figs. S7 to S11 and discussed in (*19*).

The white lines of W L_3-edge x-ray absorption near-edge structure (XANES) spectra of all samples in Fig. 3D show that W in G-FeCoW and A-FeCoW samples before and after OER has a distorted WO_6 octahedral symmetry (*24*). The W L_3 amplitude in pre-OER A-FeCoW was low, a finding attributable to the loss of bound water during annealing (*24*). When a +1.4 V bias was applied, the W L_3 intensity in G-FeCoW increased, indicating that the valence of W decreases, which is consistent with increased distortion of WO_6 octahedra (*24*). This result agrees with the results of DFT, in which W-doped CoOOH(01-12) is expected to produce W residing in a lower oxidation state. These results indicate that Fe and Co also inversely influence W in the homogeneous ternary metal oxyhydroxides.

In situ extended x-ray absorption fine structure (EXAFS) (figs. S13 and S14) on G-FeCoW showed a significant decrease in Co-O bond distance, from 2.06 to 1.91 Å, after a potential of +1.4 V was applied. This decrease is consistent with the reported results that the Co-O bond distance in CoOOH is shorter than that in $Co(OH)_2$ (*23*). EXAFS data at the Fe edge in G-FeCoW show the same trend (figs. S15 and S16). Ex situ EXAFS data before OER are also shown in figs. S17 to S20 and table S3. In contrast, the local structural arrangement in A-FeCoW remains unchanged at 1.4 V. Overall, we conclude that Co in the G-FeCoW structure is more readily oxidized to high valence, which is consistent with G-FeCoW being more active than the control annealed samples.

We compared the OER performance of our gelled sample G-FeCoW with that of the reference samples G-FeCo, LDH FeCo, and A-FeCoW. Representative OER currents of the samples were measured for spin-coated thin films (thickness ~ 30 nm) (fig. S21) (*19*) on a well-defined Au(111) single-crystal electrode (Fig. 4A) in 1 M KOH aqueous electrolyte at a scan rate of 1 mV s^{-1} (currents are uncorrected and thus include the effects of resistive losses incurred within the electrolyte). The G-FeCoW–on-Au(111) required an overpotential of only 315 mV

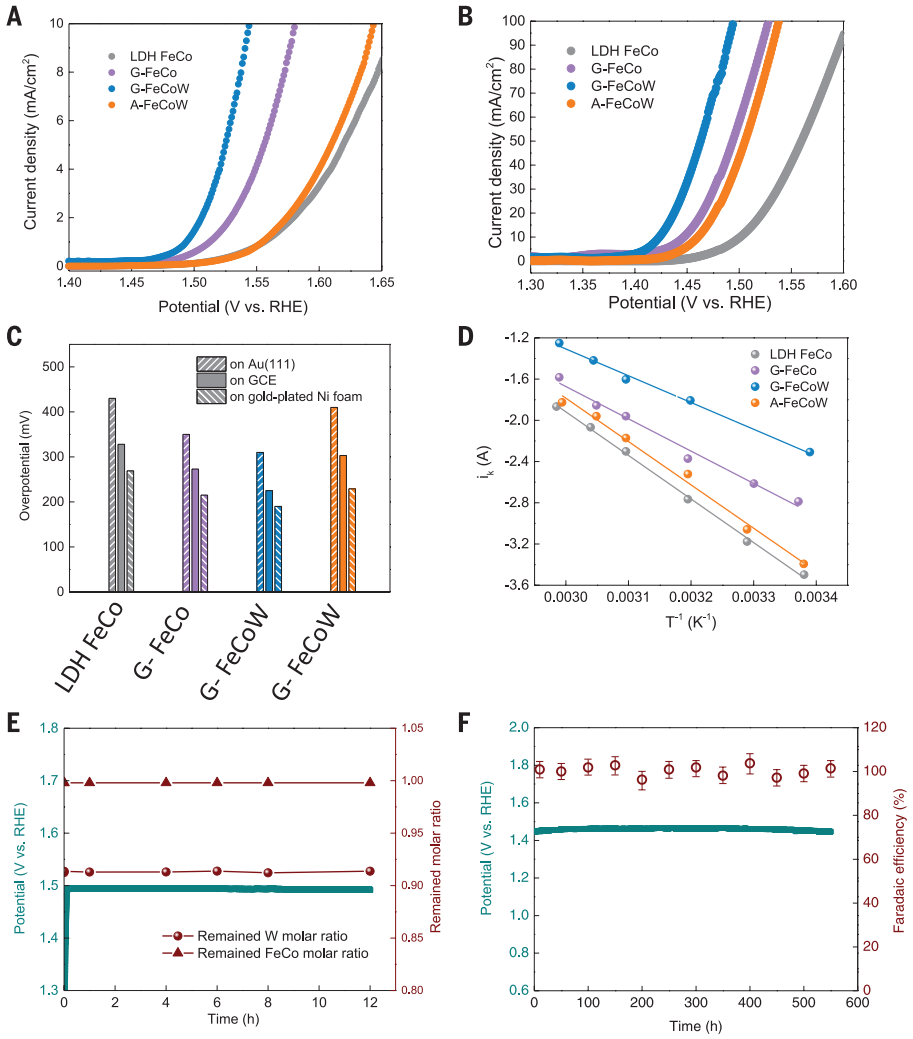

Fig. 4. Performance of G-FeCoW oxyhydroxides catalysts and controls in three-electrode configuration in 1 M KOH aqueous electrolyte. (**A** and **B**) The OER polarization curve of catalysts loaded on two different substrates with 1 mV s^{-1} scan rate, without *iR* correction: (A) Au(111) electrode and (B) gold-plated Ni foam. (**C**) Overpotentials obtained from OER polarization curves at the current density of 10 mA cm^{-2} tested on Au(111), GCE and gold-plated Ni foam, respectively, without *iR* correction. (**D**) Arrhenius plot of the kinetic current at η = 300 mV, tested on Au(111), without *iR* correction. (**E**) Chronopotentiometric curves obtained with the G-FeCoW oxyhydroxides on gold-plated Ni foam electrode with constant current densities of 30 mA cm^{-2}, and the corresponding remaining metal molar ratio in G-FeCoW calculated from ICP-AES results. (**F**) Chronopotentiometric curves obtained with the G-FeCoW oxyhydroxides on gold-plated Ni foam electrode with constant current densities of 30 mA cm^{-2}, and the corresponding Faradaic efficiency from gas chromatography measurement of evolved O_2.

at 10 mA cm^{-2} (Table 1, all current densities based on projected geometric area). This potential is 114 mV lower than that of precipitated FeCo LDH fabricated for the present study. When W was not introduced, the resultant G-FeCo gelled catalyst required an additional overpotential of 31 mV to reach a similar current density. When the gelled sample was subjected to a postsynthetic thermal treatment (500°C anneal), the overpotential of the FeCoW electrode increased to 405 mV at 10 mA cm^{-2}.

To assess the impact of the electrode support and compare the performance of the new catalysts with the state-of-the-art NiFeOOH, we tested on glassy carbon electrode (GCE) using the identical three-electrode system and with a catalyst loading mass of 0.21 mg cm^{-2}. The trend of the overpotentials remains the same (fig. S22), with the G-FeCoW–on-GCE electrode requiring an overpotential of 223 mV at 10 mA cm^{-2}. Without carbon additives, and without *iR* corrections (*i*, current; *R*, resistance), the G-FeCoW catalyst consistently outperforms the best oxide catalysts previously reported (Table 1) (*4*, *22*, *25*).

Next, we investigated whether the OER-performance of G-FeCoW originates from intrinsic catalytic activity of multimetal active sites or exclusively from an enhanced surface area. We analyzed the Brunauer-Emmett-Teller (BET) surface area, which allowed us to report normalized kinetic current density (referred to as specific activity) as a function of potential versus RHE (*7*). We confirmed that the intrinsic activity of G-FeCoW is notably higher than that of the controls and also higher than those previously reported (fig. S26) (*7*).

The intrinsic activity of G-FeCoW was further confirmed by determining the mass activities and turnover frequencies (TOFs) for this catalyst. We used data obtained on GCE with 95% *iR* correction at η = 300 mV (the remaining data in this work are not corrected by 95% *iR*, unless stated). As shown in Table 1 and tables S5 and S9 (*19*), the G-FeCoW catalysts on GCE exhibit TOFs of 0.46 s^{-1} per total 3d metal atoms and mass activities of 1175 A g^{-1} (considering the total loading mass on the lower limiting case). If only considering electrochemically active 3d metals or mass (obtained from the integration of Co redox features) (*26*), G-FeCoW catalysts exhibit much higher TOFs of 1.5 s^{-1} and 3500 A g^{-1}. These are more than three times above the TOF and mass activities of the optimized control catalysts and the repeated state-of-the-art NiFeOOH (table S9) (*5*, *26*).

To assess the kinetic barriers involved in OER, we studied the effect of temperature on the performance of the catalysts (fig. S27). OER proceeds more rapidly at elevated temperatures, reflecting the exponential temperature dependence of the chemical rate constant (*27*). The Arrhenius plots at η = 300 mV for four different catalysts (Fig. 4D) allowed us to extract electrochemical activation energies that agree well with the values reported previously (Table 1) (*27*). We found that G-FeCoW has the lowest apparent barrier value of 49 kJ mol^{-1}. The similar data obtained for all catalysts suggests that OER proceeds via the same potential-determining step on all catalysts investigated in this work.

To obtain a highly efficient catalytic electrode, we increased the conductivity of the substrate by loading our catalysts on a nickel foam that was covered with gold in order to avoid any spurious effects arising from interaction of the catalyst with Ni. The activity trends of catalysts remained the same as observed on the Au(111) surface and GCE, whereas the absolute performance of each sample was substantially improved (Fig. 4B). The G-FeCoW showed a low overpotential of 191 mV at 10 mA cm^{-2} on the gold-plated nickel foam (projected geometric area) (Table 1). On the basis of the above discussion and the overpotentials on Au(111), gold foam, GCE, and fluorine-doped tin oxide (Fig. 4C, fig. S30, and table S6), it can be seen that the catalytic activity of G-FeCoW is much higher than that of the annealed control (A-FeCoW), gelled FeCo without W (G-FeCo), and the LDH FeCo having the same structure as the state-of-the-art LDH NiFeOOH OER catalysts.

The operating stability of the OER catalysts is essential to their application (*28*). To characterize the performance stability of the G-FeCoW catalysts, we ran water oxidation on the catalyst deposited on gold-plated Ni foam under constant current of 30 mA cm^{-2} continuously for 550 hours. We observed no appreciable increase in potential in this time interval (Fig. 4, E and F). To check that the catalyst remained physically intact, we tested in situ its mass using the electrochemical quartz crystal microbalance (EQCM) technique (figs. S31 and S32) and also assessed whether any metal had leached into the electrolyte by using inductively coupled plasma atomic emission spectroscopy (ICP-AES) (figs. S33 to S36 and table S7). After the completion of an initial burn-in period in which (presumably unbound) W is shed into the electrolyte, we saw stable operation and no discernible W loss. EELS mapping of G-FeCoW after OER (fig. S37) indicates that the remaining W continues to be distributed homogeneously in the sample. By measuring the O_2 evolved from the G-FeCoW/gold-plated Ni foam catalyst, we also confirmed the high activity throughout the entire duration of stability test, obtaining quantitative (unity Faradaic efficiency) gas evolution of O_2 to within our available ±5% experimental error (Fig. 4F). These findings suggest that modulating the 3d transition in metal oxyhydroxides by using a suitable transition metal, one closely atomically coupled through homogeneous solid-state dispersion, may provide further avenues to OER optimization.

REFERENCES AND NOTES

1. C. R. Cox, J. Z. Lee, D. G. Nocera, T. Buonassisi, *Proc. Natl. Acad. Sci. U.S.A.* **111**, 14057–14061 (2014).
2. J. Luo *et al.*, *Science* **345**, 1593–1596 (2014).
3. M. Schreier *et al.*, *Nat. Commun.* **6**, 7326 (2015).
4. R. D. L. Smith *et al.*, *Science* **340**, 60–63 (2013).
5. D. Friebel *et al.*, *J. Am. Chem. Soc.* **137**, 1305–1313 (2015).
6. M. W. Kanan, D. G. Nocera, *Science* **321**, 1072–1075 (2008).
7. J. Suntivich, K. J. May, H. A. Gasteiger, J. B. Goodenough, Y. Shao-Horn, *Science* **334**, 1383–1385 (2011).
8. A. Vojvodic, J. K. Nørskov, *Science* **334**, 1355–1356 (2011).
9. Q. Yin *et al.*, *Science* **328**, 342–345 (2010).
10. M. Dincă, Y. Surendranath, D. G. Nocera, *Proc. Natl. Acad. Sci. U.S.A.* **107**, 10337–10341 (2010).
11. F. M. Toma *et al.*, *Nat. Chem.* **2**, 826–831 (2010).
12. M. S. Burke, M. G. Kast, L. Trotochaud, A. M. Smith, S. W. Boettcher, *J. Am. Chem. Soc.* **137**, 3638–3648 (2015).
13. M. W. Louie, A. T. Bell, *J. Am. Chem. Soc.* **135**, 12329–12337 (2013).
14. M. Bajdich, M. García-Mota, A. Vojvodic, J. K. Nørskov, A. T. Bell, *J. Am. Chem. Soc.* **135**, 13521–13530 (2013).
15. C. C. L. McCrory *et al.*, *J. Am. Chem. Soc.* **137**, 4347–4357 (2015).
16. J. A. Haber *et al.*, *Energy Environ. Sci.* **7**, 682–688 (2014).
17. J. A. Haber, E. Anzenburg, J. Yano, C. Kisielowski, J. M. Gregoire, *Adv. Ener. Mat.* **5**, 1402307 (2015).
18. P. Liao, J. A. Keith, E. A. Carter, *J. Am. Chem. Soc.* **134**, 13296–13309 (2012).
19. Materials and methods are available as supplementary materials on *Science* Online.
20. C. Ling, L. Q. Zhou, H. Jia, *RSC Adv.* **4**, 24692–24697 (2014).
21. V. Augustyn *et al.*, *Nat. Mater.* **12**, 518–522 (2013).
22. W. Ma *et al.*, *ACS Nano* **9**, 1977–1984 (2015).
23. R. Subbaraman *et al.*, *Nat. Mater.* **11**, 550–557 (2012).
24. A. Balerna *et al.*, *Nucl. Instrum. Methods Phys. Res. A* **308**, 240–242 (1991).
25. F. Song, X. Hu, *Nat. Commun.* **5**, 4477 (2014) .
26. A. S. Batchellor, S. W. Boettcher, *ACS Catal.* **5**, 6680–6689 (2015).
27. J. R. Swierk, S. Klaus, L. Trotochaud, A. T. Bell, T. D. Tilley, *J. Phys. Chem. C* **119**, 19022–19029 (2015).
28. N. Danilovic *et al.*, *Angew. Chem. Int. Ed. Engl.* **126**, 14240–14245 (2014).
29. F. Rosalbino, S. Delsante, G. Borzone, G. Scavino, *Int. J. Hydrogen Energy* **38**, 10170–10177 (2013).
30. D. Friebel *et al.*, *Phys. Chem. Chem. Phys.* **15**, 17460–17467 (2013).

ACKNOWLEDGMENTS

This work was supported by the Ontario Research Fund–Research Excellence Program, Natural Sciences and Engineering Research Council of Canada, and the Canadian Insititute for Advanced Research Bio-Inspired Solar Energy program. B.Z. acknowledges funding from China Scholarship Council/University of Toronto Joint Funding Program (201406745001), Shanghai Municipal Natural Science Foundation (14ZR1410200), and the National Natural Science Foundation of China (21503079). X.Z. acknowledges a scholarship from the China Scholarship Council (CSC) (20140625004). This work was also supported by the U.S. Department of Energy (DOE), Office of Basic Energy Science grant to the SUNCAT Center for Interface Science and Catalysis and the Laboratory-Directed Research and Development program funded through the SLAC National Accelerator Laboratory. M.G.-M. acknowledges funding from the Agency for Administration of University and Research Grants of Catalonia (AGAUR, 2013 BP-A 00464). This work has also benefited from the Hard X-ray Micro-Analysis and Spherical Grating Monochromator beamlines at CLS and the BL14W1 beamline at the Shanghai Synchrotron Radiation Facility (SSRF). B.Z. and R.C. acknowledge the CLS Post-Doctoral Student Travel Support Program. The TEM study in this work is supported by the Center for Functional Nanomaterials, which is a DOE Office of Science Facility, at Brookhaven National Laboratory under contract DE-SC0012704. E.Y. acknowledges a Fundação de Amparo à Pesquisa do Estado de São Paulo–Bolsa Estágio de Pesquisa no Exterior (2014/18327-9) fellowship. E.H.S. and F.P.G.A acknowledge funding from the Connaught Global Challenge program of the University of Toronto. The authors thank D. Bélanger and G. Chamoulaud at Université du Québec à Montréal for assistance in EQCM measurements and T.-O. Do and C.-C. Nguyen at Laval University for surface area analysis. The authors thank Y. J. Pang, X. Lan, L. N. Quan, and S. Hoogland for fruitful discussions; M. X. Liu and X. W. Gong for fabrication assistance; and R. Wolowiec and D. Kopilovic for assistance. B.Z., X.Z., J.X., M.L., C.T.D, and E.H.S. of the University of Toronto have filed provisional patent application no. 62288648 regarding the preparation of multimetal catalysts for oxygen evolution.

SUPPLEMENTARY MATERIALS

www.sciencemag.org/content/352/6283/333/suppl/DC1
Materials and Methods
Figs. S1 to S43
Tables S1 to S9
References (*31*–*56*)

23 December 2015; accepted 9 March 2016
10.1126/science.aaf1525

CORAL REEFS

Climate change disables coral bleaching protection on the Great Barrier Reef

Tracy D. Ainsworth,[1*†] Scott F. Heron,[2,3*] Juan Carlos Ortiz,[4,5*] Peter J. Mumby,[4,5] Alana Grech,[6] Daisie Ogawa,[1,7] C. Mark Eakin,[2] William Leggat[1,7*]

Coral bleaching events threaten the sustainability of the Great Barrier Reef (GBR). Here we show that bleaching events of the past three decades have been mitigated by induced thermal tolerance of reef-building corals, and this protective mechanism is likely to be lost under near-future climate change scenarios. We show that 75% of past thermal stress events have been characterized by a temperature trajectory that subjects corals to a protective, sub-bleaching stress, before reaching temperatures that cause bleaching. Such conditions confer thermal tolerance, decreasing coral cell mortality and symbiont loss during bleaching by over 50%. We find that near-future increases in local temperature of as little as 0.5°C result in this protective mechanism being lost, which may increase the rate of degradation of the GBR.

In the past three decades, bleaching events have caused reef-wide declines in coral across the Great Barrier Reef (GBR) (*1*). Coral bleaching is a stress response that results in the loss of intracellular symbiotic dinoflagellates (*Symbiodinium*) and/or their photosynthetic pigments; on a broad spatial scale, bleaching results from extended warm periods (*1*). The frequency and intensity of such bleaching events are expected to increase as sea surface temperature (SST) continues to rise under climate change (*2*, *3*). Acclimatization and adaptation to future temperature conditions have been suggested as mechanisms by which corals may withstand increasing SST, reducing the severity of coral bleaching and ameliorating mortality (*4*–*6*). Although the extent of adaptation remains uncertain (*7*), processes of acclimatization have been studied empirically. An important driver of thermal acclimatization in any organism is the variance of temperature to which it is exposed (*8*). Sub-lethal pre-stress events reset physiological and molecular mechanisms that underpin the innate stress response, and provide a means to survive subsequent stress events (*9*). However, the influence of pre-stress events on thermal tolerance is not well understood in marine ecosystems. Here we show that such pre-stress events do occur on the GBR and serve to increase physiological preparation for the intense thermal stress that results in coral bleaching. We provide experimental evidence to show that this mechanism has probably reduced the impact of historical bleaching events, and we predict that such protective pre-stress events could disappear within a few decades.

To quantify the thermal regimes that GBR corals have experienced, we examined 27 years of satellite-based SST records (at a resolution of 0.5°) and found that 372 thermal stress events, capable of causing bleaching, occurred across 115 reef pixels (*10*). We identified three thermal trajectories associated with past bleaching events,

[1]Australian Research Council Centre of Excellence for Coral Reef Studies, James Cook University, Townsville 4810, Australia. [2]Coral Reef Watch, U.S. National Oceanic and Atmospheric Administration (NOAA), College Park, MD 20740, USA. [3]Marine Geophysical Laboratory, College of Science, Technology and Engineering, James Cook University, Townsville 4811, Australia. [4]Marine Spatial Ecology Lab, School of Biological Sciences, University of Queensland, Brisbane 4072, Australia. [5]Australian Research Council Centre of Excellence for Coral Reef Studies, University of Queensland, Brisbane 4072, Australia. [6]Department of Environmental Sciences, Macquarie University, Sydney 2109, Australia. [7]The College of Public Health, Medical and Veterinary Sciences, James Cook University, Townsville 4810, Australia.
*These authors contributed equally to this work. **†Corresponding author. E-mail: tracy.ainsworth@jcu.edu.au**

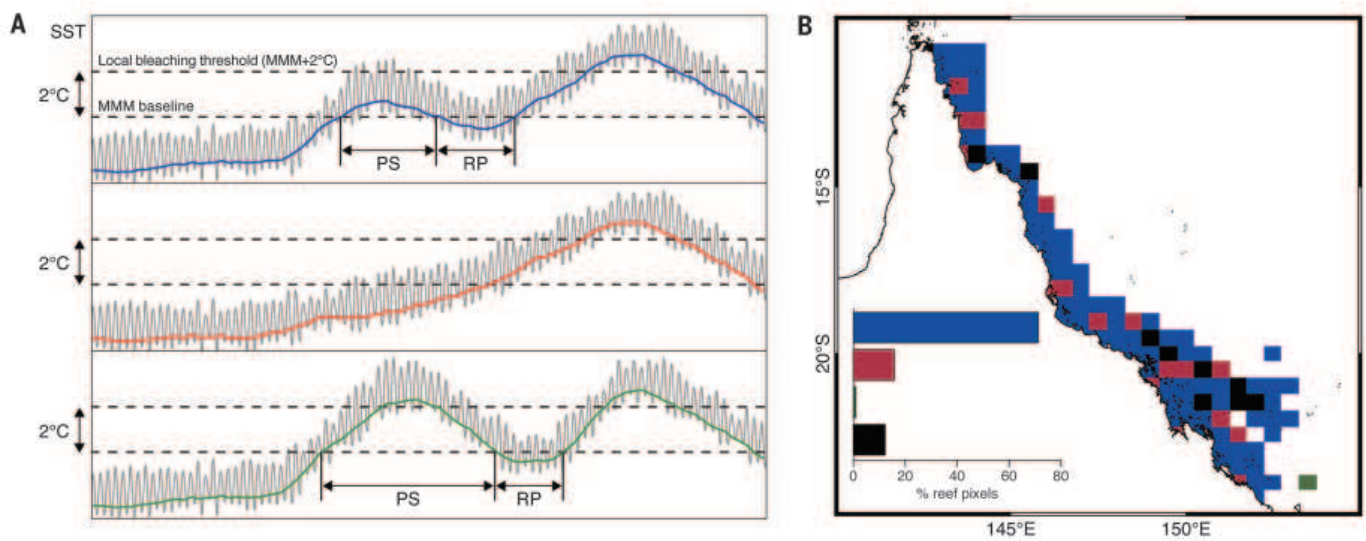

Fig. 1. Sea temperature trajectories before and during coral bleaching stress events on the GBR. (**A**) Schematic of the three temperature trajectories on the GBR during previous (the past 27 years) bleaching level thermal anomalies, where SST reached the local bleaching threshold, 2°C above the local MMM baseline. (Top, blue line) protective trajectory; (middle, red line) single bleaching trajectory; and (bottom, green line) repetitive bleaching trajectory. The black line represents diurnal temperature variation; the colored lines reflect the nighttime-only satellite data. The pre-stress period (PS) is the duration of the pre-stress pulse exceeding the MMM; the recovery period (RP) is the duration below the MMM after the pulse. The horizontal axis spans 90 days. (**B**) The predominant trajectory for each reef pixel (n = 115) is shown by color as for (A), except that green shows equal incidence of repetitive and protective trajectories (no pixels were predominated by the repetitive trajectory). Black pixels indicate that the local bleaching threshold (MMM+2°C) was never reached. The histogram (inset) shows the frequency of the predominant trajectories for reef pixels (table S2).

characterized by the presence and intensity of a pre-stress (sub-bleaching) warming period (Fig. 1A and fig. S1). Warming events were quantified relative to two thresholds: (i) the long-term maximum monthly mean (MMM) temperature, which sets a baseline from which warming can be identified; and (ii) the local coral bleaching threshold (MMM+2°C) (*11*). The predominant trajectory, accounting for 75% of thermal stress events (n = 277), was characterized by an SST event that exceeded the local MMM but remained below the bleaching threshold. The SST then returned below the MMM, for an average recovery period of 10 days, before increasing above the local bleaching threshold (Fig. 1A and table S1); we term this the protective trajectory. The second trajectory was characterized by a direct SST increase from below the MMM to exceed the local bleaching threshold, with no pre-stress or recovery period. This trajectory, which we term the single bleaching trajectory, occurred in 20% (n = 77) of thermal stress events (Fig. 1, A and B). The final trajectory exceeded the local bleaching threshold in two peaks, separated by an average recovery period of 9 days below the local MMM (Fig. 1, A and B, and table S1). We term this the repetitive bleaching trajectory, and it accounted for 5% (n = 18) of identified thermal stress events on the GBR (Fig. 1B).

Having identified three thermal trajectories in situ, we studied the physiological response of corals to each temperature trajectory under experimental conditions, using the model species *Acropora aspera* (*10*). Corals exposed to the protective trajectory underwent characteristic alterations (*12–15*) of the symbiotic organisms' photochemistry and heat stress responses that led to the acquisition of thermal tolerance and reduced bleaching and coral cell death (Fig. 2). Cell death is a conserved response to thermal stress and represents the cellular driver of partial- and whole-colony mortality (*16*). Using a multivariate analysis, we showed that the different temperature trajectories result in distinct expression profiles of stress-related genes during coral bleaching (Fig. 2A and tables S7 and S8). Specifically, the gene expression of corals under the protective trajectory differed significantly from that under both the single bleaching (P = 0.03) and repetitive bleaching (P = 0.02) trajectories, and was more similar to that found in corals not exposed to thermal stress (Fig. 2A). Gene expression in the single bleaching and repetitive bleaching trajectories was indistinguishable (P = 0.422). These gene expression profiles were associated with lower levels of localized cell death under the protective trajectory (30 ± 4% of cells) than either the single bleaching trajectory (56 ± 4%) or repetitive bleaching trajectory (70 ± 2%) (Fig. 2B, C). In addition, the extent of bleaching (*Symbiodinium* loss) was less (P < 0.01) in corals exposed to the protective than either of the other two trajectories (Fig. 2B and table S6). In short, corals and their endosymbiotic *Symbiodinium* acquired thermal tolerance after exposure to the sublethal, pre-stress protective trajectory that has predominated throughout the GBR over the past 27 years. However, corals experiencing the single bleaching and repetitive bleaching trajectories did not acquire thermal tolerance, which resulted in poorer physiological outcomes and a greater loss of symbionts and coral tissue during coral bleaching.

Given that sea temperatures are steadily rising, an obvious concern is that the sub-bleaching temperature event of the protective trajectory could eventually exceed the bleaching threshold, switching events from being protective to becoming increasingly lethal. To examine how climate change is projected to alter our three bleaching trajectories, we applied temperature offsets to the observed 27-year time series of SST (*10*), which implicitly incorporates spatially variable interannual variation and ENSO events (Fig. 3, A to T). We took this approach because climate model predictions are incapable of resolving meaningful spatial variation in the rate of warming across the GBR (*17*). This approach was validated by the correlation between historical annual maximum SST and summer-average SST [linear regression slope = 0.98, coefficient of determination (r^2) = 0.82], which supports the hypothesis that all summer temperatures will increase consistently (fig. S2). Moreover, the drivers of SST pulsing (wind speed, solar radiation, and tidal flow; see the supplementary text) are expected to exhibit less than a 2% change by 2100 under most climate models (*18*). Our simulations project that if SST increases by +2°C, as could occur by 2100 under current warming trajectories, the number of thermal stress events will increase (Fig. 3, A to E). Within these, the proportion of events benefiting from the protective trajectory falls by two-thirds, from 75% (historical) to only 22% (Fig. 3, F to J). Concurrently, the proportion of single bleaching

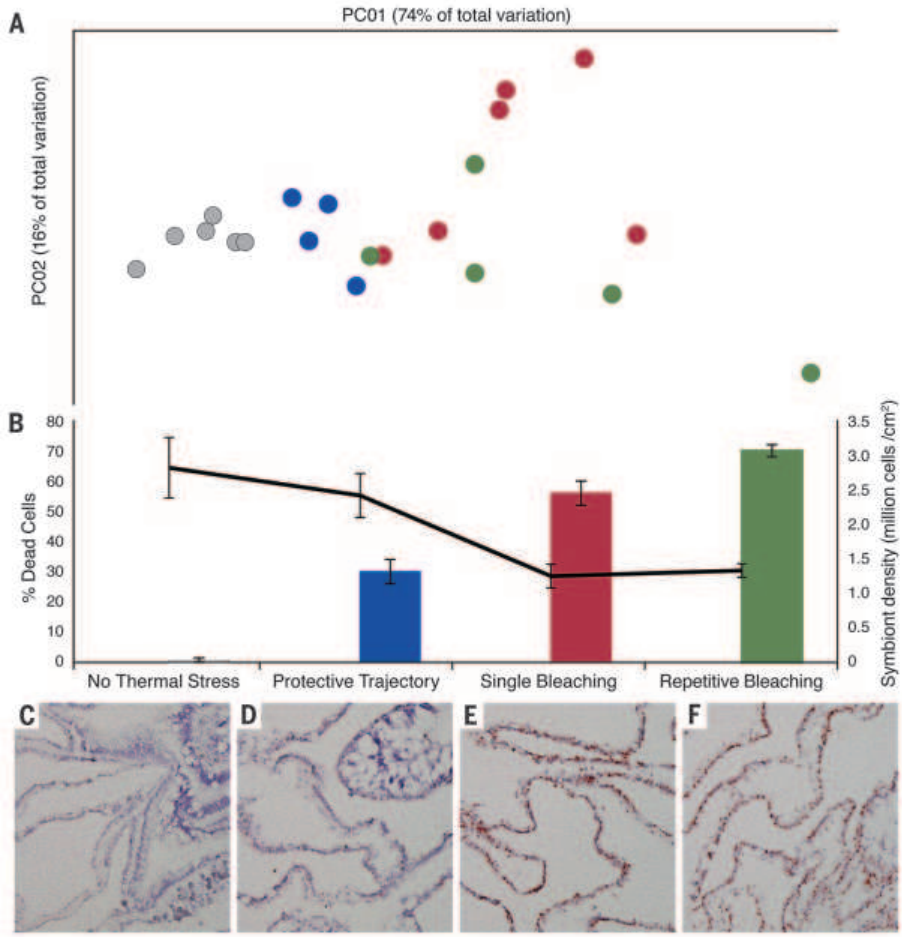

Fig. 2. Effects of temperature trajectories on cell death and *Symbiodinium* cell density of *A. aspera* at bleaching. (**A**) Principal coordinate ordination plot of the gene expression patterns of the apoptotic genes (*Bcl-2*, *Bak*, *Bok*, *Bax*, *Bak*, *Bl*, and *BlR*) under ambient conditions (no thermal stress; white) and the three temperature trajectories: protective (blue), single bleaching (red), and repetitive bleaching (green). Each point represents an individual coral. PC01, principal coordinate ordination axis 1; PC02, principal coordinate ordination axis 2. (**B**) Coral cell death (bars) and *Symbiodinium* density (lines) at bleaching; colors are as for (A). (**C** to **F**) In situ end labeling of coral tissue exposed to (C) ambient conditions and the (D) protective, (E) single bleaching, and (F) repetitive bleaching trajectories. Healthy haematoxylin-counterstained nuclei are stained blue, In situ end-labeled nuclei undergoing cell death are stained red.

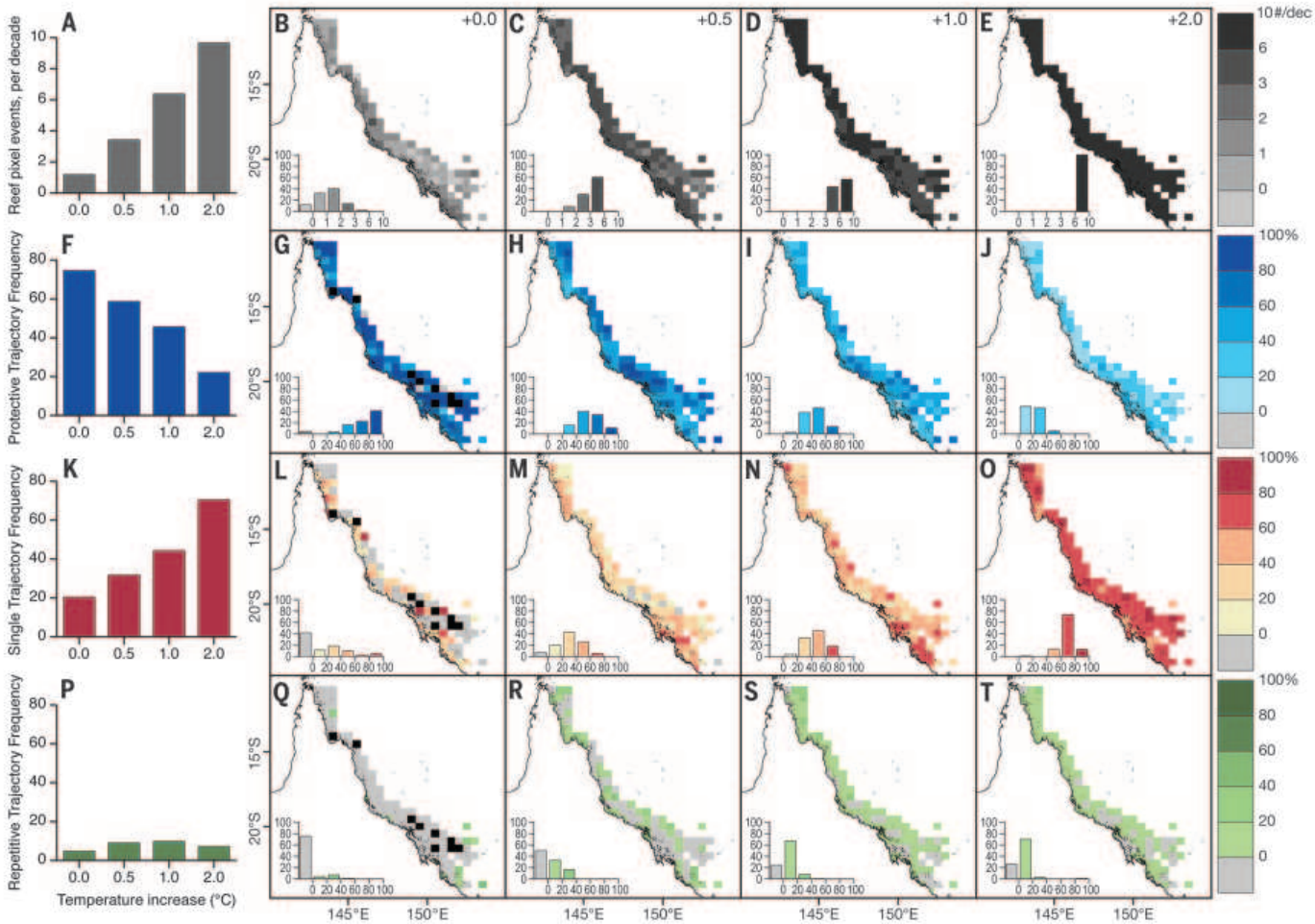

Fig. 3. Projected changes in the frequency of thermal stress events, and SST trajectories, with +0.5°C, +1.0°C, and +2.0°C SST warming. Stress event frequency at 50-km reef pixels (**A**) averaged across the GBR; and spatial distribution under (**B**) recent conditions, and (**C**) +0.5°C, (**D**) +1.0°C, and (**E**) +2.0°C projections. Proportions of events from each trajectory are as follows: (**F** to **J**) protective, (**K** to **O**) single bleaching, (**P** to **T**) repetitive bleaching. Inset histograms show the percentage of reef pixels (vertical axis) with [(B) to (E)] bleaching frequency per decade (horizontal axis) or [(G) to (J), (L) to (O), and (Q) to (T)] trajectory frequency (horizontal axis) for each projected warming. Black pixels in (B), (G), (L), and (Q) indicate that no severe stress events occurred (not present in projected warming).

trajectory events will increase from 21% (Fig. 3, K and L) to 71% (Fig. 3, K and O), implying that thermal stress events become far more lethal for corals. The proportion of repetitive bleaching did not dramatically increase (5 to 7%), but the absolute number increased from 18 to 219 reef pixels experiencing this temperature regime over a 10-year period (Fig. 3, P to T, and table S2).

We predict that most of the reefs that have only experienced the protective trajectory to date (gray in Fig. 3, L and Q) will begin to experience the single and repetitive bleaching trajectories when SST is approximately 0.5°C higher than present (Fig. 3, M and R, and insets in H, M, and R), which will be within 4 decades at historical warming rates (*19*). The sensitivity of reefs to such warming varies geographically (Fig. 3, H, M, and R). For example, reefs in the southern GBR could experience more single bleaching trajectory events at lower temperature increases than elsewhere on the GBR (Fig. 3, L to O). Once there is a 1°C increase in SST, the majority of reefs are likely to experience single trajectory bleaching at least once per decade (Fig. 3, D and N).

The prevalence of an SST trajectory on the GBR that can stimulate thermal tolerance has not previously been recognized, nor has the effect of this induced tolerance on mitigating bleaching events been examined. Acroporid corals, such as *A. aspera* used here, are some of the most important taxa in driving rapid recovery and resilience in Pacific coral reefs (*3*). We therefore integrated our experimental results into a validated simulation model for GBR coral communities (*3*) and evaluated how corals would fare under contrasting emissions scenarios being considered by the Intergovernmental Panel on Climate Change: business-as-usual representative concentration pathway 8.5 (RCP8.5) (*20*) and a low-carbon economy in which CO_2 concentrations are limited to a peak of 450 parts per million by 2040, RCP2.6 (*21*). We used the relative proportions of dead cells within corals that occurred after experimental exposure to the three SST trajectories (Fig. 2B) as a proxy for estimating the extent of coral colony mortality during each type of thermal stress event (*10*). Under business-as-usual (high) carbon emissions, the long-term outlook of reefs was bleak, irrespective of their current thermal trajectory (Fig. 4, A, C, and E); coral cover became low (<5%) toward the end of the century. However, the protective trajectory delayed the onset of this condition by approximately 20 years, which may yet prove to be evolutionarily significant. Moving to aggressive action to reduce greenhouse gas emissions, the outlook for reefs was far better, particularly on reefs experiencing the protective trajectory, where no net long-term decline was predicted (Fig. 4B). However, even under aggressive action, coral cover on reefs exposed to the single and repetitive bleaching trajectories will fall below 5% (Fig. 4, D and F).

Although our ecosystem model now allows for processes of thermal acclimatization, it does not provide for adaptation, mostly because the rates and mechanisms of adaptation in corals remain

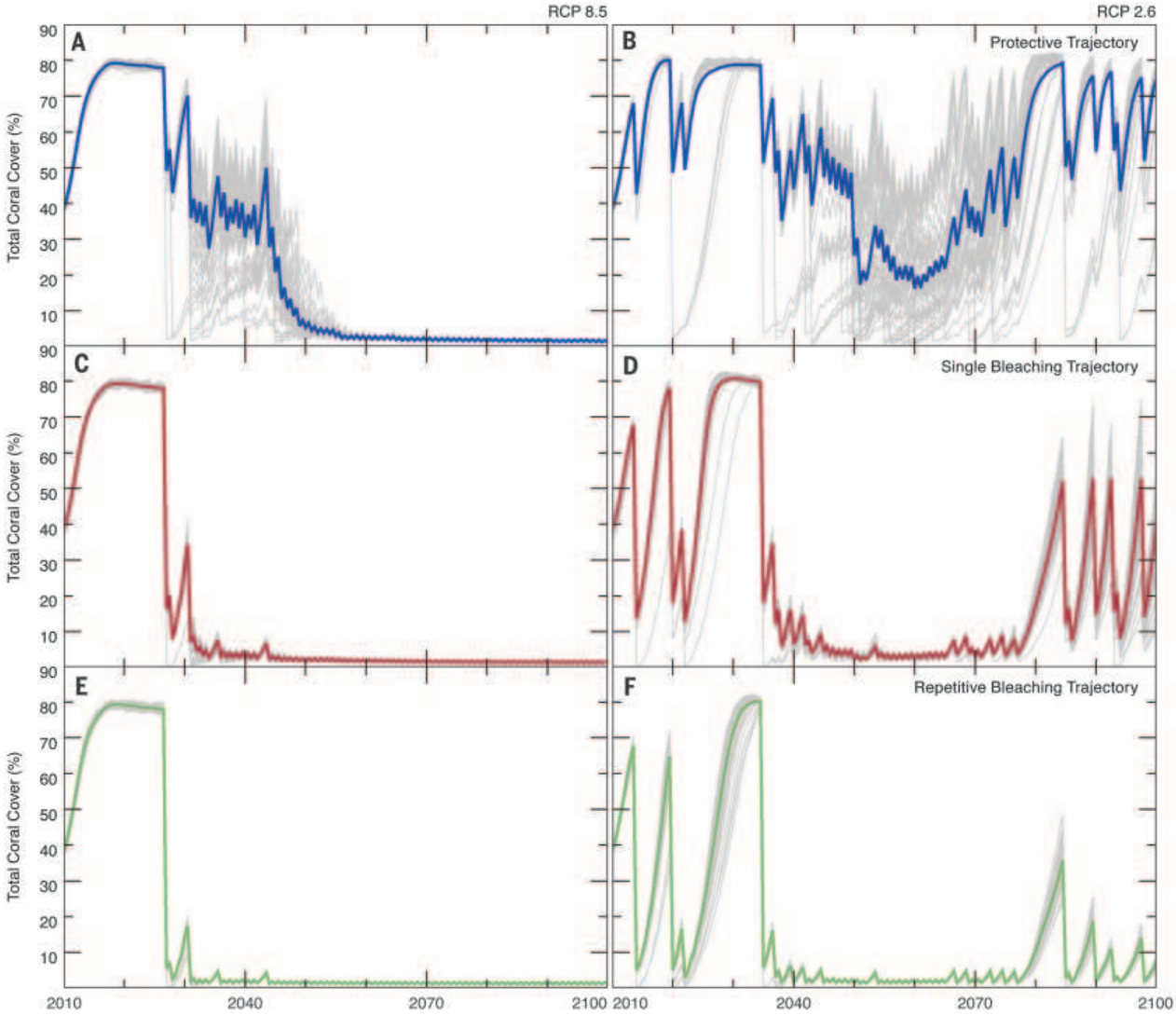

Fig. 4. Coral cover simulations under high (A, C, and E) and low (B, D, and F) CO_2 emission scenarios (RCP8.5 and RCP2.6). This incorporates differential mortality rates associated with protective [(A) and (B)] single bleaching [(C) and (D)] and repetitive bleaching [(E) and (G)] trajectories. Colored lines represent the average coral cover among simulations; gray lines represent the trajectory of each of the 50 simulations for each scenario.

uncertain (*7*). Adaptation may mitigate the impact of climate change and improve the chances of coral reef ecosystem recovery (*4*, *6*, *22–24*).

Reefs of the GBR experience a variety of disturbances, only some of which are subject to management interventions. Our analysis reveals that the exposure to sub-lethal pre-stress events varies dramatically among reefs, with some having an inherent level of "protection from" or "preparedness for" the conditions that induce coral bleaching, whereas others experience multiple stress exposures in a single event. Recognizing such spatial variability is important when targeting management actions that aim to mitigate coral reef degradation in the future. For example, local management interventions that reduce cumulative stress impacts (such as impacts caused by pollution, sedimentation, and crown-of-thorns starfish outbreaks) could be prioritized toward reefs that exhibit protective trajectories, thereby serving to minimize biological and physical stressors simultaneously and helping to build ecosystem resilience.

REFERENCES AND NOTES

1. G. De'ath, J. M. Lough, K. E. Fabricius, *Science* **323**, 116–119 (2009).
2. R. van Hooidonk, J. A. Maynard, S. Planes, *Nat. Clim. Change* **3**, 508–511 (2013).
3. J. C. Ortiz, Y.-M. Bozec, N. H. Wolff, C. Doropoulos, P. J. Mumby, *Nat. Clim. Change* **4**, 1090–1094 (2014).
4. J. M. Pandolfi, S. R. Connolly, D. J. Marshall, A. L. Cohen, *Science* **333**, 418–422 (2011).
5. C. R. Voolstra *et al.*, *PLOS One* **6**, e20392 (2011).
6. S. R. Palumbi, D. J. Barshis, N. Traylor-Knowles, R. A. Bay, *Science* **344**, 895–898 (2014).
7. P. J. Mumby, R. van Woesik, *Curr. Biol.* **24**, R413–R423 (2014).
8. J. J. Ruel, M. P. Ayres, *Trends Ecol. Evol.* **14**, 361–366 (1999).
9. D. B. Berry, A. P. Gasch, *Mol. Biol. Cell* **19**, 4580–4587 (2008).
10. Materials and methods are available as supplementary materials on *Science* Online.
11. E. T. Game, M. E. Watts, S. Wooldridge, H. P. Possingham, *Ecol. Appl.* **18**, 670–680 (2008).
12. D. J. Barshis *et al.*, *Proc. Natl. Acad. Sci. U.S.A.* **110**, 1387–1392 (2013).
13. A. J. Bellantuono, C. Granados-Cifuentes, D. J. Miller, O. Hoegh-Guldberg, M. Rodriguez-Lanetty, *PLOS One* **7**, e50685 (2012).
14. T. D. Ainsworth *et al.*, *Sci. Rep.* **1**, 160 (2011).
15. A. J. Bellantuono, O. Hoegh-Guldberg, M. Rodriguez-Lanetty, *Proc. Biol. Sci.* **279**, 1100–1107 (2012).
16. D. Tchernov *et al.*, *Proc. Natl. Acad. Sci. U.S.A.* **108**, 9905–9909 (2011).
17. L. Kwiatkowski, P. J. Halloran, P. Mumby, D. Stephenson, *Clim. Dyn.* **43**, 1483–1496 (2014).
18. D. L. Hartmann *et al.*, *The Physical Science Basis. Contribution of Working Group I to the Fifth Assessment Report of the Intergovernmental Panel on Climate Change* (Cambridge Univ. Press, 2013).
19. J. M. Lough, *J. Environ. Monit.* **10**, 21–29 (2008).
20. K. Riahi *et al.*, *Clim. Change* **109**, 33–57 (2011).
21. D. van Vuuren *et al.*, *Clim. Change* **109**, 95–116 (2011).
22. C. A. Logan, J. P. Dunne, C. M. Eakin, S. D. Donner, *Glob. Change Biol.* **20**, 125–139 (2014).

23. P. L. Munday, R. R. Warner, K. Monro, J. M. Pandolfi, D. J. Marshall, *Ecol. Lett.* **16**, 1488–1500 (2013).
24. B. M. Riegl, S. J. Purkis, A. S. Al-Cibahy, M. A. Abdel-Moati, O. Hoegh-Guldberg, *PLOS One* **6**, e24802 (2011).

ACKNOWLEDGMENTS

The authors thank the following funding bodies: Australian Research Council Discovery Program grant DP130101421 (awarded to W.L. and T.D.A.); Australian Research Council Super Science Program grant FS110200046 (awarded to Terry P. Hughes, Director, Australian Research Council Centre of Excellence for Coral Reef Studies); Australian Research Council Centre of Excellence for Coral Reef Studies grant CE0561435; the Great Barrier Reef Foundation (Coral Health Grant); the NOAA National Environmental Satellite, Data, and Information Service; and the NOAA Coral Reef Conservation Program. The authors thank N. Wolff for providing SST projections and help in analysis of ecosystem model components and M. De Freitas Prazeres for cell counts. The contents in this manuscript are solely the opinions of the authors and do not constitute a statement of policy, decision, or position on behalf of NOAA or the U.S. government. T.D.A., S.F.H., J.C.O., and W.L. designed the study. T.D.A., D.O., and W.L. conducted experimental procedures and physiological analyses. S.F.H. and C.M.E. conducted SST and oceanographic analyses. J.C.O. and P.J.M. conducted predictive modeling and model validation. T.D.A., S.F.H., J.C.O., P.J.M., A.G., C.M.E., and W.L. wrote and finalized the manuscript. Code for the analysis of SST data is available through contact and collaboration with S. Heron (scott.heron@noaa.gov). Code for the ecosystem model is available through contact and collaboration with J.-C. Ortiz (j.ortiz@uq.edu.au). The NOAA data and code are available from a dedicated web page: http://coralreefwatch.noaa.gov/publications/AinsworthEtAl_2016.php. All data and code are available at FigShare project number 12040: Ecosystems model code and scripts (DOI 10.6084/m9.figshare.3081127); Bleaching on the GBR data release (DOI 10.6084/m9.figshare.3081127); Physiology and gene expression data (DOI 10.6084/m9.figshare.3081064). D.O. is currently employed by Boehringer Ingelheim, Fremont, CA. The authors declare no competing financial interests.

SUPPLEMENTARY MATERIALS

www.sciencemag.org/content/352/6283/338/suppl/DC1
Materials and Methods
Supplementary Text
Figs. S1 to S8
Tables S1 to S8

10 September 2015; accepted 10 March 2016
10.1126/science.aac7125

FOREST ECOLOGY

Belowground carbon trade among tall trees in a temperate forest

Tamir Klein,[1]*† Rolf T. W. Siegwolf,[2] Christian Körner[1]

Forest trees compete for light and soil resources, but photoassimilates, once produced in the foliage, are not considered to be exchanged between individuals. Applying stable carbon isotope labeling at the canopy scale, we show that carbon assimilated by 40-meter-tall spruce is traded over to neighboring beech, larch, and pine via overlapping root spheres. Isotope mixing signals indicate that the interspecific, bidirectional transfer, assisted by common ectomycorrhiza networks, accounted for 40% of the fine root carbon (about 280 kilograms per hectare per year tree-to-tree transfer). Although competition for resources is commonly considered as the dominant tree-to-tree interaction in forests, trees may interact in more complex ways, including substantial carbon exchange.

Stable carbon isotope labeling at the canopy scale is a powerful tool for tracing carbon allocation in forest ecosystems (*1*, *2*). In a dense forest, large quantities of photoassimilates may be exported to mycorrhiza and rhizosphere microbes (*3*–*11*), and hyphae of mycorrhizal fungi can form "underground highways" for carbon and nutrient exchange with and between plants (*9*). It has been suggested that because of the unpredictability of disturbance events and the divergence of responses among plant communities, mycorrhizal fungi and their host plant species are under selective pressure to evolve generality (*9*, *10*). The groups of plants that are interlinked through a common mycorrhizal network are hence termed "guilds" (*10*). The identity and ensemble of fungal species may affect plant community structure and ecosystem productivity (*12*, *13*), with mycorrhiza improving plant fitness by increasing phosphorus and nitrogen uptake (*14*). As a result, mycorrhizal networks are considered an integral part of the autotrophic system (*15*, *16*) and are essential components in ecosystem resilience to change. Yet, these benefits have traditionally been studied from a nutrient supply perspective, and the mycorrhiza "pipeline" was never shown to transfer considerable amounts (>1 g) of mobile carbon compounds among trees (*4*–*10*). In addition to mycorrhizal networks, carbon can be transferred through natural root grafts, which are anatomical fusions between two or more roots. Growth of interconnected trees in situ can be affected directly by the presence of root grafts—for example, by translocation of water and carbohydrates (*17*). Transport across root grafts has been demonstrated in numerous field studies using various methods, from dye injection to the use of radioactive tracers (*18*, *19*), but these grafts are restricted to trees of the same species or, at most, of phylogenetically closely related species (*17*–*20*).

Using a tall canopy crane (*1*, *2*), we continuously labeled five 40-m-tall Norway spruce trees (*Picea abies*) as part of a 5-year free-air CO_2 enrichment experiment (FACE) in a mixed forest in northwest Switzerland (*3*, *21*, *22*) (figs. S1 to S7). Five unlabeled *Picea* trees served as controls (fig. S8). We then measured $\delta^{13}C$ from "tip to toe," including canopy twigs, stems, and fine roots of labeled and unlabeled individuals of *Picea* and of neighboring trees belonging to different taxa (*Fagus sylvatica*, *Pinus sylvestris*, and *Larix decidua*). Except for the five labeled *Picea*, none of the trees were exposed to CO_2 labeling. Using industrial, ^{13}C-depleted CO_2 gas, our canopy labeling made the $\delta^{13}C$ signal of labeled trees more negative by 5.3 per mil (‰) compared to unlabeled control trees: Twig $\delta^{13}C$ was –31.4‰ in labeled and –26.1‰ in unlabeled *Picea* (Fig. 1). New fine roots of labeled *Picea*, isolated from 90 ingrowth cores (figs. S9 and S10) had 2.6‰ lower $\delta^{13}C$ values than the control trees growing in ambient air (no ^{13}C label) (Fig. 1). Almost the same isotopic signal was found among fine roots of similarly tall nonconspecific trees in the neighborhood that were unlabeled and contributed about half of the fine roots recovered from ingrowth cores (Fig. 2A). To validate that fine roots of the other taxa were not confused with those of *Picea*, we excavated roots from *Picea* (control and labeled) and neighboring tree species and traced them to the trunk of origin (figs. S12 to S14). Again, fine roots of these non-*Picea* taxa showed a ^{13}C signal similar to that of their neighboring *Picea* (either control or labeled) but jointly at a 2.6‰ less negative level when ^{13}C-labeled *Picea* was present (Fig. 2B). Hence, both the root-ingrowth-core data (with multiple individuals' input) and the data for intact root systems from three individuals belonging to three different tree genera yielded the same signals. Sapwood $\delta^{13}C$ of the 2010 to 2014 annual rings in stem cores taken at breast height from neighboring and nonneighboring non-*Picea* trees was –27.8 ± 0.1‰ and –26.9 ± 0.1‰, respectively—still a significant difference ($P = 0.019$).

Because our FACE system operated in the canopy only (20 to 40 m aboveground), tank CO_2, and thus the ^{13}C label, were not present in the understory. This was ascertained first by ^{13}C signals in understory plants, which are exclusively vesicular-arbuscular mycorrhizal: *Paris quadrifolia*, *Mercurialis perennis*, and *Rubus fruticosus*. $\delta^{13}C$ values in rhizomes/root stocks from these three species growing under both unlabeled and labeled *Picea* showed the typical, very negative signals for deep shade plants (from –30.2 to –34.5‰) (fig. S15). Besides differences among species, however, there was absolutely no signal difference between samples collected under unlabeled and labeled *Picea* and no difference between years. Second, we checked the canopy crowns of the trees neighboring the labeled *Picea* individuals for traces

[1]Institute of Botany, University of Basel, Schönbeinstrasse 6, 4056 Basel, Switzerland. [2]Laboratory of Atmospheric Chemistry, Ecosystems Fluxes Research Group, Paul Scherrer Institute, PSI, 5323 Villigen, Switzerland.
***Corresponding author. E-mail: tamir.klein@unibas.ch** †Present address: Institute of Soil, Water, and Environmental Sciences, Agricultural Research Organization Volcani Center, Beit Dagan 50250, Israel.

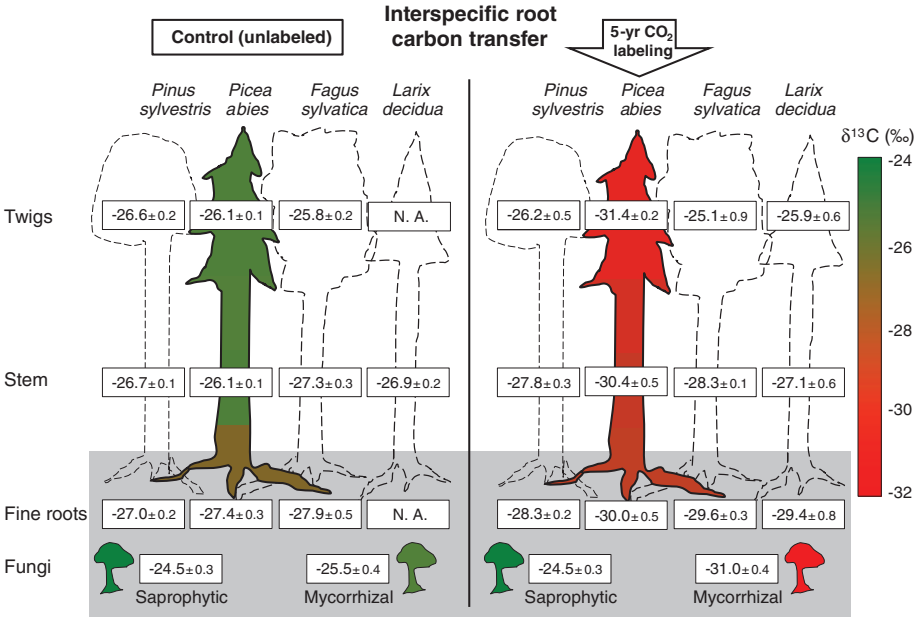

Fig. 1. Transfer of carbon from labeled spruce to fine roots of neighboring nonspruce trees. $\delta^{13}C$ gradients (means ± SE; N = 4 to 5 samples from 1 to 5 trees) within tree compartments and fungal sporocarps in the studied mixed forest stand near Basel, Switzerland. The use of industrial, ^{13}C-depleted CO_2 gas for the FACE allowed for identifying carbon allocation in and from spruce trees exposed to labeled CO_2 ($\delta^{13}C \leq -30.0‰$), compared with other carbon in wood and fungi ($\delta^{13}C > -27.5‰$). Linear gradients were assumed between measurement points.

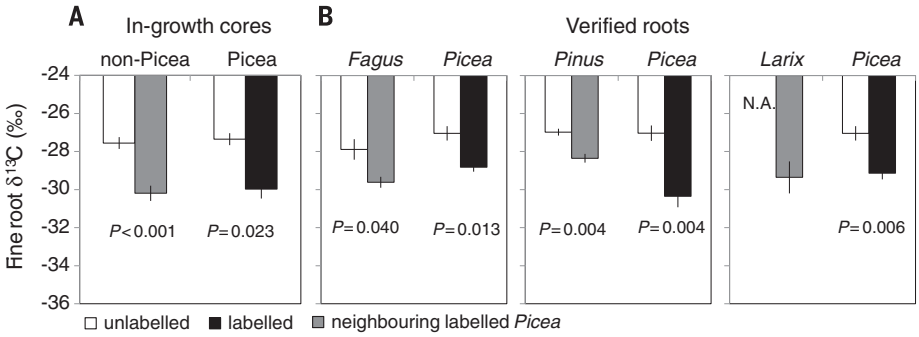

Fig. 2. Fine roots of unlabeled beech, pine, and larch trees carry the isotopic signal of labeled spruce. $\delta^{13}C$ in fine roots from ingrowth cores located in overlapping root spheres of spruce and neighboring tree species (**A**) and from three undisturbed soil volumes circumjacent to roots of spruce trees under labeled CO_2 and neighboring trees of other species (where species were absolutely verified) (**B**). Roots of labeled spruce individuals and of neighboring nonspruce trees had significantly lower $\delta^{13}C$ than trees growing in the same stand that were not exposed to labeled CO_2. Each bar is a mean ± SE of five trees, each with three core triplets (ingrowth cores) and of four root samples from one individual tree (verified roots). P values are from analysis of variance. All available *Larix* trees were neighboring the labeled *Picea*, and none were neighboring the unlabeled *Picea* (fig. S8).

of ^{13}C label in 2-year old high-canopy twigs from all four compass directions in each crown. No influence of the ^{13}C label could be found. $\delta^{13}C$ in twig xylem of *Picea* was −26.1 ± 0.1‰ and −31.4 ± 1.1‰ in unlabeled and labeled trees, respectively. In twig xylems of the three neighboring tree species (*Fagus*, *Pinus*, and *Larix*), $\delta^{13}C$ was −25.1 ± 0.9, −26.2 ± 0.5, and −25.9 ± 0.6‰, respectively, as previously observed in these trees (*23*). Only in twigs sampled in the small crown fraction immediately next to the crowns of the labeled *Picea* (<20% of the crown circumference), $\delta^{13}C$ was slightly lowered compared with the aforementioned values (−28.1, −29.2, and −28.8 in twigs of *Fagus*, *Pinus*, and *Larix*, respectively). The remainder of the crown periphery and the crown center showed no label, and hence the overall crown volume that was slightly influenced by the isotope label was <10%. Moreover, the $\delta^{13}C$ values in those proximal twigs were still 2.2 to 3.3‰ above those in the labeled *Picea* twigs.

The tree-to-tree transfer of labeled carbon was so strong in this study that roots of different tree taxa (of which only *Picea* was labeled) shared an almost similar isotopic signature: −30.0‰ and −29.1‰ in labeled and neighbor trees, respectively (Fig. 1). The decrease in $\delta^{13}C$ of unlabeled neighbor roots, and the parallel increase in $\delta^{13}C$ of labeled roots relative to their source tissues (Fig. 1), indicate a bidirectional carbon exchange. To estimate the direction and magnitude of the carbon exchange, we compared the aforementioned $\delta^{13}C$ values with those prevailing without any labeled carbon transfer ("baseline" signatures). We then applied a simple carbon isotope mixing calculation between roots of labeled and neighbor trees using the equation $a \times n + (100 - a) \times m = p$, where a is the contribution of one of two sources to a mixture (in %), n is its isotopic signature, m is the isotopic signature of the other source, and p that of the mixed product. In the neighbor roots, the $\delta^{13}C$ value of −29.1‰ reflects a decrease by 1.7‰ from a mean baseline value of −27.4‰ observed in roots of the same tree species growing around unlabeled *Picea* (Fig. 1). However, a baseline signature in the labeled *Picea* roots is harder to estimate, because we had no reference observation of labeled *Picea* that did not exchange carbon with non-*Picea* neighbors. To this mixing, one must add an intrinsic dilution by the contribution of older, unlabeled carbon to current fine root growth (*3*, *24*). We do know that in control *Picea*, $\delta^{13}C$ of roots was 1.3‰ more negative than that of the canopy twigs (Fig. 1) (a common observation), and hence a premixed baseline for the labeled *Picea* root would be −32.7‰ (−31.4 minus 1.3‰). Thus, our isotope mixing calculation had to solve for a mixing ratio that would satisfy (i) a 2.7‰ increase in the labeled *Picea* root signal (−30.0 minus −32.7‰); (ii) a 1.7‰ decrease in the neighbor root signal; and account for (iii) the intrinsic dilution ratio with old stored carbon. We found that a 20% contribution of older, unlabeled carbon to current fine-root growth of labeled *Picea*, and an isotope-mixing ratio of 60% self and 40% exchanged carbon between fine roots of labeled and unlabeled trees, satisfied the ^{13}C signal changes at both sides of the transfer (Fig. 3).

The magnitude of the exchange can be estimated: *Picea* fine-root biomass production estimated from our ingrowth cores (*11*) was 60 g m^{-2} a^{-1}

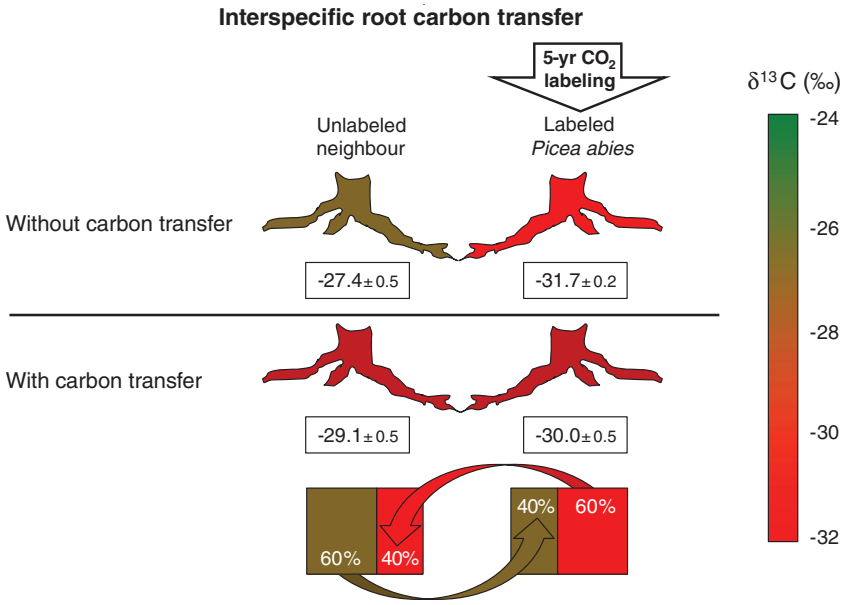

Fig. 3. Bidirectional root carbon transfer between mature forest trees. Estimation of the magnitude of the interspecific root carbon exchange in the studied mixed forest stand based on the observed $\delta^{13}C$ values. An isotope mixing ratio of 60% self and 40% exchanged carbon between fine roots of labeled and unlabeled trees satisfies the ^{13}C signals in both.

at 1- to 12-cm depth, upscaled linearly to 150 g m^{-2} a^{-1} for the entire 30-cm soil profile. Assuming an average root carbon concentration of 46%, this corresponds to a fine-root production of 69 g carbon m^{-2} a^{-1}. If 40% of this fine-root carbon came from an exchange via mycorrhiza, this carbon transfer flux equals 28 g carbon m^{-2} a^{-1}—i.e., 280 kg ha^{-1} a^{-1}, which is equivalent to 4% of the forest net carbon uptake (net primary production).

The carbon transfer that we observed most likely occurred through common ectomycorrhiza networks, which are very abundant at this site (table S1), and also exhibited the labeled carbon in their "fruit" bodies near labeled *Picea* (*3*) and are a substantial carbon sink in Norway spruce forests (*16*). Host specificity is a known trait among ectomycorrhiza taxa, yet common networks and the formation of trophic guilds play a crucial role in forest dynamics (*25*). For example, in a mixed Central European forest, 75 ectomycorrhiza taxa were identified on *Fagus sylvatica* roots (*26*); 29% and 10% of the ectomycorrhiza species were shared with one or two other tree species, respectively; however, it is noteworthy that the 61% host-specific ectomycorrhiza species colonized only 20% of the root tips (*24*). The ectomycorrhiza species *Russula ochroleuca* (Pers.) has been previously identified on roots of all four tree species studied here (*27*), and a *Russula* species was identified in our forest site (table S1). A taxonomic search in the ectomycorrhiza database (www.deemy.de) (*28*) revealed three other genera found at our site that are common symbionts to our four study tree species—namely, *Cortinarius*, *Lactarius*, and *Tricholoma*.

Our earlier study on this site (*3*) also showed zero $\delta^{13}C$ labeling in saprophytic fungi (Fig. 1) and decreasing mycorrhizal $\delta^{13}C$ with decreasing distance from the labeled *Picea*. Our results indicate a bidirectional carbon exchange (Fig. 3) rather than a one-way transfer (*17*), which is not along a demand-supply gradient as previously reported (*10*, *17*). Considering that all studied trees were dominant, healthy, and tall individuals, growing without obvious carbon limitation, no a priori source-sink gradients might be expected here (*29*). It has been suggested that carbon transfer between trees via mycorrhiza is rather regulated to satisfy the needs of the mycorrhiza itself (*7*). In our case, it is still possible that labeled *Picea* transferred excess carbon belowground (*3*) and, in turn, enhanced mycorrhizal activity and proliferation.

The mild, yet significant increase in sapwood $\delta^{13}C$ at the base of trees neighboring the labeled *Picea* (Fig. 1) indicates slight aboveground allocation of imported carbon. So far, root carbon uptake was shown in "green-to-ground" corn and in willow cuttings using labeled carbonate ($NaH^{14}CO_3$ and $H^{13}CO_3^-$) (*31*), as well as in pine seedlings (*30*), but not in mature trees in the field.

Finally, the observed interspecific carbon transfer among tall trees in our study can become increasingly important for forests under stress conditions (e.g., drought or spring frost) or after disturbance such as wildfire, when divergence in species' responses come into play (*5–10*, *14*, *20*, *23*). The magnitude, direction, and control of these transfer fluxes and their importance are yet to be resolved, and they add a new dimension and level of complexity to known ecosystem processes.

REFERENCES AND NOTES

1. S. Pepin, C. Körner, *Oecologia* **133**, 1–9 (2002).
2. C. Körner *et al.*, *Science* **309**, 1360–1362 (2005).
3. M. Mildner, M. K. F. Bader, S. Leuzinger, R. T. W. Siegwolf, C. Körner, *Oecologia* **175**, 747–762 (2014).
4. M. C. Hirrel, J. W. Gerdemann, *New Phytol.* **83**, 731–738 (1979).
5. R. Francis, D. J. Read, *Nature* **307**, 53–56 (1984).
6. C. P. P. Reid, F. W. Woods, *Ecology* **50**, 179–187 (1969).
7. A. H. Fitter, J. D. Graves, N. K. Watkins, D. Robinson, C. Scrimgeour, *Funct. Ecol.* **12**, 406–412 (1998).
8. D. Robinson, A. Fitter, *J. Exp. Bot.* **50**, 9–13 (1999).
9. D. A. Perry, T. Bell, M. P. Amaranthus, in *The Ecology of Mixed-Species Stands of Trees*, M. G. R. Cannell, D. C. Malcolm, P. A. Robertson, Eds. (Blackwell, Oxford, 1992), pp. 151–179.
10. S. W. Simard *et al.*, *Nature* **388**, 579–582 (1997).
11. P. Högberg *et al.*, *New Phytol.* **177**, 220–228 (2008).
12. M. G. van der Heijden, T. Boller, A. Wiemken, I. R. Sanders, *Ecology* **79**, 2082–2091 (1998).
13. M. G. van der Heijden *et al.*, *Nature* **396**, 69–72 (1998).
14. N. C. Johnson, G. W. Wilson, M. A. Bowker, J. A. Wilson, R. M. Miller, *Proc. Natl. Acad. Sci. U.S.A.* **107**, 2093–2098 (2010).
15. N. A. Hynson, S. Mambelli, A. S. Amend, T. E. Dawson, *Oecologia* **169**, 307–317 (2012).
16. H. Wallander, A. Ekblad, J. Bergh, *For. Ecol. Manage.* **262**, 999–1007 (2011).
17. E. C. Fraser, V. J. Lieffers, S. M. Landhäusser, *Tree Physiol.* **26**, 1019–1023 (2006).
18. B. F. Graham, *Ecology* **41**, 56–64 (1960).
19. F. W. Woods, K. Brock, *Ecology* **45**, 886–889 (1964).
20. B. F. Graham, F. H. Bormann, *Bot. Rev.* **32**, 255–292 (1966).
21. M. Mildner, M. K. F. Bader, C. Baumann, C. Körner, *Biogeochemistry* **124**, 95–111 (2015).
22. Materials and methods are available as supplementary materials on *Science* Online.
23. V. S. Chevillat, R. T. W. Siegwolf, S. Pepin, C. Körner, *Basic Appl. Ecol.* **6**, 519–534 (2005).
24. R. Vargas, S. E. Trumbore, M. F. Allen, *New Phytol.* **182**, 710–718 (2009).
25. E. Bent, P. Kiekel, R. Brenton, D. L. Taylor, *Appl. Environ. Microbiol.* **77**, 3351–3359 (2011).
26. C. Lang, J. Seven, A. Polle, *Mycorrhiza* **21**, 297–308 (2011).
27. A. Pillukat, R. Agerer, *Z. Mykol.* **58**, 211–242 (1992).
28. R. Agerer, G. Rambold, DEEMY: An Information System for Characterization and Determination of Ectomycorrhizae [first posted 2004-06-01; most recent update: 2011-01-10] (Munich, 2004); www.deemy.de.
29. C. Körner, *J. Ecol.* **91**, 4–17 (2003).
30. C. R. Ford, N. Wurzburger, R. L. Hendrick, R. O. Teskey, *Tree Physiol.* **27**, 375–383 (2007).
31. D. M. Matarese, thesis, Portland State University, Oregon (2011).

ACKNOWLEDGMENTS

Research at the Swiss canopy crane site was funded by the Swiss National Fund project FORCARB (31003A_14753/1 to C.K.). T.K. was cofunded by the Plant Fellows program of the Zürich-Basel Plant Science Center (PSC) through the EU FP7 Marie Curie action. We thank J. Grünzweig (Hebrew University of Jerusalem, Israel) and R. Milo (Weizmann Institute of Science, Israel) for providing comments on an earlier version of the paper; M. Saurer and L. Schmid at the Paul Scherrer Institute for stable isotope analyses; S. G. Keel, R. Keller, and M. Wilhelm for collection and taxonomic classification of mycorrhizal fungi; E. Amstutz and L. Rizzelli for crane operation; and G. Grun for electronics and CO_2 control. Data showing the experimental set-up, mycorrhiza species list, supplementary figs. S1 to S15, and materials and methods are available in the supplementary materials. The authors declare no conflict of interest and that there are no material transfer agreements or patent applications involved in the study. Author contributions: C.K. designed the experiment, T.K. initiated the fine-root study, C.K. and T.K. sampled the plant materials, and R.T.W.S. did the isotope analyses. All authors wrote the paper jointly.

SUPPLEMENTARY MATERIALS

www.sciencemag.org/content/352/6283/342/suppl/DC1
Materials and Methods
SupplementaryText
Figs. S1 to S15
Table S1
References

11 October 2015; accepted 2 March 2016
10.1126/science.aad6188

ZIKA VIRUS OUTBREAK

Zika virus in the Americas: Early epidemiological and genetic findings

Nuno Rodrigues Faria,[1,2]* Raimunda do Socorro da Silva Azevedo,[3]* Moritz U. G. Kraemer,[2] Renato Souza,[4] Mariana Sequetin Cunha,[4] Sarah C. Hill,[2] Julien Thézé,[2] Michael B. Bonsall,[2] Thomas A. Bowden,[5] Ilona Rissanen,[5] Iray Maria Rocco,[4] Juliana Silva Nogueira,[4] Adriana Yurika Maeda,[4] Fernanda Giseli da Silva Vasami,[4] Fernando Luiz de Lima Macedo,[4] Akemi Suzuki,[4] Sueli Guerreiro Rodrigues,[3] Ana Cecilia Ribeiro Cruz,[3] Bruno Tardeli Nunes,[3] Daniele Barbosa de Almeida Medeiros,[3] Daniela Sueli Guerreiro Rodrigues,[3] Alice Louize Nunes Queiroz,[3] Eliana Vieira Pinto da Silva,[3] Daniele Freitas Henriques,[3] Elisabeth Salbe Travassos da Rosa,[3] Consuelo Silva de Oliveira,[3] Livia Caricio Martins,[3] Helena Baldez Vasconcelos,[3] Livia Medeiros Neves Casseb,[3] Darlene de Brito Simith,[3] Jane P. Messina,[2,6] Leandro Abade,[2] José Lourenço,[2] Luiz Carlos Junior Alcantara,[7] Maricélia Maia de Lima,[8] Marta Giovanetti,[7] Simon I. Hay,[9,5] Rodrigo Santos de Oliveira,[1] Poliana da Silva Lemos,[1] Layanna Freitas de Oliveira,[1] Clayton Pereira Silva de Lima,[1] Sandro Patroca da Silva,[1] Janaina Mota de Vasconcelos,[1] Luciano Franco,[1] Jedson Ferreira Cardoso,[1] João Lídio da Silva Gonçalves Vianez-Júnior,[1] Daiana Mir,[10] Gonzalo Bello,[10] Edson Delatorre,[10] Kamran Khan,[11,12] Marisa Creatore,[13] Giovanini Evelim Coelho,[14] Wanderson Kleber de Oliveira,[14] Robert Tesh,[15] Oliver G. Pybus,[2,6]†‡ Marcio R. T. Nunes,[1,15]†‡ Pedro F. C. Vasconcelos[3]†‡

Brazil has experienced an unprecedented epidemic of Zika virus (ZIKV), with ~30,000 cases reported to date. ZIKV was first detected in Brazil in May 2015, and cases of microcephaly potentially associated with ZIKV infection were identified in November 2015. We performed next-generation sequencing to generate seven Brazilian ZIKV genomes sampled from four self-limited cases, one blood donor, one fatal adult case, and one newborn with microcephaly and congenital malformations. Results of phylogenetic and molecular clock analyses show a single introduction of ZIKV into the Americas, which we estimated to have occurred between May and December 2013, more than 12 months before the detection of ZIKV in Brazil. The estimated date of origin coincides with an increase in air passengers to Brazil from ZIKV-endemic areas, as well as with reported outbreaks in the Pacific Islands. ZIKV genomes from Brazil are phylogenetically interspersed with those from other South American and Caribbean countries. Mapping mutations onto existing structural models revealed the context of viral amino acid changes present in the outbreak lineage; however, no shared amino acid changes were found among the three currently available virus genomes from microcephaly cases. Municipality-level incidence data indicate that reports of suspected microcephaly in Brazil best correlate with ZIKV incidence around week 17 of pregnancy, although this correlation does not demonstrate causation. Our genetic description and analysis of ZIKV isolates in Brazil provide a baseline for future studies of the evolution and molecular epidemiology of this emerging virus in the Americas.

Zika virus (ZIKV) is a single-stranded, positive-sense RNA virus with a 10.7-kb genome encoding a single polyprotein that is cleaved into three structural proteins (C, prM/M, E) and seven nonstructural proteins (NS1, NS2A, NS2B, NS3, NS4A, NS4B, and NS5) (*1*). ZIKV is a member of the family *Flaviviridae*, genus *Flavivirus*, and is transmitted among humans by *Aedes* mosquito species such as *A. aegypti*, *A. albopictus*, and *A. africanus*. The virus was first isolated in 1947 from a sentinel rhesus monkey in the Zika forest in Uganda (*2*) and is classified by sequence analysis into two genotypes, African and Asian (*3*). In humans, ZIKV infection typically causes a mild and self-limiting illness known as Zika fever (*4*), which is accompanied by maculopapular rash, headache, conjunctivitis, and myalgia. In April 2007, a large epidemic of Asian genotype ZIKV was reported in Yap Island and Guam, Micronesia (*5*, *6*). Between 2013 and 2014, the ZIKV Asian genotype caused epidemics reported in several Pacific Islands, including French Polynesia (*7*), New Caledonia (*8*), the Cook Islands (*9*), Tahiti (*10*), and Easter Island (*11*).

By May 2015, ZIKV was reported in Brazil (*12*) and, subsequently, in several Central and South American countries and in the Caribbean. In Brazil, nearly 30,000 cases of ZIKV infection had been reported by 30 January 2016 (supplementary materials section 1.4). These occurrences point to an epidemic peak in mid-July 2015 (Fig. 1A), and most Brazilian ZIKV cases (93%) were reported in Bahia state (Fig. 1B). Surveillance of ZIKV in Brazil began after the country's first reported case and is conducted through the national Notifiable Diseases Information System (SINAN), which currently relies on passive case detection and reporting and therefore underestimates incidence (*13*). ZIKV is now widespread in Brazil, with autochthonous transmission and high incidence notified in 22 of 27 administrative states (*14*). ZIKV infection during pregnancy has been hypothesized to cause microcephaly and congenital abnormalities (*15*–*20*). The detection of ZIKV in fetal brain tissue (*17*, *20*) and amniotic fluid (*21*) supports the hypothesis that the virus is transmitted from mother to child (*22*); further, the virus infects neural progenitor cells in vitro (*23*). In Brazil, between November 2015 and 30 January 2016, 4783 suspected cases of microcephaly were reported electronically to the RESP database (www.resp.saude.gov.br; Ministry of Health, Brazil) (supplementary materials section 1.4) (Fig. 1C), although most suspected cases are still under investigation and a substantial proportion may represent misdiagnosis and overreporting (*24*). Using the 4 March 2016 World Health Organization guidelines for microcephaly diagnosis (*25*), we identified a total of 1118 suspected microcephaly cases suitable for analysis. The relation between total per-capita ZIKV incidence (Fig. 1B) and per-capita suspected microcephaly cases (Fig. 1C) in each state is weak and only significant under nonparametric correlation ($P < 0.01$) (fig. S1A); noise and uncertainty probably affect both variables. However, the relation is strengthened if suspected microcephaly cases are measured per pregnancy (fig. S1B). For municipalities with reported ZIKV incidence and cases of suspected microcephaly, we used a simple linear model to link microcephaly cases as a function of past ZIKV incidence (supplementary materials section 1.5). On average, suspected microcephaly cases are best predicted by ZIKV incidence during week 17 of pregnancy (95% confidence interval of mean = ±0.11 weeks) or week 14 for suspected

[1]Center for Technological Innovation, Evandro Chagas Institute, Ministry of Health, Ananindeua, PA 67030-000, Brazil. [2]Department of Zoology, University of Oxford, South Parks Road, Oxford OX1 3PS, UK. [3]Department of Arbovirology and Hemorrhagic Fevers, Evandro Chagas Institute, Ministry of Health, Ananindeua, Pará State, Brazil. [4]Instituto Adolfo Lutz, University of São Paulo, São Paulo, Brazil. [5]Wellcome Trust Centre for Human Genetics, University of Oxford, Oxford, UK. [6]Metabiota, San Francisco, CA 94104, USA. [7]Oswaldo Cruz Foundation (FIOCRUZ), Salvador, Bahia, Brazil. [8]Centre of Post Graduation in Collective Health, Department of Health, Universidade Estadual de Feira de Santana, Feira de Santana, Bahia, Brazil. [9]Institute for Health Metrics and Evaluation, University of Washington, Seattle, WA 98121, USA. [10]Laboratório de AIDS and Imunologia Molecular, Instituto Oswaldo Cruz, FIOCRUZ, Rio de Janeiro, Brazil. [11]Li Ka Shing Knowledge Institute, St. Michael's Hospital, Toronto, Ontario, Canada. [12]Department of Medicine, Division of Infectious Diseases, University of Toronto, Toronto, Ontario, Canada. [13]Dalla Lana School of Public Health, University of Toronto, Toronto, Ontario, Canada. [14]Brazilian Ministry of Health, Brasília, Brazil. [15]Department of Pathology, University of Texas Medical Branch, Galveston, TX 77555, USA. *These authors contributed equally to this work. †These authors contributed equally to this work. **‡Correspondening author. E-mail: oliver.pybus@zoo.ox.ac.uk (O.G.P.); marcionunesbrasil@yahoo.com.br (M.R.T.N.); pedrovasconcelos@iec.pa.gov.br (P.F.C.V.)**

severe microcephaly cases (±0.08 weeks). These findings are in general agreement with individual reports of the timing of ZIKV symptoms in mothers of infants with microcephaly (*16*, *19*, *21*). We stress that these results quantify only the correlation between ZIKV and suspected microcephaly and do not demonstrate a causal link. Ongoing studies are aiming to establish whether ZIKV is a causal factor in microcephaly and other conditions (*15*–*17*, *23*, *26*).

We used phylogenetic, epidemiological, and mobility data to quantify ZIKV evolution and explore the introduction of the virus to the Americas. As part of ongoing surveillance by the Brazilian Ministry of Health, national laboratories, and other institutions, we used next-generation sequencing to generate seven complete ZIKV coding region sequences from samples collected during the outbreak. Our samples include one from a deceased newborn with microcephaly and congenital malformations collected in Ceará and one from a fatal adult case with lupus and rheumatoid disease from Maranhão state (Fig. 1B). None of the Brazilian patients reported overseas travel (information unavailable in one case), and one individual was a blood donor (supplementary materials section 2). A comparison of our genomes with other available Brazilian strains reveals that Brazilian ZIKV isolates differ at multiple nucleotide sites across the 10.3-kb coding region. The ZIKV genome recovered from isolate ZIKSP, from São Paulo, had 32 nucleotide changes compared with the microcephaly case (BeH823339) and 34 compared with the fatal case from Maranhão (BeH818305). Isolates BeH819966 (from Belém), BeH815744 (from Paraíba), and BeH18995 (from Belém) had a maximum of five nucleotide changes.

Maximum likelihood analysis of complete coding regions from our and other ZIKV genome sequences revealed that all viruses sampled in the Americas, including those from Brazil, form a robust monophyletic cluster (bootstrap score = 94%) within the Asian genotype (Fig. 2 and fig. S2) and share a common ancestor with the ZIKV strain that circulated in French Polynesia in November 2013 (Fig. 3). Previous analyses of outbreaks of related flaviviruses (*27*, *28*) suggest that, to be informative, molecular epidemiological studies of the current ZIKV epidemic should use full or near-complete coding region sequences.

We used a phylogenetic molecular clock approach to further explore the molecular epidemiology of ZIKV in the Americas. A strong correlation between genetic divergence and sampling time within the outbreak lineage (Fig. 2, inset) shows that our approach is appropriate, provided that whole genomes are used. The estimated time-scaled phylogeny (Fig. 3A) again contains a well-supported clade of American ZIKV strains [denoted B; posterior probability (*PP*) = 1.00] that share a common ancestor (denoted A) with the French Polynesian lineage (*PP* = 0.92). Within the American ZIKV lineage (clade B), Brazilian isolates are interspersed among isolates from elsewhere in the Americas. The mingling of ZIKV genomes from different countries reveals ZIKV movement within the Americas since its introduction to the continent. Two observations suggest that the common ancestor of the American ZIKV lineage existed in Brazil. First, Brazil was the first country in the Americas to detect ZIKV (*29*), and second, Brazilian strains are phylogenetically more diverse within clade B than those from elsewhere. However, these observations may reflect differences in surveillance intensity among countries, and more data are required before we can exclude the scenario that ZIKV was introduced to Brazil multiple times from other locations. Although two of three ZIKV-associated microcephaly isolates group together in the phylogeny, there is no reason to posit that this lineage is associated with increased disease severity.

Estimated rates of ZIKV molecular evolution are consistent among different evolutionary models and vary from 0.98×10^{-3} to 1.06×10^{-3} nucleotide substitutions per site per year (table S3). Although these rates are high compared with whole-genome rates for other flaviviruses (*28*), they are consistent with retrospective analyses of previous epidemics, which show that evolutionary rate estimates decline as the epidemic progresses (*30*, *31*). Hence, this result should not be interpreted as implying that ZIKV in the Americas is unusually mutable. We estimate that the date of the most recent common ancestor (TMRCA) of all Brazilian genomes (clade B) is Aug 2013 to Apr 2014 [95% Bayesian credible intervals (BCIs); point estimate = mid-December 2013] (Fig. 3B). The common ancestor of the French Polynesian and America lineages (clade A) was dated from December 2012 to September 2013 (BCIs; point estimate = late May 2013) (Fig. 3B). The posterior distribution for the age of clade B encompasses the recorded duration of the ZIKV outbreak in three of five island groups of French Polynesia (*4*) (Fig. 3C). Divergence date estimates are robust among different combinations of prior distributions, molecular clock models, and coalescent models (supplementary materials sections 4 and 5) and are more likely to shift into the past than toward the present as virus genomes accumulate through time (*30*).

To explore the possible routes of entry of ZIKV in Brazil, we collated airline flight data from all countries with reported ZIKV outbreaks between 2012 and the end of 2014. From late 2012, we find an increase in the number of travelers arriving in Brazil from these countries, rising from 3775 passengers per month in early 2013 to 5754 passengers per month a year later (Fig. 3C). This increase in visitors to Brazil from ZIKV-affected countries coincides with the period during which ZIKV is estimated to have entered the Americas (i.e., between TMRCAs of clades A and B) (Fig. 3B and supplementary materials section 5). If the ZIKV epidemic in Brazil did indeed arise from a single introduction, then the virus must have circulated in the country for at least 12 months before the first case was reported in May 2015. ZIKV clinical symptoms may be confused with those caused by

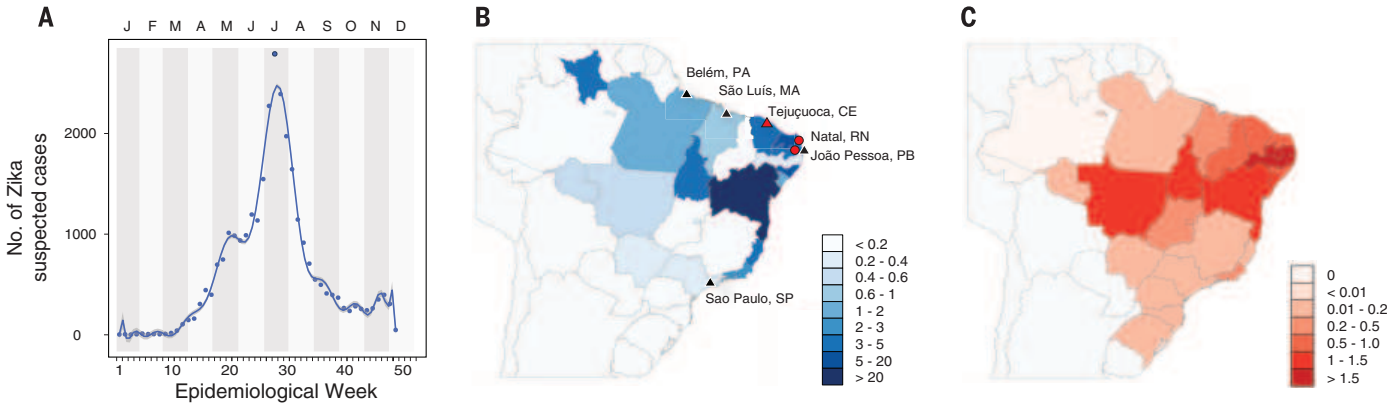

Fig. 1. Time series and cartography of reported Zika virus and microcephaly cases in Brazil. (**A**) Number of suspected cases of ZIKV per week in 5596 municipalities in Brazil. The epidemic peaked from 12 to 18 July 2015 (*n* = 2791 cases). Letters indicate months. (**B**) Total incidence of ZIKV cases per 100,000 people in each federal state. Triangles indicate sampling locations of the sequences reported here; circles indicate locations of other genomes from Brazil [municipality of Natal in Rio Grande do Norte state (*16*) and an unknown municipality in Paraiba state (*21*)]. Red symbols indicate ZIKV genomes isolated from microcephaly cases. Federal states are indicated by two-letter codes: PA, Pará; MA, Maranhão; CE, Ceará; RN, Rio Grande do Norte; PB, Paraíba; SP, São Paulo. Per-capita incidences in each state were calculated using high-resolution gridded human population–size data sets for Brazil (*45*). (**C**) Incidence of suspected microcephaly cases per 100,000 people in each federal state. Per-capita incidences for each state were calculated as described for (B).

dengue and chikungunya viruses, two endemic and epidemic viruses that cocirculate and share mosquito vectors with ZIKV in Brazil (*27*, *32*, *33*). Reliable differential diagnosis is possible only by using improved surveillance and laboratory diagnostics, which are now being implemented throughout the country.

There are two published hypotheses for how ZIKV came to be introduced into Brazil: during (i) the 2014 World Cup soccer tournament (12 June to 13 July 2014) (*29*) or (ii) the Va'a canoe event held in Rio de Janeiro between 12 and 17 August 2014 (*34*). Alternatively, introduction could have occurred during (iii) the 2013 Confederations Cup soccer tournament (15 to 30 June 2013). Notably, events (ii) and (iii) included competitors from French Polynesia. Our results suggest that the introduction of ZIKV to the Americas predated events (i) and (ii). Although the molecular clock dates are more consistent with the Confederations Cup tournament, that event ended before ZIKV cases were first reported in French Polynesia (*4*). Consequently, we believe that large-scale patterns in human mobility will provide more useful and testable hypotheses about viral introduction and emergence (*33*, *35*, *36*) than ad hoc hypotheses focused on specific events.

The ZIKV genome we obtained from a microcephaly case in Ceará, Brazil, contains eight amino acid changes not observed in any other complete genome in our data set. However, none of these mutations are shared with either of two recently published genomes from microcephaly cases (*16*, *21*). Thus, if a causal link between Asian lineage ZIKV and microcephaly is confirmed, it is possible that putative viral genetic determinants of disease will be found among the amino acid changes that occur on the ZIKV phylogeny branches ancestral to the French Polynesian and American ZIKV lineages (i.e., the two lineages associated with reports of microcephaly, Guillain-Barré syndrome, and congenital abnormalities) (*37*). Phylogenetic character mapping using parsimony reveals 11 amino acid changes on the four internal branches (Fig. 2, asterisks; and fig. S3) leading to these two lineages. We identified the structures of homologous proteins most closely related to the ZIKV proteins (supplementary materials section 7) and used them to map 7 of the 11 amino acid changes, in a structural context, to five proteins: the pr-peptide region of prM [changes Val^{123}→Ala^{123} (V123A) and S139N (S, Ser; N, Asn)], NS1 (A982V), the RNA helicase [NS3; N1902H and Y2086H (H, His; Y, Tyr)], the FtsJ-like methyl transferase domain [NS5; M2634V (M, Met)], and the thumb domain of RNA-directed RNA polymerase (NS5; M3392V) (fig. S7). None of these mutations are predicted to substantially affect the physicochemical properties of the protein environment, except possibly Y2086H (in the helicase; fig. S8), which may increase the hydrophilicity of the region. The remaining four amino acid changes could not be accurately mapped due to the absence of suitable related x-ray structures (supplementary materials section 7). Notably, none of the observed changes map to the E glycoprotein ectodomain, the primary target of humoral immune responses against flaviviruses (*38*, *39*). Factors other than viral genetic differences may be important for the proposed pathogenesis of ZIKV; hypothesized factors include coinfection with chikungunya virus (*40*), previous infection with dengue virus (*41*), or differences in human genetic predisposition to disease.

Besides vector-borne and mother-to-child transmission, Zika virus may also spread via sexual

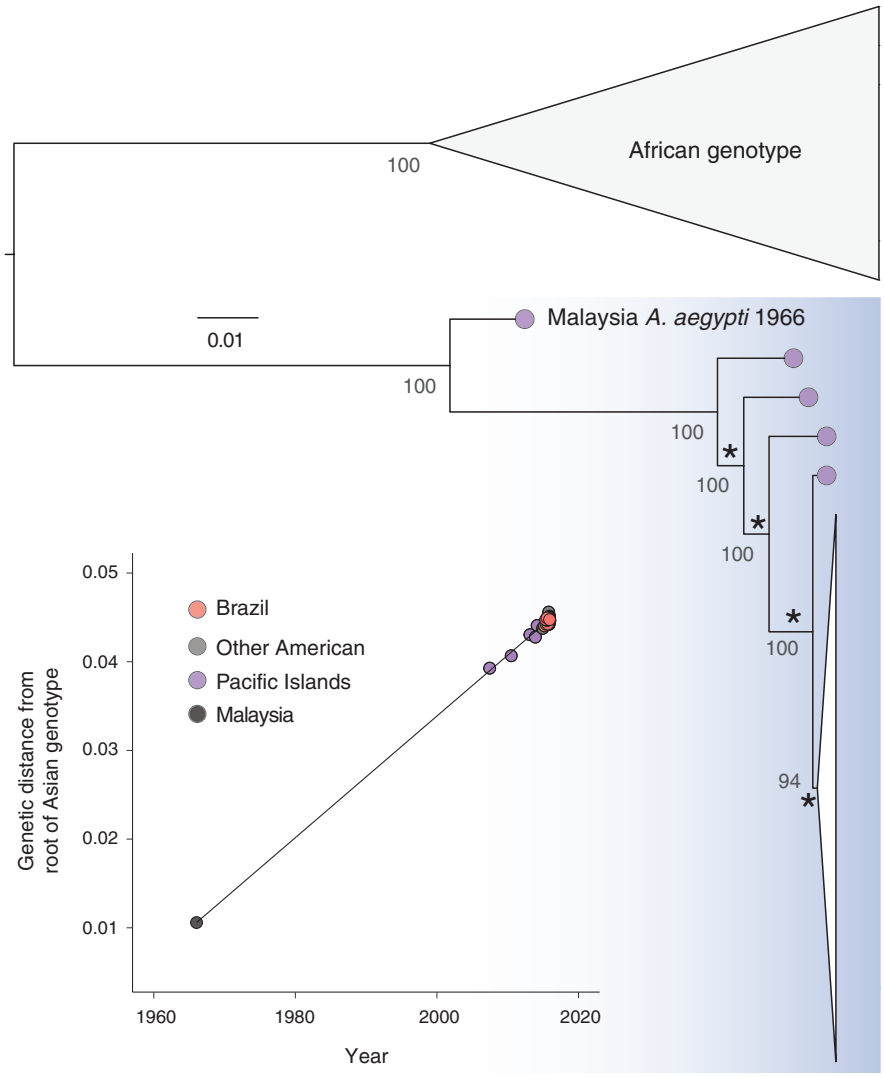

Fig. 2. Maximum likelihood phylogeny of ZIKV complete coding region sequences. Bootstrap scores are shown next to well-supported nodes, and the phylogeny was midpoint rooted. A fully annotated tree is provided in fig. S2. The American ZIKV outbreak clade is drawn as a narrow white triangle and is shown in detail in Fig. 3. Asterisks highlight the four internal branches that are ancestral to the American ZIKV lineage (see main text and fig. S3). There is a correlation between the sampling date of each sequence and the genetic distance of that sequence from the root of a maximum likelihood phylogeny of the Asian genotype (correlation coefficient R^2 = 0.997). A molecular clock phylogeny of these data is shown in Fig. 3. The Malaysian strain (HQ234499) sampled in 1966 is the oldest representative of the Asian genotype and falls on the regression line, indicating that it does not appear to be unusually divergent for its age. A similar analysis with the HQ234499 strain excluded is shown in fig. S5C.

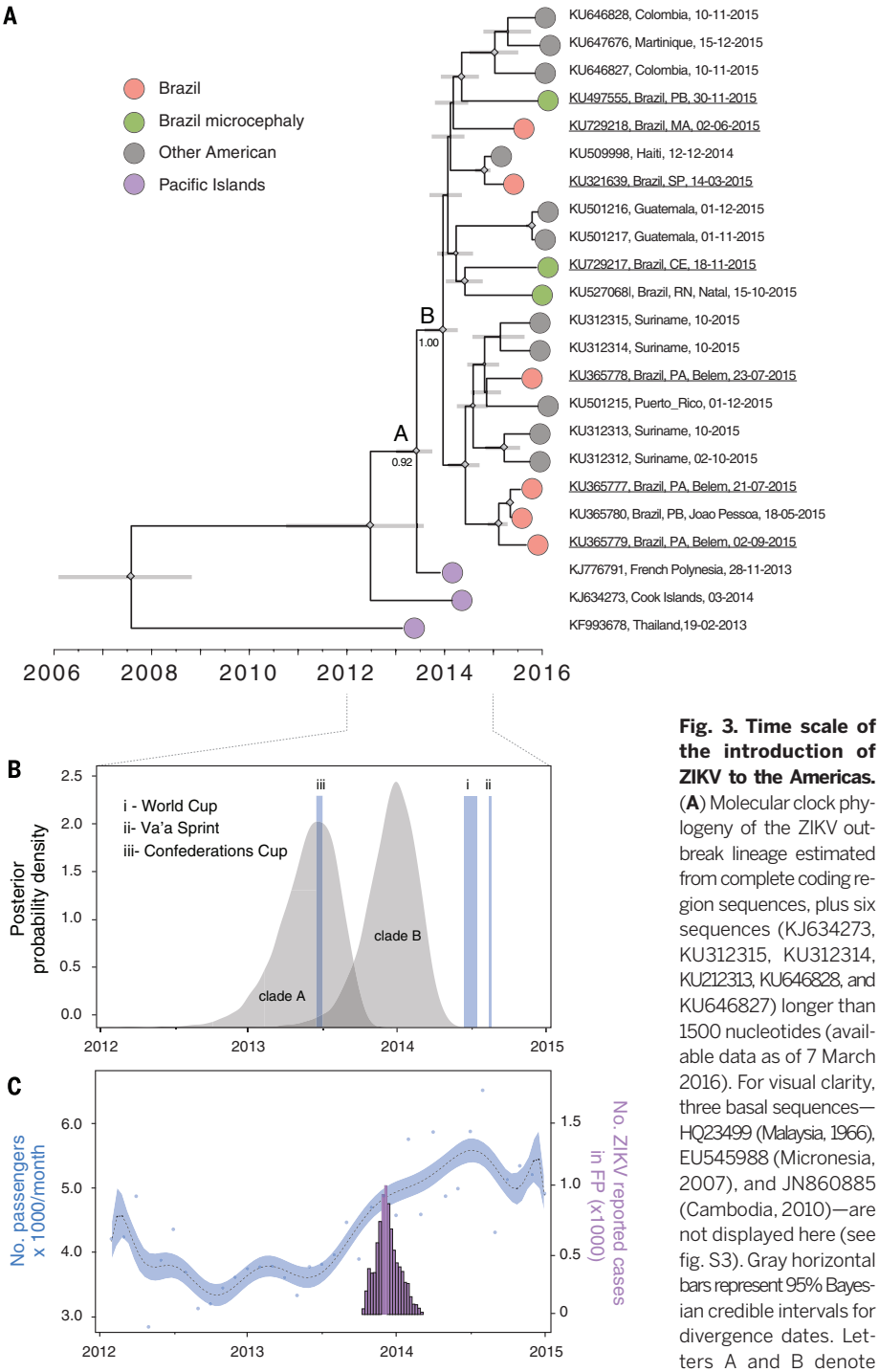

Fig. 3. Time scale of the introduction of ZIKV to the Americas. (**A**) Molecular clock phylogeny of the ZIKV outbreak lineage estimated from complete coding region sequences, plus six sequences (KJ634273, KU312315, KU312314, KU212313, KU646828, and KU646827) longer than 1500 nucleotides (available data as of 7 March 2016). For visual clarity, three basal sequences—HQ23499 (Malaysia, 1966), EU545988 (Micronesia, 2007), and JN860885 (Cambodia, 2010)—are not displayed here (see fig. S3). Gray horizontal bars represent 95% Bayesian credible intervals for divergence dates. Letters A and B denote clades discussed in the main text; numbers under the clade letters denote posterior probabilities. Diamond sizes represent, at each node, the posterior probability support of that node. Taxa are labeled with accession number, sampling location, and sampling date. Names of sequences generated in this study are underlined. (**B**) Posterior distributions of the estimated ages (TMRCAs) of clades A and B, estimated with BEAST software using the best-fitting evolutionary model (table S2). The time and duration of the three events (i to iii) discussed in the main text are shown. (**C**) Number of airline passengers from specific countries arriving in Brazil per month versus number of suspected cases of ZIKV in French Polynesia. The blue curve (left *y* axis) shows a polynomial fitting of the number of travelers (blue points) from countries with recorded ZIKV outbreaks between 2012 and 2015 (French Polynesia, Thailand, Indonesia, Malaysia, Cambodia, and New Caledonia) (supplementary materials section 6), aggregated across 20 Brazilian national airports. The purple bars represent weekly numbers of suspected ZIKV cases (right *y* axis) in French Polynesia (FP) from 30 October 2013 to 14 February 2014 (*4*).

contact (*42*, *43*) and blood transfusion (*44*). The evidence of ZIKV in blood donors raises the possibility of ZIKV transmission through transfusion and indicates that it may be prudent to consider the screening of blood donors.

REFERENCES AND NOTES

1. B. D. Lindenbach, C. M. Rice, *Adv. Virus Res.* **59**, 23–61 (2003).
2. G. W. Dick, S. F. Kitchen, A. J. Haddow, *Trans. R. Soc. Trop. Med. Hyg.* **46**, 509–520 (1952).
3. O. Faye *et al.*, *Virol. J.* **10**, 311 (2013).
4. S. Ioos *et al.*, *Med. Mal. Infect.* **44**, 302–307 (2014).
5. M. R. Duffy *et al.*, *N. Engl. J. Med.* **360**, 2536–2543 (2009).
6. A. D. Haddow *et al.*, *PLOS Negl. Trop. Dis.* **6**, e1477 (2012).
7. V. M. Cao-Lormeau *et al.*, *Emerg. Infect. Dis.* **20**, 1085–1086 (2014).
8. M. Dupont-Rouzeyrol *et al.*, *Emerg. Infect. Dis.* **21**, 381–382 (2015).
9. A. T. Pyke *et al.*, *PLOS Curr.* 10.1371/currents.outbreaks.4635a54dbffba2156fb2fd76dc49f65e (2014).
10. T. Wæhre, A. Maagard, D. Tappe, D. Cadar, J. Schmidt-Chanasit, *Emerg. Infect. Dis.* **20**, 1412–1414 (2014).
11. J. Tognarelli *et al.*, *Arch. Virol.* **161**, 665–668 (2016).
12. M. Hennessey, M. Fischer, J. E. Staples, *MMWR Morb. Mortal. Wkly. Rep.* **65**, 55–58 (2016).
13. M. M. O. Silva *et al.*, *Emerg. Infect. Dis.* **22**, 336–339 (2016).
14. Secretaria de Vigilância em Saúde, "Boletim epidemiológico: Monitoramento dos casos de dengue, febre de chikungunya e febre pelo vírus Zika até a semana epidemiológica 4, 2016" (in Portuguese) (Ministério da Saúde do Brasil, 2016); vol. 47, no. 7; http://portalsaude.saude.gov.br/images/pdf/2016/fevereiro/29/2016-005—Dengue-SE4-publica—-o.pdf.
15. European Centre for Disease Prevention and Control (ECDC), "Rapid risk assessment: Microcephaly in Brazil potentially linked to the Zika virus epidemic" (ECDC, 2015); http://ecdc.europa.eu/en/publications/Publications/zika-microcephaly-Brazil-rapid-risk-assessment-Nov-2015.pdf.
16. J. Mlakar *et al.*, *N. Engl. J. Med.* **374**, 951–958 (2016).
17. L. Schuler-Faccini *et al.*, *MMWR Morb. Mortal. Wkly. Rep.* **65**, 59–62 (2016).
18. C. V. Ventura *et al.*, *Arq. Bras. Oftalmol.* **79**, 1–3 (2016).
19. R. B. Martines *et al.*, *MMWR Morb. Mortal. Wkly. Rep.* **65**, 159–160 (2016).
20. Pan American Health Organization (PAHO), World Health Organization (WHO), "Epidemiological alert: Neurological syndrome, congenital malformations, and Zika virus infection. Implications for public health in the Americas" (PAHO/WHO, 2015).
21. G. Calvet *et al.*, *Lancet Infect. Dis.* 10.1016/S1473-3099(16)00095-5 (2016).
22. M. Besnard, S. Lastere, A. Teissier, V. Cao-Lormeau, D. Musso, *Euro Surveill.* **19**, 20751 (2014).
23. H. Tang *et al.*, *Cell Stem Cell* 10.1016/j.stem.2016.02.016 (2016).
24. C. G. Victora *et al.*, *Lancet* **387**, 621–624 (2016).
25. WHO, "Assessment of infants with microcephaly in the context of Zika virus" (WHO Interim Report, 2016); http://apps.who.int/iris/bitstream/10665/204475/1/WHO_ZIKV_MOC_16.3_eng.pdf.
26. C. V. Ventura, M. Maia, V. Bravo-Filho, A. L. Góis, R. Belfort Jr., *Lancet* **387**, 228 (2016).
27. M. R. Nunes *et al.*, *Emerg. Infect. Dis.* **18**, 1858–1864 (2012).
28. O. G. Pybus *et al.*, *Proc. Natl. Acad. Sci. U.S.A.* **109**, 15066–15071 (2012).
29. C. Zanluca *et al.*, *Mem. Inst. Oswaldo Cruz* **110**, 569–572 (2015).
30. A. G. Meyer, S. J. Spielman, T. Bedford, C. O. Wilke, *Virus Evol.* **1**, vev006 (2015).
31. D. J. Park *et al.*, *Cell* **161**, 1516–1526 (2015).
32. M. R. Nunes *et al.*, *BMC Med.* **13**, 102 (2015).
33. M. R. Nunes *et al.*, *PLOS Negl. Trop. Dis.* **8**, e2769 (2014).
34. D. Musso, *Emerg. Infect. Dis.* **21**, 1887 (2015).
35. P. Lemey *et al.*, *PLOS Pathog.* **10**, e1003932 (2014).
36. O. G. Pybus, A. J. Tatem, P. Lemey, *Proc. Biol. Sci.* **282**, 20142878 (2015).
37. V. M. Cao-Lormeau *et al.*, *Lancet* 10.1016/S0140-6736(16)00562-6 (2016).
38. K. A. Dowd, T. C. Pierson, *Virology* **411**, 306–315 (2011).
39. J. T. Roehrig, *Adv. Virus Res.* **59**, 141–175 (2003).
40. P. Gérardin *et al.*, *PLOS Negl. Trop. Dis.* **8**, e2996 (2014).
41. A. Fagbami, S. B. Halstead, N. Marchette, K. Larsen, *Am. J. Trop. Med. Hyg.* **38**, 205–207 (1988).
42. B. D. Foy *et al.*, *Emerg. Infect. Dis.* **17**, 880–882 (2011).
43. D. Musso *et al.*, *Emerg. Infect. Dis.* **21**, 359–361 (2015).

44. D. Musso *et al.*, *Euro Surveill.* **19**, 20761 (2014).
45. A. Sorichetta *et al.*, *Sci. Data* **2**, 150045 (2015).

ACKNOWLEDGMENTS

We thank X. de Lamballerie and J. Lednicky for permission to include their unpublished ZIKV genomes in our analysis. We thank the Death Verification Service (SVO); Central Laboratories of Public Health (LACEN); and health departments of the Ceará State and Maranhão State, Brazil, for collaboration. O.G.P. is supported by the European Research Council (ERC) under the European Union's Seventh Framework Programme (FP7/2007-2013)/ERC grant 614725-PATHPHYLODYN. J.L. is supported by the ERC under the European Union's Seventh Framework Programme (FP7/2007-2013)/ERC grant 268904-DIVERSITY. O.G.P. received consulting fees from Metabiota between 2015 and 2016. This study is made possible in part by the generous support of the American people through the United States Agency for International Development (USAID) Emerging Pandemic Threats Program - PREDICT. The contents are the responsibility of the authors and do not necessarily reflect the views of USAID or the U.S. government. S.I.H. is funded by a Senior Research Fellowship from the Wellcome Trust (095066) and grants from the Bill and Melinda Gates Foundation (OPP1119467, OPP1093011, OPP1106023, and OPP1132415). M.R.T.N. is funded as an associated researcher in public health by the Evandro Chagas Institute, Brazilian Ministry of Health, and as a researcher in scientific productivity by CNPq (Brazilian National Council for Scientific and Technological Development) grants 302032/2011-8 and 200024/2015-9 and is also supported in part by the National Institute of Science and Technology for Viral Hemorrhagic Fevers. R.T. is funded by grant R24 AT 120942 from the U.S. NIH. S.C.H. is supported by a Wellcome Trust grant (102427). T.A.B. and I.R. are supported by grants from the UK Medical Research Council (MR/L009528/1) and the Wellcome Trust (090532/Z/09/Z). P.F.C.V. is supported by CNPq–National Agency for Scientific and Technologic Development (grants 573739/2008-0, 301641/2010-2, and 457664/2013-4). All samples were obtained from persons visiting local clinics or hospitalized by the Brazilian Ministry of Health personnel as part of dengue, chikungunya, and Zika fever surveillance activities. In these cases, patient consent was oral and not recorded. The study was authorized by the Coordination of the National Program for Dengue, Chikungunya, and Zika Control coordinated by Brazil's Ministry of Health. The data are available at DRYAD (DOI: 10.5061/dryad.6kn23). The ZIKV genomes reported in this study are deposited in GenBank under accession numbers KU321639, KU365777 to KU365780, KU729217, and KU729218.

SUPPLEMENTARY MATERIALS

www.sciencemag.org/content/352/6283/345/suppl/DC1
Materials and Methods
Supplementary Text
Figs. S1 to S8
Tables S1 to S5
References (*46*–*78*)

18 February 2016; accepted 16 March 2016
Published online 24 March 2016
10.1126/science.aaf5036

MALARIA DRUGS

Parasites resistant to the antimalarial atovaquone fail to transmit by mosquitoes

Christopher D. Goodman,[1]*† Josephine E. Siregar,[1,2,6]† Vanessa Mollard,[1] Joel Vega-Rodríguez,[3] Din Syafruddin,[2,4] Hiroyuki Matsuoka,[5] Motomichi Matsuzaki,[6] Tomoko Toyama,[1] Angelika Sturm,[1] Anton Cozijnsen,[1] Marcelo Jacobs-Lorena,[3] Kiyoshi Kita,[6,7] Sangkot Marzuki,[2]‡ Geoffrey I. McFadden[1]*‡

Drug resistance compromises control of malaria. Here, we show that resistance to a commonly used antimalarial medication, atovaquone, is apparently unable to spread. Atovaquone pressure selects parasites with mutations in cytochrome *b*, a respiratory protein with low but essential activity in the mammalian blood phase of the parasite life cycle. Resistance mutations rescue parasites from the drug but later prove lethal in the mosquito phase, where parasites require full respiration. Unable to respire efficiently, resistant parasites fail to complete mosquito development, arresting their life cycle. Because cytochrome *b* is encoded by the maternally inherited parasite mitochondrion, even outcrossing with wild-type strains cannot facilitate spread of resistance. Lack of transmission suggests that resistance will be unable to spread in the field, greatly enhancing the utility of atovaquone in malaria control.

Atovaquone, a component of the safe and effective antimalarial medication Malarone, kills both the blood and liver stages of malaria (*1*). The rollout of cheap generics should see increased atovaquone usage, and atovaquone derivatives are in development (*1*). Atovaquone is prone to resistance (*1*), and it has been assumed that this resistance will spread (*2*, *3*), as it has for other antimalarials (*4*, *5*). However, the target of atovaquone, cytochrome *b* (*cytB*) (*6*–*9*), has unique genetics (*10*–*12*) and experiences differential selection across the malaria parasite life cycle (*13*), which prompted us to investigate whether atovaquone resistance can spread via the mosquito vector.

We tested three atovaquone-resistant strains of the rodent malaria parasite *Plasmodium berghei*, each with different mutations in their mitochondrial DNA-encoded *cytB* gene (*14*, *15*), for transmissibility from mouse to mosquito and back to mouse (Table 1). *Anopheles stephensi* mosquitoes were fed on mice infected with either the parental *Pb*ANKA strain or one of the three atovaquone-resistant mutants, and sexual development of parasites in mosquitoes was assayed (Table 1). All three atovaquone-resistant parasite lines produced wild-type numbers of active male gametes (exflagellation) (Table 1). Parasites carrying the *Pb*M133I and *Pb*Y268C mutations in their *cytB* gene were able to self-fertilize, generate ookinetes, and successfully produce oocysts, but the oocysts produced had developmental defects (Fig. 1, A and B, and Table 1). Parasites with the *Pb*Y268N mutation were defective in the ability to self-fertilize and infect the mosquito host (Table 1) due to severely impaired female gamete activation (Fig. 1C). From 17 attempted mosquito infections, no parasite carrying an atovaquone-resistant *cytB* mutation was able to generate the sporozoite stages in the mosquito salivary glands or was able to infect a naïve mouse (Table 1). We conclude that the rodent malaria atovaquone-resistant *cytB* mutants tested—which represent a good cross section of the clinical atovaquone-resistant genotypes, including the common Y268 locus (*16*)—are unable to transmit from mouse to mouse via *A. stephensi* mosquitoes when self-fertilizing.

To determine whether outcrossing with atovaquone-sensitive parasites could help transmit the atovaquone resistance genes, we generated crosses of our atovaquone-resistant *P. berghei* lines with atovaquone-sensitive parasites. These experiments simulate what might happen if a mosquito bit an individual (or separate individuals) infected with both atovaquone-resistant and atovaquone-sensitive parasites, which can then mate in the mosquito gut. They allow us to assess whether the presence of wild-type copies of the *cytB* genes from one parent can complement a mutation in the other, as observed with deletions of electron transport components encoded in the nuclear genome (*17*). We first crossed *Pb*Y268C with an atovaquone-sensitive line (wild-type *cytB*) carrying a mutation (*15*) in the nucleus-encoded dihydrofolate reductase (*dhfr*) gene conferring pyrimethamine resistance (*Pbdhfr*S110N) by pooling blood from separate infected mice and then membrane-feeding mosquitoes. Sporozoites were produced, and all 14 naïve mice bitten by these mosquitoes (three trials) developed blood-stage infections. Genotyping of these progeny [passage

[1]School of BioSciences, University of Melbourne, Melbourne, VIC 3010, Australia. [2]Eijkman Institute for Molecular Biology, Jl Diponegoro no. 69, Jakarta, 10430, Indonesia. [3]Johns Hopkins University Bloomberg School of Public Health, Department of Molecular Microbiology and Immunology, Malaria Research Institute, Baltimore, MD 21205, USA. [4]Department of Parasitology, Faculty of Medicine, Hasanuddin University, Jalan Perintis Kemerdekaan Km10, Makassar 90245, Indonesia. [5]Division of Medical Zoology, Jichi Medical University, 3311-1 Yakushiji, Shimotsuke, Tochigi 329-0498, Japan. [6]Department of Biomedical Chemistry, Graduate School of Medicine, The University of Tokyo, Hongo, Bunkyo-ku, Tokyo 113-0033, Japan. [7]School of Tropical Medicine and Global Health, Nagasaki University, Sakamoto, Nagasaki 852-8523, Japan.
***Corresponding author. E-mail: gim@unimelb.edu.au (G.I.M.); deang@unimelb.edu.au (C.D.G.)** †These authors contributed equally to this work; order is alphabetical. ‡These authors contributed equally to this work; order is alphabetical.

zero (P0)] showed that outcrossing had occurred because 2 out of 14 mice carried parasites with both the wild-type and pyrimethamine-resistant (S110N) alleles of *Pbdhfr*. However, all 14 mice carried parasites with only wild-type, atovaquone-sensitive *cytB* alleles; outcrossing did not facilitate transmission of atovaquone resistance.

To explore this further, and quantify the level of outcrossing, we fed *A. stephensi* mosquitoes from mice infected with equal numbers of an atovaquone-sensitive line that constitutively expresses green fluorescent protein (GFP) from the nucleus (*18*) and one of our three atovaquone-resistant lines (*Pb*M133I, *Pb*Y268C, or *Pb*Y268N), which lack GFP. All crosses between sensitive (*Pb*GFP) parasites and our atovaquone-resistant parasites successfully infected the mosquitoes, and these mosquitoes were able to infect naïve mice by biting (Table 2). Presence in the progeny of both the GFP and the wild-type (no GFP) nuclear markers confirmed outcrossing (Table 2). However, all the progeny had wild-type *cytB* genotype and were sensitive to atovaquone (Table 2 and fig. S1), reaffirming that the resistance mutations cannot be complemented and transmitted, even when one parent carries a wild-type version of the gene. We conclude that outcrossing cannot assist transmission of the commonly occurring *cytB* mutations conferring atovaquone resistance.

The malaria parasite *cytB* gene is encoded on maternally inherited mitochondrial DNA (*10–12*), which implies that known forms of atovaquone resistance must be maternally inherited. We reasoned that the block in mosquito-stage development when atovaquone-resistant parasites attempt to self-fertilize (Table 1) is due to the mutation in the cytochrome *b* protein in the mitochondrion, which is only carried by the female gamete and effectively renders *cytB* mutant females sterile. To confirm this, we crossed our three *P. berghei* atovaquone-resistant lines with parasites genetically modified to be either male sterile (genotype *Pbs*48|45ko) or female sterile (genotype *Pb*nek-4ko) (*19*, *20*). If atovaquone resistance is indeed linked to mitochondrial inheritance, we expect normal genetic recombination from crosses to male-deficient parasites but no progeny from attempted crosses to a second female-deficient line. After confirming the phenotypes of the tester parasite lines (*18–20*), we crossed each of them with our three *P. berghei* *cytB* mutants. Crosses to the male-deficient line resulted in recombinant progeny (Table 2), confirming previous results from outcrossing to wild type. Again, though, all progeny from these crosses had wild-type, atovaquone-sensitive *cytB* genotype (Table 2), so they must have acquired their mitochondria from *Pbs*48|45ko female gametes (Fig. 2C).

Crossing atovaquone-resistant lines with the female infertile *Pb*nek-4ko (*20*) resulted in no progeny in 16 of 17 attempts to transmit to a naïve mouse (Table 2), largely confirming our hypothesis that the atovaquone-resistant mutants are effectively female sterile. In a single instance, parasites carrying the Y268C mutation were transmitted but with a markedly reduced efficiency (8 days to patency) (Table 2). Three independent cloned lines of the parasites recovered from this sole transmission event (named *Pb*Y268C P0) were unable to retransmit when either self-fertilized or backcrossed to *Pb*nek-4ko parasites (Tables 1 and 2); passage had not improved their transmissibility. In sum, from 44 separate transmission attempts involving 750 mosquito bites, atovaquone resistance transmission was only observed once, and this mutant was unable to transmit further despite seven attempts. We conclude that the *cytB* mutations in the mitochondrial DNA of atovaquone-resistant rodent malaria parasites render them effectively female sterile and hence largely unable to pass on the resistance gene,

Table 1. Atovaquone-resistant mutants in rodent and human malaria parasites fail to produce sporozoites in mosquitoes, and bite-back experiments with mice yielded no resistance transmission. All values are ±SEM. IC_{50}, median inhibitory concentration; wt, wild type; nd, no data available; na, not applicable.

Parasite genotype nuclear/mitochondrial	Atovaquone IC_{50} (nM)	Number of infections	Exflagellations per 10^4 red blood cells	Ookinetes per mosquito (*n* = no. of mosquitoes)	Midgut infection % infected oocytes per mosquito (*n* = no. of mosquitoes)	Sporozoites per mosquito (*n* = no. of mosquitoes)	Transmission to naïve mice	Time to patency (days)
Pb wt/wt	9.1 ± 0.4	6	5.3 ± 1.6	2327.6 ± 810.7 (58)	100 109.8 ± 21.7 (85)	10,348 ± 3279	3/3	4.3 ± 0.3
Pb wt/M133I	250 ± 41	4	5.5 ± 1.9	1488 ± 549 (38)	59 ± 16 23.2 ± 9.8 (69)	0	0/4	na
Pb wt/Y268C	23,695 ± 915	3	4.5 ± 1.3	725 ± 52.0 (30)	50 ± 10 7.0 ± 2.9 (47)	0	0/5	na
Pb wt/Y268C P0	19,080 ± 1119	4	6.7 ± 1.4	347 ± 97.0 (29)	52 ± 17 17.1 ± 10.2 (85)	0	0/6	na
Pb wt/Y268N	11,625 ± 1225	6	7.3 ± 1.9	41.7 ± 41.7* (81)	17± 11 2.7 ± 1.7 (80)	0	0/5	na
*Pf*NF54e/wt	2.25 ± 1.13	4	20.0 ± 9.3	1918 ± 225 (30)	97.3 ± 1.7 98.5 ± 38.5 (83)	nd	na	na
Pf NF54e/M133I	16.2 ± 3.9	4	9.3 ± 3.8	0	1.5 ± 1.5 0.02 ± 0.02* (144)	nd	na	na
Pf NF54e/V259L	35.3 ± 2.5	4	7.0 ± 4.3	0	3 ± 1 0.03 ± 0.01 (154)	nd	na	na

*Parasites were detected from only a single experiment.

which must be inherited through the mitochondrion (Fig. 2).

To determine whether the impact of *cytB* mutations conferring atovaquone resistance on transmission is similar in the human malaria parasite (*P. falciparum*), we selected atovaquone-resistant lines by repeated exposure to sublethal concentrations of a drug during in vitro culture (*16*). Two clones, with different mutations in *cytB* (M133I and V259L), were established (Table 1). In vitro cultured gametocytes were fed to *A. gambiae* mosquitoes, and oocyst numbers were counted 7 days after infection (Table 1). The parental line (NF54e) retained normal mosquito infectivity (Table 1). However, the two atovaquone-resistant mutants were severely impaired in their mosquito infectivity and in the number of oocysts produced when infection did occur (Table 1). The severe defect in activation of female gametes phenocopies the reduced number of activated females in the rodent malaria *Pb*Y268N (Fig. 1C). We conclude that human *P. falciparum* malaria parasites carrying atovaquone resistance mutations in *cytB* are unable to successfully infect

Table 2. Outcrossing atovaquone-resistant rodent malaria lines to sensitive lines does not facilitate resistance transmission because resistance is maternally inherited. All values are ±SEM; wt, wild type; nd, no data available; na, not applicable.

Cross nuclear genotype/ mitochondrial genotype	Number of infections	Exflagellations per 10^4 red blood cells	Midgut infection % infected oocytes per mosquito (*n* = no. of mosquitoes)	Sporozoites per mosquito (*n* = no. of mosquitoes)	Transmission to naïve mice	Time to patency (days)	Nuclear genotype P0	Mitochondrial genotype P0
GFP/wt x GFP/wt	3	6.07 ± 1.88	93 ± 6 211.2 ± 40.4 (30)	12,433 ± 1822 (29)	4/4	4 ± 0	100% GFP	wt
wt/M133I x GFP/wt	3	6.77 ± 2.16	91 ± 6 140.7 ± 76.3 (31)	10,600 ± 3139 (55)	4/4	4.25 ± 0.3	60 ± 4% GFP	wt
wt/Y268C x GFP/wt	3	1.83 ± 0.73	69 ± 6 27.0 ± 15.0 (42)	3133 ± 2533 (57)	3/4	4 ± 0	50 ± 8% GFP	wt
wt/Y268N x GFP/wt	3	6.73 ± 2.13	77 ± 12 16.8 ± 8.1 (29)	6076 ± 2899 (45)	4/4	4.5 ± 0.3	72 ± 17% GFP	wt
s48|45ko/wt × s48|45ko/wt	1	1.7	0	0	0/1	na	na	na
nek-4ko/wt x nek-4ko/wt	2	9.0 ± 6.2	0 (27)	na	na	na	na	na
s48|45ko/wt x nek-4ko/wt	1	10.2	44 9.9 (15)	750 (17)	1/1	5	s48|45ko and nek-4ko	nd
GFP/wt x nek-4ko/wt	2	11 ± 3.8	85 ± 15 31.8 ± 26.8 (22)	4575 ± 4425 (25)	2/2	4 ± 0	57 ± 5% GFP	wt
wt/M133I x s48|45ko/wt	1	2.2	67 7.3 (12)	18,900 (10)	1/1	4	wt and s48|45ko	wt
wt/Y268C x s48|45ko/wt	1	6.4	100 16 (5)	8500 (10)	1/1	4	wt and s48|45ko	wt
wt/Y268N x s48|45ko/wt	1	8.1	90 8.9 (9)	2125 (10)	1/1	4	wt and s48|45ko	wt
wt/M133I x nek-4ko/wt	4	5.5 ± 1.5	48 ± 14 8.9 ± 3.6 (73)	0 (80)	0/5	na	na	na
wt/Y268C x nek-4ko/wt	5	7.3 ± 4.3	24 ± 15 5.6 ± 3.6 (99)	500* (108)	1/7	8	wt	Y268C
wt/Y268CP0 × nek-4ko/wt	3	9.3± 4.5	41 ± 10 6.2 ± 2.6 (73)	0 (76)	0/5	na	na	na
wt/Y268N x nek-4ko/wt	3	12.6 ± 2.1	43 ± 21 18.8 ± 16.7 (4)	0 (31)	0/3	na	na	na

*Sporozoites detected in only one infection trial.

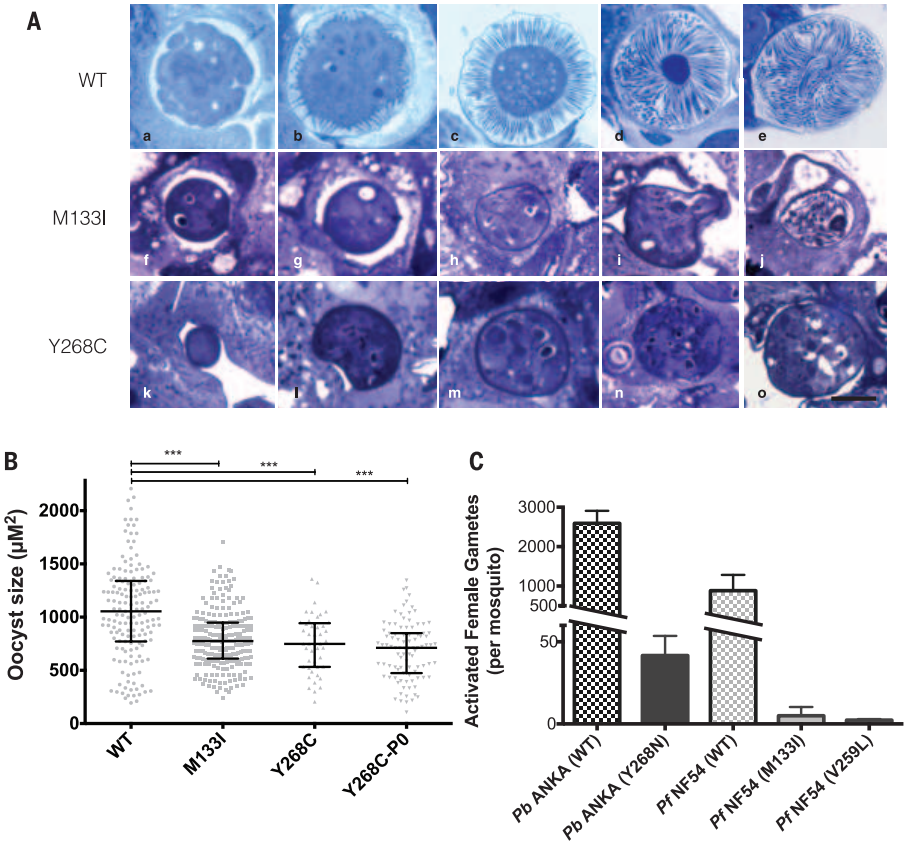

Fig. 1. Atovaquone-resistant parasites generate small, malformed oocysts in the mosquito that fail to form infectious sporozoites. (**A**) (a to e) Developmental series of oocyst sporogony in *Pb*ANKA (atovaquone sensitive and wild type) over ~18 days. The sporoblast buds off hundreds of long, thin sporozoites within the cyst wall. (f to j) Atovaquone-resistant mutant (*Pb*M133I) has smaller oocysts with dense cytoplasm, and sporozoite budding is minimal. Rare oocysts (j) form short, thick sporozoites that do not emerge. (k to o) Atovaquone-resistant mutant (*Pb*Y268C) also has small, dense, misshapen oocysts that fail to bud off any sporozoites. Scale bar, 25 μm. (**B**) Quantification of oocyst area at 12 days after feeding, showing reduced size of atovaquone-resistant parasites. Bars represent median with interquartile range. ***$P < 0.001$); difference between three atovaquone-resistant lines is not significant ($P > 0.05$); Dunn's multiple comparison test. (**C**) Number of activated females in *P. berghei* (all activated forms 24 hours after feeding) and *P. falciparum* (females and zygotes present 20 hours after feeding).

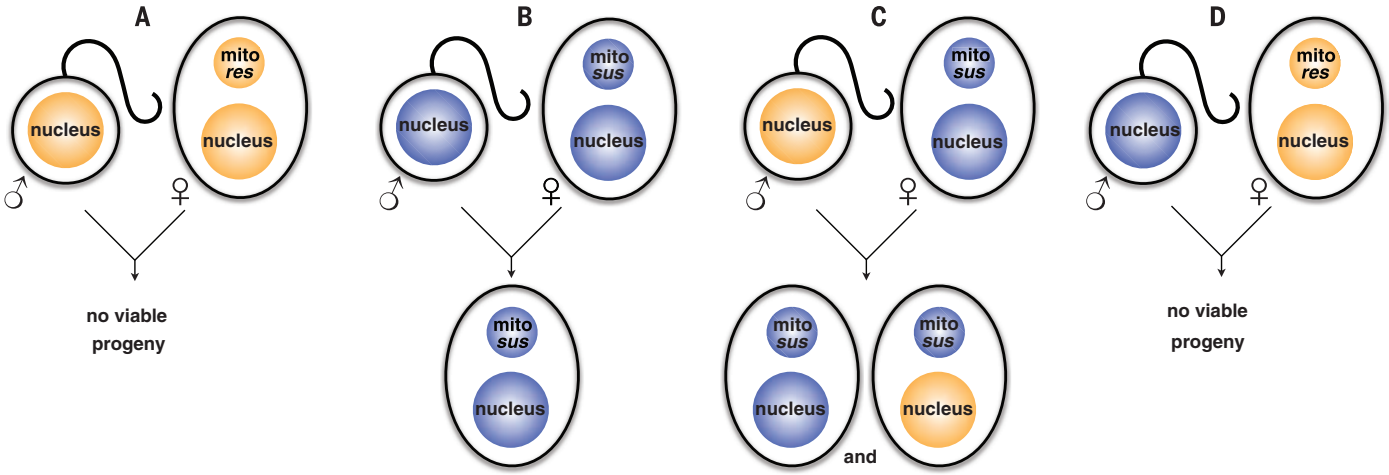

Fig. 2. The genetics of inheritance of mitochondrial DNA–encoded atovaquone resistance mutations in *cytB* prevent transmission. (**A**) Parasites with atovaquone-resistant *cytB* genes in their mitochondrion (mito *res*) cannot generate viable progeny by self-fertilization and cannot transmit. (**B**) Susceptible (mito *sus*) parasites produce susceptible progeny when self-fertilizing. (**C**) Sperm from resistant lines are able to fertilize eggs from susceptible lines and recombinant progeny ensue, but all inherit a susceptible mitochondrion from the female parent. (**D**) Sperm from susceptible lines fertilizing eggs carrying a mitochondrion-encoded resistance allele. The progeny develop poorly in mosquitoes, are not viable, and cannot transmit.

A. gambiae mosquitoes, which strongly suggests that human malaria parasites will also be unable to transmit atovaquone-resistant mutations efficiently.

Our findings show that common, clinically relevant atovaquone resistance mutations block transmission of malaria by the mosquito vector and that this phenotype is a consequence of maternal inheritance of the mitochondrion. Why are *cytB* mutations "genetic time bombs" that affect the mosquito stages of the parasite so severely? All clinically recovered atovaquone resistance mutations are in the quinol oxidase (Q^o) site of the mitochondrion-encoded cytochrome *b* protein and prevent atovaquone from displacing ubiquinone from complex III in the mitochondrial electron transport chain (*1*, *6*–*9*, *16*). Importantly, ubiquinone → cytochrome *b* electron transport operates at only

minimal levels during the malaria parasite blood phase, which relies solely on aerobic glycolysis (*21*). Nevertheless, nominal transport is essential, primarily as an electron sink for pyrimidine biosynthesis (*22*). We hypothesize that the modest levels of mitochondrial electron transport during blood phase offer relaxed selection on *cytB*—which is multicopy and easily mutable (*3*, *23*)—allowing respiration-deficient mutants (*8*, *24*) with reduced atovaquone binding (*9*) to be readily selected by drug pressure. However, when these mutants switch to the mosquito phase—which relies on full aerobic respiration with an active tricarboxylic acid cycle (*25*), robust electron transport (*17*, *26*, *27*), and mitochondrial adenosine triphosphatase activity (*28*)—the respiration deficits of the *cytB* mutants (*8*, *24*) prevent them from completing their development and generating infectious sporozoites. This results in a block of transmission of atovaquone resistance genotypes to new hosts—a block that cannot be overcome by outcrossing because *cytB* is maternally inherited.

Cytochrome *b* is thus a rather unique malaria drug target. Its genetics are constrained by maternal inheritance (*10*–*12*, *29*), there is no recombination of mitochondrial DNA (*23*), and markedly different selection regimes in the mammalian versus the mosquito hosts (*17*, *25*, *26*, *28*) all combine to restrict the parasite's options to disseminate mutations conferring resistance to atovaquone, even though they can arise relatively quickly in patients (*2*, *3*). These constraints likely apply to other cytochrome *b* targeting drugs currently under development (*30*–*32*) and perhaps to drugs targeting the maternally inherited apicoplast (*10*–*12*, *29*), an endosymbiotic organelle drug target that also has differential activity across the life cycle.

REFERENCES AND NOTES

1. G. L. Nixon *et al*., *J. Antimicrob. Chemother.* **68**, 977–985 (2013).
2. R. J. Maude, C. Nguon, A. M. Dondorp, L. J. White, N. J. White, *Malar. J.* **13**, 380 (2014).
3. G. Cottrell, L. Musset, V. Hubert, J. Le Bras, J. Clain, *Antimicrob. Agents Chemother.* **58**, 4504–4514 (2014).
4. E. Y. Klein, *Int. J. Antimicrob. Agents* **41**, 311–317 (2013).
5. E. A. Ashley *et al*., *N. Engl. J. Med.* **371**, 411–423 (2014).
6. M. Fry, M. Pudney, *Biochem. Pharmacol.* **43**, 1545–1553 (1992).
7. I. K. Srivastava, J. M. Morrisey, E. Darrouzet, F. Daldal, A. B. Vaidya, *Mol. Microbiol.* **33**, 704–711 (1999).
8. J. E. Siregar *et al*., *Parasitol. Int.* **64**, 295–300 (2015).
9. D. Birth, W. C. Kao, C. Hunte, *Nat. Commun.* **5**, 4029 (2014).
10. A. Creasey *et al*., *Mol. Biochem. Parasitol.* **65**, 95–98 (1994).
11. A. M. Creasey *et al*., *Curr. Genet.* **23**, 360–364 (1993).
12. A. B. Vaidya, J. Morrisey, C. V. Plowe, D. C. Kaslow, T. E. Wellems, *Mol. Cell. Biol.* **13**, 7349–7357 (1993).
13. D. Jacot, R. F. Waller, D. Soldati-Favre, D. A. MacPherson, J. I. MacRae, *Trends Parasitol.* **32**, 56–70 (2016).
14. D. Syafruddin, J. E. Siregar, S. Marzuki, *Mol. Biochem. Parasitol.* **104**, 185–194 (1999).
15. J. E. Siregar, D. Syafruddin, H. Matsuoka, K. Kita, S. Marzuki, *Parasitol. Int.* **57**, 229–232 (2008).
16. M. Korsinczky *et al*., *Antimicrob. Agents Chemother.* **44**, 2100–2108 (2000).
17. K. E. Boysen, K. Matuschewski, *J. Biol. Chem.* **286**, 32661–32671 (2011).
18. B. Franke-Fayard *et al*., *Mol. Biochem. Parasitol.* **137**, 23–33 (2004).
19. M. R. van Dijk *et al*., *Cell* **104**, 153–164 (2001).
20. L. Reininger *et al*., *J. Biol. Chem.* **280**, 31957–31964 (2005).
21. J. I. MacRae *et al*., *BMC Biol.* **11**, 67 (2013).
22. H. J. Painter, J. M. Morrisey, M. W. Mather, A. B. Vaidya, *Nature* **446**, 88–91 (2007).
23. M. D. Preston *et al*., *Nat. Commun.* **5**, 4052 (2014).
24. N. Fisher *et al*., *J. Biol. Chem.* **287**, 9731–9741 (2012).
25. H. Ke *et al*., *Cell Reports* **11**, 164–174 (2015).
26. A. Hino *et al*., *J. Biochem.* **152**, 259–268 (2012).
27. T. Q. Tanaka, M. Hirai, Y. Watanabe, K. Kita, *Parasitol. Int.* **61**, 726–728 (2012).
28. A. Sturm, V. Mollard, A. Cozijnsen, C. D. Goodman, G. I. McFadden, *Proc. Natl. Acad. Sci. U.S.A.* **112**, 10216–10223 (2015).
29. N. Okamoto, T. P. Spurck, C. D. Goodman, G. I. McFadden, *Eukaryot. Cell* **8**, 128–132 (2009).
30. T. G. Nam *et al*., *ACS Chem. Biol.* **6**, 1214–1222 (2011).
31. A. M. Stickles *et al*., *Am. J. Trop. Med. Hyg.* **92**, 1195–1201 (2015).
32. C. K. Dong *et al*., *Chem. Biol.* **18**, 1602–1610 (2011).

ACKNOWLEDGMENTS

This work was supported by grants from the National Health and Medical Research Council (Australia); the Australian Research Council; the Indonesian Ministry of Research, Technology, and Higher Education; the U.S. National Institutes of Health (grants AI031478 and RR00052); the Japanese Society for Promotion of Science (JSPS) KAKENHI (grant 23117004 to M. M. and 26253025 to K. K.); and Japanese Science and Technology Agency/Japan International Cooperation Agency Science and Technology Research Partnership for Sustainable Development (SATREPS; no. 10000284 to K. K.). We acknowledge support of the Program for Promotion of Basic and Applied Researches for Innovations in Bio-oriented Industry (BRAIN) and the Science and Technology Research Promotion Program for Agriculture, Forestry, Fisheries and Food Industry. J.E.S. was a JSPS Ph.D. fellow (RONPAKU program) and an Endeavor Fellow from Scope Global, Australia. A.S. is affiliated with TropIQ Health Sciences (http://tropiq.nl). We thank the Johns Hopkins Malaria Research Institute mosquito and parasite core facilities for help with mosquito rearing and *P. falciparum* cultures, S. Narulitha of the Eijkman Institute for Molecular Biology for the novel *P. berghei* PbM133I atovaquone resistance mutant, and Walter Reed Army Institute of Research for the *P. falciparum* NF54e parasites. Data are archived at figshare (https://figshare.com) under doi 10.4225/49/56DE29B278684.

SUPPLEMENTARY MATERIALS

www.sciencemag.org/content/352/6283/349/suppl/DC1
Materials and Methods
Fig. S1
References (*33*–*39*)

23 November 2015; accepted 10 March 2016
10.1126/science.aad9279

CELL BIOLOGY

Nuclear envelope rupture and repair during cancer cell migration

Celine M. Denais,[1]* Rachel M. Gilbert,[1]* Philipp Isermann,[1]* Alexandra L. McGregor,[1] Mariska te Lindert,[2] Bettina Weigelin,[2] Patricia M. Davidson,[1] Peter Friedl,[2,3,4] Katarina Wolf,[2] Jan Lammerding[1]†

During cancer metastasis, tumor cells penetrate tissues through tight interstitial spaces, which requires extensive deformation of the cell and its nucleus. Here, we investigated mammalian tumor cell migration in confining microenvironments in vitro and in vivo. Nuclear deformation caused localized loss of nuclear envelope (NE) integrity, which led to the uncontrolled exchange of nucleo-cytoplasmic content, herniation of chromatin across the NE, and DNA damage. The incidence of NE rupture increased with cell confinement and with depletion of nuclear lamins, NE proteins that structurally support the nucleus. Cells restored NE integrity using components of the endosomal sorting complexes required for transport III (ESCRT III) machinery. Our findings indicate that cell migration incurs substantial physical stress on the NE and its content and requires efficient NE and DNA damage repair for cell survival.

The nuclear envelope (NE), comprising the inner and outer nuclear membranes, nuclear pore complexes, and the nuclear lamina, presents a physical barrier between the nuclear interior and the cytoplasm that protects the genome from cytoplasmic components and establishes a separate compartment for DNA and RNA synthesis and processing (*1*). Loss of NE integrity and nuclear pore selectivity has been linked to the normal aging process and a variety of human diseases, including cancer (*2*). In cancer progression, key steps of tumor cell invasion depend upon deformation of the nucleus into available spaces within the three-dimensional tissue (*3*–*6*). Whereas the cytoplasm of migrating cells can penetrate even submicron-sized pores, the deformation of the large and relatively rigid nucleus becomes a rate-limiting factor in migration through pores <25 μm^2 in cross section (*4*, *6*–*10*). We hypothesized that migration through such tight spaces provides a substantial mechanical challenge to the integrity of the nucleus. Thus, we investigated whether cell migration through confining spaces induces NE rupture and compromises DNA integrity

[1]Nancy E. and Peter C. Meinig School of Biomedical Engineering and Weill Institute for Cell and Molecular Biology, Cornell University, Ithaca, NY, USA. [2]Department of Cell Biology, Radboud University Medical Center, Nijmegen, Netherlands. [3]Department of Genitourinary Medical Oncology, The University of Texas MD Anderson Cancer Center, Houston, TX, USA. [4]Cancer Genomics Center, Netherlands (CGC.nl).
*These authors contributed equally to this work. **†Corresponding author. E-mail: jan.lammerding@cornell.edu**

and how cells repair such NE ruptures during interphase.

To model cancer cell invasion with precise control over cell confinement, we designed a microfluidic device containing constrictions with fixed height and varying widths mimicking interstitial pore sizes (fig. S1, A and B) (*11*). We detected NE rupture using previously established fluorescent reporters consisting of green or red fluorescent proteins fused to a nuclear localization sequence (NLS-GFP and NLS-RFP, respectively) that rapidly escape into the cytoplasm when NE integrity is lost (*12–14*). Breast cancer, fibrosarcoma, and human skin fibroblast cells displayed transient loss of NE integrity, which coincided with the nucleus passing through the constrictions (Fig. 1, A and B; fig. S1, C to L; and movie S1). NE rupture was associated with transient influx of fluorescently

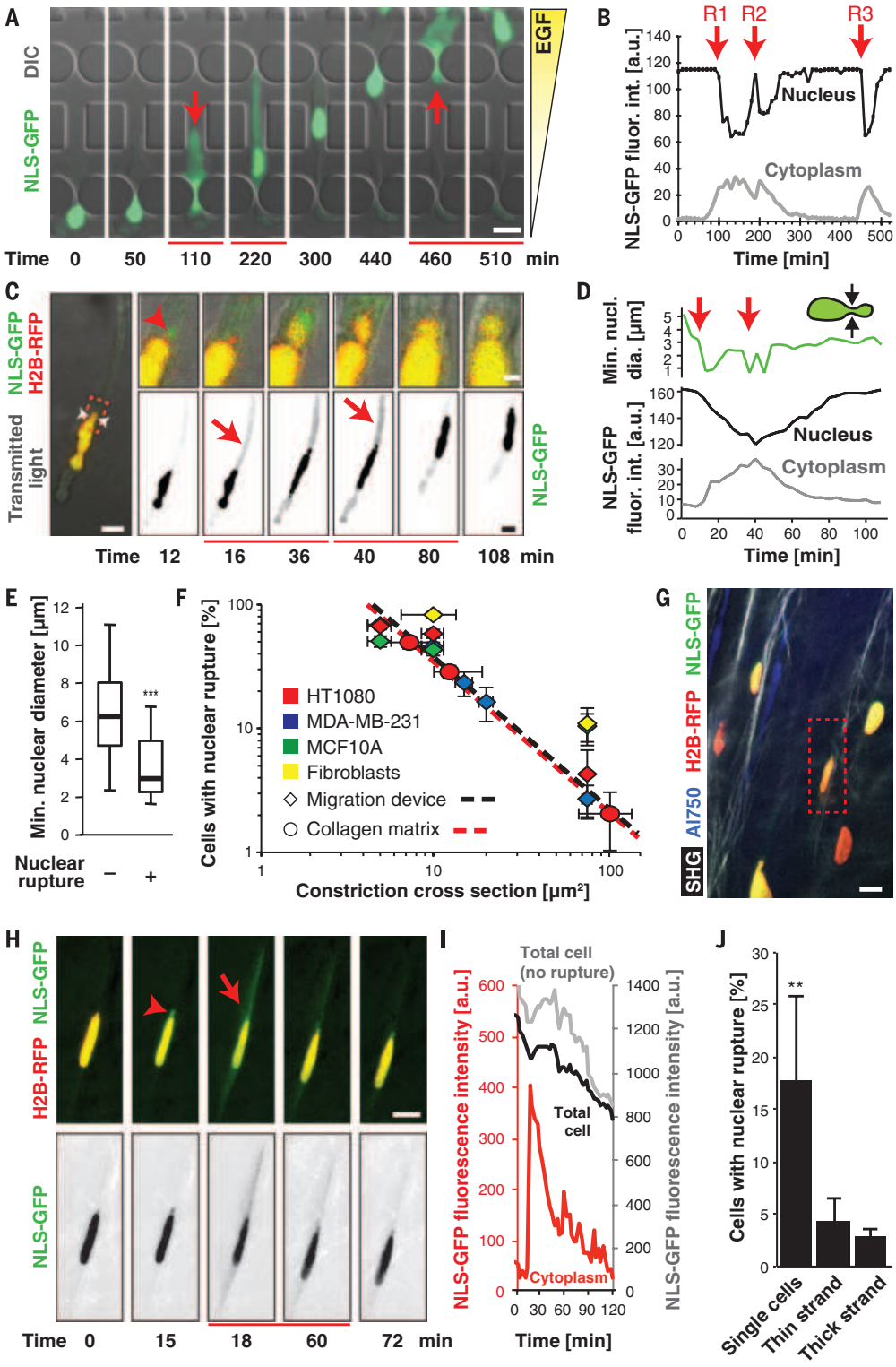

Fig. 1. Nuclear rupture during migration through confining environments. (**A**) Image sequence of an MDA-MB-231 breast cancer cell that exhibited multiple NE ruptures while moving through 2- × 5-µm^2 constrictions. See also movie S1. DIC, differential interference contrast; EGF, epidermal growth factor. Here and in all other figures, red arrows and lines below frames indicate beginning and duration of NE rupture(s). Scale bar, 20 µm. (**B**) Fluorescence intensity (arbitrary units) of nuclear and cytoplasmic NLS-GFP of the cell in (A), showing loss of nuclear signal and concomitant increase in cytoplasmic fluorescence upon NE rupture, followed by gradual reimport of NLS-GFP into the nucleus. R1 to R3 indicate NE rupture events. (**C**) NE rupture in an HT1080 fibrosarcoma cell coexpressing NLS-GFP and fluorescently labeled histones (H2B-RFP) migrating inside a collagen matrix (2.5 mg/ml) with MMP inhibitor GM6001. See also movie S2. White arrowheads indicate the minimal nuclear diameter. (Insets, top row) Close-up of nuclear bleb formation (red arrowhead). Scale bar, 10 µm; insets, 2 µm. (**D**) Minimal nuclear diameter and nuclear and cytoplasmic NLS-GFP fluorescence intensity for the cell in (C). (**E**) Minimal nuclear diameter in rupturing and nonrupturing HT1080 cells in collagen matrix. ***$P < 0.001$; $n = 159$ and 62 cells, respectively. (**F**) Incidences of NE rupture as a function of constriction sizes in collagen matrices [slope = –1.224; coefficient of determination (R^2) = 0.999] and microfluidic devices during a ~12-hour period (slope = –1.219; $R^2 = 0.974$). Regression based on HT1080 and MDA-MB-231 cells; $n = 55$ to 445 cells per condition. (**G** and **H**) Multiphoton image of HT1080 fibrosarcoma cells 5 days after implantation into the mouse dermis. Dashed box in (G) indicates cell with NE rupture and nuclear bleb (arrowhead) shown in (H). Collagen fibers detected by second harmonic generation (SHG); blood vessels visualized by AlexaFluor-750–labeled 70 kD dextran. Scale bar, 20 µm. (**I**) Fluorescence intensity of cytoplasmic (red) and total (black and gray) NLS-GFP signal in rupturing (red and black) and nonrupturing (gray) cell(s) in the same field of view. (**J**) Incidence of NE rupture as function of migration mode. **$P < 0.01$ versus thin and thick strands; $n = 22$ to 211 cells per condition. Error bars, SE.

labeled cytoplasmic proteins into the nucleus (fig. S2) and could also be detected by accumulation of the fluorescently labeled DNA-binding proteins' barrier-to-autointegration factor (BAF) (*15*) and guanosine 3′,5′-monophosphate–adenosine 3′,5′-monophosphate (cyclic GMP-AMP) synthase (cGAS) (*16*) at sites of NE rupture (fig. S3).

We then tested whether NE rupture also occurs during cancer cell migration in biological environments. Fibrosarcoma cells and skin fibroblasts exhibited NE rupture during migration in fibrillar collagen matrices (Fig. 1, C and D; fig. S4; and movie S2), with kinetics similar to those recorded in the constriction channels (fig. S1M). NE rupture typically occurred when the minimal nuclear diameter, which closely matches the pore size encountered by the cell (*6*), dropped to 3 μm (Fig. 1, D and E) and so linked NE rupture to cell movement through narrow spaces. Accordingly, NE ruptures were rare (i.e., below 5% per ~12-hour observation period) for cells migrating on glass, in low-density collagen matrices, or through channels 15 × 5 μm^2 wide, in line with previously reported rates of spontaneous NE rupture in cancer cell lines (*13*). However, when matrix pore sizes were reduced to 5 to 20 μm^2 and below by increasing collagen concentration and/or by

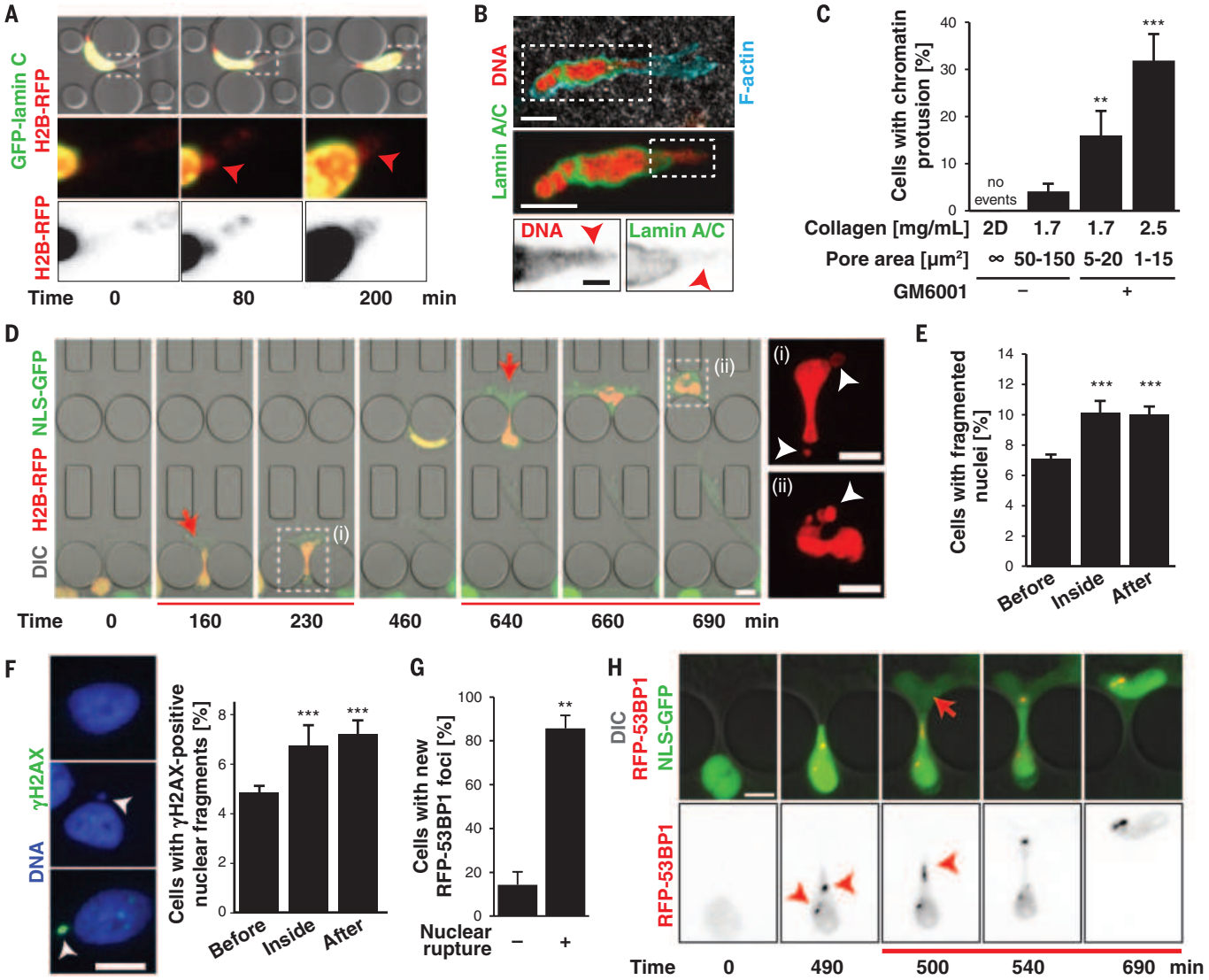

Fig. 2. Confined migration leads to chromatin protrusions, nuclear fragmentation, and DNA damage. (**A**) Representative image of an MDA-MB-231 cell coexpressing GFP-lamin C and H2B-RFP developing chromatin protrusion (arrowhead) during migration through a microfluidic constriction. Scale bar, 5 μm. (**B**) HT1080 cell in a collagen matrix (2.5 mg/ml + GM6001) with chromatin protrusion (arrowheads) across the nuclear lamina, stained for lamin A/C (green), DNA (red), and F-actin (turquoise). Scale bars, 10 μm; bottom inset, 2 μm. (**C**) Percentage of cells with chromatin protrusions as a function of collagen matrix pore size. 2D, unconfined migration on glass slide. $^{**}P < 0.01$; $^{***}P < 0.0001$; n = 50 to 146 cells per condition. (**D**) Representative image sequence of the formation of chromatin-filled nuclear membrane blebs (white arrowheads) and subsequent nuclear fragmentation in an MDA-MB-231 breast cancer cell coexpressing NLS-GFP (green) and H2B-RFP (red) during migration through consecutive 2- × 5-μm^2 constrictions. Insets are indicated by dashed lines. See also movie S6. (**E**) Percentage of cells with fragmented nuclei before entry into constriction channel, inside the channel, and after exit. $^{***}P < 0.001$; n = 9775, 1376, and 3072, respectively. (**F**) Example of an intact nucleus (left top), a nucleus with a small fragment (arrowhead) (left middle), and a nucleus with a γ-H2AX–positive fragment (left bottom). Scale bar, 10 μm. Percentage of cells with γ-H2AX–positive nuclear fragments before, inside, and after migration through constriction channels (right). $^{***}P < 0.001$; n = 1376 to 3072 cells per condition. (**G**) Percentage of HT1080 cells migrating through 2- × 5-μm^2 or 1- × 5-μm^2 constrictions that formed 53BP1-RFP foci as a function of nuclear rupture. $^{**}P < 0.01$, n = 35 cells total. (**H**) Representative example of formation of 53BP1 foci (arrowheads) in U2OS cell coexpressing NLS-GFP and RFP-53BP1 during migration through 2- × 5-μm^2 constriction and NE rupture. Scale bar, 10 μm. Error bars, SE.

blocking the cells' ability to cleave collagen fibers and widen pores by addition of a matrix metalloprotease (MMP) inhibitor, the incidence of NE rupture increased 10-fold and more (fig. S5, A and B). Similarly, reducing the pore size of the microfluidic channels to <20 μm^2 increased NE rupture more than 10-fold (fig. S5, C and D). Irrespective of the experimental model, the incidence of NE rupture increased exponentially with decreasing pore size (Fig. 1F) and reached >90% when the nuclear height was confined to 3 μm (fig. S5E). Imaging HT1080 fibrosarcoma cells invading the collagen-rich mouse dermis in live tumors after orthotopic implantation confirmed that migration-induced NE rupture also occurs in vivo, particularly in individually disseminating cells (Fig. 1, G to J; fig. S6; and movie S3). NE rupture was less prevalent in cells moving as multicellular collective strands (Fig. 1J and fig. S6), which typically follow linear tracks of least resistance and undergo less pronounced nuclear deformations (*3*, *7*).

NE rupture in vitro and in vivo was often accompanied by protrusion of chromatin through the nuclear lamina (Fig. 2, A and B; fig. S7, A to I; and movies S4 and S5). The incidence of such "chromatin herniations" increased significantly with decreasing pore sizes (Fig. 2C and fig. S7H). In severe cases, small pieces of the nucleus were pinched off from the primary nucleus as cells

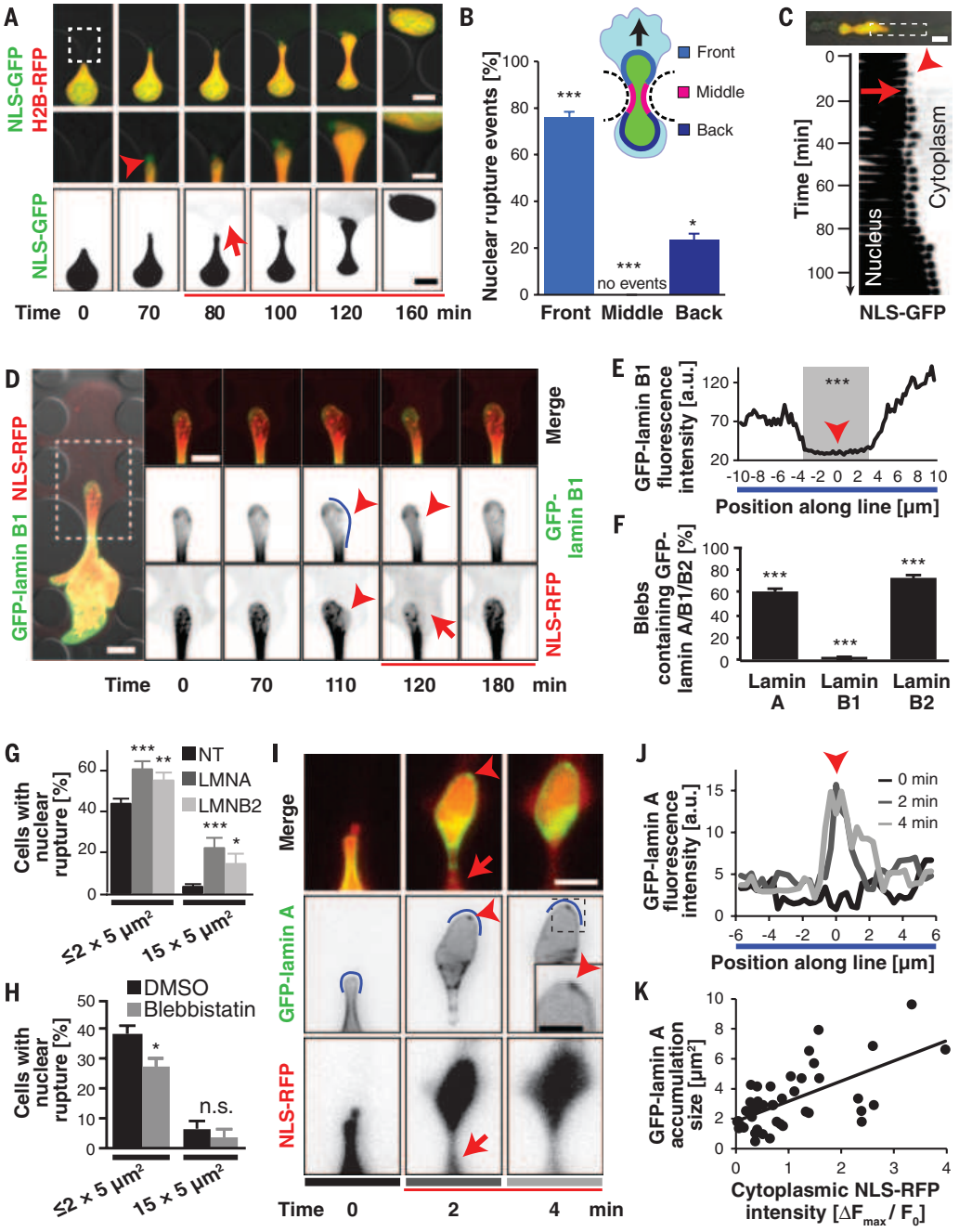

Fig. 3. Molecular sequence of nuclear rupture. (**A**) Nuclear membrane bleb formation (arrowhead) and collapse upon NE rupture. Scale bars, top and bottom rows, 10 μm; inset, 5 μm. (**B**) Distribution of NE rupture sites along nuclear periphery. Regions are based on the migration direction (black arrow) and denoted in the cartoon. n = 352 cells; $^*P < 0.05$; $^{***}P < 0.001$; all comparisons relative to the hypothetical uniform distribution of 33%. (**C**) Kymograph of nuclear bleb formation (arrowhead) and collapse during subsequent NE rupture, corresponding to the image sequence in Fig. 1C. (**D**) Nuclear membrane blebs formed at sites of low GFP-lamin B1 intensity and were devoid of GFP-lamin B1 (arrowheads). Intensity along the blue line is quantified in (E). The gray area indicates the local absence of lamin B1. Representative cell out of 178 cells observed. (**E**) GFP-lamin B1 fluorescence intensity profile. The gray area and arrowhead indicate the section where the nuclear bleb forms. $^{***}P < 0.001$; comparing values inside and outside the gray area. (**F**) Percentage of nuclear blebs containing detectable amounts of lamin A, B1, or B2. $^{***}P < 0.001$; compared with the expected value of 100% for the primary nucleus; n = 178 to 199 cells per condition. (**G**) Incidence of NE rupture after small interfering RNA (siRNA) treatment against lamin A/C, lamin B2, or nontarget (NT) control. $^*P < 0.05$; $^{**}P < 0.01$; $^{***}P < 0.001$; n = 384, 150, and 163 cells for constrictions ≤2 × 5 μm^2; n = 166, 68, and 49 for 15- × 5-μm^2 constrictions. (**H**) Blebbistatin treatment reduced NE rupture incidence during migration in constriction channels, but not in 15- × 5-μm^2 control channels. DMSO, dimethyl sulfoxide as a control. $^*P < 0.05$; n = 286 and 194 for constrictions ≤2 × 5 μm^2; n = 122, and 54 for cells in constrictions 15 × 5 μm^2. (**I**) GFP-lamin A accumulated at sites of NE rupture, forming lamin scars (arrowheads). Gray and black bars under images correspond to line profiles at different times in (J). Scale bar, 10 μm. (**J**) GFP-lamin A signal intensity along a section of the nuclear rim [blue line in (I)]. (**K**) GFP-lamin A accumulation increases with the severity of NE rupture. $P < 0.0001$; n = 46 cells (slope = 1.345, R^2 = 0.3945). Error bars, SE.

passed through narrow constrictions (Fig. 2D and movie S6), which resulted in an elevated and persistent fraction of cells with fragmented nuclei (Fig. 2E and fig. S7J). Furthermore, cells that had passed through microfluidic constrictions had more nuclear fragments positive for γ-H2AX, a marker of DNA double-strand breaks (*17*), than cells that had not yet entered the constrictions (Fig. 2F), consistent with recent reports that loss of NE integrity in micronuclei can cause DNA damage (*14*) and chromothripsis (*18*). Intense γ-H2AX staining could also be found at chromatin protrusions (fig. S8A). To confirm that DNA damage was caused by migration-induced nuclear deformation and NE rupture, we performed live-cell imaging on cells coexpressing NLS-GFP and fluorescently labeled 53BP1 (RFP-53BP1), another marker of DNA damage (*19*, *20*). NE rupture, and even severe nuclear deformation alone, resulted in rapid formation of new RFP-53BP1 foci as cells squeezed through the constrictions (Fig. 2, G and H; and fig. S8, B to G), consistent with previous reports of increased activation of DNA damage response genes after compression-induced chromatin herniation and NE rupture (*21*).

To gain further insights into the biophysical processes underlying NE rupture, we analyzed

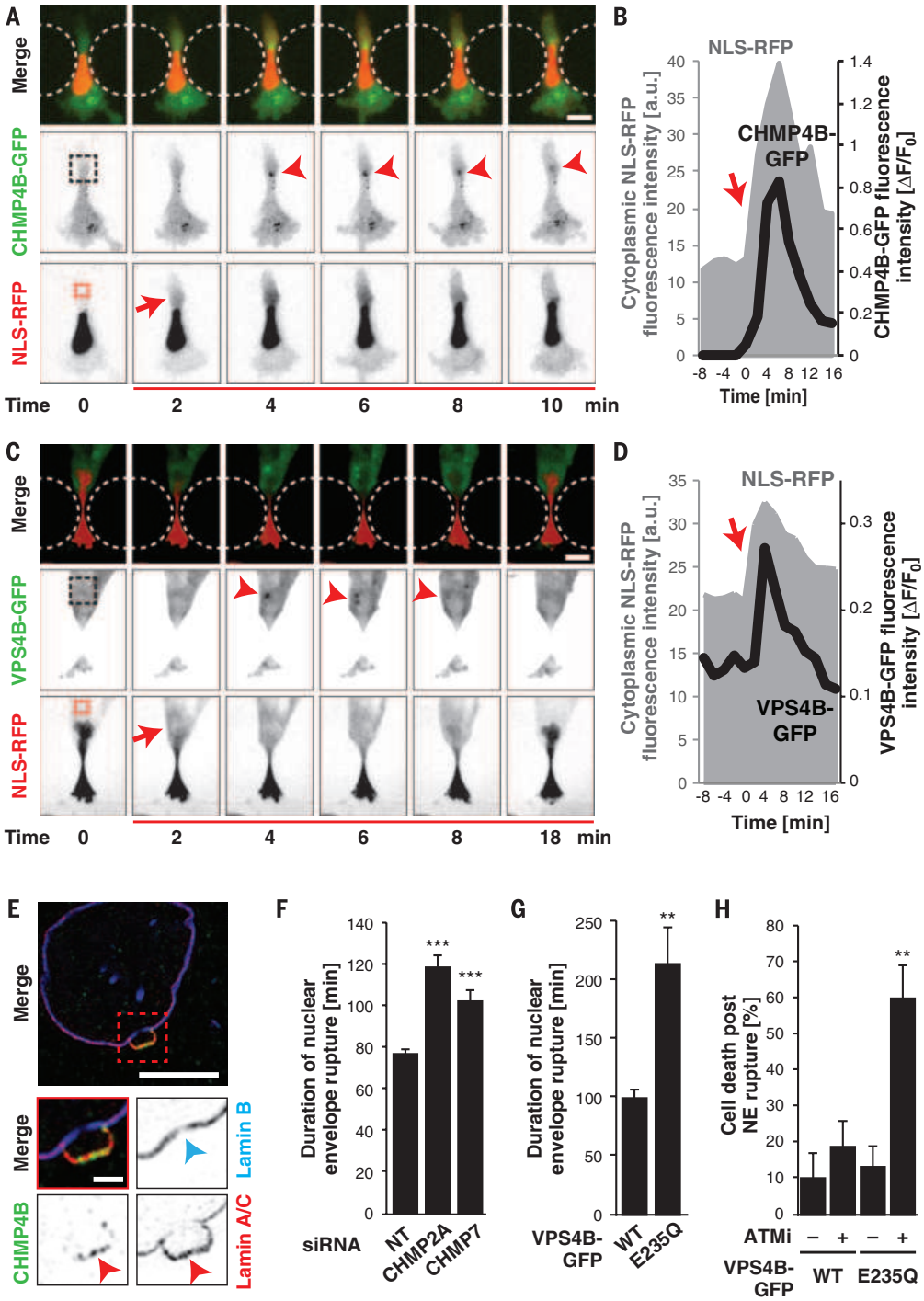

Fig. 4. ESCRT III mediates nuclear envelope repair. (**A**) CHMP4B-GFP was transiently recruited to the site of nuclear membrane damage (arrowhead). See also movie S7. Dashed boxes indicate areas used for measurements in (B). Representative sequence from 12 HT1080 cells total. Scale bar, 10 μm. (**B**) CHMP4B-GFP fluorescence intensity at rupture site (black), normalized to prerupture intensity, increased after NE rupture, indicated by increase in cytoplasmic NLS-RFP signal (gray). Red arrow indicates time of NE rupture. $\Delta F/F_0$, the change of the intensity from the original intensity before stimulation. (**C**) Recruitment of VPS4B-GFP to sites of NE rupture (arrowhead) in an MDA-MB-231 cell. Dashed boxes indicate areas used for measurements in (D). Representative example from 18 cells total. Scale bar, 10 μm. (**D**) VPS4B-GFP fluorescence intensity in the cytoplasm (black) increased rapidly after NE rupture, detected by increase in cytoplasmic NLS-RFP signal (gray). Red arrow indicates time of NE rupture. (**E**) Representative superresolution image (from 12 cells total) of endogenous CHMP4B accumulation at NE rupture site. Lamin A/C accumulation confirmed rupture site (red arrowhead). Blue arrowhead indicates decreased lamin B intensity at the base of the bleb. Scale bars, 5 μm; inset, 1 μm. (**F**) siRNA-mediated depletion of ESCRT III proteins CHMP7 and CHMP2A in HT1080 cells resulted in an increased duration of NLS-GFP in the cytoplasm after migration induced NE rupture compared with nontarget (NT) controls. ***$P < 0.001$; $n = 137$ and 107, respectively. (**G**) Expression of the dominant-negative mutant VPS4B^{E235Q}-GFP increased the duration of NLS-GFP in the cytoplasm after migration induced NE rupture in HT1080 cells, which indicated impaired nuclear membrane repair. **$P < 0.005$; $n = 17$ and 10, respectively. (**H**) Percentage of HT1080 cells dying after migration induced NE rupture, in the absence or presence of inhibition of ESCRT III by dominant-negative VPS4B^{E235Q}-GFP and/or DNA repair with the ataxia telangiectasia mutated kinase (ATM) inhibitor KU-55933 (ATMi). **$P < 0.01$, comparing ATMi$^+$/E235Q to ATMi$^+$/WT and ATMi$^-$/E235Q; $n = 20$, 32, 38, 30, respectively. Error bars, means ± SEM.

the timing and location of NE rupture in regard to nuclear deformation, local membrane curvature, NE composition, and cytoskeletal forces. NE rupture occurred predominantly (~76%) at the leading edge of the nucleus (Fig. 3, A and B) and was almost always (89.9 ± 2.14%, n = 198 cells) preceded by, or coincided with, the formation of nuclear membrane protrusions ("blebs") as the nuclei moved through the constrictions (Fig. 1, C and H; Fig. 3, A and C; and fig. S9). Nuclear membrane blebs typically (96.1 ± 1.38%, n = 178 blebs) formed at sites where the nuclear lamina signal, particularly the lamin B1 network, was weak or absent (Fig. 3, D to F, and fig. S10, A and B). These findings indicate that blebs form when segments of the nuclear membrane detach from the nuclear lamina and bulge into the cytoplasm. Depletion of the lamins A/C and lamin B2 significantly increased the likelihood of NE rupture (Fig. 3G and fig. S10C), which together with previous studies (*4*, *12*, *13*, *21*–*23*) suggest that lamins are important for stabilizing the NE.

Consistent with previous observations (*13*, *21*, *22*, *24*, *25*), the expanding nuclear blebs were devoid of GFP-lamin B1 (Fig. 3, D to F) and nuclear pores (fig. S10D), and initially contained little or no GFP-lamin A and B2 (fig. S10, A and B). Upon NE rupture the blebs retracted and collapsed (Fig. 1, C and H; Fig. 3, A and C; fig. S9; and fig. S10, E to H), which suggested that hydrostatic pressure was released from the fluid-filled blebs. Although the NE contains pores, recent studies have shown that the NE can provide an effective barrier to support intracellular pressure gradients (*26*, *27*). Nuclear pressurization could arise from actomyosin contraction at the rear of the nucleus that is required to move the nucleus through tight spaces (*5*, *6*), which effectively mimicks cellular compression experiments (*21*, *22*). Supporting this idea, treatment with low concentrations of blebbistatin, a myosin II inhibitor, significantly decreased the incidence of nuclear rupture (Fig. 3H) without inhibiting the ability of cells to migrate through larger channels (fig. S10I)

The transient nature of NE rupture suggests that cells can efficiently restore nuclear membrane integrity during interphase. We observed rapid (<2 min) accumulation of GFP-lamin A at the site of rupture that correlated with the severity of nuclear rupture and that often persisted for hours (Fig. 3, I to K, and fig. S11). Subsequent ruptures within the same cell occurred at distinct sites (fig. S11A), which implied local protection by these "lamin scars." Two recent reports have shown that members of the endosomal sorting complexes required for transport III (ESCRT III) family are involved in resealing the nuclear membrane during late anaphase (*28*, *29*). To assess whether ESCRT proteins have a similar function in interphase NE repair, we generated GFP-fusion constructs of the ESCRT III subunit CHMP4B, involved in recruiting other ESCRT III proteins and facilitating membrane scission, and the ESCRT III–associated VPS4B, which is required for disassembly and recycling of ESCRT III proteins (*30*). Upon NE rupture induced by confined migration or laser ablation, CHMP4B-GFP and VPS4B-GFP rapidly (in ≤2 min) formed transient foci at the site of nuclear membrane damage (Fig. 4, A to D; fig. S12; fig. S13, A to C; and movie S7). Superresolution microscopy confirmed recruitment of endogenous ESCRT III proteins to sites of NE rupture into complexes ≤160 nm in size (Figs. 4E and fig. S13, D to H). Recruitment of the ESCRT III machinery was independent of microtubules (fig. S14). Depletion of the ESCRT III subunit CHMP2A, CHMP7, or ectopic expression of a dominant-negative VPS4B mutant (GFP-VPS4B^{E235Q}) that prevents ESCRT III subunit recycling significantly increased the time required for nucleo-cytoplasmic recompartmentalization (Figs. 4, F and G, and fig. S13, I to N), which indicated a crucial role of ESCRT III proteins in restoring nuclear membrane integrity. To assess the functional relevance of NE repair, we quantified cell viability after NE rupture. Under normal conditions, the vast majority (>90%) of cells survived even repeated NE rupture (Figs. 1A and 4H and fig. S4A). Inhibiting either ESCRT III–mediated NE repair or DNA damage repair pathways alone did not reduce cell viability, but inhibition of both NE and DNA repair substantially increased cell death after NE rupture (Fig. 4H).

Taken together, our studies demonstrate that cell migration through confining spaces, as frequently encountered during cancer cell invasion, can challenge the integrity of the NE and DNA content, which could promote DNA damage, aneuploidy, and genomic rearrangements, and—in the absence of efficient repair—cell death (*31*). We propose a biophysical model in which cytoskeletal-generated nuclear pressure results in the formation and eventual rupture of nuclear membrane blebs at sites of high membrane curvature and weakness in the underlying nuclear lamina (fig. S15). These events could be particularly prominent in cells with reduced levels of lamins, whose expression is deregulated in many cancers and often correlates with negative outcomes (*32*, *33*). Although NE rupture, and resulting genomic instability, may promote cancer progression, it may also represent a particular weakness of metastatic cancer cells and an opportunity to develop novel antimetastatic drugs by specifically targeting these cells, for example, by blocking NE repair and inhibiting DNA damage repair.

REFERENCES AND NOTES

1. B. Burke, C. L. Stewart, *Curr. Top. Dev. Biol.* **109**, 1–52 (2014).
2. E. Hatch, M. Hetzer, *J. Cell Biol.* **205**, 133–141 (2014).
3. B. Weigelin, G.-J. Bakker, P. Friedl, *Intravital* **1**, 32–43 (2012).
4. T. Harada *et al.*, *J. Cell Biol.* **204**, 669–682 (2014).
5. D. G. Thomas *et al.*, *J. Cell Biol.* **210**, 583–594 (2015).
6. K. Wolf *et al.*, *J. Cell Biol.* **201**, 1069–1084 (2013).
7. P. Friedl, K. Wolf, J. Lammerding, *Curr. Opin. Cell Biol.* **23**, 55–64 (2011).
8. P. M. Davidson, C. Denais, M. C. Bakshi, J. Lammerding, *Cell. Mol. Bioeng.* **7**, 293–306 (2014).
9. A. C. Rowat *et al.*, *J. Biol. Chem.* **288**, 8610–8618 (2013).
10. Y. Fu, L. K. Chin, T. Bourouina, A. Q. Liu, A. M. VanDongen, *Lab Chip* **12**, 3774–3778 (2012).
11. P. M. Davidson, J. Sliz, P. Isermann, C. Denais, J. Lammerding, *Integr. Biol. (Camb.)* **7**, 1534–1546 (2015).
12. W. H. De Vos *et al.*, *Hum. Mol. Genet.* **20**, 4175–4186 (2011).
13. J. D. Vargas, E. M. Hatch, D. J. Anderson, M. W. Hetzer, *Nucleus* **3**, 88–100 (2012).
14. E. M. Hatch, A. H. Fischer, T. J. Deerinck, M. W. Hetzer, *Cell* **154**, 47–60 (2013).
15. A. Jamin, M. S. Wiebe, *Curr. Opin. Cell Biol.* **34**, 61–68 (2015).
16. F. Civril *et al.*, *Nature* **498**, 332–337 (2013).
17. A. J. Nakamura, V. A. Rao, Y. Pommier, W. M. Bonner, *Cell Cycle* **9**, 389–397 (2010).
18. C. Z. Zhang *et al.*, *Nature* **522**, 179–184 (2015).
19. S. Bekker-Jensen, C. Lukas, F. Melander, J. Bartek, J. Lukas, *J. Cell Biol.* **170**, 201–211 (2005).
20. A. Loewer, K. Karanam, C. Mock, G. Lahav, *BMC Biol.* **11**, 114 (2013).
21. M. Le Berre, J. Aubertin, M. Piel, *Integr. Biol. (Camb.)* **4**, 1406–1414 (2012).
22. J. L. Broers *et al.*, *Hum. Mol. Genet.* **13**, 2567–2580 (2004).
23. J. Lammerding *et al.*, *J. Clin. Invest.* **113**, 370–378 (2004).
24. T. Shimi *et al.*, *Genes Dev.* **22**, 3409–3421 (2008).
25. T. Shimi *et al.*, *Mol. Biol. Cell* **26**, 4075–4086 (2015).
26. R. J. Petrie, H. Koo, K. M. Yamada, *Science* **345**, 1062–1065 (2014).
27. S. Neelam *et al.*, *Proc. Natl. Acad. Sci. U.S.A.* **112**, 5720–5725 (2015).
28. Y. Olmos, L. Hodgson, J. Mantell, P. Verkade, J. G. Carlton, *Nature* **522**, 236–239 (2015).
29. M. Vietri *et al.*, *Nature* **522**, 231–235 (2015).
30. J. H. Hurley, *EMBO J.* **34**, 2398–2407 (2015).
31. M. Raab *et al.*, *Science* **352**, aad7611 (2016).
32. C. J. Hutchison, *Adv. Exp. Med. Biol.* **773**, 593–604 (2014).
33. A. Matsumoto *et al.*, *Cancer Med.* **4**, 1547–1557 (2015).

ACKNOWLEDGMENTS

The authors thank G. Lahav, A. Loewer, M. Zwerger, M. Smolka, S. Emr, N. Buchkovich, B. Burke, H. Worman, S. Young, L. Fong, D. Discher, J. Broers, J. Goedhart, H. Yu, and W. Zipfel for cells, reagents, and helpful discussion. The authors acknowledge E. Wagena for mouse surgery and cell transfection, C. Paus for generation of in vitro collagen data, and K. Zhang, E. Ghazoul, D. Huang, G. Fedorchak, G.-J. Bakker, and F. Ahmadpour for help with image analysis. The authors are grateful to M. Piel and colleagues for sharing their unpublished data and manuscript. This work was supported by awards from NIH (R01 HL082792 and R01 NS059348); the Department of Defense Breast Cancer Research Program (BC102152 and BC150580); NSF (CBET-1254846); the National Cancer Institute, NIH, through the Cornell Center on the Microenvironment and Metastasis (U54 CA143876); and an NSF Graduate Research Fellowship to A.L.M (DGE-1144153). This work was further supported by the Netherlands Science Organization (NWO-VIDI 917.10.364 to K.W. and NWO-VICI 918.11.626 to P.F.) and the Cancer Genomics Center, Netherlands. This work was performed in part at the Cornell NanoScale Science and Technology Facility, which is supported by NSF (grant ECCS-15420819). Imaging was performed in part through the Cornell University Biotechnology Resource Center, which is supported by New York Stem Cell Foundation (NYSTEM) (CO29155), NIH (S10OD018516), and NSF (1428922), and by the Radboud University Medical Center Microscopic Imaging Center and Preclinical Animal Imaging Center (PRIME). Additional experimental details and data are available in the supplementary materials.

SUPPLEMENTARY MATERIALS

www.sciencemag.org/content/352/6283/353/suppl/DC1
Materials and Methods
Figs. S1 to S15
Movie Captions S1 to S7
References (*34*–*43*)
Movies S1 to S7

26 October 2015; accepted 25 February 2016
Published online 24 March 2016
10.1126/science.aad7297

CELL BIOLOGY

ESCRT III repairs nuclear envelope ruptures during cell migration to limit DNA damage and cell death

M. Raab,[1,2] M. Gentili,[3] H. de Belly,[1] H. R. Thiam,[1] P. Vargas,[1,2] A. J. Jimenez,[1] F. Lautenschlaeger,[1*] Raphaël Voituriez,[4,5] A. M. Lennon-Duménil,[3] N. Manel,[3] M. Piel[1,2]†

In eukaryotic cells, the nuclear envelope separates the genomic DNA from the cytoplasmic space and regulates protein trafficking between the two compartments. This barrier is only transiently dissolved during mitosis. Here, we found that it also opened at high frequency in migrating mammalian cells during interphase, which allowed nuclear proteins to leak out and cytoplasmic proteins to leak in. This transient opening was caused by nuclear deformation and was rapidly repaired in an ESCRT (endosomal sorting complexes required for transport)–dependent manner. DNA double-strand breaks coincided with nuclear envelope opening events. As a consequence, survival of cells migrating through confining environments depended on efficient nuclear envelope and DNA repair machineries. Nuclear envelope opening in migrating leukocytes could have potentially important consequences for normal and pathological immune responses.

The nuclear envelope (NE) functions as a barrier to separate the chromatin from the cytoplasm and is considered to remain intact during interphase. Only under pathological circumstances is the NE thought to open in nonmitotic cells. It can bud during viral infection (*1*) or be completely breached in laminopathies, pathologies associated with mutations in genes coding for nuclear lamina proteins, especially in LMN A/C (*2*, *3*). Many cancer cells express lower levels of LMN A/C, which correlates with a higher degree of metastatic potential (*4*). This is because nuclei lacking LMN A/C can be more easily deformed (*5*), which allows them to migrate through narrower pores and to invade tissues (*6*). Complete removal of LMN A/C leads to an increase in cell death during migration through pores and, eventually, reduces the extent of metastasis (*4*). The cause of this cell death remains unknown. Similarly to cancer cells, several types of immune cells express lower levels of LMN A/C. These cells also have the capacity to migrate through dense tissues (*7*). Their response to pathogens is tightly associated with their migratory capacities. Do specific survival mechanisms exist to allow highly migratory cells to survive their journey through tissues, despite a large degree of nuclear deformation?

[1]Institut Curie, PSL Research University, CNRS, UMR 144, F-75005 Paris, France. [2]Institut Pierre-Gilles de Gennes, PSL Research University, F-75005 Paris, France. [3]Institut Curie, PSL Research University, INSERM, U 932, F-75005 Paris, France. [4]Laboratoire de Physique Théorique de la Matière Condensée, CNRS UMR 7600, Université Pierre et Marie Curie, Paris, France. [5]Laboratoire Jean Perrin, CNRS UMR 8237, Université Pierre et Marie Curie, Paris, France.
*Present address: Department of Physics, Saarland University, Saarbrucken, Germany. **†Corresponding author. E-mail: matthieu.piel@curie.fr**

We compared bone marrow–derived mouse dendritic cells (mDCs), migrating between two surfaces spaced 5 μm apart either without (Fig. 1A and fig. S1A) or with collagen filling (Fig. 1B), as well as cells migrating through mice ear explants (Fig. 1C and fig. S1B). In collagen or ear explants, nuclei were more irregularly shaped (Fig. 1D), and the minimum diameter of the nucleus was reduced (Fig. 1E). This reflected pinched or dumbbell-shaped nuclei (arrows, Fig. 1C), as has been observed previously in migrating cancer and immune cells (*8*, *9*). Thus, DCs deform their nucleus during migration through physiological environments.

We recorded mDCs expressing green fluorescent protein (GFP) linked to a nuclear localization sequence (NLS-GFP). We followed cells migrating through a collagen gel (fig. S1C), or in an ear explant (fig. S1, D and E, and movie S1). Cells undergoing strong nuclear deformations displayed a decrease in the GFP nuclear signal and an increase in the cytoplasmic signal (Fig. 1F). This suggests that the nucleo-cytoplasmic barrier was transiently abrogated and then restored, which likely corresponds to an opening of the NE.

Collagen gels and ear explants offer poor control over the degree of nuclear deformation. We thus used a migration assay consisting of microchannels with constrictions of various sizes (fig. S2, A and B) (*10*), which matched the range of sizes observed in vivo for nuclear deformation (Fig. 1E) (*11*). To extend our findings to human cells, we investigated monocyte-derived human DCs (hDCs) (Fig. 2A and movie S2), as well as cultured cancer cells (HeLa) (Fig. 2B, fig. S2C, and movie S2) and normal cultured immortalized cells (RPE-1) (fig. S2D and movie S2). The NLS-GFP nuclear signal strongly decreased and the cytoplasmic signal increased while the nucleus was crossing the constriction (fig. S3, A and B). Cytoplasmic signal remained high as long as the nucleus was engaged within the constriction, independently of cell speed.

The slow passage of HeLa cells allowed us to observe several individual leakage events (bursts in fig. S3, B to E), which corresponded to the formation and rapid disappearance of bleblike structures at the tip of the passing nucleus (fig. S3, B to D, and movie S2). This suggests a mechanism by which deformation of the nucleus generates increased internal pressure and the formation of NE blebs that eventually rupture, followed by a resealing process, until the next bleb forms and ruptures. This is reminiscent of compressed nonmigrating cells (*12*). Consistently, the amount of NLS-GFP cytoplasmic leakage increased when the constriction size was narrower (Fig. 2C). Thus, migrating cells, when deforming their nucleus, display a high survival rate (Fig. 2D and fig. S3F) despite frequent opening of their NEs (Fig. 2E).

To assess the precise timing and location of NE opening, we used cells expressing a cytoplasmic DNA binding probe fused to GFP [cyclic guanosine monophosphate–adenosine monophosphate (GMP-AMP) synthase, cGAS]. Upon compression of hDCs, nuclear blebs were induced (*12*) (fig. S4A and movie S3). GFP-cGAS localized to chromatin at the exact location where the nuclear bleb had formed and ruptured (fig. S4A). Using this probe, we confirmed that hDCs opened their NEs (Fig. 2F and movie S4) at a higher frequency (Fig. 2G and fig. S4B) and earlier in the constriction (Fig. 2H and fig. S4C) for smaller constrictions, and that openings were mostly localized at the front tip of the nucleus. This was also observed during bleb bursting in HeLa cells (Fig. 2I and fig. S4, D to G). Staining of NE components showed that the nuclear lamina also ruptured (fig. S5, A and B) and that nuclear pores were excluded from the rupture region at the tip of the nucleus (fig. S5, B and C). Recording GFP-tagged Lap2β (Lap2β-GFP), an inner NE protein bound to the nuclear lamina, confirmed that the NE formed blebs devoid of lamina, that blebs eventually ruptured, and that they could contain chromatin (fig. S5, D to F, and movie S5). These observations are consistent with a simple physical model of deformation-induced blebbing followed by NE opening and resealing (fig. S6).

Plasma membrane repair and postmitotic NE resealing both require the ESCRT III complex (*13*–*15*). We therefore used cells coexpressing GFP-tagged CHMP4B (CHMP4B-GFP) (*16*), an ESCRT III complex subunit, and RFP-cGAS. Nearly all nuclear blebs that burst subsequently recruited CHMP4B-GFP (95%; $n = 62$) (fig. S7A and movie S6). We could also induce recruitment of CHMP4B-GFP using laser ablation aimed at the nuclear edge (fig. S7, B to D; fig. S8; and movie S7), associated with NLS-mCherry leakage into the cytoplasm (fig. S9). In cells migrating through constrictions, CHMP4B-GFP was transiently recruited to sites of

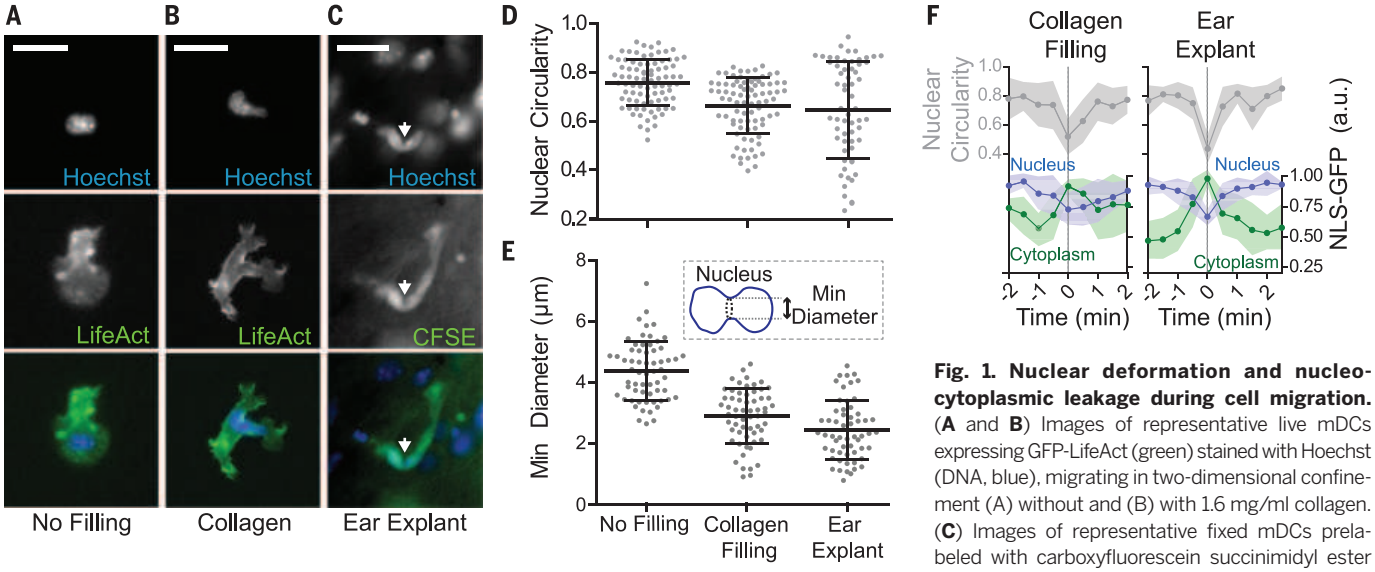

Fig. 1. Nuclear deformation and nucleo-cytoplasmic leakage during cell migration. (**A** and **B**) Images of representative live mDCs expressing GFP-LifeAct (green) stained with Hoechst (DNA, blue), migrating in two-dimensional confinement (A) without and (B) with 1.6 mg/ml collagen. (**C**) Images of representative fixed mDCs prelabeled with carboxyfluorescein succinimidyl ester (CFSE) (green) migrating in a mouse ear explant. Hoechst staining (blue). (**D**) Nuclear circularity and (**E**) minimum diameter of Hoechst-labeled nuclei in migrating cells ($n > 50$ cells for each condition, $N = 2$). (**F**) Nuclear circularity (gray) and NLS-GFP mean intensity (a.u., arbitrary units) inside the nucleus (blue) and in the cytoplasm (green) for mDCs passing through a confined space in collagen with a CCL21 gradient (left, $n = 13$ cells) or in an ear explant (right, $n = 15$ cells). Time zero corresponds to lowest value of circularity. Error bars, SD. Scale bars, 20 µm.

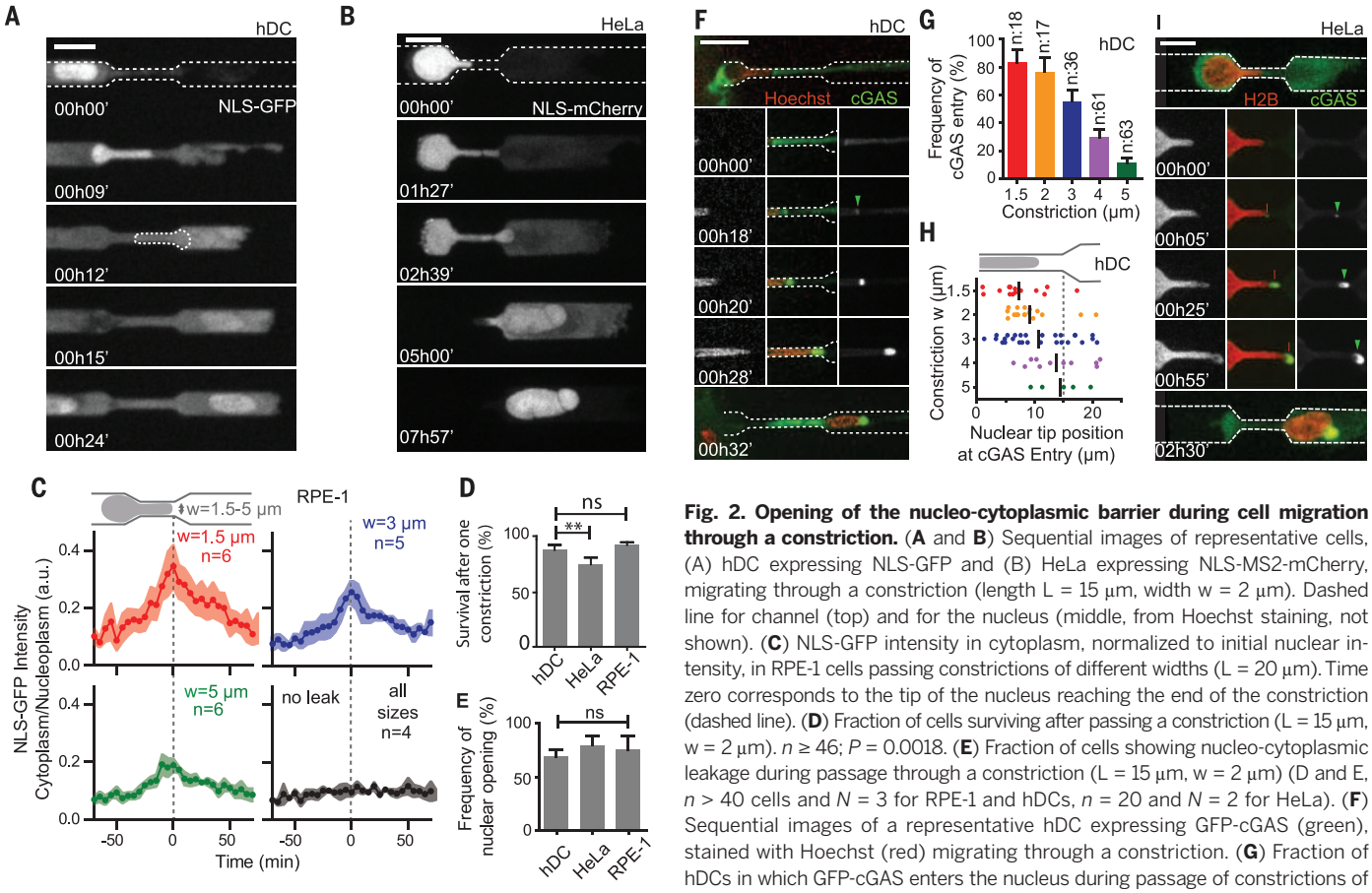

Fig. 2. Opening of the nucleo-cytoplasmic barrier during cell migration through a constriction. (**A** and **B**) Sequential images of representative cells, (A) hDC expressing NLS-GFP and (B) HeLa expressing NLS-MS2-mCherry, migrating through a constriction (length L = 15 µm, width w = 2 µm). Dashed line for channel (top) and for the nucleus (middle, from Hoechst staining, not shown). (**C**) NLS-GFP intensity in cytoplasm, normalized to initial nuclear intensity, in RPE-1 cells passing constrictions of different widths (L = 20 µm). Time zero corresponds to the tip of the nucleus reaching the end of the constriction (dashed line). (**D**) Fraction of cells surviving after passing a constriction (L = 15 µm, w = 2 µm). $n \geq 46$; $P = 0.0018$. (**E**) Fraction of cells showing nucleo-cytoplasmic leakage during passage through a constriction (L = 15 µm, w = 2 µm) (D and E, $n > 40$ cells and $N = 3$ for RPE-1 and hDCs, $n = 20$ and $N = 2$ for HeLa). (**F**) Sequential images of a representative hDC expressing GFP-cGAS (green), stained with Hoechst (red) migrating through a constriction. (**G**) Fraction of hDCs in which GFP-cGAS enters the nucleus during passage of constrictions of different widths (L = 15 µm). (**H**) Position along the constriction where GFP-cGAS first entered the nucleus. (**I**) Sequential images of a representative HeLa cell expressing GFP-cGAS (green) and H2B-mCherry (red). Green arrowheads show entry of GFP-cGAS at the nuclear tip. Time is hours (h):minutes (′). Scale bars, 10 µm. ns, not significant.

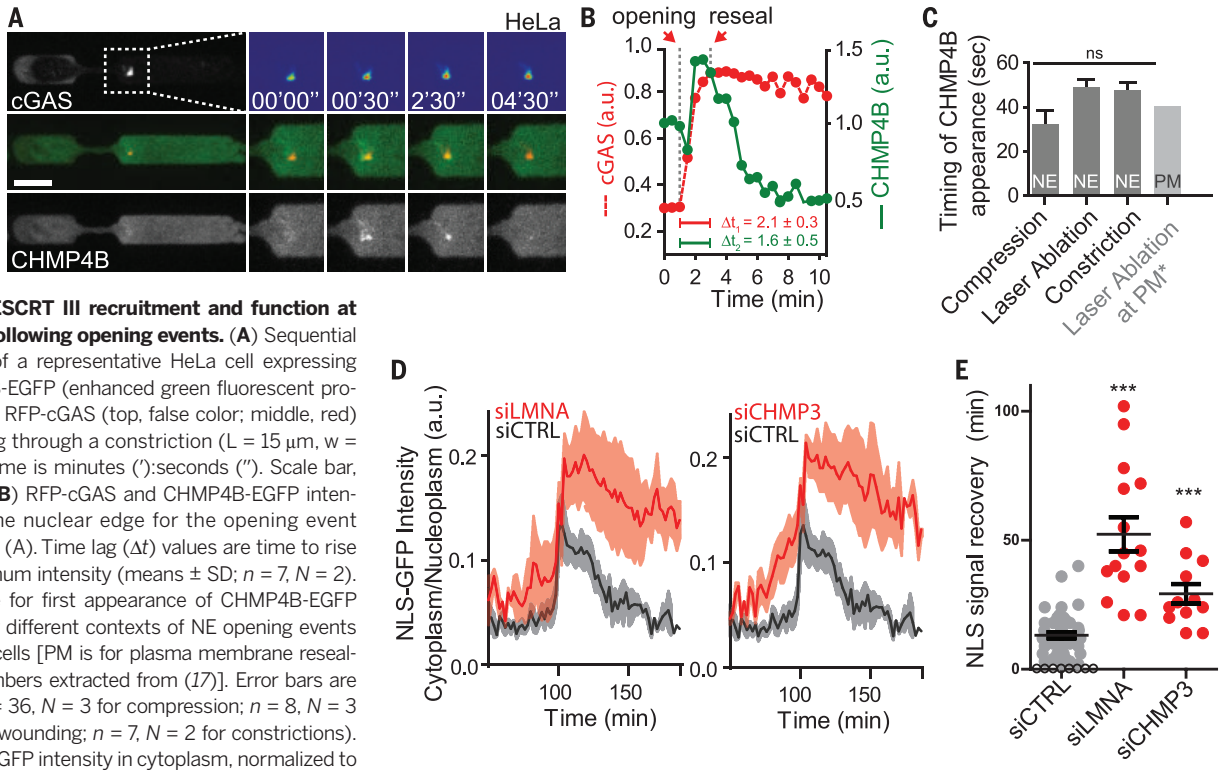

Fig. 3. ESCRT III recruitment and function at the NE following opening events. (**A**) Sequential images of a representative HeLa cell expressing CHMP4B-EGFP (enhanced green fluorescent protein) and RFP-cGAS (top, false color; middle, red) migrating through a constriction (L = 15 μm, w = 2 μm). Time is minutes (′):seconds (″). Scale bar, 20 μm. (**B**) RFP-cGAS and CHMP4B-EGFP intensity at the nuclear edge for the opening event shown in (A). Time lag (Δ*t*) values are time to rise to maximum intensity (means ± SD; *n* = 7, *N* = 2). (**C**) Time for first appearance of CHMP4B-EGFP at NE for different contexts of NE opening events in HeLa cells [PM is for plasma membrane resealing, *numbers extracted from (*17*)]. Error bars are SEM (*n* = 36, *N* = 3 for compression; *n* = 8, *N* = 3 for laser wounding; *n* = 7, *N* = 2 for constrictions). (**D**) NLS-GFP intensity in cytoplasm, normalized to initial nuclear intensity, in RPE-1 cells treated with control small interfering RNA (siRNA); siCTRL, black curves; and with LMNA (left) and CHMP3 (right) siRNAs (red curves). *n* ≥ 6 cells for each curve (*N* = 2). Error bars are SEM. (**E**) Quantification of the time needed for full recovery of NLS-GFP in the nucleus. Time zero is nuclear exit from the constriction (open circles are for recovery before exit; *n* = 46, 15, and 12; *N* = 2; error bars, SEM; ***$P < 0.0001$).

RFP-cGAS entry, at the nucleus tip (Fig. 3A and movie S8). CHMP4B-GFP localized to the site of NE opening just after the opening occurred and decreased after resealing (Fig. 3B and fig. S10, A and B). Thus, NE opening induced with these three different methods (compression, laser, and confined migration), recruited CHMP4B-GFP with kinetics similar to those observed after plasma membrane wounding (Fig. 3C) (*13*, *17*). This suggests that the resealing of the NE after opening caused by nuclear deformation in migrating cells might also require the ESCRT III complex machinery.

To test the function of ESCRT III in NE resealing, we depleted (knocked down) CHMP3 (*14*), which delayed recruitment of CHMP4B-GFP after laser wounding (fig. S10C). We also knocked down LMN A/C, whose depletion, as expected (*18*, *19*), caused random bursts of NLS-GFP into the cytoplasm even in the absence of nuclear constriction (fig. S10D and movie S9). CHMP3-depleted cells did not show any leakage of NLS-GFP in the cytoplasm outside constrictions, which indicated that CHMP3 depletion did not make the NE more susceptible to spontaneous opening. However, when CHMP3-depleted cells passed through constrictions, they showed increased GFP signal in the cytoplasm, as did LMN A/C–depleted cells, and the cytoplasmic signal remained for prolonged periods of time after the cells passed the constriction (Fig. 3, D and E; fig. S10, E to G; fig. S11, A and B; and movie S9). Thus the ESCRT III complex is essential to reseal the NE in migrating cells.

We hypothesized that efficient resealing was responsible for the high survival rate of cells passing through constrictions. As expected (*4*), we observed increased death in LMN A/C–depleted cells (Fig. 4A), even inside straight channels, but more so when cells were passing constrictions. CHMP3 depletion did not induce any increase in cell death (Fig. 4A); thus, prolonged nuclear opening alone was not enough to cause cell death. LMN A/C–depleted cells exhibit defects in DNA damage response (*20*). We thus imaged RPE-1 cells expressing 53BP1-GFP, a protein recruited to DNA double-strand breaks (*21*). These cells showed a transient increase in the number and intensity of 53BP1-GFP foci during passage of the nucleus through a constriction (Fig. 4, B to D, and movie S10), with kinetics similar to NLS-GFP leakage into the cytosol. This suggested that DNA double-strand breaks might result from NE opening, although we cannot fully exclude that mechanical constrains exerted on the DNA during nuclear deformation also play a role. We imaged cells expressing both 53BP1-GFP and RFP-cGAS and found that the formation of 53BP1-GFP foci always followed the recruitment of RFP-cGAS into the nucleus (Fig. 4, B and E). Furthermore, only cells that exhibited entry of RFP-cGAS into the nucleus also showed an increase in 53BP1-GFP foci (Fig. 4F), which were dispersed throughout the nucleus (Fig. 4G). This suggests that diffusing cytoplasmic factors might enter during NE opening, and in turn induce DNA damage. 53BP1-GFP foci disappeared a few tens of minutes after cells exited the constriction, which implies efficient DNA repair. We thus inhibited DNA repair using an ataxia telangiectasia mutated (ATM) inhibitor (ATMi) (fig. S11C) (*22*). Upon ATMi treatment, the level of cell death was increased only in LMN A/C- and in CHMP3-depleted cells migrating through constrictions (Fig. 4A). Together these experiments show that DNA damage caused by prolonged NE opening can lead to cell death provided that DNA repair is also affected.

Here, we have shown that nuclear deformation during cell migration leads to transient opening of the NE and that the ESCRT III complex, similarly to what happens at mitotic exit (*14*, *15*), is required for fast resealing of the nucleo-cytoplasmic barrier (fig. S12). This transient opening leads to nucleo-cytoplasmic mixing, which potentially causes DNA damage owing to entry of cytoplasmic factors (fig. S13) (*23*–*26*). We propose that this phenomenon might be particularly relevant for immune and cancer cells (*27*). We anticipate that in various developmental, immunological or pathological contexts, nuclear deformation-associated NE rupture could lead to a large range of cellular responses, as well as to genomic instability, cell aging, or cell death (*28*–*30*). Such responses could be important physiologically or pathologically.

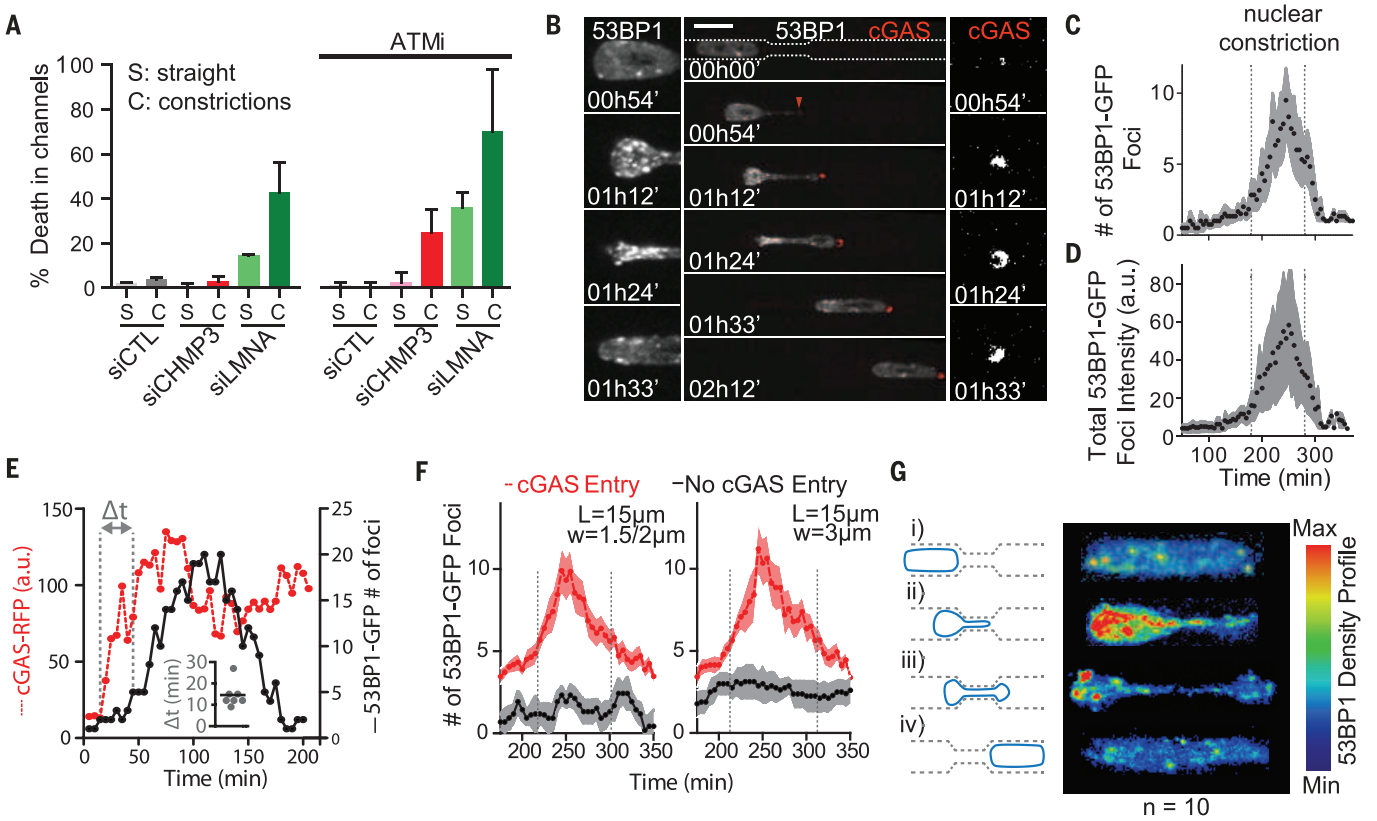

Fig. 4. DNA damage associated with nuclear deformation and NE opening. (**A**) Fraction of RPE-1 cells dying after passing one constriction. siCTL, siRNA control. "Straight" is for cells moving across the same distance in channels without constrictions (L = 20 μm, w = 3 μm; left to right, n = 300, 300, 240, 240, 90, 90, 300, 300, 120, 60, 60, 60; N = 3 for each condition). (**B**) Sequential images of a representative RPE-1 cell expressing 53BP1-GFP (gray levels) and RFP-cGAS (red) migrating through a constriction (L = 15 μm, w = 2 μm). Red arrow shows first RFP-cGAS entry at nuclear tip. Time is hours (h):minutes (′); scale bar, 20 μm. Number (**C**) and total intensity (**D**) of 53BP1-GFP foci in the nucleus while passing a constriction (L = 15 μm, w = 1.5 μm; n = 7 cells, N = 3). (**E**) RFP-cGAS intensity (red curve) inside the nucleus and number of 53BP1-GFP foci (black curve) for a representative cell. (Inset) Time lag (Δt) between the entry of RFP-cGAS and the increase in number of 53BP1-GFP foci (n = 7, N = 2). (**F**) Number of 53BP1-GFP foci in the nucleus, for cells which showed entry of RFP-cGAS in the nucleus (red curve) compared with cells that did not show entry of RFP-cGAS (black curve), for the same size of constrictions (L = 15 μm, left: w = 1.5 μm and 2 μm, n = 25 and 5 cells; right: w = 3 μm, n = 13 and 9; N = 3). (**G**) 53BP1-GFP density profile in nuclei at different stages of passing constrictions: (i) before entering, (ii) nuclear tip reaching the end of the constriction, (iii) nucleus halfway through the constriction, and (iv) after exiting (N = 2). Constrictions are (L = 15 μm, w = 2 μm). Error bars, SEM.

REFERENCES AND NOTES

1. C. P. Lee *et al.*, *PLOS Pathog.* **8**, e1002904 (2012).
2. E. Hatch, M. Hetzer, *J. Cell Biol.* **205**, 133–141 (2014).
3. A. Fidziańska *et al.*, *J. Neurol. Sci.* **271**, 91–96 (2008).
4. T. Harada *et al.*, *J. Cell Biol.* **204**, 669–682 (2014).
5. A. C. Rowat *et al.*, *J. Biol. Chem.* **288**, 8610–8618 (2013).
6. P. M. Davidson, C. Denais, M. C. Bakshi, J. Lammerding, *Cell. Mol. Bioeng.* **7**, 293–306 (2014).
7. M. Sixt, *Immunol. Lett.* **138**, 32–34 (2011).
8. K. Wolf *et al.*, *J. Cell Biol.* **201**, 1069–1084 (2013).
9. H. Pflicke, M. Sixt, *J. Exp. Med.* **206**, 2925–2935 (2009).
10. M. L. Heuzé, O. Collin, E. Terriac, A. M. Lennon-Duménil, M. Piel, *Methods Mol. Biol.* **769**, 415–434 (2011).
11. M. Krause, K. Wolf, *Cell Adhes. Migr.* **9**, 357–366 (2015).
12. M. Le Berre, J. Aubertin, M. Piel, *Integr. Biol. (Camb.)* **4**, 1406–1414 (2012).
13. A. J. Jimenez *et al.*, *Science* **343**, 1247136 (2014).
14. Y. Olmos, L. Hodgson, J. Mantell, P. Verkade, J. G. Carlton, *Nature* **522**, 236–239 (2015).
15. M. Vietri *et al.*, *Nature* **522**, 231–235 (2015).
16. I. Poser *et al.*, *Nat. Methods* **5**, 409–415 (2008).
17. L. L. Scheffer *et al.*, *Nat. Commun.* **5**, 5646 (2014).
18. W. H. De Vos *et al.*, *Hum. Mol. Genet.* **20**, 4175–4186 (2011).
19. J. D. Vargas, E. M. Hatch, D. J. Anderson, M. W. Hetzer, *Nucleus* **3**, 88–100 (2012).
20. S. Gonzalo, R. Kreienkamp, *Curr. Opin. Cell Biol.* **34**, 75–83 (2015).
21. A. Janssen, M. van der Burg, K. Szuhai, G. J. Kops, R. H. Medema, *Science* **333**, 1895–1898 (2011).
22. I. Hickson *et al.*, *Cancer Res.* **64**, 9152–9159 (2004).
23. J. Maciejowski, Y. Li, N. Bosco, P. J. Campbell, T. de Lange, *Cell* **163**, 1641–1654 (2015).
24. S. Sarbajna, D. Davies, S. C. West, *Genes Dev.* **28**, 1124–1136 (2014).
25. D. Gritenaite *et al.*, *Genes Dev.* **28**, 1604–1619 (2014).
26. Y. W. Chan, S. C. West, *Nat. Commun.* **5**, 4844 (2014).
27. C. M. Denais *et al.*, *Science* **352**, aad7297 (2016).
28. T. Shimi, R. D. Goldman, *Adv. Exp. Med. Biol.* **773**, 415–430 (2014).
29. E. M. Hatch, A. H. Fischer, T. J. Deerinck, M. W. Hetzer, *Cell* **154**, 47–60 (2013).
30. C. Soria-Valles *et al.*, *Nat. Cell Biol.* **17**, 1004–1013 (2015).

ACKNOWLEDGMENTS

The authors thank I. Poser, M. Hetzer, R. Medema, B. Baum, and M. Petronczki for kindly providing cell lines and plasmids and E. Zlotek-Zlotkieviz for help with the figures. We are grateful to J. Lammerding and coauthors for sharing their unpublished results and manuscripts. We also thank P. Maiuri, F. Perez, and M. Le Berre for helpful discussions and help with the methods and analysis; V. Fraisier; L. Sengmanivong; the Nikon imaging center and the BioImaging Cell and Tissue Core Facility of the Institut Curie (PICT IBiSA) platform at Institut Curie for technical support in microscopy; the Institut Curie animal facility; S. Kitchen-Goosen for animal husbandry and technical support; and M. Maurin for help in image analysis. This work was supported by European Research Council (ERC) grant 311205 for proliferation and migration under external constraints (PROMICO) to M.P., Human Frontier Science Program Fellowship to M.R., Agence Nationale de Research grant for cell migration in confined environments (MICEMICO) to M.P. and A.M.L.-D., ERC grant for spatio-temporal regulation of antigen presentation and cell migration (STRAPACEMI) to A.M.L.-D., ERC grant 309848 for innate sensing of HIV and immune responses (HIVINNATE) to N.M.; Ville de Paris Emergence program; Dendritic Cell Biology (DCBIOL) Laboratories of Excellence (LabEx DCBIOL); Fondation Acting on European Research in Immunology and Allergology (ACTERIA Foundation); and Fondation Schlumberger (FSER). Additional experimental details and data are available in the supplementary materials.

SUPPLEMENTARY MATERIALS

www.sciencemag.org/content/352/6283/359/suppl/DC1
Materials and Methods
Figs. S1 to S13
Movie Captions S1 to S10
References (*31–39*)
Movies S1 to S10

29 October 2015; accepted 25 February 2016
Published online 24 March 2016
10.1126/science.aad7611

STRUCTURAL BIOLOGY

Molecular architecture of the inner ring scaffold of the human nuclear pore complex

Jan Kosinski,[1*] Shyamal Mosalaganti,[1*] Alexander von Appen,[1*] Roman Teimer,[2] Amanda L. DiGuilio,[3] William Wan,[1] Khanh Huy Bui,[4] Wim J.H. Hagen,[1] John A. G. Briggs,[1,5] Joseph S. Glavy,[3] Ed Hurt,[2] Martin Beck[1,5]†

Nuclear pore complexes (NPCs) are 110-megadalton assemblies that mediate nucleocytoplasmic transport. NPCs are built from multiple copies of ~30 different nucleoporins, and understanding how these nucleoporins assemble into the NPC scaffold imposes a formidable challenge. Recently, it has been shown how the Y complex, a prominent NPC module, forms the outer rings of the nuclear pore. However, the organization of the inner ring has remained unknown until now. We used molecular modeling combined with cross-linking mass spectrometry and cryo-electron tomography to obtain a composite structure of the inner ring. This architectural map explains the vast majority of the electron density of the scaffold. We conclude that despite obvious differences in morphology and composition, the higher-order structure of the inner and outer rings is unexpectedly similar.

Nuclear pore complexes (NPCs) are the major mediators of nucleocytoplasmic exchange and are of fundamental importance to all eukaryotic cells. Alterations of the nucleocytoplasmic transport system have been linked to various types of cancer, autoimmune diseases, and aging (*1*, *2*). Experimentally testable structural models of the vertebrate NPC could provide a mechanistic basis for understanding clinically relevant mutations. Generating predictive structural models, however, is extremely challenging because of the size and intricate composition of the NPC (*3*). Nucleoporins (Nups) preassemble into several distinct subcomplexes, which oligomerize to form an eightfold rotationally symmetric structure. Many intra-subcomplex interactions have been biochemically and structurally characterized. In contrast, the weaker inter-subcomplex interactions have remained poorly understood, mainly because of their instability ex situ. To overcome this hurdle, it has been essential to combine biochemical and classical structure determination methods with in situ structural analysis and integrative molecular modeling (*4*).

Previous studies revealed that 16 copies of the Y complex (also called the Nup107 complex or Nup84 complex in fungi) form a reticulated double-ring arrangement within both the nuclear and cytoplasmic rings (*4*). However, our understanding of how the inner ring (IR) scaffold is assembled in situ has been sparse. The Nup93 and Nup62 complexes—composed of Nup62, Nup58, and Nup54 and Nup205, Nup188, Nup155, Nup93, and Nup53, respectively—have been shown to localize to the IR (Nic96 and Nsp1 complexes in fungi; fig. S1) (*5*). More recently, it has been shown that Nup205 binds to the IR complexes mutually exclusively with respect to its homolog Nup188 (*6*) and also interacts with Nup98 (*7*, *8*). Most domains of Nup93 complex members have been analyzed by x-ray crystallography (*4*), and some of these show homology to Y complex members. A tomographic study (*9*) revealed possible locations of 32 copies each of Nup155 and the large N-terminal domain (NTD) of Nup205 or Nup188 (fig. S2) (*10*). However, various other components—such as Nup93, the Nup62 complex, and the C-terminal domains (CTDs) of Nup205 and Nup188—remained unassigned and left large patches of the observed electron optical density unexplained.

Recent studies structurally and biochemically analyzed the Nup62-Nup58-Nup54 heterotrimer (*8*, *11*), the CTD of Nup205 (*8*), and interactions between the Nup62 and Nup93 complexes (*7*, *8*). In this study, we fitted all of the available structures into the tomographic map of the IR (*9*), in consensus with the well-established domain connectivity, interactions, and symmetry that have been observed by means of cryo-electron microscopy (cryo-EM) (details are provided in fig. S2, database S2, movies S1 to S3, and the supplementary materials). We found that 32 copies each of Nup205 or Nup188 (*10*), Nup93, Nup155, and the Nup62 complex fit seamlessly into the IR (Fig. 1, A and B, and fig. S2); another 16 copies of Nup155 connect it to the outer rings (*9*). The asymmetric unit of the IR is composed of four core modules. Each core module contains one copy of the aforementioned Nups. The inner and outer copies of the core modules are rotationally shifted with respect to each other and have slightly different conformations, but they engage in identical intra-subcomplex interactions (Fig. 1C). They form heterotypic inter-subcomplex interactions and oligomerize into four horizontally stacked rings. Each ring contains eight core modules. The inner and outer pairs of the core module are symmetric with respect to the nuclear envelope plane (Fig. 1C). These architectural principles are unexpectedly similar to the Y complex of the outer rings (*9*, *12*, *13*), highlighting a potential evolutionary relationship. An obvious difference is that the inner copies of the IR core modules form a C_2 symmetric interface with each other, whereas the outer rings are spatially separated.

A further-refined tomographic map of the IR solidifies the assignments (fig. S3 and database S2). It resolves the subdomain structures of Nup205 and Nup188 and the asymmetric features of Nup93, and it facilitates an unambiguous determination of the orientation of those proteins that could not be positioned previously (*9*).

Next, we generated spatial restraints by using cross-linking mass spectrometry. We affinity-purified Nup205-Nup93 complex (fig. S4) and Nup62 complex from human cells and reconstituted a complex in vitro, which consisted of the fungal orthologs of Nup205, Nup155, Nup93, Nup53, and Nup98 (fig. S5), as previously described (*7*). Spatial restraints were combined and mapped onto human proteins where necessary (Fig. 2A and fig. S6). Our composite structure is consistent with most of the spatial restraints (table S1), and the cross-links confirm several of the key features (Fig. 2, B to D). The very few cross-links that are violated in the structure are well in line with the false-positive discovery rate of cross-linking mass spectrometry. They may also arise from conformational heterogeneity due to the ex situ cross-linking (table S1 and figs. S4B and S7). We systematically validated our model by imposing biochemical restraints that were generated by several previous studies. We extracted 89 restraints from 35 publications and found strong agreement with our composite structure (table S2). To assess whether the available data could converge into alternative configurations of the IR structure, we used the Integrative Modeling Platform software suite (*14*) to set up an unbiased computational modeling approach that takes into account the matching of the high-resolution structures with the tomographic map, the cross-links, and domain connectivity. A set of seven top-scoring solutions were highly similar to the composite structure (fig. S8A). We therefore conclude that our composite structure is an objective and robust representation of the IR architecture. It is also in line with independent analyses of stoichiometry (*15*) and spatial proximities (*16*).

Nup155 is homologous to Nup133 and Nup160 of the Y complex, whereas Nup93 is homologous to Nup107 and Nup85 of the Y complex (*17*–*19*). The interface of Nup133 and Nup107 (*13*) also seamlessly superimposes with that of Nup160 and Nup85 (fig. S9) (*20*). In our blueprint of the IR architecture, Nup155 and Nup93 are similarly positioned (Fig. 3, A and B, and fig. S9). A potential direct interface between Nup155 and Nup93 would have to be much weaker than its outer ring

[1]Structural and Computational Biology Unit, European Molecular Biology Laboratory (EMBL), Heidelberg, Germany. [2]Biochemistry Center of Heidelberg University, Im Neuenheimer Feld 328, D-69120 Heidelberg, Germany. [3]Department of Chemistry, Chemical Biology and Biomedical Engineering, Stevens Institute of Technology, 507 River Street, Hoboken, NJ 07030, USA. [4]Department of Anatomy and Cell Biology, McGill University, Montreal, Quebec, Canada. [5]Cell Biology and Biophysics Unit, EMBL, Heidelberg, Germany.
*These authors contributed equally to this work.
†Corresponding author. E-mail: martin.beck@embl.de

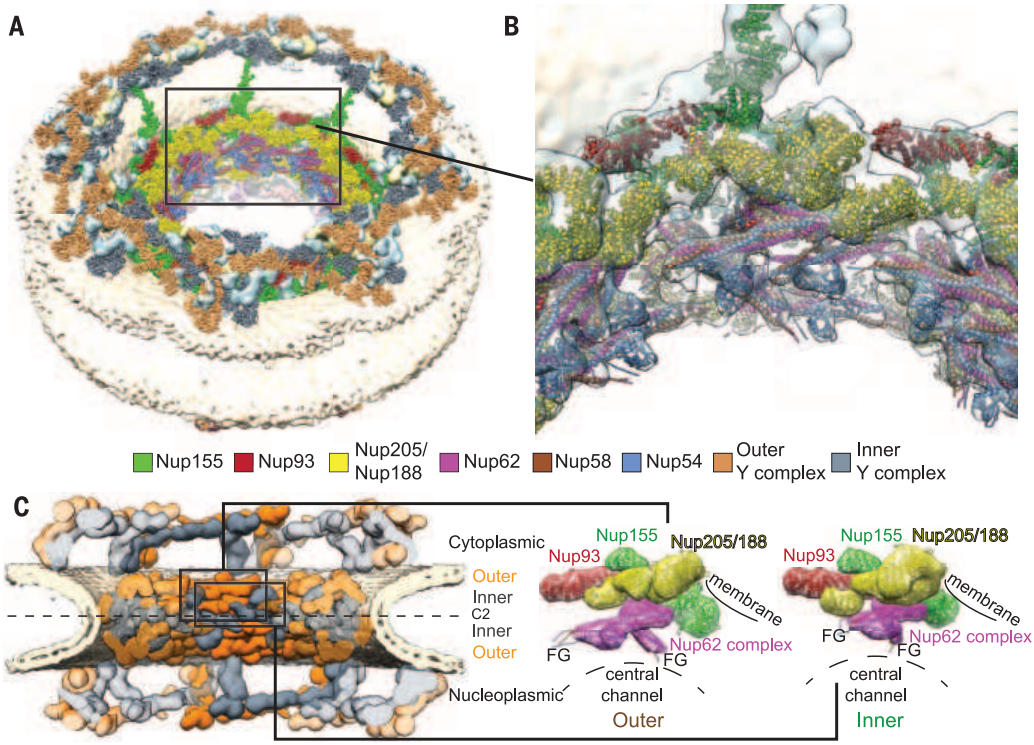

Fig. 1. Composite structure of the human NPC. (**A**) Overview of the composite structure of the entire NPC, in which previous structural assignments in the outer rings (*9*, *13*) are represented together with the assignments in the IR that were undertaken in this study (details are shown in fig. S2). Unassigned density is shown in cyan; the nuclear ring is facing up. (**B**) Zoomed-in view of the IR region framed in (A). High-resolution structures (colored ribbons) are shown in the context of the tomographic map (transparent isosurface). (**C**) Conceptual outline of the NPC architecture. Inner (gray) and outer (orange) copies of the Y complex (top and bottom) and the IR core module (middle) are shown in comparison. The configurations of the outer and inner copies of the IR core module are shown enlarged on the right. FG repeat domains can readily reach out into the central channel (F, phenylalanine; G, glycine).

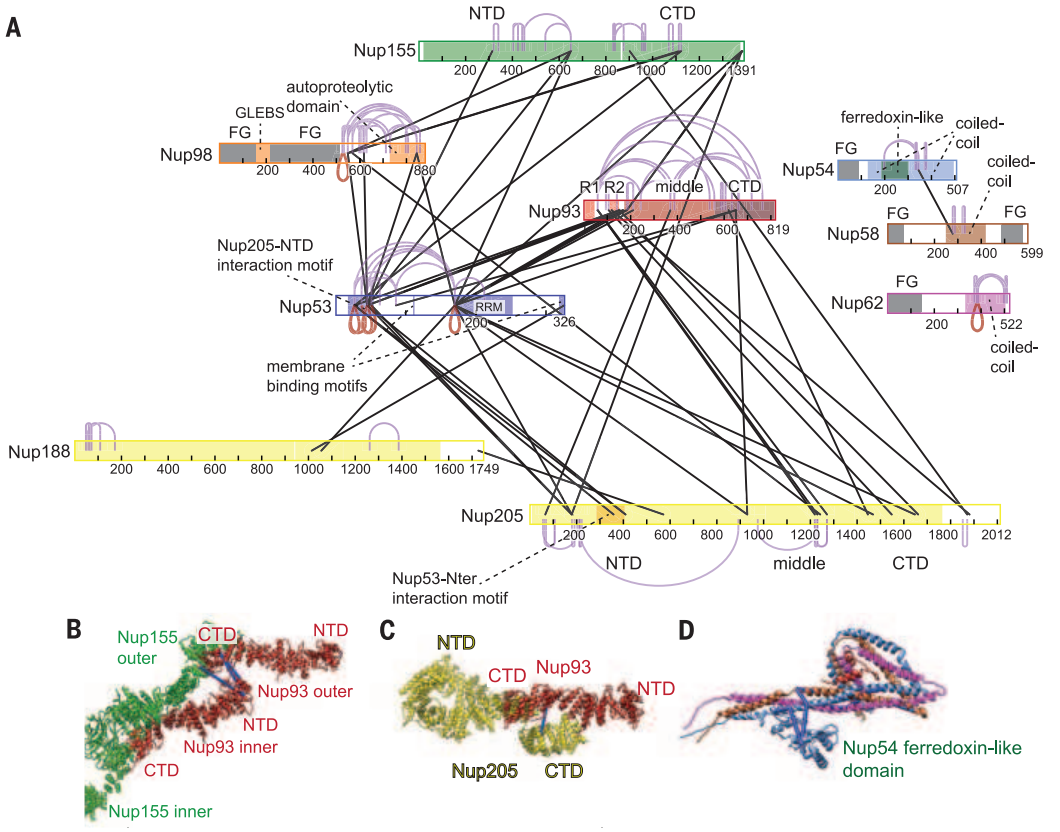

Fig. 2. Cross-linking mass spectrometry confirms intra- and inter-subcomplex interactions of the IR architecture. (**A**) Primary schematic of the IR proteins, showing the cross-links obtained by mass spectrometry. Inter-protein cross-links are shown in black, intra-protein links in light purple, and homodimeric cross-links (linking the same residues of a protein) in red. For clarity, Nup53 is not drawn to scale. Colored areas within the primary structures mark domains and motifs as individually labeled (residues are indicated below). A larger version is shown in fig. S6, and table S1 provides details on the cross-link data sets. The cross-links [blue lines in (B) to (D)] confirm specific features suggested by the composite structure, such as (**B**) head-to-tail arrangement of the inner and outer copy of Nup93, (**C**) interaction between Nup93 and Nup205, and (**D**) positioning of the Nup54 ferredoxin-like domain within the Nup62 complex.

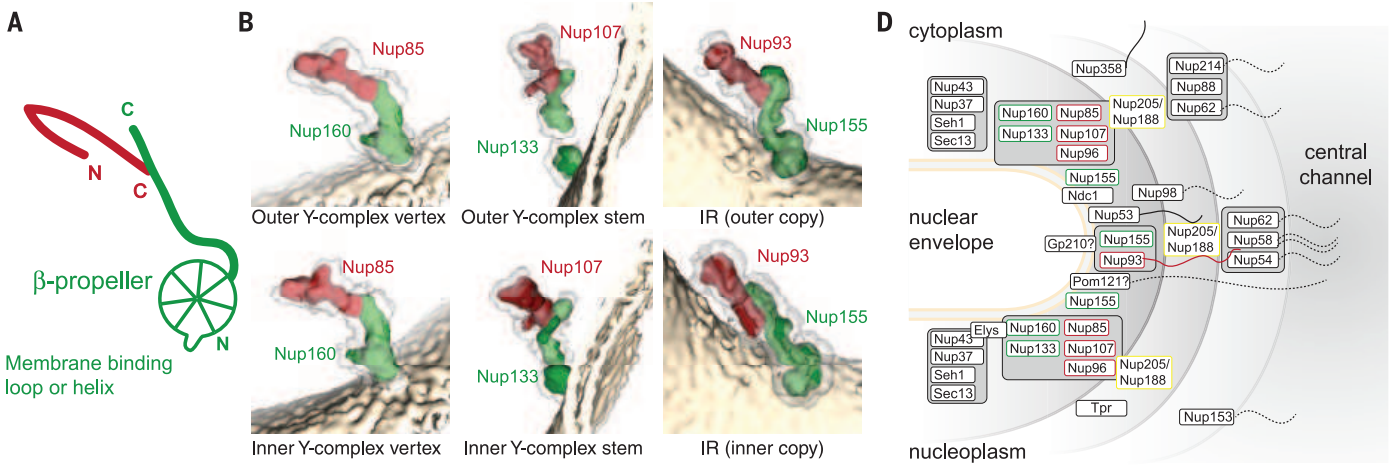

Fig. 3. Simple and highly similar organizational principles govern the architecture of the inner and outer rings of the NPC. (**A**) Schematic representation of the branching motif formed by the different heterodimers. (**B**) Structural similarity of the Nup155-Nup93 dimer to the Nup107-Nup133 and Nup120-Nup85 dimers. The structures are shown in low-resolution representation within the corresponding segments of the tomographic map. Homologous Nups are colored identically. (**C**) Arrangement of the branching motifs within the NPC membrane-binding coat [homologous Nups are colored as in (B)]. (**D**) Schematic of the human NPC architecture (details are shown in figs. S9 to S11). Trailing lines indicate FG repeats.

counterparts, because it has escaped biochemical characterization. However, it would be in agreement with the high sequence conservation of the respective surfaces (figs. S9C and S10) (*19*, *21*) and the observation that the CTD of Nup93 is necessary and sufficient for the assembly of the NPC scaffold (*22*). Complex formation is strengthened in the presence of Nup53, as reported by various studies (table S2). This structural signature reoccurs throughout the inner and outer rings and directly engages with the membrane through the β-propellers of Nup160, Nup133, and Nup155, thereby forming a membrane-binding NPC coat (Fig. 3C).

It has been previously assumed that the Y and Nup93 complexes are spatially separated into the morphological features observed with classical EM—namely, the outer and inner rings, respectively. Our analysis, taken together with previous work on the outer rings (*9*), suggests that multiple copies of Nup205 or Nup188 independently bind to the coat of the NPC in both the IR and the outer rings (Fig. 3D and fig. S11). The Nup62 complex binds to this scaffold (Fig. 3D), whereby short linear motifs in Nup53, Nup98, and Nup93 are important for the interconnection of subcomplexes (*6*–*8*). Our composite structure of the IR explains both the bulk of the electron optical density observed in situ and the biochemical data. In the future, cryo-EM maps at subnanometer resolution will be required to enable flexible fitting of x-ray structures and to precisely determine the orientations of Nup53, Ndc1, Nup98, and the linker regions of Nup53 and Nup93. Intersubcomplex interfaces must be targeted by x-ray crystallography. Our model is suggestive of various such interfaces and will remain a cornerstone for further crystallographic analysis. It also highlights the anchoring positions of the intrinsically disordered Nup domains that facilitate the translocation of cargo, and it lays the foundation for understanding their spatial organization and functional role in healthy and diseased tissues.

REFERENCES AND NOTES

1. M. Raices, M. A. D'Angelo, *Nat. Rev. Mol. Cell Biol.* **13**, 687–699 (2012).
2. A. Mor, M. A. White, B. M. Fontoura, *Curr. Opin. Cell Biol.* **28**, 28–35 (2014).
3. A. Hoelz, E. W. Debler, G. Blobel, *Annu. Rev. Biochem.* **80**, 613–643 (2011).
4. E. Hurt, M. Beck, *Curr. Opin. Cell Biol.* **34**, 31–38 (2015).
5. B. Vollmer, W. Antonin, *Biol. Chem.* **395**, 515–528 (2014).
6. S. Amlacher *et al.*, *Cell* **146**, 277–289 (2011).
7. J. Fischer, R. Teimer, S. Amlacher, R. Kunze, E. Hurt, *Nat. Struct. Mol. Biol.* **22**, 774–781 (2015).
8. T. Stuwe *et al.*, *Science* **350**, 56–64 (2015).
9. A. von Appen *et al.*, *Nature* **526**, 140–143 (2015).
10. As noted by von Appen *et al.* (*9*), the structural homologs Nup205 and Nup188 cannot be distinguished at the given resolution of the tomographic map, although biochemical data point to an association of Nup188 with the outer rings.
11. H. Chug, S. Trakhanov, B. B. Hülsmann, T. Pleiner, D. Görlich, *Science* **350**, 106–110 (2015).
12. K. H. Bui *et al.*, *Cell* **155**, 1233–1243 (2013).
13. T. Stuwe *et al.*, *Science* **347**, 1148–1152 (2015).
14. D. Russel *et al.*, *PLOS Biol.* **10**, e1001244 (2012).
15. A. Ori *et al.*, *Mol. Syst. Biol.* **9**, 648 (2013).
16. D. I. Kim *et al.*, *Proc. Natl. Acad. Sci. U.S.A.* **111**, E2453–E2461 (2014).
17. D. Devos *et al.*, *PLOS Biol.* **2**, e380 (2004).
18. S. G. Brohawn, N. C. Leksa, E. D. Spear, K. R. Rajashankar, T. U. Schwartz, *Science* **322**, 1369–1373 (2008).
19. J. R. Whittle, T. U. Schwartz, *J. Biol. Chem.* **284**, 28442–28452 (2009).
20. T. Boehmer, S. Jeudy, I. C. Berke, T. U. Schwartz, *Mol. Cell* **30**, 721–731 (2008).
21. S. Jeudy, T. U. Schwartz, *J. Biol. Chem.* **282**, 34904–34912 (2007).
22. R. Sachdev, C. Sieverding, M. Flötenmeyer, W. Antonin, *Mol. Biol. Cell* **23**, 740–749 (2012).

ACKNOWLEDGMENTS

We thank A. Andres-Pons for technical support and critical reading of the manuscript. We acknowledge support from EMBL's Electron Microscopy and Proteomics Core Facilities. W.W. and J.A.G.B. thank N. Grigorieff for sharing data before publication. J.K. was supported by the EMBL Interdisciplinary Postdoc Programme under Marie Curie COFUND actions. A.L.D. was supported by the Robert Crooks Stanley Fellowship at the Stevens Institute of Technology and National Institute on Aging (NIA) grant 1R21AG047433-01. J.S.G. was supported by an Ignition Grant Initiative from Stevens Institute of Technology and NIA grant 1R21AG047433-01. M.B. acknowledges funding by EMBL and the European Research Council (grant 309271-NPCAtlas). The density maps have been deposited in the Electron Microscopy Data Bank with accession numbers 8085, 8086, and 8087. The composite structure and the top-scoring automated models have been deposited in the Protein Data Bank with accession numbers 5IJN and 5IJO.

SUPPLEMENTARY MATERIALS

www.sciencemag.org/content/352/6283/363/suppl/DC1
Materials and Methods
Figs. S1 to S11
Tables S1 to S4
References (*23*–*34*)
Movies S1 to S3
Databases S1 and S2

15 December 2015; accepted 19 March 2016
10.1126/science.aaf0643

BIOMATERIALS

Developing a pro-regenerative biomaterial scaffold microenvironment requires T helper 2 cells

Kaitlyn Sadtler,[1,5] Kenneth Estrellas,[1,5] Brian W. Allen,[1,5] Matthew T. Wolf,[1,5] Hongni Fan,[2,5] Ada J. Tam,[2,5] Chirag H. Patel,[2,5] Brandon S. Luber,[3,5] Hao Wang,[3,5] Kathryn R. Wagner,[4] Jonathan D. Powell,[2,5] Franck Housseau,[2,5] Drew M. Pardoll,[2,5] Jennifer H. Elisseeff[1,5]*

Immune-mediated tissue regeneration driven by a biomaterial scaffold is emerging as an innovative regenerative strategy to repair damaged tissues. We investigated how biomaterial scaffolds shape the immune microenvironment in traumatic muscle wounds to improve tissue regeneration. The scaffolds induced a pro-regenerative response, characterized by an mTOR/Rictor-dependent T helper 2 pathway that guides interleukin-4–dependent macrophage polarization, which is critical for functional muscle recovery. Manipulating the adaptive immune system using biomaterials engineering may support the development of therapies that promote both systemic and local pro-regenerative immune responses, ultimately stimulating tissue repair.

Immune homeostasis is indispensable to tissue development, regeneration, and repair (*1*). Trauma initiates a cascade of local and systemic immune events that trigger the mobilization of cells into the damaged site to initiate host defense and tissue repair. The limited success achieved to date in rebuilding human tissues may be due in part to the tendency for therapeutic strategies to target later processes in wound healing and regeneration, such as stem cell differentiation. Conversely, the immune system is a highly flexible network that serves as a guardian of tissue integrity and is adapted to the nature of the local microenvironment (*2*). The immune system participates in tissue repair by scavenging debris and dead cells (*3*), recruiting and supporting the proliferation of tissue progenitor cells (*4*), and inducing vascularization (*5*). Previously, immune responses to biomaterials were related to rejection (*6–8*); however, subsets of innate immune cells have been identified as important mediators of scaffold remodeling (*9–11*) and can be targeted for immune-mediated tissue regeneration. We explored the role of adaptive immunity in tissue regeneration, identifying T_H2 responses as critical in driving the repair of traumatic tissue injury.

To model a traumatic wound, we surgically excised a portion of the quadriceps muscle group in C57BL/6 mice, provoking an irreversible volumetric muscle loss (VML) injury (*12*). Based on the regenerative potential and clinical use of tissue-derived extracellular matrix (ECM) scaffolds (*10*, *11*), we screened and selected bone- and cardiac muscle–derived tissue ECM scaffolds (B-ECM and C-ECM) for their immunomodulatory properties [fig. S1 (*13*)]. The presence of scaffolds in damaged muscle significantly increased the number of myeloid cells ($F4/80^+$ macrophages and $CD11c^+$ dendritic cells; $P < 0.0001$) and lymphocytes ($CD3^+$ T cells and $CD19^+$ B cells; $P < 0.05$) present at the injury site as compared to a saline-treated control after 1 and 3 weeks (Fig. 1A and fig. S2). At 1 week, collagen-treated wounds recruited the highest number of immune cells into the defect region (36.0% of total live cells, 13.6 million cells) followed by B-ECM– and C-ECM–treated wounds (39.3%, 5.32 million; and 45.4%, 5.44 million cells), with saline-treated wounds containing significantly fewer cells (36.4%, 0.97 million). The proportion of myeloid cells in the damaged muscle peaked at 1 week after injury, and the T cell fraction, consisting of both $CD4^+$ and $CD8^+$ cells, peaked in all treatment groups at 3 weeks after injury. In the muscle wound, biomaterial scaffolds skewed the ratio of CD4:CD8 T cells toward a higher fraction of $CD4^+$ helper T cells (~70% in scaffold-treated, versus ~50% in saline-treated wounds) at 1 week after injury (Fig. 1B). $CD4^+FoxP3^+$ regulatory T cells were also present at low levels and increased over time (fig. S3).

The expression of *interleukin 4* (*Il4*), a gene encoding a canonical type 2 helper T cell (T_H2) cytokine that is also important in muscle healing (*14–17*), increased in the presence of the scaffold (Fig. 1C). Therefore, we sought to understand the role of cells of the adaptive immune system on the formation of the regenerative immune microenvironment. Scaffolds were implanted into B6.129S7-*Rag1*^{tm1Mom}/J (*Rag1*$^{-/-}$) mice, which lack mature T and B cells. In *Rag1*$^{-/-}$ mice, scaffold-mediated *Il4* up-regulation was lost, suggesting a T_H2-driven scaffold immune microenvironment. $CD3^+$ cells were sorted out of muscle injuries at 1 week after injury for detailed gene expression analysis (Fig. 1D, fig. S4, and table S1). Scaffolds induced a T_H2-type gene expression profile as characterized by increased *Il4* expression and decreased expression of *Ifng* and *Tbx21* (T_H1 canonical genes). In addition, *Jag2*, which encodes the Notch ligand Jagged 2, was elevated. Jagged2 helps direct T_H differentiation away from T_H1 and toward T_H2 (*18*). *Il10*, which encodes a general anti-inflammatory cytokine that is not T_H-specific, was also up-regulated. Other genes that are more selectively expressed by T_H1 cells, such as *Fasl* and *Cd28* (the costimulatory receptor for CD86), were likewise down-regulated.

The regenerative outcome of tissue-derived ECM scaffolds in animals and humans is correlated with an immunoregulatory M2 macrophage phenotype during remodeling (*9–11*). Biomaterials increased the expression of genes associated with a pro-regenerative type 2 immune response, including hallmark genes of M2 myeloid cells, more specifically macrophages that are stimulated by IL-4, known as M(IL-4) macrophages (fig. S5) (*19*). As with *Il4* expression, induction of these M(IL-4) markers was almost completely lost in *Rag1*$^{-/-}$ mice (fig. S5). In the presence of adaptive immune cells, biomaterial scaffolds inhibited macrophage CD86 up-regulation (a costimulatory molecule expressed at high levels by classical M1 macrophages) at 3 weeks after surgery (Fig. 2A and fig. S6H). In *Rag1*$^{-/-}$ mice, however, down-regulation of CD86 expression was mitigated, and ECM scaffold–treated wounds returned to a macrophage polarization profile resembling that of saline-treated control animals (Fig. 2A). On the other hand, CD206 expression (a mannose receptor and classical M2 marker) was similar between ECM scaffold–treated and saline-treated mice at 1 week after implantation, with increased expression at 3 weeks (Fig. 2B). However, this increase in CD206 was ablated in *Rag1*$^{-/-}$ mice in both scaffold- and saline-treated wounds, suggesting that the adaptive immune system also has a scaffold-independent role in shaping the wound healing response. Moreover, this CD206 up-regulation was also impaired in B6.129S2-*Cd4*^{tm1Mak}/J (*Cd4*$^{-/-}$) mice, which maintain B cells and $CD8^+$ T cells but lack $CD4^+$ helper T cells (fig. S6A). Additionally, in *Cd4*$^{-/-}$ mice, the recruitment of B cells (a commonly T_H2-driven adaptive effector cell) was diminished (fig. S6G).

To further elucidate the role of $CD4^+$ T cells, and more specifically T_H2 T cells on the polarization of myeloid cells, we evaluated myeloid CD206 expression in *Rag1*$^{-/-}$ mice that were repopulated with either wild-type (WT) $CD4^+$ T cells or *Rictor*$^{-/-}$ $CD4^+$ T cells (Fig. 2, C and D, and fig. S7). Rictor is a critical component of the mTORC2 complex that integrates signals from the environment and drives the polarization of T_H2 cells (*20*). Myeloid cells in *Rag1*$^{-/-}$ mice expressed lower levels of CD206 as compared to WT mice; however, when repopulated with WT $CD4^+$ T cells (T-WT cells), this phenotype was rescued. When

[1]Translational Tissue Engineering Center, Wilmer Eye Institute and Department of Biomedical Engineering, Johns Hopkins University, Baltimore, MD 21287, USA. [2]Department of Oncology, Sidney Kimmel Comprehensive Cancer Center, Johns Hopkins University School of Medicine, Baltimore, MD 21231, USA. [3]Division of Biostatistics and Bioinformatics, Sidney Kimmel Comprehensive Cancer Center, Johns Hopkins University School of Medicine, Baltimore, MD 21231, USA. [4]Hugo W. Moser Research Institute at Kennedy Krieger Institute, Baltimore, MD 21205, USA, and Departments of Neurology and Neuroscience, Johns Hopkins University School of Medicine, Baltimore, MD, USA. [5]Bloomberg-Kimmel Institute for Cancer Immunotherapy, Johns Hopkins University School of Medicine, Baltimore, MD, USA.
***Corresponding author. E-mail: jhe@jhu.edu**

mice received T_H2-deficient T cells (T-*Rictor*$^{-/-}$ cells), CD206 expression was not rescued, proving that T_H2 T cells, dependent on mTORC2 signaling, are necessary for pro-regenerative myeloid polarization. To confirm the role of IL-4 in T_H2-dependent myeloid polarization, we characterized the phenotype of macrophages in BALB/c-*Il4ra*^{tm1Sz}/J (*Il4ra*$^{-/-}$) mice that cannot receive signals from IL-4 (Fig. 2, C and D). Compared to WT controls, myeloid cells in *Il4ra*$^{-/-}$ wounds expressed far lower levels of CD206, suggesting that the macrophage activation was controlled by IL-4, and verifying that the pro-regenerative profile is associated with M(IL-4) cells.

The pleiotropic nature of immune responses typically results in complex expression profiles beyond stereotypical M1 versus M2 "poles" (*19*). The expression of CD86 and the expression of CD206 on macrophages (classically M1 versus M2) were not mutually exclusive; however, these scaffold-associated macrophages also up-regulated the expression of genes encoding *Arg1* and *Retnla* (encoding Fizz1), similar to the results from quantitative reverse transcription polymerase chain reaction (qRT-PCR) analyses of the whole wound (Fig. 2E and fig. S5). Additionally, *Cebpb*, and *Timp1* were up-regulated, whereas *Mmp16* and *Mmp9* were down-regulated, further suggesting a pro-regenerative function of the scaffold-associated macrophages (*21–23*). In *Rag1*$^{-/-}$ mice, which cannot mount a T_H2 immune response, scaffold-associated macrophages lost their pro-regenerative transcriptome (Fig. 2F, fig. S8, and table S2). Several genes directly implicated in muscle regeneration such as *Igf1* (insulin-like growth factor-1) (*24–26*) and *Vegfa* (vascular endothelial growth factor) (*27*) decreased significantly in *Rag1*$^{-/-}$ mice. Gene ontology enrichment analysis of genes differentially expressed in *Rag1*$^{-/-}$ versus WT macrophages shows enrichment in programs associated with morphogenesis and differentiation, suggesting a reliance on the adaptive immune system for up-regulation of developmentally active immune genes (fig. S9).

The detection of a local scaffold-associated T_H2 polarization led us to investigate the potential systemic T cell response (*28*). Subcutaneous scaffold implants produce a systemic T_H2-like

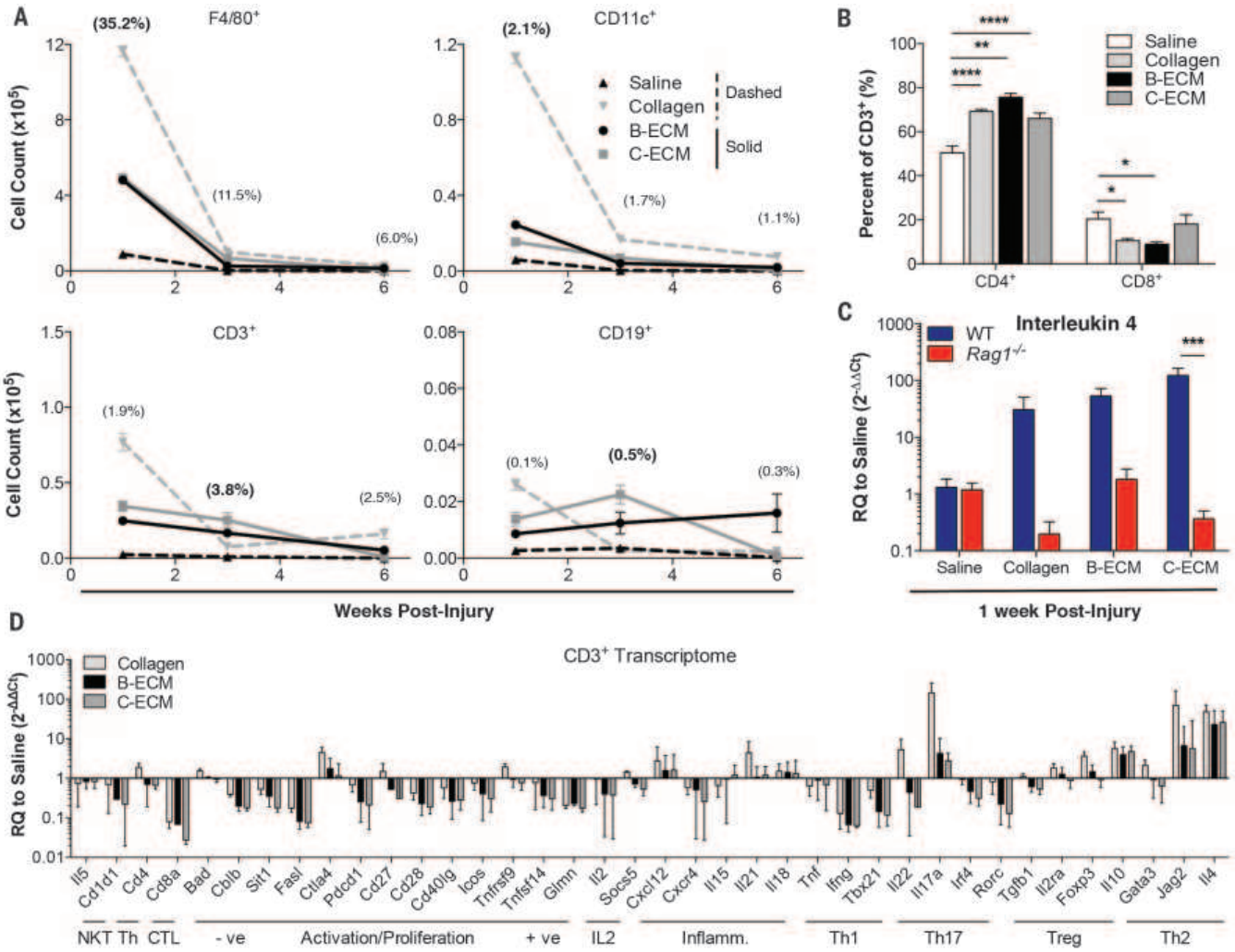

Fig. 1. Biomaterial scaffolds induce a T_H2 response in volumetric muscle wounds. C57BL/6 (WT) and *Rag1*$^{-/-}$ mice received a critical-size quadriceps muscle injury and were treated immediately with 0.05 ml of saline, particulate collagen, B-ECM, or C-ECM. (**A**) Proportions of myeloid (F4/80$^+$ macrophages and CD11c$^+$ dendritic cells) and lymphoid (CD3$^+$ T cells and CD19$^+$ B cells) cell populations in the WT wound environment, determined by flow cytometry (% = mean fraction of live cells across all treatments, with peak level shown in bold text). The greatest cell numbers were in scaffold-treated wounds. (**B**) Proportion of CD3$^+$ T cells that are CD4$^+$ T_H cells or CD8$^+$ cytotoxic T lymphocytes at 1 week after injury treated with saline, collagen, B-ECM, or C-ECM by flow cytometry. (**C**) qRT-PCR analysis of *Il4* gene expression in WT and *Rag1*$^{-/-}$ mice at 1 week after injury. (**D**) One week after injury, transcriptome of CD3 cells sorted from wounded muscles treated with saline, collagen, B-ECM, or C-ECM, determined by qRT-PCR. Data are displayed as relative quantification (RQ) to saline-treated wounds. Data are means ± SEM, n = 4 mice (2 legs pooled per mouse, representative of at least two independent experiments), analysis of variance (ANOVA): ****$P < 0.0001$, ***$P < 0.001$, **$P < 0.01$, *$P < 0.05$.

response in the bloodstream, but the connection to wound healing and regeneration is unknown (*28*, *29*) (Fig. 3 and fig. S10). Scaffold treatment induced hypertrophy of local draining lymph nodes (Fig. 3A), which accompanied a robust increase in *Il4* expression (Fig. 3B and fig. S10). This *Il4* induction was absent at 1 week after injury in *Rag1*$^{-/-}$ mice but present after 3 weeks, suggesting an early adaptive immune–dependent *Il4* up-regulation followed by an innate immune–driven *Il4* up-regulation later in the wound healing and regeneration processes. Additionally, *Cd4*$^{-/-}$ mice displayed a significant decrease in scaffold-mediated *Il4* up-regulation in inguinal lymph nodes at 3 weeks after injury in C-ECM–treated animals (Fig. 3B). This *Il4* expression level was higher than that in *Rag1*$^{-/-}$ mice, demonstrating an important role of CD4^{+} T cells in

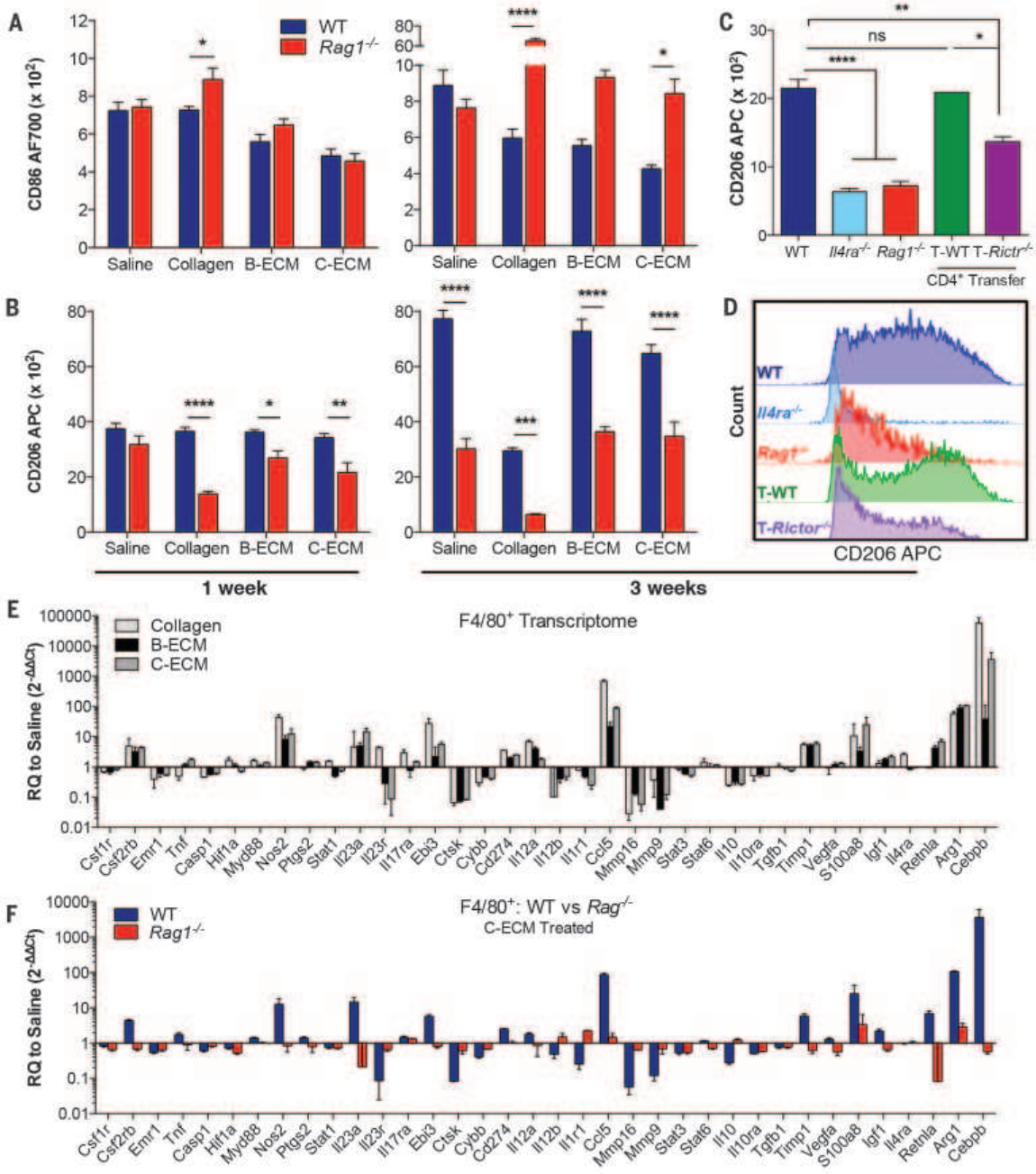

Fig. 2. M(IL-4) pro-regenerative myeloid polarization induced by scaffolds is T_H2-dependent. (**A** and **B**) Macrophages in wounded muscle were characterized for CD86 (A) and CD206 (B) expression by flow cytometry at 1 and 3 weeks after injury in the presence of saline or ECM scaffold in WT (blue bars) and *Rag1*$^{-/-}$ (red bars) mice. The mean of fluorescence is shown. (**C**) CD206 expression at 3 weeks after injury in C-ECM–treated WT, *Il4ra*$^{-/-}$, *Rag1*$^{-/-}$, and *Rag1*$^{-/-}$ mice reconstituted with either WT CD4^{+} T cells (T-WT, $n = 2$) or *Rictor*$^{-/-}$ CD4^{+} T cells (T-*Rictr*$^{-/-}$; T_H2-deficient). (**D**) Representative comparison of CD206 expression between WT, *Il4ra*$^{-/-}$, *Rag1*$^{-/-}$, and *Rag1*$^{-/-}$ reconstituted with WT and *Rictor*$^{-/-}$ CD4^{+} T cells. (**E**) qRT-PCR gene expression analysis in cell-sorted macrophages from wounded muscles 1 week after injury and treated with collagen (light gray–striped bars), B-ECM (black solid bars), or C-ECM (gray solid bars) compared to saline control. RQ to saline $= 2^{-\Delta\Delta Ct}$. (**F**) RQ to saline in WT and *Rag1*$^{-/-}$ mice when wounds were treated with C-ECM. The figure shows a loss of scaffold-mediated macrophage polarization in *Rag1*$^{-/-}$ mice. WT, blue bars; *Rag1*$^{-/-}$, red bars. Data are means ± SEM, $n = 4$ mice unless otherwise stated (representative of one or two independent experiments); ANOVA [(A) and (B)] and Student's *t* test (D): ****$P < 0.0001$, ***$P < 0.001$, **$P < 0.01$, *$P < 0.05$.

scaffold-induced systemic type 2 immunity, but with potential further contributions by B cells or $CD8^+$ T cells.

Functionally, WT animals recovered to be able to run distances similar to those of healthy uninjured counterparts after 6 weeks (Fig. 4A). However, this restoration of running capacity was ablated in the absence of T and B cells (*Rag1*$^{-/-}$) in ECM scaffold–treated wounds. At 3 weeks after

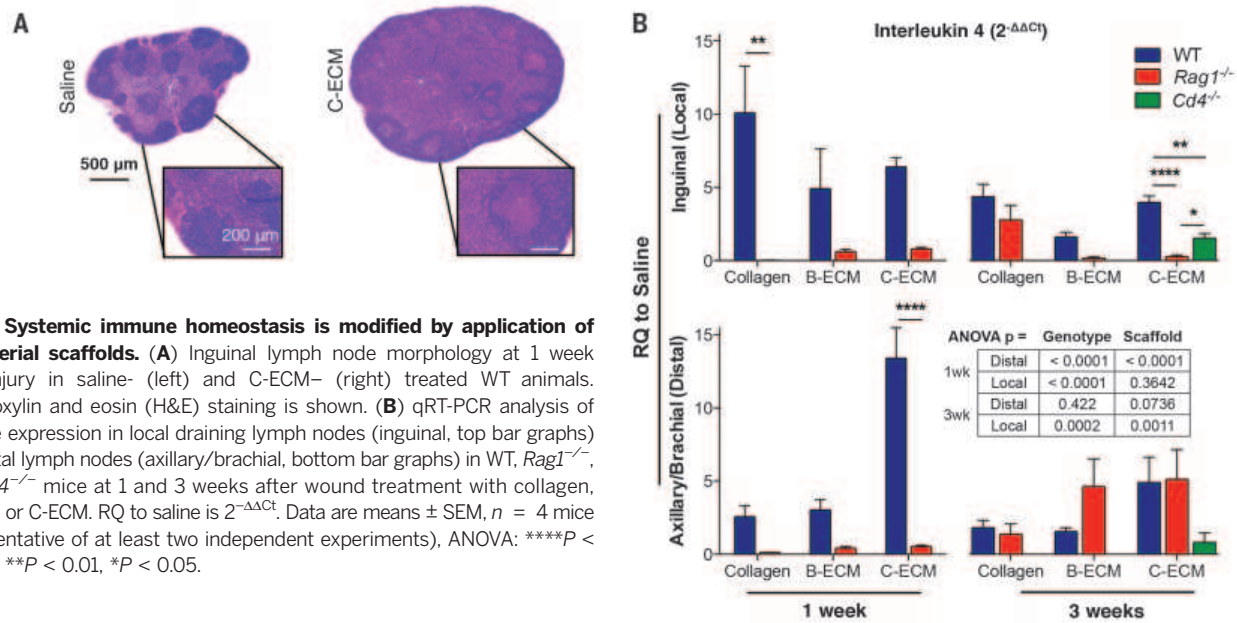

Fig. 3. Systemic immune homeostasis is modified by application of biomaterial scaffolds. (**A**) Inguinal lymph node morphology at 1 week after injury in saline- (left) and C-ECM– (right) treated WT animals. Hematoxylin and eosin (H&E) staining is shown. (**B**) qRT-PCR analysis of *Il4* gene expression in local draining lymph nodes (inguinal, top bar graphs) and distal lymph nodes (axillary/brachial, bottom bar graphs) in WT, *Rag1*$^{-/-}$, and *Cd4*$^{-/-}$ mice at 1 and 3 weeks after wound treatment with collagen, B-ECM, or C-ECM. RQ to saline is $2^{-\Delta\Delta Ct}$. Data are means ± SEM, n = 4 mice (representative of at least two independent experiments), ANOVA: ****P < 0.0001, **P < 0.01, *P < 0.05.

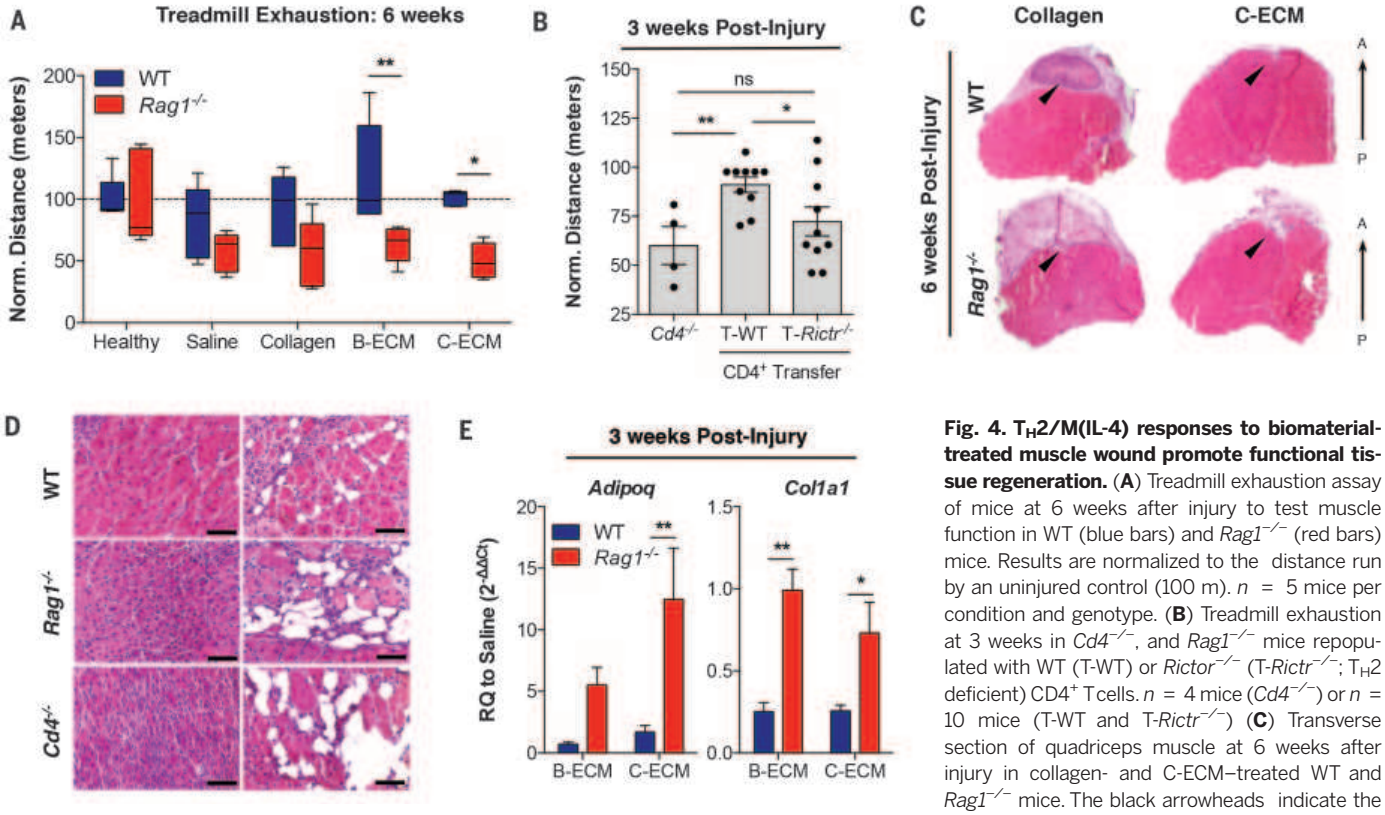

Fig. 4. T_H2/M(IL-4) responses to biomaterial-treated muscle wound promote functional tissue regeneration. (**A**) Treadmill exhaustion assay of mice at 6 weeks after injury to test muscle function in WT (blue bars) and *Rag1*$^{-/-}$ (red bars) mice. Results are normalized to the distance run by an uninjured control (100 m). n = 5 mice per condition and genotype. (**B**) Treadmill exhaustion at 3 weeks in *Cd4*$^{-/-}$, and *Rag1*$^{-/-}$ mice repopulated with WT (T-WT) or *Rictor*$^{-/-}$ (T-*Rictr*$^{-/-}$; T_H2 deficient) $CD4^+$ T cells. n = 4 mice (*Cd4*$^{-/-}$) or n = 10 mice (T-WT and T-*Rictr*$^{-/-}$) (**C**) Transverse section of quadriceps muscle at 6 weeks after injury in collagen- and C-ECM–treated WT and *Rag1*$^{-/-}$ mice. The black arrowheads indicate the injury/treatment area. A, anterior, P, posterior, with H&E staining shown. (**D**) C-ECM–treated VML at 3 weeks after injury in WT, *Rag1*$^{-/-}$, and *Cd4*$^{-/-}$ mice stained with H&E. Small muscle fibers and ectopic adipogenesis are present in *Rag1*$^{-/-}$ and *Cd4*$^{-/-}$ wounds. Scale bars, 50 µm. (**E**) Gene expression (qRT-PCR) of *Adipoq* (adipose marker) and *Col1a1* (collagen I) showing increased adipose gene expression in *Rag1*$^{-/-}$ as well as increased collagen gene expression, suggesting alterations in connective tissue deposition and possible scarring. n = 4 mice unless otherwise stated (representative of at least two independent experiments). Data are means ± SEM; ANOVA [(A) and (D)] and Student's t test (E): ****P <0.0001, ***P < 0.001, **P < 0.01, *P < 0.05.

injury, repopulation of *Rag1*$^{-/-}$ mice with WT T cells rescued their functional capacity, and the animals could run greater distances as compared to mice lacking the CD4 subset (Fig. 4B; 91.11 ± 3.83 versus 60.06 ± 9.69, P = 0.0032). Furthermore, *Rag1*$^{-/-}$ mice repopulated with WT CD4 T cells performed better than those repopulated with *Rictor*$^{-/-}$ CD4^{+} T cells (72.31 ± 7.40, P = 0.0368), confirming the role of T_H2 CD4^{+} T cells in functional muscle regeneration.

Muscle structure correlated with the differences in functional capacity. Histologically, at 6 weeks after injury, the quadriceps muscle treated with the C-ECM scaffold appeared similar to that of healthy controls, with minimal scaffold visible and repair tissue fully integrated within the surrounding musculature. A large region of fibrous tissue with active inflammation was present in muscles treated with the collagen scaffold (Fig. 4C and fig. S11). *Rag1*$^{-/-}$ mice displayed increased adipose deposition, fibrosis, scaffold persistence, and smaller-diameter muscle fibers than their WT counterparts. At 3 weeks after injury, centrally nucleated muscle fibers, which are indicative of active regeneration or recovery from injury, were present within the biomaterial scaffold and around the defect site (Fig. 4D and fig. S12). WT mice produced muscle with larger, more rounded fibers, whereas *Rag1*$^{-/-}$ mice muscles contained smaller, irregularly shaped fibers, indicating a defect in muscle regeneration. In addition, the pathologic *Rag1*$^{-/-}$ histomorphology was recapitulated in *Cd4*$^{-/-}$ mice, confirming the role of CD4^{+} T cells in fibro-adipogenic lineage commitment (Fig. 4D). Increased gene expression of *Adipoq* (adiponectin) confirmed ectopic adipogenesis in *Rag1*$^{-/-}$ whole muscle. Similarly, the expression of *Col1a1* (type I collagen) increased in *Rag1*$^{-/-}$ mice muscles, highlighting increased fibrosis (Fig. 4E and fig. S13). Although scaffold treatment reduced fibro- and adipogenesis markers in WT animals, this benefit was lost in *Rag1*$^{-/-}$ mice.

We have demonstrated that tissue-derived biomaterial scaffolds enhance the development of a pro-regenerative immune environment and have implicated adaptive immune cells, specifically mTORC2-dependent CD4^{+} T_H2 T cells, in the process of functional tissue restoration (fig. S14). Just as cancer research has made great strides in T cell therapies, these concepts can be translated to biomaterials design to improve tissue repair and regeneration (*30–33*).

REFERENCES AND NOTES

1. T. A. Wynn, A. Chawla, J. W. Pollard, *Nature* **496**, 445–455 (2013).
2. P. Matzinger, T. Kamala, *Nat. Rev. Immunol.* **11**, 221–230 (2011).
3. Y. Peng *et al.*, *J. Autoimmun.* **29**, 303–309 (2007).
4. J. S. Otis *et al.*, *PLOS One* **9**, e92363 (2014).
5. S. Frantz, K. A. Vincent, O. Feron, R. A. Kelly, *Circ. Res.* **96**, 15–26 (2005).
6. J. M. Anderson, *Annu. Rev. Mater. Res.* **31**, 81–110 (2001).
7. J. M. Anderson, K. M. Miller, *Biomaterials* **5**, 5–10 (1984).
8. J. M. Anderson, *ASAIO Trans.* **34**, 101–107 (1988).
9. B. M. Sicari *et al.*, *Sci. Transl. Med.* **6**, 234ra58 (2014).
10. V. J. Mase Jr. *et al.*, *Orthopedics* **33**, 511 (2010).
11. B. N. Brown *et al.*, *Acta Biomater.* **8**, 978–987 (2012).
12. B. M. Sicari *et al.*, *Tissue Eng. Part A* **18**, 1941–1948 (2012).
13. V. Z. Beachley *et al.*, *Nat. Methods* **12**, 1197–1204 (2015).
14. V. Salmon-Ehr *et al.*, *Lab. Invest. J. Tech. Methods Pathol.* **80**, 1337–1343 (2000).
15. W. C. Gause, T. A. Wynn, J. E. Allen, *Nat. Rev. Immunol.* **13**, 607–614 (2013).
16. J. E. Heredia *et al.*, *Cell* **153**, 376–388 (2013).
17. V. Horsley, K. M. Jansen, S. T. Mills, G. K. Pavlath, *Cell* **113**, 483–494 (2003).
18. T. C. Fang *et al.*, *Immunity* **27**, 100–110 (2007).
19. P. J. Murray *et al.*, *Immunity* **41**, 14–20 (2014).
20. G. M. Delgoffe *et al.*, *Nat. Immunol.* **12**, 295–303 (2011).
21. D. Ruffell *et al.*, *Proc. Natl. Acad. Sci. U.S.A.* **106**, 17475–17480 (2009).
22. J. Blackwell *et al.*, *J. Physiol. Sci.* **65**, 145–150 (2015).
23. M. E. Davis, J. P. Gumucio, K. B. Sugg, A. Bedi, C. L. Mendias, *J. Appl. Physiol.* **115**, 884–891 (2013).
24. F. Mourkioti, N. Rosenthal, *Trends Immunol.* **26**, 535–542 (2005).
25. A. Musarò *et al.*, *Nat. Genet.* **27**, 195–200 (2001).
26. J. P. Liu, J. Baker, A. S. Perkins, E. J. Robertson, A. Efstratiadis, *Cell* **75**, 59–72 (1993).
27. N. Arsic *et al.*, *Molecular Therapy: J. Am. Soc. Gene Therapy* **10**, 844–854 (2004).
28. A. J. Allman *et al.*, *Transplantation* **71**, 1631–1640 (2001).
29. A. J. Allman, T. B. McPherson, L. C. Merrill, S. F. Badylak, D. W. Metzger, *Tissue Eng.* **8**, 53–62 (2002).
30. S. A. Rosenberg, J. C. Yang, N. P. Restifo, *Nat. Med.* **10**, 909–915 (2004).
31. O. A. Ali *et al.*, *Cancer Res.* **74**, 1670–1681 (2014).
32. J. Kim, D. J. Mooney, *Nano Today* **6**, 466–477 (2011).
33. O. A. Ali, P. Tayalia, D. Shvartsman, S. Lewin, D. J. Mooney, *Adv. Funct. Mater.* **23**, 4621–4628 (2013).

ACKNOWLEDGMENTS

The authors acknowledge the Sidney Kimmel Comprehensive Cancer Center Flow Cytometry Research Core and L. Blosser for their help on flow cytometric studies; A. Anderson for assistance with adipogenesis studies; S. Sommerfeld and X. Wang for assistance with the clinical product testing; A. Rittenbach for assistance with computed tomography imaging; M. de Palma for generous donation of the iBMM macrophage cell line; M. Swartz and the Swartz lab for assistance in the pilot studies and J.H.E. sabbatical hosting; A. Ewald for helpful discussions; and J. Schneck for critical review. The data presented in this manuscript are tabulated in the main paper and in the supplementary materials. K.S., F.H., D.P., and J.H.E. are inventors on provisional patent application no. 48317-502P01US, filed by Johns Hopkins University (JHU) related to regenerative immunology. J.H.E. holds equity in Aegeria Soft Tissue, a company that has licensed JHU intellectual property not directly related to the materials used in this study but similar enough that it may benefit from the results. The conflict is being managed by the Johns Hopkins Office of Policy Coordination. This work was funded by the Maryland Stem Cell Research Fund (MSCRF), grant 113345; the Armed Forces Institute for Regenerative Medicine; and U.S. Department of Defense grant W81XWH-11-2-0022 (awarded to J.H.E.) and the Jules Stein Professorship from the Research to Prevent Blindness Foundation. M.T.W. was supported by a postdoctoral fellowship from the Hartwell Foundation. D.M.P., J.D.P., B.S.L. and H.W. were supported by Cancer Center Core grant P30CA006973. J.D.P. was supported by a grant from the National Institutes of Health, R01AI077610. J.D.P, J.H.E., and D.M.P acknowledge support from the Bloomberg-Kimmel Institute for Cancer Immunotherapy.

SUPPLEMENTARY MATERIALS

www.sciencemag.org/content/352/6283/366/suppl/DC1
Materials and Methods
Figs. S1 to S14
Tables S1 and S2
References (*34*, *35*)

23 November 2015; accepted 4 March 2016
10.1126/science.aad9272

NEW ENGLAND BioLabs® Inc.

Time for change.

Introducing Monarch™ Nucleic Acid Purification Kits

It's time to transform your DNA purification experience. NEB's Monarch Nucleic Acid Purification Kits are optimized for maximum performance and minimal environmental impact. With an innovative column design, buffer retention is prevented, eliminating risk of carryover contamination and enabling elution in smaller volumes. The result – highly pure DNA for your downstream applications.

Make the change and migrate to Monarch today.

Optimized design of Monarch Miniprep Columns

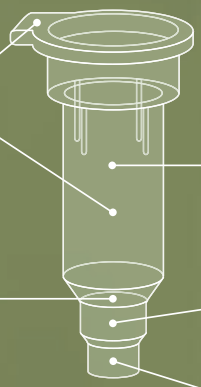

Request your free sample at **NEBMonarch.com**

NEW ENGLAND BIOLABS® and NEB® are registered trademarks of New England Biolabs, Inc.
MONARCH™ is a trademark of New England Biolabs, Inc.

BOYALIFE & Science Science Translational Medicine Award in Stem Cells and Regenerative Medicine

The first global award for stem cells and regenerative medicine

Stem cells and regenerative medicine is the new frontier in life sciences. *Boyalife, Science, and Science Translational Medicine* jointly establish a global award to recognize and reward scientists in the fields of stem cells and/or regenerative medicine with a focus on developing cell-based treatments for cancer, degenerative disorders, immunotherapy and stem cells transplantation.

The 2016 award ceremony will be held in San Francisco, on 23rd June, 2016.

The winners will receive:

☆A Grand Prize of $25,000 and a Runner-Up Prize of $5,000 will be awarded.

☆The Grand Prize Winning Essay will be published in Science; a brief abstract of the Runner-Up Essay will be published in Science.

Learn more about the Prize,
visit : *www.sciencemag.org/prize/boyalife/rules*

BOYALIFE Stem Cell

Science AAAS

Science Translational Medicine AAAS

CALL FOR NOMINATIONS FOR A $1 MILLION PRIZE

THE BIGGEST PRIZE IN THE WORLD

FOR INNOVATION IN THE FIELD OF ALTERNATIVE FUELS FOR TRANSPORTATION

THE 2016 ERIC AND SHEILA SAMSON PRIME MINISTER'S PRIZE IS A $ 1 MILLION INTERNATIONAL PRIZE FOR INNOVATION IN ALTERNATIVE FUELS FOR TRANSPORTATION.

If you are actively engaged in innovative, paradigm-shifting research or groundbreaking technological development worthy of significant and widespread attention, you can qualify for this prestigious prize.

For more information visit
prize.fuelchoicesinitiative.com

DEADLINE FOR NOMINATIONS

MAY 15, 2016

OPEN TO CITIZENS OF ALL COUNTRIES

For further information and forms:
Go to: prize.fuelchoicesinitiative.com
Or contact: avi@most.gov.il

Fuel Choices Initiative

KEREN HAYESOD קרן היסוד UNITED ISRAEL APPEAL

Israel

Ministry of Science, Technology and Space

Don't miss the debut of *Science Immunology*.

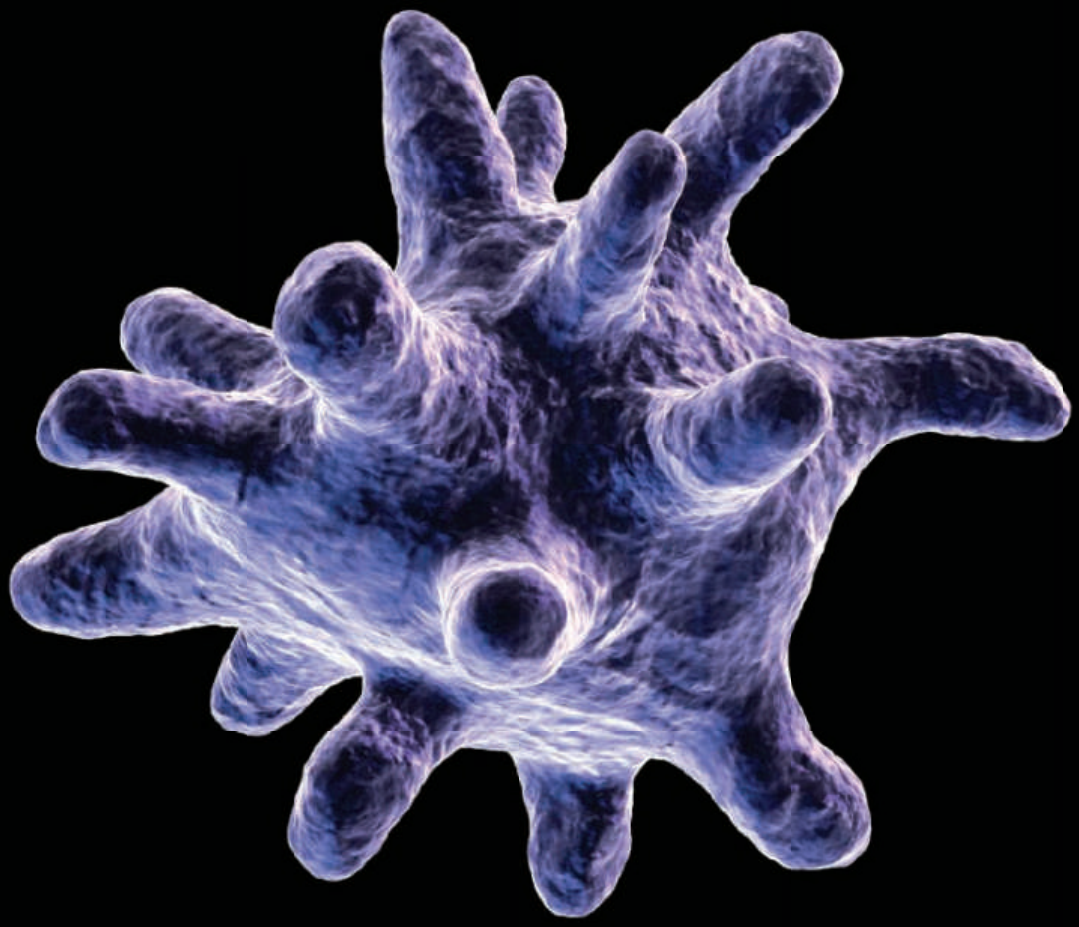

Image: Eraxion / iStockPhoto

NOW ACCEPTING PAPERS

Science is expanding its reach into immunology—now offering the newest online-only, weekly journal in the *Science* family of publications. *Science Immunology* will provide original, peer-reviewed research articles that report critical advances in all areas of immunological research, including studies that provide insight into the human immune response in health and disease.

Be a part of the *Science Immunology* debut issue publishing Summer 2016!

Submit your manuscript today at **ScienceImmunology.org.**

Science Immunology

AAAS

Join our live webinar!

Metabolic regulation of immunity

Exploring programs that drive immune development and function

To register, go to:
bit.ly/ScienceWebinarApr27

Wednesday,
April 27, 2016

12 noon Eastern,
9 a.m. Pacific,
5 p.m. UK,
6 p.m. CEST

Science
AAAS

Sponsored by Seahorse Bioscience
A part of Agilent Technologies

AAAS *Travels*

In Search of
AMELIA EARHART
Explore one of the greatest mysteries of all time!
On the 80th Anniversary of
Amelia's World Flight & Disappearance!

Amelia 2017 Adopt an Expert!
June 21–July 11, 2017

Help in search of Amelia Earhart!

1) You can join us yourself.
2) You can also *Adopt-an-Expert* and help pay the way of one of the research scientists.

For further information please visit
http://niku2017.strikingly.com

You can adopt an expert for just $8,995 + airfare of $1,695 from Los Angeles.

For a detailed brochure, call (800) 252-4910
All prices are per person twin share + air

BETCHART EXPEDITIONS Inc.
17050 Montebello Rd, Cupertino, CA 95014
Email: AAASInfo@betchartexpeditions.com
www.betchartexpeditions.com

myIDP:
A career plan customized for you, by you.

For your career in science, there's only one Science

my IDP
Science Careers

Recommended by leading professional societies and the NIH

Features in myIDP include:

- Exercises to help you examine your skills, interests, and values
- A list of 20 scientific career paths with a prediction of which ones best fit your skills and interests
- A tool for setting strategic goals for the coming year, with optional reminders to keep you on track
- Articles and resources to guide you through the process
- Options to save materials online and print them for further review and discussion
- Ability to select which portion of your IDP you wish to share with advisors, mentors, or others
- A certificate of completion for users that finish myIDP.

Visit the website and start planning today!
myIDP.sciencecareers.org

Science Careers In partnership with:

FASEB
UCSF University of California San Francisco
Medical College of Wisconsin
Burroughs Wellcome Fund

Gas Sorption Analyzers

Hiden Isochema's new MultiPort inlet selector is now available for the manufacturer's intelligent gravimetric analyzer (IGA) and XEMIS series gas sorption analyzers. The MultiPort expands the number of gases that can be simultaneously connected and the level of automation available. There are connections for up to 12 gas species, and control is integrated within Hiden Isochema's HIsorp.NET software suite. The MultiPort not only allows the user to determine consecutive gravimetric sorption isotherms with more species at one or more gas temperatures, but also offers the user full control of the inlet for advanced method development. The MultiPort inlet selector also provides an affordable solution for increasing the level of automation of existing IGA or XEMIS gas sorption analyzers as part of an in-the-field upgrade package.

Hiden Isochema
For info: +44-(0)-1925-244678
www.hidenisochema.com

Filtration System

The SARTOFLOW Smart is a smart and easy benchtop crossflow system for optimized ultra- and diafiltration applications. It can ideally be used in many downstream processes, such as purification of vaccines, monoclonal antibodies, and recombinant proteins. The system is suitable for flexible use in laboratory environments for process development and clinical trials as well as for current good manufacturing practice (cGMP) environments. The new system is equipped with a low-shear, four-piston membrane pump enabling the highest product yields. The pump also provides a wide range of flow rates, allowing the user to choose between membrane surface areas from 50 cm^2 up to 0.14 m^2. The crossflow system is supplied with Sartorius Stedim Biotech's intuitive and easy-to-use DCU-4 control unit, which when combined with the company's BioPAT SCADA MFCS-4 software, provides data logging and export. Its touchscreen offers instant access to all critical process parameters and displays control and alarm functions.

Sartorius Stedim Biotech
For info: +49-(0)-551-308-3324
www.sartorius.com

Gel Imager

The Bio-1000F is an innovative, user-friendly, and cost-effective device that integrates image capture, gel preview, and gel extraction essential for routine nucleic acid gel electrophoresis. With the combination of a high-sensitivity charge-coupled device (CCD) system and blue-light emitting diode (LED) illuminators, the Bio-1000F is compatible with all ethidium bromide (EtBr)-alternative fluorescent stains, and provides publication-quality images up to 0.04 ng per band, significantly enhancing fluorescent signal expression over other gel documentation systems that depend on ultraviolet and blue-LED light sources. Thanks to its removable filter plate and intuitive MiBioFluo software interface, users can visualize banding patterns and conduct gel extraction directly on the Bio-1000F without moving between the transilluminator and gel imager. The Bio-1000F's compact design enables it to fit in crowded laboratory spaces. The Bio-1000F features an integrated, environment-friendly, and ultrasensitive gel imager for researchers dedicated to improving laboratory safety and the efficiency of gel electrophoresis.

Microtek International
For info: +886-3-577-2155
www.microtek.com

3D X-Ray Microscope

The new Zeiss FPX flat panel extension for the Zeiss Xradia Versa 500 series of 3D X-ray microscopes (XRMs) delivers large-sample, high-throughput scanning with best-in-class image quality. Combined with the high resolution of the Xradia Versa XRMs, the new Zeiss FPX enhances imaging flexibility and creates workflow efficiencies with an all-in-one system for industrial development and academic research. The Xradia Versa with FPX enables engineers, developers, and researchers to scout large samples two to five times faster to identify a region of interest (ROI), and then zoom to image areas at high resolution with the exclusive Zeiss Xradia Versa RaaD dual magnification microscope objectives, which enable resolution at a distance. The Zeiss FPX extends the ability of the Xradia Versa XRM to achieve full-field-of-view, whole-sample imaging up to five inches in diameter.

Zeiss
For info: +49-3641-64-3949
www.zeiss.com

Protein Gel Casting

Researchers can now access a device that enables reliable, leak-free custom development of protein gels for electrophoresis. Developed for simplicity and intuitively designed, the SureCast Gel Handcast System also helps to save time, money, and precious samples. While precast gels for separating proteins are popular among researchers, handcasting polyacrylamide gels continues to be the favored method used by labs around the world. But leakage and the loss of precious samples are recurring issues with many systems on the market. One main advantage of the SureCast Gel Handcast System is its ultradurable glass plates, which are more than 3 times thicker and up to 20 times more durable than currently available glass plates. A single-motion, load-and-lock system also creates a securely sealed assembly for confident protein gel casting.

Thermo Fisher Scientific
For info: 800-955-6288
www.thermofisher.com/surecast

Electronically submit your new product description or product literature information! Go to www.sciencemag.org/about/new-products-section for more information.

Newly offered instrumentation, apparatus, and laboratory materials of interest to researchers in all disciplines in academic, industrial, and governmental organizations are featured in this space. Emphasis is given to purpose, chief characteristics, and availability of products and materials. Endorsement by *Science* or AAAS of any products or materials mentioned is not implied. Additional information may be obtained from the manufacturer or supplier.

Join the Conversation!

Twitter is a great way to connect with AAAS members and staff about the issues that matter to you most. Be a part of the discussion while staying up-to-date on the latest news and information about your personal member benefits.

Follow us @AAASmember and join the conversation with #AAAS

AAAS MemberCentral

MemberCentral.aaas.org

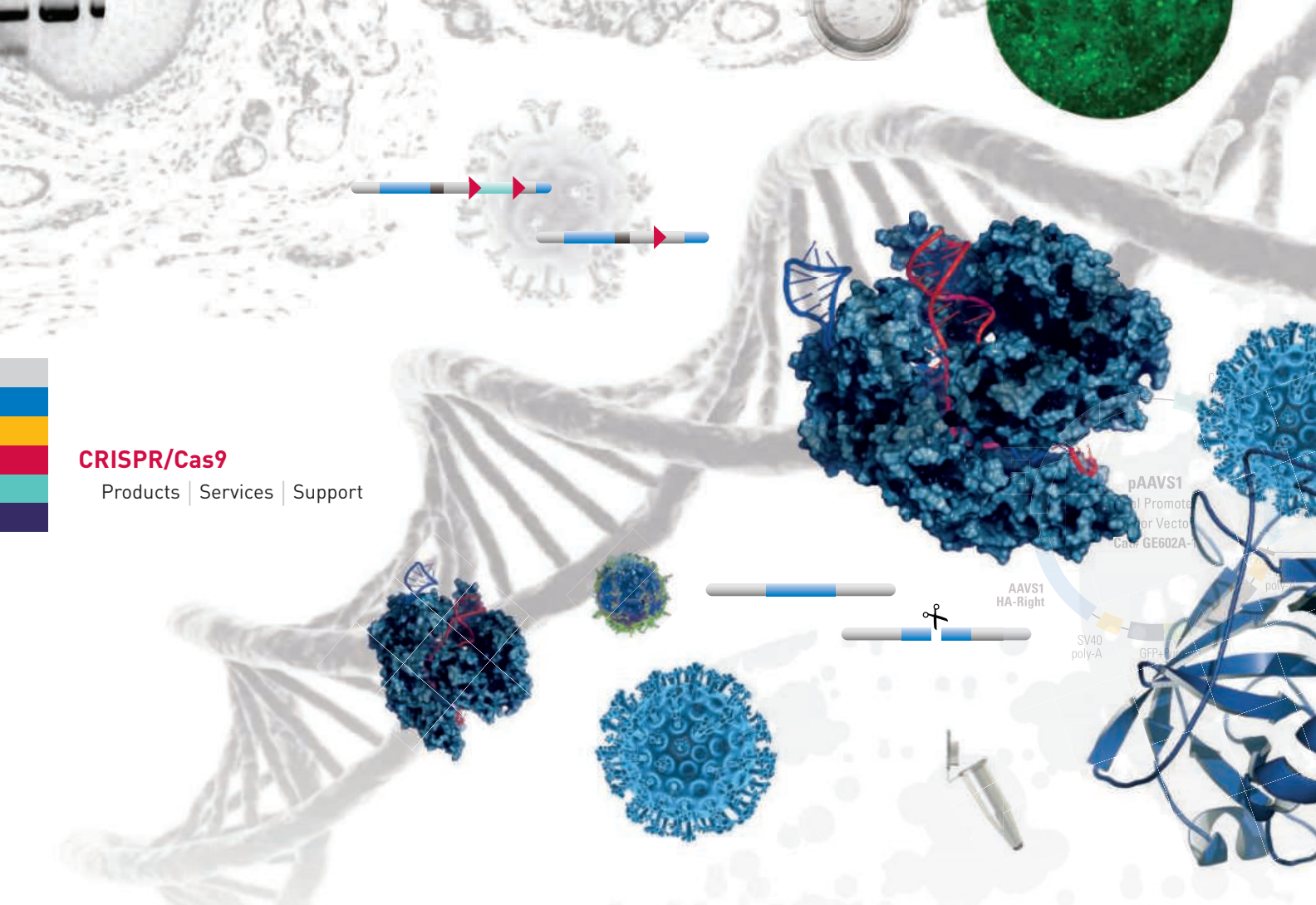

CRISPR/Cas9

Products | Services | Support

GETTING STARTED WITH CRISPR/Cas9

CRISPR/Cas9 is revolutionizing biology, giving scientists unparalleled power and precision for genome engineering. But like many other life science tools, there's a learning curve. To help you bring this innovative technology into your lab, SBI has put together a series of tutorials on how to use CRISPR/Cas9.

Start using CRISPR/Cas9 today, watch the tutorials at: *systembio.com/crispr-cas9-tutorials*

Or, to speed up your research, take advantage of SBI's expertise and have our team of scientists design and build custom constructs and/or engineered cell lines. Contact us to learn more at *services@systembio.com*

SBI System Biosciences
Harnessing innovation to drive discoveries

There's only one Science

Science Careers Advertising

For full advertising details, go to ScienceCareers.org and click For Employers, or call one of our representatives.

Tracy Holmes
Worldwide Associate Director
Science Careers
Phone: +44 (0) 1223 326525

THE AMERICAS

E-mail: advertise@sciencecareers.org
Fax: +1 (202) 289 6742

Tina Burks
Phone: +1 (202) 326 6577

Nancy Toema
Phone: +1 (202) 326 6578

Online Job Posting Questions
Phone: +1 (202) 312 6375

EUROPE / INDIA / AUSTRALIA / NEW ZEALAND / REST OF WORLD

E-mail: ads@science-int.co.uk
Fax: +44 (0) 1223 326532

Sarah Lelarge
Phone: +44 (0) 1223 326527

Kelly Grace
Phone: +44 (0) 1223 326528

Online Job Posting Questions
Phone: +44 (0) 1223 326528

JAPAN

Katsuyoshi Fukamizu (Tokyo)
E-mail: kfukamizu@aaas.org
Phone: +81 3 3219 5777

Hiroyuki Mashiki (Kyoto)
E-mail: hmashiki@aaas.org
Phone: +81 75 823 1109

CHINA / KOREA / SINGAPORE / TAIWAN / THAILAND

Ruolei Wu
E-mail: rwu@aaas.org
Phone: +86 186 0082 9345

All ads submitted for publication must comply with applicable U.S. and non-U.S. laws. *Science* reserves the right to refuse any advertisement at its sole discretion for any reason, including without limitation for offensive language or inappropriate content, and all advertising is subject to publisher approval. *Science* encourages our readers to alert us to any ads that they feel may be discriminatory or offensive.

ScienceCareers
FROM THE JOURNAL SCIENCE AAAS

ScienceCareers.org

Postdoctoral Research Associate
Three Positions Available

The Institute of Marine and Environmental Technology (IMET) of the University System of Maryland (USM) seeks applications for three Postdoctoral Research Associate positions. IMET scientists study the biology of coastal marine biosystems and ensure their sustainable use (www.imet.usmd.edu). IMET brings together faculty members from three major USM research institutions - the University of Maryland Baltimore (UMB), the University of Maryland Baltimore County (UMBC), and the University of Maryland Center for Environmental Science (UMCES) - in a state-of-the-art research facility located at Baltimore's Inner Harbor. These positions are in collaboration with the National Institute of Standards and Technology (NIST), Hollings Marine Laboratory in Charleston, South Carolina. The postdocs will be jointly trained in Baltimore and Charleston and successful candidates will tentatively work at IMET for 6 months (Baltimore, MD) and at NIST for 6 months (Charleston, SC) each year. Appointments are for one year with extension possible depending on performance and funding availability.

1. IMET-UMBC seeks a Postdoctoral Research Associate in the laboratory of Dr. Colleen Burge to study coral holobiont function in a changing ocean. The position requires a PhD in Biology/Molecular Biology/Marine Science or related field. The position is in collaboration with Dr. Rusty Day at NIST. The postdoc will focus on integrating genomics and biogeochemistry approaches to understand coral physiology across a pH gradient. We seek an individual with strong experience in molecular biology, microbiology, and bioinformatics. Highly qualified candidates will also have experience in coral reef biology and/or biogeochemistry, including field sample collection via SCUBA, and laboratory processing of coral specimens. Salary is commensurate with experience. Interested applicants should send a letter of application, statement of research goals & curriculum vitae including three references (name, affiliation, phone number, and e-mail address) in PDF format via email to **mupload.Postdoc.fyznkra096@u.box.com**. Applicants will receive an e-mail from "Box" confirming receipt of the e-mail with attached files.

2. IMET-UMCES seeks a Postdoctoral Research Associate who is self-motivated, independent, dedicated, and career-oriented with a strong publication record and with expertise in invertebrate neuroendocrinology or NMR analysis to study Crustacean Metabolomics: Identification of potential growth and reproductive indicators for aquaculture using NMR and MS approaches. The position is in the laboratory of Dr. Sook Chung (IMET) in collaboration with Dr. Tracey Schock (NIST). The role of this position involves defining the ecdysteroidogenesis pathway using molecular biology and transcriptomic data analysis and NMR and MS analysis and an alternative ecdysteroidogenesis site in adult female blue crab, *Callinectes sapidus*; organizing experimental animals; conducting experiments; and analyzing data. Proposal and manuscript writing ability preferred. Among other shared responsibilities, this position will order supplies and arrange experiment services required. The successful candidate will tentatively work at IMET for 6 months (Baltimore, MD) and at NIST for 6 months (Charleston, SC) each year and must be able to work independently, as well as be a team leader/player working with students and other laboratory staff. Please submit your CV, cover letter, and contact information for three references to **imethr@umces.edu**.

3. IMET-UMB seek an outstanding candidate for a Postdoctoral Research Associate position (full-time) to study the metabolomics of extremophiles. Funding is available from the NIST/IMET Postdoctoral Program for applying high field NMR to study stress-related metabolites including compatible solutes. The position requires a PhD or equivalent degree in biological chemistry and/or molecular biology. Previous experience in microbial physiology, NMR spectroscopy or related disciplines is advantageous. The position is in a collaboration between Prof. Frank Robb (IMET) and Dr. Dan Bearden (NIST). Salary negotiable. Send CV with training, list of publications, a brief statement of career objectives, and plans for research in the research area listed above. Include the names and telephone numbers of three references to: Dr. Frank Robb, Ph.D. at **Frobb@som.umaryland.edu**.

To receive full consideration, application materials should be submitted by **7 May, 2016** (the positions will be open until filled).

The USM is an Equal Opportunity, Affirmative Action Employer. The University of Maryland, Baltimore is an Equal Opportunity/Affirmative Action Employer. Minorities, women, individuals with disabilities, and protected veterans are encouraged to apply.

Institute of Marine and Environmental Technology

NIST
National Institute of Standards and Technology
U.S. Department of Commerce

NORTH CAROLINA CENTRAL UNIVERSITY
FOUNDED 1910

Director
Biomanufacturing Research Institute and Technology Enterprise

North Carolina Central University (NCCU) invites applications for the position of Director for the Biomanufacturing Research Institute and Technology Enterprise (BRITE) to provide overall leadership and supervision of the unit. The Director reports directly to the Vice Chancellor for Research and Economic Development. BRITE is one of NCCU's major research institutes and houses the College of Arts and Science's Department of Pharmaceutical Sciences. BRITE is located in a $20.1 million state-of-the-art facility and features 21,000 sq. ft. of classroom and office space, and 31,000 sq. ft. of laboratory space for faculty and students to conduct applied research in areas related to drug discovery, biomanufacturing and biotechnology.

Purpose of Position: The BRITE Director will lead and manage teams of scientists conducting translational research encompassing biomanufacturing and drug discovery activities in various therapeutic areas that include diabetes, cancer, neurodegenerative diseases and other metabolic disorders. The Institute owns a 460,000 compound library which is the largest academic collection in the USA. BRITE serves approximately 200 students annually who are majoring in Pharmaceutical Sciences at the undergraduate or graduate level. The newest graduate program within the unit is the Ph.D. in Integrated Biosciences/Pharmaceutical Sciences Track. The unit has approximately 38 research, faculty and staff members. The Director, in collaboration with the Chair of Pharmaceutical Sciences, will manage the recruitment of new students, BRITE scholarships, student mentoring and career development, internships, student leadership development and outreach activities for K-12. The Director will participate as a leader representing BRITE at NCBioImpact, a state initiative for workforce development. The Director is also expected to establish and manage internal and external collaborations; contribute to the assessment of external business alliances; and, out-licensing opportunities for technologies developed in BRITE.

Qualifications: The Director is expected to have an earned Ph.D. (or M.D. or PharmD) in Biochemistry, Chemistry, Biology or a related field and an in-depth understanding of the pharmaceutical industry. It is expected the Director will qualify for full professor and tenure. A minimum of 5 years of managerial experience working in the pharmaceutical/ biotechnology industry is required. The Director will have a demonstrated record of leading translational research in drug discovery to advance leads and candidate drugs; a record of effective project leadership and an in-depth understanding of drug discovery and development from target to clinical trials; demonstrated track record of innovation and development; strong interpersonal, leadership and collaboration skills to work in a team-oriented, matrix environment. Academic experience and a successful track-record of obtaining external funding are encouraged.

The Division anticipates filling the Position of Director, BRITE by July 1, 2016; however, review of applications will commence immediately and continue until the position is filled.
Applicants should apply at the following web address **https://jobs.nccu.edu/**.

Director
Julius L. Chambers Biomedical/Biotechnology Research Institute

North Carolina Central University (NCCU) invites applications for the position of Director, Julius L. Chambers Biomedical/Biotechnology Research Institute (JLC-BBRI). The Director of the JLC-BBRI reports directly to the Vice Chancellor for Research and Economic Development; and, provides leadership for a broadly based research portfolio which includes cancer, cardio-metabolic disorders, neuroscience and nutrition. Established in 1999, the JLC-BBRI facility provides 40,000 sq. ft. of basic research space. The JLC-BBRI is an innovative research and training institute dedicated to the advancement of fundamental knowledge of human diseases, particularly those that disproportionately affect underrepresented minority groups.

Purpose of Position: The Director serves as the scientific leader of NCCU's JLC-BBRI research facilities in Durham and Kannapolis, NC (North Carolina Research Campus-NCRC) and holds a tenured faculty position as Professor. The Director's responsibilities include the following: assure the quality and competitiveness of research conducted in the Institute; evaluate, plan, direct and implement activities related to the mission and function of the JLC-BBRI as a constituent body of the University; manage the Institute's budget and provide overall administrative leadership; supervises and mentors faculty and non-tenure track scientists in securing external research funding; facilitate student research experiences within the JLC-BBRI and with the Institute's internal and external partners; forge long-term successful partnerships among various academic and research units at NCCU as well as with agencies, corporations and academic research institutions within Research Triangle Park, throughout the state and beyond.

Qualifications: The Director will have an earned doctorate degree (Ph.D.) or equivalent doctoral degree in the biomedical sciences; or (M.D.) degree with relevant research experience from an accredited institution. The Director will have a distinguished record of leadership, research, grantsmanship, publications, and other scholarly activities. Sustained contribution to the sciences will be evidenced by productivity in funded research and publications. Continuous experience as a principal investigator on externally funded biomedically-related research projects is also required. A record of administration in higher education is highly preferred.

The Division anticipates filling the Position of Director, JLC-BBRI by July 1, 2016; however, review of applications will commence immediately and continue until the position is filled. Applicants should apply at the following web address, **https://jobs.nccu.edu/**.

COLUMBIA UNIVERSITY MEDICAL CENTER

Postdoctoral Research Scientist

We are seeking a highly motivated candidate with a background in Genetics, Bioinformatics, Computer Science or Statistical Genetics for a Post-Doctoral position within an independent research group at the Columbia University Medical Center Campus. The research will focus on Essential Tremor and neurodegenerative disease. This position will involve analysis of Whole Genome Sequence data in families with Essential Tremor using state of the art statistical methods.

Job Requirements:

- Ph.D. in Genetics, Bioinformatics, Computer Science, Statistical Genetics, or a related field is required
- Experience using bioinformatics to analyze high-throughput genetic and genomic data
- Experience running statistical tests on next-generation sequencing data particularly in family-based study design
- Experience with variant interpretation and classification
- Familiarity and working knowledge with standard bioinformatics tools, packages, algorithms, and databases
- Familiarity with statistical analysis methods and tools for bioinformatics
- Excellent written and verbal communication
- Effective judgment and problem solving with little supervision is imperative for this position

2016 High-Level Global Experts Recruitment Program
Beijing Institute of Technology

Beijing Institute of Technology (BIT) is a prestigious national key university in China and enjoys a high reputation in research and education in science, technology and other areas of scholarship. Founded in 1940,it is one of the first Chinese universities to run a graduate school and has been listed into national "Project 211" and "Project 985 " since the founding of the People's Republic of China. It is now under the administration of the Ministry of Industry and Information Technology of China.

I. Positions available in the following disciplines:

Discipline Category	Mechanical and Vehicle Engineering	Information and Electronics	Science and Materials	Humanities and Social Sciences
Discipline	Mechanics	Optical Engineering	Mathematics	Theoretical Economics
	Aeronautic and Astronautic Science and Technology	Instrumentation Science and Technology	Statistics	Marxist Theory
	Armament Science and Technology	Electronic Science and Technology	Physics	Applied Economics
	Mechanical Engineering	Information and Telecommunications	Chemistry	Management Science and Engineering
	Power Engineering and Engineering Thermo-physics	Control Science and Engineering	Biology	Business Administration
	Safety Science and Technology	Computer Science and Technology	Biomedical Engineering	Law
		Software Engineering	Materials Science and Engineering	Foreign Language and Literature
			Chemical Engineering and Technology	

II. Talent programs

1. Global experts: experts engaged by the Recruitment Program of Global Experts (Thousand Talents Program), Distinguished Professors with the Chang Jiang Scholars Program, National Outstanding Youth Fund Winners, etc.; Youth Scholars engaged by the Thousand Talents Program, Youth Scholars with the Chang Jiang Scholars Program, National Excellent Youth Science Fund Winners, and the Youth Top-notch Talent Support Program, etc.
2. Young scholars: associateship of associate or assistant professor

III. Pay and benefits

We offer exceptional benefits and competitive salaries, including:

1. A competitive annual salary according to performance;
2. Startup research funds, and support for the creation of a research team;
3. Helps in accommodation.

To view the full job listing, please visit our website http://renshichu.bit.edu.cn/docs/20160325183439075120.pdf

VI. Application and contact us

Applicants please send a curriculum vitae and at least 5 published academic papers via email to: bitrcb@bit.edu.cn, or sscsr@bit.edu.cn. Please note the program you apply for in the subject of your email.

Contacts: Mr. Shi
Tel.: +8610-68918577
For more faculty positions, please visit our website http://renshichu.bit.edu.cn/

北京理工大學
BEIJING INSTITUTE OF TECHNOLOGY

ScienceCareers online @sciencecareers.org
OPPORTUNITIES IN CHINA

Center for Immunology & Microbial Disease
Albany Medical College

Assistant/Associate Professor

The Center for Immunology & Microbial Disease at Albany Medical College invites applications for a tenure-track faculty position from individuals who have a doctoral degree, postdoctoral experience, and demonstrated research productivity. The successful candidate will be expected to establish an independent, extramurally-funded research program and participate in the teaching of medical and graduate students. The basic science departments at Albany Medical College are organized as interdisciplinary research centers and the Center for Immunology & Microbial Disease has a focus on microbial pathogenesis and immune defense, particularly as related to host-pathogen interactions. Faculty at the Albany Medical College receive competitive salaries, attractive start-up packages, and access to the Center's ABSL-3/BSL-3, Microbiology and Immunology Core Labs. In addition, we have established a close relationship with the New York State Department of Health Wadsworth Laboratories, providing a diverse environment that is rich in infectious disease expertise. Albany Medical College is located in a mid-sized city within the upstate New York Capital Region, and has easy access to Boston, New York City, and the Adirondack Mountains.

Applicants should send their curriculum vitae, a statement of research plans, and three letters of reference to:

Faculty Search Committee
Center for Immunology & Microbial Disease
Albany Medical College
47 New Scotland Avenue, MC-151
Albany, NY 12208

For further information about the Center, visit
http://www.amc.edu/Research/IMD/

An Equal Opportunity/Affirmative Action Employer.
Women and minorities are encouraged to apply.

Funding Available: Collaborative & Interdisciplinary Team-Based Synthesis Research

The National Socio-Environmental Synthesis Center (SESYNC) invites proposals for collaborative, interdisciplinary synthesis research projects focused on socio-environmental problems. These theme-based proposals should lead to scientific knowledge, tools, and methods and contribute to actionable outcomes.

SESYNC provides:
- Travel and logistical support
- Meeting facilities at our center in Annapolis, Maryland
- Computational and collaboration support
- Planning and facilitation for the team science process
- Opportunities to engage with on-site scholars

Proposals must be received by May 16, 2016.

For compelte details, visit: http://sesync.us/dv

SESYNC is funded by an award to the University of Maryland from the National Science Foundation.

www.jobs.cam.ac.uk

G. I. Taylor Professorship of Fluid Mechanics

Department of Applied Mathematics and Theoretical Physics

The Board of Electors to the GI Taylor Professorship of Fluid Mechanics invite applications from persons whose work falls within the general field of fluid mechanics and its applications, to take up appointment on 1 October 2016 or as soon as possible thereafter.

Candidates will have an outstanding research record of international stature. They will hold a PhD or equivalent postgraduate qualification. In keeping with the scientific legacy of GI Taylor, we particularly welcome applicants whose work involves close contact with experiment.

Standard professorial duties include teaching and research, examining, supervision and administration. The Professor will be based in Cambridge. A competitive salary will be offered.

To apply online for this vacancy and to view further information about the role, please visit: http://www.jobs.cam.ac.uk/job/9977.

Further information is available at: www.admin.cam.ac.uk/offices/academic/secretary/professorships/ or contact the Academic Secretary, University Offices, The Old Schools, Cambridge, CB2 1TT, (email: ibise@admin.cam.ac.uk).

Applications, consisting of a letter of application, a statement of current and future research plans, a curriculum vitae and a publications list, along with details of three referees should be made online no later than 9 May 2016.

Informal enquiries may be directed to Professor Nigel Peake, Head of Department of Applied Mathematics and Theoretical Physics, telephone 01223 339058 or email n.peake@damtp.cam.ac.uk. Further information about the Department can be found at http://www.damtp.cam.ac.uk/.

Please quote reference LE08764 on your application and in any correspondence about this vacancy.

The University values diversity and is committed to equality of opportunity.

The University has a responsibility to ensure that all employees are eligible to live and work in the UK.

UT Southwestern Medical Center

Chair, Department of Immunology

The University of Texas Southwestern Medical Center (Dallas, TX), a premier academic medical center, invites applications for the position of Chair of the Department of Immunology. The Chair will lead a faculty that is internationally recognized for outstanding achievements in many aspects of immunology. The incoming Chair will be responsible for recruiting new faculty members, overseeing research and training programs, and promoting an environment in which excellence in interdisciplinary immunological research is fostered and achieved. The Chair will direct a creative and productive research program, as evidenced by a distinguished track-record of external funding and high-impact publications. Qualified applicants must possess a doctorate with focus in biomedical research.

Interested candidates with exceptional records of scholarship and achievement, strong interpersonal and administrative skills, and institutional vision should send a curriculum vitae and brief cover letter to:

Michael V. Norgard, Ph.D.
UT Southwestern Medical Center
Department of Microbiology
5323 Harry Hines Blvd.
Dallas, TX 75390-9048
recruiting@utsouthwestern.edu

UT Southwestern is an Affirmative Action/Equal Opportunity Employer. Women, minorities, veterans, and individuals with disabilities are encouraged to apply.

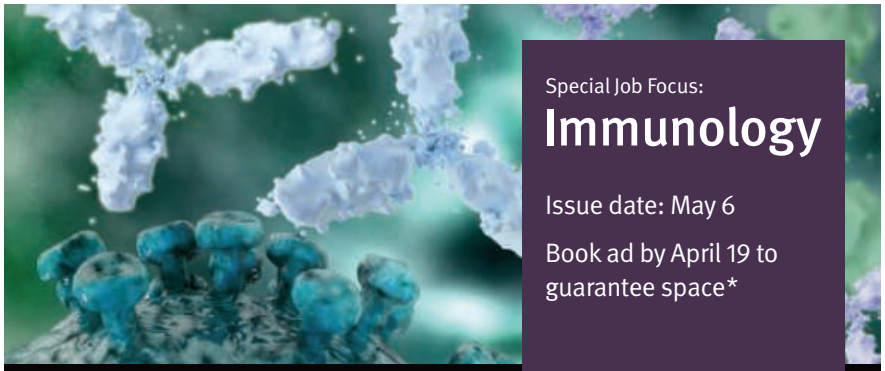

For recruitment in science, there's only one *Science*.

Special Job Focus:

Immunology

Issue date: May 6

Book ad by April 19 to guarantee space*

Why choose this Immunology Focus for your advertisement?

- Relevant ads lead off the career section with special immunology banner
- Bonus distribution to Immunology 2016 (AAI), May 13–17, Seattle, WA.

*Ads accepted until April 29 if space allows.
Produced by the *Science*/AAAS Custom Publishing Office.

SCIENCECAREERS.ORG

Science Careers AAAS

To book your ad: **advertise@sciencecareers.org**

The Americas
202 326 6582

Europe/RoW
+44(0)1223 326500

Japan
+81 3 3219 5777

China/Korea/Singapore/Taiwan
+86 186 0082 9345

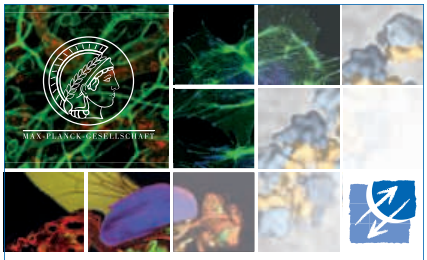

Your Career at the Max Planck Institute of Biochemistry

Martinsried / Munich - Germany

The Max Planck Institute of Biochemistry (MPIB) in Martinsried near Munich is inviting nominations and self-nominations for a position as

Department Director

to complement its existing 10 departments and 20 research groups ranging from **biochemistry**, **structural** and **cell biology** to **biophysics**. The position is equivalent to that of a tenured Full Professor fully devoted to research. The offer includes a highly competitive package with substantial core funding and generous lab space.

We are seeking candidates who study the **molecular mechanisms of fundamental biological problems**. We especially encourage expressions of interest from, and nominations of, candidates with a strong track record and several years of experience as principal investigators, but still at a relatively early career stage.

The Max Planck Society, an equal opportunity employer, is committed to diversity and inclusion in all aspects of recruiting and employment. The Max Planck Society is aiming at increasing the percentage of women among its scientific leadership, particularly at the director level, and therefore strongly encourages expressions of interest from, or nominations of, qualified female scientists.

Please e-mail applications and nominations including CV, list of publications, a brief summary of past and current research and the names of 3 references to the Office of the Managing Board of Directors (gl@biochem.mpg.de).

The deadline for application is **Tuesday, 31 May, 2016**.

WORKING LIFE

By **Jeffrey J. McDonnell**

Orchestrating a powerful group

As I entered my assistant professor years in the early 1990s and worked to assemble my research team, I considered each candidate individually. I took on students based on grades and test scores, and my relationships with them were one-on-one. I didn't consider their teamwork abilities or soft skills—or the group dynamic as a whole. This approach gave me a somewhat productive lab group as measured by single member outputs, but over many years, I came to appreciate that the collective matters—a lot. Beyond the individual output of the graduate students and postdocs lies a parallel universe of teamwork, peer-to-peer mentoring, and—most important—discovery for the research group as a whole.

I found this quite by accident, 10 years into my faculty appointment, with the arrival of a European postdoc who insisted that the group have daily morning coffee like he had "back home." This ritual evolved from nonacademic conversations over pastries to daily check-ins about what the group was working on to discussions of new ideas. Over the years, these conversations have been the most satisfying part of my job and have led to some of my group's better papers.

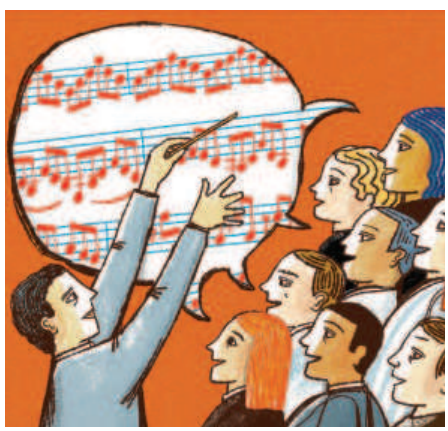

"Using the powerful group as a way to think is like conducting an orchestra."

I now think of each group member as a critical puzzle piece for my collective. I assemble teams of individuals with different but complementary scientific backgrounds and play off of the (healthy) tension between them, where they question one another's approaches and perspectives. Research group members will have their own theses, projects, and papers, but one can orchestrate a group dynamic that promotes discussion about where the field should be headed and the best new questions to ask.

The first step toward creating this environment and fostering a powerful research group is building relationships. Regular social activities outside of work can help break down walls and create a team spirit. Weekly lab meetings, morning coffee, group lunches, or Friday after-work beers can engineer serendipity across the entire group, or smaller subgroups that head into new directions with curiosity-driven side projects. The team building also creates a sense of safety, trust, and belonging. In my lab, there are high expectations for unselfish cooperation and maintaining one another's reputations. We adhere to the old adage that if you do not have something nice to say about someone, then say nothing at all. Foibles are tolerated; disagreements are settled quickly.

Lab diversity, be it scientific or cultural, can make building community challenging, but that diversity itself can add immense power to the team. Certainly I have found that my most productive groups over the years have been the ones with the greatest gender balance and range of cultural and scientific backgrounds. A group leader can learn to leverage this diversity and draw out ideas from some who may be timid in group discussions. Something as simple as not letting anyone dominate during discussions can help. Inviting a gifted member to throw out an idea and having the group discuss it can also be effective.

Using the powerful group as a way to think is like conducting an orchestra. It involves assembling a varied group of musicians, each with solo skills, and helping them play together, creating a piece I could never accomplish myself or with a single student or postdoc.

I have in no way mastered the powerful research group, which is an evolving and ever-changing thing. New lab members bring in new opportunities and challenges. But one thing I now understand is that as old members fledge, the powerful group extends well beyond the faculty member's home institution. The group becomes a ready-made network for collaboration among lab alumni who go on to develop their own orchestras, repeating the cycle of the powerful research group elsewhere. ■

Jeffrey J. McDonnell is a professor in the School of Environment and Sustainability at the University of Saskatchewan in Saskatoon, Canada, and Sixth Century Chair at the University of Aberdeen in the United Kingdom. *He thanks Paul Axtell for early discussions and the Global Institute for Water Security postdocs and his lab members for feedback.*

ILLUSTRATION: ROBERT NEUBECKER

Published by AAAS